

Doctoral thesis

Doctoral theses at NTNU, 2023:218

Lina Johnsen Kamra

Proximity effects, spin transport, and phase transitions in superconducting hybrids

NTNU
Norwegian University of Science and Technology
Thesis for the Degree of
Philosophiae Doctor
Faculty of Natural Sciences
Department of Physics



Norwegian University of
Science and Technology

Lina Johnsen Kamra

Proximity effects, spin transport, and phase transitions in superconducting hybrids

Thesis for the Degree of Philosophiae Doctor

Trondheim, June 2023

Norwegian University of Science and Technology
Faculty of Natural Sciences
Department of Physics



Norwegian University of
Science and Technology

NTNU

Norwegian University of Science and Technology

Thesis for the Degree of Philosophiae Doctor

Faculty of Natural Sciences

Department of Physics

© Lina Johnsen Kamra

ISBN 978-82-326-7134-2 (printed ver.)

ISBN 978-82-326-7133-5 (electronic ver.)

ISSN 1503-8181 (printed ver.)

ISSN 2703-8084 (online ver.)

Doctoral theses at NTNU, 2023:218

Printed by NTNU Grafisk senter

ABSTRACT

This thesis presents our work on the theory of spin-dependent effects and transport in heterostructures involving superconductors, magnets, and non-centrosymmetric materials. The results are roughly divided into those concerning i) the superconducting phase transition and its influence on adjacent materials, and ii) spin transport. Our study of the superconducting phase transition is focused around spin-valve effects where the superconducting critical temperature can be controlled by the magnetic configuration or inversion symmetry breaking in materials in proximity to the superconductor. We also consider the reciprocal effect where decreasing the temperature below the superconducting transition temperature alters the magnetic anisotropy of an adjacent magnet. Furthermore, we consider how the superconducting critical temperature of an unconventional p -wave superconductor can be enhanced by proximity-coupling it via a ferromagnetic interlayer to a conventional superconductor with a higher critical temperature. Finally, we study the magnetic field-driven superconducting transition in a highly disordered hole-overdoped d -wave cuprate superconductor where superconducting pairing remains above the critical field where phase coherence is lost. Our work on spin transport includes the study of both dissipationless Cooper pair and resistive quasi-particle transport. We predict that due to interfacial exchange coupling, a supercurrent of spin-polarized Cooper pairs can induce a non-reciprocity in the magnon dispersion of a ferromagnetic insulator giving rise to magnon spin currents. We also study how non-equilibrium quasi-particle transport is affected by the pairing symmetry of the superconductor, how the inverse spin-Hall effect and spin-swapping are renormalized by a spin-splitting field, and how the coupling between two ferromagnetic insulators can be mediated by a superconductor thus affecting spin-pumping.

P R E F A C E

This thesis is submitted as part of fulfilling the criteria for the degree of philosophiae doctor (PhD). Most of the research was conducted at the Center for Quantum Spintronics (QuSpin) at the Norwegian University of Science and Technology (NTNU) under the supervision of Prof. Jacob Linder. I have also visited Universidad Autónoma de Madrid several times collaborating with the group of Prof. Farkhad G. Aliev and the group of Dr. Akashdeep Kamra. The work presented herein is part of a four-year graduate programme in physics. The workload also included 30 ECTS credits of course work and one year of teaching in the labs of the first year bachelor courses FY1001 Mechanical Physics, FY1003 Electricity and Magnetism, and TFY4163 Wave Physics and Fluid Mechanics. Funded by the QuSpin mobility grant awarded to two PhD students every year, I spent nearly four months at RIKEN in Japan working under the supervision of Prof. Naoto Nagaosa and Prof. Yukio Tanaka. The research performed during this period is not part of this thesis and will be published separately. Also not enclosed is a News & Views article [1] published in Nature Physics that I was invited to contribute to.

The most important part of this thesis is the collection of publications attached. These are rather self contained, and include detailed descriptions of the methods in appendices or supplementary documentation. In order to not repeat myself, I have therefore chosen to devote the chapters of my thesis to explain the main results in terms of simpler physical pictures, more or less the way I would have explained them in a seminar or over a cup of coffee. I have also included brief introductions to the main theoretical frameworks. I hope this will serve as a pleasant reading experience by itself, or as a warm up before diving into the details of the publications.

Lina Johnsen Kamra,
Madrid, April 2023

ACKNOWLEDGEMENTS

My PhD would not have been so enjoyable without all the wonderful people I have gotten the chance to meet and spend time with, both through collaborations and social gatherings. In addition to working from my home university NTNU in Trondheim, I have been lucky to get the chance to visit several other places including longer stays at Universidad Autónoma de Madrid in Spain and at RIKEN in Japan.

First, I would like to thank my collaborators at QuSpin in Trondheim. My supervisor Prof. Jacob Linder has always been available for discussions and eager to get things done. Thank you for giving me the opportunity to take part in so many interesting projects and collaborations. I also want to thank Dr. Haakon T. Simensen and Prof. Arne Brataas for two successful collaborations and for sharing their expertise on magnetic materials. A big thank you to Dr. Sol H. Jacobsen for inviting me into a very interesting collaboration exploring the effects of compensated antiferromagnetic interfaces on the superconducting pairing. Thank you to Kristian Svalland for discussions about non-centrosymmetric materials and for sharing his method of symmetrizing the Rashba term.

I was also very happy to have Dr. Linde A. B. Olde Olthof from the University of Cambridge visiting us in Trondheim. During our project together, we had many interesting physics discussions. Most of all, I appreciated her unique perspective from having hands-on experience with both experiments and theory. I would also like to thank Prof. Jason W. A. Robinson for his valuable contributions to this project, and for not giving up on arranging a visit to his group in Cambridge despite inconveniently timed Corona outbreaks. During my stay, I enjoyed discussions with him and his group members, as well as a tour through the labs with the amazing guide Dr. Nadia Stelmashenko.

I also learned a lot from the two collaborations with Prof. Farkhad G. Aliev, César González-Ruano, and Diego Caso at Universidad Autónoma de Madrid. During my first visit to Madrid, I appreciated Farkhad taking the time to show me around the lab. I also admire his attitude towards always promoting and talking warmly about his students. During these collaborations, and also during my first attempt at doing research in my Master's, I have gained from the valuable insights of Dr. Niladri Banerjee at Loughborough University and lately at Imperial College London. I also want to thank Prof. Michel Hehn and Prof. Coriolan Tiusan for their contributions to these projects.

During my stay at RIKEN in Tokyo, I had the great pleasure to work with Prof. Naoto Nagaosa and Prof. Yukio Tanaka. I admire Nagaosa-sensei's broad knowledge across a number of fields and his passion for physics. I am also thankful for his career advice. I highly appreciate Tanaka-sensei sharing his deep knowledge about the McMillan Green's function method and heterostructures including topological materials. Most of all, I enjoyed our physics discussions where the time of day was not an issue, even if the meeting ended quarter past midnight. Thank you also to Tokuyoshi-san for organizing my visa application and housing, making my move to Japan as smooth as possible.

I also want to thank my most recent collaborators, Dr. Akashdeep Kamra and Simran Chourasia at Universidad Autónoma de Madrid, and Prof. Irina V. Bobkova at Moscow Institute of Physics and Technology. In our project together, I got the chance to try out the role of co-supervisor. I am greatly thankful for this opportunity.

Also thank you to Akash for giving me the chance to contribute to his invited Nature Physics News & Views article, and for introducing me to so many great people.

I also want to thank some of the people I have visited during the last years for their hospitality. It has not been easy to travel during a worldwide pandemic. First, thank you to Prof. Wolfgang Belzig who welcomed me and Akash in Konstanz in the short time window the borders were open. Upon my and Akash's arrival in Spain, I would especially like to thank Prof. Juan Carlos Cuevas and his wife Ana for all the help they gave us, for showing us around Madrid, and for making us feel welcome. Also a great thank you to Prof. Justin W. Wells and Dr. Kristin Høydalsvik Wells for inviting me to stay at their home when I visited Oslo. I was very happy that Justin let me visit his lab and discuss with his group. I am grateful to Prof. Liang Fu for letting me visit him at MIT and for taking the time to discuss with me. I am also very thankful that he let me give a seminar at his department. During this visit, I had the great pleasure to spend a day together with Dr. Jagadeesh Moodera. I am humbled that he invited me to discuss with him and his group, and that he with great enthusiasm showed me his many impressive labs containing the instrument likely to hold the record for producing the highest number of PRLs.

The PhD would not have been the same without all the people I have spent time with. Among my friends at QuSpin, I especially want to mention Atousa, Eirik E., Matthias, Even, Håvard, Jeroen, Nicolay, Martin, Øyvind, Payel, and Jonas – who introduced me to the good life as a PhD student back when I was young and ignorant. Later, I also got to know Verena and Max, who's cooking is highly recommended. I also enjoyed going for walks and chatting with Anna Cecilie, and meeting up with Ali and Faiga. Thank you also to my office mates Bjørnulf, Eirik H. F., Morten, and for a short while Vetle. Luckily, Bjørnulf and Morten shared my passion for taking breaks after a good session of work. A great thank you also goes to Karen-Elisabeth for nice conversations in the lunch room and for supporting me in all of my travel plans. In addition to those already mentioned, I also very much enjoyed the company of Max K., Frode, Håkon, Jinbang, Longfei, Vasil, Arnau, Alireza, Haakon, Therese, Sverre, Henning, Tancredi, Kristian, Christian, Niels Henrik, Vemund, Jacob B., and Thanos. Thank you also to my office mates at RIKEN for countless conversations in the coffee corner. Thank you Oh-san, Liu-san, Jimmy-san, Chen-san, Siqi-san, Murakami-san, and Sakai-san.

I would also like to thank *mamma* and *far* for always helping me out when I got myself into trouble. Like when I was stuck in a quarantine hotel with only my hand luggage, or left homeless when testing positive for Corona just before my flight to Japan.

Most of all, I want to thank Akash a thousand times for being the perfect husband. Thank you for all your love and support, for always knowing the right things to do and say, and for long walks along the beaches of Spain talking about physics.

Dedicated to Akka and Tusse.

PUBLICATIONS

1. **Lina G. Johnsen, Niladri Banerjee, and Jacob Linder,**
Magnetization reorientation due to the superconducting transition in heavy-metal heterostructures,
[Phys. Rev. B **99**, 134516 \(2019\).](#)
2. **César González-Ruano, Lina G. Johnsen, Diego Caso, Coriolan Tiusan, Michel Hehn, Niladri Banerjee, Jacob Linder, and Farkhad G. Aliev,**
Superconductivity-induced change in magnetic anisotropy in epitaxial ferromagnet-superconductor hybrids with spin-orbit interaction,
[Phys. Rev. B **102**, 020405\(R\) \(2020\).](#) (Rapid communication)
3. **Lina G. Johnsen, Kristian Svalland, and Jacob Linder,**
Controlling the Superconducting Transition by Rotation of an Inversion Symmetry Breaking Axis,
[Phys. Rev. Lett. **125**, 107002 \(2020\).](#)
4. **Haakon T. Simensen, Lina G. Johnsen, Jacob Linder, and Arne Brataas,**
Spin pumping between noncollinear ferromagnetic insulators through thin superconductors,
[Phys. Rev. B **103**, 024524 \(2021\).](#)
5. **Lina G. Johnsen, Sol H. Jacobsen, and Jacob Linder,**
Magnetic control of superconducting heterostructures using compensated antiferromagnets,
[Phys. Rev. B **103**, L060505 \(2021\).](#) (Letter)
6. **César González-Ruano, Diego Caso, Lina G. Johnsen, Coriolan Tiusan, Michel Hehn, Niladri Banerjee, Jacob Linder, and Farkhad G. Aliev,**
Superconductivity assisted change of the perpendicular magnetic anisotropy in V/MgO/Fe junctions,
[Sci. Rep. **11**, 19041 \(2021\).](#)
7. **Lina G. Johnsen, and Jacob Linder,**
Spin injection and spin relaxation in odd-frequency superconductors,
[Phys. Rev. B **104**, 144513 \(2021\).](#)
8. **Lina G. Johnsen, Haakon T. Simensen, Arne Brataas, and Jacob Linder,**
Magnon spin current induced by triplet Cooper pair supercurrents,
[Phys. Rev. Lett. **127**, 207001 \(2021\).](#)
9. **Linde A. B. Olde Olthof, Lina G. Johnsen, Jason W. A. Robinson, and Jacob Linder,**
Controllable enhancement of p-wave superconductivity via magnetic coupling to a conventional superconductor,
[Phys. Rev. Lett. **127**, 267001 \(2021\).](#)

10. **Lina G. Johnsen**,
The magnetic field driven superconductor–metal transition in disordered hole-overdoped cuprates,
[J. Phys.: Condens. Matter](#) **35**, 115601 (2023).
11. **Akashdeep Kamra, and Lina G. Johnsen**,
Nanoscale spin waves get excited,
[Nat. Phys.](#) **19**, 469 (2023). (Invited News & Views article)
12. **Simran Chourasia, Lina Johnsen Kamra, Irina V. Bobkova, and Akashdeep Kamra**,
Generation of spin-triplet Cooper pairs via a canted antiferromagnet,
[arXiv:2303.18145](#) (2023).
13. **Lina Johnsen Kamra, and Jacob Linder**,
Inverse spin-Hall effect and spin-swapping in spin-split superconductors,
[Manuscript under preparation](#).

From this full list of publications, papers 2-10, 12, and 13 are [attached](#) and included as part of this PhD thesis. We label these eleven papers I to XI in the following.

CONTENTS

1	Introduction	1
1.1	Conventional superconductors	1
1.2	The proximity effect	3
1.3	Unconventional superconductors	5
1.4	Structure of thesis	6
2	Theoretical frameworks	9
2.1	The Bogoliubov–de Gennes equations	9
2.2	The McMillan Green’s function	12
2.3	The Schrieffer-Wolff transformation	17
2.4	The Usadel equation	18
3	The superconducting phase transition	23
3.1	Hybrids with misaligned ferromagnets	23
3.2	Hybrids with one ferromagnet and spin-orbit coupling	24
3.3	Non-magnetic hybrids	28
3.4	Hybrids containing antiferromagnets	30
3.5	Hybrids containing canted antiferromagnets	32
3.6	T_c enhancement by proximity to a stronger superconductor	34
3.7	The critical field in highly disordered superconductors	36
4	Spin transport	41
4.1	From Cooper pair currents to magnon currents	41
4.2	Spin transport in odd-frequency superconductors	44
4.3	Transversal currents in spin-split superconductors	49
4.4	Spin pumping	52
5	Conclusions and outlook	57
	Bibliography	61

INTRODUCTION

This chapter gives a brief introduction to some of the concepts that will be discussed in this thesis. We try to explain these in terms of simple pictures. For a complete review and derivation of the fundamental concepts, see *e.g.* Refs. [2, 3]. For the more specialized topics, many good review articles have published over the years. The most central ones to the discussion below are Refs. [4–7].

1.1 CONVENTIONAL SUPERCONDUCTORS

Since its discovery in 1911 [8], superconductivity has been one of the main research topics within condensed matter physics. Even today, the field is constantly evolving with new directions being pursued. In the initial experiment by Kamerlingh-Onnes, mercury was cooled down in liquid helium resulting in the remarkable discovery of near zero resistance below 4K [8, 9]. In the metallic state, each individual electron taking part in the electric current can be scattered, thus causing a finite resistance. In superconductors, electrons instead condense into a collective state where all electrons and holes within an certain energy interval take part. In this case, the behavior of each individual electron is less important since the current is carried by the condensate as a whole. Superconductors can therefore carry supercurrents with perfect conductivity [2, 3].

The second characteristic trait of superconductors is the Meissner effect – the expulsion of magnetic fields [10]. This perfect diamagnetism is related to the supercurrents screening the external magnetic field by inducing an equal and oppositely oriented magnetic field. However, if these shielding currents were to explain the Meissner effect alone, flux might as well be trapped inside the superconductor instead of expelled upon lowering the temperature through the superconducting transition. The complete expulsion of the magnetic field is quantum mechanical in nature, and has no classical analogue [3].

These two characteristics were first described by F. and H. London [11] through the equations

$$\mathbf{E} = \partial_t \Lambda \mathbf{J}_S, \tag{1}$$

$$\mathbf{H} = -c \nabla_r \times \Lambda \mathbf{J}_S. \tag{2}$$

The first equation describes the supercurrent through resistance-free acceleration by a local electric field \mathbf{E} , and allows for a constant current \mathbf{J}_S at $\mathbf{E} = 0$. The second equation together with the Maxwell equation $\nabla_r \times \mathbf{H} = 4\pi \mathbf{J}_S / c$ describes the exponential decay of the local magnetic field \mathbf{H} inside the superconductor, characterized by the penetration depth $\lambda = \sqrt{c^2 \Lambda / 4\pi}$. Here, c is the speed of light. The penetration depth diverges at a critical temperature T_c as the superconductor transitions to the normal state [3].

While the London equations are a good starting point for describing the basic properties superconductors, they are subject to several assumptions such as the

external magnetic field being weak [2]. When increasing the external magnetic field, we have to separate the superconductors into two different classes. In type I superconductors, superconductivity vanishes abruptly at a critical field H_c . In type II superconductors [12–14], there is an intermediate regime between the two critical field strengths H_{c1} and H_{c2} , where the magnetic field punches holes into the superconducting condensate. Through each such hole, called a vortex, a field corresponding to a single superconducting flux quanta $\Phi_{SC} = hc/2e$ can penetrate the superconductor. Here, h is Planck’s constant and $2e$ is the twice the electron charge. The field through the superconductor increases gradually between H_{c1} and H_{c2} as the number of vortices increases [15, 16]. As a consequence, a current exerts a Lorentz force pushing the vortices sideways thus causing a finite resistance [17].

Having defined the most fundamental experimentally observable properties of superconductors takes us next to the microscopic origin. The most important development on this front was the Bardeen-Cooper-Schrieffer (BCS) theory [18] which was published in 1957, but still stands as a main building block for the description of many conventional materials studied to this date. While a gap around the Fermi level of the superconducting energy spectrum had already been proposed and observed [2, 19, 20], the BCS theory explained this by proposing that electrons are attracted to each other and form pairs. From a classical perspective, this attraction can be illustrated as a two-step process where an electron attracts the positively charged ions in a lattice, and the slower-moving ions attract a second electron, as illustrated in Fig. 1(a) and (b). In the quantum mechanical picture, the lattice vibrations are quantized and represented by phonons which mediate the attractive interaction between two electrons, see Fig. 1(c). To destroy a pair, the two electrons must overcome the gap in the energy spectrum by acquiring an energy $2|\Delta|$.

The electron pairs, called Cooper pairs, are formed between electrons of opposite momentum. This lowers the kinetic energy of the pair. It also gives the largest number of available directions to scatter to after the momentum-conserving process in Fig. 1(c), since any momentum \mathbf{q} results in zero center-of-mass momentum. Two equivalent electrons, having a fermionic nature, cannot exist in the same position. Since the attractive interaction is localized to a specific position in the lattice, the spin of the two electrons must therefore be opposite. This results in the conventional spin-singlet pairing ($\uparrow\downarrow - \downarrow\uparrow$) which is odd under inversion of spin. This type of

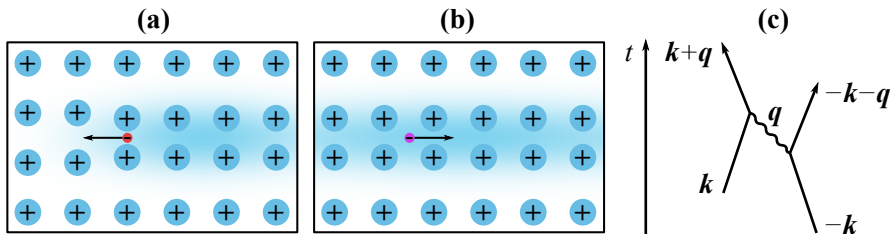


Figure 1: In the classical picture, the attraction between two electrons is mediated by the crystal lattice. Due to its negative charge, the first electron (red) attracts the positively charged ions comprising the crystal lattice (blue), as shown in panel (a). Since the electron moves much faster than the heavier ions, the lattice remains distorted after the first electron has left. The second electron (purple) is attracted to the accumulation of positive charge, as shown in panel (b). This is a classical analog to the process in panel (c), where two electrons (solid lines) of opposite momenta $\pm\mathbf{k}$ interacts via a phonon (wiggly line) of momentum \mathbf{q} . The vertical axis represents the time t [2].

conventional pairing is found in many materials such as Nb, Al, V, etc. where such local interactions are preferred. However, as we will see, a whole fauna of pairing types exist in unconventional superconductors, or can be created in conventional ones by combining them with other materials.

Having introduced the Cooper pairs, we now come back to the transport properties of superconductors. While the magnitude of the superconducting gap protects the Cooper pairs from breaking up into individual electrons, the superconducting pairing $\Delta = |\Delta|e^{i\varphi}$ is also associated with a phase φ . A finite phase gradient $\nabla_r\varphi$ gives rise to a supercurrent. This kind of dissipationless transport is however only allowed for energies below the superconducting gap [3]. For energies above the gap, electron and hole energy bands hybridize so that transport is instead carried by electron-like and hole-like quasi-particles. This transport is dissipative, but highly dependent on the superconductivity due to the alteration of the energy band structure and the associated density of states. Scattering rates can also be renormalized by superconductivity, especially when the scattering process is spin dependent [21]. We will discuss both quasi-particle [22, 23] and Cooper pair [24] transport later on.

A large part of this thesis revolve around systems where we try to control the factors that limit superconductivity. The superconducting transition is most commonly defined as the temperature, field, or current that causes the superconducting gap to close so that the superconducting pairing vanishes [2, 3]. However, in some cases including highly disordered materials, the superconducting transition can instead be determined by the loss of phase coherence when the superfluid stiffness vanishes. In this case, superconducting pairing can survive in grains even though the material cannot carry a supercurrent [25]. The superconducting condensate is weakened by spin-splitting fields and orbital depairing from proximitized magnets and external magnetic fields [26–28]. We will also see that inversion symmetry breaking from Rashba spin-orbit coupling can cause a similar suppression [29–32]. While spin-splitting fields weaken superconductivity, they also cause the creation of more exotic types of superconducting pairing. As we will discuss below, these are relevant both for carrying spin currents and for controlling the properties of a heterostructure.

1.2 THE PROXIMITY EFFECT

Let us first consider what happens when a superconductor (SC) is put into contact with a normal-metal (NM). Electrons from the normal-metal cannot be transmitted into the superconductor if their energy is below the superconducting gap, since there are no states available. The superconductor therefore partially behaves as an insulator where electrons are reflected at the interface. However, another possibility exists – Andreev reflection [33, 34]. In this process, shown in Fig. 2, the electron is reflected as a hole of opposite spin, and a Cooper pair is transmitted into the superconductor. Andreev reflection is a phase coherent process. This means that there is a correlation between the phases of the electron and hole in the normal-metal and the Cooper pair in the superconductor. Andreev reflection is therefore the main ingredient in the proximity effect where electrons and holes remain phase coherent so that superconducting pairing can leak into the normal-metal [35–38]. In clean materials, this phase coherence is lost over a length scale called the coherence length. Since superconducting pairing leaks out of the superconductor, the superconducting gap is also weakened over a similar length scale inside the superconductor [6].

When interfacing a superconductor with a normal-metal, superconducting pairing penetrates into the latter. However, the pairing remains conventional. The simplest way of creating other types of superconducting pairing is replacing the normal-metal

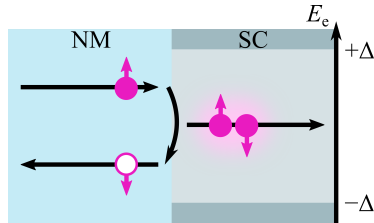


Figure 2: When a normal-metal (NM) is interfaced with a superconductor (SC), a spin-up electron (pink) of energy E_e below the superconducting gap Δ can be scattered as a spin-down hole (white) of energy $E_h = E_e$. This results in the propagation of a Cooper pair of energy $E_e - E_h = 0$ inside the superconductor.

with a ferromagnetic metal (FM). At each lattice site of a magnet, there is a magnetic moment. In ferromagnets, these are all oriented in the same direction. This leads to a splitting of the energy bands of spin-up and spin-down electrons, as shown in the inset of Fig. 3(a). As a result, the spin-up and spin-down electrons at the Fermi energy have different momenta $k_{F,\uparrow} \neq k_{F,\downarrow}$. With an interface normal along \mathbf{x} , this causes the Cooper pairs pick up a phase depending on the momentum difference. This leads to a modulation

$$\begin{aligned} (\uparrow\downarrow - \downarrow\uparrow) &\rightarrow \left(\uparrow\downarrow e^{i(k_{F,\uparrow} - k_{F,\downarrow})x} - \downarrow\uparrow e^{-i(k_{F,\uparrow} - k_{F,\downarrow})x} \right) \\ &= (\uparrow\downarrow - \downarrow\uparrow) \cos[(k_{F,\uparrow} - k_{F,\downarrow})x] + i(\uparrow\downarrow + \downarrow\uparrow) \sin[(k_{F,\uparrow} - k_{F,\downarrow})x] \end{aligned} \quad (3)$$

between conventional pairing and opposite-spin triplet pairing ($\uparrow\downarrow + \downarrow\uparrow$) [6]. The spins are assumed to be oriented along the magnetization direction \mathbf{z} . Since both the conventional and opposite-spin triplet pairing consists of Cooper pairs with opposite spin, the Cooper pairs cannot be formed between electrons of exactly opposite momenta. The Cooper pairs therefore easily lose phase coherence inside the ferromagnet. The oscillation and decay of the two pairing types is sketched in Fig. 3(a). A similar phase shift is accumulated when a Cooper pair is reflected at an insulating ferromagnetic interface [6].

The modulation between spin-singlets and opposite-spin triplets discussed above can be seen as a precession of the magnetic moments of the spin-up and spin-down electrons in opposite directions around the magnetization. The spin component along the magnetization is conserved, but the in-plane component can have zero or net spin depending on whether the two in-plane components are parallel or antiparallel. The spin-triplets discussed above therefore have a net spin $\mathbf{S} = 1$, but zero spin projection along the magnetization direction \mathbf{z} . Since the SC/FM bilayer is invariant under rotation of the magnetization, we can define a spin-triplet vector

$$[-(\uparrow\uparrow - \downarrow\downarrow), -i(\uparrow\uparrow + \downarrow\downarrow), (\uparrow\downarrow + \downarrow\uparrow)]/2, \quad (4)$$

where the x and y components represent the zero-spin triplets with respect to a magnetization oriented along \mathbf{x} or \mathbf{y} , respectively. The spins are still defined with respect to the z axis. As we can see, there are two additional types of spin-triplet pairing ($\uparrow\uparrow$) and ($\downarrow\downarrow$) with origin in the finite in-plane spin components. Their spin projections along \mathbf{z} are $S_z = 1$ and $S_z = -1$, respectively.

The existence of the equal-spin triplets in the plane perpendicular to the magnetization direction hints that we can break the spin conservation along \mathbf{z} by introducing a second noncollinear ferromagnet, as shown in Fig. 3(b). Since the spin-triplets created in one ferromagnet look like equal-spin triplets in a second perpendicular ferromagnet,

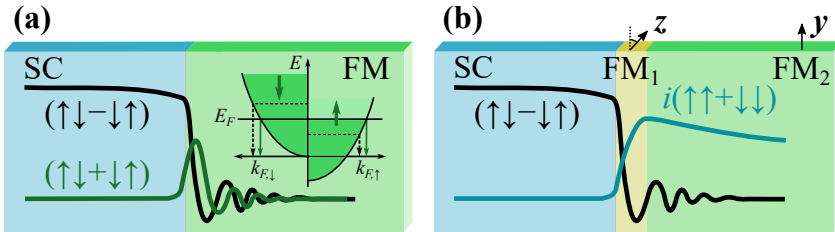


Figure 3: (a) When a superconductor (SC) is put into contact with a ferromagnetic metal (FM), the superconducting pairing can leak into the ferromagnet. However, due to the spin-splitting of the spin-up and spin-down energy bands in the ferromagnet (inset), electrons at the Fermi energy E_F have different Fermi momenta $k_{F,\uparrow}$ and $k_{F,\downarrow}$ depending on their spin. This results in a mixing between conventional $(\uparrow\downarrow - \downarrow\uparrow)$ and opposite-spin triplet $(\uparrow\downarrow + \downarrow\uparrow)$ pairs, as well as a rapid decay of both types of pairing. (b) If we add a thin interfacial ferromagnetic layer FM_1 with the magnetization oriented perpendicular to the second ferromagnet FM_2 , the opposite-spin triplets created in FM_1 are equal-spin triplets $(\uparrow\uparrow)$ and $(\downarrow\downarrow)$ with respect to the magnetization of FM_2 . Due to the electrons having equal spin, this pairing is not affected by the spin-splitting of the energy bands in FM_2 and decays over much longer distances.

they are not broken by loss of phase coherence. This is a simple, but powerful, way of creating spin-polarized triplet Cooper pairs that have been demonstrated in many magnetic heterostructures such as magnetic multilayers [39–41], single magnets with non-collinear magnetization [42, 43], systems with spin-orbit coupling [29–32], etc.

There are many benefits of creating spin-polarized triplet Cooper pairs. In this thesis, the two properties we will focus on are their above-mentioned ability to survive a spin-splitting field, and their capacity to carry a net spin through spin-polarized supercurrents. The first property opens the possibility for spin-valve effects where the critical temperature of the superconductor is modulated depending on the alignment between the quantization axis of the triplets and a field imposed by the proximitized material [39–41]. It also allows for change in the magnetic anisotropy of a heterostructure below the superconducting transition temperature, as we will show later [31, 44, 45]. The second property allows for dissipationless transport of spin. We will see that such spin transport can be transferred between different types of materials [24].

1.3 UNCONVENTIONAL SUPERCONDUCTORS

While unconventional pairing can be created in heterostructures, it can also exist intrinsically in materials. In conventional s -wave superconductors, the superconducting gap is homogenous and does not depend on the direction of the quasi-particle momentum. This is related to the pairing being highly localized so that all directions in the lattice look the same. If we loosen this constraint, we open the possibility for Cooper pairing with different symmetries with regards to spin and momentum. Some of these possibilities are illustrated in Fig. 4, where the sign of the superconducting pairing depends on the propagation direction [7].

The overall symmetry with respect to spin, position, orbital, and time inversion must be conserved following the Pauli principle [7]. In Fig. 4, where we consider the position, or equivalently the momentum symmetry, we see that p -wave pairing has an odd symmetry under inversion of momentum. The p -wave pairing can therefore have a spin-triplet symmetry. Although the d -wave pairing changes sign under inversion of

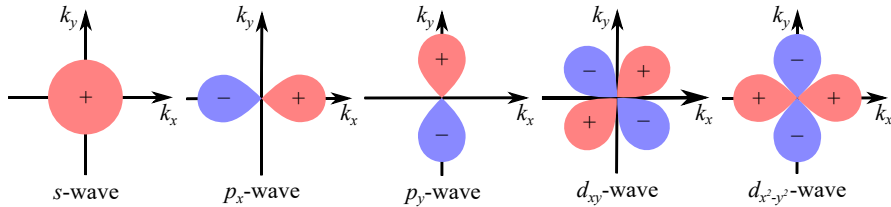


Figure 4: Some possible pairing symmetries that exist in superconductors. Red (blue) lobes represents momentum directions where the superconducting pairing has a positive (negative) sign. While the s -wave and d -wave pairings are even under inversion of the total momentum $\mathbf{k} = (k_x, k_y)$, the p -wave pairing changes sign.

k_x and k_y individually, it is symmetric under inversion of the total momentum \mathbf{k} . The d -wave pairing is therefore spin-singlet, just like the conventional s -wave pairing. What about the proximity-induced spin-triplet pairing discussed in the previous section? Anderson's theorem states that s -wave pairing is robust to impurity scattering [46]. This is because the pairing does not change sign when the momentum changes during the scattering process. In heterostructures, particularly those containing many impurities and lattice defects, the dominant pairing is therefore s -wave. The spin-triplet symmetry can be obtained by breaking the symmetry under time inversion, resulting in odd-frequency s -wave spin-triplet pairing [5, 7]. Intrinsic p -wave and d -wave superconductivity is highly sensitive to impurity scattering, and only exist when the material is sufficiently clean.

The d -wave superconducting pairing can be found in the high- T_c cuprates. As the name suggests, these have much higher critical temperatures than conventional superconductors. High- T_c superconductivity was first discovered in 1986 by Bednorz and Müller in LaBaCuO. They found a critical temperature of 30K [47]. The critical temperatures of the cuprates can however reach well above 100K, even at atmospheric pressure [48]. For comparison, the common conventional superconductor Nb has a critical temperature of approximately 9K [49]. The cuprates also have a rich phase diagram both above and below the critical temperature hosting strange metal behavior, the pseudogap phase, competition between antiferromagnetic and superconducting order, and so on [50]. We will later discuss how the cuprates, in the most conventional limit of high hole-doping, behave under disorder and an external magnetic field [51].

Candidates for p -wave spin-triplet superconductors are rare and hotly debated. Sr_2RuO_4 has been challenged as the main candidate by unexplained observations suggesting that the pairing symmetry might not be p -wave after all [52]. The p -wave superconductors are however promising platforms for exotic phenomena such as Majorana fermions and chiral edge states [53]. From a theory perspective they also provide a convenient way of studying spin-polarized supercurrents. However, due to their fragile nature, proximity-induced odd-frequency superconductivity could be a useful replacement. We will discuss how such supercurrents can be coupled to magnons later in the thesis [24]. For all of the above-mentioned reasons, increasing the critical temperature of p -wave superconductors would be beneficial. We will propose a possible way of doing this in a heterostructure [54].

1.4 STRUCTURE OF THESIS

This concludes our brief introduction to the fundamental concepts relevant for the research presented in this thesis. In Chapter 2, we will proceed to discuss the relevant theoretical tools. The research presented can loosely be divided into two categories.

Studies of the superconducting phase transition are discussed in Chapter 3. Here we will discuss: a) How the superconducting critical temperature can be controlled by proximity to ferromagnets, antiferromagnets, materials with Rashba spin-orbit coupling, and superconductors with a higher critical temperature (papers II, IV, VIII, and X), b) How the magnetic anisotropy of a magnet in a superconducting heterostructure can be altered through the superconducting transition (papers I, IV, and V), and c) How the field-driven superconducting transition in a d -wave superconductor under an external magnetic field is affected by strong disorder (paper IX). Studies of spin transport are discussed in Chapter 4. Here we will discuss: a) How supercurrents carried by spin-polarized Cooper pairs can induce a magnon current in an adjacent ferromagnetic insulator (paper VII), b) How quasi-particle spin transport and scattering is affected by the symmetry of the superconducting pairing (paper VI), c) How the inverse spin-Hall and spin-swap effects are renormalized by a spin-splitting field (paper XI), and d) How spin-pumping from a ferromagnetic insulator is affected by the orientation of a second ferromagnetic insulator through coupling via a superconductor (paper III). In both Chapter 3 and 4, we will provide a brief introduction to and physical interpretation of the results in each paper. Chapter 5 provides a summary and outlook. Finally, we attach the main results – The manuscripts that we have published and submitted as a part of this thesis.

THEORETICAL FRAMEWORKS

In this Chapter, we outline the most important methods used in this thesis. A complete description of the derivation of each method in the context of each paper can be found in the appendices or attached supplemental material. We here focus on when the different frameworks are useful, what their limitations are, and describe them using simple examples.

2.1 THE BOGOLIUBOV–DE GENNES EQUATIONS

The Bogoliubov–de Gennes (BdG) equations [2, 55] is a set of equations that can be solved analytically or numerically in order to diagonalize a fermionic Hamiltonian. The Hamiltonian can either be a tight binding model in real space, a continuum model in momentum space, or a combination where we only consider real space coordinates along certain directions. While this method is a powerful tool for studying a wide range of phenomena, its main limitation is that it is useful only in equilibrium.

The BdG method provides information about the energy band structure, making it a useful tool for predicting behavior based on simple analytical models. From numerical studies, we can extract information about physical observables such as the density of states, the superconducting gap and pair correlations, the superconducting critical temperature, the superfluid stiffness, the magnetization, currents in the system, etc. We can also calculate the free energy which provides information about the ground state of the system. This is less straightforward in quasi-classical theory [56].

The BdG equations are mostly used for clean systems and assumes a perfectly periodic lattice structure. Impurities can only be included in real space through averaging over a large number of impurity potentials that effectively adds randomness to the chemical potential. Interface barriers can be included through a chemical potential mismatch at the interface. A complication is that the lattice size has to be scaled down in the numerical computation. This restricts the ability to make quantitative predictions since all parameters must be scaled down accordingly for length scales such as the superconducting coherence length to scale correctly with the system size. The down-scaling and ballistic behavior makes the system more sensitive to changes in the normal-state band structure and exaggerates behavior such as Friedel oscillations. Great care must therefore be taken in interpreting the numerical results.

As a simple demonstration of the method, we consider the real space Hamiltonian

$$H = - \sum_{\langle i,j \rangle, \sigma} t_{i,j} c_{i,\sigma}^\dagger c_{j,\sigma} - \sum_{i,\sigma} \mu_i c_{i,\sigma}^\dagger c_{i,\sigma} + \sum_i \frac{|\Delta_i|^2}{U_i} + \sum_i (\Delta_i c_{i,\uparrow}^\dagger c_{i,\downarrow}^\dagger + \text{h.c.}) \quad (5)$$

describing a conventional superconductor with a mean field superconducting gap $\Delta_i = U_i \langle c_{i,\uparrow} c_{i,\downarrow} \rangle$. We assume a square lattice structure and include hopping between nearest neighboring lattice sites i and j . Above, $t_{i,j}$ is the hopping parameter, μ_i is the chemical potential, and $c_i^{(\dagger)}$ is the annihilation (creation) operator of an electron at site i with spin σ . All parameters in the above Hamiltonian are position dependent.

We can therefore consider *e.g.* a NM/SC bilayer by letting U_i be zero in one region and finite in another. The boundary conditions at the edges of the material can either be towards vacuum, or they can be periodic by allowing hopping between the last and the first lattice site.

We start by defining a basis vector

$$\psi_i = \left(c_{i,\uparrow} \ c_{i,\downarrow} \ c_{i,\uparrow}^\dagger \ c_{i,\downarrow}^\dagger \right)^\top, \quad (6)$$

so that the Hamiltonian can be written in the form

$$H = H_0 + \frac{1}{2} \sum_{i,j} \psi_i^\dagger H_{i,j} \psi_j, \quad (7)$$

where H_0 is a constant and $H_{i,j}$ a 4×4 matrix. We can write the above Hamiltonian in a diagonal form

$$H = H_0 + \frac{1}{2} \sum_n E_n \gamma_n^\dagger \gamma_n. \quad (8)$$

by solving the BdG equations

$$\sum_j H_{i,j} \phi_{j,n} = E_n \phi_{i,n}. \quad (9)$$

The BdG equations above provide the eigenenergies E_n and the eigenvectors $\phi_{i,n}$. These are labeled by $n \in [0, 4N]$, where N is the total number of lattices sites. These eigenenergies and eigenvectors are essentially what we need in order to calculate physical observables. We can solve the above set of equations by constructing a $4N \times 4N$ matrix containing all $H_{i,j}$, and diagonalizing it numerically.

The final ingredient for calculating physical observables is a way of evaluating expectation values of the operators. In Eq. (5), we started out with $2N$ fermionic operators $c_{i,\sigma}$ when counting two spins for all lattices sites. This means that the number of fermionic operators γ_n in Eq. (8) is twice that of the original number of fermionic operators. We can show that the above BdG equations have two equivalent solutions

$$E_n, \phi_{i,n} = \left(u_{i,n\uparrow} \ u_{i,n\downarrow} \ v_{i,n\uparrow} \ v_{i,n\downarrow} \right)^\top, \quad (10)$$

$$-E_n, \phi_{i,n} = \left(v_{i,n\uparrow}^* \ v_{i,n\downarrow}^* \ u_{i,n\uparrow}^* \ u_{i,n\downarrow}^* \right)^\top. \quad (11)$$

By taking this degeneracy into account, we can write the Hamiltonian in terms of independent fermionic operators as

$$H = H_0 - \frac{1}{2} \sum_{n \text{ for } E_n > 0} E_n + \sum_{n \text{ for } E_n > 0} E_n \gamma_n^\dagger \gamma_n, \quad (12)$$

where we sum over positive eigenenergies only. Since the operators are now independent, expectation values can be evaluated from the Fermi-Dirac distribution $f_{\text{FD}}(E_n)$ as

$$\langle \gamma_n^\dagger \gamma_m \rangle = f_{\text{FD}}(E_n) \delta_{n,m}, \quad (13)$$

$$\langle \gamma_n^\dagger \gamma_m^\dagger \rangle = \langle \gamma_n \gamma_m \rangle = 0. \quad (14)$$

To calculate physical observables, we start by expressing them in terms of the old fermionic operators. These are related to the new ones by

$$c_{i,\sigma} = \sum_{n \text{ for } E_n > 0} \left(u_{i,n,\sigma} \gamma_n + v_{i,n,\sigma}^* \gamma_n^\dagger \right). \quad (15)$$

By taking the expectation value and inserting Eqs. (13) and (14), we can express the physical observables fully by the eigenenergies and the elements of the eigenvectors.

In the absence of spin-mixing terms from *e.g.* spin-splitting fields and spin-orbit coupling, as is the case in our Hamiltonian in Eq. (5), the size of the matrix that we need to diagonalize can be reduced. We notice that the matrix in Eq. 9,

$$H_{i,j} = \begin{pmatrix} \epsilon_{i,j} & 0 & 0 & \Delta_i \delta_{i,j} \\ 0 & \epsilon_{i,j} & -\Delta_j \delta_{i,j} & 0 \\ 0 & -\Delta_i^* \delta_{i,j} & -\epsilon_{i,j} & 0 \\ \Delta_i^* & 0 & 0 & -\epsilon_{i,j} \end{pmatrix}, \quad (16)$$

$$\epsilon_{i,j} = -t_{i,j} - \mu_i \delta_{i,j}, \quad (17)$$

is block diagonal. By using the relations in Eqs. (10) and (11), we can reduce the BdG equations to

$$\sum_j \begin{pmatrix} \epsilon_{i,j} & \Delta_i \delta_{i,j} \\ \Delta_i^* \delta_{j,i} & -\epsilon_{j,i} \end{pmatrix} \begin{pmatrix} u_{j,n} \\ v_{j,n} \end{pmatrix} = E_n \begin{pmatrix} u_{i,n} \\ v_{i,n} \end{pmatrix}. \quad (18)$$

We now only have to diagonalize a matrix of size $2N \times 2N$. We obtain a diagonal Hamiltonian

$$H = H_0 - \frac{1}{2} \sum_n |E_n| + \sum_n |E_n| \gamma_n^\dagger \gamma_n, \quad (19)$$

where expectation values are evaluated according to

$$\langle \gamma_n^\dagger \gamma_m \rangle = f_{\text{FD}}(|E_n|) \delta_{n,m}, \quad (20)$$

$$\langle \gamma_n^\dagger \gamma_m^\dagger \rangle = \langle \gamma_n \gamma_m \rangle = 0, \quad (21)$$

and the operators are related by

$$c_{i,\uparrow} = \sum_{n \text{ for } E_n > 0} u_{i,n} \gamma_n + \sum_{n \text{ for } E_n < 0} u_{i,n} \gamma_n^\dagger, \quad (22)$$

$$c_{i,\downarrow} = \sum_{n \text{ for } E_n > 0} v_{i,n}^* \gamma_n^\dagger + \sum_{n \text{ for } E_n < 0} v_{i,n}^* \gamma_n. \quad (23)$$

This greatly enhances the speed of the numerical calculation. In the case where orbital depairing creates vortices in a periodic array, we can furthermore improve the calculation speed by dividing the Hamiltonian into magnetic supercells. This is described in paper IX [51].

Finally, we briefly discuss the case where we instead have a momentum space Hamiltonian

$$H = \sum_{\mathbf{k}, \sigma} \epsilon_{\mathbf{k}} c_{\mathbf{k}, \sigma}^\dagger c_{\mathbf{k}, \sigma} + \frac{N|\Delta|^2}{U} + \sum_{\mathbf{k}} \left(\Delta c_{\mathbf{k}, \uparrow}^\dagger c_{-\mathbf{k}, \downarrow}^\dagger + \text{h.c.} \right), \quad (24)$$

which can be obtained by performing a Fourier transform on the Hamiltonian in Eq. (5). We have assumed the system to be completely uniform and periodic. Above, $\epsilon_{\mathbf{k}} = -2t[\cos(k_x) + \cos(k_y)] - \mu$. If we want to study the system analytically, we can derive a continuum model, where the momentum \mathbf{k} is assumed to be small and no longer discrete. In this case, the first term in $\epsilon_{\mathbf{k}}$ is typically replaced with the kinetic energy so that $\epsilon_{\mathbf{k}} = k^2/2m - \mu$. By following the above procedure, the BdG equations now take a much simpler form

$$\begin{pmatrix} \epsilon_{\mathbf{k}} & \Delta \\ \Delta^* & -\epsilon_{\mathbf{k}} \end{pmatrix} \begin{pmatrix} u_{n,\mathbf{k}} \\ v_{n,\mathbf{k}} \end{pmatrix} = E_{n,\mathbf{k}} \begin{pmatrix} u_{n,\mathbf{k}} \\ v_{n,\mathbf{k}} \end{pmatrix}. \quad (25)$$

This set of equations can easily be solved analytically. We find that the eigenenergies are given by

$$E_{\mathbf{k}}^{\pm} = \pm\sqrt{\epsilon_{\mathbf{k}}^2 + |\Delta|^2}. \quad (26)$$

Without loss of generality, we choose to only consider positive energies $E_{\mathbf{k}}^+ = E > 0$. As shown in Eqs. (10) and (11) for the real space model, the solution for positive and negative energies are closely related. Consider now $\mu > 0$ so that the Fermi level intersects the bands. We can then define two corresponding eigenvectors

$$\phi^e = \begin{pmatrix} u \\ v \end{pmatrix}, \quad \phi^h = \begin{pmatrix} v \\ u \end{pmatrix}, \quad (27)$$

where

$$u = \sqrt{\frac{1}{2} \left(1 + \frac{\sqrt{E^2 - |\Delta|^2}}{E} \right)}, \quad (28)$$

$$v = \sqrt{\frac{1}{2} \left(1 - \frac{\sqrt{E^2 - |\Delta|^2}}{E} \right)}. \quad (29)$$

By letting $|\Delta| \rightarrow 0$, we see that ϕ^e (ϕ^h) reduces to the eigenvector of an electron (hole) in a normal-metal. We therefore call the above eigenvectors electron-like and hole-like, respectively. We have thus obtained analytic expressions for the energy band structure and eigenvectors of the system. The band structure can in itself reveal important properties of the system such as the presence of non-reciprocity [57]. Furthermore, the above expressions can be used to construct wave functions describing scattering at an interface, as will be discussed in the next section.

2.2 THE MCMILLAN GREEN'S FUNCTION

McMillan's method [58] can be used to construct the retarded and advanced Green's function from wave functions describing scattering at an interface. It is a useful tool for obtaining analytic expressions describing the behavior in bi- and tri-layer structures. Since it starts out from a fully continuum BdG model for each of the materials involved, the limitations are similar to those described for the momentum space BdG method in the previous section. While the McMillan Green's function can be used to describe rather complex behavior such as currents in Josephson junctions [59, 60] and edge modes in ferromagnetic insulator/topological superconductor bi-layers [61], the complexity of the problem increases with the number of layers and the dimensions of the eigenvectors. We here describe how the method by using the superconductor described by Eqs. (26) and (27) as a simple example.

Let us first set up the scattering wave functions for a NM/SC interface based on the results in the previous section. We assume the interface normal to be oriented along the x axis and the momentum k_y along the y direction to be conserved. The wave function in the normal-metal is given by

$$\psi_j(\mathbf{r}) = \left[\psi_j^{\text{in}}(x) + r_e \begin{pmatrix} 1 \\ 0 \end{pmatrix} e^{-ik_x x} + r_h \begin{pmatrix} 0 \\ 1 \end{pmatrix} e^{ik_x x} \right] e^{ik_y y}, \quad x < 0 \quad (30)$$

where

$$\psi_1^{\text{in}}(x) = \begin{pmatrix} 1 \\ 0 \end{pmatrix} e^{ik_x x}, \quad \psi_2^{\text{in}}(x) = \begin{pmatrix} 0 \\ 1 \end{pmatrix} e^{-ik_x x}, \quad \psi_3^{\text{in}}(x) = \psi_4^{\text{in}}(x) = 0, \quad x < 0. \quad (31)$$

The wave function in the superconductor is given by

$$\psi_j(\mathbf{r}) = \left[\psi_j^{\text{in}}(x) + t_e \begin{pmatrix} u \\ v \end{pmatrix} e^{ik_x x} + t_h \begin{pmatrix} v \\ u \end{pmatrix} e^{-ik_x x} \right] e^{ik_y y}, \quad x > 0 \quad (32)$$

where

$$\psi_1^{\text{in}}(x) = \psi_2^{\text{in}}(x) = 0, \quad \psi_3^{\text{in}}(x) = \begin{pmatrix} u \\ v \end{pmatrix} e^{-ik_x x}, \quad \psi_4^{\text{in}}(x) = \begin{pmatrix} v \\ u \end{pmatrix} e^{ik_x x}, \quad x > 0. \quad (33)$$

Above, we have taken into account four possible processes resulting from an incoming electron or hole from the left or right. The coefficients $r_{e(h)}$ and $t_{e(h)}$ can be obtained by applying suitable boundary conditions for the wave function at the interface $x = 0$. The momentum along the x direction is derived from the expression for the eigenenergies in Eq. (26). We find that

$$k_x^{e(h)} = \sqrt{2m[\mu \pm \sqrt{E^2 - |\Delta|^2}] - k_y^2}, \quad (34)$$

where the energy $E > 0$ and the momentum k_y are now a fixed parameters. In the normal state, we can assume that $\mu \gg E$, and find that

$$k_x = \sqrt{2m\mu - k_y^2} \quad (35)$$

for both electrons and holes. In the superconducting state, we must be very careful if we want to make the assumption $\mu \gg \sqrt{E^2 - |\Delta|^2}$ for the reason that the latter is imaginary below the gap edge. Not taking this into account results in a propagating rather than decaying wave function for energies below the gap.

How are the wave functions related to the retarded Green's function? Let us start from the definition of the retarded Green's function,

$$G_{i,j}^{\text{R}}(\mathbf{r}, \mathbf{r}', t, t') = -i\Theta(t - t') \langle \{C_i(\mathbf{r}, t), C_j^\dagger(\mathbf{r}', t')\} \rangle, \quad (36)$$

where

$$C(\mathbf{r}, t) = [c_\uparrow(\mathbf{r}, t) \quad c_\downarrow(\mathbf{r}, t) \quad c_\uparrow^\dagger(\mathbf{r}, t) \quad c_\downarrow^\dagger(\mathbf{r}, t)]^T \quad (37)$$

is the vector of electron annihilation and creation operators¹. Above, \mathbf{r} and t are spatial and time coordinates, and $\Theta(t - t')$ is the Heaviside step function. Writing the Green's function in matrix form, it can equivalently be expressed as

$$G^{\text{R}}(\mathbf{r}, \mathbf{r}', t, t') = \begin{pmatrix} g^{\text{R}}(\mathbf{r}, \mathbf{r}', t, t') & f^{\text{R}}(\mathbf{r}, \mathbf{r}', t, t') \\ -[f^{\text{R}}(\mathbf{r}, \mathbf{r}', t, t')]^* & -[g^{\text{R}}(\mathbf{r}, \mathbf{r}', t, t')]^* \end{pmatrix}, \quad (38)$$

where

$$g_{\alpha,\beta}^{\text{R}}(\mathbf{r}, \mathbf{r}', t, t') = -i\Theta(t - t') \langle \{c_\alpha(\mathbf{r}, t), c_\beta^\dagger(\mathbf{r}', t')\} \rangle, \quad (39)$$

$$f_{\alpha,\beta}^{\text{R}}(\mathbf{r}, \mathbf{r}', t, t') = -i\Theta(t - t') \langle \{c_\alpha(\mathbf{r}, t), c_\beta(\mathbf{r}', t')\} \rangle \quad (40)$$

are the ordinary and anomalous retarded Green's functions. We can perform a Fourier transform on Eq. (38), thus realizing that even though we consider $E > 0$ when constructing the wave functions, the lower elements of the Green's function matrix

¹ A more common notation in continuum theory is $\Psi(\mathbf{r}, t) = [\psi_\uparrow(\mathbf{r}, t) \quad \psi_\downarrow(\mathbf{r}, t) \quad \psi_\uparrow^\dagger(\mathbf{r}, t) \quad \psi_\downarrow^\dagger(\mathbf{r}, t)]^T$. We use the notation in Eq. (37) to avoid confusion between the operators and wave functions.

can be used to describe the lower half of the energy spectrum. The above notation is useful when the 4×4 Hamiltonian is not block diagonal due to spin-mixing. In our example, we can simplify the problem further by reducing the basis in Eq. (37) to

$$C(\mathbf{r}, t) = [c_{\uparrow}(\mathbf{r}, t) \ c_{\downarrow}^{\dagger}(\mathbf{r}, t)]^T, \quad (41)$$

thus producing a 2×2 Green's function matrix.

We now let $\mathbf{k} \rightarrow -i\nabla_{\mathbf{r}}$ in our Hamiltonian in Eq. (24). By evaluating $-i\partial_t c_{\sigma}(\mathbf{r}) = [H, c_{\sigma}(\mathbf{r})]$, we find that

$$i\partial_t C(\mathbf{r}, t) = H_{\mathbf{r}} C(\mathbf{r}, t), \quad (42)$$

$$-i\partial_t C^{\dagger}(\mathbf{r}, t) = C^{\dagger}(\mathbf{r}, t) H_{\mathbf{r}}^{\dagger}, \quad (43)$$

where $H_{\mathbf{r}} = H_{\mathbf{k}}(\mathbf{k} \rightarrow -i\nabla_{\mathbf{r}})$, and $H_{\mathbf{k}}$ is the matrix in Eq. (25). In this particular context, the \dagger operator is defined as a matrix operation and only acts on the matrix elements as a complex conjugate and matrix transpose. As a result, the retarded Green's function therefore satisfy the equations

$$(i\partial_t - H_{\mathbf{r}})G^{\text{R}}(\mathbf{r}, \mathbf{r}', t, t') = \delta(t - t')\delta(\mathbf{r} - \mathbf{r}')\sigma_0, \quad (44)$$

$$G^{\text{R}}(\mathbf{r}, \mathbf{r}', t, t')(-i\partial_{t'} - H_{\mathbf{r}}^{\dagger}) = \delta(t - t')\delta(\mathbf{r} - \mathbf{r}')\sigma_0, \quad (45)$$

where σ_0 is the 2×2 unit matrix. Assuming the Green's function to be independent of the absolute time coordinate $T = (t + t')/2$ and performing a Fourier transform over the relative time coordinate $t_{\text{rel}} = t - t'$, we find that the above equations can be expressed as

$$(E - H_{\mathbf{r}})G^{\text{R}}(\mathbf{r}, \mathbf{r}') = \delta(\mathbf{r} - \mathbf{r}')\sigma_0, \quad (46)$$

$$G^{\text{R}}(\mathbf{r}, \mathbf{r}')(E - H_{\mathbf{r}}^{\dagger}) = \delta(\mathbf{r} - \mathbf{r}')\sigma_0. \quad (47)$$

The Green's functions depends on the energy E , although this is not written out explicitly.

Let us next make the ansatz that the Green's function $G^{\text{R}}(\mathbf{r}, \mathbf{r}') = \psi(\mathbf{r})\tilde{\psi}^T(\mathbf{r}')$ can be constructed from two wave functions

$$\psi(\mathbf{r}) = \sum_n c_n \psi_n(\mathbf{r}), \quad (48)$$

$$\tilde{\psi}(\mathbf{r}) = \sum_m \tilde{c}_m \tilde{\psi}_m(\mathbf{r}). \quad (49)$$

Here, c_n and \tilde{c}_m are constants that in the case of scattering at an interface relates to transmission and reflection amplitudes for the specific quasi-particle described by $\psi_n(\mathbf{r})$ or $\tilde{\psi}_m(\mathbf{r})$. If we assume that

$$\psi_n(\mathbf{r}) = \phi_{n, \mathbf{k}_n} e^{i\mathbf{k}_n \cdot \mathbf{r}}, \quad (50)$$

$$\tilde{\psi}_m(\mathbf{r}) = \tilde{\phi}_{m, \mathbf{k}_m} e^{i\mathbf{k}_m \cdot \mathbf{r}}, \quad (51)$$

we find that the eigenvectors ϕ_{n, \mathbf{k}_n} and $\tilde{\phi}_{m, \mathbf{k}_m}$ satisfy the equations

$$H_{\mathbf{k}_n} \phi_{n, \mathbf{k}_n} = E \phi_{n, \mathbf{k}_n}, \quad (52)$$

$$H_{-\mathbf{k}_m}^* \tilde{\phi}_{m, \mathbf{k}_m} = E \tilde{\phi}_{m, \mathbf{k}_m}, \quad (53)$$

The first of these two equations, is equivalent to the BdG equation in Eq. (25). We have already calculated the eigenenergies and eigenvectors in Eqs. (26) and (27). In this simple case, there are no \mathbf{k} -linear terms in the Hamiltonian and the only

complex quantity is the superconducting gap that only enters the eigenenergies and eigenvectors as $|\Delta|^2$. Therefore, $H_{-\mathbf{k}}^*$ gives the same eigenenergies and eigenvectors as $H_{\mathbf{k}}$. In conclusion, the wave functions in Eqs. (48) and (49) used to construct the retarded Green's function can be written in terms of the wave functions $\psi_j(\mathbf{r})$ of the normal-metal and superconductor in Eqs. (30) and (32). For generality, we name the wave function related to Eqs. (49) and (53) the conjugated wave function $\tilde{\psi}_j(\mathbf{r})$.

What now remains is to choose which wave functions $\psi_j(\mathbf{r})$ and $\tilde{\psi}_j(\mathbf{r}')$ we should combine in order to construct the retarded Green's function. In our particular case of a NM/SC junction, we have 4 distinct processes associated with an incoming electron and hole from the left, and an incoming electron-like and hole-like quasi-particle from the right. We will be looking for solutions where the wave function $\tilde{\psi}_j(\mathbf{r}')$ describes the conjugated processes compared to $\psi_j(\mathbf{r})$. The resulting eight scattering processes are sketched in Fig. 5. We assume conservation of the momentum parallel to the interface so that the retarded Green's function is given by $G^R(\mathbf{r}, \mathbf{r}') = G^R(x, x')e^{ik_y(y-y')}$. The Green's function can be constructed from particles incoming from the left (1 and 2) and particles incoming from the right (3 and 4) as

$$G^R(x, x') = \alpha_1 \psi_1(x) \tilde{\psi}_3^T(x') + \alpha_2 \psi_1(x) \tilde{\psi}_4^T(x') + \alpha_3 \psi_2(x) \tilde{\psi}_3^T(x') + \alpha_4 \psi_2(x) \tilde{\psi}_4^T(x'), \quad x > x', \quad (54)$$

$$G^R(x, x') = \beta_1 \psi_3(x) \tilde{\psi}_1^T(x') + \beta_2 \psi_4(x) \tilde{\psi}_1^T(x') + \beta_3 \psi_3(x) \tilde{\psi}_2^T(x') + \beta_4 \psi_4(x) \tilde{\psi}_2^T(x'), \quad x < x'. \quad (55)$$

The coefficients α_j and β_j are obtained from the boundary conditions of the Green's function at $x = x'$. These can be derived by integrating the Fourier transform of Eq. (46),

$$(E - H_{x,k_y})G^R(x, x') = \delta(x - x')\sigma, \quad (56)$$

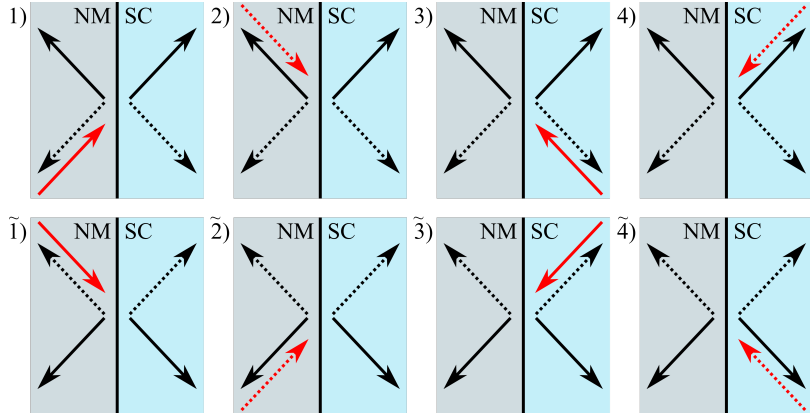


Figure 5: In processes 1) and 2) respectively, an electron and a hole incoming from the left normal-metal (NM) is scattered at the interface. In processes 3) and 4) respectively, an electron-like and a hole-like quasi-particle incoming from the right superconductor (SC) is scattered at the interface. Processes $\tilde{1}$), $\tilde{2}$), $\tilde{3}$), and $\tilde{4}$) show the corresponding conjugated processes for an electron from the left, a hole from the left, an electron-like quasi-particle from the right, and a hole-like quasi-particle from the right, respectively. Red lines represent incoming particles and black lines represent outgoing particles. Solid lines represent electrons and electron-like quasi-particles, while dotted lines represent holes and hole-like quasi-particles.

as

$$\lim_{\delta \rightarrow 0} \int_{x'-\delta}^{x'+\delta} dx \int_{-\infty}^x dx'', \quad \text{and} \quad \lim_{\delta \rightarrow 0} \int_{x'-\delta}^{x'+\delta} dx. \quad (57)$$

In the first integration, the x coordinate in Eq. (56) is replaced with x'' . The boundary conditions depend on the particular form of the Hamiltonian. In this case, where the spatial derivative only enters through the kinetic energy, the first integration reveals that the Green's function must be continuous at $x = x'$,

$$\lim_{\delta \rightarrow 0} [G^{\text{R}}(x' + \delta, x') - G^{\text{R}}(x' - \delta, x')] = 0. \quad (58)$$

This can be used when evaluating the second integration. We find that the second boundary condition is

$$\lim_{\delta \rightarrow 0} \partial_x G^{\text{R}}(x, x') \Big|_{x=x'-\delta}^{x=x'+\delta} = 2m\sigma_3, \quad (59)$$

where σ_3 is the third Pauli matrix.

We now have everything we need to calculate the Green's function. The process of solving the Green's function for the full scattering process is a straightforward, but rather tedious problem. As a demonstration, we therefore only consider the bulk Green's function of a superconductor. In this case, the wave functions are simply

$$\begin{aligned} \psi_1(x) &= \tilde{\psi}_1(x) = \begin{pmatrix} u \\ v \end{pmatrix} e^{ik_x^e x}, & \psi_2(x) &= \tilde{\psi}_2(x) = \begin{pmatrix} v \\ u \end{pmatrix} e^{-ik_x^h x}, \\ \psi_3(x) &= \tilde{\psi}_3(x) = \begin{pmatrix} u \\ v \end{pmatrix} e^{-ik_x^e x}, & \psi_4(x) &= \tilde{\psi}_4(x) = \begin{pmatrix} v \\ u \end{pmatrix} e^{ik_x^h x}. \end{aligned} \quad (60)$$

Inserting these wave functions into Eqs. (54) and (55), we find that the retarded Green's function is given by

$$\begin{aligned} G^{\text{R}}(x, x') &= \alpha_1 \begin{pmatrix} u^2 & uv \\ uv & v^2 \end{pmatrix} e^{ik_x^e(x-x')} + \alpha_2 \begin{pmatrix} uv & u^2 \\ v^2 & uv \end{pmatrix} e^{ik_x^e x + ik_x^h x'} \\ &+ \alpha_3 \begin{pmatrix} uv & v^2 \\ u^2 & uv \end{pmatrix} e^{-ik_x^h x - ik_x^e x'} + \alpha_4 \begin{pmatrix} v^2 & uv \\ uv & u^2 \end{pmatrix} e^{-ik_x^h(x-x')}, \quad x > x', \end{aligned} \quad (61)$$

$$\begin{aligned} G^{\text{R}}(x, x') &= \beta_1 \begin{pmatrix} u^2 & uv \\ uv & v^2 \end{pmatrix} e^{-ik_x^e(x-x')} + \beta_2 \begin{pmatrix} uv & v^2 \\ u^2 & uv \end{pmatrix} e^{ik_x^h x + ik_x^e x'} \\ &+ \beta_3 \begin{pmatrix} uv & u^2 \\ v^2 & uv \end{pmatrix} e^{-ik_x^e x - ik_x^h x'} + \beta_4 \begin{pmatrix} v^2 & uv \\ uv & u^2 \end{pmatrix} e^{ik_x^h(x-x')}, \quad x < x'. \end{aligned} \quad (62)$$

It can be seen directly from the above Green's function that the continuity at $x = x'$ imposed by Eq. (58) requires $\alpha_1 = \beta_1$, $\alpha_4 = \beta_4$, and $\alpha_2 = \beta_2 = \alpha_3 = \beta_3 = 0$. From the second boundary condition, Eq. (59), we derive that

$$\alpha_1 = -\frac{im}{k_x^e(u^2 - v^2)}, \quad (63)$$

$$\alpha_4 = -\frac{im}{k_x^h(u^2 - v^2)}. \quad (64)$$

Inserting the expressions for the coefficients, we find that the retarded Green's function of a bulk superconductor is given by

$$G^{\text{R}}(x, x') = -\frac{im}{2\sqrt{E^2 - |\Delta|^2}} \left[\frac{1}{k_x^{\text{e}}} \begin{pmatrix} E + \sqrt{E^2 - |\Delta|^2} & |\Delta| \\ |\Delta| & E - \sqrt{E^2 - |\Delta|^2} \end{pmatrix} e^{ik_x^{\text{e}}|x-x'|} + \frac{1}{k_x^{\text{h}}} \begin{pmatrix} E - \sqrt{E^2 - |\Delta|^2} & |\Delta| \\ |\Delta| & E + \sqrt{E^2 - |\Delta|^2} \end{pmatrix} e^{-ik_x^{\text{h}}|x-x'|} \right]. \quad (65)$$

A number of equilibrium properties can be derived from the retarded Green's function. One example that is captured by the simple model above is the superconducting density of states $\sim \text{Re}[E/\sqrt{E^2 - |\Delta|^2}]$ calculated from the imaginary part of the trace. The retarded Green's function calculated here can also be extended to the Matsubara formalism by analytic continuation.

2.3 THE SCHRIEFFER-WOLFF TRANSFORMATION

In some cases, the Hamiltonian includes terms that makes it impossible to diagonalize it exactly. This is for instance the case when we have a coupling between a fermionic and bosonic Hamiltonian in the form

$$H_{\text{c}} = \lambda \sum_{\mathbf{k}, \mathbf{q}} (c_{\mathbf{k}+\mathbf{q}, \uparrow}^{\dagger} c_{\mathbf{k}, \downarrow} a_{-\mathbf{q}}^{\dagger} + c_{\mathbf{k}+\mathbf{q}, \downarrow}^{\dagger} c_{\mathbf{k}, \uparrow} a_{\mathbf{q}}). \quad (66)$$

This term will be used to describe coupling between electron operators $c_{\mathbf{k}, \sigma}$ in a superconductor and magnon operators $a_{\mathbf{q}}$ in a ferromagnetic insulator later on [24]. We can use perturbation theory to diagonalize the Hamiltonian in terms of the bosonic operators.

Assume that the Hamiltonian can be written as $H = H_0 + H_{\text{c}}$, where H_0 is already quadratic in the bosonic operators and $H_{\text{c}} \sim \lambda$. We define an effective Hamiltonian $H_{\text{eff}} = e^{iS} H e^{-iS}$, and use the Baker–Campbell–Hausdorff formula to expand it as

$$H_{\text{eff}} = H_0 + H_{\text{c}} + i[S, H_0 + H_{\text{c}}] + \frac{i^2}{2!}[S, [S, H_0 + H_{\text{c}}]] + \dots \quad (67)$$

By requiring that

$$H_{\text{c}} = -i[S, H_0], \quad (68)$$

we project out terms of order $\mathcal{O}(\lambda)$. Keeping terms up to order $\mathcal{O}(\lambda^2)$, the effective Hamiltonian can be written as

$$H_{\text{eff}} = H_0 + \frac{i}{2}[S, H_{\text{c}}]. \quad (69)$$

In this effective Hamiltonian, S is derived from the condition in Eq. (68). The effective Hamiltonian is now quadratic in the bosonic operators and can be diagonalized. The perturbative approach described above is called a Schrieffer-Wolff transformation [62, 63]. It is justified when the first order terms are irrelevant for the physics we wish to investigate and the perturbation $\sim \lambda$ is small compared to the unperturbed Hamiltonian.

2.4 THE USADEL EQUATION

So far, we have discussed tight binding and continuum models that disregard disorder in the system. We will now consider the Green's function in the opposite limit of diffusive transport. To this end, we will describe the system by the Usadel equation [64], which is suitable for superconductors where the scattering rate is so large that only *s*-wave pairing is present. The advantage of the quasi-classical theory presented here, is that we can introduce the Keldysh Green's function that captures non-equilibrium properties [65–67].

Let us go through the relevant approximations by starting with a the Hamiltonian

$$\begin{aligned} H(\mathbf{r}, t) = & \int d\mathbf{r} \sum_{\sigma} \psi_{\sigma}^{\dagger}(\mathbf{r}, t) \left(-\frac{1}{2m} \nabla_{\mathbf{r}}^2 - \mu \right) \psi_{\sigma}(\mathbf{r}, t) \\ & + \frac{1}{2} \int d\mathbf{r} \left[\Delta(\mathbf{r}) \psi_{\uparrow}^{\dagger}(\mathbf{r}, t) \psi_{\downarrow}^{\dagger}(\mathbf{r}, t) + \text{h.c.} \right] \\ & + \int d\mathbf{r} \sum_{\sigma, \sigma'} \psi_{\sigma}^{\dagger}(\mathbf{r}, t) U_{\sigma, \sigma'}^{\text{tot}}(\mathbf{r}) \psi_{\sigma'}(\mathbf{r}, t), \end{aligned} \quad (70)$$

as an example. We follow the approach in the appendix of paper VI [23]. Above, $\psi_{\sigma}^{(\dagger)}(\mathbf{r}, t)$ is an operator annihilating (creating) a spin- σ electron at position \mathbf{r} and time t . The first term introduces the chemical potential μ and the kinetic energy for electrons of mass m . The second term describes superconducting attractive interaction with a mean-field superconducting gap $\Delta(\mathbf{r}) = V \langle \psi_{\uparrow}(\mathbf{r}) \psi_{\downarrow}(\mathbf{r}) \rangle$. The last term is the hardest one to treat as it describes the total scattering potential $U^{\text{tot}}(\mathbf{r})$ and depends on the positions of all of the impurities in the system. This term includes the ordinary impurity scattering that makes the system diffusive. It can however also include other types of scattering potentials such as spin-flip and spin-orbit scattering.

We first need to derive the equations of motion of the Green's function for the relevant Hamiltonian. We begin by defining

$$\hat{\psi}(\mathbf{r}, t) = [\psi_{\uparrow}(\mathbf{r}, t) \quad \psi_{\downarrow}(\mathbf{r}, t) \quad \psi_{\uparrow}^{\dagger}(\mathbf{r}, t) \quad \psi_{\downarrow}^{\dagger}(\mathbf{r}, t)]^T, \quad (71)$$

which is a four-vector field operator in Nambu \otimes spin space. We also define the 8×8 Green's function in Keldysh space

$$\check{G}(1, 2) = \begin{pmatrix} \hat{G}^{\text{R}}(1, 2) & \hat{G}^{\text{K}}(1, 2) \\ 0 & \hat{G}^{\text{A}}(1, 2) \end{pmatrix}, \quad (72)$$

where the elements are the retarded, advanced, and Keldysh Green's functions in Nambu \otimes spin space defined as

$$[\hat{G}^{\text{R}}(1, 2)]_{i,j} = -i\Theta(t_1 - t_2) \sum_k (\hat{\rho}_3)_{ik} \langle \{ [\hat{\psi}(1)]_k, [\hat{\psi}^{\dagger}(2)]_j \} \rangle, \quad (73)$$

$$[\hat{G}^{\text{A}}(1, 2)]_{i,j} = i\Theta(t_2 - t_1) \sum_k (\hat{\rho}_3)_{ik} \langle \{ [\hat{\psi}(1)]_k, [\hat{\psi}^{\dagger}(2)]_j \} \rangle, \quad (74)$$

$$[\hat{G}^{\text{K}}(1, 2)]_{i,j} = -i \sum_k (\hat{\rho}_3)_{ik} \langle [[\hat{\psi}(1)]_k, [\hat{\psi}^{\dagger}(2)]_j] \rangle, \quad (75)$$

respectively. Above, $(1, 2)$ is short-hand notation for $(\mathbf{r}_1, t_1, \mathbf{r}_2, t_2)$. Note that the hat and the check refers to vectors or matrices in Nambu \otimes spin space and Keldysh space, respectively. From the Heisenberg equations of motion for the field operators, we derive the equations of motion for the Keldysh space Green's function,

$$[i\partial_{t_1} \hat{\rho}_3 - \hat{H}(\mathbf{r}_1)] \check{G}(1, 2) = \delta(1-2) \check{\rho}_0, \quad (76)$$

$$\check{G}(1, 2) [i\partial_{t_2} \hat{\rho}_3 - \hat{\rho}_3 \hat{H}(\mathbf{r}_2) \hat{\rho}_3]^{\dagger} = \delta(1-2) \check{\rho}_0. \quad (77)$$

Above, $\hat{\rho}_3 = \text{diag}(1, 1, -1, -1)$, and $\check{\rho}_0$ ($\hat{\rho}_0$) is the unit matrix in Keldysh (Nambu \otimes spin) space. The Hamiltonian matrix is given by

$$\hat{H}(\mathbf{r}) = \left(-\frac{1}{2m} \nabla_{\mathbf{r}}^2 - \mu \right) \hat{\rho}_0 - \hat{\Delta}(\mathbf{r}) + \hat{U}_{\text{tot}}(\mathbf{r}), \quad (78)$$

where $\hat{\Delta}(\mathbf{r}) = \text{antidiag}(\Delta, -\Delta, \Delta^*, -\Delta^*)$. The scattering potential matrix $\hat{U}_{\text{tot}}(\mathbf{r})$ can hold a number of different terms, but must at least include scattering on non-magnetic impurities

$$U(\mathbf{r}) = \sum_i u(\mathbf{r} - \mathbf{r}_i), \quad (79)$$

where $u(\mathbf{r} - \mathbf{r}_i)$ is the scattering potential of a single non-magnetic impurity at position \mathbf{r}_i .

Our strategy for treating the difficult scattering terms in Eqs. (76) and (77) is to replace the impurity potentials with self-energies. To do so, we split the Hamiltonian up into two parts, $\hat{H}(\mathbf{r}) = \hat{H}_0(\mathbf{r}) + \hat{U}_{\text{tot}}(\mathbf{r})$, where $\hat{H}_0(\mathbf{r})$ describes the system in the absence of impurity scattering. The self-energies are introduced through the Dyson equations

$$\check{G}(1, 2) = \check{G}_0(1, 2) + \check{G}_0 \bullet \check{\Sigma} \bullet \check{G}(1, 2), \quad (80)$$

$$\check{G}(1, 2) = \check{G}_0(1, 2) + \check{G} \bullet \check{\Sigma}^\dagger \bullet \check{G}_0(1, 2), \quad (81)$$

where we have defined $\check{\Sigma}(1, 2) = \delta(1 - 2) \hat{U}_{\text{tot}}(\mathbf{r}_2)$, and $\check{G}_0(1, 2)$ is the Green's function in the absence of impurity scattering. We have introduced the bullet product

$$A \bullet B(1, 2) = \int d3 A(1, 3) B(3, 2). \quad (82)$$

The Dyson equations are exact and include an infinite sum of self-energy diagrams. We solve the Dyson equations iteratively within the self-consistent Born approximation, where terms above second order in $\check{\Sigma} \bullet \check{G}$ and $\check{G} \bullet \check{\Sigma}^\dagger$ are neglected. More self-energy diagrams can be included to capture higher order effects such as transversal currents from spin-Hall and spin-swapping effects [68]. Since we are not interested in one specific impurity configuration, we average over all impurities by performing the integral

$$\langle \dots \rangle_{\text{av}} = \prod_{n=1}^N \left(\frac{1}{\mathcal{V}} \int d\mathbf{r}_n \right) \dots, \quad (83)$$

Here, \mathcal{V} is the volume of the system. The Green's function is assumed to be approximately equal to its impurity-averaged value $\check{G}_{\text{av}}(1, 2)$. By acting with $[i\partial_{t_1} \hat{\rho}_3 - \hat{H}_0(\mathbf{r}_1)]$ and $[i\partial_{t_2} \hat{\rho}_3 - \hat{\rho}_3 \hat{H}_0(\mathbf{r}_2) \hat{\rho}_3]$ on the resulting equations, we obtain expressions in a similar form as Eqs. (76) and (77). However, the impurity potentials are now replaced by expressions involving self-energies and impurity averaged Green's functions. By subtracting the two equations that we have obtained, we find that

$$\begin{aligned} & [i\partial_{t_1} \hat{\rho}_3 - \hat{H}_0(\mathbf{r}_1)] \check{G}_{\text{av}}(1, 2) - \check{G}_{\text{av}}(1, 2) [i\partial_{t_2} \hat{\rho}_3 - \hat{\rho}_3 \hat{H}_0(\mathbf{r}_2) \hat{\rho}_3]^\dagger \\ & - [\langle \check{\Sigma} \bullet \check{G}_{\text{av}} \bullet \check{\Sigma} \rangle_{\text{av}} \bullet \check{G}_{\text{av}}](1, 2) = 0. \end{aligned} \quad (84)$$

To proceed, we need to introduce several approximations to this equation.

First of all, we wish to express the problem in terms of a more sensible choice of coordinates so that we can make assumptions about the spatial and time dependencies

of physical observables. We first introduce the center-of-mass coordinate $\mathbf{R} = (\mathbf{r}_1 + \mathbf{r}_2)/2$ and the relative coordinate $\mathbf{r} = \mathbf{r}_1 - \mathbf{r}_2$, together with absolute and relative time coordinates $T = (t_1 + t_2)/2$ and $t = t_1 - t_2$. In this treatment, we assume that the Green's function is independent of the absolute time coordinate. We will discuss time dependent problems further in paper III [69]. We also assume that all quantities vary slowly in space compared to the Fermi wavelength. This allows us to keep only the first order gradients in the center of mass coordinate. Since it is more convenient to study the problem in terms of momentum \mathbf{p} and energy ϵ , we introduce the Fourier transform and its inverse,

$$\check{G}_{\text{av}}(\mathbf{R}, \mathbf{p}, \epsilon) = \int d\mathbf{r} \int dt e^{-i\mathbf{p}\cdot\mathbf{r} + i\epsilon t} \check{G}_{\text{av}}(\mathbf{R}, \mathbf{r}, t), \quad (85)$$

$$\check{G}_{\text{av}}(\mathbf{R}, \mathbf{r}, t) = \int \frac{d\mathbf{p}}{(2\pi)^3} \int \frac{d\epsilon}{2\pi} e^{i\mathbf{p}\cdot\mathbf{r} - i\epsilon t} \check{G}_{\text{av}}(\mathbf{R}, \mathbf{p}, \epsilon). \quad (86)$$

Under the above assumptions, the Fourier transform of the bullet product between two functions $A(\mathbf{R}, \mathbf{p}, \epsilon)$ and $B(\mathbf{R}, \mathbf{p}, \epsilon)$ is given by

$$\begin{aligned} A \bullet B(\mathbf{R}, \mathbf{p}, \epsilon) &= A(\mathbf{R}, \mathbf{p}, \epsilon)B(\mathbf{R}, \mathbf{p}, \epsilon) + \frac{i}{2}[\nabla_{\mathbf{R}}A(\mathbf{R}, \mathbf{p}, \epsilon) \cdot \nabla_{\mathbf{p}}B(\mathbf{R}, \mathbf{p}, \epsilon) \\ &\quad - \nabla_{\mathbf{p}}A(\mathbf{R}, \mathbf{p}, \epsilon) \cdot \nabla_{\mathbf{R}}B(\mathbf{R}, \mathbf{p}, \epsilon)]. \end{aligned} \quad (87)$$

We next apply the quasi-classical approximation, where we assume that the absolute value of the momentum p is approximately equal to the Fermi momentum p_{F} . As a result, integrations over the momentum components are then simplified as

$$\int \frac{d\mathbf{p}}{(2\pi)^3} \check{G}_{\text{av}}(\mathbf{R}, \mathbf{p}, \epsilon) \approx N_0 \int d\xi_{p_{\text{F}}} \int \frac{d\mathbf{e}_{p_{\text{F}}}}{4\pi} \check{G}_{\text{av}}(\mathbf{R}, \mathbf{p}_{\text{F}}, \epsilon). \quad (88)$$

Above, N_0 is the DOS at the Fermi level, $\xi_{p_{\text{F}}} = p_{\text{F}}^2/2m$, and $\mathbf{e}_{p_{\text{F}}} = \mathbf{p}_{\text{F}}/p_{\text{F}}$ describes the direction of the momentum. We will use the short-hand notation $\langle \dots \rangle_{p_{\text{F}}} = \int (d\mathbf{e}_{p_{\text{F}}}/4\pi)$ for the average over all directions of the momentum. We introduce the quasi-classical Green's function

$$\check{g}_{\text{av}}(\mathbf{R}, \mathbf{p}_{\text{F}}, \epsilon) = \frac{i}{\pi} \int d\xi_{p_{\text{F}}} \check{G}_{\text{av}}(\mathbf{R}, \mathbf{p}_{\text{F}}, \epsilon), \quad (89)$$

which we will approximate further.

The approximations we have made so far are those necessary to derive a quasi-classical theory for the Green's function based on our Hamiltonian. To derive the Usadel equation, we take a step further and assume that the system is in the diffusive limit. In this case, the quasi-classical Green's function can be approximated as

$$\check{g}_{\text{av}}(\mathbf{R}, \mathbf{p}_{\text{F}}, \epsilon) \approx \check{g}_{\text{av}}^{\text{s}}(\mathbf{R}, \epsilon) + \mathbf{e}_{p_{\text{F}}} \cdot \check{g}_{\text{av}}^{\text{D}}(\mathbf{R}, \epsilon). \quad (90)$$

We assume that $|\check{g}_{\text{av}}^{\text{D}}(\mathbf{R}, \epsilon)| \ll \check{g}_{\text{av}}^{\text{s}}(\mathbf{R}, \epsilon)$ and neglect terms of second order in $\check{g}_{\text{av}}^{\text{D}}(\mathbf{R}, \epsilon)$. In this treatment, we have essentially assumed that the system is so disordered that only the s -wave superconductivity survives.

After applying all these approximations to Eq. (84), we separate out the even contributions in $\mathbf{e}_{p_{\text{F}}}$ by averaging over all $\mathbf{e}_{p_{\text{F}}}$. We next separate out the odd contributions in $\mathbf{e}_{p_{\text{F}}}$ by multiplying the equation by $\mathbf{e}_{p_{\text{F}}}$ before doing the averaging. In the odd equation, we use the normalization condition

$$\check{g}_{\text{av}}(\mathbf{R}, p_{\text{F}}, \epsilon) \check{g}_{\text{av}}(\mathbf{R}, p_{\text{F}}, \epsilon) = \check{\rho}_0 \quad (91)$$

to express $\check{g}_{\text{av}}^{\text{p}}(\mathbf{R}, \epsilon)$ in terms of $\check{g}_{\text{av}}^{\text{s}}(\mathbf{R}, \epsilon)$. When including only ordinary scattering on non-magnetic impurities, we find that

$$\check{g}_{\text{av}}^{\text{p}}(\mathbf{R}, \epsilon) = -\tau v_{\text{F}} \check{g}_{\text{av}}^{\text{s}}(\mathbf{R}, \epsilon) \nabla_{\mathbf{R}} \check{g}_{\text{av}}^{\text{s}}(\mathbf{R}, \epsilon). \quad (92)$$

Oftentimes, the above form of $\check{g}_{\text{av}}^{\text{p}}(\mathbf{R}, \epsilon)$ is assumed even in the presence of other types of scattering. This is because the impurity scattering length for ordinary scattering on non-magnetic impurities is assumed much shorter than all other length scales. The final step is to insert Eq. (92) into the even equation. The resulting Usadel equation is commonly expressed as

$$\nabla_{\mathbf{R}} \cdot \check{\mathbf{I}}(\mathbf{R}, \epsilon) = i[\check{\sigma}(\mathbf{R}, \epsilon), \check{g}_{\text{av}}^{\text{s}}(\mathbf{R}, \epsilon)]. \quad (93)$$

The left-hand side describes the divergence of the matrix current $\check{\mathbf{I}}(\mathbf{R}, \epsilon)$, which originates from the odd equation. Under the assumption in Eq. (92), the matrix current is given by

$$\check{\mathbf{I}}(\mathbf{R}, \epsilon) = -D \check{g}_{\text{av}}^{\text{s}}(\mathbf{R}, \epsilon) \nabla_{\mathbf{R}} \check{g}_{\text{av}}^{\text{s}}(\mathbf{R}, \epsilon), \quad (94)$$

where $D = \tau v_{\text{F}}^2/3$ is the diffusion coefficient. The diffusion coefficient is determined by the Fermi velocity $v_{\text{F}} = p_{\text{F}}/m$, and the scattering time τ associated with scattering on non-magnetic impurities. The scattering time is given by

$$\frac{1}{\tau} = 2\pi n N_0 \left\langle |u(\mathbf{e}_{p_{\text{F}}} - \mathbf{e}_{q_{\text{F}}})|^2 \right\rangle_{p_{\text{F}}, q_{\text{F}}}, \quad (95)$$

where n is the density of non-magnetic impurities, and $u(\mathbf{e}_{p_{\text{F}}} - \mathbf{e}_{q_{\text{F}}})$ is the scattering potential of a single non-magnetic impurity. The right-hand side of the Usadel equation contains the self-energy matrix $\check{\sigma}(\mathbf{R}, \epsilon)$. The self-energy matrix depends on what kind of Hamiltonian we started out with, but it typically at least contains the contribution $\epsilon \hat{\rho}_3 + \hat{\Delta}(\mathbf{R})$. These terms arise from the first line of Eq. (84), and enter through the even equation. The Usadel equation can also include torque terms if higher-order self-energy terms are included [68].

The Usadel equation can be solved analytically or numerically depending on its complexity. The superconducting pairing obeys a gap equation so that the superconducting gap can be solved self-consistently in the numerical calculation. To solve the Usadel equation analytically, we typically assume the gap and the retarded part of the Green's function to take a constant value. Non-equilibrium phenomena can be conveniently studied by considering the Keldysh component of the Usadel equation [66, 67]. In the case where *e.g.* a voltage or thermal gradient is injected from another material, we also need to include boundary conditions. Boundary conditions have been derived for a number of different interfaces [70–77]. For further details, we refer to the wide array of literature discussing quasi-classical theory and the Usadel equation, *e.g.* Refs. [65–67].

 THE SUPERCONDUCTING PHASE TRANSITION

In this chapter, we discuss how the superconducting transition temperature of a material can be controlled by proximity to other magnetic, inversion symmetry breaking, and superconducting materials (papers II, IV, VIII, and X). We also discuss how the magnetic anisotropy of a material changes as the temperature drops below the critical temperature of an adjacent superconductor (papers I and V). In the end, we discuss the critical field in highly disordered hole-overdoped cuprate superconductors (paper IX).

3.1 HYBRIDS WITH MISALIGNED FERROMAGNETS

The critical temperature of a superconductor can be altered by connecting it to a ferromagnetic material [26–28]. However, for a homogenous ferromagnet, the Zeeman splitting of the energy bands is entirely independent of the direction of the magnetization with respect to the interface. It was therefore realized that to achieve control of the critical temperature, one must break this symmetry by engineering heterostructures consisting of misaligned ferromagnets or magnetic materials with non-collinear magnetization [6, 78].

Consider the case of a FM/SC/FM trilayer where the relative orientation of the magnetization in the two ferromagnetic layers can be controlled by an external magnetic field. In this case, there are two competing effects controlling the superconducting critical temperature. The first and most dominant one is the mutual compensation of the ferromagnetic exchange fields. When the magnetizations of the two ferromagnets are parallel, both contribute to inducing an exchange field inside the superconducting region. This weakens the superconducting condensate resulting in a lower critical temperature. If instead the magnetization of the two ferromagnets are antiparallel, the contributions to the induced exchange field from the two ferromagnets cancel in

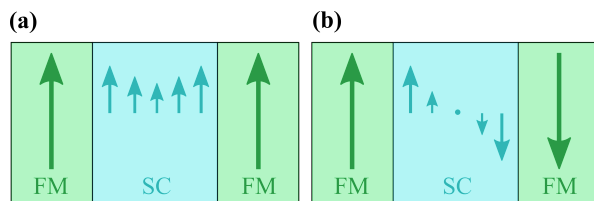


Figure 6: When the magnetization (green arrows) of the two ferromagnets (FM) are aligned (panel (a)), there is a finite induced exchange field (blue arrows) in the superconductor (SC). When the magnetization of the two ferromagnets are antiparallel (panel (b)), the exchange field vanishes in the middle of the superconducting region. The superconducting critical temperature is therefore expected to be higher for the configuration in panel (b) than for the configuration in panel (a).

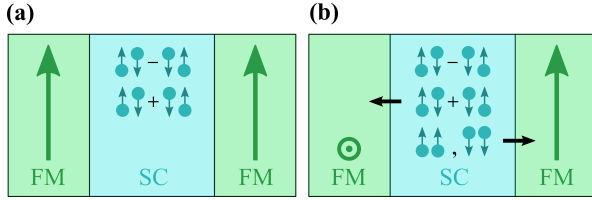


Figure 7: When the magnetization (green arrows) of the two ferromagnets (FM) are aligned (panel (a)), the only superconducting correlations present are the conventional spin-singlets ($\uparrow\downarrow - \downarrow\uparrow$) and the opposite-spin triplets ($\uparrow\downarrow + \downarrow\uparrow$). When the magnetization of the two ferromagnets are perpendicular (panel (b)), the spin-triplet correlations created due to the leftmost FM are equal-spin triplets ($\uparrow\uparrow$ and $\downarrow\downarrow$) in the reference frame of the rightmost FM. These are robust to the spin-splitting field and can easily leak out into the rightmost ferromagnet (indicated by right-going black arrow). This weakens the superconducting condensate. Similarly, spin-triplets that have equal spin with respect to the leftmost FM can leak into this region (left-going black arrow). The leakage of spin-triplet pairing is therefore expected to weaken the superconducting condensate for the configuration in panel (b) compared to the configuration in panel (a).

the middle of the superconducting region. The critical temperature is therefore less affected by the ferromagnets. This is depicted in Fig. 6.

The second contribution is the leakage of equal-spin triplets into the ferromagnetic regions. As long as the ferromagnets are aligned, the only spin-triplet Cooper pairs present in the system are those with zero spin along the magnetization direction. If the ferromagnets are misaligned, the opposite-spin triplets created due to the spin-splitting field of one ferromagnet has an equal-spin triplet component in the reference frame of the other ferromagnet. When both electrons in the Cooper pair have the same spin aligned parallel or antiparallel to the magnetization direction, the Cooper pair does not lose phase coherence due to the Zeeman splitting of the spin-up and spin-down energy bands. These can therefore leak into the ferromagnetic region and cause a weakening of the superconducting condensate. The suppression is strongest when the two ferromagnets have perpendicular magnetization. This is depicted in Fig. 7.

While the first of the two mechanisms has been observed to be stronger in FM/SC/FM structures [39, 40], the contribution from the second one is more likely to be observed in FM/FM/SC structures [41]. In this case, the induced exchange field has a dominant contribution from the ferromagnet closest to the superconductor. Since the ferromagnetic layers are close to each other, spin-triplet pairs can leak efficiently into the ferromagnetic region. Similar control of the superconducting critical temperature has also been observed in systems where the magnetization of a single magnetic region can be tuned from spiral to aligned by applying an external magnetic field [42, 43].

3.2 HYBRIDS WITH ONE FERROMAGNET AND SPIN-ORBIT COUPLING

A natural next question to ask is whether we can introduce some other kind of symmetry breaking so that we can control the superconducting critical temperature in a simple SC/FM bilayer. It turns out that this is indeed possible by introducing strong interfacial Rashba spin-orbit coupling [22, 29, 80]. The interfacial Rashba spin-orbit coupling breaks the symmetry under inversions around the interface normal. The critical temperature can therefore be tuned by applying an external magnetic field that rotates the magnetization from an in-plane to an out-of-plane direction [30].

In Refs. [31, 79], and papers I and V [44, 45], we studied this system numerically by solving the Bogoliubov-de Gennes equations on a cubic lattice for the Hamiltonian

$$H = -t \sum_{\langle i,j \rangle, \sigma} c_{i,\sigma}^\dagger c_{j,\sigma} - \sum_i \mu_i c_{i,\sigma}^\dagger c_{i,\sigma} - \sum_i U_i n_{i,\uparrow} n_{i,\downarrow} - \frac{i}{2} \sum_{\langle i,j \rangle, \alpha, \beta} \lambda_j c_{i,\alpha}^\dagger \mathbf{n} \cdot (\boldsymbol{\sigma} \times \mathbf{d}_{i,j})_{\alpha,\beta} c_{j,\beta} + \sum_{i,\alpha,\beta} c_{i,\alpha}^\dagger (\mathbf{h}_i \cdot \boldsymbol{\sigma})_{\alpha,\beta} c_{i,\beta}. \quad (96)$$

Above, $c_{i,\sigma}^{(\dagger)}$ is the electron annihilation (creation) operator, $n_{i,\sigma} = c_{i,\sigma}^\dagger c_{i,\sigma}$ is the number operator, t is the hopping parameter for hopping between nearest neighbors, and μ is the chemical potential. The third term describes conventional on-site attractive interaction between electrons of opposite spin when $U_i > 0$. This term is treated by a mean field approximation, and the superconducting gap $\Delta_i = U_i \langle c_{i,\uparrow} c_{i,\downarrow} \rangle$ is treated self-consistently. The fourth term describes Rashba spin-orbit coupling with the magnitude λ_i . As we are considering interfacial Rashba interaction, the inversion symmetry breaking axis \mathbf{n} is taken to be the interface normal. The vector $\mathbf{d}_{i,j}$ is the vector from site i to site j , and $\boldsymbol{\sigma}$ is the vector of Pauli matrices. The fifth term introduces a Zeeman splitting in the magnetic region through the local magnetic exchange field \mathbf{h}_i . The three last terms are only nonzero in their respective regions.

In the above lattice model, we are able to study the behavior of T_c in clean systems, contrary to previous works considering the dirty limit [22, 29, 30, 80]. Since electrons are more likely to hop to nearest-neighboring lattice sites in the crystal structure, the inversion symmetry breaking effectively acts only along these axes. The critical temperature can therefore also be controlled by rotating the magnetization in the plane of the interface [31]. The modulation of T_c for an out-of-plane and in-plane rotation of the magnetization is demonstrated in Fig. 8.

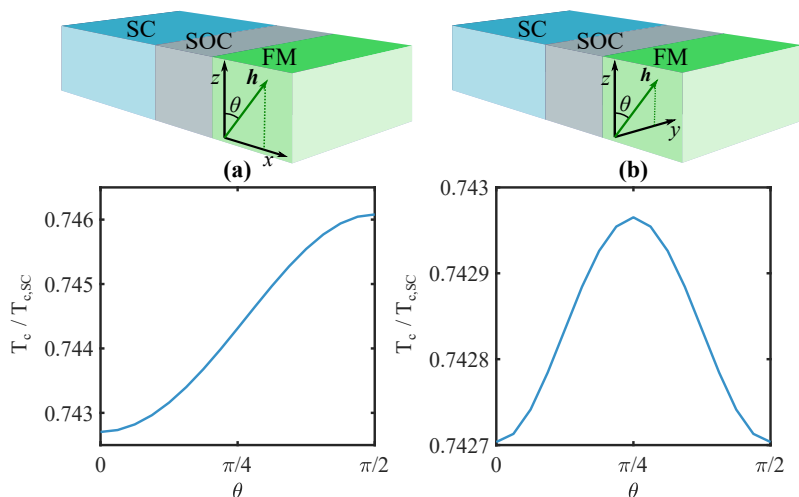


Figure 8: The critical temperature T_c in a trilayer consisting of a superconductor (SC), a thin heavy-metal layer boosting the interfacial Rashba spin-orbit coupling (SOC), and a ferromagnet (FM) can be controlled by rotating the exchange field \mathbf{h} out-of-plane (panel (a)) or in-plane (panel (b)). The $\pi/2$ period of the modulations in panel (b) is caused by the cubic lattice structure. The critical temperature is normalized by its value $T_{c,SC}$ in a superconductor without proximity to the SOC/FM layers. The figure is adapted from Refs. [31, 79], where full information about the parameters can be found.

While the orientation of the magnetization can be used to control the critical temperature, the onset of the superconducting state can also affect the magnetization direction in the adjacent ferromagnet. When the material enters the superconducting state, the free energy decreases as the electrons are bound in Cooper pairs resulting in a finite condensation energy. The superconducting contribution to the free energy therefore increases when the critical temperature is decreased and shows opposite behavior under magnetization reorientation compared to the critical temperature in Fig. 8. This was predicted in our earlier works, Refs. [31, 79].

In our experimental collaborations, papers I and V [44, 45], we show that the superconducting contribution to the free energy can affect the magnetic anisotropy of the ferromagnetic layer. The physical origin of the modulation is illustrated in Fig. 9 for an in-plane magnetization (paper I). The measurements were performed on V/MgO/Fe. The MgO boosted the Rashba spin-orbit coupling at the interface between the conventional superconductor vanadium and the ferromagnetic iron. A second hard Fe/Co ferromagnetic layer was added for measuring the magnetization direction of the soft Fe layer. In the normal-state, the magnetic anisotropy of V/MgO/Fe favors in-plane magnetization along the main crystalline (cubic) axes. The Fe/Co layer caused an additional preference for anti-parallel alignment between the soft and hard magnetic layers.

In paper I, we studied the in-plane magnetic anisotropy. The starting point for the experimental measurements were either a parallel or an anti-parallel alignment between the two magnetic layers. An external magnetic field was rotated by an in-plane angle 2π or π , respectively. During this rotation of the external magnetic field, the magnetization switched from one allowed orientation to the next, so that the effective magnetic anisotropy of the soft magnetic layer could be identified. These

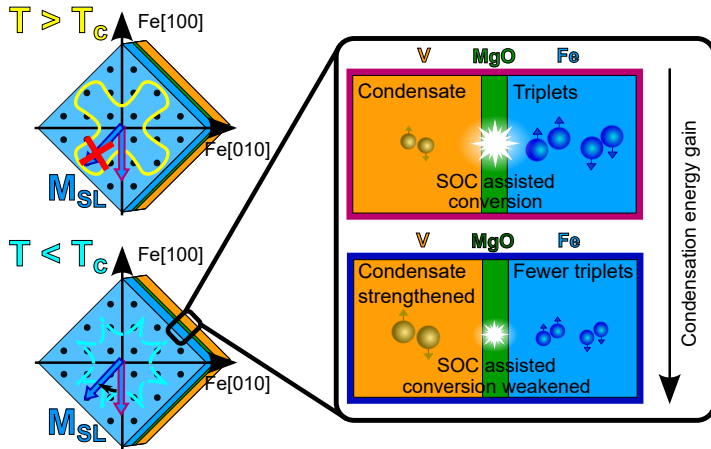


Figure 9: We consider the magnetic anisotropy of a thin ferromagnetic film with in-plane shape anisotropy. Above the critical temperature of the superconductor ($T > T_c$), the anisotropy (yellow) favors magnetization along the cubic axes (top left). When the temperature decreases below the critical temperature ($T < T_c$), local energy minima (cyan) appear at $\pi/4$ angles with respect to these axes (bottom left). This is because these magnetization directions allow for fewer spin-triplet Cooper pairs to leak into the ferromagnetic region (right). The condensate is thus strengthened causing a gain in condensation energy and local minima in the free energy. At sufficiently low temperatures, the magnetization can be trapped in these minima. The figure is adapted from paper I [44].

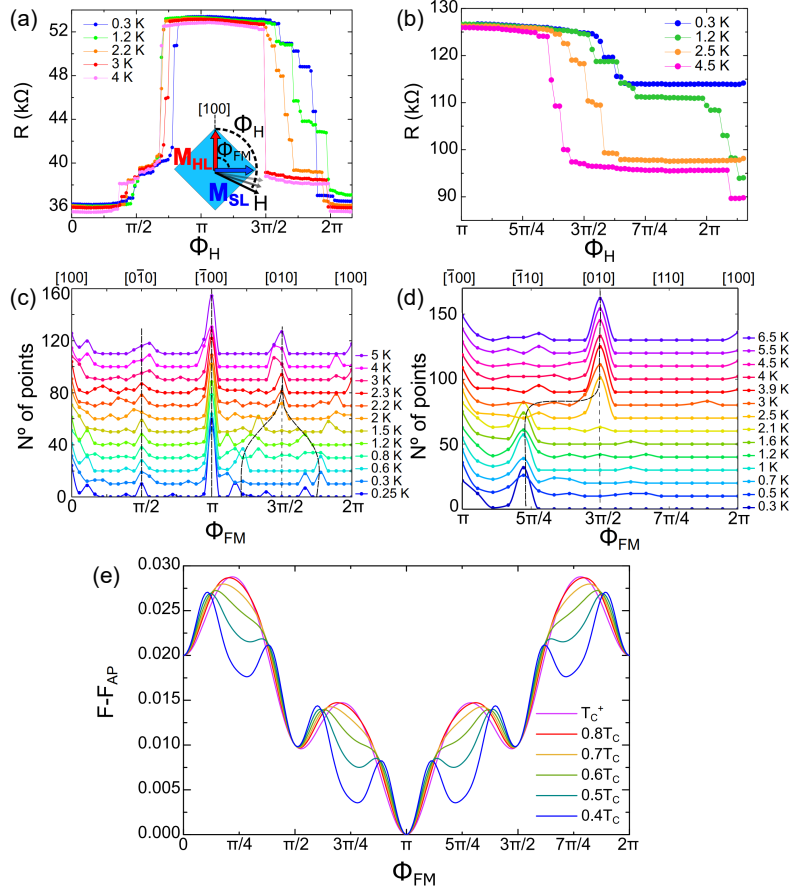


Figure 10: Panel (a) and (b) show the resistance of a V/MgO/Fe/MgO/Fe/Co junction as a function of the angle Φ_H of the external magnetic field with respect to the magnetization of the hard Fe/Co layer (see inset). Panel (c) and (d) show the same experimental data presented in the form of histograms. The height of the peaks represents the range of angles Φ_H for which the magnetization of the soft ferromagnetic layer remains at a certain angle Φ_{FM} . In panel (a) and (c), the initial magnetization alignment is parallel ($\Phi_{FM} = 0$), and in panel (b) and (d) it is anti-parallel ($\Phi_{FM} = \pi$). At $T \approx T_c/2$, the peak at $3\pi/2$ in panel (c) splits, thus establishing two additional peaks at intermediate angles (black dotted lines). In panel (d) where the initial magnetization is anti-parallel, the magnetization is completely trapped at $\Phi_{FM} = 5\pi/4$. Panel (e) shows theoretical results for the free energy F with respect to the free energy at anti-parallel alignment F_{AP} . As the temperature decreases below T_c , local minima develop at $\pi/4$ angles. Because anti-parallel alignment is favored, the energy barrier for rotating the magnetization from one local minima to the next is higher when we rotate towards parallel alignment. This explains why the magnetization is only trapped in the local minima when rotating the field towards parallel alignment (panel (c) and (d)). The difference between panel (c) and (d) can most likely be explained by an improved macrospin alignment when starting at anti-parallel alignment which increases the energy cost of rotating the magnetization. The figure is adapted from paper I [44], where full information about the parameters and experimental procedure can be found. Figure credit (panel (a)-(d)) to C. González-Ruano.

measurements were performed at different temperatures from above to well below T_c so that we could study how the magnetic anisotropy evolved with temperature. The results in Fig. 10 show that new allowed magnetization directions develop at $\pi/4$ angles with respect to the main crystalline axes as the temperature drops below $T_c/2$, as predicted by theory [31].

In paper V [45], we studied the perpendicular magnetic anisotropy of the same structure. The superconducting contribution to the free energy favors an out-of-plane magnetization direction [31]. However, compared to the in-plane reorientation discussed above, a reorientation from in-plane to out-of-plane magnetization is in principle harder to achieve due to the strong in-plane shape anisotropy. The experimental measurements [45] showed a field-free partial reorientation where the magnetization close to the interface was out-of-plane below the critical temperature for samples with small lateral size ($10 \times 10 \mu\text{m}^2$). The out-of-plane external magnetic field required to reorient the magnetization of the whole sample to an out-of-plane orientation also decreased below T_c for these samples. For larger lateral sizes, the external magnetic field required to reorient the magnetization slightly increased below T_c . This could be due to a magnetostatic interaction between vortices and magnetic inhomogeneities.

3.3 NON-MAGNETIC HYBRIDS

We have now established that including Rashba spin-orbit coupling at the interface between a superconductor and a ferromagnet can break the rotational invariance of the system. This is why T_c can be tuned by rotating the magnetization, and the magnetic anisotropy can be altered by decreasing the temperature below T_c . Rashba spin-orbit coupling is characterized by an axis \mathbf{n} around which inversion symmetry is broken. Although the Rashba spin-orbit coupling is commonly associated with interfaces, at which \mathbf{n} is simply the interface normal, Rashba-like spin-orbit coupling also exists intrinsically in some noncentrosymmetric materials. These are typically layered materials with weaker coupling between atoms in the direction perpendicular to the layers. This results in an inversion symmetry breaking axis oriented perpendicular to the layers. It is therefore in principle possible to create materials where Rashba-like spin-orbit coupling is a bulk property, and the bulk inversion symmetry breaking axis \mathbf{n} differs from the interfacial one \mathbf{n}_{int} .

To describe Rashba spin-orbit coupling where \mathbf{n} has a nonzero component along the interface, the Rashba term in Eq. (96) must be generalized to

$$-\frac{i}{2} \sum_{\langle i,j \rangle, \alpha, \beta} c_{i,\alpha}^\dagger (\lambda_{i,j} \mathbf{n} + \lambda_{j,\text{int}} \mathbf{n}_{\text{int}}) \cdot \left\{ \boldsymbol{\sigma} \times \left[\frac{1}{2} (1 + \zeta) (\mathbf{d}_{i,j})_x + (\mathbf{d}_{i,j})_{\parallel} \right] \right\}_{\alpha, \beta} c_{j,\beta} \quad (97)$$

to ensure hermiticity at the interface. Above, $(\mathbf{d}_{i,j})_x$ and $(\mathbf{d}_{i,j})_{\parallel}$ are the projections of the vector from site \mathbf{i} to site \mathbf{j} onto the interface normal \mathbf{x} and the yz plane, respectively. The factor ζ accounts for the fact that site \mathbf{i} and \mathbf{j} might be on opposite sides of the interface. If site \mathbf{i} and \mathbf{j} are both inside the SOC layer, $\zeta = 1$, and otherwise $\zeta = 0$.

In paper II [32], we consider a SC/SOC bilayer consisting of a superconductor and a material with such Rashba-like spin orbit coupling. Interfacial Rashba spin-orbit coupling is included at the lattice sites closest to the interface. Although T_c cannot be controlled by the orientation of a single ferromagnet (in the absence of spin-orbit coupling), it turns out that T_c depends on the orientation of the inversion symmetry breaking axis \mathbf{n} with respect to the interface. This is demonstrated through our numerical results in Fig. 11.

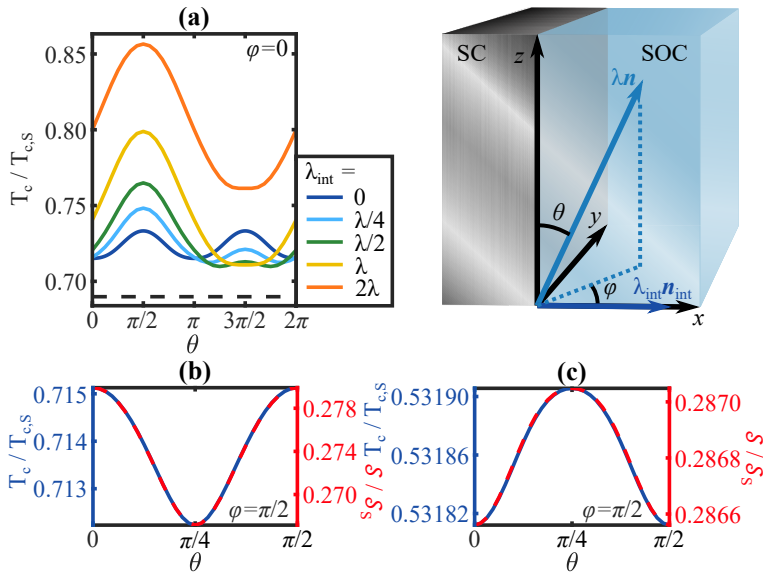


Figure 11: We consider a superconductor (SC) interfaced with a material (SOC) with an intrinsic inversion symmetry breaking axis along \mathbf{n} giving rise to Rashba spin-orbit coupling of strength λ . We additionally include interfacial Rashba spin-orbit coupling of strength λ_{int} with an inversion symmetry breaking axis along the interface normal \mathbf{n}_{int} . If the interfacial Rashba spin-orbit coupling is weak, T_c always increases when rotating \mathbf{n} from an in-plane to an out-of-plane direction (panel (a), $\lambda_{\text{int}} < \lambda$). If the interfacial spin-orbit coupling is stronger, the dominant contribution is whether the two axes are parallel or anti-parallel (panel (a), $\lambda_{\text{int}} \geq \lambda$). When \mathbf{n} is rotated in-plane, the change in T_c is smaller and $\pi/2$ periodic (panel (b) and (c)). The exact behavior depends on material parameters, but closely follows the s -wave singlet pairing amplitude \mathcal{S} . The critical temperature and spin-singlet pairing amplitude are both normalized by their values without proximity to the SOC layer, $T_{c,S}$ and \mathcal{S}_S . This figure is adapted from paper II [32], where full information about the parameters can be found.

In the case where the interfacial Rashba spin-orbit coupling is weak, the dominant effect controlling T_c is the conversion of s -wave spin-singlet correlations into other types of correlations. The correlations were investigated analytically by constructing the McMillan anomalous Green's function from scattering wave functions. If we first consider a SC/FM bilayer, conventional pairing is converted into odd-frequency s -wave and even-frequency p_x -wave spin-triplets regardless of the magnetization direction. In an SC/SOC bilayer in the case when \mathbf{n} is perpendicular to the interface, conventional pairing is instead converted into even-frequency d_{xy} -wave spin-singlets and p_y -wave spin-triplets. This is because the inversion symmetry breaking parallel to the interface causes the superconducting correlations to have negative parity under in-plane inversion. To satisfy the Pauli principle [7], this also causes the parity of the correlations perpendicular to the interface to change sign compared to the SC/FM case. The most important difference compared to the SC/FM case is the lack of odd-frequency s -wave spin-triplets. In the presence of impurity scattering, we expect these to give the dominant contribution to the T_c modulation. To create such odd-frequency s -wave triplets, we must let the axis \mathbf{n} have an in-plane component. In the case where \mathbf{n} is in-plane, we obtain a mix of all spatial pairing symmetries, as well as a mix

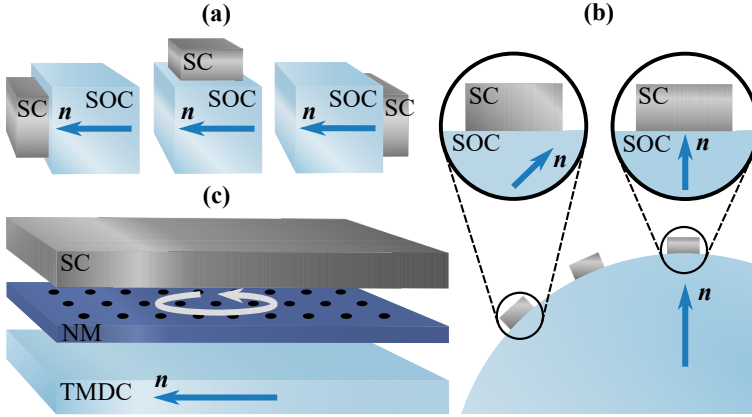


Figure 12: For observing the variation in T_c under an in-plane to out-of-plane reorientation of the inversion-symmetry breaking axis \mathbf{n} , we suggest growing the superconductor (SC) on different surfaces (panel (a)), or on a curved noncentrosymmetric material (panel (b)). For observing the in-plane variation (panel (c)), we suggest growing a normal-metal (NM) with a square lattice structure on top of a transition-metal dichalcogenide (TMDC) with in-plane \mathbf{n} . The NM/TMDC effectively enables a rotation of \mathbf{n} with respect to the lattice by growing the square lattice at different angles with respect to \mathbf{n} , so that the critical temperature of an adjacent superconductor can be studied. This figure is adapted from paper II [32].

between opposite-spin and equal-spin triplets. As seen in Fig. 11(a), this causes a suppression of T_c for in-plane \mathbf{n} .

In the case where the interfacial Rashba spin-orbit coupling becomes stronger than the intrinsic bulk spin-orbit coupling, the dominant effect is instead the mutual compensation between these. When \mathbf{n} and \mathbf{n}_{int} are parallel, the spin-orbit interaction is effectively stronger than if they are anti-parallel. Increased spin-orbit coupling causes an increase in the Fermi vector mismatch at the interface and thus increased normal-reflection [81] so that the SOC influences the critical temperature of the superconductor less. This is shown in Fig. 11(a).

While the magnetization of a ferromagnet can be rotated by applying an external magnetic field, the orientation of the inversion symmetry breaking axis \mathbf{n} cannot be controlled by any type of external field. Instead, the inversion symmetry axis is fixed during the growth of the material. We therefore suggest some possible ways of comparing different orientations of \mathbf{n} in Fig. 12.

3.4 HYBRIDS CONTAINING ANTIFERROMAGNETS

The magnets we have considered so far are ferromagnets with a net spin along the magnetization direction. Antiferromagnets have magnetic moments at each lattice site, but a zero net spin. Their interfaces can either be compensated with a finite spin or uncompensated with zero spin, as shown in Fig. 13.

Due to their zero net spin, antiferromagnets do not emit stray fields to their surroundings and they are also insensitive to disturbing magnetic fields [83]. However, the rapid spacial oscillations of magnetization makes it far from obvious whether antiferromagnets can affect experimentally observable quantities in a heterostructure. Previous studies of quasi-particle reflection [84, 85], Josephson effects [86–88], the superconducting critical temperature [89–91], and the critical field [91] in

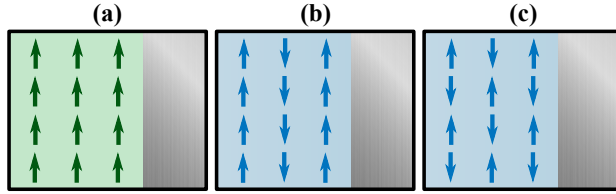


Figure 13: Ferromagnets (panel(a)) have a net magnetization, because all spins are aligned along the same axis. Uncompensated antiferromagnets (panel (b)) have zero net magnetization, but a finite magnetization at the interface since the spins in each layer are oppositely aligned. Compensated antiferromagnets (panel (c)) have zero net spin both in the bulk and at the interface since all nearest neighboring spins are oppositely orientated.

superconductor/antiferromagnet heterostructures have proved that uncompensated antiferromagnets are able to manipulate the superconducting condensate. Moreover, an uncompensated antiferromagnetic insulator can induce spin-splitting in an adjacent superconductor due to the net spin at the interface [92]. In paper IV [82], we instead consider hybrids containing compensated antiferromagnets with zero net spin at the interface. These can be studied numerically by letting the exchange field \mathbf{h}_i in Eq. (96) have opposite signs on neighboring lattice sites. We show that these interfaces can be considered spin-active despite their zero net spin. This is because spin-triplet Cooper pairs created at an interface between a superconductor and ferromagnet are scattered differently at the compensated antiferromagnetic interface depending on whether they have a net spin with respect to the Néel vector of the antiferromagnet, see Fig. 14.

Because the compensated antiferromagnetic interface differentiates between opposite-spin and equal-spin triplets, we can consider the dependence of the superconducting critical temperature on the magnetization direction of a ferromagnet in the antiferromagnetic insulator/superconductor/ferromagnet (AFI/SC/FM) structure shown in Fig. 14. The FM/SC/FM structures discussed in Sec. 3.1 has a dominant contribution to the T_c modulation from the total Zeeman splitting induced in the superconducting

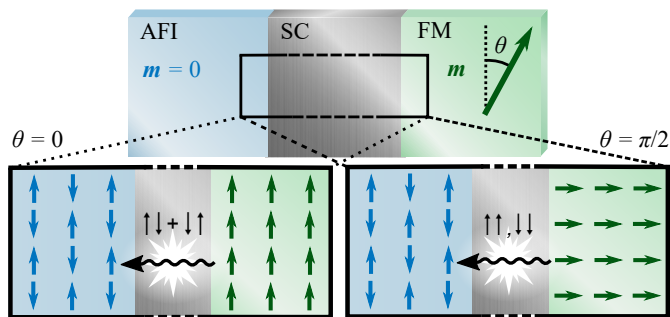


Figure 14: Although the net spin of the compensated antiferromagnetic insulator (AFI) is zero, spin-triplet Cooper pairs scatter differently at the interface depending on whether the electrons in the Cooper pair have opposite (left) or equal (right) spin with respect to the Néel vector (which is parallel to the blue arrows). Cooper pairs are created at the superconductor/ferromagnet (SC/FM) interface and their spin with respect to the Néel vector can be controlled by rotating the magnetization. The perpendicular alignment thus weakens the superconducting condensate compared to the parallel alignment. Note that this effect can be captured by rotating the magnetization in-plane. This figure is adapted from paper IV [82].

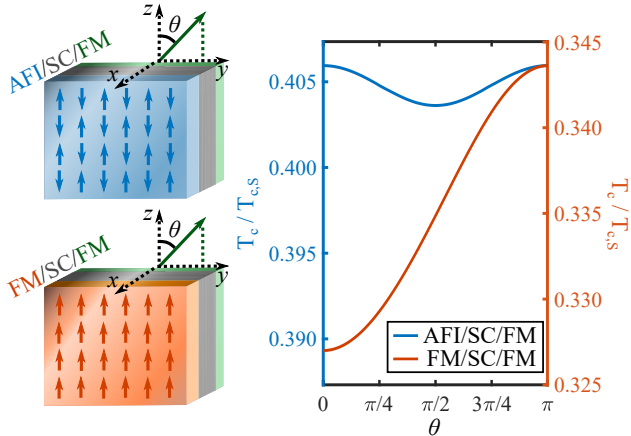


Figure 15: We consider rotating the magnetization of a ferromagnet in an uncompensated antiferromagnet/superconductor/ferromagnet (AFI/SC/FM) structure (top left) and in an FM/SC/FM structure (bottom left). For the AFI/SC/FM structure, the superconducting critical temperature T_c is suppressed when the magnetization is perpendicular to the spins in the antiferromagnet (blue). For the FM/SC/FM structure, T_c is suppressed when the magnetizations of the two ferromagnets are parallel (orange). The critical temperature is normalized by its value $T_{c,s}$ in the absence of the magnetic layers. This figure is adapted from paper IV [82], where full information about the parameters can be found.

region. The net Zeeman splitting in the AFI/SC/FM structure is independent of the magnetization direction since the antiferromagnet gives a contribution that oscillates over an atomic length scale [93]. The spin-triplet generation therefore gives the only contribution to the T_c modulation, and the critical temperature is most suppressed when the magnetic moments in the ferromagnet and antiferromagnet are perpendicular, see Fig. 15.

In paper IV [82], we also show that the free energy of the system depends on the relative orientation of the magnetic moments in the ferromagnet and antiferromagnet. This implies that the magnetic anisotropy of the system is altered when the temperature drops below the critical temperature of the superconductor as in the SC/SOC/FM systems discussed in Sec. 3.2. This opens the possibility that the superconductivity-mediated interaction between the magnetic moments can be used to control the orientation of the Néel vector by rotation of the magnetization.

3.5 HYBRIDS CONTAINING CANTED ANTIFERROMAGNETS

In the system discussed in the previous section, we needed two magnetic layers to control the triplet generation. In paper X [94], we consider an antiferromagnet where the magnetic spins can be canted so that the two sublattices are non-collinear. We find that canting gives rise to unique triplet pairs not present in the antiferromagnetic or ferromagnetic configuration. It can also be used to distinguish the recently predicted interband Néel pairing [93]. Canting is induced intrinsically in materials such as hematite [95] by Dzyaloshinskii-Moriya interaction, and can also be achieved by applying an external magnetic field [96].

To understand what happens in a canted antiferromagnet, we first have to consider the results of Ref. [93]. In this work, they considered spin-triplet generation in a

superconductor/antiferromagnet bilayer in the absence of canting. The antiferromagnet enforces a Brillouin zone periodicity of $Q = \pi/a$. Due to this periodicity, a single normal-state conduction band therefore becomes two separate bands in the reduced Brillouin zone [97]. Consider a Fermi level in the lower band, where superconducting pairing takes place between electrons with momentum k and $-k$. The spatially oscillating spin-splitting field in the superconductor induced by the adjacent antiferromagnet causes scattering by a momentum Q , thus creating Cooper pairs where the electrons have momentum $-k + Q$ and k and exist in the upper and lower band, respectively. We call this pairing an interband pairing. Since the two bands exist at different energy, the two electrons differ by an energy 2μ and there is an energy cost associated the interband pairing. The interband pairing is therefore favored close to $\mu = 0$ corresponding to half-filling.

In paper X [94], we find that while interband pairing is dominant close to half-filling, intraband pairing with an oscillating Néel character is still present away from half-filling. This intraband pairing is caused by an imprinting of the Néel pattern on the normal state wave functions. When introducing canting to the antiferromagnet, an additional ferromagnetic component appears with a spin-zero triplet component along the direction of the net magnetization. Away from half-filling, a third type of pairing also appears. This pairing has a Néel-like spatially oscillating character and has its zero-spin component along the axis perpendicular to both sublattice spins. Its absence at half-filling is explained by the perfect decoupling of the two sublattices at this particular filling factor. In a canted antiferromagnet away from half-filling, all three components of the triplet vector $[-(\uparrow\uparrow - \downarrow\downarrow), -i(\uparrow\uparrow + \downarrow\downarrow), (\uparrow\downarrow + \downarrow\uparrow)]/2$ are therefore nonzero.

The interband Néel pairing close to half-filling has a much higher amplitude than the intraband Néel pairing away from half-filling. The ferromagnetic component is less affected by the filling factor. As shown in Fig. 16, the critical temperature behaves qualitatively different at half-filling than away from half-filling. In the former case, the interband pairing in the antiferromagnetic configuration causes a stronger

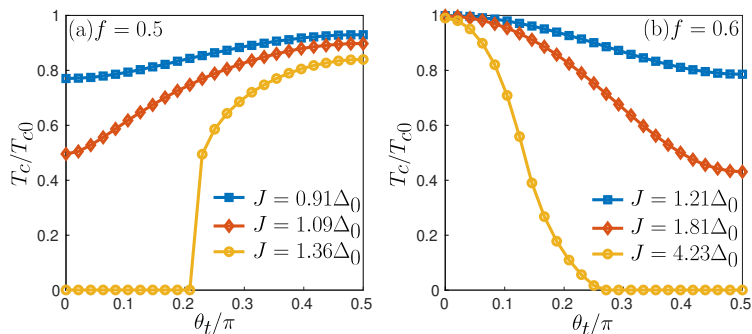


Figure 16: The superconducting critical temperature T_c at (a) half-filling ($f = 0.5$) and (b) away from half-filling ($f = 0.6$) is plotted as a function of the canting angle θ for different values of the spin-splitting J . At half-filling, the interband Néel pairing in the antiferromagnetic configuration ($\theta = 0$) suppresses T_c more strongly than in the ferromagnetic configuration ($\theta = 0.5\pi$). Away from half-filling, the weaker intraband pairing hardly affects T_c , and it is instead suppressed in the ferromagnetic configuration. Here, T_{c0} and Δ_0 are the critical temperature and superconducting gap at zero temperature and in the absence of spin-splitting. This figure and the details about the parameters are published in paper X [94]. Figure credit to S. Chourasia.

suppression of the superconducting critical temperature than in the ferromagnetic alignment. If the spin-splitting is sufficiently strong, a complete suppression of superconductivity can happen due to the opening of the antiferromagnetic gap. Away from half-filling, the antiferromagnetic intraband pairing has almost no influence on the critical temperature, and it is instead suppressed when canting the magnetic moments towards a ferromagnetic alignment. As a result, the qualitative behavior of the superconducting critical temperature can be used to distinguish the interband and intraband pairing. Note that we have here focused on the clean limit. Far away from half-filling, highly disordered superconductors have been shown to be affected by a third mechanism where non-magnetic impurities effectively act as magnetic impurities due to electrons of a particular spin having a higher probability to exist on one sublattice than the other. The magnetic scattering causes a suppression of the superconductivity [98, 99].

The results in Fig. 16 were produced for a one-dimensional superconducting chain with a spatially-oscillating spin splitting induced by an adjacent canted antiferromagnetic insulator. These results fit well with the results for thin films. As already discussed in Ref. [93], the Néel pairing forms a checkerboard pattern in the superconductor continuing the pattern of the spatially oscillating magnetic moments in the antiferromagnet. The spin-triplet pairing survives over surprisingly long distances away from the interface. In paper X [94], we further show that both the Néel component, perpendicular Néel-like component, and ferromagnetic component of the spin-triplet pairing survives over similar length scales. Away from half-filling, Friedel oscillations can cause skipping of the sign change in the alternating pattern, so that the same sign is repeated in the direction perpendicular to the interface.

3.6 T_c ENHANCEMENT BY PROXIMITY TO A STRONGER SUPERCONDUCTOR

In all of the systems discussed so far, the superconducting critical temperature has been suppressed by proximity to another material. Is it possible to instead increase the critical temperature of a superconductor by proximity to a superconductor with a higher critical temperature? Due to their spin-triplet symmetry, p -wave superconductors contain spinful Cooper pairs and can therefore carry spin-polarized supercurrents. They are also interesting from the viewpoint of quantum computation due to their topologically protected edge states [100]. However, candidate materials have a low critical temperature and are sensitive to disorder. One possible candidate could be Sr_2RuO_4 with $T_c = 1.5\text{K}$, although the pairing symmetry of this material has been debated [52, 101–103]. Previous attempts at increasing the critical temperature of Sr_2RuO_4 includes local enhancements close to Ru inclusions [104, 105] and dislocations [106], applying uniaxial pressure [107, 108], as well as piezoelectric techniques [109, 110].

In paper VIII [54], we demonstrate an alternative way of increasing the critical temperature of a p -wave superconductor by converting s -wave spin-singlet pairing from an adjacent conventional superconductor into p -wave spin-triplet pairing via a ferromagnetic layer, see Fig. 17. For the conventional superconductor and magnetic layer, we use the same Hamiltonian as before. To describe the p -wave spin-triplet pairing, we must include a nearest neighbor attraction $V_i > 0$ though the term

$$-\frac{1}{2} \sum_{i,j,\sigma} V_{i,j} n_{i,\sigma} n_{j,-\sigma}. \quad (98)$$

This term is also treated self-consistently, and we calculate a pairing correlation $F_{i,j} = \langle c_{i,\uparrow} c_{j,\downarrow} \rangle$. We further calculate the spin-triplet correlations as $F_{i,j}^{(T)} = (F_{i,j} - F_{j,i})/2$, and the p -wave spin-triplet pairing as

$$F_{p_x,i} = \frac{1}{2} (F_{i,i+x}^{(T)} - F_{i,i-x}^{(T)}), \quad (99)$$

$$F_{p_y,i} = \frac{1}{2} (F_{i,i+y}^{(T)} - F_{i,i-y}^{(T)}). \quad (100)$$

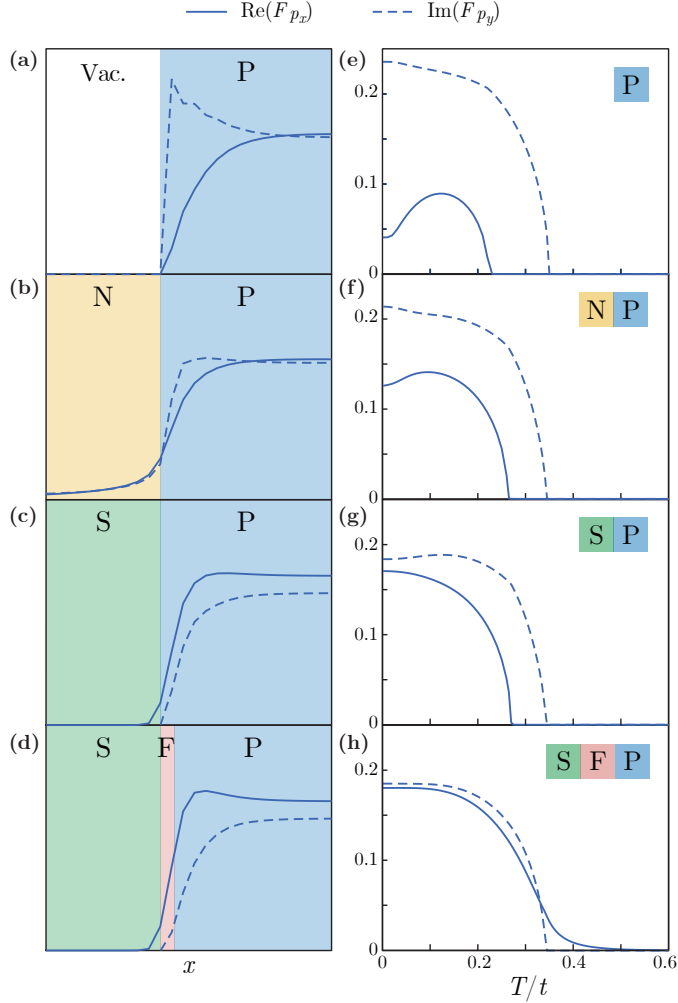


Figure 17: Panel (a)-(d) shows the p_x - and p_y -wave pairing correlations of a p -wave superconductor (P) close to its interface towards vacuum (Vac.), a normal-metal (N), an s -wave superconductor (S), and when including a thin ferromagnetic layer (F) between the s -wave and p -wave superconductor. The interface normal is oriented along x so that interface reflections suppress the p_x -wave pairing. Panel (e)-(h) shows the corresponding pairing amplitudes as a function of temperature normalized by the hopping parameter. The ferromagnetic layer provides a conversion channel between the s -wave and p_x -wave pairing causing an increase in the critical temperature of the p_x -wave pairing in panel (h). This figure and information about the parameters are published in paper VIII [54]. Figure credit to L. A. B. Olde Olthof.

We study $p_x + ip_y$ -wave pairing where $\text{Re}(F_{p_x})$ and $\text{Im}(F_{p_y})$ are nonzero.

When a p -wave superconductor has a surface towards vacuum so that the x component of the quasi-particle momentum changes sign upon reflection, the p_x -wave pairing is suppressed as the pairing correlations are odd under such a momentum inversion. This frees up electrons resulting in an increased p_y -wave pairing at the interface (Fig. 17(a)). If we replace the vacuum with a normal-metal, superconductivity can leak into the normal-metal, reducing the influence of reflections (Fig. 17(b)). This proximity effect is reduced when interfacing the p -wave superconductor with an s -wave superconductor, since the electrons in the adjacent material are already forming Cooper pairs of an incompatible pairing symmetry (Fig. 17(c)). Moreover, normal reflections are decreased. In order to mix the two pairing symmetries, we can introduce a thin ferromagnetic layer at the interface. This layer offers a conversion channel between s -wave spin-singlet and p_x -wave spin-triplet pairing. The critical temperature of the p_x -wave pairing is therefore enhanced (Fig. 17(h)) compared to the case where there is no conversion (Fig. 17(g)). A similar but stronger enhancement can be achieved by instead providing the Zeeman-splitting by applying an in-plane external magnetic field. In this case, we can choose to consider a field strength that completely suppresses the p_y wave pairing, leaving more electrons available for the p_x -wave type. However, this also produces a contamination of s -wave pairing inside the bulk of the p -wave superconductor.

The conversion channel between the conventional and spin-triplet pairing can be controlled by rotating the magnetization of the ferromagnet in-plane. This is because the quantization axis of the spin-triplets in the p -wave superconductor must be the same as the magnetization direction of the ferromagnet. If not, pairing with a different quantization axis is fed into the p -wave superconductor causing a competition between the different pairing types ($\uparrow\downarrow + \downarrow\uparrow$), ($\uparrow\uparrow$), and ($\downarrow\downarrow$) that in fact decreases the critical temperature.

Although Fig. 17 demonstrates the T_c enhancement by proximity to an s -wave superconductor, the same should be true for a $d_{x^2-y^2}$ -wave superconductor. These have the same spin-singlet symmetry as well as inversion symmetry under $x \rightarrow -x$, and should therefore mix with the p_x -wave pairing through the same conversion channel. This would offer the possibility of an even higher T_c enhancement by interfacing the p -wave superconductor with a high- T_c cuprate.

3.7 THE CRITICAL FIELD IN HIGHLY DISORDERED SUPERCONDUCTORS

In the previous sections, the superconducting phase transition has been characterized by the temperature at which the mean-field superconducting pairing correlations, or in the s -wave case the superconducting gap, vanishes. The fact that pairing correlations are present in the system is however not a guarantee for phase coherence. In highly disordered systems, the superconductivity can become granular and lose its ability to carry supercurrents [25]. In this case, the superconducting phase transition is instead characterized by the temperature at which the superfluid stiffness vanishes.

Recently, the superconducting phase transition of the hole-overdoped cuprates has attracted attention due to some surprising observations. These have often been considered more conventional than their underdoped and optimally doped counterparts [48, 111–113]. While the latter enter a strange metal or pseudogap phase in the normal-state [50], the hole-overdoped cuprates have a large Fermi surface with well-defined quasi-particles that is better described by Fermi-liquid theory [114, 115]. In the superconducting state, the superconducting transition of the underdoped and optimally doped cuprates is determined by the onset of superfluid stiffness [116].

Moreover, a competition with antiferromagnetic order can cause magnetic structures to arise around vortices [117–121] and impurities [122–124]. While the overdoped cuprates have shown a better fit with BCS-theory [50, 125], puzzling observations include the formation of Cooper pairs above the critical temperature [126–128], a large fraction of uncondensed electrons below the critical temperature [129–133], a linear decrease in the superfluid stiffness with increasing temperature and the dependence of the critical temperature on the zero-temperature superfluid stiffness [132, 134, 135]. How far these observations surpass the conventional description is still debated [136–139].

In a theoretical work studying hole-overdoped $\text{Bi}_2\text{Sr}_2\text{CaCu}_2\text{O}_{8+x}$ (Bi2212), it was shown that granular superconducting pairing survives in strongly disordered systems with vanishing superfluid stiffness [140]. In paper IX [51], we further show that when applying an out-of-plane external magnetic field to the type-II superconductor, granular superconducting pairing survives beyond the magnetic field driven superconducting transition where the superfluid stiffness vanishes. These results were obtained by solving the Bogoliubov–de Gennes equations numerically and self-consistently for the Hamiltonian

$$H = - \sum_{i,j,\sigma} t_{i,j} e^{i\phi_{i,j}} c_{i,\sigma}^\dagger c_{j,\sigma} - \sum_{i,\sigma} (\mu - V_i) n_{i,\sigma} + \sum_{\langle i,j \rangle} (\Delta_{i,j} c_{i,\uparrow}^\dagger c_{j,\downarrow}^\dagger + \text{h.c.}). \quad (101)$$

Compared to the Hamiltonian in Eq. (96), we have here included hopping up to the third nearest neighbor so that we can better control the band structure. Instead of considering an in-plane field giving rise to Zeeman splitting, we consider an out-of-plane magnetic field giving rise to orbital depairing through the Peierls phase

$$\phi_{i,j} = - \frac{\pi}{\Phi_0^{\text{SC}}} \int_{r_j}^{r_i} d\mathbf{r} \cdot \mathbf{A}(\mathbf{r}) \quad (102)$$

Above, $\Phi_0^{\text{SC}} = hc/2e$ is the superconducting flux quantum, and $\mathbf{A}(\mathbf{r}) = B(0, x, 0)$ is the vector potential in the Landau gauge resulting from a homogeneous external magnetic field B . The disorder is included by the random box potential $V_i \in [-V, V]$. The chemical potential must be adjusted in order to fix the hole density

$$x = \frac{1}{N_x N_y} \sum_{i,\sigma} \langle 1 - n_{i,\sigma} \rangle. \quad (103)$$

while considering different disorder strengths. We consider hole-doped superconductors ($0 < x \leq 1$) far away from half-filling ($x = 0$). The pairing correlation $\Delta_{i,j} = J \langle c_{i,\uparrow} c_{j,\downarrow} \rangle$ is used to calculate the spin-singlet pairing $\Delta_{i,j}^{\text{S}} = (\Delta_{i,j} + \Delta_{j,i})/2$, and the d -wave spin-singlet pairing

$$\Delta_i^{\text{d}} = \frac{1}{4} (\Delta_i^{+x} + \Delta_i^{-x} - \Delta_i^{+y} - \Delta_i^{-y}), \quad (104)$$

where $\Delta_i^{\pm x(y)} = \Delta_{i,i\pm x(y)}^{\text{S}} \exp(i\phi_{i,i\pm x(y)})$. By using this method, we demonstrate that the phase transition may be bounded by the superfluid stiffness even when the system is fully described within dirty-BCS theory.

While the superconducting pairing and superfluid stiffness is expected to vanish simultaneously at the critical field in clean systems described within BCS theory, disorder explains the remaining granular pairing in our study. In clean systems, the repulsion between vortices causes them to form a regular lattice. In Fig. 18, we show how disorder causes the vortices induced by the external magnetic field to be attracted to regions of high disorder. In these regions, the gap in the local density of states is

slightly more filled up than the average gap of the whole system. Since the vortices tend to penetrate regions where the superconductivity is already weak, superconducting islands survive well beyond the critical field where the superfluid stiffness goes to zero. In the material studied here, flat bands in the anti-nodal regions of the Fermi surface increases the sensitivity to disorder by increased scattering between momenta where the pairing correlations have opposite sign [128, 140]. Similar results have however

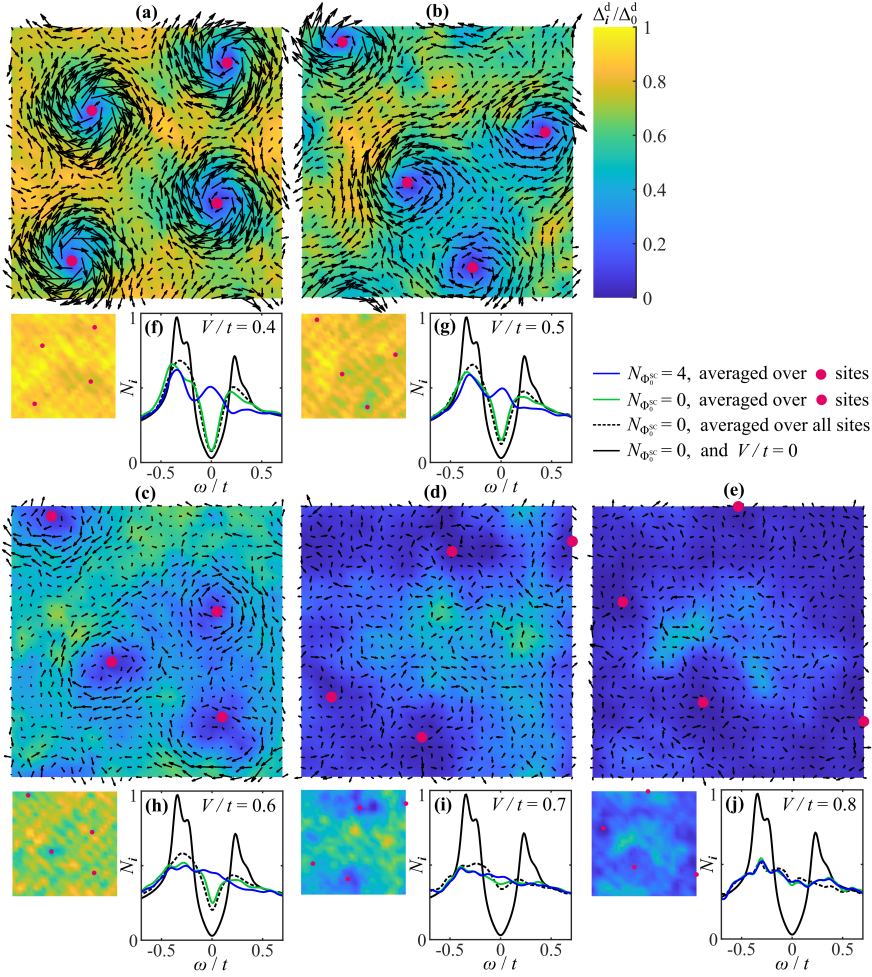


Figure 18: Panel (a)-(e) shows the d -wave superconducting pairing Δ_i^d in a magnetic unit cell penetrated by 4 vortices for an increasing disorder potential V . The corresponding plots in the absence of an external magnetic field is shown below each panel. The pairing is normalized by the superconducting pairing Δ_0^d in a clean system without an applied magnetic field. The red dots mark the centers of the vortex cores and the black arrows represent the net current through each lattice site. Panel (f)-(j) show the local density of states averaged over the vortex cores (blue), over the corresponding lattice sites (green) and over the whole lattice (dotted black) in the absence of a magnetic field (black). This figure and information about the parameters are published in paper IX [51].

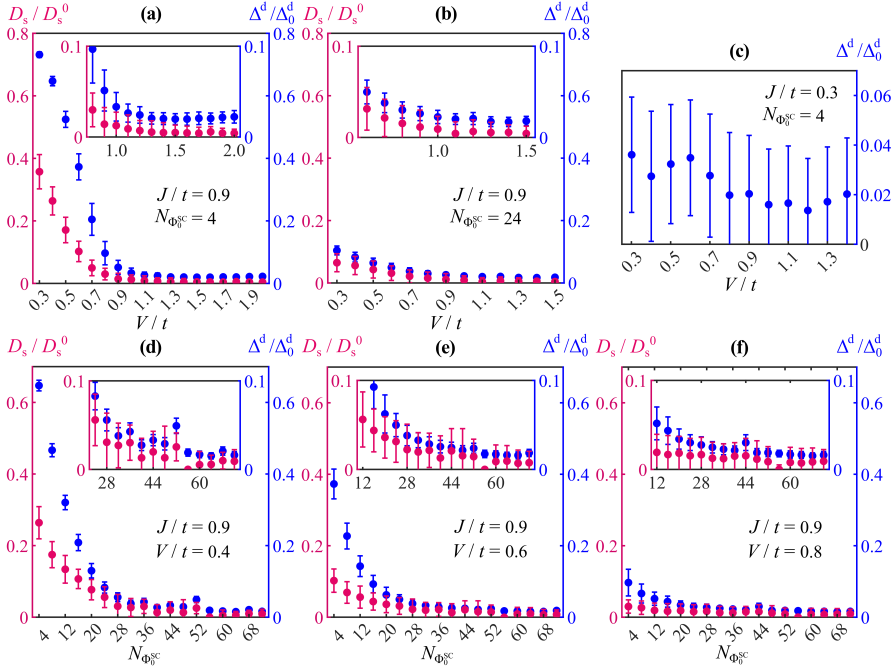


Figure 19: Panels (a) and (b) show the superfluid stiffness D_s and superconducting pairing Δ^d as a function of the disorder potential V for a magnetic unit cell penetrated by 4 and 24 superconducting flux quanta, respectively. The superfluid stiffness and superconducting pairing are normalized by their values D_s^0 and Δ_0^d in a clean system in the absence of an external magnetic field, and are averaged over space and 70-100 impurity configurations. As the error bars of the superfluid stiffness start to fall below zero, an increasing number of impurity configurations result in zero superfluid stiffness. This marks the superconducting phase transition. The superconducting pairing is finite for all disorder strengths and impurity configurations. Panel (c) shows the superconducting pairing at a lower pairing strength, and demonstrates that there is a second transition where also the superconducting pairing vanishes. Panels (d)-(f) show the superfluid stiffness and superconducting pairing as a function of the number of flux quanta penetrating a magnetic unit cell for three different disorder potentials. These panels demonstrate that a similar superconducting transition to the disorder-driven one in panel (a) and (b) can be achieved by applying an external magnetic field. The non-monotonous behavior in these plots is an artifact of the finite system size not allowing all magnetic field strengths to produce a regular vortex lattice in the clean limit. This figure and information about the parameters are published in paper IX [51].

also been found for conventional s -wave superconductors [141]. An additional physical observable related to this behavior is the absence of the Caroli-de Gennes-Matricorn (CdGM) zero-bias peak at the vortex cores of the disordered systems. The CdGM zero-bias peak have been observed in conventional superconductors [142], and in the cuprate $\text{YBa}_2\text{Cu}_3\text{O}_{7-\delta}$ (Y123) [143]. It has however proven difficult to observe in most cuprate studies [144–148], and the sensitivity towards disorder shown here could be a contributing factor.

In Fig. 19, we show impurity averaged results for the superfluid stiffness and superconducting pairing under increasing disorder and external magnetic fields. Although the small system size results in a rather large standard deviation, it is clear that the

fraction of impurity configurations resulting in zero superfluid stiffness increases as the disorder and external magnetic field increases. The superconducting pairing on the other hand is nonzero for all disorder strengths and impurity configurations in panel (a), (b), and (d)-(f). In panel (c), we demonstrate that the superconducting pairing also eventually vanishes for an increasing fraction of the impurity configurations. However, due to the robustness of the granular pairing, we have demonstrated this for a lower superconducting pairing strength so that this second transition can be captured within realistic disorder and field strengths. Thus, we expect granular superconducting pairing to survive for a wide range of field and disorder strengths beyond the superconducting transition.

While we have studied the low-temperature limit, it is likely that thermal fluctuations could lead to loss of phase coherence closer to the critical temperature. It is also unclear whether a pseudogap may appear beyond the disorder and field driven superconducting transition, as observed in the antinodal regions of the Fermi surface of the underdoped to weakly overdoped samples [149]. Also, the BdG framework is not suitable for determining the nature of the normal-state. Experiments have suggested that hole-overdoped cuprates are metallic in the normal state, suggesting that they could still be conducting beyond the two transitions [136]. The aim of this study is not to capture all aspects of the behavior of the hole-overdoped cuprates. Rather, we have considered properties that at least partially can be explained within dirty-BCS theory in order to investigate how far we can get with such a simple description.

 SPIN TRANSPORT

In this chapter, we discuss spin transport carried by Cooper pairs and quasi-particles. First, we consider how a supercurrent of spin-polarized Cooper pairs can give rise to a magnon current in an adjacent ferromagnetic insulator (paper VII). Next, we consider how quasi-particle spin transport in a superconductor is affected by an odd-frequency spin-triplet pairing symmetry (paper VI), and how the inverse spin-Hall and spin-swapping effects are renormalized by a spin-splitting field (paper XI). Finally, we discuss spin-pumping from a ferromagnetic insulator into a superconductor (paper III).

4.1 FROM COOPER PAIR CURRENTS TO MAGNON CURRENTS

Ferromagnetic insulators have a large gap in the energy spectrum that inhibits electron transport. Fluctuations in the local magnetic moments can however carry pure spin currents over long distances [150]. These are called magnon currents, as the spin fluctuations can be represented by a bosonic particle called a magnon. Conversion between these long-range magnon currents and electron-based charge and spin currents have been studied for a number of years [151–153].

Superconductors can carry spin currents via quasi-particles above the superconducting gap, similar to the electron transport in normal-metals. This transport is however dissipative, contrary to the Cooper-pair transport below the gap. In conventional superconductors, supercurrents only carry charge because the Cooper pairs consist of two electrons of opposite spin. To have dissipationless spin transport in a superconductor, we therefore need spin-polarized Cooper pairs. As described in Secs. 1.2 and 1.3, these can be induced by the proximity effect or they can exist intrinsically in p -wave superconductors.

In paper VII [24], we study how a supercurrent carried by spin-polarized Cooper pairs can induce a magnon spin current in an adjacent ferromagnetic insulator. For simplicity, we consider the case of a one-dimensional p -wave superconductor coupled to a chain of z oriented magnetic moments. We consider both charge and spin supercurrents by changing the relative center-of-mass momentum of the spin-up and spin-down Cooper pairs. The setup is shown in Fig. 20.

To describe the supercurrent, we assume the spin- σ Cooper pairs to have a center-of-mass momentum $2Q^\sigma$ by introducing a phase factor in the mean-field superconducting pairing. This results in a Hamiltonian

$$H_S = \sum_{\mathbf{k},\sigma} \epsilon_{\mathbf{k}} c_{\mathbf{k},\sigma}^\dagger c_{\mathbf{k},\sigma} - \frac{1}{2} \sum_{\mathbf{k},\sigma} \left(\Delta_{\mathbf{k},\sigma}^\delta c_{\mathbf{k}+Q^\sigma,\sigma}^\dagger c_{-\mathbf{k}+Q^\sigma,\sigma}^\dagger + \text{H.c.} \right), \quad (105)$$

where $c_{\mathbf{k},\sigma}^{(\dagger)}$ describes the annihilation (creation) of an electron with momentum \mathbf{k} and spin σ . Above, $\epsilon_{\mathbf{k}}$ is the normal-state energy dispersion, and $\Delta_{\mathbf{k},\sigma}^\delta \sim \sin(\mathbf{k} \cdot \boldsymbol{\delta})$, where $\boldsymbol{\delta} = \mathbf{x}$ in the one-dimensional x oriented chain. The important point to note about the above Hamiltonian is that the two electron operators no longer have opposite

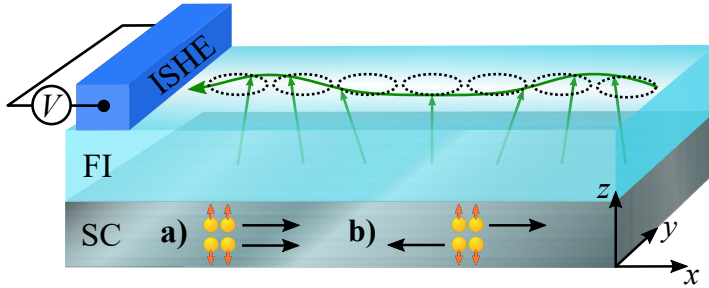


Figure 20: We let a charge supercurrent (a) or a spin supercurrent (b) carried by spin-polarized triplet Cooper pairs run through a superconductor (SC). Due to a coupling at the interface, the supercurrent can induce a magnon spin current in an adjacent ferromagnetic insulator (FI). This equilibrium magnon current alters the propagation length of an injected non-equilibrium magnon current which can be measured via the inverse spin Hall effect [154]. Although the spin of the Cooper pairs must be aligned with the magnetization, the orientation of the interface is not restricted by our model. For the experimental realization it would be beneficial to choose the magnetization in-plane. This figure is adapted from paper VII [24].

momentum due to the finite center-of-mass momentum. This produces an energy spectrum that is asymmetric with respect to inversion of momentum.

The ferromagnetic insulator is described a coupling between nearest neighbouring magnetic moments favoring parallel spins. In addition we include an anisotropy term favoring spins along the positive z direction. After performing a Holstein-Primakoff transformation, we can describe the ferromagnetic insulator by the Hamiltonian

$$H_{\text{FI}} = \sum_{\mathbf{q}} \omega_{\mathbf{q}} a_{\mathbf{q}}^{\dagger} a_{\mathbf{q}}, \quad (106)$$

where $a_{\mathbf{q}}^{(\dagger)}$ describes the annihilation (creation) of a magnon with momentum \mathbf{q} . The eigenenergy spectrum $\omega_{\mathbf{q}}$ is gapped due to the anisotropy term and symmetric under inversion of the momentum \mathbf{q} .

In order to induce a magnon spin current in the ferromagnetic insulator, we must find a way to transfer the asymmetry in the eigenenergy spectrum of the superconductor to the eigenenergy spectrum of the magnons. We do this by introducing an exchange coupling between quasi-particle spins in the superconductor and the magnetic moments in the ferromagnetic insulator. After a Holstein-Primakoff transformation, this coupling produces three terms. One term introduces a spin-splitting that can be absorbed into the Hamiltonian of the superconductor. It turns out not to be important for the magnon current generation. The second term gives a renormalization of the magnon gap. This renormalization depends on whether the system is superconducting or not, but is present also in the normal state. The most interesting term is given by

$$H_c^{2c1a} = -\lambda \sum_{\mathbf{k}, \mathbf{q}} \left(c_{\mathbf{k}+\mathbf{q}, \uparrow}^{\dagger} c_{\mathbf{k}, \downarrow} a_{-\mathbf{q}}^{\dagger} + c_{\mathbf{k}+\mathbf{q}, \downarrow}^{\dagger} c_{\mathbf{k}, \uparrow} a_{\mathbf{q}} \right). \quad (107)$$

Above, λ represents the coupling strength. In order to extract the interesting physics from this term, we perform a Schrieffer-Wolff transformation, thus projecting out first order terms in the perturbation theory, *e.g.* the term renormalizing the magnon gap. To the second order in the perturbation theory, this term allows for a momentum transfer between the electrons and the magnons, as depicted in Fig. 21.

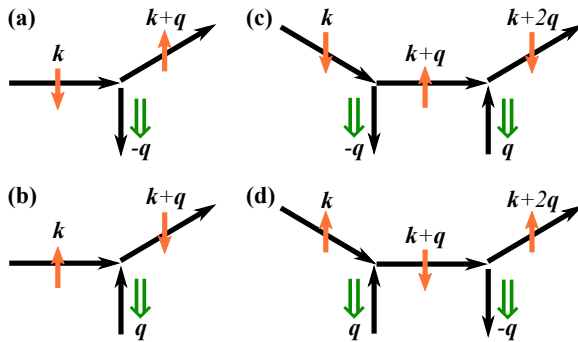


Figure 21: Equation (107) describes a process where an electron of spin $\mp 1/2$ can flip its spin (orange) by creating (panel (a)) or absorbing (panel (b)) a magnon of spin -1 (green). If we glue the two diagrams in panel (a) and (b) together, we obtain the second order processes (panels (c) and (d)). These allow for a momentum transfer between electrons and magnons.

Due to this momentum transfer, the non-reciprocity of the eigenenergy spectrum of the superconductor can be transferred to that of the magnons. We obtain an effective Hamiltonian

$$H_{\text{eff}} = \sum_{\mathbf{q}} \Omega_{\mathbf{q}} \alpha_{\mathbf{q}}^{\dagger} \alpha_{\mathbf{q}}, \quad (108)$$

with new magnon operators $\alpha_{\mathbf{q}}^{(\dagger)}$ and an eigenenergy spectrum $\Omega_{\mathbf{q}}$ that is asymmetric under inversion of \mathbf{q} . This asymmetry is demonstrated in the inset of Fig. 22. As a result, we find a finite magnon spin current density

$$j_{\delta}^z = \frac{1}{N} \sum_{\mathbf{q}} v_{\mathbf{q}}^{\delta} \langle S_{\mathbf{q}}^z \rangle_{\alpha}, \quad (109)$$

as shown in Fig. 22. Here, N is the number of lattice sites, $v_{\mathbf{q}}^{\delta}$ is the velocity and $\langle S_{\mathbf{q}}^z \rangle_{\alpha}$ the spin associated with the new magnon modes. From Fig. 22, we see that a charge and a spin supercurrent results in the same magnon spin current. Although this might seem counter intuitive, it is simply a result of the contribution from the spin-down Cooper pairs being negligible compared to the contribution from the spin-up Cooper pairs. This is because the ferromagnetic insulator breaks the symmetry between spin-up and spin-down.

Although we have here considered a p -wave superconductor, it is important to point out that the main ingredients for inducing a magnon spin current are: 1) Cooper pairs that have a spin-polarization along the magnetization direction of the ferromagnetic insulator, and 2) a coupling between the magnetic moments in the ferromagnetic insulator and the quasi-particle spins in the superconductor. It is therefore likely that a similar magnon spin current can be induced by odd-frequency s -wave Cooper pairs. This would simplify the experimental realization of the results discussed above, as the odd-frequency triplets can be conveniently created in magnetic heterostructures. In fact, a recent theoretical work [155] showed that in a conventional superconductor/ferromagnetic insulator bilayer, magnons induce spin-triplet Cooper pairs that screen the magnon spin. Notably, these spin-polarized Cooper pairs can transfer a spin signal from one ferromagnetic insulator lead to another. This ability of the magnon spin wave to act as a noncollinear magnetization, thus inducing spin-polarized Cooper pairs, makes it possible to couple magnon currents to supercurrents in conventional superconductors.

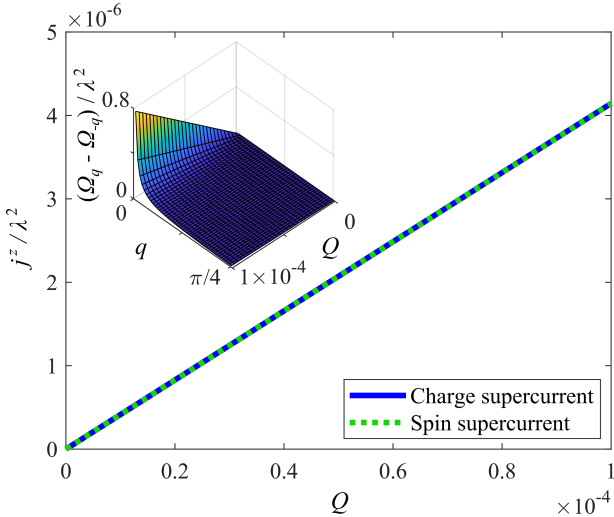


Figure 22: Both a charge ($Q^\uparrow = Q^\downarrow = Q$) and a spin ($Q^\uparrow = -Q^\downarrow = Q$) supercurrent associated with a Cooper pair center-of-mass momentum Q induce the same magnon spin current density j^z , because the contribution from spin-up Cooper pairs dominates. The inset shows the difference between the magnon energy spectrum at positive and negative magnon momenta q . The asymmetry in the eigenenergy spectrum of the superconductor is transferred to the eigenenergy spectrum of the magnons via the coupling, thus resulting in a magnon spin current. This figure and complete information about the parameters is published in paper VII [24].

To experimentally measure the induced magnon spin current, it is important to note that a supercurrent is an equilibrium phenomenon. The magnon spin current is therefore a drift current that cannot in itself perform a torque. One way of observing such a current is to inject an additional magnon current and measure the magnon propagation length in both directions. The magnon current can be injected from a spin accumulation produced by a current through the spin-Hall effect. The propagation length is longer in the direction of the magnon drift [154]. By measuring the inverse spin Hall signal from the resulting spin accumulation at a second contact [156, 157], one can compare the signal in the forward and backward direction to evaluate the magnon drift velocity.

4.2 SPIN TRANSPORT IN ODD-FREQUENCY SUPERCONDUCTORS

We will now consider quasi-particle spin transport in superconductors. Although electron transport in normal-metals and quasi-particle transport in superconductors are both dissipative, an important difference arises from the density of states. Conventional spin-singlet superconductors have a gap in the density of states. At the gap edge, there is a large increase in the density of states. These peaks ensure that the total number of states is conserved. The effect of the gap is two-fold. First, it blocks spin injections for energies below the gap. This is because conventional Cooper pairs cannot carry spin. Second, the scattering length for spin-flip scattering on magnetic impurities is greatly reduced for energies close to the gap edge [21].

In paper VI [23], we study how the quasi-particle spin transport is affected by the pairing symmetry of the Cooper pairs. In particular, we compare the non-equilibrium spin-accumulation in a material with an odd-frequency s -wave spin-triplet pairing

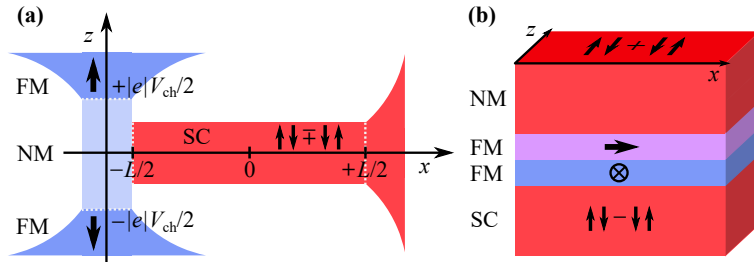


Figure 23: (a) We study the non-equilibrium spin accumulation in a conventional spin-singlet ($\uparrow\downarrow - \downarrow\uparrow$) and odd-frequency spin-triplet ($\uparrow\downarrow + \downarrow\uparrow$) superconductor (SC). A spin dependent voltage $|e|V$ is injected from a normal-metal (NM) contact. The resulting quasi-particle spin transport is relaxed by spin-orbit and spin-flip scattering inside the superconductor. The spin-dependent voltage can be obtained by applying a voltage $|e|V_{\text{ch}}$ between two oppositely oriented ferromagnets (FM). (b) An odd-frequency spin-triplet superconductor can be obtained by using misaligned ferromagnets. Spin-singlet Cooper pairs are converted into spin-triplet ones in the first ferromagnet (blue). If the second ferromagnet (pink) is sufficiently thick, only Cooper pairs that have equal spin with respect to the magnetization of this ferromagnet survives and effectively makes the normal-metal a spin-triplet superconductor. This figure is published in paper VI [23].

symmetry with the accumulation in a conventional superconductor. This can be studied in the system shown in Fig. 23. Odd-frequency superconductivity is expected to result in a different density-of-states and quasi-particle spin transport than in the conventional case. Instead of always being gapped, the density of states can also be peaked at zero energy [158, 159]. While the spin-flip scattering time remains the same as in the normal state, the quasi-particle transport in odd-frequency pairing is expected to be renormalized by spin-orbit scattering [5, 160, 161].

Since we now need to consider non-equilibrium properties, we study the conventional and odd-frequency superconductors within the quasi-classical theory by solving the Usadel equation analytically in the presence of spin-flip and spin-orbit scattering. We assume the superconducting pairing to be spatially independent. This assumption is reasonable when there is no conversion between quasi-particle current and supercurrent, a condition that applies as long as the Cooper pairs cannot carry a net spin. This is true also for the spin-triplet pairing as long as the electrons in the pair have opposite spin with respect to the injected spin. In practice, there will be a local suppression of superconductivity close to the interface. This suppression can be reduced by using a tunneling contact that reduces the proximity effect. The conventional superconducting gap follows the Bardeen-Cooper-Schrieffer temperature dependence

$$\Delta^S(T) = \Delta_0 f(T), \quad \Delta_0 = 1.76k_{\text{B}}T, \quad f(T) = \tanh\left(1.74\sqrt{\frac{T_c}{T}} - 1\right). \quad (110)$$

In order to model the odd-frequency spin-triplet superconductivity we have to make two changes to the superconducting contribution of the Usadel equation (see Sec. 2.4, Eq. (93)). First, we have to change the spin symmetry to an opposite-spin triplet one by letting $\uparrow\downarrow$ and $\downarrow\uparrow$ contributions to the gap matrix have the same sign. Second, we

need the superconducting pairing to be odd under inversion of energy. This can be captured by one of the following simple models [159]

$$\Delta^T(\epsilon, T) = \frac{Cf(T)\epsilon}{1 + \left(\frac{C\epsilon}{2\Delta_{\max}}\right)^2}, \quad \Delta^T(\epsilon, T) = \frac{Cf(T)\epsilon}{\sqrt{1 + \left(\frac{C\epsilon}{\Delta_{\infty}}\right)^2}}. \quad (111)$$

The first model describes a pairing that has a linear form $Cf(T)$ at small energies ϵ , reaches its maximum Δ_{\max} , and then decays as $\sim 1/\epsilon$. The second model has the same linear form for small energies, and approaches a constant value Δ_{∞} at large energies. We assume the temperature dependence to be inherited from the spin-singlet pairing through the proximity effect as shown in Fig. 23(b). In the figures in this section, we use the first of these two models, however they give similar results.

Focusing first on the density of states in Fig. 24(a) and (b), we see that the density of states of the spin-triplet superconductor can either be gapped around or peaked at zero energy depending on the value of $Cf(T)$. This means that if the density of states is gapped at zero temperature, an increase in temperature must cause a transition to a peaked density of states as $Cf(T)$ drops below one. Furthermore, note that when the density of states is peaked or has a narrow gap, the number of states is not conserved in our simple model. However, it has been shown that this is compensated by a dip in the density of states at higher energies [159]. If the applied spin voltage is small enough that only the lower energies are relevant, we can achieve a non-equilibrium spin accumulation that is larger than in the normal state, as shown in Fig. 24(c) and (d).

To further understand the results in Fig. 24(c) and (d), we must consider how the scattering length is renormalized by superconductivity. In a conventional superconductor, the inverse scattering length is given by

$$\frac{1}{L_{\text{sc}}(\epsilon)} = \sqrt{\frac{1}{l_{\text{so}}^2} + \frac{1}{l_{\text{sf}}^2} \frac{\epsilon^2 + |\Delta^{\text{S}}|^2}{\epsilon^2 - |\Delta^{\text{S}}|^2}}. \quad (112)$$

Thus, the spin-flip scattering length is renormalized by superconductivity and goes to zero at the gap edge. In the odd-frequency spin-triplet superconductor, the inverse scattering length is instead given by

$$\frac{1}{L_{\text{sc}}(\epsilon)} = \sqrt{\frac{1}{l_{\text{sf}}^2} + \frac{1}{l_{\text{so}}^2} \frac{\epsilon^2 + |\Delta^{\text{T}}(\epsilon)|^2}{\epsilon^2 - |\Delta^{\text{T}}(\epsilon)|^2}}. \quad (113)$$

Compared to the conventional superconductor, the spin-orbit and spin-flip scattering has changed roles. The energy dependence of the spin-triplet pairing makes the energy dependence of the renormalization a bit more complicated. It turns out that there is still a large renormalization at the gap edge, if a gap edge exists. The decay of the non-equilibrium spin accumulation in the conventional superconductor under spin-flip scattering can be seen from Fig. 24(c) and in the odd-frequency spin-triplet superconductor under spin-orbit scattering in Fig. 24(d).

Further, we explore the temperature dependence of the non-equilibrium spin accumulation. In Fig. 25, we show the results in the presence of spin-flip scattering. If the density of states is peaked at zero energy already at zero temperature, the non-equilibrium spin accumulation of the odd-frequency spin-triplet superconductor is larger than in the normal state for all temperatures up to the critical temperature as shown in panel (a). The spin accumulation in the conventional superconductor vanishes rapidly as the temperature is decreased due to the opening of the gap. If we start out with an odd-frequency spin-triplet superconductor with a gapped density

of states where the gap hinders all spin transport at zero temperature, the density of states must become peaked when the temperature increases. At the transition point $Cf(T) = 1$, the non-equilibrium spin-accumulation diverges. This is shown in panel (b).

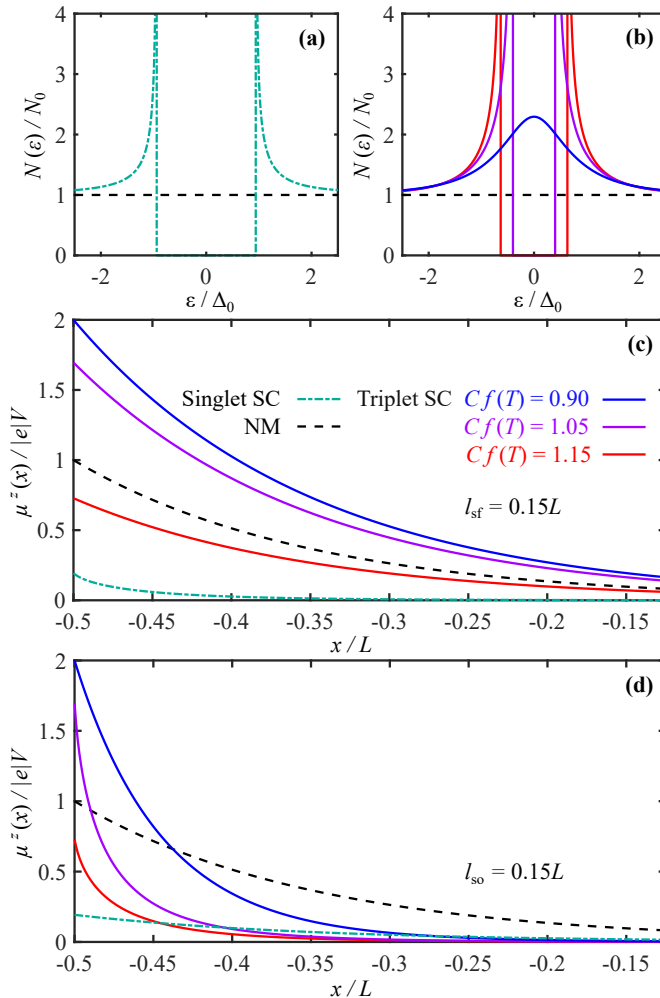


Figure 24: While the density of states of a conventional superconductor (panel (a)) is gapped, the density of states of an odd-frequency spin-triplet superconductor (panel (b)) is peaked at zero energy if $Cf(T) < 1$ and has a narrow gap if $Cf(T) > 1$. The density of states is normalized by its normal-state value (dotted black line). Due to the density of states being higher at low energies, the non-equilibrium spin accumulation μ^z can be higher than in the normal state (panel (c) and (d)). The spin-flip scattering length l_{sf} is strongly renormalized in conventional superconductors leading to a rapid decay of the non-equilibrium spin accumulation (green dotted line in panel (c)). In odd-frequency spin-triplet superconductors, the spin-orbit scattering length l_{so} is instead reduced (see the solid lines in panel (d)). The length scales are normalized by the length of the superconductor L , and the spin accumulation by the spin dependent voltage $|e|V$. This figure and complete information about the parameters are published in paper VI [23].

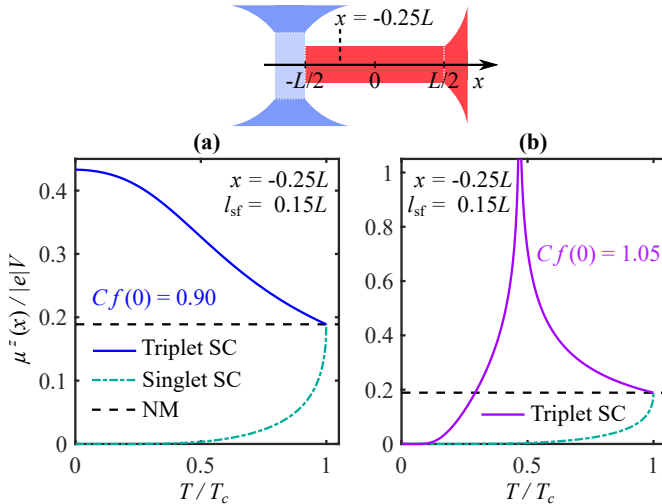


Figure 25: We consider the non-equilibrium spin accumulation μ^z normalized by the spin dependent voltage $|e|V$ in the presence of spin-flip scattering. The spin-flip scattering length l_{sf} is only renormalized for the conventional pairing. (a) For an odd-frequency spin-triplet superconductor with a density of states that is peaked at all temperatures, the spin accumulation can be larger than in the normal state. (b) When the density of states is instead gapped at low temperatures and becomes peaked at zero energy for higher temperatures, the spin-accumulation diverges at the transition point before it decreases towards the normal state value at the critical temperature T_c . In both panels, the length scales are normalized by the length of the superconductor L . This figure and complete information about the parameters are published in paper VI [23].

In the presence of spin-orbit scattering, the non-equilibrium spin accumulation in the spin-triplet superconductor decays rapidly inside the superconductor and can for a peaked density of states be either larger or smaller than in the normal state depending on how far away from the interface the spin accumulation is measured, see Fig. 26(a) and (b). The decay also smears out the peak in the non-equilibrium spin accumulation as the density of states transitions from gapped to peaked. In panel (c), this peak is still visible. In panel (d), at a distance further away from the interface, the peak has completely vanished and the spin accumulation is even smaller than in a conventional superconductor.

We have thus shown that due to the spin-symmetry and energy-dependence of the odd-frequency spin-triplet pairing, the density of states and scattering length is qualitatively different compared to the case of conventional pairing, thus resulting in a renormalized spin accumulation. The model used here is a rather simple analytical one, and there are several things that could be implemented in order to investigate other interesting effects. First, it has been shown that a gapped density of states can lead to an increased spin accumulation as the injected spin-polarized current cause an accumulation of spin at the interface [162–164]. Second, additional spin-transport can be carried by Cooper pairs if the spin-triplet pairing is spin-polarized along the polarization axis of the injected spin. This would however require a self-consistent solution as the superconducting pairing would be renormalized. Third, a spin-splitting field could allow for a coupling between the spin and energy modes, allowing for an enhanced long-range spin accumulation as predicted for conventional spin-split superconductors [165–169]. Finally, we have here assumed the spin distribution to

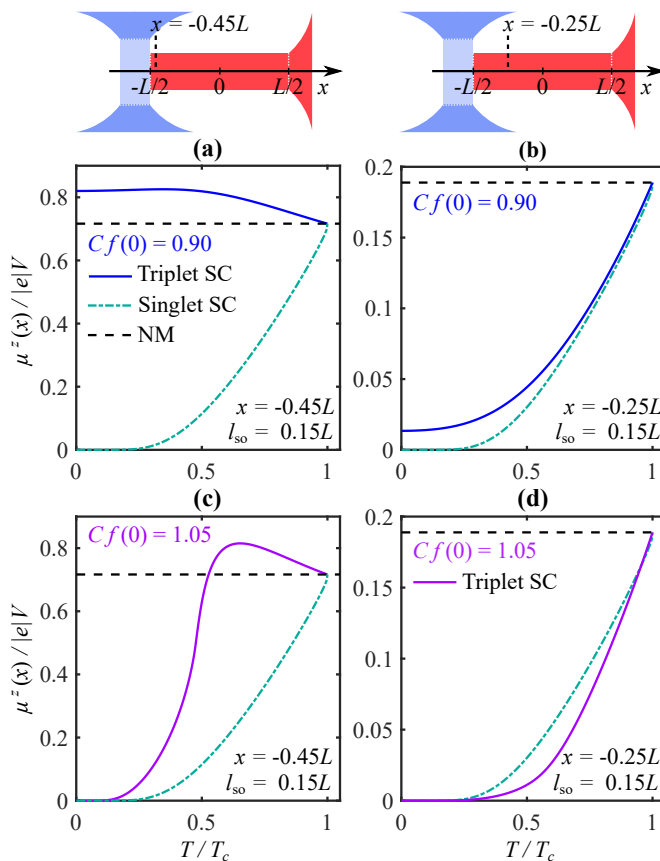


Figure 26: We consider the non-equilibrium spin accumulation μ^z normalized by the spin dependent voltage $|e|V$ in the presence of spin-orbit scattering. The spin-orbit scattering length l_{so} is only renormalized for the spin-triplet pairing. In panel (a) and (b), the density of states of the spin-triplet superconductor is peaked at zero energy for all temperatures. In panel (c) and (d), the density of states transitions from gapped to peaked as the temperature increases. At positions close to the interface (panel (a) and (c)), the results are qualitatively similar to those in Fig. 25. However, the peak in panel (c) is smeared out by the spin-orbit scattering as compared to Fig. 25(b). Further away from the interface (panel (b) and (d)), the spin accumulation decreases rapidly below the critical temperature T_c due to the renormalization of the spin-orbit scattering length. In all panels, the length scales are normalized by the length of the superconductor L . This figure and complete information about the parameters are published in paper VI [23].

be continuous at the interface, thus assuming a perfectly transparent contact. In reality, the injected spin should therefore be smaller, although this is at least partially compensated for in our results by normalizing with the normal-state spin accumulation.

4.3 TRANSVERSAL CURRENTS IN SPIN-SPLIT SUPERCONDUCTORS

In the previous section, we focused on how spin-orbit and spin-flip scattering caused the injected spin current to decay inside the superconductor. However, spin-orbit scattering can also cause generation of transversal currents. If we inject a spin current

polarized in a direction perpendicular to its propagation direction, a transversal charge current will be generated through the inverse spin-Hall effect [170, 171]. This allows for spin currents to be detected through a transverse electric voltage. The efficiency of the spin-to-charge conversion is quantified by a spin-Hall angle. For maximal detection sensitivity, it is desirable to make the spin-Hall angle as large as possible. Previous works have investigated the spin-Hall effect and its inverse in superconducting systems, both theoretically [172] and experimentally [173]. Theoretical works found a renormalization of the spin-Hall angle in the superconducting state compared to the normal state [172].

Injected spin currents with perpendicular spin polarization also lead to the generation of transversal spin currents where the spin polarization and propagation direction are swapped compared to the injected current. This effect is called spin-swapping [174]. Spin-swapping can also happen when the injected spin current is polarized along its propagation direction, in which case also the transversal spin currents have parallel spin polarization and propagation direction. The transversal spin currents cause a spin accumulation across the material so that the spin-swap signals can be measured through a spin-dependent voltage. The spin-swap angle is the same in the superconducting and normal state [172].

In paper XI, we study the inverse spin-Hall effect and spin-swapping in a superconductor under a spin-splitting field. While superconductivity have been shown to renormalize the spin-Hall angle, we show that adding spin-splitting causes a further renormalization. Moreover, we find transversal charge and spin currents that only appear in the presence of a spin-splitting field. Spin-splitting causes the spin and spin-energy currents polarized along the spin-splitting field to be coupled to the energy and charge currents, respectively. Moreover, the spin currents polarized perpendicular to the spin-splitting field are coupled together due to a precession of the spin around the spin-splitting field [67, 169]. The pairwise coupling between different types of currents opens the possibility that the energy current can contribute to the relevant transversal currents, and also enables spin-energy currents to contribute to the charge accumulation. In this context, we show that inelastic scattering plays an important role as it allows for a flow and decay of the injected energy current [67], and also leads to a huge renormalization of some of the spin-Hall and spin-swap angles in certain energy intervals.

To capture these effects, we must include corrections to the first order in the spin-orbit parameter compared to the Usadel equation derived in Sec. 2.4. In order to describe spin-swapping currents, we include third order self-energies going beyond the self-consistent Born approximation. The resulting Usadel equation is given by [68]

$$\nabla_{\mathbf{R}} \cdot \check{\mathcal{I}}(\mathbf{R}, \epsilon) = i[\check{\sigma}(\mathbf{R}, \epsilon), \check{g}_{\text{av}}^{\text{s}}(\mathbf{R}, \epsilon)] + \check{\mathcal{T}}(\mathbf{R}, \epsilon), \quad (114)$$

with the matrix current

$$\begin{aligned} \check{\mathcal{I}}(\mathbf{R}, \epsilon) = & -D \left(\check{g}_{\text{av}}^{\text{s}}(\mathbf{R}, \epsilon) \nabla_{\mathbf{R}} \check{g}_{\text{av}}^{\text{s}}(\mathbf{R}, \epsilon) \right. \\ & \left. - \frac{\theta}{2} [\hat{\rho}_3 \hat{\sigma} \times, \nabla_{\mathbf{R}} \check{g}_{\text{av}}^{\text{s}}(\mathbf{R}, \epsilon)] - \frac{i\kappa}{2} \{ \hat{\rho}_3 \hat{\sigma} \times, \check{g}_{\text{av}}^{\text{s}}(\mathbf{R}, \epsilon) \nabla_{\mathbf{R}} \check{g}_{\text{av}}^{\text{s}}(\mathbf{R}, \epsilon) \} \right). \end{aligned} \quad (115)$$

The additional terms in the second line describes the transversal currents with θ and κ being the normal-state spin-Hall and spin-swap angles, respectively. These are both of first order in the spin-orbit parameter. Above, we have defined $\hat{\rho}_3 = \text{diag}(1, 1, -1, -1)$, and $\hat{\sigma} = \text{diag}(\boldsymbol{\sigma}, \boldsymbol{\sigma}^*)$, where $\boldsymbol{\sigma}$ is the vector of Pauli matrices. The self-energy matrix $\check{\sigma}(\mathbf{R}, \epsilon)$ describes a diffusive spin-split superconductor where spin-orbit, spin-flip and inelastic scattering causes decay of the injected currents. The torque $\check{\mathcal{T}}(\mathbf{R}, \epsilon)$ is only

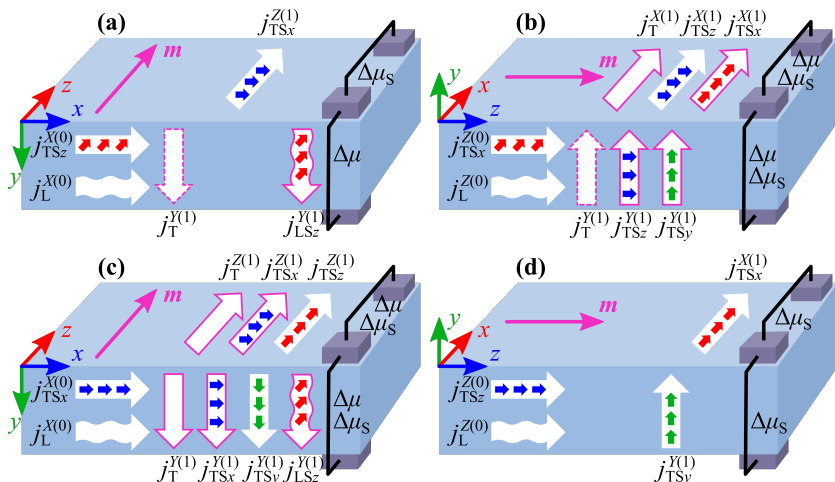


Figure 27: We inject a spin current $\mathbf{j}_{\text{TS}x_i}^{(0)}$ polarized along x_i and an energy current $\mathbf{j}_L^{(0)}$ (horizontal white arrows) into a spin-split superconductor with a spin-splitting field \mathbf{m} (pink arrow). We consider the cases where the spin polarization (small arrows) of the injected current is perpendicular (panel (a) and (b)) or parallel (panel (c) and (d)) to the direction of the injected current. From panel (a) to (b) and from panel (c) to (d), we rotate \mathbf{m} by $\pi/2$. The resulting transversal currents lead to charge and spin accumulations $\Delta\mu$ and $\Delta\mu_S$, respectively, across the superconductor. The transversal currents that are renormalized by the presence of spin-splitting are outlined by a pink dashed line, and the currents that are only present in a spin-split superconductor are outlined by a solid pink line.

non-zero in the presence of supercurrents and is therefore not included in our results where we only consider quasi-particle transport. We calculate the transversal currents and their associated spin-Hall and spin-swap angles from the Keldysh part of the above matrix current.

The transversal currents relevant for producing charge and spin accumulations across the superconductor are illustrated in Fig. 27. We consider the cases where the spin polarization is in-plane and either perpendicular or parallel to the direction of the injected spin current. For each of these two cases, we also consider a rotation of the spin-splitting field. The main features to be noted are: i) The out-of-plane inverse spin-Hall signal is renormalized in different ways in panel (a) and (b). For the magnetization direction in panel (a), the charge accumulation has a contribution from both the charge current $j_T^{Y(1)}$ and the spin-energy current $j_{LSz}^{Y(1)}$. Their spin-Hall and energy-Hall angles describing the conversion efficiency of the incoming spin and energy currents are both strongly renormalized due to the coupling between the incoming currents. When rotating the field to the alignment in panel (b), only the injected spin current contributes, and the spin-Hall angles are smaller. ii) Additional spin-Hall signals appear in panels (b) and (c). The in-plane charge currents are a result of precession of the spin around the spin-splitting field, while the out-of-plane charge current in panel (c) only has a contribution from the energy current. The associated energy-Hall angle is strongly increased between the inner and outer gap edges of the spin-split density of states where only one quasi-particle spin species is present. iii) The spin-swap angles of the transversal currents present in the normal-state are neither renormalized by superconductivity nor spin-splitting. However, additional spin currents appear that only exist in the spin-split superconductor. Most of these are

converted through the normal-state spin-swap angle κ . However, the currents $j_{\text{TS}x}^{Z(1)}$ in panel (c) as well as $j_{\text{TS}x}^{X(1)}$ and $j_{\text{TS}y}^{Y(1)}$ in panel (b) depend on the injected energy current through a spin-swap angle that is strongly increased for energies between the inner and outer gap edges of the spin-split density-of-states.

In conclusion, spin-splitting not only causes a renormalization of the spin-Hall angle allowing for increased spin detection sensitivity. It also allows for transversal charge and spin currents that can be turned completely on and off by a $\pi/2$ rotation of the spin-splitting field. Superconductors can therefore provide efficient and tunable inverse spin-Hall and spin-swapping signals.

4.4 SPIN PUMPING

Another way of injecting spin currents into a material is via spin pumping [175–177]. When applying an external magnetic field to a ferromagnet, the magnetization \mathbf{m} precesses around the effective magnetic field \mathbf{B}_{eff} . The magnetization of the ferromagnet can be described by the Landau-Lifshitz-Gilbert (LLG) equation

$$\dot{\mathbf{m}} = -\gamma_0 \mathbf{m} \times \mathbf{B}_{\text{eff}} + \alpha_0 \mathbf{m} \times \dot{\mathbf{m}}. \quad (116)$$

Here, $\dot{\mathbf{m}} = \partial \mathbf{m} / \partial t$ is the time derivative of the magnetization. The $\mathbf{m} \times \mathbf{B}_{\text{eff}}$ term describes the precession resulting from the effective magnetic field, where γ_0 is the gyromagnetic ratio. The second term describes the damping of the precession, where α_0 is the Gilbert damping parameter.

The above magnetization precession causes spin to be injected into an adjacent material via a spin pumping current. The spin accumulation in turn results in a backflow spin current into the ferromagnet. The former depends on what kind of material the ferromagnet is attached to. The spin current enters the LLG equation as

$$\dot{\mathbf{m}} = -\gamma_0 \mathbf{m} \times \mathbf{B}_{\text{eff}} + \alpha_0 \mathbf{m} \times \dot{\mathbf{m}} - \frac{\gamma_0}{M_s d} \mathbf{j}^s \quad (117)$$

and renormalizes the gyromagnetic ratio and Gilbert damping parameter. Above, M_s is the saturation magnetization and d the thickness of the ferromagnetic insulator. The current can be written in terms of a reactive and dissipative part

$$\mathbf{j}^s = C_r \dot{\mathbf{m}} + C_d \mathbf{m} \times \dot{\mathbf{m}}, \quad (118)$$

respectively. The reactive part of the spin current is directed along the precession direction of the magnetization and renormalizes the ferromagnetic resonance (FMR) frequency. The dissipative term relaxes the magnetization towards its principal axis, thus increasing the Gilbert damping coefficient [178] and broadening the FMR linewidth [176, 179].

When the adjacent material is a superconductor, quasi-particle spin transport is only allowed above the superconducting gap. This causes decreased spin pumping below the superconducting critical temperature [180, 181]. Other works found a coherence peak in the Gilbert damping just below the superconducting critical temperature [182, 183] and enhancement under an exchange field [184]. The observation of an increased FMR linewidth showed that the presence of spin-polarized Cooper pairs can lead to an enhanced dissipative component of the spin current in the superconducting state [185]. There has been many theoretical advances in explaining spin pumping into superconductors in superconductor/ferromagnet bilayers [181, 186–190] and Josephson junctions [191] with one precessing ferromagnet, also in the presence of a spin-splitting field [192].

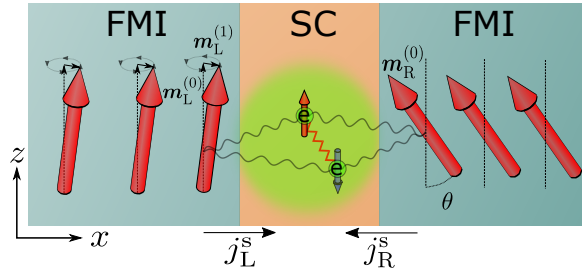


Figure 28: We consider spin currents j_L^s and j_R^s into a superconductor (SC) from two ferromagnetic insulators (FMIs) connected to the left and right interface of the superconducting film. The magnetic moments in the left FMI precess around the z axis. They have a static and a dynamic component $\mathbf{m}_L^{(0)}$ and $\mathbf{m}_L^{(1)}$, respectively. The magnetic moments of the right FMI are static and oriented with an angle θ with respect to the z axis. When the superconducting film is much thinner than the coherence length, the exchange interaction at the interface (grey wiggly line) between the electrons in the SC and the magnetic moments in the FMI induces a magnetic field in the superconductor, which we assume to be homogeneous. Electrons in the SC are further coupled together via an attractive interaction giving rise to superconductivity (red sawtooth-like line). This figure is published in paper III [69]. Figure credit to H. T. Simensen.

In paper III [69], we study spin-pumping into a thin superconducting film sandwiched between two weakly magnetized ferromagnetic insulators (FMIs). As shown in Fig. 28, we assume the left FMI to have a precessing magnetization and the right FMI to have a static magnetization. The principal axes of the two FMIs can be misaligned with respect to each other. We assume the thickness of the superconductor to be much shorter than the coherence length and the interface resistance to be larger than the bulk normal-state resistance. In this case, the ferromagnetic insulators induce a constant effective magnetic field $\mathbf{m}(t) = m_{\text{eff}}[\mathbf{m}_L(t) + \mathbf{m}_R(t)]$ in the superconductor and the Green's function can be assumed constant throughout the superconductor. Here, $\mathbf{m}_{L(R)}(t)$ is the unit vector of the magnetization in the left (right) FMI, and m_{eff} is the magnitude of the effective magnetization.

The aim of paper III [69] is to study the spin currents inside the superconductor. The current is given by

$$\mathbf{j}_X^s = \frac{N_0 m_{\text{eff}}}{4} \int_{-\infty}^{\infty} dE \left[\frac{1}{2} \left(\frac{\partial G_0^K}{\partial E} \right) \left(\frac{\partial \mathbf{m}_X}{\partial t} \right) + (\mathbf{G}^K \times \mathbf{m}_X) \right], \quad (119)$$

where N_0 is the normal-metal density of states, and $X = (L, R)$. The components of the Keldysh Green's functions are defined as $G_0^K = G_{30}^K$, and $\mathbf{G}^K = [G_{0x}^K, G_{3y}^K, G_{0z}^K]$, where $G_{ij} = \text{Tr}(\hat{G} \tau_i \sigma_j) / 4$ is a Green's function in particle-hole \otimes spin space, and τ_i and σ_j the Pauli matrices in the respective spaces. The first term in the above current is the spin-pumping current from the imaginary part of the mixing conductance. The spin-pumping current is the same in the superconducting and normal state. We can disregard the real part of the mixing conductance under the assumption that the magnetization from the FMIs is weak. The second term is the backflow current \mathbf{j}^b due to the spin accumulation in the superconductor. This is the current we will focus on, as it depends on the material properties. While we focus on the quasi-particle current contribution, a more recent work [193] have considered the magnetization dynamics of two misaligned ferromagnetic insulators coupled by spin supercurrents as well as spin pumping. Induced spin supercurrent in an FMI/FMI/SC system with two precessing magnets have also been studied recently [194].

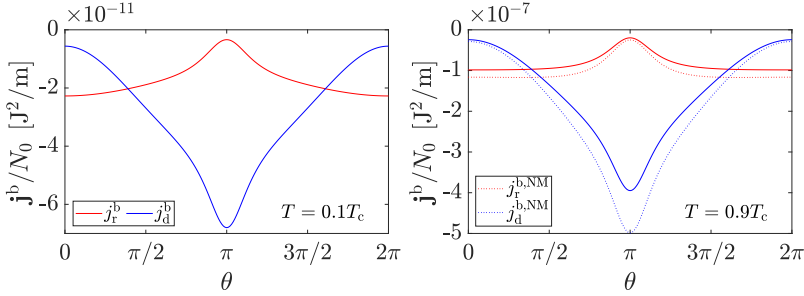


Figure 29: The backflow current \mathbf{j}^b normalized by the normal state density of states is plotted as a function of the misalignment angle θ between the magnetization in the two ferromagnetic insulators for two different temperatures below the superconducting critical temperature T_c . The red and blue curves correspond to the reactive and dissipative components, respectively. The dotted curves show the corresponding currents in the normal state. This figure is adapted from paper III [69], where complete information about the parameters can be found. Figure credit to H. T. Simensen.

To find the backflow current at the left interface, we solve the Usadel equation of the system described in Fig. 28. To obtain a realistic solution, we include spin relaxation through coupling to a normal-metal reservoir so that the Green's function can relax towards the equilibrium value around the Fermi level in the normal-metal reservoir. In order to solve the Usadel equation analytically, we make some important assumptions. We assume the gap to be constant and avoid solving the gap equation. When neglecting fluctuations in the superconducting gap $\partial\Delta/\partial t$, the equations for the Keldysh component decouples from the equations for the retarded and advanced Green's function. We decompose the effective magnetization into a static and dynamic component and keep only first order terms in the magnitude of the dynamic component by assuming that this magnitude is much smaller than the superconducting gap. This also allows us to expand the Keldysh Green's function in the dynamic component keeping only terms up to first order.

The resulting backflow current turns out to have both a reactive and dissipative component, even though the spin pumping current is purely reactive. The backflow current is plotted as a function of the misalignment angle between the two FMIs in Fig. 29. The spin pumping current is purely reactive and equal to $\mathbf{j}^p/N_0 = 10^{-5} \text{ J}^2/\text{m}$. The reactive and dissipative backflow currents is four orders of magnitude larger at $T = 0.9T_c$ than at $T = 0.1T_c$. This is because singlet pair formation hinders spin injection into the superconductor. At parallel alignment $\theta = 0$, the reactive component of the current dominates. This is because the effective magnetization inside the superconductor is large, and Hanle precession of \mathbf{G}^K around the effective magnetization suppresses the reactive component by a factor m_{eff}^{-1} and the dissipative component by a factor m_{eff}^{-2} . At antiparallel alignment $\theta = \pi$, the effective magnetization inside the superconductor is small and the dissipative component instead dominates. This is because the dissipative component is suppressed by a factor V^{-1} , while the reactive component is suppressed by a factor V^{-2} , where V quantifies the strength of the coupling to the normal-metal reservoir.

We next study the total spin current. The reactive component of the backflow spin current, dominating at parallel alignment, counteracts the spin-pumping current. The number of available quasi-particle states in an interval $\pm\beta^{-1}$ around the Fermi energy is larger when the temperature approaches T_c and when the effective magnetic

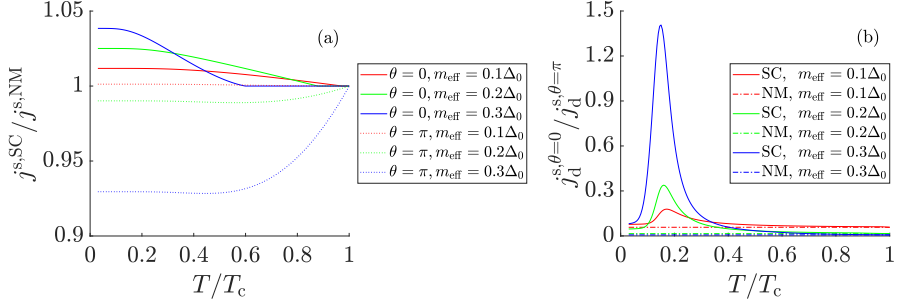


Figure 30: (a) The temperature dependence of the total spin current $j^{\text{s,SC}}$ normalized by its value in the normal state $j^{\text{s,NM}}$ is plotted for parallel ($\theta = 0$) and antiparallel ($\theta = \pi$) magnetization alignment. (b) The ratio between the dissipative part of the spin current at parallel and antiparallel alignment is plotted as a function of temperature. T_c is the superconducting critical temperature. This figure is adapted from paper III [69], where complete information about the parameters can be found. Figure credit to H. T. Simensen.

field is strong. The spin accumulation and thus the backflow spin current is therefore larger in the normal state and for strong magnetic fields. This causes the total spin current to be larger below the critical temperature and field than in the normal state, as shown by the solid curves ($\theta = 0$) in Fig. 30(a). The dissipative component of the backflow spin current is oriented almost perpendicular to the spin pumping current, thus adding to the total spin current. Due to the increased spin accumulation and backflow spin current in the normal state, the total current is therefore smaller below the critical temperature, as shown by the dotted curves ($\theta = \pi$) in Fig. 30(a). In Fig. 30(b), we see that the ratio between the dissipative backflow current in the parallel and antiparallel alignment has a peak at a temperature well below T_c . This peak appears at the temperature $\beta^{-1} \approx \Delta$ where the coherence peaks at the gap edge of the density of states becomes important for the quasi-particle spin injection.

CONCLUSIONS AND OUTLOOK

In this thesis, we have studied the theory of spin-dependent effects and transport in heterostructures involving superconductors, magnets, and non-centrosymmetric materials. Our results are roughly divided into those concerning the superconducting phase transition and its influence on adjacent materials, and those describing different kinds of spin-transport.

We started out by investigating the superconducting phase transition. We considered spin-valve effects where the superconducting critical temperature depends on the magnetic configuration or asymmetries in the system. When the temperature is close to the superconducting transition temperature, superconducting spin valves allow for superconductivity to be turned on or off. This way, we can control whether the system carries resistive or dissipationless currents [39–41]. The structures studied in this thesis have the advantage that they contain no more than one ferromagnetic layer. We thus avoid exchange coupling between two or more ferromagnets, and minimize stray fields. Moreover, we are able to study the impact of spin-triplet Cooper pair generation without the net spin-splitting field in the superconducting region being modulated much.

In this line of study, we built upon previous works on superconductor/ferromagnet structures with interfacial Rashba spin-orbit coupling showing magnetic control of the superconducting critical temperature [22, 29, 30, 80]. We demonstrated that in the clean limit, the transition temperature depends not only on the orientation of the magnetization with respect to the interface, but also on its orientation with respect to the crystal structure [31]. We then showed that a similar modulation of the superconducting critical temperature can originate from Rashba-like spin-orbit coupling in an adjacent non-centrosymmetric material [32]. The transition temperature depends on the orientation of the inversion symmetry-breaking axis with respect to the interface. We further considered a superconductor sandwiched between an antiferromagnet and a ferromagnet, and showed that the compensated antiferromagnetic interface is spin-active allowing for control of the superconducting transition temperature depending on the relative alignments between the magnetization and Néel vector [82]. Taking this a step further, we realized spin-triplet generation and critical temperature modulation from a single canted antiferromagnetic insulator where the canting angle can be controlled by an external magnetic field [94]. This work also revealed possible experimental signatures of the Néel interband pairing predicted in a recent work [93].

While spin-valve effects allow for switching supercurrents on and off, another direction that has attracted attention lately is non-reciprocal transport. The superconducting diode effect provides control of the allowed direction of supercurrents [195, 196]. The basic requirements are time reversal symmetry breaking *e.g.* from an external magnetic field, and some kind of inversion symmetry breaking [197, 198]. Experiments have shown a strong superconducting diode effect in conventional superconductors without the need for exotic physics [199–201]. This is an exciting new direction that

together with spin-valve effects allows for full control of the dissipationless transport in superconductors.

Following our earlier work on superconductor/ferromagnet structures with interfacial Rashba spin-orbit coupling [31], our experimental collaborators demonstrated how the generation of spin-triplet Cooper pairs leads to changes in the magnetic anisotropy below the superconducting phase transition [44, 45]. Spin-triplet Cooper pair generation can thus be used to alter the magnetization with respect to the crystal structure, or to lower the barrier for perpendicular magnetic anisotropy. We further demonstrated that this control of the magnetic anisotropy can be used to rotate the Néel vector through rotation of the magnetization of a ferromagnet coupled to the antiferromagnet via a conventional superconductor [82]. A future direction could be to use spin-triplet generation to control more complicated magnetic structures with two or more sublattices or inhomogeneous magnetization.

We also studied the superconducting transition in unconventional superconductors. We predicted an increase in the superconducting critical temperature of a p -wave superconductor when coupled to a conventional superconductor with a higher critical temperature [54]. This coupling is mediated by an interfacial ferromagnetic metal or an external Zeeman field. We also studied the magnetic field-driven superconducting phase transition in a strongly disordered hole-overdoped d -wave cuprate [51]. Beyond the field-driven transition where phase coherence is lost, we found remnant superconducting pairing.

All of the systems mentioned so far were studied by solving the Bogoliubov–de Gennes equations self-consistently (Sec. 2.1) or by calculating triplet correlations from the McMillan Green’s function (Sec. 2.2). These theoretical frameworks can be used to study a wide array of systems. In addition to the systems described above, they have also been used for predictions regarding topological materials and Majorana modes [202–204], non-reciprocal critical currents [205, 206], honeycomb structures such as graphene [207], and so on. While there is still room for studying new combinations of materials numerically, the simple analytical counterparts offer predictive power as a starting point before employing more sophisticated models.

In our study of spin transport, we have considered both Cooper pair and quasi-particle transport. We showed that currents carried by spin-polarized Cooper pairs in a superconductor can give rise to a magnon current in a ferromagnetic insulator [24]. Thus, the non-reciprocity in the energy spectrum of the superconductor caused by the supercurrents induces a non-reciprocity in the magnon dispersion. Similar non-reciprocity has been shown as a result of interfacial Dzyaloshinskii-Moriya interaction and the magnon Hanle effect in non-superconducting systems [156, 157]. Due to the supercurrent being an equilibrium phenomenon, the spin transport in the ferromagnetic insulator is also an equilibrium current. It would be advantageous to instead be able to induce non-equilibrium magnon spin transport.

Although quasi-particle currents are dissipative, we have seen that quasi-particle transport in superconductors is of interest due to the superconductor’s ability to renormalize the currents. This is both a result of its influence in the density of states and the renormalization of the scattering rates resulting from different kinds of spin-dependent scattering [21, 23]. Moreover, we have seen that coupling between two ferromagnetic insulators can be mediated by a superconductor affecting spin-pumping [69]. Replacing the second ferromagnet with other symmetry breaking materials could be of interest. These ideas have already partially been explored by several groups [189, 190, 192–194].

In this thesis, we have mostly focused on heterostructures containing conventional superconductors. A few of the works consider unconventional d -wave cuprates or

spin-triplet p -wave superconductors. There are however many other unconventional materials that could harbor spin-triplet superconductivity and unveil interesting physics in heterostructures. One example is the strongly correlated doped insulators in two-dimensional honeycomb materials such as graphene, where the valley degree of freedom offer possibilities of spin-triplet pairing symmetries [208]. Superconductivity in such materials can moreover be controlled by the twist angle between two layers [209]. In these two-dimensional materials, even more exotic types of superconductivity such as Ising [210], nematic [211] and charge-4e [212] superconductivity is expected to arise. The variety of different materials that are possible to create in the lab offers a rich playground for studying the interplay between different superconducting and magnetic orders within a single material or in heterostructures.

BIBLIOGRAPHY

- [1] A. Kamra and L. G. Johnsen, *Nat. Phys.* **19**, 469 (2023).
- [2] P.-G. de Gennes, *Superconductivity of metals and alloys* (Westview Press, 1966).
- [3] M. Tinkham, *Introduction to superconductivity* (McGraw-Hill, Inc., 1996).
- [4] A. I. Buzdin, *Rev. Mod. Phys.* **77**, 935 (2005).
- [5] F. S. Bergeret *et al.*, *Rev. Mod. Phys.* **77**, 1321 (2005).
- [6] M. Eschrig, *Rep. Prog. Phys.* **78**, 104501 (2015).
- [7] J. Linder and A. V. Balatsky, *Rev. Mod. Phys.* **91**, 045005 (2019).
- [8] H. Kamerlingh-Onnes, *Commun. Phys. Lab. Univ. Leiden* **1226**, 264 (1911).
- [9] D. van Delft and P. Kes, *Phys. Today* **63**, 38 (2010).
- [10] W. Meissner and R. Ochsenfeld, *Naturwissenschaften* **21**, 787 (1933).
- [11] F. London and H. London, *Proc. Roy. Soc.* **A149**, 71 (1935).
- [12] A. A. Abrikosov, *Zh. Eksp. Teor. Fiz.* **32**, 1442 (1957).
- [13] A. A. Abrikosov, *Sov. Phys.–JETP* **5**, 1174 (1957).
- [14] A. A. Abrikosov, *Rev. Mod. Phys.* **76**, 975 (2004).
- [15] J. N. Rjabinin and L. Shubnikow, *Nature* **135**, 581 (1935).
- [16] L. V. Shubnikov *et al.*, *Zh. Eksp. Teor. Fiz.* **7**, 221 (1937).
- [17] J. Bardeen and M. J. Stephen, *Phys. Rev.* **140**, A1197 (1965).
- [18] J. Bardeen *et al.*, *Phys. Rev.* **108**, 1175 (1957).
- [19] J. G. Daunt *et al.*, *Proc. Roy. Soc. London A* **185**, 225 (1946).
- [20] W. S. Corak *et al.*, *Phys. Rev.* **96**, 1442 (1954).
- [21] J. P. Morten *et al.*, *Phys. Rev. B* **70**, 212508 (2004).
- [22] H. T. Simensen and J. Linder, *Phys. Rev. B* **97**, 054518 (2018).
- [23] L. G. Johnsen and J. Linder, *Phys. Rev. B* **104**, 144513 (2021).
- [24] L. G. Johnsen *et al.*, *Phys. Rev. Lett.* **127**, 207001 (2021).
- [25] I. S. Beloborodov *et al.*, *Rev. Mod. Phys.* **79**, 469 (2007).
- [26] A. I. Buzdin and M. Y. Kypriyanov, *JETP Lett.* **52**, 487 (1990).
- [27] Z. Radović *et al.*, *Phys. Rev. B* **44**, 759 (1991).
- [28] A. I. Buzdin and M. Y. Kupriyanov, *JETP Lett.* **53**, 321 (1991).
- [29] S. H. Jacobsen *et al.*, *Phys. Rev. B* **92**, 024510 (2015).
- [30] N. Banerjee *et al.*, *Phys. Rev. B* **97**, 184521 (2018).
- [31] L. G. Johnsen *et al.*, *Phys. Rev. B* **99**, 134516 (2019).
- [32] L. G. Johnsen *et al.*, *Phys. Rev. Lett.* **125**, 107002 (2020).
- [33] A. F. Andreev, *Sov. Phys.–JETP* **19**, 1228 (1964).
- [34] P. G. de Gennes and D. Saint-James, *Phys. Lett.* **4**, 151 (1963).
- [35] P. G. de Gennes and E. Guyon, *Phys. Lett.* **3**, 168 (1963).

- [36] P. G. de Gennes, *Rev. Mod. Phys.* **36**, 225 (1964).
- [37] N. R. Werthamer, *Phys. Rev.* **132**, 2440 (1963).
- [38] J. J. Hauser *et al.*, *Phys. Rev.* **136**, A637 (1964).
- [39] J. Y. Gu *et al.*, *Phys. Rev. Lett.* **89**, 267001 (2002).
- [40] I. C. Moraru *et al.*, *Phys. Rev. Lett.* **96**, 037004 (2006).
- [41] P. V. Leksin *et al.*, *Phys. Rev. Lett.* **109**, 057005 (2012).
- [42] C.-T. Wu *et al.*, *Phys. Rev. Lett.* **108**, 117005 (2012).
- [43] F. Chiodi *et al.*, *Europhys. Lett.* **101**, 37002 (2013).
- [44] C. González-Ruano *et al.*, *Phys. Rev. B* **102**, 020405(R) (2020).
- [45] C. González-Ruano *et al.*, *Sci. Rep.* **11**, 19041 (2021).
- [46] P. W. Anderson, *J. Phys. Chem. Solids* **11**, 26 (1959).
- [47] J. G. Bednorz and K. A. Müller, *Z. Physik B – Condens. Matter* **64**, 189 (1986).
- [48] A. Damascelli *et al.*, *Rev. Mod. Phys.* **75**, 473 (2003).
- [49] J. Rairden and C. Neugebauer, *Proc. IEEE* **52**, 1234 (1964).
- [50] H. Alloul *et al.*, *Rev. Mod. Phys.* **81**, 45 (2009).
- [51] L. G. Johnsen, *J. Phys.: Condens. Matter* **35**, 115601 (2023).
- [52] A. P. Mackenzie and Y. Maeno, *Rev. Mod. Phys.* **75**, 657 (2003).
- [53] M. Sato and S. Fujimoto, *J. Phys. Soc. Jpn.* **85**, 072001 (2016).
- [54] L. A. B. Olde Olthof *et al.*, *Phys. Rev. Lett.* **127**, 267001 (2021).
- [55] J.-X. Zhu, *Bogoliubov-de Gennes method and its applications* (Springer, 2016).
- [56] P. Virtanen *et al.*, *Phys. Rev. B* **101**, 094507 (2020).
- [57] N. F. Q. Yuan and L. Fu, *PNAS* **119**, e2119548119 (2022).
- [58] W. L. McMillan, *Phys. Rev.* **175**, 559 (1968).
- [59] A. Furusaki and M. Tsukada, *Sol. State Commun.* **78**, 299 (1991).
- [60] B. Lu *et al.*, *arXiv:2211.10572* (2022).
- [61] B. Lu and Y. Tanaka, *Phil. Trans. Roy. Soc. A* **376**, 20150246 (2018).
- [62] J. R. Schrieffer and P. A. Wolff, *Phys. Rev.* **149**, 491 (1966).
- [63] S. Bravyi *et al.*, *Ann. Phys.* **326**, 2793 (2011).
- [64] K. D. Usadel, *Phys. Rev. Lett.* **25**, 507 (1970).
- [65] N. B. Kopnin, *Theory of nonequilibrium superconductivity* (Oxford Uni., 2001).
- [66] W. Belzig *et al.*, *Superlatt. Microstruct.* **25**, 1251 (1999).
- [67] F. S. Bergeret *et al.*, *Rev. Mod. Phys.* **90**, 041001 (2018).
- [68] C. Huang *et al.*, *Phys. Rev. B* **98**, 144515 (2018).
- [69] H. T. Simensen *et al.*, *Phys. Rev. B* **103**, 024524 (2021).
- [70] M. Y. Kuprianov and V. F. Lukichev, *Zh. Eksp. Teor. Fiz* **94**, 149 (1988).
- [71] A. Millis *et al.*, *Phys. Rev. B* **38**, 4504 (1988).
- [72] C. J. Lambert *et al.*, *Phys. Rev. B* **55**, 6015 (1997).
- [73] Y. V. Nazarov, *Superlatt. Microstruct.* **25**, 1221 (1999).
- [74] T. Tokuyasu *et al.*, *Phys. Rev. B* **38**, 8823 (1988).

- [75] F. S. Bergeret *et al.*, *Phys. Rev. B* **86**, 214516 (2012).
- [76] P. Machon *et al.*, *Phys. Rev. Lett.* **110**, 047002 (2013).
- [77] M. Eschrig *et al.*, *New J. Phys.* **17**, 083037 (2015).
- [78] M. Eschrig, *Phys. Today* **64**, 43 (2011).
- [79] L. G. Johnsen, *Controllable superconducting phase transition and magnetization reorientation due to spin-orbit interactions* (Master Thesis, Norwegian University of Science and Technology, 2019).
- [80] J. A. Ouassou *et al.*, *Sci. Rep.* **6**, 1 (2016).
- [81] Y. Tanaka and M. Tsukada, *Phys. Rev. B* **42**, 2066 (1990).
- [82] L. G. Johnsen *et al.*, *Phys. Rev. B* **103**, L060505 (2021).
- [83] T. Jungwirth *et al.*, *Nat. Nanotech.* **11**, 231 (2016).
- [84] I. V. Bobkova *et al.*, *Phys. Rev. Lett.* **94**, 037005 (2005).
- [85] B. M. Andersen *et al.*, *Phys. Rev. B* **72**, 184510 (2005).
- [86] C. Bell *et al.*, *Phys. Rev. B* **68**, 144517 (2003).
- [87] B. M. Andersen *et al.*, *Phys. Rev. Lett.* **96**, 117005 (2006).
- [88] P. Komissinskiy *et al.*, *Phys. Rev. Lett.* **99**, 017004 (2007).
- [89] M. Hübener *et al.*, *J. Phys.: Condens. Matter* **14**, 8687 (2002).
- [90] K. Westerholt *et al.*, *Phys. Rev. Lett.* **95**, 097003 (2005).
- [91] B. L. Wu *et al.*, *Appl. Phys. Lett.* **103**, 152602 (2013).
- [92] A. Kamra *et al.*, *Phys. Rev. Lett.* **121**, 247702 (2018).
- [93] G. A. Bobkov *et al.*, *Phys. Rev. B* **106**, 144512 (2022).
- [94] S. Chourasia *et al.*, [arXiv:2303.18145](https://arxiv.org/abs/2303.18145) (2023).
- [95] A. H. Morrish, *Canted antiferromagnetism: hematite* (World Scientific, 1994).
- [96] T. Wimmer *et al.*, *Phys. Rev. Lett.* **125**, 247204 (2020).
- [97] V. Baltz *et al.*, *Rev. Mod. Phys.* **90**, 015005 (2018).
- [98] E. H. Fyhn *et al.*, [arXiv:2210.09325](https://arxiv.org/abs/2210.09325) (2022).
- [99] G. A. Bobkov *et al.*, [arXiv:2303.14225](https://arxiv.org/abs/2303.14225) (2023).
- [100] N. V. Gnezdilov *et al.*, *Phys. Rev. B* **92**, 121406 (2015).
- [101] Y. Maeno *et al.*, *Nature* **372**, 532 (1994).
- [102] A. P. Mackenzie *et al.*, *Phys. Rev. Lett.* **80**, 161 (1998).
- [103] C. Kallin, *Rep. Prog. Phys.* **75**, 042501 (2012).
- [104] Y. Maeno *et al.*, *Phys. Rev. Lett.* **81**, 3765 (1998).
- [105] S. Acharya *et al.*, *Commun. Phys.* **2**, 163 (2019).
- [106] Y. A. Ying *et al.*, *Nat. Commun.* **4**, 2596 (2013).
- [107] S. Kittaka *et al.*, *J. Phys. Soc. Jpn.* **78**, 103705 (2009).
- [108] S. Kittaka *et al.*, *Phys. Rev. B* **81**, 180510 (2010).
- [109] C. W. Hicks *et al.*, *Science* **344**, 283 (2014).
- [110] A. Steppke *et al.*, *Science* **355**, eaaf9398 (2017).
- [111] C. M. Varma *et al.*, *Phys. Rev. Lett.* **63**, 1996 (1989).
- [112] H. Alloul *et al.*, *Phys. Rev. Lett.* **63**, 1700 (1989).

- [113] J. Rossat-Mignod *et al.*, *Phys. C: Supercond.* **185**, 86 (1991).
- [114] M. Platé *et al.*, *Phys. Rev. Lett.* **95**, 077001 (2005).
- [115] B. Vignolle *et al.*, *Nature* **455**, 952 (2008).
- [116] V. J. Emery and S. A. Kivelson, *Nature* **374**, 434 (1995).
- [117] B. Lake *et al.*, *Science* **291**, 1759 (2001).
- [118] E. Demler *et al.*, *Phys. Rev. Lett.* **87**, 067202 (2001).
- [119] J.-X. Zhu and C. S. Ting, *Phys. Rev. Lett.* **87**, 147002 (2001).
- [120] J. E. Hoffman *et al.*, *Science* **295**, 466 (2002).
- [121] J.-X. Zhu *et al.*, *Phys. Rev. Lett.* **89**, 067003 (2002).
- [122] M.-H. Julien *et al.*, *Phys. Rev. Lett.* **84**, 3422 (2000).
- [123] Z. Wang and P. A. Lee, *Phys. Rev. Lett.* **89**, 217002 (2002).
- [124] B. M. Andersen *et al.*, *Phys. Rev. Lett.* **99**, 147002 (2007).
- [125] O. Simard *et al.*, *Phys. Rev. B* **100**, 094506 (2019).
- [126] K. K. Gomes *et al.*, *Nature* **447**, 569 (2007).
- [127] A. N. Pasupathy *et al.*, *Science* **320**, 196 (2008).
- [128] Y. He *et al.*, *Phys. Rev. X* **11**, 031068 (2021).
- [129] Y. J. Uemura *et al.*, *Nature* **364**, 605 (1993).
- [130] C. Niedermayer *et al.*, *Phys. Rev. Lett.* **71**, 1764 (1993).
- [131] P. M. C. Rourke *et al.*, *Nat. Phys.* **7**, 455 (2011).
- [132] I. Božović *et al.*, *Nature* **536**, 309 (2016).
- [133] F. Mahmood *et al.*, *Phys. Rev. Lett.* **122**, 027003 (2019).
- [134] J. Wu *et al.*, *Nature* **547**, 432 (2017).
- [135] C. Herrera *et al.*, *Phys. Rev. B* **103**, 024528 (2021).
- [136] I. Božović *et al.*, *J. Supercond. Nov. Magn.* **31**, 2683 (2018).
- [137] N. R. Lee-Hone *et al.*, *Phys. Rev. B* **96**, 024501 (2017).
- [138] N. R. Lee-Hone *et al.*, *Phys. Rev. Res.* **2**, 013228 (2020).
- [139] D. Wang *et al.*, *Phys. Rev. Lett.* **128**, 137001 (2022).
- [140] Z.-X. Li *et al.*, *npj Quantum Mater.* **6**, 36 (2021).
- [141] A. Datta *et al.*, *arXiv:2001.00220* (2021).
- [142] H. F. Hess *et al.*, *Phys. Rev. Lett.* **62**, 214 (1989).
- [143] C. Berthod *et al.*, *Phys. Rev. Lett.* **119**, 237001 (2017).
- [144] C. Renner *et al.*, *Phys. Rev. Lett.* **80**, 3606 (1998).
- [145] B. W. Hoogenboom *et al.*, *Physica C: Supercond.* **332**, 440 (2000).
- [146] S. H. Pan *et al.*, *Phys. Rev. Lett.* **85**, 1536 (2000).
- [147] G. Levy *et al.*, *Phys. Rev. Lett.* **95**, 257005 (2005).
- [148] S. Yoshizawa *et al.*, *J. Phys. Soc. Jpn.* **82**, 083706 (2013).
- [149] E. Fradkin *et al.*, *Rev. Mod. Phys.* **87**, 457 (2015).
- [150] L. J. Cornelissen *et al.*, *Nat. Phys.* **11**, 1022 (2015).
- [151] A. V. Chumak *et al.*, *Nat. Phys.* **11**, 453 (2015).

- [152] W. Han *et al.*, *Nat. Mater.* **19**, 139 (2020).
- [153] A. Brataas *et al.*, *Phys. Rep.* **885**, 1 (2020).
- [154] S. De-La-Peña *et al.*, *J. Phys.: Condens. Matter* **34**, 295801 (2022).
- [155] I. V. Bobkova *et al.*, *Commun. Mater.* **3**, 95 (2022).
- [156] R. Schlitz *et al.*, *Phys. Rev. Lett.* **126**, 257201 (2021).
- [157] J. Gückelhorn *et al.*, *arXiv:2209.09040* (2022).
- [158] Y. Tanaka *et al.*, *Phys. Rev. Lett.* **99**, 037005 (2007).
- [159] P. O. Sukhachov and A. V. Balatsky, *Phys. Rev. B* **100**, 134516 (2019).
- [160] E. A. Demler *et al.*, *Phys. Rev. B* **55**, 15174 (1997).
- [161] T. Rachataruangsit and S. Yoksan, *Physica C: Supercond.* **467**, 156 (2007).
- [162] F. J. Jedema *et al.*, *Phys. Rev. B* **60**, 16549 (1999).
- [163] S. Takahashi and S. Maekawa, *Phys. Rev. B* **67**, 052409 (2003).
- [164] N. Poli *et al.*, *Phys. Rev. Lett.* **100**, 136601 (2008).
- [165] H. Yang *et al.*, *Nat. Mater.* **9**, 586 (2010).
- [166] F. Hübler *et al.*, *Phys. Rev. Lett.* **109**, 207001 (2012).
- [167] C. H. L. Quay *et al.*, *Nat. Phys.* **9**, 84 (2013).
- [168] M. J. Wolf *et al.*, *Phys. Rev. B* **87**, 024517 (2013).
- [169] M. Silaev *et al.*, *Phys. Rev. Lett.* **114**, 167002 (2015).
- [170] M. I. Dyakonov and V. I. Perel, *Phys. Lett. A* **35**, 459 (1971).
- [171] J. E. Hirsch, *Phys. Rev. Lett.* **83**, 1834 (1999).
- [172] C. Espedal *et al.*, *Phys. Rev. B* **95**, 054509 (2017).
- [173] T. Wakamura *et al.*, *Nat. Mater.* **14**, 675 (2015).
- [174] M. B. Lifshits and M. I. Dyakonov, *Phys. Rev. Lett.* **103**, 186601 (2009).
- [175] A. Brataas *et al.*, *Phys. Rev. B* **66**, 060404 (2002).
- [176] Y. Tserkovnyak *et al.*, *Phys. Rev. Lett.* **88**, 117601 (2002).
- [177] Y. Tserkovnyak *et al.*, *Phys. Rev. B* **66**, 224403 (2002).
- [178] T. L. Gilbert, *IEEE Trans. Magn.* **40**, 3443 (2004).
- [179] Y. Tserkovnyak *et al.*, *Rev. Mod. Phys.* **77**, 1375 (2005).
- [180] C. Bell *et al.*, *Phys. Rev. Lett.* **100**, 047002 (2008).
- [181] J. P. Morten *et al.*, *Europhys. Lett.* **84**, 57008 (2008).
- [182] M. Inoue *et al.*, *Phys. Rev. B* **96**, 024414 (2017).
- [183] Y. Yao *et al.*, *Phys. Rev. B* **97**, 224414 (2018).
- [184] K.-R. Jeon *et al.*, *Phys. Rev. B* **99**, 024507 (2019).
- [185] K.-R. Jeon *et al.*, *Nat. Mater.* **17**, 499 (2018).
- [186] T. Yokoyama and Y. Tserkovnyak, *Phys. Rev. B* **80**, 104416 (2009).
- [187] T. Kato *et al.*, *Phys. Rev. B* **99**, 144411 (2019).
- [188] M. A. Silaev, *Phys. Rev. B* **102**, 180502 (2020).
- [189] M. A. Silaev, *Phys. Rev. B* **102**, 144521 (2020).
- [190] M. Tanhayi Ahari and Y. Tserkovnyak, *Phys. Rev. B* **103**, L100406 (2021).

- [191] M. Houzet, *Phys. Rev. Lett.* **101**, 057009 (2008).
- [192] R. Ojajärvi *et al.*, *Phys. Rev. B* **101**, 115406 (2020).
- [193] R. Ojajärvi *et al.*, *Phys. Rev. Lett.* **128**, 167701 (2022).
- [194] X. Montiel and M. Eschrig, *arXiv:2106.13988* (2023).
- [195] F. Ando *et al.*, *Nature* **584**, 373 (2020).
- [196] A. Daido *et al.*, *Phys. Rev. Lett.* **128**, 037001 (2022).
- [197] J. J. He *et al.*, *New J. Phys.* **24**, 053014 (2022).
- [198] M. Davydova *et al.*, *Sci. Adv.* **8**, eabo0309 (2022).
- [199] Y. Hou *et al.*, *arXiv:2205.09276* (2022).
- [200] D. Suri *et al.*, *Appl. Phys. Lett.* **121**, 102601 (2022).
- [201] A. Gutfreund *et al.*, *arXiv:2301.07121* (2023).
- [202] L. Fu and C. L. Kane, *Phys. Rev. Lett.* **100**, 096407 (2008).
- [203] Y. Tanaka *et al.*, *Phys. Rev. Lett.* **103**, 107002 (2009).
- [204] G. Francica *et al.*, *Phys. Rev. B* **101**, 094504 (2020).
- [205] K. M. D. Hals, *Phys. Rev. B* **95**, 134504 (2017).
- [206] Y. Tanaka, B. Lu, and N. Nagaosa, *Phys. Rev. B* **106**, 214524 (2022).
- [207] Y. Su and S.-Z. Lin, *Phys. Rev. B* **98**, 195101 (2018).
- [208] V. Crépel and L. Fu, *PNAS* **119**, e2117735119 (2022).
- [209] E. Y. Andrei and A. H. MacDonald, *Nat. Mater.* **19**, 1265 (2020).
- [210] D. Wickramaratne and I. I. Mazin, *arXiv:2304.03759* (2023).
- [211] Y. Cao *et al.*, *Science* **372**, 264 (2021).
- [212] R. M. Fernandes and L. Fu, *Phys. Rev. Lett.* **127**, 047001 (2021).

I

REFERENCE

César González-Ruano, Lina G. Johnsen, Diego Caso, Coriolan Tiusan, Michel Hehn, Niladri Banerjee, Jacob Linder, and Farkhad G. Aliev,
Superconductivity-induced change in magnetic anisotropy in epitaxial ferromagnet-superconductor hybrids with spin-orbit interaction,
Phys. Rev. B **102**, 020405(R) (2020).

CONTRIBUTIONS

FGA and CT designed the device, and CT and MH fabricated the junctions. The measurements were performed by CG-R with the participation of DC and CT. The modelling was developed by LGJ and JL with participation of NB. CT carried out ab-initio and DC micro-magnetic calculations. FGA, CG-R, JL, NB and LGJ analysed the data and wrote the manuscript. All authors contributed to the study, discussed the results, commented and revised the manuscript. FGA supervised the work.

Superconductivity-induced change in magnetic anisotropy in epitaxial ferromagnet-superconductor hybrids with spin-orbit interactionCésar González-Ruano,¹ Lina G. Johnsen,² Diego Caso,¹ Coriolan Tiusan,^{3,4} Michel Hehn,⁴ Niladri Banerjee,⁵ Jacob Linder,² and Farkhad G. Aliev^{1,*}¹*Departamento Física de la Materia Condensada C-III, Instituto Nicolás Cabrera (INC) and Condensed Matter Physics Institute (IFIMAC), Universidad Autónoma de Madrid, Madrid 28049, Spain*²*Center for Quantum Spintronics, Department of Physics, Norwegian University of Science and Technology, NO-7491 Trondheim, Norway*³*Department of Physics and Chemistry, Center of Superconductivity Spintronics and Surface Science C4S, Technical University of Cluj-Napoca, Cluj-Napoca 400114, Romania*⁴*Institut Jean Lamour, Nancy Université, 54506 Vandoeuvre-les-Nancy Cedex, France*⁵*Department of Physics, Loughborough University, Epinal Way, Loughborough LE11 3TU, United Kingdom*

(Received 10 March 2020; revised 1 July 2020; accepted 1 July 2020; published 15 July 2020)

The interaction between superconductivity and ferromagnetism in thin film superconductor/ferromagnet heterostructures is usually reflected by a change in superconductivity of the S layer set by the magnetic state of the F layers. Here we report the converse effect: transformation of the magnetocrystalline anisotropy of a single Fe(001) layer, and thus its preferred magnetization orientation, driven by the superconductivity of an underlying V layer through a spin-orbit coupled MgO interface. We attribute this to an additional contribution to the free energy of the ferromagnet arising from the controlled generation of triplet Cooper pairs, which depends on the relative angle between the exchange field of the ferromagnet and the spin-orbit field. This is fundamentally different from the commonly observed magnetic domain modification by Meissner screening or domain wall-vortex interaction, and it offers the ability to fundamentally tune magnetic anisotropies using superconductivity—a key step in designing future cryogenic magnetic memories.

DOI: [10.1103/PhysRevB.102.020405](https://doi.org/10.1103/PhysRevB.102.020405)

Superconductivity (S) is usually suppressed in the presence of ferromagnetism (F) [1–5]. For example, in F/S/F spin-valves the transition temperature T_C of the S layer is different for a parallel alignment of the F layer moments compared to an antiparallel alignment [6–9]. Interestingly, for noncollinear alignment of the F layer moments in spin-valves [10–12] or Josephson junctions [13–22], an enhancement in the proximity effect is found due to the generation of long-range triplet Cooper pairs, immune to the pair-breaking exchange field in the F layers. So far, the reciprocal modification of the static properties of the ferromagnet by superconductivity has been limited to restructuring [23] and pinning of magnetic domain walls (DWs) by Meissner screening and vortex-mediated pinning of DWs [24–27].

Modification of the magnetization dynamics in the presence of superconductivity has been studied in [28–36]. Recently, theoretical and experimental results have indicated an underlying role of Rashba spin-orbit coupling (SOC), resulting in an enhancement of the proximity effect and a reduction of the superconducting T_C , along with enhanced spin pumping and Josephson current in systems with a single F layer coupled to Nb through a heavy-metal (Pt) [37–43]. In this context, V/MgO/Fe [44] has been shown to be an effective system to study the effect of SOC in S/F structures with fully epitaxial layers.

At first glance, altering the magnetic order in S/F heterostructures leading to a change in the direction of magnetization appears nontrivial due to the difference in the energy scales associated with the order parameters. The exchange splitting of the spin-bands and the superconducting gap are about 10^3 and 10^1 K, respectively. However, this fundamentally changes if one considers the possibility of controlling the magnetocrystalline anisotropy (MCA) by manipulating the competing anisotropy landscape with superconductivity, since the MCA energy scales are comparable to the superconducting gap energy. Interestingly, emergent triplet superconducting phases in S/SOC/F heterostructures offer the possibility to observe MCA modification of a F layer coupled to a superconductor through a spin-orbit coupled interface, triggered by the superconducting phase [45].

In this paper, we present evidence that cubic in-plane MCA in a V/MgO/Fe(001) system is modified by the superconductivity of V through SOC at the MgO/Fe interface [46]. Our detailed characterization of the coercive fields of the rotated soft Fe(001) and sensing hard (Fe/Co) ferromagnetic layers by the tunneling magnetoresistance effect (TMR) [47] along with numerical simulations dismisses the Meissner screening and DW-vortex interactions as a source of the observed effects.

The magnetic tunnel junction (MTJ) multilayer stacks have been grown by molecular beam epitaxy (MBE) in a chamber with a base pressure of 5×10^{-11} mbar following the procedure described in [48]. The samples were grown on [001]

*farkhad.aliev@uam.es

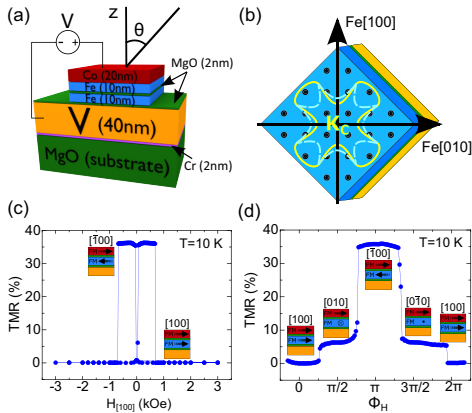


FIG. 1. (a) Sketch of the junctions under study. Fe(10 nm)/Co(20 nm) is the hard (sensing) layer while Fe(10 nm) is the soft ferromagnet where spin reorientation transitions are investigated. (b) Sketch showing the top view without the hard Fe/Co layer, with the fourfold in-plane magnetic energy anisotropy expected for the Fe(001) atomic plane of the magnetically free layer, for temperatures above T_C and well below T_C (dashed cyan). Note that during the epitaxial growth, the Fe lattice is rotated by 45° with respect to MgO. Parts (c) and (d) show in-plane spin reorientation transitions between parallel (P), perpendicular in plane (PIP), and antiparallel (AP) relative magnetization alignments of the soft and hard F layers for a $30 \times 30 \mu\text{m}^2$ junction at $T = 10$ K (above T_C). Indices above the inset sketches indicate the direction of the soft layer. The in-plane rotation has been carried out with the angle Φ_H of the magnetic field relative to the Fe[100] axis going from -30° to 390° .

MgO substrates. Then a 10-nm-thick seed of antidiffusion MgO underlayer is grown on the substrate to trap the C from it before the deposition of the Fe (or V). Then the MgO insulating layer is epitaxially grown by e-beam evaporation, the thickness is approximately ~ 2 nm, and so on with the rest of the layers. Each layer is annealed at 450°C for 20 min for flattening. After the MBE growth, all the MTJ multilayer stacks are patterned in $10\text{--}40\text{-}\mu\text{m}$ -sized square junctions (with the diagonal along [100]) by UV lithography and Ar-ion etching, controlled step-by-step *in situ* by Auger spectroscopy. The measurements are performed inside a JANIS® He³ cryostat. The magnetic field is varied using a three-dimensional (3D) vector magnet. For the in-plane rotations, the magnetic-field magnitude was kept at $70\text{--}120$ Oe, far away from the soft Fe(001) and hard Fe/Co layer switching fields obtained from in-plane TMRs (see the Supplemental Material S1 and S2 [49], which also includes Refs. [50–55]). This way, only the soft layer is rotated, and the difference in resistance can be attributed to the angle between the soft and hard layers.

Figure 1(a) shows the device structure with the Fe/Co hard layer sensing the magnetization alignment of the 10-nm-thick Fe(001) soft layer. A typical TMR plot above T_C is shown in Fig. 1(c). The resistance switching shows a standard TMR between the P and AP states. However, the epitaxial Fe(001)

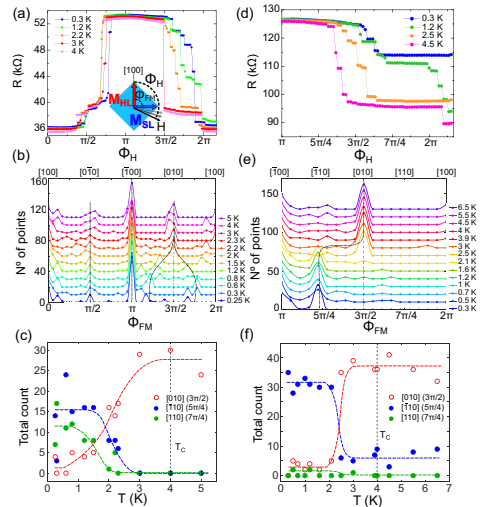


FIG. 2. Typical angular dependence of the resistance of a V/MgO/Fe/MgO/Fe/Co junction on the orientation of the in-plane field with respect to the main crystalline axes from above to below T_C when the rotation is initiated from a P state (a)–(c) and from an AP state (d)–(f). The inset sketches the experimental configuration, showing the angles between the ferromagnetic layers (Φ_{FM}) and of the external magnetic field (Φ_H). Parts (b),(e) correspondingly represent the experimental data shown in (a),(d) in the form of histograms, dividing the $0\text{--}2\pi$ interval into 36 zones. Parts (c),(f) plot the histograms in (b),(e) as counts vs temperature for the intermediate states (AP + $\pi/4$ or the $[\bar{1}10]$ axis, AP + $\pi/2$ = PIP or [010], and AP + $3\pi/4$ or [110]) for the second half of the rotation.

has a fourfold in-plane anisotropy with two orthogonal easy axes—[100] and [010]—[Fig. 1(b)]. These MCA states could be accessed by an in-plane rotation of the Fe(001) layer with respect to the Fe/Co layer using a field greater than the coercive field of the Fe(001) layer without disrupting the Fe/Co magnetization (see also the Supplemental Material S1 [49] for the magnetic characterization of the Fe/Co layer). This is shown in Fig. 1(d), where TMR is plotted as a function of the in-plane field angle with respect to the [100] direction angle Φ_H . This gives rise to four distinct magnetization states with P, perpendicular in-plane (PIP), and AP states reflected by the TMR values. Supplemental Material S3 [49] discusses the weak magnetostatic coupling between the two FM layers (detected through resistances in-between the P and AP states in the virgin state of different samples), showing that it does not affect the capability to reorient the soft layer independently of the hard one. It also demonstrates that the soft layer retains different magnetic directions at zero field.

Figure 2 analyzes the most probable in-plane magnetization orientations of the Fe(001) layer through magnetic field rotations at fixed temperatures from above to below T_C . Typically, no qualitative changes in TMR are observed

above and below T_C in the $0 - \pi$ field rotation angle (Φ_H) span [Fig. 2(a)]. However, in the $\pi - 2\pi$ range, the TMR qualitatively changes below $T_C/2$, possibly indicating new stable magnetization states along different directions from the ones established by the principal crystallographic axes [Fig. 2(a)].

To ascertain the exact angle Φ_{FM} between the two F layers, we have calibrated the magnetization direction of the soft layer with respect to the hard Fe/Co using the Slonczewski formula (Supplemental Material S4 [49]). The applicability of the macrospin approach to describe TMRs and magnetization reorientation resides in the high effective spin polarization obtained ($P = 0.7$) [47], approaching the values typically reported for Fe/MgO in a fully saturated state [56,57]. Figure 2(b) is a histogram representing the probability of obtaining a specific Φ_{FM} as temperature is lowered from above to below T_C . We observe that the most probable Fe(001) directions are oriented along the [100] and [010] principal axes above $T_C/2$, while below $T_C/2$ it splits in three branches roughly oriented along $\pi/4$ angles. The split of the [010] state into three branches is also visualized in Fig. 2(e), with a plot of the counts versus temperature around the $[\bar{1}\bar{1}0]$, [010], and $[\bar{1}10]$ magnetization directions.

Interestingly, once the rotation is initiated in the AP configuration, the magnetization apparently locks in the $(\pi + \pi/4)$ (or $[\bar{1}\bar{1}0]$) state [Figs. 2(b), 2(d) and 2(f)]. This probably arises due to the improved initial macrospin alignment, which is not fully achieved in the AP state with a preceding P-AP rotation. We believe that with the full 2π field rotation, magnetization inhomogeneities or local DWs created during the P-AP state rotation help to overcome MCA energy barriers more easily. The suggested suppression of the local DWs with the magnetization rotation initiated from the AP state can be indirectly inferred from the broadening of the $[\bar{1}\bar{1}0]$ to [010] transition in the normal state detected as a small (extrinsic) number of counts around $[\bar{1}\bar{1}0]$ [Fig. 2(f)].

For a more systematic analysis, we performed a series of in-plane TMR measurements along different directions relative to the symmetry axes. The first experiment (i) was performed with an initial saturation field of ± 1 kOe in the [100] direction, followed by a TMR in the [210] direction (between [100] and [110]). The second experiment (ii) initially saturates both the hard and soft layers along the [100] direction. Then, a minor loop is performed starting from zero field and going up to 150 Oe along the [110] axis.

Both experiments further suggest the possibility of superconductivity-induced changes of MCA. The inset of Fig. 3(a) shows the full field sweep range in the first (i) configuration, and Fig. 3(a) zooms in close to the AP configuration. When we sweep the field in the [210] direction, we detect a weak but robust resistance upturn at temperatures below approximately $T_C/2$ (Fig. 3). This additional TMR increase [shown by the arrows in Fig. 3(a)] roughly corresponds to an 8–10 degree rotation in the relative spin direction between the soft and hard layer toward their AP alignment (see the Supplemental Material S4 [49] for an analysis of the calculated angle error). Within the proposed macrospin approximation, this could be understood as a redirection of the soft layer magnetization forced by the external field, from the initially blocked [110] direction toward the external

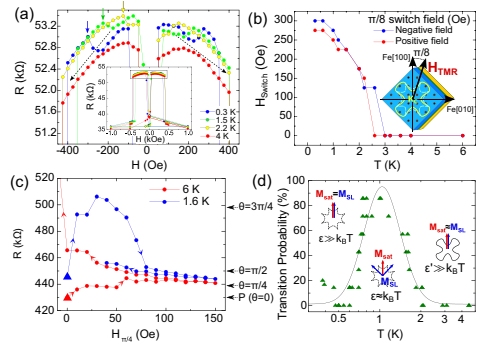


FIG. 3. (a) TMR measurements on an S/F/F $30 \times 30 \mu\text{m}^2$ junction with H oriented along [210] [inset in (b)] for various temperatures. The increase in R is associated with a transition from the [110] magnetization orientation to a forced [210] direction of the soft layer. (b) Variation of the transition field with T for the positive and negative field branches. Inset: exchange energy anisotropy and direction of the applied field (H_{TMR}). (c) Two TMRs performed on a $10 \times 10 \mu\text{m}^2$ junction in the [110] direction at $T = 6$ and 1.6 K, after applying 1 kOe in the [100] direction. The 6 K TMR starts in a P state, while the 1.6 K TMR starts already in a tilted state. Right axis: estimation of the angle θ between the two F layers based on the Slonczewski formula. (d) Probability of finding a tilted state at $H = 0$ [triangular points in (b)] vs T (in log scale), averaged with seven experimental points around each T . The line is a guide for the eye. Insets: sketch of the magnetic anisotropy below and above T_C , with the saturation magnetization (M_{sat}) and the zero-field magnetization state measured for the soft layer (M_{SL}). ε and ε' represent the energy barrier separating the [100] magnetization direction from the closest minimum below and above T_C , respectively.

field [210] direction. A strong increase of the characteristic field, H_{switch} , required to reorient the soft layer from [110] toward [210] when T decreases below $T_C/2$, could reflect the superconductivity-induced MCA energy minimum along the [110] direction.

The minor TMR loops along [110] [Fig. 3(c)] realized after saturation along [100] point on a thermally induced magnetization reorientation from [100] toward [110] even at zero field, in a temperature range below T_C where the barrier between adjacent energy minima is comparable to $k_B T$. The zero-field reorientation becomes less probable when the thermal energy is insufficient to overcome the barrier [Fig. 3(d)]. An estimation of the in-plane normal-state MCA energy barrier done through magnetization saturation along [100] and [110] provides a value of only a few $\mu\text{eV}/\text{at}$ (Supplemental Material S5 [49]). However, the real barrier is determined by the nucleation volume, which depends on the exchange length in the material. With a DW width of about 3 nm for Fe(001), we estimate the MCA barrier to be at least $10^0 - 10^1$ mV.

Before describing our explanation of the MCA modification of Fe(001) in the superconducting state of the V(40 nm)/MgO(2 nm)/Fe(10 nm) system, we discard alternative

interpretations of the observed effects. Meissner screening [24,25], if present, would introduce about a 10% correction to the actual magnetic field independently of the external field direction (see Supplemental Material S2 [49]). The reason for the weak in-plane field screening could be the small superconductor thickness (40 nm), only slightly exceeding the estimated coherence length (26 nm). On the other hand, intermediate multidomain states are expected to be absent when magnetization is directed along [110] (Supplemental Material S6 [49]). Indeed, our experiments show that magnetization, when locked below T_C in the $(\pi + \pi/4)$ angle, hardly depends on the absolute value of the external field along [110] varied between 0 and 100 Oe. Moreover, simulations of the vortex-DW interaction using MUMAX3 [58] and TDGL codes [59] discard the vortex-mediated DW pinning [26,27] scenario including when interfacial magnetic defects created by misfit dislocations [60] are considered (see Supplemental Material S6 [49]). The vortex pinning mechanism also contradicts that only the $(0 - \pi)$ field rotation span [Fig. 2(a)] gets affected below $T_C/2$. The observed irrelevance of the junction area (Supplemental Material S7 [49]) contradicts the importance of the vortex-edge DW interaction. The shape and vortex-DW interaction effects, if relevant, would strengthen magnetization pinning along [100], but not [110] (Supplemental Material S6 and S7 [49]). Finally, we also indicate that the MCA modification from singlet superconductivity would not enable any zero-field rotation to noncollinear misalignment angles, in contrast to our data [Fig. 3(d)].

To explain our results, we consider the possibility in which the invariance of the superconducting proximity effect to magnetization rotation is broken in the presence of SOC. It has been predicted that triplet-superconductivity is effectively generated even for weakly spin-polarized ferromagnets with a small spin-orbit field [61]. In addition to generating triplet pairs, the SOC also introduces an angle-dependent anisotropic depairing field for the triplets [43,45]. In V/MgO/Fe, the Rashba field is caused by a structural broken inversion symmetry at the MgO interfaces [44]. We model our experimental results using a tight-binding Bogoliubov-de Gennes Hamiltonian on a lattice and compute the free energy (Supplemental Material S8 [49]). The Hamiltonian includes electron hopping in and between the different layers, a Rashba-like SOC at the MgO/Fe interface, an exchange splitting between spins in the Fe layers, and conventional s -wave superconductivity in the V layer. The free energy determined from this Hamiltonian includes the contribution from the superconducting proximity effect, and an effective in-plane magnetocrystalline anisotropy favoring magnetization along the [100] and [010] axes. Experimentally, we see a weak antiferromagnetic coupling between the Fe(100) and Fe/Co layers (which does not affect the capability to reorient the soft layer independently of the hard one) described by an additional contribution $f_{AF} \cos(\Phi_{FM})$ with a constant parameter $f_{AF} > 0$.

Figure 4 shows the total free energy of the system as a function of the IP magnetization angle Φ_{FM} for decreasing temperatures. Due to the increase in the superconducting proximity effect, additional local minima appear at $\Phi_{FM} = n\pi/2 + \pi/4$, where $n = 0, 1, 2, \dots$ (i.e., [110], $[\bar{1}10]$, $[\bar{1}\bar{1}0]$, and $[1\bar{1}0]$, respectively). This is a clear signature for the proximity-induced triplet correlations. These are most efficiently generated at

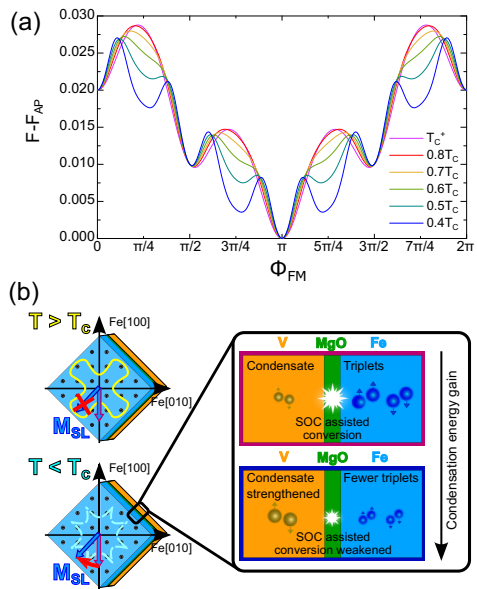


FIG. 4. Numerical modeling. (a) Free energy F vs in-plane magnetization angle Φ_{FM} for temperatures below the superconducting critical temperature and just above the critical temperature (T_C^+). The free energy is plotted relative to the free energy in the AP configuration F_{AP} and has been normalized to the hopping parameter t used in the tight-binding model. (b) Illustration of the physical origin of the change in magnetic anisotropy induced by the superconducting layer. Above T_C , V is a normal metal and the soft Fe layer has a fourfold in-plane magnetic energy anisotropy (yellow line). Below T_C , V is superconducting and influences the soft Fe layer via the proximity effect: a leakage of Cooper pairs into the ferromagnet. Due to the SOC at the interface, a magnetization-orientation-dependent generation of triplet Cooper pairs occurs. The generation of triplets is at its weakest for a magnetization pointing in the $[\bar{1}\bar{1}0]$ direction, giving a maximum for the superconducting condensation energy gain. This modifies the magnetic anisotropy of the soft Fe layer (cyan line), enabling magnetization switching to the $[\bar{1}\bar{1}0]$ direction (blue arrow). The magnetic anisotropy does not show the weak AP coupling between the two Fe layers, causing an absolute minimum in $\Phi_{FM} = \pi$ (a).

angles $\Phi_{FM} = n\pi/2$ (i.e., [100], [010], $[\bar{1}00]$, and $[0\bar{1}0]$) for a heterostructure with a magnetic layer that has a cubic crystal structure like Fe [45]. As a result, the decrease in the free energy is stronger at angles $\Phi_{FM} = n\pi/2 + \pi/4$, where more singlet Cooper pairs survive. Our numerical results thus confirm that the experimentally observed modification of the anisotropy can be explained by the presence of SOC in the S/F structure alone, without including superconducting proximity effects from misalignment between the Fe(100) and Fe/Co layers. Moreover, Fig. 4 illustrates why the $\Phi_{FM} = n\pi/2 + \pi/4$ states only appear experimentally when the external field

is rotated from an AP to P alignment (Fig. 2). Because of the weak AP coupling between the ferromagnetic layers, the energy thresholds for reorienting the magnetization from one local minimum to the next are higher under a rotation from AP to P alignment.

In conclusion, we present experimental evidence for superconductivity-induced change in magnetic anisotropy in epitaxial ferromagnet-superconductor hybrids with spin-orbit interaction. We believe that this mechanism is fundamentally different from the previous reports of magnetization modification arising from Meissner screening and vortex-induced domain wall pinning, even though the spin-triplet mechanism and performed simulations require many assumptions. Our results establish superconductors as tunable sources of magnetic anisotropies and active ingredients for future low dissipation superspintronic technologies. Specifically, they could provide an opportunity to employ spin-orbit proximity effects in magnetic Josephson junction technology and apply it to Fe/MgO-based junctions that are widely used in commercial spintronic applications.

We acknowledge Mairbek Chshiev and Antonio Lara for help with simulations, Yuan Lu for help in sample preparations, and Igor Zutic and Alexandre Buzdin for the discussions. The work in Madrid was supported by Spanish Ministry of Science and Innovation (MAT2015-66000-P, RTI2018-095303-B-C55, EUIN2017-87474) and Consejería de Educación e Investigación de la Comunidad de Madrid (NANOMAGCOST-CM Ref. P2018/NMT-4321) grants. F.G.A. acknowledges financial support from the Spanish Ministry of Science and Innovation, through the María de Maeztu Programme for Units of Excellence in *R&D* (MDM-2014-0377, CEX2018-000805-M). N.B. was supported by EPSRC through the New Investigator Grant EP/S016430/1. The work in Norway was supported by the Research Council of Norway through its Centres of Excellence funding scheme grant 262633 QuSpin. C.T. acknowledges “EMER-SPIN” grant ID PN-IIMP4-ID-PCE-2016-0143, No. UEFIS-CDI: 22/12.07.2017. The work in Nancy was supported by CPER MatDS and the French PIA project “Lorraine Université d’Excellence,” reference ANR-15-IDEX-04-LUE.

-
- [1] V. L. Ginzburg, Ferromagnetic superconductors, *Zh. Eksp. Teor. Fiz.* **31**, 202 (1956) [*Sov. Phys. JETP* **4**, 153 (1957)].
- [2] B. T. Matthias, H. Suhl, and E. Corenzwit, Spin Exchange in Superconductors, *Phys. Rev. Lett.* **1**, 152 (1958).
- [3] A. I. Buzdin, L. N. Bulaevskii, M. L. Kulich, and S. V. Panyukov, Magnetic superconductors, *Sov. Phys. Usp.* **27**, 927 (1984).
- [4] J. Y. Gu, C.-Y. You, J. S. Jiang, J. Pearson, Y. B. Bazaliy, and S. D. Bader, Magnetization-Orientation Dependence of the Superconducting Transition Temperature in the Ferromagnet-Superconductor-Ferromagnet System: CuNi/Nb/CuNi, *Phys. Rev. Lett.* **89**, 267001 (2002).
- [5] I. C. Moraru, W. P. Pratt, Jr., and N. O. Birge, Observation of standard spin-switch effects in ferromagnet/superconductor/ferromagnet trilayers with a strong ferromagnet, *Phys. Rev. B* **74**, 220507(R) (2006).
- [6] L. R. Tagirov, Low-Field Superconducting Spin Switch Based on a Superconductor/Ferromagnet Multilayer, *Phys. Rev. Lett.* **83**, 2058 (1999).
- [7] A. I. Buzdin, A. V. Vedyayev, and N. V. Ryzhanova, Spin-orientation dependent superconductivity in F/S/F structures, *Europhys. Lett.* **48**, 686 (1999).
- [8] I. Baladíé, A. Buzdin, N. Ryzhanova, and A. Vedyayev, Interplay of superconductivity and magnetism in superconductor/ferromagnet structures, *Phys. Rev. B* **63**, 054518 (2001).
- [9] P. V. Leksin, N. N. Garif’yanov, I. A. Garifullin, J. Schumann, V. Kataev, O. G. Schmidt, and B. Büchner, Manifestation of New Interference Effects in a Superconductor-Ferromagnet Spin Valve, *Phys. Rev. Lett.* **106**, 067005 (2011).
- [10] X. L. Wang, A. Di Bernardo, N. Banerjee, A. Wells, F. S. Bergeret, M. G. Blamire, and J. W. A. Robinson, Giant triplet proximity effect in superconducting pseudo spin valves with engineered anisotropy, *Phys. Rev. B* **89**, 140508(R) (2014).
- [11] A. Singh, S. Voltan, K. Lahabi, and J. Aarts, Colossal Proximity Effect in a Superconducting Triplet Spin Valve Based on the Half-Metallic Ferromagnet CrO₂, *Phys. Rev. X* **5**, 021019 (2015).
- [12] P. V. Leksin, N. N. Garif’yanov, I. A. Garifullin, Ya. V. Fominov, J. Schumann, Y. Krupskaya, V. Kataev, O. G. Schmidt, and B. Büchner, Evidence for Triplet Superconductivity in a Superconductor-Ferromagnet Spin Valve, *Phys. Rev. Lett.* **109**, 057005 (2012).
- [13] R. S. Keizer, S. T. B. Goennenwein, T. M. Klapwijk, G. Miao, G. Xiao, and A. A. Gupta, A spin triplet supercurrent through the half-metallic ferromagnet CrO₂, *Nature (London)* **439**, 825 (2006).
- [14] T. S. Khaire, M. A. Khasawneh, W. P. Pratt, Jr., and N. O. Birge, Observation of Spin-Triplet Superconductivity in Co-Based Josephson Junctions, *Phys. Rev. Lett.* **104**, 137002 (2010).
- [15] M. S. Anwar, F. Czeschka, M. Hesselberth, M. Porcu, and J. Aarts, Long-range supercurrents through half-metallic ferromagnetic CrO₂, *Phys. Rev. B* **82**, 100501(R) (2010).
- [16] J. W. A. Robinson, J. D. S. Witt, and M. G. Blamire, Controlled injection of spin-triplet supercurrents into a strong ferromagnet, *Science* **329**, 59 (2010).
- [17] C. Visani, Z. Sefrioui, J. Tornos, C. Leon, J. Briatico, M. Bibes, A. Barthélémy, J. Santamaría, and J. E. Villegas, Equal-spin Andreev reflection and long-range coherent transport in high-temperature superconductor/halfmetallic ferromagnet junctions, *Nat. Phys.* **8**, 539 (2012).
- [18] N. Banerjee, J. W. A. Robinson, and M. G. Blamire, Reversible control of spin-polarized supercurrents in ferromagnetic Josephson junctions, *Nat. Commun.* **5**, 4771 (2014).
- [19] A. Iovan, T. Golod, and V. M. Krasnov, Controllable generation of a spin-triplet supercurrent in a Josephson spin valve, *Phys. Rev. B* **90**, 134514 (2014).
- [20] J. Linder and J. W. A. Robinson, Superconducting spintronics, *Nat. Phys.* **11**, 307 (2015).
- [21] M. Eschrig, Spin-polarized supercurrents for spintronics: a review of current progress, *Rep. Prog. Phys.* **78**, 104501 (2015).

- [22] M. G. Flokstra, N. Satchell, J. Kim, G. Burnell, P. J. Curran, S. J. Bending, J. F. K. Cooper, C. J. Kinane, S. Langridge, A. Isidori, N. Pugach, M. Eschrig, H. Luethkens, A. Suter, T. Prokscha, and S. L. Lee, Remotely induced magnetism in a normal metal using a superconducting spin-valve, *Nat. Phys.* **12**, 57 (2016).
- [23] A. I. Buzdin and L. N. Bulaevskii, Ferromagnetic film on the surface of a superconductor: Possible onset of inhomogeneous magnetic ordering, *Zh. Eksp. Teor. Fiz.* **94**, 256 (1988) [*Sov. Phys. JETP* **67**, 576 (1988)].
- [24] L. N. Bulaevskii and E. M. Chudnovsky, Ferromagnetic film on a superconducting substrate, *Phys. Rev. B* **63**, 012502 (2000).
- [25] S. V. Dubonos, A. K. Geim, K. S. Novoselov, and I. V. Grigorieva, Spontaneous magnetization changes and nonlocal effects in mesoscopic ferromagnet-superconductor structures, *Phys. Rev. B* **65**, 220513R (2002).
- [26] J. Fritzsche, R. B. G. Kramer, and V. V. Moshchalkov, Visualization of the vortex-mediated pinning of ferromagnetic domains in superconductor-ferromagnet hybrids, *Phys. Rev. B* **79**, 132501 (2009).
- [27] P. J. Curran *et al.*, Irreversible magnetization switching at the onset of superconductivity in a superconductor ferromagnet hybrid, *Appl. Phys. Lett.* **107**, 262602 (2015).
- [28] X. Weintal and P. W. Brouwer, Magnetic exchange interaction induced by a Josephson current, *Phys. Rev. B* **65**, 054407 (2002).
- [29] Y. Tserkovnyak and A. Brataas, Current and spin torque in double tunnel barrier ferromagnet-superconductor-ferromagnet systems, *Phys. Rev. B* **65**, 094517 (2002).
- [30] C. Bell, S. Milikisyants, M. Huber, and J. Aarts, Spin Dynamics in a Superconductor-Ferromagnet Proximity System, *Phys. Rev. Lett.* **100**, 047002 (2008).
- [31] B. Braude and Ya. M. Blanter, Triplet Josephson Effect with Magnetic Feedback in a Superconductor-Ferromagnet Heterostructure, *Phys. Rev. Lett.* **100**, 207001 (2008).
- [32] E. Zhao and J. A. Sauls, Theory of nonequilibrium spin transport and spin-transfer torque in superconducting-ferromagnetic nanostructures, *Phys. Rev. B* **78**, 174511 (2008).
- [33] F. Konschelle and A. Buzdin, Magnetic Moment Manipulation by a Josephson Current, *Phys. Rev. Lett.* **102**, 017001 (2019).
- [34] J. Linder and T. Yokoyama, Supercurrent-induced magnetization dynamics in a Josephson junction with two misaligned ferromagnetic layers, *Phys. Rev. B* **83**, 012501 (2011).
- [35] J. Linder, A. Brataas, Z. Shomali, and M. Zareyan, Spin-Transfer and Exchange Torques in Ferromagnetic Superconductors, *Phys. Rev. Lett.* **109**, 237206 (2012).
- [36] N. G. Pugach and A. I. Buzdin, Magnetic moment manipulation by triplet Josephson current, *Appl. Phys. Lett.* **101**, 242602 (2012).
- [37] F. S. Bergeret and I. V. Tokatly, Singlet-Triplet Conversion and the Long-Range Proximity Effect in Superconductor-Ferromagnet Structures with Generic Spin Dependent Fields, *Phys. Rev. Lett.* **110**, 117003 (2013).
- [38] N. Banerjee, J. A. Ouassou, Y. Zhu, N. A. Stelmashenko, J. Linder, and M. G. Blamire, Controlling the superconducting transition by spin-orbit coupling, *Phys. Rev. B* **97**, 184521 (2018).
- [39] K.-R. Jeon, C. Ciccarelli, A. J. Ferguson, H. Kurebayashi, L. F. Cohen, X. Montiel, M. Eschrig, J. W. A. Robinson, and M. G. Blamire, Enhanced spin pumping into superconductors provides evidence for superconducting pure spin currents, *Nat. Mater.* **17**, 499 (2018).
- [40] K.-R. Jeon, C. Ciccarelli, A. J. Ferguson, H. Kurebayashi, L. F. Cohen, X. Montiel, M. Eschrig, S. Komori, J. W. A. Robinson, and M. G. Blamire, Exchange-field enhancement of superconducting spin pumping, *Phys. Rev. B* **99**, 024507 (2019).
- [41] N. Satchell and N. O. Birge, Supercurrent in ferromagnetic Josephson junctions with heavy metal interlayers, *Phys. Rev. B* **97**, 214509 (2018).
- [42] N. Satchell, R. Loloee, and N. O. Birge, Supercurrent in ferromagnetic Josephson junctions with heavy-metal interlayers. II. Canted magnetization, *Phys. Rev. B* **99**, 174519 (2019).
- [43] S. H. Jacobsen, J. A. Ouassou, and J. Linder, Critical temperature and tunneling spectroscopy of superconductor-ferromagnet hybrids with intrinsic Rashba-Dresselhaus spin-orbit coupling, *Phys. Rev. B* **92**, 024510 (2015).
- [44] I. Martínez, P. Högl, C. González-Ruano, J. P. Cascales, C. Tiusan, Y. Lu, M. Hehn, A. Matos-Abiague, J. Fabian, I. Zutic, and F. G. Aliev, Interfacial Spin-Orbit Coupling: A Platform for Superconducting Spintronics, *Phys. Rev. Appl.* **13**, 014030 (2020).
- [45] L. G. Johnsen, J. Linder, and N. Banerjee, Magnetization reorientation due to superconducting transition in heavy metal heterostructures, *Phys. Rev. B* **99**, 134516 (2019).
- [46] H. X. Yang, M. Chshiev, and B. Dieny, First-principles investigation of the very large perpendicular magnetic anisotropy at Fe/MgO and Co/MgO interfaces, *Phys. Rev. B* **84**, 054401 (2011).
- [47] I. Martínez, C. Tiusan, M. Hehn, M. Chshiev, and F. G. Aliev, Symmetry broken spin reorientation transition in epitaxial MgO/Fe/MgO layers with competing anisotropies, *Sci. Rep.* **8**, 9463 (2018).
- [48] C. Tiusan, F. Greullet, M. Hehn, F. Montaigne, S. Andrieu, and A. Schuhl, Spin tunneling phenomena in single crystal magnetic tunnel junction systems, *J. Phys.: Condens. Matter* **19**, 165201 (2007).
- [49] See Supplemental Material at <http://link.aps.org/supplemental/10.1103/PhysRevB.102.020405> for more details about the magnetic characterization of the samples, the micromagnetic and TDGL simulations, and the theoretical modelling.
- [50] E. Jal *et al.*, Interface Fe magnetic moment enhancement in MgO/Fe/MgO trilayers, *Appl. Phys. Lett.* **107**, 092404 (2015).
- [51] P. Blaha, K. Schwarz, F. Tran, R. Laskowski, G. K. H. Madsen, and L. D. Marks, An APW+lo program for calculating the properties of solids, *J. Chem. Phys.* **152**, 074101 (2020).
- [52] A. Manchon, H. C. Koo, J. Nitta, S. M. Frolov, and R. A. Duine, New perspectives for Rashba spin-orbit coupling, *Nat. Mater.* **14**, 871 (2015).
- [53] J. C. Slonczewski, Conductance and exchange coupling of two ferromagnets separated by a tunneling barrier, *Phys. Rev. B* **39**, 6995 (1989).
- [54] A. N. Anisimov, M. Farle, P. Pouloupoulos, W. Platon, K. Baberschke, P. Isberg, R. Wüppling, A. M. N. Niklasson, and O. Eriksson, Orbital Magnetism and Magnetic Anisotropy Probed with Ferromagnetic Resonance, *Phys. Rev. Lett.* **82**, 2390 (1999).
- [55] J. Bardeen, L. N. Cooper, and J. R. Schrieffer, Theory of superconductivity, *Phys. Rev.* **108**, 1175 (1957).

- [56] S. S. P. Parkin, C. Kaiser, A. Panchula, P. M. Rice, B. Hughes, M. Samant, and S.-H. Yang, Giant tunneling magnetoresistance at room temperature with MgO (100) tunnel barriers, *Nat. Mater.* **3**, 862 (2004).
- [57] S. Yuasa, T. Nagahama, A. Fukushima, Y. Suzuki, and K. Ando, Giant room temperature magnetoresistance in single-crystal Fe/MgO/Fe magnetic tunnel junctions, *Nat. Mater.* **3**, 868 (2004).
- [58] A. Vansteenkiste, J. Leliaert, M. Dvornik, M. Helsen, F. Garcia-Sanchez, and B. Van Waeyenberge, The design and verification of MuMax3, *AIP Adv.* **4**, 107133 (2014).
- [59] A. Lara, C. González-Ruano, and F. G. Aliev, Time-dependent Ginzburg-Landau simulations of superconducting vortices in three dimensions, *Low Temp. Phys.* **46**, 316 (2020).
- [60] D. Herranz, F. Bonell, A. Gomez-Ibarlucea, S. Andrieu, F. Montaigne, R. Villar, C. Tiusan, and F. G. Aliev, Strongly suppressed $1/f$ noise and enhanced magnetoresistance in epitaxial Fe-V/MgO/Fe magnetic tunnel junctions, *Appl. Phys. Lett.* **96**, 202501 (2010).
- [61] T. Vezin, C. Shen, J. E. Han, and I. Žutić, Enhanced spin-triplet pairing in magnetic junctions with s-wave superconductors, *Phys. Rev. B* **101**, 014515 (2020).

Supplementary material
Superconductivity-induced change in magnetic anisotropy in epitaxial ferromagnet-superconductor hybrids with spin-orbit interaction

César González-Ruano,¹ Lina G. Johnsen,² Diego Caso,¹ Coriolan Tiusan,^{3,4}
 Michel Hehn,⁴ Niladri Banerjee,⁵ Jacob Linder,² and Farkhad G. Aliev^{1,*}

¹*Departamento Física de la Materia Condensada C-III, Instituto Nicolás Cabrera (INC) and Condensed Matter Physics Institute (IFIMAC), Universidad Autónoma de Madrid, Madrid 28049, Spain*

²*Center for Quantum Spintronics, Department of Physics, Norwegian University of Science and Technology, NO-7491 Trondheim, Norway*

³*Department of Physics and Chemistry, Center of Superconductivity Spintronics and Surface Science C4S, Technical University of Cluj-Napoca, Cluj-Napoca, 400114, Romania*

⁴*Institut Jean Lamour, Nancy Université, 54506 Vandoeuvre-les-Nancy Cedex, France*

⁵*Department of Physics, Loughborough University, Epinal Way, Loughborough, LE11 3TU, United Kingdom*

Abstract

In the supplementary material, the section S1 presents a magnetic characterization of the hard Fe/Co layer of the junctions under study. Section S2 presents a magnetic characterization of the soft Fe(001) layer and studies the possible influence of the Meissner screening on the coercive fields of the soft and hard layers. Section S3 estimates the strength of the weak antiferromagnetic coupling between magnetically soft and hard electrodes. Section S4 provides details about the calibration of the angle between the soft and hard layers using the Slonczewski formula, as well as discussing the possible sources of error for this calibration and their magnitude. Section S5 provides an estimation for the magneto-anisotropic energy barrier between the [110] and [100] magnetization directions, normalized per volume or per atom. Section S6 numerically evaluates the possible domain walls pinning by superconducting vortices. Section S7 discusses the contribution of the shape to the magnetic anisotropy. Finally, section S8 provides details on the theoretical modelling of the observed effects.

S1. Magnetic characterization of the hard Fe/Co layer

Figure S1 shows the magnetic characterization of the hard Fe/Co bilayer, determined from a typical spin-valve M-H loop on a standard Fe/MgO/Fe/Co single crystal MTJ system (continuous layers, unpatterned). The nominal thickness of the layers on this sample, MgO(100)/Fe(30 nm)/MgO(2 nm)/Fe(10 nm)/Co(20 nm), has been chosen to optimize the magnetic properties of the MTJ stack [1]. The TMR measurements of the coercive fields of the hard ($H_{C,Hard}$) and soft ($H_{C,Soft}$) layers in MTJs under study show that they are well sep-

arated from the external field values used to rotate the soft layer. Figure S2 shows that the hard layer switching fields obtained from TMRs along [100], [010] and [110] measured in our junctions remain far above the typical range of 70-120 Oe which is used to rotate the soft layer. Moreover, Figure S3 also shows the typical temperature dependence of $H_{C,Hard}$, demonstrating its independence with temperature from well above to well below T_C .

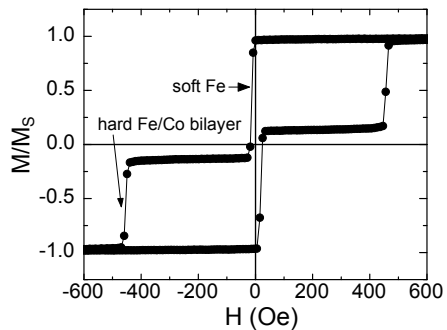


Fig. S 1: Magnetic characterization of a Fe(30 nm)/MgO/Fe(10 nm)Co(20 nm) structure, at room temperature, along the [100] direction.

S2. Magnetic characterization of the soft Fe(001) layer and estimation of the Meissner screening

The magnetostatic Meissner screening has been discussed mainly in studies with perpendicular magnetiza-

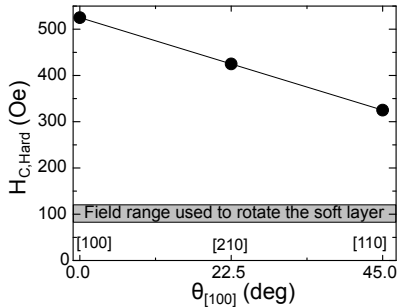


Fig. S2: Coercive field of the hard Fe/Co layer for magnetic field oriented along different crystallographic directions [100], [110] and [210], above the superconducting critical temperature ($T = 5$ K). The grey band shows the typical field range used to manipulate the magnetization of the soft Fe(100) layer in the rotation experiments.

tion [2]. In the case of the experiments with in-plane field rotation which we carry out, such field expulsion could induce some screening of the external magnetic field applied to invert or rotate the magnetization of the soft Fe(001) layer (which is the closest to the superconductor), and with less probability affect the switching of the more distant hard Fe/Co layer.

Figure S4 shows the typical variation of the coercive field of the soft Fe(001) ferromagnetic layer with temperature from above to below the critical temperature. We observe some weak increase of the coercive field below 10 Oe, which could be due to spontaneous Meissner screening and/or vortex interaction with domain walls. These changes, however, are an order of magnitude below the typical magnetic fields applied to rotate the Fe(001) layer (70-120 Oe). As we also show in Figure S3, the coercive field of the hard FeCo layer (typically above 400-500 Oe) shows practically no variation (within the error bars) within a wide temperature range, from $3T_C$ to $0.1T_C$, discarding the influence of the Meissner screening on the hard layer.

As the superconducting layer is much larger in area than the ferromagnetic one, these experiments point out that the possible existing Meissner screening would introduce about a 10% correction to the actual external field acting on the soft ferromagnet, regardless of the external field direction.

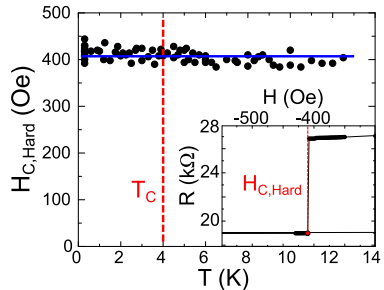


Fig. S3: Typical temperature dependence of the coercive field of the hard Fe/Co ferromagnetic layer along the [100] direction. The critical temperature is marked with a dashed red line. We relate the excess scatter observed in the hard layer with the extra structural disorder at the Fe/Co interface, providing an enhanced coercive field for the Fe/Co layer. The blue line is a guide for the eye. The inset shows the method for determining the coercive field: it's the field of the first point after the hard layer transition from in each TMR experiment.

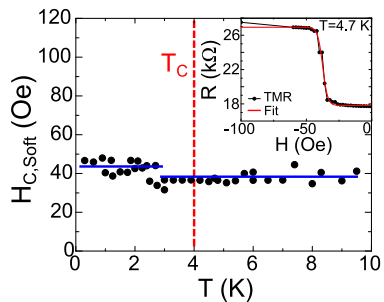


Fig. S4: Typical temperature dependence of the coercive field of the soft Fe(001) ferromagnetic layer measured along [100] direction. The critical temperature is marked with a dashed red line. Blue lines are guides for the eye. The inset shows the method for determining the coercive field: a logistic fit was performed for the transition, and the coercive field was defined as the mid-height value of the fit.

S3. Estimation of the weak antiferromagnetic coupling of the two ferromagnetic layers.

In order to quantify the unavoidable weak antiferromagnetic magnetostatic coupling between the rotated soft Fe(001) and the practically fixed hard FeCo layer, we show low field TMR measurements where the AP state is achieved and then maintained at zero field (Figure S5a). One clearly observes that the AP and P states can be

obtained as two different non-volatile states, and therefore the antiferromagnetic coupling is not sufficient to antiferromagnetically couple the two layers at zero field. The stability of the P state against the antiferromagnetic coupling is confirmed by the temperature dependence of the resistance in the P and AP states. The P state shows stable resistance values at least below 15 K (Figure S5b). This means that the antiferromagnetic coupling energy is well below 2 mV.

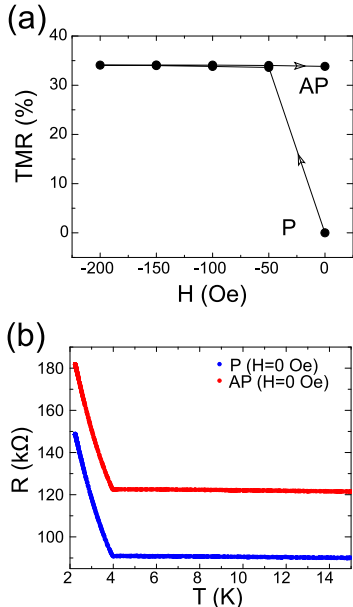


Fig. S5: Two experiments demonstrating the stability of the P and AP states at zero field. (a) TMR to AP state before a critical temperature measurement: the sample was first saturated in the P state with $H = 1000$ Oe in the [100] direction, and then a negative field sweeping was performed to -200 Oe and back to 0 Oe in the same direction in order to switch the soft layer into the AP state, where it remained at zero field. (b) Two critical temperature measurements: the sample was saturated in the P state, and then switched to AP state as described in (a) for the AP measurement. After this, the temperature was risen to 15 K and let to slowly cool down to $T \sim 2$ K. The increase in resistance below 4 K corresponds to the opening and deepening of the superconducting gap, since the voltage used was only a few microvolts in order to distinguish the superconducting transition from its appearance. Both experiments show no sudden changes in resistance, as would happen if any magnetic transition took place.

S4. Calibration of the angle between the two ferromagnetic layers

In order to estimate the angle between the two ferromagnets for the TMR measurements and rotations, we used the Slonczewski model [3]. By using values of the resistance in the AP, P and PIP states established above T_C , we can calculate the desired angle θ with the following expression:

$$G^{-1} = G_1^{-1} + [G_2 (1 + p^2 \cos \theta)]^{-1}. \quad (1)$$

Here, G is the total conductance of the sample, G_1 and G_2 are the conductances of each of the two tunnel barriers, and p is the spin polarization in the ferromagnets, for which we obtain values between 0.7 and 0.8 depending on the sample (the value being robust for each individual one).

In order to ascertain the precision of this calibration method, an analysis of the different errors has been performed. First, a standard error propagation calculation was done to estimate the uncertainty in the resistance values, taking typical values for the current and voltage of 100 nA and 5 mV, respectively, which gives us a typical resistance value of 50 kΩ. The current is applied using a Keithley 220 Current Source, which has an error of 0.3% in the operating range according to the user manual. The voltage is measured using a DMM-522 PCI multimeter card. In the specifications, the voltage precision is said to be 5 1/2 digits. With all this, the resistance error obtained is $\Delta R = 75.08 \Omega$ or a 0.15% of relative error. Using this value, the error bars in the measurements shown in the main text would be well within the experimental points.

For the calculated angle, the error propagation method is not adequate. It gives errors bigger than 360 degrees for some angles, and in general over 30 degrees. This is clearly not what it is observed in reality: the performed fits are quite robust, showing little variance in the estimated angle when changing the input parameters all that is reasonable. Instead, we have used a typical rotation performed on a $30 \times 30 \mu\text{m}^2$ sample. The fitting to the Slonczewski formula needs three input values: the resistance in the P state (R_P), the resistance in the AP state (R_{AP}) and the resistance in the PIP state (R_{PIP}). Using these, a numerical algorithm calculates the spin polarization (p), the resistance of the F/F barrier (R_{FF}), and the resistance of the F/S (F/N) barrier (R_{NIF}). These give us the total resistance of the sample as a function of the angle Φ_{FM} between the two ferromagnets or, reciprocally, the angle as a function of resistance. For our estimation, we have varied the value of the R_{PIP} input parameter from the lowest to the highest possible in the PIP state of the rotation, as well as taking an intermediate value which would be used in a normal analysis

(the P and AP resistance values are always taken as the minimum and maximum resistance values in the rotation respectively). The calculated parameters for the resistance of each barrier and the polarization may slightly vary from one fitting to another, but the overall fitting remains remarkably stable, as shown in Figure 6.

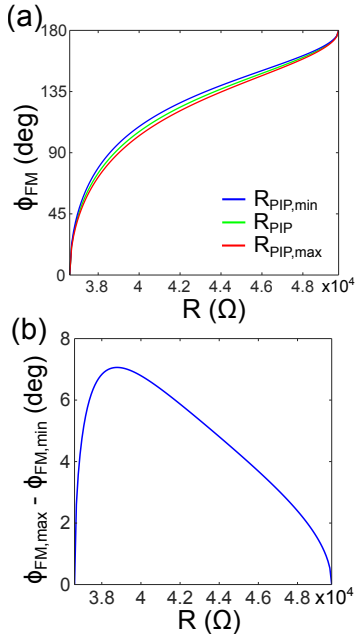


Fig. S6: (a) ϕ_{FM} as a function of resistance for the fittings with maximum, usual, and minimum R_{PIP} used, in the P-AP resistance range. (b) difference of calculated angle vs resistance (in the P-AP resistance range) for the fittings with maximum and minimum R_{PIP} used.

As expected, the difference is higher for the PIP state, and minimum in the P and AP state that are “fixed”. The difference doesn’t exceed 7 degrees, and it keeps below 2 degrees near the P and AP states.

S5. Saturation magnetization for thin Fe(001) films in [100] and [110] directions

Different M vs H measurements were performed at room temperature on a 10 nm thick Fe films, both for the easy [100] and hard [110] crystallographic axes, in order to estimate the magnetocrystalline anisotropy (MCA) energy. The results are depicted in Fig. S7. Using the

saturation field for the two directions, the anisotropy energy can be estimated as $K_{Fe} = M_{Fe}H_{Sat}/2 = 5.1 \times 10^5 \text{ erg} \cdot \text{cm}^{-3}$, where $M_{Fe} = 1714 \text{ emu/cm}^3$ is used. The anisotropy energy per unit cell is therefore MAE= $6.674 \mu\text{eV}$, or $3.337 \mu\text{eV}$ per atom. The obtained energy barrier is similar to the one measured using ferromagnetic resonance [4].

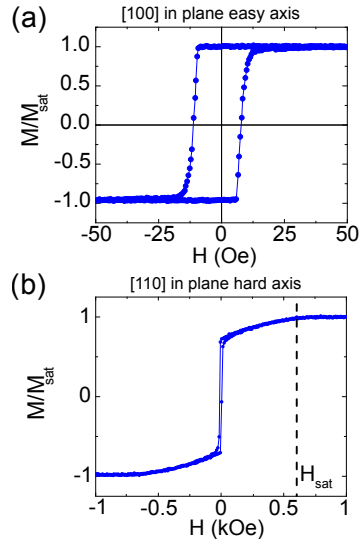


Fig. S7: M vs H measurements on a 10 nm thick Fe film for the easy [100] (a) and hard [110] (b) crystallographic axis. The saturation field (H_{sat}) for the easy axis is around 10 Oe, while for the hard direction it reaches up to 600 Oe.

As shown in Fig.S8, the experimental MCA energy values have been theoretically confronted with theoretical/numerical calculations of the angular in-plane variation of magnetic anisotropy, using the ab-initio Wien2k FP-LAPW code [5]. The calculations were based on a supercell model for a V/MgO/Fe/MgO slab similar to the experimental samples. To insure the requested extreme accuracy in MCA energy values (μeV energy range), a thoroughly well-converged k grid with significantly large number of k -points has been involved. Within these circumstances, our theoretical results for the Fe(001) thin films show standard fourfold anisotropy features and reasonable agreement with the experimentally estimated figures with a maximum theoretical MAE of $4.9 \mu\text{eV}$ per atom (expected theoretical under-estimation of the magnetocrystalline energy within the GGA approach). Note that the superconducting-V induced MCA modulation features cannot be described within the ab-initio

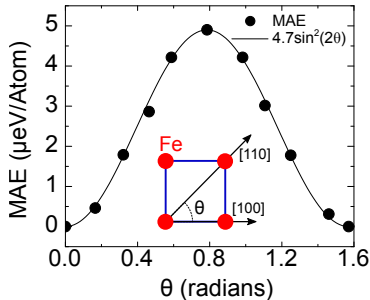


Fig. S 8: Ab-initio calculation of magnetocrystalline anisotropy energy (MAE) as a function of the in-plane orientation angle θ , defined in the inset. Solid line is a phenomenological fit to a $\sin^2(2\theta)$ function.

FP-LAPW approach, describing the V in its normal metallic state. Therefore, the below T_C experimentally observed MCA energy modulations have to be clearly related to the proximity effect in the superconducting V/MgO/Fe(001) system and not to any specific MCA feature of Fe(001) in the V/MgO/Fe(001)/MgO complex stacking sequence.

S6. Evaluation of the vortex induced pinning of domain walls

Using MuMax3 [6], we have compared numerically the DWs formation along the [100] and [110] magnetization directions. The simulations took place in samples with $3 \times 3 \mu\text{m}^2$ lateral dimensions (100 nm rounded corners were used as the devices have been fabricated by optical lithography), with $512 \times 512 \times 16$ cells, at $T = 0$. The rest of the parameters used were $A_{ex} = 2.1 \times 10^{-11}$ J/m for the exchange energy, $M_{\text{sat}} = 1.7 \times 10^6$ A/m for the saturation magnetization, a damping parameter $\alpha = 0.02$, and crystalline anisotropy parameters $K_{C1} = 4.8 \times 10^4$ J/m³ and $K_{C3} = -4.32 \times 10^5$ J/m³. The goal of the simulations was to evaluate the DW formation and their interaction with the superconducting vortices induced by the vertical component of the stray fields at a 2-3 nm from the Fe(001) surface. We observed that, depending on the external field, in the range of 70-1000 Oe both edge-type and inner-type DWs are formed when the field is directed along [100], and mainly edge type DWs are formed with field along [110] (Figure S9a).

We have also calculated the interaction \mathcal{I} between the DW related excess exchange energy E_{ex} and the vertical component of the stray fields, B_{eff} (Figure S9b):

$$\mathcal{I} = \int_0^{N_x} \int_0^{N_y} |B_{\text{eff}}| E_{\text{ex}} \mathcal{F} dx dy \quad (2)$$

Where N_x and N_y are the total number of cells in each dimension of the simulation, and \mathcal{F} is a filter “Vortex generation function” that takes into account the simulated dependence of the number of vortices on the vertically applied field (Figure S9c). The vortices were simulated using the Time Dependent Ginzburg Landau code developed in Madrid described in [7]. The TDGL simulations took place in $5 \times 5 \mu\text{m}^2$ Vanadium samples with 200×200 cells, at $T = 2$ K, with a coherence length $\xi_0 = 2.6 \times 10^{-8}$ based on our experimental estimations for the studied devices, $\kappa = 3$ and $T_C = 4$ K. A uniform field was applied in the perpendicular direction, its magnitude varying from $0.1H_{C2}$ to $0.6H_{C2}$, and the number of vortices generated in the relaxed state were counted.

The second critical field in the vertical direction ($H_{c2} = 3$ kOe) was determined experimentally. The estimated interaction shows that in the weakly saturated regime, when the inner DWs could emerge and the DW-vortex interaction increases, such interaction should pin the magnetization along the [100] direction, corresponding to the MCA already present in the normal state, therefore blocking any magnetization rotation towards the [110] direction, contrary to our experimental observations. The possible reason for the irrelevance of the DW-vortex interaction in our system is that inner DWs are expected to be of Neel-type for the thickness considered [8].

Finally we mention that our numerical evaluations show that, if present, the vortex-DW interaction should remain dominant for the magnetization directed along [100] respect [110] and for the magnetic field range 70-1000 Oe also without K_{C3} parameter providing the MCA energy minima along [110]. In these simulations the Fe(001) layer has been considered to be smooth. In order to further approach simulations to the experiment, we have also verified that the conclusions above are not affected by the introduction of interfacial magnetic disorder due to mismatch defects (every 30 lattice periods) with 25% excess of Fe moment at the Fe/MgO interface [9]. More detailed simulations involving also interface roughness could be needed to further approach the real experimental situation.

S7. Magnetization alignment along [110] and irrelevance of the junction area for the superconductivity induced MCA modification

As we mentioned in the main text, our experiments point that Fe(001) layers are close to a highly saturated state when the magnetization is directed along [100] or equivalent axes. On the other hand, micromagnetic simulations (Figure S9a) show that the magnetization align-

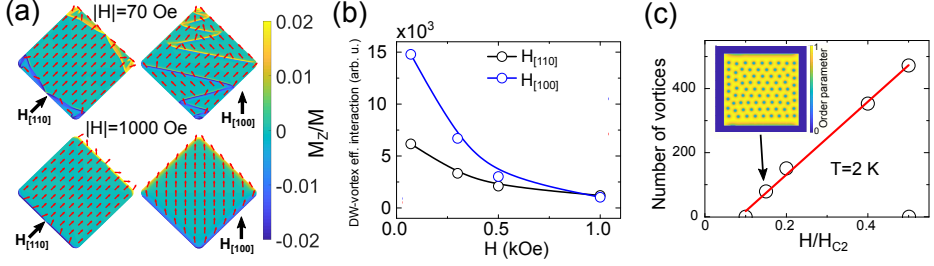


Fig. S9: (a) Typical DW formation mapped by MuMax3 simulations for the $[110]$ and $[100]$ applied field directions in the non-saturated (70 Oe) and saturated (1000 Oe) field regimes. The color map represents the out of plane component of the magnetization, while the red arrows indicate the in plane direction. (b) Values of the 2D integral \mathcal{I} between the local exchange energy (DWs) and the perpendicular component of the stray fields at a distance of 2-3 nm from the ferromagnet, taking into account the vortex generation function \mathcal{F} . (c) Vortex generation function \mathcal{F} , represented as number of vortices formed in a $5 \times 5 \mu\text{m}^2$ square 40 nm thick superconducting Vanadium film as a function of the applied perpendicular field (normalized by the second critical field H_{c2}), simulated at $T = 2$ K by using the TDGL code described in [7]. The insert shows a typical image of the vortices at $H = 0.15H_{c2}$.

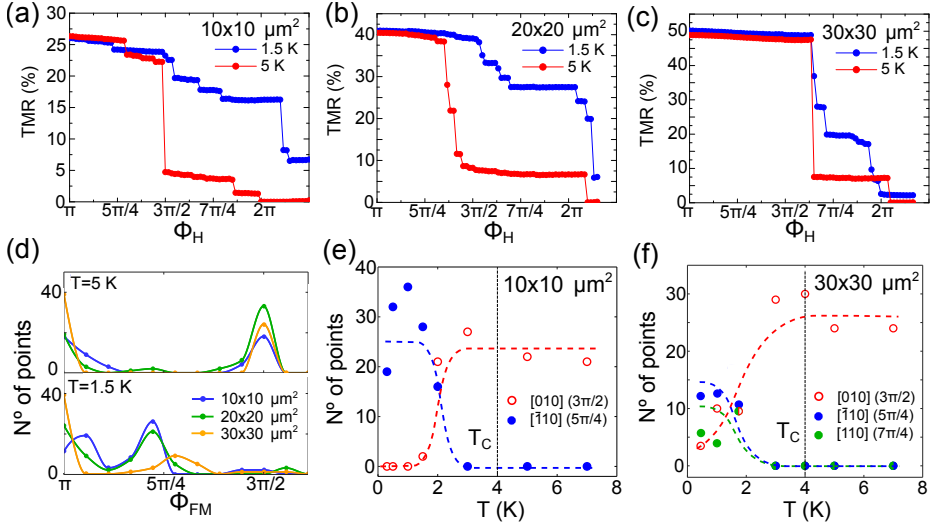


Fig. S10: In-plane field rotation experiments with $H = 70$ Oe below (blue) and above (red) T_C for 10×10 (a), 20×20 (b) and 30×30 (c) μm^2 junctions. (d) Histograms of the calculated angle between the two FM layers ϕ_{FM} for these same rotations, above and below T_C , showing the $[\bar{1}10]$ states for low temperatures. (e) and (f) show the evolution of the $[110]$, $[\bar{1}10]$ and $[010]$ (PIP) states with temperature for the same 10×10 and $30 \times 30 \mu\text{m}^2$ junctions (qualitatively similar evolution is shown in Figure 2f in the main text for the $20 \times 20 \mu\text{m}^2$ junction).

ment is more robust in the [110] direction (or equivalent) rather than in the [100] direction (or equivalent). So, if we indeed reach a highly saturated state in the [100] direction, this should also be the case for the [110] direction. Therefore, the emergent stable tunneling magnetoresistance states we observe experimentally below T_c , cannot be explained in terms of the intermediate multi-domain states but rather correspond to the dominant [110] magnetization alignment of the Fe(001) layer.

As shown in Figure S10, our experiments shows that the observed effects remain qualitatively unchanged when the junction area is varied about an order of magnitude.

S8. Modelling

We describe the V/MgO/Fe structure by the Hamiltonian [10]

$$\begin{aligned}
H = & -t \sum_{\langle i,j \rangle, \sigma} c_{i,\sigma}^\dagger c_{j,\sigma} - \sum_{i,\sigma} (\mu_i - V_i) c_{i,\sigma}^\dagger c_{i,\sigma} \\
& - \sum_i U_i n_{i,\uparrow} n_{i,\downarrow} + \sum_{i,\alpha,\beta} c_{i,\alpha}^\dagger (\mathbf{h}_i \cdot \boldsymbol{\sigma})_{\alpha,\beta} c_{i,\beta} \\
& - \frac{i}{2} \sum_{\langle i,j \rangle, \alpha,\beta} \lambda_i c_{i,\alpha}^\dagger \hat{n} \cdot (\boldsymbol{\sigma} \times \mathbf{d}_{i,j})_{\alpha,\beta} c_{j,\beta}
\end{aligned} \quad (3)$$

defined on a cubic lattice. The first term describes nearest-neighbor hopping. The second term includes the the chemical potential and the potential barrier at the insulating MgO layers. The remaining terms describes superconducting attractive on-site interaction, ferromagnetic exchange interaction, and Rashba spin-orbit interaction, respectively. These are only nonzero in their respective regions. In the above, t is the hopping integral, μ_i is the chemical potential, V_i is the potential barrier that is nonzero only for the MgO layer, $U > 0$ is the attractive on-site interaction giving rise to superconductivity, λ_i is the local spin-orbit coupling magnitude, \hat{n} is a unit vector normal to the interface, $\boldsymbol{\sigma}$ is the vector of Pauli matrices, $\mathbf{d}_{i,j}$ is a vector from site i to site j , and \mathbf{h}_i is the local magnetic exchange field. The number operator used above is defined as $n_{i,\sigma} \equiv c_{i,\sigma}^\dagger c_{i,\sigma}$, and $c_{i,\sigma}^\dagger$ and $c_{i,\sigma}$ are the second-quantization electron creation and annihilation operators at site i with spin σ . The superconducting term in the Hamiltonian is treated by a mean-field approach, where we assume $c_{i,\uparrow} c_{i,\downarrow} = \langle c_{i,\uparrow} c_{i,\downarrow} \rangle + \delta$ and neglect terms of second order in the fluctuations δ .

We consider a system of size $N_x \times N_y \times N_z$ setting the interface normals parallel to the x axis and assuming periodic boundary conditions in the y and z directions. To simplify notation in the following, we define $i \equiv i_x$, $j \equiv j_x$, $\mathbf{i}_{||} \equiv (\hat{i}_x, \hat{i}_y)$ and $\mathbf{k} \equiv (k_y, k_z)$. We apply the Fourier transform

$$c_{i,\sigma} = \frac{1}{\sqrt{N_y N_z}} \sum_{\mathbf{k}} c_{i,\mathbf{k},\sigma} e^{i(\mathbf{k} \cdot \mathbf{i}_{||})} \quad (4)$$

to the above Hamiltonian and use that

$$\frac{1}{N_y N_z} \sum_{\mathbf{i}_{||}} e^{i(\mathbf{k} - \mathbf{k}') \cdot \mathbf{i}_{||}} = \delta_{\mathbf{k}, \mathbf{k}'}. \quad (5)$$

We choose a new basis

$$B_{i,\mathbf{k}}^\dagger = [c_{i,\mathbf{k},\uparrow}^\dagger, c_{i,\mathbf{k},\downarrow}^\dagger, c_{i,-\mathbf{k},\uparrow}, c_{i,-\mathbf{k},\downarrow}] \quad (6)$$

spanning Nambu \times spin space, and rewrite the Hamiltonian as

$$H = H_0 + \frac{1}{2} \sum_{i,j,\mathbf{k}} B_{i,\mathbf{k}}^\dagger H_{i,j,\mathbf{k}} B_{i,\mathbf{k}}. \quad (7)$$

Above, the Hamiltonian matrix is given by

$$\begin{aligned}
H_{i,j,\mathbf{k}} = & \epsilon_{i,j,\mathbf{k}} \hat{\tau}_3 \hat{\sigma}_0 + \delta_{i,j} \left[i \Delta_i \hat{\tau}^+ \hat{\sigma}_y - i \Delta_i^* \hat{\tau}^- \hat{\sigma}_y \right. \\
& + h_i^x \hat{\tau}_3 \hat{\sigma}_x + h_i^y \hat{\tau}_0 \hat{\sigma}_y + h_i^z \hat{\tau}_3 \hat{\sigma}_z \\
& \left. - \lambda_i \sin(k_y) \hat{\tau}_0 \hat{\sigma}_z + \lambda_i \sin(k_z) \hat{\tau}_3 \hat{\sigma}_y \right],
\end{aligned} \quad (8)$$

where Δ_i is the superconducting gap which we solve for self-consistently, $\hat{\tau}_i \hat{\sigma}_j \equiv \hat{\tau}_i \otimes \hat{\sigma}_j$ is the Kronecker product of the Pauli matrices spanning Nambu and spin space, $\hat{\tau}^\pm \equiv (\hat{\tau}_1 \pm i \hat{\tau}_2)/2$, and

$$\begin{aligned}
\epsilon_{i,j,\mathbf{k}} \equiv & -2t [\cos(k_y) + \cos(k_z)] \delta_{i,j} \\
& - t (\delta_{i,j+1} + \delta_{i,j-1}) \\
& - (\mu_i - V_i) \delta_{i,j}.
\end{aligned} \quad (9)$$

The constant term in Eq. (7) is given by

$$\begin{aligned}
H_0 = & - \sum_{i,\mathbf{k}} \{2t [\cos(k_y) + \cos(k_z)] + \mu_i - V_i\} \\
& + N_y N_z \sum_i \frac{|\Delta_i|^2}{U_i}.
\end{aligned} \quad (10)$$

We absorb the sum over lattice sites in Eq. (7) into the matrix product by defining a new basis

$$W_{\mathbf{k}}^\dagger = [B_{1,\mathbf{k}}^\dagger, \dots, B_{i,\mathbf{k}}^\dagger, \dots, B_{N_x,\mathbf{k}}^\dagger]. \quad (11)$$

Eq. (7) can then be rewritten as

$$H = H_0 + \frac{1}{2} \sum_{\mathbf{k}} W_{\mathbf{k}}^\dagger H_{\mathbf{k}} W_{\mathbf{k}}, \quad (12)$$

where

$$H_{\mathbf{k}} = \begin{bmatrix} H_{1,1,\mathbf{k}} & \cdots & H_{1,N_x,\mathbf{k}} \\ \vdots & \ddots & \vdots \\ H_{N_x,1,\mathbf{k}} & \cdots & H_{N_x,N_x,\mathbf{k}} \end{bmatrix} \quad (13)$$

is Hermitian and can be diagonalized numerically. We obtain eigenvalues $E_{n,\mathbf{k}}$ and eigenvectors $\Phi_{n,\mathbf{k}}$ given by

$$\begin{aligned}
\Phi_{n,\mathbf{k}}^\dagger = & [\phi_{1,n,\mathbf{k}}^\dagger, \dots, \phi_{N_x,n,\mathbf{k}}^\dagger], \\
\phi_{i,n,\mathbf{k}}^\dagger = & [u_{i,n,\mathbf{k}}^* v_{i,n,\mathbf{k}}^* w_{i,n,\mathbf{k}}^* x_{i,n,\mathbf{k}}^*].
\end{aligned} \quad (14)$$

The diagonalized Hamiltonian can be written on the form

$$H = H_0 + \frac{1}{2} \sum_{n,\mathbf{k}} E_{n,\mathbf{k}} \hat{\gamma}_{n,\mathbf{k}}^\dagger \gamma_{n,\mathbf{k}}, \quad (15)$$

where the new quasi-particle operators are related to the old operators by

$$\begin{aligned} c_{i,\mathbf{k},\uparrow} &= \sum_n u_{i,n,\mathbf{k}} \gamma_{n,\mathbf{k}}, \\ c_{i,\mathbf{k},\downarrow} &= \sum_n v_{i,n,\mathbf{k}} \gamma_{n,\mathbf{k}}, \\ c_{i,-\mathbf{k},\uparrow}^\dagger &= \sum_n w_{i,n,\mathbf{k}} \gamma_{n,\mathbf{k}}, \\ c_{i,-\mathbf{k},\downarrow}^\dagger &= \sum_n x_{i,n,\mathbf{k}} \gamma_{n,\mathbf{k}}. \end{aligned} \quad (16)$$

The superconducting gap is given by $\Delta_i \equiv U_i \langle c_{i,\uparrow} c_{i,\downarrow} \rangle$. We apply the Fourier transform in Eq. (4) and use Eq. (16) in order to rewrite the expression in terms of the new quasi-particle operators. Also using that $\langle \gamma_{n,\mathbf{k}}^\dagger \gamma_{m,\mathbf{k}} \rangle = f(E_{n,\mathbf{k}}/2) \delta_{n,m}$, we obtain the expression

$$\Delta_i = -\frac{U_i}{N_y N_z} \sum_{n,\mathbf{k}} v_{i,n,\mathbf{k}} w_{i,n,\mathbf{k}}^* [1 - f(E_{n,\mathbf{k}}/2)] \quad (17)$$

for the gap, that we use in computing the eigenenergies iteratively. Above, $f(E_{n,\mathbf{k}}/2)$ is the Fermi-Dirac distribution.

Using the obtained eigenenergies, we compute the free energy,

$$F = H_0 - \frac{1}{\beta} \sum_{n,\mathbf{k}} \ln(1 + e^{-\beta E_{n,\mathbf{k}}/2}), \quad (18)$$

where $\beta = (k_B T)^{-1}$. The preferred magnetization directions are described by the local minima of the free energy. In the main body of the paper, we use this to explain the possible magnetization directions of the soft ferromagnet when rotating an IP external magnetic field over a 2π angle starting at a parallel alignment with the hard ferromagnet.

Other relevant quantities to consider in modelling the experimental system is the superconducting coherence length and the superconducting critical temperature. In the ballistic limit, the coherence length is given by $\xi = \hbar v_F / \pi \Delta_0$, where $v_F = \frac{1}{\hbar} \frac{dE_{\mathbf{k}}}{dk} \Big|_{k=k_F}$ is the Fermi velocity related to the normal-state eigenenergy $E_{\mathbf{k}} = -2t[\cos(k_x) + \cos(k_y) + \cos(k_z)] - \mu$, and Δ_0 is the zero-temperature superconducting gap [11]. The critical temperature is found by a binomial search, where we decide if a temperature is above or below T_c by determining whether $\Delta_{N_x^S/2}$ increases towards a superconducting solution or decreases towards a normal state solution from the initial guess under iterative recalculations of Δ_i . We choose an initial guess with a magnitude very close to

zero and with a lattice site dependence similar to that of the gap just below T_c .

In the main plot showing the free energy under IP rotations of the magnetization, we have chosen parameters $t = 1$, $\mu_S = \mu_{\text{SOC}} = \mu_F = 0.9$, $V = 2.1$, $U = 1.35$, $\lambda = 0.4$, $h = 0.8$, $N_x^S = 30$, $N_x^{\text{SOC}} = 3$, $N_x^F = 8$, and $N_y = N_z = 60$. All length scales are scaled by the lattice constant a , all energy scales are scaled by the hopping parameter t , and the magnitude of the spin-orbit coupling λ is scaled by ta . In order to make the system computationally manageable, the lattice size is scaled down compared to the experimental system, however the results should give qualitatively similar results as long as the ratios between the coherence length and the layer thicknesses are reasonable compared to the experimental system. For this set of parameters, the superconducting coherence length is approximately $0.6N_x^S$. Since the coherence length is inversely proportional to the superconducting gap, U has been chosen to be large in order to allow for a coherence length smaller than the thickness of the superconducting layer. Although this results in a large superconducting gap, the modelling will qualitatively fit the experimental results as long as the other parameters are adjusted accordingly. We therefore choose the local magnetic exchange field so that $h \gg \Delta$, as in the experiment. For this parameter set, $h \approx 20\Delta$. The order of magnitude of λ is $1 \text{ eV}\text{\AA}$, given that $t \sim 1 \text{ eV}$ and $a \sim 4 \text{ \AA}$. This is realistic considering Rashba parameters measured in several materials [12]. The Rashba spin-orbit field at the interfaces of V/MgO/Fe is caused by a structural inversion asymmetry across the MgO layer, and breaks the inversion symmetry at the MgO interfaces [13]. This causes generation of triplet-superconductivity even for weakly spin-polarized ferromagnets with a small spin-orbit field [14]. We are therefore not dependent upon a strong magnetic exchange field and a strong spin-orbit field for realizing the observed effects. For the AF coupling contribution to the free energy, we set $f_{\text{AF}} = 0.01$ in order to fit the anisotropy of the experimental system just above T_c .

* e-mail: farkhad.aliev@uam.es

- [1] C. Tiusan, F. Greullet, M. Hehn, F. Montaigne, S. Andrieu and A. Schuhl, Spin tunnelling phenomena in single-crystal magnetic tunnel junction systems, *Journal of Physics: Condensed Matter*, **19**, 16 (2007).
- [2] L. N. Bulaevskii and E. M. Chudnovsky, Ferromagnetic film on a superconducting substrate, *Phys. Rev. B* **63**, 012502 (2000).
- [3] J. C. Slonczewski, Conductance and exchange coupling of two ferromagnets separated by a tunneling barrier. *Phys. Rev. B* **39**, 6995 (1989).
- [4] A. N. Anisimov, M. Farle, P. Pouloupoulos, W. Plатов, K. Baberschke, P. Isberg, R. Wappling, A. M. N. Niklasson and O. Eriksson, *Orbital Magnetism and Magnetism*

- Anisotropy Probed with Ferromagnetic Resonance, *Phys. Rev. Lett.* **82**, 2390 (1999).
- [5] P. Blaha, K. Schwarz, F. Tran, R. Laskowski, G.K.H. Madsen and L.D. Marks, An APW+lo program for calculating the properties of solids, *J. Chem. Phys.* **152**, 074101 (2020).
- [6] A. Vansteenkiste, J. Leliaert, M. Dvornik, M. Helsen, F. Garcia-Sanchez and B. Van Waeyenberge, The design and verification of MuMax3, *AIP Advances* **4**, 107133 (2014).
- [7] A. Lara, C. González-Ruano and F.G. Aliev, Time-dependent Ginzburg-Landau simulations of superconducting vortices in three dimensions, *Low Temperature Physics* **46**, 316 (2020).
- [8] A. Hubert and R. Schäfer, *Magnetic domains. The analysis of magnetic microstructures* (Springer, Berlin, 1999).
- [9] E. Jal et al; Interface Fe magnetic moment enhancement in MgO/Fe/MgO trilayers, *Appl. Phys. Lett.* **107**, 092404 (2015).
- [10] L. G. Johnsen, N. Banerjee, and J. Linder, Magnetization reorientation due to the superconducting transition in heavy-metal heterostructures, *Phys. Rev. B* **99**, 134516 (2019).
- [11] J. Bardeen, L. N. Cooper and J. R. Schrieffer, Theory of Superconductivity, *Phys. Rev.* **108**, 1175 (1957).
- [12] A. Manchon, H. C. Koo, J. Nitta, S. M. Frolov, and R. A. Duine, New perspectives for Rashba spin-orbit coupling, *Nat. Mater.* **14**, 871 (2015).
- [13] I. Martínez, P. Högl, C. González-Ruano, J. P. Cascales, C. Tiusan, Y. Lu, M. Hehn, A. Matos-Abiague, J. Fabian, I. Žutić and F. G. Aliev, Interfacial Spin-Orbit Coupling: A Platform for Superconducting Spintronics, *Phys. Rev. Appl.* **13**, 014030 (2020).
- [14] T. Vezin, C. Shen, J. E. Han, and I. Žutić, Enhanced spin-triplet pairing in magnetic junctions with *s*-wave superconductors, *Phys. Rev. B*, **101**, 014515 (2020).

II

REFERENCE

Lina G. Johnsen, Kristian Svalland, and Jacob Linder,

Controlling the Superconducting Transition by Rotation of an Inversion Symmetry Breaking Axis,

Phys. Rev. Lett. **125**, 107002 (2020).


CONTRIBUTIONS

LGJ performed most of the analytical calculations, all of the numerical calculations, and wrote the paper. KS derived the symmetrized expression for the Rashba spin-orbit coupling. All authors contributed to discussions and revision of the paper. JL initiated and supervised the project.

Controlling the Superconducting Transition by Rotation of an Inversion Symmetry-Breaking Axis

Lina G. Johnsen[✉], Kristian Svalland[✉], and Jacob Linder

Center for Quantum Spintronics, Department of Physics, Norwegian University of Science and Technology, NO-7491 Trondheim, Norway

 (Received 3 September 2019; revised 28 April 2020; accepted 10 August 2020; published 3 September 2020)

We consider a hybrid structure where a material with Rashba-like spin-orbit coupling is proximity coupled to a conventional superconductor. We find that the superconducting critical temperature T_c can be tuned by rotating the vector \mathbf{n} characterizing the axis of broken inversion symmetry. This is explained by a leakage of s -wave singlet Cooper pairs out of the superconducting region, and by conversion of s -wave singlets into other types of correlations, among these s -wave odd-frequency pairs robust to impurity scattering. These results demonstrate a conceptually different way of tuning T_c compared to the previously studied variation of T_c in magnetic hybrids.

DOI: 10.1103/PhysRevLett.125.107002

Introduction.—Over the last years, research on combining superconducting and magnetic materials has shown that the physical properties of the resulting hybrid structure may be drastically altered compared to those of the individual materials [1–3]. In a conventional superconductor (S), electrons combine into s -wave singlet Cooper pairs [4]. A decrease in the s -wave singlet amplitude leads to a loss of superconducting condensation energy, and thus also a suppression of the superconducting critical temperature T_c . Such a decrease can be obtained by leakage of Cooper pairs into a nonsuperconducting material in proximity to the superconductor, and by conversion of s -wave singlets into different singlet and triplet Cooper pairs. For the latter to happen, the nonsuperconducting material must introduce additional symmetry breaking. This is the case in superconductor-ferromagnet hybrids where the spin splitting of the energy bands of the homogeneous ferromagnetic material (F) leads to creation of opposite-spin triplets [2,3,5].

A single, homogeneous ferromagnet cannot alone cause variation in the s -wave singlet amplitude under rotations of the magnetization \mathbf{m} . However, experiments [6–10] have demonstrated that the critical temperature of $F/S/F$ and $S/F/F$ structures can be modulated by changing the relative orientation of the magnetization of the ferromagnets. The misalignment opens all three triplet channels, leading to a stronger decrease in the superconducting condensation energy associated with the singlet amplitude. Recent work [11–15] has shown that the rotational invariance of the S/F structure can also be broken by adding thin heavy normal-metal layers that boost the interfacial Rashba spin-orbit coupling. Spin-orbit coupling (SOC) introduces inversion symmetry breaking perpendicular to an axis, here characterized by the vector \mathbf{n} .

While ferromagnetism only leads to spin splitting of the energy bands of spin-up and spin-down electrons, Rashba

SOC is in addition odd under inversion of the momentum component perpendicular to \mathbf{n} . This raises an interesting question. While the proximity effect and accompanying change in T_c in a S/F bilayer is invariant under rotations of \mathbf{m} , is it possible that T_c in a S/SOC bilayer is *not* invariant under rotations of \mathbf{n} (see Fig. 1)?

Motivated by this, we explore the possibility of T_c modulation under reorientations of the inversion symmetry-breaking vector \mathbf{n} in a bilayer consisting of a conventional superconductor and a material with Rashba-like SOC in the bulk. We also include interfacial Rashba SOC with an inversion symmetry-breaking vector \mathbf{n}_{int} perpendicular to the interface. This simple model illustrates the concept of tuning T_c via rotation of \mathbf{n} .

When the bulk SOC is stronger than the interfacial contribution, we discover a suppression of T_c when rotating \mathbf{n} from an out-of-plane (OOP) to an in-plane (IP) orientation. This effect is enhanced by increasing the interfacial SOC, provided that $\mathbf{n} \parallel \mathbf{n}_{\text{int}}$ when \mathbf{n} is OOP. The difference in T_c for IP and OOP orientations of \mathbf{n} can at least partly be accounted for by the absence of s -wave odd-frequency triplets for an OOP orientation of \mathbf{n} . Since s -wave triplets are robust with respect to impurity scattering, we expect our prediction of an IP suppression of T_c to be observable

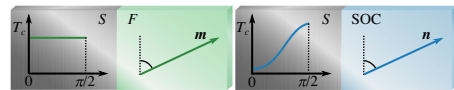


FIG. 1. In a S/F bilayer (left), T_c is invariant under a rotation of \mathbf{m} . In a S/SOC bilayer (right), the inversion symmetry perpendicular to \mathbf{n} is broken. This opens up the possibility for a variation in T_c under a rotation of \mathbf{n} .

not only in the ballistic limit covered by our theoretical framework, but also in the diffusive limit. When interfacial SOC dominates, the T_c modulation changes qualitatively. The critical temperature is instead suppressed for antiparallel compared to parallel \mathbf{n} and \mathbf{n}_{int} . This is explained by a reduced leakage of s -wave singlets into the non-superconducting region when the total SOC magnitude is increased. Moreover, we demonstrate a variation in T_c even when \mathbf{n} is varied solely in the plane of the SOC layer.

The lattice Bogoliubov–de Gennes framework.—We consider a 3D cubic S /SOC lattice structure of size $N_x \times N_y \times N_z$ with interface normal along the x axis. We assume periodic boundary conditions along the y and z axes. The inversion symmetry breaking in the nonsuperconducting layer is accounted for by the existence of a Rashba SOC term in the Hamiltonian, with a constant magnitude λ . In addition, we include a perpendicular Rashba contribution with $\mathbf{n}_{\text{int}} = \mathbf{x}$ and magnitude λ_{int} at the atomic layer closest to the interface. Our Hamiltonian thus accounts for both a Rashba-like SOC field in the bulk of the nonsuperconducting material, and interfacial Rashba SOC. We use the ballistic-limit tight-binding Bogoliubov–de Gennes framework, following a similar approach to that in Refs. [15–17]. Our Hamiltonian is given by

$$\begin{aligned}
 H = & -t \sum_{\langle ij \rangle, \sigma} c_{i, \sigma}^\dagger c_{j, \sigma} - \sum_i \mu_i c_{i, \sigma}^\dagger c_{i, \sigma} \\
 & - \sum_i U_i n_{i, \uparrow} n_{i, \downarrow} - \frac{i}{2} \sum_{\langle ij \rangle, \alpha, \beta} c_{i, \alpha}^\dagger (\lambda \mathbf{n} + \lambda_{\text{int}} \mathbf{n}_{\text{int}}) \\
 & \cdot \left\{ \boldsymbol{\sigma} \times \left[\frac{1}{2} (1 + \zeta) (\mathbf{d}_{ij})_x + (\mathbf{d}_{ij})_{\parallel} \right] \right\}_{\alpha, \beta} c_{j, \beta}. \quad (1)
 \end{aligned}$$

Above, t is the hopping integral, μ_i is the chemical potential at lattice site i , $U_i > 0$ is the attractive on-site interaction giving rise to superconductivity, $\boldsymbol{\sigma}$ is the vector of Pauli matrices, \mathbf{d}_{ij} is the vector from site i to site j , and $(\mathbf{d}_{ij})_x$ and $(\mathbf{d}_{ij})_{\parallel}$ are its projections onto the x axis and yz plane, respectively. If site i and j are both inside the SOC layer, $\zeta = 1$. Otherwise, $\zeta = 0$. $c_{i, \sigma}^\dagger$ and $c_{i, \sigma}$ are the second quantization electron creation and annihilation operators at site i with spin σ , and $n_{i, \sigma} \equiv c_{i, \sigma}^\dagger c_{i, \sigma}$ is the number operator. The Rashba term [18] has been symmetrized in order to allow for IP components of \mathbf{n} while ensuring a Hermitian Hamiltonian. The superconducting term is treated by a mean-field approach, assuming $c_{i, \uparrow} c_{i, \downarrow} = \langle c_{i, \uparrow} c_{i, \downarrow} \rangle + \delta$ and neglecting terms of second order in the fluctuations δ . The terms of the Hamiltonian are only nonzero in their respective regions.

We diagonalize the Hamiltonian numerically and compute the physical quantities of interest as outlined in the Supplemental Material [19]. The superconducting gap $\Delta_i \equiv U_i \langle c_{i, \uparrow} c_{i, \downarrow} \rangle$ is treated iteratively. We calculate T_c by a binomial search [20] where we for each of the N_T

temperatures considered decide whether the gap increases toward a superconducting state or decreases toward a normal state from an initial guess much smaller than the zero-temperature gap. In this way, we do not calculate the exact value for the gap, and we can thus get high accuracy in T_c for a low number of iterations N_Δ .

In order to confirm that the modulation of T_c is caused by conversion of s -wave even-frequency singlets into other singlet and triplet correlations, we consider the even-frequency s -wave singlet amplitude $S_{s,i} \equiv \langle c_{i, \uparrow} c_{i, \downarrow} \rangle - \langle c_{i, \downarrow} c_{i, \uparrow} \rangle$. As a measure of the total s -wave singlet amplitude of the superconductor, we introduce the quantity $\mathcal{S} \equiv (1/N_{x,S}) \sum_i |S_{s,i}|$, where the sum is taken over the superconducting region only. We also define the opposite- and equal-spin odd-frequency s -wave triplet amplitudes $S_{0i}(\tau) \equiv \langle c_{i, \uparrow}(\tau) c_{i, \downarrow}(0) \rangle + \langle c_{i, \downarrow}(\tau) c_{i, \uparrow}(0) \rangle$ and $S_{\sigma i}(\tau) \equiv \langle c_{i, \sigma}(\tau) c_{i, \sigma}(0) \rangle$ [17], where the time-dependent electron annihilation operator is given by $c_{i, \sigma}(\tau) \equiv e^{iH\tau} c_{i, \sigma} e^{-iH\tau}$ [21]. The s -wave triplet amplitude is of particular interest as it is the only triplet amplitude robust to impurity scattering. Other superconducting correlations, such as p -wave and d -wave correlations, also appear due to the presence of SOC, as will be discussed later in this work.

The superconducting critical temperature.—By following the above approach, we plot the critical temperature and the total s -wave singlet amplitude in Fig. 2. To ensure that the effect is robust, we use two different parameter sets. The parameters are given in the figure caption. All length scales are scaled by the lattice constant a , the SOC magnitudes are scaled by ta , and the remaining energy scales are scaled by t . For $t \sim 1$ eV and $a \sim 5$ Å, the order of magnitude of λ is 10^{-10} eVm, which corresponds well to Rashba parameters found in several materials [22]. In order to make the system computationally manageable, the lattice size and coherence length $\xi \propto \Delta^{-1}$ must be scaled down, leading to an overestimation of Δ and thus T_c . The results in Fig. 2 must therefore be seen mainly as qualitative.

For both sets of parameters, we see a qualitatively similar behavior for rotations of \mathbf{n} in the xz plane [see Fig. 2(a) for the first set of parameters]. When $\lambda_{\text{int}} = 0$, we find a suppression of T_c for an IP \mathbf{n} compared to an OOP \mathbf{n} . When $0 < \lambda_{\text{int}} < \lambda$, there are still maxima at the OOP directions $\mathbf{n} \parallel \mathbf{n}_{\text{int}}$ and $(-\mathbf{n}) \parallel \mathbf{n}_{\text{int}}$, but when increasing λ_{int} the magnitude of the former increases while the magnitude of the latter decreases. As long as \mathbf{n} is parallel to \mathbf{n}_{int} in the OOP configuration, the T_c modulation from IP to OOP is thus enhanced by the additional interface contribution. For $\lambda_{\text{int}} > \lambda$, T_c is maximal for $\mathbf{n} \parallel \mathbf{n}_{\text{int}}$ and minimal for $(-\mathbf{n}) \parallel \mathbf{n}_{\text{int}}$. The change in T_c from the parallel to the antiparallel configuration increases with an increasing λ_{int} . The results presented here only depend on the relative orientations of \mathbf{n} and \mathbf{n}_{int} , and are independent of whether \mathbf{n}_{int} is directed out of or into the nonsuperconducting material. Notice that in all cases, nonzero SOC increases T_c compared to when $\lambda = \lambda_{\text{int}} = 0$. This is explained by a

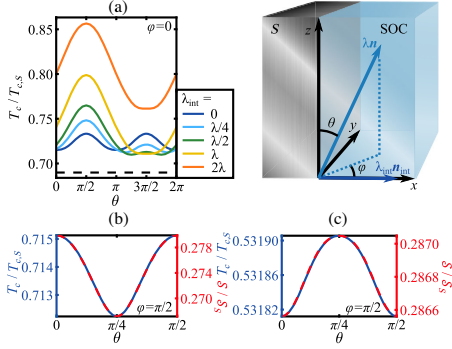


FIG. 2. The T_c modulation under rotation of \mathbf{n} between IP and OOP orientations (a) is qualitatively different for $\lambda_{\text{int}} < \lambda$ and $\lambda_{\text{int}} > \lambda$. The dashed line marks T_c for $\lambda = \lambda_{\text{int}} = 0$. Depending on the material parameters, T_c can have either its IP maxima (b) or minima (c) along the cubic axes. Notice the strong correlation between T_c and the total s -wave singlet amplitude at $T = T_c$. Above, $T_{c,S}$ and S_S corresponds to when the superconductor is not very proximity to the SOC layer. We have used parameters $N_{x,S} = 7$, $N_{x,HM} = 3$, $N_y = N_z = 85$, $\mu_S = 1.9$, $\mu_{HM} = 1.7$, $U = 2.1$, $\lambda = 0.8$, $N_T = 20$, and $N_\Delta = 35$ for panels (a) and (b), and $N_{x,S} = 5$, $N_{x,HM} = 2$, $N_y = N_z = 100$, $\mu_S = 1.9$, $\mu_{HM} = 1.7$, $U = 1.9$, $\lambda = 0.2$, $N_T = 25$, and $N_\Delta = 40$ for panel (c), corresponding to coherence lengths $\xi = 4$ and $\xi = 7$, respectively. In panels (b) and (c), $\lambda_{\text{int}} = 0$.

decreased leakage of conventional singlets into the non-superconducting region.

From panels (b) and (c), we see that there is also an IP variation in T_c , that may give the strongest in-plane suppression either when \mathbf{n} is oriented at a $\pi/4$ angle with respect to the cubic axes, or when \mathbf{n} is oriented along the cubic axes. As we find a similar variation in the normal-state free energy, which only depends on the eigenenergy spectrum of the system, this varying modulation of the IP component of T_c is likely to be caused by band-structure effects due to the crystal structure of the cubic lattice. In order to demonstrate the IP modulation, the interfacial SOC should preferably be as small as possible.

To demonstrate that the T_c modulation can be attributed to the variation of the s -wave singlet amplitude in the superconducting region, we plot the total s -wave singlet amplitude as a function of the IP angle of \mathbf{n} [panels (b) and (c)]. As expected, it is of a similar form as the variation in T_c . The slight deviation between T_c and S is caused by S being calculated at a temperature T_c slightly below T_c . We have verified that the variation in S and T_c is similar also for panel (a).

The variation in the s -wave singlet amplitude inside the superconducting region is caused by a reduced leakage of s -wave singlets out of the superconducting region, and conversion of s -wave singlets into other singlet and triplet

correlations. When λ_{int} is nonzero, the length of $\lambda\mathbf{n} + \lambda_{\text{int}}\mathbf{n}_{\text{int}}$ changes under rotations of \mathbf{n} , leading to an effective change in the magnitude of the SOC. Increased SOC causes an increase in the Fermi vector mismatch [23], due to a change in the Fermi surface in the nonsuperconducting material. Since the overlap between the Fermi surfaces of the two materials decreases, there is an increase in the normal reflection at the interface, as our analytical results verify. For large λ_{int} , the T_c modulation is dominated by variation in the Fermi vector mismatch. If we further investigate the triplet amplitudes present for different orientations of \mathbf{n} , we find that the s -wave odd-frequency triplet amplitude is absent for $\mathbf{n} = \mathbf{x}$, i.e., when \mathbf{n} has no IP component. For all other orientations of \mathbf{n} , the s -wave odd-frequency anomalous triplet amplitude is nonzero. This suggests that the OOP to IP change in T_c is at least partly caused by the increase in the s -wave triplet amplitude from zero when \mathbf{n} points OOP to an increasing finite value as the IP component of \mathbf{n} increases. When λ_{int} is small, so that the length of $\lambda\mathbf{n} + \lambda_{\text{int}}\mathbf{n}_{\text{int}}$ is approximately constant, we may therefore expect an IP suppression of T_c not only in the ballistic-limit materials covered by our theoretical framework, but also in diffusive materials. Below, we perform analytical calculations which prove that odd-frequency pairing is absent when \mathbf{n} points OOP.

The continuum Bogoliubov–de Gennes framework.—In order to explain the absence of s -wave odd-frequency triplets when \mathbf{n} is OOP, we consider two 2D continuum systems that can be treated analytically within the Bogoliubov–de Gennes framework [24–31]: a SOC/ S bilayer with an OOP $\mathbf{n} = \mathbf{x}$, and a F/S bilayer with magnetization $\mathbf{m} \parallel \mathbf{z}$. We use conventions similar to those in Refs. [30,31]. Our systems are located in the xy plane, with interface normal along x and the interface at $x = 0$.

We find the scattering wave functions $\Psi_n(x_1)$ and $\tilde{\Psi}_m(x_2)$ that we will use to construct the Green's functions in the system from the time-independent Schrödinger equations [30–32]

$$\begin{aligned} H(p_y)\Psi_n(x_1) &= (\omega + i\delta)\Psi_n(x_1), \\ H^*(p_y)\tilde{\Psi}_m(x_2) &= (\omega + i\delta)\tilde{\Psi}_m(x_2), \end{aligned} \quad (2)$$

respectively, where

$$\begin{aligned} H(p_y) &= (-\partial_x^2/\eta + p_y^2/\eta - \mu)\hat{\tau}_3\hat{\sigma}_0 \\ &+ \Delta i\hat{\tau}^+\hat{\sigma}_y - \Delta^* i\hat{\tau}^-\hat{\sigma}_y + h_x\hat{\tau}_3\hat{\sigma}_x + h_y\hat{\tau}_0\hat{\sigma}_y + h_z\hat{\tau}_3\hat{\sigma}_z \\ &- \lambda(n_x p_y + n_y i\partial_x)\hat{\tau}_0\hat{\sigma}_z + i\lambda n_z\partial_x\hat{\tau}_3\hat{\sigma}_y + \lambda n_z p_y\hat{\tau}_0\hat{\sigma}_x. \end{aligned} \quad (3)$$

Above, $\delta > 0$ is real and infinitesimal, $\eta \equiv 2m/\hbar^2$, p_y is the momentum in the y direction, and $\mathbf{h} = (h_x, h_y, h_z)$ is the magnetic exchange field. The terms are only nonzero in their respective regions. The four components of the

scattering wave functions correspond to spin-up and spin-down electrons, and spin-up and spin-down holes, respectively. The spins are defined with respect to the z axis. The indices n and m refer to the eight possible wave functions describing scattering of quasiparticles incoming from the left and right. In the continuum model, the symmetrization of the Rashba term enters through the boundary conditions of the wave functions at $x = 0$ rather than through the Hamiltonian [33]. From the scattering wave functions, we construct the retarded Green's function in Nambu \otimes spin space for $x_1 > x_2$ and $x_1 < x_2$, and apply boundary conditions at $x_1 = x_2$.

The even-(odd)-frequency singlet and triplet retarded anomalous Green's functions can be written in terms of the center of mass coordinate $X \equiv (x_1 + x_2)/2$ and the relative coordinate $x \equiv x_1 - x_2$ as [30,31]

$$\begin{aligned} F_0^{r,E(O)}(X, x, p_y; \omega) &= [F_0^r(X, x, p_y; \omega) \begin{pmatrix} + \\ - \end{pmatrix} F_0^r(X, -x, -p_y; \omega)]/2, \\ F_i^{r,E(O)}(X, x, p_y; \omega) &= [F_i^r(X, x, p_y; \omega) \begin{pmatrix} - \\ + \end{pmatrix} F_i^r(X, -x, -p_y; \omega)]/2, \end{aligned} \quad (4)$$

where $i = \{1, 2, 3\}$, and

$$\begin{aligned} F_0^r(X, x, p_y; \omega) &= [F_{\uparrow\downarrow}^r(X, x, p_y; \omega) - F_{\downarrow\uparrow}^r(X, x, p_y; \omega)]/2, \\ F_1^r(X, x, p_y; \omega) &= F_{\uparrow\uparrow}^r(X, x, p_y; \omega), \\ F_2^r(X, x, p_y; \omega) &= F_{\downarrow\downarrow}^r(X, x, p_y; \omega), \\ F_3^r(X, x, p_y; \omega) &= [F_{\uparrow\downarrow}^r(X, x, p_y; \omega) + F_{\downarrow\uparrow}^r(X, x, p_y; \omega)]/2 \end{aligned} \quad (5)$$

represents the singlet amplitude, the equal-spin triplet amplitudes ($i = 1, 2$), and the opposite-spin triplet amplitude ($i = 3$), respectively. The retarded anomalous Green's functions $F_{\sigma\sigma'}^r(X, x, p_y; \omega)$ are anomalous elements of the retarded Green's function in Nambu \otimes spin space. Odd (even) frequency refers to the sum of the retarded and advanced Green's functions being odd (even) under inversion of relative time, or equivalently under inversion of the sign of ω .

The analytical expressions obtained for the even- and odd-frequency singlet and triplet retarded anomalous Green's functions are given in the Supplemental Material [19]. Their spatial symmetries are determined by their parities under inversion of x and p_y . Although the s -wave and $d_{x^2-y^2}$ -wave triplets have the same parities along the x and y axis, the presence of the s -wave triplet is proven by a nonzero result when integrating over all spatial coordinates.

Singlet and triplet amplitudes.—For the 2D SOC/ S structure with $\mathbf{n} = \mathbf{x}$, we find that s - and p_x -wave singlets, and p_y - and d_{xy} -wave opposite-spin triplets are present.

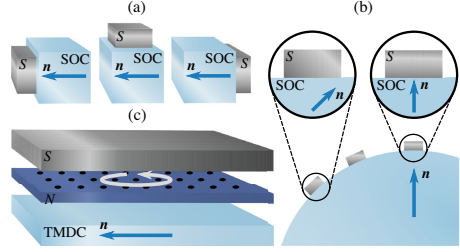


FIG. 3. For the experimental observation of the IP to OOP T_c modulation, we suggest growing the superconductor on (a) different surfaces of a noncentrosymmetric material or (b) on a curved noncentrosymmetric material. For observing IP variations, we suggest (c) growing a normal metal with a cubic lattice structure at different angles compared to a TMDC with IP inversion symmetry breaking, and then growing the superconductor on top. The N /TMDC bilayer effectively enables a rotation of \mathbf{n} compared to the lattice.

At the first glance, it might seem strange that the odd-frequency s -wave triplet amplitude is zero, when it is nonzero for a 2D F/S structure with magnetization along the z axis. Although the Hamiltonians of these systems are of a similar form, they allow for the existence of different triplet amplitudes. The crucial difference leading to a generation of p_y - and d_{xy} -wave triplets in the SOC/ S system rather than s - and p_x -wave triplets as in the F/S system, is the momentum dependence of the Rashba term.

We have also investigated a 2D SOC/ S structure for an IP orientation $\mathbf{n} = \mathbf{z}$ numerically and find additional equal-spin triplets with an odd-frequency symmetry. For a 3D SOC/ S system with \mathbf{n} OOP, the Rashba term depends on the momentum both along the y and z axes. Similarly as in 2D, we expect this to allow for triplets that are odd under inversion of p_y and p_z . This is ultimately the reason for the absence of s -wave triplets.

Experimental realization.—We finally comment on the possibilities of an experimental realization of the predicted T_c variation upon redirecting \mathbf{n} . We suggest cleaving a noncentrosymmetric metal, such as BiPd [34–36], in different directions and growing a superconductor (with a higher T_c) on the surface, see Fig. 3(a). This requires a material that can be cleaved along at least two axes. Alternatively, one could deposit superconductors on the surface of a curved noncentrosymmetric material with a long edge (several mm), see Fig. 3(b) [37]. In both scenarios, different samples would have their inversion symmetry-breaking axis in different directions, corresponding to a systematic rotation of \mathbf{n} from IP to OOP. We underline that although \mathbf{n} rotates along with the lattice in the nonsuperconducting region, the difference in T_c as \mathbf{n} changes from IP to OOP is robust. The reason is that the corresponding change in the proximity effect

exists even in our continuum model without the underlying lattice.

In order to observe IP variations, we suggest growing a normal metal (N) with a cubic lattice structure at different angles compared to a transition metal dichalcogenide (TMDC) with IP inversion symmetry breaking [38], see Fig. 3(c). This corresponds to an effective IP rotation of \mathbf{n} compared to the lattice. The superconductor is grown on top of the normal metal, which should be a light element with as little interfacial SOC as possible. The ideal scenario, albeit challenging, would be to induce an *in situ* rotation of \mathbf{n} in the nonsuperconducting region via electric gating in different directions, that induces an inversion-symmetry-breaking field. However, since \mathbf{n} is rotated inside the noncentrosymmetric material, λ may in principle vary. This is not the case for our previous suggestions, since we do not rotate \mathbf{n} inside the noncentrosymmetric material, but instead change the position of the superconductor.

Concluding, we have shown that the superconducting transition temperature T_c can be altered by rotating the inversion symmetry-breaking axis \mathbf{n} in a proximate material, providing a conceptually different way of controlling T_c compared to previous studies. Moreover, we have shown that when in addition an interfacial spin-orbit coupling perpendicular to the interface is present and substantial, the behavior of T_c as \mathbf{n} is varied can change qualitatively.

The authors would like to thank J. A. Ouassou, and J. W. Wells for helpful discussions. This work was supported by the Research Council of Norway through its Centres of Excellence funding scheme Grant No. 262633 QuSpin.

*Corresponding author.
lina.g.johnsen@ntnu.no

- [1] J. Linder and J. W. A. Robinson, Superconducting spintronics, *Nat. Phys.* **11**, 307 (2015).
- [2] M. Eschrig, Spin-polarized supercurrents for spintronics: a review of current progress, *Phys. Today* **64**, No. 1, 43 (2011).
- [3] M. Eschrig, Spin-polarized supercurrents for spintronics: a review of current progress, *Rep. Prog. Phys.* **78**, 104501 (2015).
- [4] J. Bardeen, L. N. Cooper, and J. R. Schrieffer, Theory of superconductivity, *Phys. Rev.* **108**, 1175 (1957).
- [5] J. Linder and A. V. Balatsky, Odd-frequency superconductivity, *Rev. Mod. Phys.* **91**, 045005 (2019).
- [6] J. Y. Gu, C. Y. You, J. S. Jiang, J. Pearson, Y. B. Bazaliy, and S. D. Bader, Magnetization-Orientation Dependence of the Superconducting Transition Temperature in the Ferromagnet-Superconductor-Ferromagnet System: CuNi/Nb/CuNi, *Phys. Rev. Lett.* **89**, 267001 (2002).
- [7] I. C. Moraru, W. P. Pratt, and N. O. Birge, Magnetization-Dependent T_c Shift in Ferromagnet/Superconductor/Ferromagnet Trilayers with a Strong Ferromagnet, *Phys. Rev. Lett.* **96**, 037004 (2006).
- [8] P. V. Leksin, N. N. Garif'yanov, I. A. Garifullin, Y. V. Fominov, J. Schumann, Y. Krupskaya, V. Kataev, O. G. Schmidt, and B. Büchner, Evidence for Triplet Superconductivity in a Superconductor-Ferromagnet Spin Valve, *Phys. Rev. Lett.* **109**, 057005 (2012).
- [9] N. Banerjee, C. B. Smiet, R. G. J. Smits, A. Ozaeta, F. S. Bergeret, M. G. Blamire, and J. W. A. Robinson, Evidence for spin selectivity of triplet pairs in superconducting spin valves, *Nat. Commun.* **5**, 3048 (2014).
- [10] X. L. Wang, A. Di Bernardo, N. Banerjee, A. Wells, F. S. Bergeret, M. G. Blamire, and J. W. A. Robinson, Giant triplet proximity effect in superconducting pseudo spin valves with engineered anisotropy, *Phys. Rev. B* **89**, 140508(R) (2014).
- [11] S. H. Jacobsen, J. A. Ouassou, and J. Linder, Critical temperature and tunneling spectroscopy of superconductor-ferromagnet hybrids with intrinsic Rashba-Dresselhaus spin-orbit coupling, *Phys. Rev. B* **92**, 024510 (2015).
- [12] J. A. Ouassou, A. D. Bernardo, J. W. A. Robinson, and J. Linder, Electric control of superconducting transition through a spin-orbit coupled interface, *Sci. Rep.* **6**, 29312 (2016).
- [13] H. T. Simensen and J. Linder, Tunable superconducting critical temperature in ballistic hybrid structures with strong spin-orbit coupling, *Phys. Rev. B* **97**, 054518 (2018).
- [14] N. Banerjee, J. A. Ouassou, Y. Zhu, N. A. Stelmashenko, J. Linder, and M. G. Blamire, Controlling the superconducting transition by spin-orbit coupling, *Phys. Rev. B* **97**, 184521 (2018).
- [15] L. G. Johnsen, N. Banerjee, and J. Linder, Magnetization reorientation due to the superconducting transition in heavy-metal heterostructures, *Phys. Rev. B* **99**, 134516 (2019).
- [16] D. Terrade, Proximity effects and Josephson currents in ferromagnet-spin-triplet superconductors junctions, Ph.D. thesis, Max-Planck-Institut für Festkörperforschung, Universität Stuttgart, 2015.
- [17] J. Linder, M. Amundsen, and V. Risinggård, Intrinsic superspin Hall current, *Phys. Rev. B* **96**, 094512 (2017).
- [18] Y. A. Bychkov and E. I. Rashba, Oscillatory effects and the magnetic susceptibility of carriers in inversion layers, *J. Phys. C* **17**, 6039 (1984).
- [19] See Supplemental Material at <http://link.aps.org/supplemental/10.1103/PhysRevLett.125.107002> for a further description of the lattice Bogoliubov-de Gennes framework, where we derive the symmetrized Rashba contribution to the Hamiltonian, diagonalize the Hamiltonian, and calculate the relevant physical quantities such as the superconducting critical temperature and the total *s*-wave singlet amplitude, and for a further description of the continuum Bogoliubov-de Gennes framework, where we give explicit expressions for the wave functions, and for the even- and odd-frequency singlet and triplet retarded anomalous Green's functions as well as tables of their symmetries.
- [20] J. A. Ouassou, Density of states and critical temperature in superconductor/ferromagnet structures with spin-orbit coupling, Master's thesis, Norwegian University of Science and Technology, 2015.
- [21] A. L. Fetter and J. D. Walecka, *Quantum Theory of Many-Particle Systems* (Dover Publications Inc., Mineola, New York, 2003).

- [22] A. Manchon, H. C. Koo, J. Nitta, S. M. Frolov, and R. A. Duine, New perspectives for Rashba spin-orbit coupling, *Nat. Mater.* **14**, 871 (2015).
- [23] Y. Tanaka and M. Tsukada, Theory of superconducting proximity effect in a three-dimensional system in the clean limit, *Phys. Rev. B* **42**, 2066 (1990).
- [24] W. L. McMillan, Theory of superconductor-normal-metal interfaces, *Phys. Rev.* **175**, 559 (1968).
- [25] C. Ishii, Josephson currents through junctions with normal metal barriers, *Prog. Theor. Phys.* **44**, 1525 (1970).
- [26] A. Furusaki and M. Tsukada, Dc Josephson effect and Andreev reflection, *Solid State Commun.* **78**, 299 (1991).
- [27] S. Kashiwaya and Y. Tanaka, Tunnelling effects on surface bound states in unconventional superconductors, *Rep. Prog. Phys.* **63**, 1641 (2000).
- [28] R. T. W. Koperdraad, R. E. S. Otadoy, M. Blaauboer, and A. Lodder, Multiple-scattering theory for clean superconducting layered structures, *J. Phys. Condens. Matter* **13**, 8707 (2001).
- [29] B. Lu and Y. Tanaka, Study on Green's function on topological insulator surface, *Phil. Trans. R. Soc. A* **376**, 20150246 (2018).
- [30] J. Cayao and A. M. Black-Schaffer, Odd-frequency superconducting pairing and subgap density of states at the edge of a two-dimensional topological insulator without magnetism, *Phys. Rev. B* **96**, 155426 (2017).
- [31] J. Cayao and A. M. Black-Schaffer, Odd-frequency superconducting pairing in junctions with Rashba spin-orbit coupling, *Phys. Rev. B* **98**, 075425 (2018).
- [32] G. E. Blonder, M. Tinkham, and T. M. Klapwijk, Transition from metallic to tunneling regimes in superconducting microconstrictions: Excess current, charge imbalance, and supercurrent conversion, *Phys. Rev. B* **25**, 4515 (1982).
- [33] C. R. Reeg and D. L. Maslov, Proximity-induced triplet superconductivity in Rashba materials, *Phys. Rev. B* **92**, 134512 (2015).
- [34] N. N. Zhuravlev, Structure of superconductors. X: Thermal, microscopic and X-ray investigation of the bismuth-palladium system, *Sov. Phys. JETP* **5**, 1064 (1957), http://www.jetp.ac.ru/cgi-bin/dn/e_005_06_1064.pdf.
- [35] Y. Bhatt and K. Schubert, Kristallstruktur von PdBi₂, *J. Less-Common Met.* **64**, P17 (1979).
- [36] Z. Sun, M. Enayat, A. Maldonado, C. Lithgow, E. Yelland, D. C. Peets, A. Yaresko, A. P. Schnyder, and P. Wahl, Dirac surface states and nature of superconductivity in Noncentrosymmetric BiPd, *Nat. Commun.* **6**, 6633 (2015).
- [37] J. E. Ortega, M. Corso, Z. M. Abd-el-Fattah, E. A. Goiri, and F. Schiller, Interplay between structure and electronic states in step arrays explored with curved surfaces, *Phys. Rev. B* **83**, 085411 (2011).
- [38] M. A. U. Absor, I. Santoso, Harsojo, K. Abrasha, H. Kotaka, F. Ishii, and M. Saito, Polarity tuning of spin-orbit-induced spin splitting in two-dimensional transition metal dichalcogenides, *J. Appl. Phys.* **122**, 153905 (2017).

Supplemental material to: Controlling the superconducting transition by rotation of an inversion symmetry breaking axis

Lina G. Johnsen, Kristian Svalland, and Jacob Linder
 Center for Quantum Spintronics, Department of Physics,
 Norwegian University of Science and Technology, NO-7491 Trondheim, Norway
 (Dated: July 16, 2020)

THE LATTICE BOGOLIUBOV-DE GENNES FRAMEWORK

If the inversion symmetry breaking axis directed along \mathbf{n} has an in-plane component, a Rashba Hamiltonian of the form

$$-\frac{i}{2} \sum_{\langle i,j \rangle, \alpha, \beta} \lambda_i c_{i,\alpha}^\dagger \mathbf{n} \cdot (\boldsymbol{\sigma} \times \mathbf{d}_{i,j})_{\alpha,\beta} c_{j,\beta} \quad (1)$$

is in general non-Hermitian. This term is the second quantized form of $\hat{h} = (\mathbf{n} \times \boldsymbol{\sigma}) \cdot \lambda(x) \hat{\mathbf{p}}$, where $\boldsymbol{\sigma}$ is the vector of Pauli matrices, $\lambda(x)$ is the x dependent Rashba spin-orbit coupling strength, and $\hat{\mathbf{p}} = (\hat{p}_x, \hat{p}_y, \hat{p}_z) = -i\hbar\nabla$ is the momentum operator [1]. Above, $\mathbf{d}_{i,j}$ is the vector from lattice site i to site j . More generally, the symmetrized version of the first quantized Rashba spin-orbit coupling operator is

$$\hat{h} = \frac{1}{2} (\mathbf{n} \times \boldsymbol{\sigma}) \cdot \{\lambda(x), \hat{\mathbf{p}}\}. \quad (2)$$

We write this on a second quantized form as $H_\lambda = \sum_{i,j,\alpha,\beta} \langle i, \alpha | \hat{h} | j, \beta \rangle c_{i,\alpha}^\dagger c_{j,\beta}$. The spatial part of the overlap integral can be written

$$\begin{aligned} \langle i | \hat{h} | j \rangle &= \frac{1}{2} (\mathbf{n} \times \boldsymbol{\sigma}) \cdot x [\langle i | \lambda(x) \hat{p}_x | j \rangle + \langle j | \lambda(x) \hat{p}_x | i \rangle^*] \\ &+ (\mathbf{n} \times \boldsymbol{\sigma}) \cdot \mathbf{y} \langle i | \lambda(x) \hat{p}_y | j \rangle \\ &+ (\mathbf{n} \times \boldsymbol{\sigma}) \cdot \mathbf{z} \langle i | \lambda(x) \hat{p}_z | j \rangle, \end{aligned} \quad (3)$$

where

$$\langle i | \lambda(x) \hat{p}_m | j \rangle = \int_{-\infty}^{\infty} dm \phi_i^*(\mathbf{r}) \lambda(x) \hat{p}_m \phi_j(\mathbf{r}) \quad (4)$$

for $m = x, y, z$. Here, $\phi_j(\mathbf{r}) \equiv \phi(\mathbf{r} - \mathbf{R}_j)$, where \mathbf{R}_j describes the position of lattice site j . We assume each ϕ_j to be highly localized. Then $\lambda(x)$ can be approximated to be constant inside each Wigner-Seitz cell, the derivative can be discretized as

$$\partial_m \phi_j(\mathbf{r}) = \frac{1}{2} [\phi_{j-\hat{\mathbf{m}}}(\mathbf{r}) - \phi_{j+\hat{\mathbf{m}}}(\mathbf{r})], \quad (5)$$

and

$$\int d\mathbf{r} \phi_i^*(\mathbf{r}) \phi_j(\mathbf{r}) = \delta_{i,j}. \quad (6)$$

We also assume that $\lambda(x) = \lambda$ is constant and nonzero inside the material with spin-orbit coupling, and that $\lambda(x)$ acts as a

step function at the interface. It follows that the symmetrized spin-orbit coupling contribution to the Hamiltonian is

$$H_\lambda = -\frac{i}{2} \sum_{\langle i,j \rangle, \alpha, \beta} \lambda c_{i,\alpha}^\dagger \mathbf{n} \cdot \left\{ \boldsymbol{\sigma} \times \left[\frac{1}{2} (1 + \zeta) (\mathbf{d}_{i,j})_x + (\mathbf{d}_{i,j})_{||} \right] \right\}_{\alpha,\beta} c_{j,\beta}. \quad (7)$$

Above, $\mathbf{d}_{i,j}$ is decomposed into a part $(\mathbf{d}_{i,j})_x$ perpendicular to the interface, and a part $(\mathbf{d}_{i,j})_{||}$ parallel to the interface. If site i and j are both inside the material with spin-orbit coupling, $\zeta = 1$, while if site i and site j are on opposite sides of the interface, $\zeta = 0$.

Using the symmetrized Rashba contribution, our Hamiltonian is given by Eq. (1) in the letter. In the following, we use a similar approach to that in Refs. [2–4]. For brevity of notation, we introduce $i \equiv i_x$, $i_{||} \equiv (i_y, i_z)$, and $\mathbf{k} \equiv (k_y, k_z)$. We assume periodic boundary conditions in the y and z directions, and introduce the Fourier transform along the y and z axes,

$$c_{i,\sigma} = \frac{1}{\sqrt{N_y N_z}} \sum_{\mathbf{k}} c_{i,\mathbf{k},\sigma} e^{i(\mathbf{k} \cdot i_{||})}, \quad (8)$$

where the sum is taken over the allowed \mathbf{k} inside the first Brillouin zone. In the following, we also use the relation

$$\frac{1}{N_y N_z} \sum_{i_{||}} e^{i(\mathbf{k} - \mathbf{k}') \cdot i_{||}} = \delta_{\mathbf{k}, \mathbf{k}'}. \quad (9)$$

By choosing the basis

$$B_{i,\mathbf{k}}^\dagger \equiv [c_{i,\mathbf{k},\uparrow}^\dagger \quad c_{i,\mathbf{k},\downarrow}^\dagger \quad c_{i,-\mathbf{k},\uparrow} \quad c_{i,-\mathbf{k},\downarrow}], \quad (10)$$

and applying the Fourier transform as well as Eq. (9), we rewrite the Hamiltonian as

$$H = H_0 + \frac{1}{2} \sum_{i,j,\mathbf{k}} B_{i,\mathbf{k}}^\dagger H_{i,j,\mathbf{k}} B_{i,\mathbf{k}}. \quad (11)$$

The constant term H_0 is of no importance for our further calculations. Above,

$$\begin{aligned} H_{i,j,\mathbf{k}} &= \epsilon_{i,j,\mathbf{k}} \hat{\tau}_3 \hat{\sigma}_0 \\ &+ (\Delta_i \hat{\tau}^+ - \Delta_j^* \hat{\tau}^-) i \hat{\sigma}_y \delta_{i,j} \\ &- \{ (\lambda n_x + \lambda_{\text{int}} |\mathbf{n}_{\text{int}}|) [\sin(k_y) \hat{\tau}_0 \hat{\sigma}_z - \sin(k_z) \hat{\tau}_3 \hat{\sigma}_y] \\ &- \lambda [n_z \sin(k_y) - n_y \sin(k_z)] \hat{\tau}_0 \hat{\sigma}_x \} \delta_{i,j} \\ &+ i \lambda (1 + \zeta) (n_y \hat{\tau}_0 \hat{\sigma}_z - n_z \hat{\tau}_3 \hat{\sigma}_y) \\ &\cdot (\delta_{i,j+1} - \delta_{i,j-1}) / 4, \end{aligned} \quad (12)$$

where $\hat{\tau}^{\pm} \equiv (\hat{\tau}_1 \pm i\hat{\tau}_2)/2$, $\hat{\tau}_i \hat{\sigma}_j \equiv \tau_i \otimes \sigma_j$ is the Kronecker product of the Pauli matrices spanning Nambu and spin space,

$$\epsilon_{i,j,\mathbf{k}} \equiv \{-2t[\cos(k_y) + \cos(k_z)] - \mu_i\}\delta_{i,j} - t(\delta_{i,j+1} + \delta_{i,j-1}), \quad (13)$$

and Δ_i is the superconducting gap at site i . By rewriting the Hamiltonian as

$$H = H_0 + \frac{1}{2} \sum_{\mathbf{k}} W_{\mathbf{k}}^{\dagger} H_{\mathbf{k}} W_{\mathbf{k}} \quad (14)$$

in terms of the basis

$$W_{\mathbf{k}}^{\dagger} \equiv [B_{1,\mathbf{k}}^{\dagger}, \dots, B_{i,\mathbf{k}}^{\dagger}, \dots, B_{N_x,\mathbf{k}}^{\dagger}], \quad (15)$$

the Hamiltonian can be diagonalized numerically as

$$H = H_0 + \frac{1}{2} \sum_{n,\mathbf{k}} E_{n,\mathbf{k}} \gamma_{n,\mathbf{k}}^{\dagger} \gamma_{n,\mathbf{k}}. \quad (16)$$

This yields eigenenergies $E_{n,\mathbf{k}}$, and eigenvectors $\Phi_{n,\mathbf{k}}$ given by

$$\begin{aligned} \Phi_{n,\mathbf{k}}^{\dagger} &\equiv [\phi_{1,n,\mathbf{k}}^{\dagger} \quad \dots \quad \phi_{N_x,n,\mathbf{k}}^{\dagger}], \\ \phi_{i,n,\mathbf{k}}^{\dagger} &\equiv [u_{i,n,\mathbf{k}}^* \quad v_{i,n,\mathbf{k}}^* \quad w_{i,n,\mathbf{k}}^* \quad x_{i,n,\mathbf{k}}^*]. \end{aligned} \quad (17)$$

The new quasiparticle operators introduced above are related to the old operators by

$$\begin{aligned} c_{i,\mathbf{k},\uparrow} &= \sum_n u_{i,n,\mathbf{k}} \gamma_{n,\mathbf{k}}, \\ c_{i,\mathbf{k},\downarrow} &= \sum_n v_{i,n,\mathbf{k}} \gamma_{n,\mathbf{k}}, \\ c_{i,-\mathbf{k},\uparrow}^{\dagger} &= \sum_n w_{i,n,\mathbf{k}} \gamma_{n,\mathbf{k}}, \\ c_{i,-\mathbf{k},\downarrow}^{\dagger} &= \sum_n x_{i,n,\mathbf{k}} \gamma_{n,\mathbf{k}}. \end{aligned} \quad (18)$$

The eigenenergies and eigenvectors are used for computing the singlet and triplet amplitudes and the superconducting critical temperature. In finding the eigenenergies and eigenvectors, the superconducting gap must be calculated iteratively. The superconducting gap is defined by $\Delta_i \equiv U_i \langle c_{i,\uparrow} c_{i,\downarrow} \rangle$. By Fourier transforming along the y and z axes, rewriting to the new quasi-particle operators, and using that $\langle \gamma_{n,\mathbf{k}}^{\dagger} \gamma_{m,\mathbf{k}} \rangle = f(E_{n,\mathbf{k}}/2) \delta_{n,m}$, we find that the gap is given by

$$\Delta_i = -\frac{U_i}{N_y N_z} \sum_{n,\mathbf{k}} v_{i,n,\mathbf{k}} w_{i,n,\mathbf{k}}^* [1 - f(E_{n,\mathbf{k}}/2)], \quad (19)$$

where $f(E_{n,\mathbf{k}}/2)$ is the Fermi-Dirac distribution.

We define the even-frequency s -wave singlet amplitude as $S_{s,i} \equiv \langle c_{i,\uparrow} c_{i,\downarrow} \rangle - \langle c_{i,\downarrow} c_{i,\uparrow} \rangle$. The even-frequency s -wave singlet amplitude inside the superconducting region is related to the superconducting gap by $S_{s,i} = 2\Delta_i/U_i$. By the same

method as used for finding the expression for the superconducting gap, we find that the odd-frequency s -wave triplet amplitudes are given by

$$\begin{aligned} S_{0,i}(\tau) &= \frac{1}{N_y N_z} \sum_{n,\mathbf{k}} [u_{i,n,\mathbf{k}} x_{i,n,\mathbf{k}}^* + v_{i,n,\mathbf{k}} w_{i,n,\mathbf{k}}^*] \\ &\quad \cdot e^{-iE_{n,\mathbf{k}}\tau/2} [1 - f(E_{n,\mathbf{k}}/2)], \\ S_{\uparrow,i}(\tau) &= \frac{1}{N_y N_z} \sum_{n,\mathbf{k}} u_{i,n,\mathbf{k}} w_{i,n,\mathbf{k}}^* \\ &\quad \cdot e^{-iE_{n,\mathbf{k}}\tau/2} [1 - f(E_{n,\mathbf{k}}/2)], \\ S_{\downarrow,i}(\tau) &= \frac{1}{N_y N_z} \sum_{n,\mathbf{k}} v_{i,n,\mathbf{k}} x_{i,n,\mathbf{k}}^* \\ &\quad \cdot e^{-iE_{n,\mathbf{k}}\tau/2} [1 - f(E_{n,\mathbf{k}}/2)]. \end{aligned} \quad (20)$$

Our binomial search algorithm [5] for the superconducting critical temperature, is as follows. We divide our temperature interval N_T times. For each of the N_T iterations, we recalculate the gap N_{Δ} times from the initial guess with a magnitude $\Delta_0/1000$, where Δ_0 is the zero-temperature superconducting gap. If the gap has increased towards a superconducting solution after N_{Δ} iterations, we conclude that the current temperature is below T_c . If the gap has decreased towards a normal-state solution, we conclude that the current temperature is above T_c . We measure the magnitude of the gap in the middle of the superconducting region. The advantage of this algorithm, is that we are not dependent upon recalculating the gap until it converges. The parameter N_{Δ} must only be large enough that the increase or decrease in Δ_i at site $i = N_x S/2$ reflects the overall behavior of the gap under recalculation. When we choose an initial guess so that the gap as a function of lattice site has a similar shape as for the gap very close to T_c , it more likely that the gap increases for all lattice sites, or decreases for all lattice sites, under recalculation. We can then get a high accuracy with a low N_{Δ} .

The superconducting coherence length is given by $\xi \equiv \hbar v_F / \pi \Delta_0$ [6], where $v_F \equiv \frac{1}{\hbar} \frac{dE_{\mathbf{k}}}{dk} \Big|_{k=k_F}$ is the normal-state Fermi velocity [6], $E_{\mathbf{k}}$ is the normal-state eigenenergies when introducing periodic boundary conditions along all three axes, and k_F is the corresponding Fermi momentum averaged over the Fermi surface. We round ξ down to the closest integer number of lattice points.

THE CONTINUUM BOGOLIUBOV-DE GENNES FRAMEWORK

The continuum Bogoliubov-de-Gennes framework [7–14] allows us to obtain analytical expressions for the singlet and triplet retarded anomalous Green's functions of the 2D SOC/S system with $\mathbf{n} = x$ and the 2D F/S system with $m||z$. We have not given these expressions in the letter, as we are mainly interested in their symmetries under spatial inversion. Here, we provide the analytical expressions for the wave functions

and the singlet and triplet retarded anomalous Green's functions for these two systems, as well as the wave functions for the 2D SOC/S system with $\mathbf{n} = \mathbf{z}$.

The scattering wave functions

We find expressions for the scattering wave functions $\Psi_n(x_1)$ and $\tilde{\Psi}_m(x_2)$ by using the time-independent Schrödinger equations given in Eq. (2) in the letter. The indices n and m refers to the different possible scattering processes. These contain reflection and transmission coefficients that are determined by the boundary conditions at the interface. The wave functions $\Psi_n(x_1)$ satisfies the boundary conditions [15]

$$\begin{aligned} [\Psi_n(x_1)]_{x_1=0^+} &= [\tilde{\Psi}_n(x_1)]_{x_1=0^-} \\ [\hat{v}\Psi_n(x_1)]_{x_1=0^+} &= [\hat{v}\tilde{\Psi}_n(x_1)]_{x_1=0^-} \end{aligned} \quad (21)$$

where $\hat{v} \equiv \partial H(p_y)/\partial(-i\partial_{x_1})$ is the velocity operator. The conjugate wave functions $\tilde{\Psi}_m(x_2)$ satisfies a similar set of boundary conditions with $\hat{v} \equiv \partial H^*(p_y)/\partial(-i\partial_{x_2})$.

In the following, we give expressions for the scattering wave functions inside a 2D superconductor, a 2D material with Rashba-like spin-orbit coupling for $\mathbf{n} = \mathbf{x}$ and $\mathbf{n} = \mathbf{z}$, and a 2D ferromagnet with $\mathbf{h} = h\mathbf{z}$, treating each material separately. We choose the superconducting region to be located at $x > 0$, while the non-superconducting region is located at $x < 0$.

The superconducting region

The scattering wave functions on the superconducting side of the interface are

$$\begin{aligned} \Psi_n(x_1) &= \Psi_{\text{in},n}^R(x_1) \\ &+ c_{n,1}[u_0 \ 0 \ 0 \ v_0]^T e^{iq_x^+ x_1} \\ &+ c_{n,2}[0 \ -u_0 \ v_0 \ 0]^T e^{iq_x^+ x_1} \\ &+ d_{n,1}[0 \ -v_0 \ u_0 \ 0]^T e^{-iq_x^- x_1} \\ &+ d_{n,2}[v_0 \ 0 \ 0 \ u_0]^T e^{-iq_x^- x_1}, \quad x_1 > 0, \\ \tilde{\Psi}_m(x_2) &= \tilde{\Psi}_{\text{in},m}^R(x_2) \\ &+ \tilde{c}_{m,1}[u_0 \ 0 \ 0 \ v_0]^T e^{iq_x^+ x_2} \\ &+ \tilde{c}_{m,2}[0 \ -u_0 \ v_0 \ 0]^T e^{iq_x^+ x_2} \\ &+ \tilde{d}_{m,1}[0 \ -v_0 \ u_0 \ 0]^T e^{-iq_x^- x_2} \\ &+ \tilde{d}_{m,2}[v_0 \ 0 \ 0 \ u_0]^T e^{-iq_x^- x_2}, \quad x_2 > 0, \end{aligned} \quad (22)$$

where the quasi-particles incoming from the right are described by the wave functions

$$\begin{aligned} \Psi_{\text{in},5}^R(x_1) &= [u_0 \ 0 \ 0 \ v_0]^T e^{-iq_x^+ x_1} \\ \Psi_{\text{in},6}^R(x_1) &= [0 \ -u_0 \ v_0 \ 0]^T e^{-iq_x^+ x_1}, \\ \Psi_{\text{in},7}^R(x_1) &= [0 \ -v_0 \ u_0 \ 0]^T e^{iq_x^- x_1}, \\ \Psi_{\text{in},8}^R(x_1) &= [v_0 \ 0 \ 0 \ u_0]^T e^{iq_x^- x_1}, \end{aligned} \quad (24)$$

and

$$\begin{aligned} \tilde{\Psi}_{\text{in},5}^R(x_2) &= [u_0 \ 0 \ 0 \ v_0]^T e^{-iq_x^+ x_2}, \\ \tilde{\Psi}_{\text{in},6}^R(x_2) &= [0 \ -u_0 \ v_0 \ 0]^T e^{-iq_x^+ x_2}, \\ \tilde{\Psi}_{\text{in},7}^R(x_2) &= [0 \ -v_0 \ u_0 \ 0]^T e^{iq_x^- x_2}, \\ \tilde{\Psi}_{\text{in},8}^R(x_2) &= [v_0 \ 0 \ 0 \ u_0]^T e^{iq_x^- x_2}. \end{aligned} \quad (25)$$

$\Psi_{\text{in},1}^R(x_1) = \Psi_{\text{in},2}^R(x_1) = \Psi_{\text{in},3}^R(x_1) = \Psi_{\text{in},4}^R(x_1) = \tilde{\Psi}_{\text{in},1}^R(x_2) = \tilde{\Psi}_{\text{in},2}^R(x_2) = \tilde{\Psi}_{\text{in},3}^R(x_2) = \tilde{\Psi}_{\text{in},4}^R(x_2) = 0$. We reserve the indices $n, m = \{1, 2, 3, 4\}$ for scattering processes with particles or quasi-particles scattering at the interface from the left. Above,

$$q_x^\pm = \{-v_y^2 + \eta[\mu \pm \sqrt{(\omega + i\delta)^2 - |\Delta|^2}]\}^{1/2} \quad (26)$$

are the allowed k_x values, and

$$u_0^2 \equiv \frac{1}{2}[1 + \sqrt{(\omega + i\delta)^2 - |\Delta|^2}/(\omega + i\delta)], \quad (27)$$

$$v_0^2 \equiv \frac{1}{2}[1 - \sqrt{(\omega + i\delta)^2 - |\Delta|^2}/(\omega + i\delta)]. \quad (28)$$

The region with Rashba spin-orbit coupling, $\mathbf{n} = \mathbf{x}$

The scattering wave functions on the side of the interface with Rashba-like spin-orbit coupling are

$$\begin{aligned} \Psi_n(x_1) &= \Psi_{\text{in},n}^L(x_1) \\ &+ a_{n,1}[1 \ 0 \ 0 \ 0]^T e^{-ik_x^{\sigma,\uparrow} x_1} \\ &+ a_{n,2}[0 \ 1 \ 0 \ 0]^T e^{-ik_x^{\sigma,\downarrow} x_1} \\ &+ b_{n,1}[0 \ 0 \ 1 \ 0]^T e^{ik_x^{h,\uparrow} x_1} \\ &+ b_{n,2}[0 \ 0 \ 0 \ 1]^T e^{ik_x^{h,\downarrow} x_1}, \quad x_1 < 0, \\ \tilde{\Psi}_m(x_2) &= \tilde{\Psi}_{\text{in},m}^L(x_2) \\ &+ \tilde{a}_{m,1}[1 \ 0 \ 0 \ 0]^T e^{-ik_x^{\sigma,\uparrow} x_2} \\ &+ \tilde{a}_{m,2}[0 \ 1 \ 0 \ 0]^T e^{-ik_x^{\sigma,\downarrow} x_2} \\ &+ \tilde{b}_{m,1}[0 \ 0 \ 1 \ 0]^T e^{ik_x^{h,\uparrow} x_2} \\ &+ \tilde{b}_{m,2}[0 \ 0 \ 0 \ 1]^T e^{ik_x^{h,\downarrow} x_2}, \quad x_2 < 0, \end{aligned} \quad (29)$$

if $\mathbf{n} = \mathbf{x}$. The particles incoming from the left are described by

$$\begin{aligned}\Psi_{\text{in},1}^L(x_1) &= [1 \ 0 \ 0 \ 0]^T e^{ik_x^{\epsilon,\uparrow} x_1}, \\ \Psi_{\text{in},2}^L(x_1) &= [0 \ 1 \ 0 \ 0]^T e^{ik_x^{\epsilon,\downarrow} x_1}, \\ \Psi_{\text{in},3}^L(x_1) &= [0 \ 0 \ 1 \ 0]^T e^{-ik_x^{h,\uparrow} x_1}, \\ \Psi_{\text{in},4}^L(x_1) &= [0 \ 0 \ 0 \ 1]^T e^{-ik_x^{h,\downarrow} x_1},\end{aligned}\quad (31)$$

and

$$\begin{aligned}\tilde{\Psi}_{\text{in},1}^L(x_2) &= [1 \ 0 \ 0 \ 0]^T e^{ik_x^{\epsilon,\uparrow} x_2}, \\ \tilde{\Psi}_{\text{in},2}^L(x_2) &= [0 \ 1 \ 0 \ 0]^T e^{ik_x^{\epsilon,\downarrow} x_2}, \\ \tilde{\Psi}_{\text{in},3}^L(x_2) &= [0 \ 0 \ 1 \ 0]^T e^{-ik_x^{h,\uparrow} x_2}, \\ \tilde{\Psi}_{\text{in},4}^L(x_2) &= [0 \ 0 \ 0 \ 1]^T e^{-ik_x^{h,\downarrow} x_2}.\end{aligned}\quad (32)$$

$\Psi_{\text{in},5}^L(x_1) = \Psi_{\text{in},6}^L(x_1) = \Psi_{\text{in},7}^L(x_1) = \Psi_{\text{in},8}^L(x_1) = \tilde{\Psi}_{\text{in},5}^L(x_2) = \tilde{\Psi}_{\text{in},6}^L(x_2) = \tilde{\Psi}_{\text{in},7}^L(x_2) = \tilde{\Psi}_{\text{in},8}^L(x_2) = 0$. We reserve the indices $n, m = \{5, 6, 7, 8\}$ for scattering processes with particles incoming from the right. Above,

$$k_x^{\epsilon(h),\uparrow(\downarrow)} = \{-p_y^2 + \eta[\mu \pm (\omega + i\delta \pm' \lambda p_y)]\}^{1/2} \quad (33)$$

are the allowed k_x values. \pm correspond to electrons and holes, respectively, while \pm' correspond to spin up and spin down, respectively.

The ferromagnetic scattering wave functions

The scattering wave functions for a ferromagnet with $\mathbf{h} = h\mathbf{z}$, are on the same form as for a material with Rashba spin-orbit coupling where $\mathbf{n} = \mathbf{x}$, and are thus given by Eqs. (29), (30), (31), and (32). The allowed k_x values are in this case given by

$$k_x^{\epsilon(h),\uparrow(\downarrow)} = \{-p_y^2 + \eta[\mu \pm (\omega + i\delta) \mp' h]\}^{1/2}. \quad (34)$$

\pm refers to electrons and holes, respectively, and \mp' refers to spin up and spin down, respectively.

The region with Rashba spin-orbit coupling, $\mathbf{n} = \mathbf{z}$

The scattering wave functions on the side of the interface with Rashba-like spin-orbit coupling are

$$\begin{aligned}\Psi_n(x_1) &= \Psi_{\text{in},n}^L(x_1) \\ &+ a_{n,1}[1 \ i e^{i\phi} \ 0 \ 0]^T e^{-ik_x^{\epsilon,\uparrow} x_1} \\ &+ a_{n,2}[-1 \ i e^{i\phi} \ 0 \ 0]^T e^{-ik_x^{\epsilon,\downarrow} x_1} \\ &+ b_{n,1}[0 \ 0 \ 1 \ i e^{-i\phi}]^T e^{ik_x^{h,-} x_1} \\ &+ b_{n,2}[0 \ 0 \ -1 \ i e^{-i\phi}]^T e^{ik_x^{h,+} x_1}, \quad x_1 < 0,\end{aligned}\quad (35)$$

$$\begin{aligned}\tilde{\Psi}_m(x_2) &= \tilde{\Psi}_{\text{in},m}^L(x_2) \\ &+ \tilde{a}_{m,1}[1 \ i e^{i\phi} \ 0 \ 0]^T e^{-ik_x^{\epsilon,+} x_2} \\ &+ \tilde{a}_{m,2}[-1 \ i e^{i\phi} \ 0 \ 0]^T e^{-ik_x^{\epsilon,-} x_2} \\ &+ \tilde{b}_{m,1}[0 \ 0 \ 1 \ i e^{-i\phi}]^T e^{ik_x^{h,-} x_2} \\ &+ \tilde{b}_{m,2}[0 \ 0 \ -1 \ i e^{-i\phi}]^T e^{ik_x^{h,+} x_2}, \quad x_2 < 0,\end{aligned}\quad (36)$$

if $\mathbf{n} = \mathbf{z}$. The particles incoming from the left are described by

$$\begin{aligned}\Psi_{\text{in},1}^L(x_1) &= [1 \ i e^{i\phi} \ 0 \ 0]^T e^{ik_x^{\epsilon,+} x_1}, \\ \Psi_{\text{in},2}^L(x_1) &= [-1 \ i e^{i\phi} \ 0 \ 0]^T e^{ik_x^{\epsilon,-} x_1}, \\ \Psi_{\text{in},3}^L(x_1) &= [0 \ 0 \ 1 \ i e^{-i\phi}]^T e^{-ik_x^{h,-} x_1}, \\ \Psi_{\text{in},4}^L(x_1) &= [0 \ 0 \ -1 \ i e^{-i\phi}]^T e^{-ik_x^{h,+} x_1}\end{aligned}\quad (37)$$

and

$$\begin{aligned}\tilde{\Psi}_{\text{in},1}^L(x_2) &= [1 \ i e^{i\phi} \ 0 \ 0]^T e^{ik_x^{\epsilon,+} x_2}, \\ \tilde{\Psi}_{\text{in},2}^L(x_2) &= [-1 \ i e^{i\phi} \ 0 \ 0]^T e^{ik_x^{\epsilon,-} x_2}, \\ \tilde{\Psi}_{\text{in},3}^L(x_2) &= [0 \ 0 \ 1 \ i e^{-i\phi}]^T e^{-ik_x^{h,-} x_2}, \\ \tilde{\Psi}_{\text{in},4}^L(x_2) &= [0 \ 0 \ -1 \ i e^{-i\phi}]^T e^{-ik_x^{h,+} x_2}.\end{aligned}\quad (38)$$

$\Psi_{\text{in},5}^L(x_1) = \Psi_{\text{in},6}^L(x_1) = \Psi_{\text{in},7}^L(x_1) = \Psi_{\text{in},8}^L(x_1) = \tilde{\Psi}_{\text{in},5}^L(x_2) = \tilde{\Psi}_{\text{in},6}^L(x_2) = \tilde{\Psi}_{\text{in},7}^L(x_2) = \tilde{\Psi}_{\text{in},8}^L(x_2) = 0$. Above, $k_x^{\epsilon(h),+(-)} = k^{\epsilon(h),+(-)} \cos(\phi)$ are the allowed k_x values, where

$$k^{\epsilon(h),+(-)} = \{[(\lambda\eta/2)^2 + \eta(\mu \pm \omega + i\delta)]^{1/2} \pm \lambda\eta/2\}^{1/2}. \quad (39)$$

\pm correspond to electrons and holes, respectively, and \pm' correspond to the two different spin-mixed states. We define $k_x^{\epsilon(h),+(-)}$ to be positive by setting $\phi \in [-\pi/2, \pi/2]$.

The singlet and triplet retarded anomalous Green's functions

From the scattering wave functions, we construct the retarded Green's function in Nambu \otimes spin space [13, 14],

$$G^r(x_1 > x_2, p_y; \omega) = \sum_{n,m=1}^4 \alpha_{nm} \Psi_n(x_1, p_y) \tilde{\Psi}_{m+4}^T(x_2, p_y), \quad (40)$$

$$G^r(x_1 < x_2, p_y; \omega) = \sum_{n,m=1}^4 \beta_{nm} \Psi_{n+4}(x_1, p_y) \tilde{\Psi}_m^T(x_2, p_y). \quad (41)$$

The coefficients α_{nm} and β_{nm} are found from the boundary conditions of the retarded Green's function at $x_1 = x_2$ [13, 14],

$$\begin{aligned} [G^r(x_1 > x_2, p_y; \omega)]_{x_1=x_2} &= [G^r(x_1 < x_2, p_y; \omega)]_{x_1=x_2}, \\ [\partial_{x_1} G^r(x_1 > x_2, p_y; \omega)]_{x_1=x_2} \\ - [\partial_{x_1} G^r(x_1 < x_2, p_y; \omega)]_{x_1=x_2} &= \eta \hat{\tau}_3 \hat{\sigma}_0, \end{aligned} \quad (42)$$

We rewrite to the center of mass coordinate $X \equiv (x_1 + x_2)/2$, and the relative coordinate $x \equiv x_1 - x_2$, and calculate the even- and odd-frequency singlet and triplet anomalous contributions to the retarded Green's functions according to Eqs. (4) and (5) in the letter. We use that

$$\begin{aligned} F_0^r(X, x, p_y; \omega) &\equiv [G_{1,4}^r(X, x, p_y; \omega) \\ &\quad - G_{2,3}^r(X, x, p_y; \omega)]/2, \\ F_1^r(X, x, p_y; \omega) &\equiv G_{1,3}^r(X, x, p_y; \omega), \\ F_2^r(X, x, p_y; \omega) &\equiv G_{2,4}^r(X, x, p_y; \omega), \\ F_3^r(X, x, p_y; \omega) &\equiv [G_{1,4}^r(X, x, p_y; \omega) \\ &\quad + G_{2,3}^r(X, x, p_y; \omega)]/2. \end{aligned} \quad (43)$$

The SOC/S system, $n = x$

For simplicity of notation, we define $k_{e1} \equiv k_x^{e,\uparrow}$, $k_{e2} \equiv k_x^{e,\downarrow}$, $k_{h1} \equiv k_x^{h,\downarrow}$, and $k_{h2} \equiv k_x^{h,\uparrow}$. On the side of the interface with Rashba-like spin-orbit coupling, where $x_1, x_2 < 0$, the nonzero even- and odd-frequency singlet and triplet retarded

anomalous Green's functions are given by

$$\begin{aligned} F_0^{r,E}(X, x, p_y; \omega) &= \frac{\eta}{2i} u_0 v_0 (q_x^+ + q_x^-) \\ &\quad \sum_{l=1,2} \frac{1}{D_l} e^{-i(k_{el} - k_{hl})X} \cos[(k_{el} + k_{hl})x/2], \\ F_0^{r,O}(X, x, p_y; \omega) &= \frac{\eta}{2} u_0 v_0 (q_x^+ + q_x^-) \\ &\quad \sum_{l=1,2} \frac{1}{D_l} e^{-i(k_{el} - k_{hl})X} \sin[(k_{el} + k_{hl})x/2], \\ F_3^{r,E}(X, x, p_y; \omega) &= \frac{\eta}{2i} u_0 v_0 (q_x^+ + q_x^-) \\ &\quad \sum_{l=1,2} (-1)^{l-1} \frac{1}{D_l} e^{-i(k_{el} - k_{hl})X} \cos[(k_{el} + k_{hl})x/2], \\ F_3^{r,O}(X, x, p_y; \omega) &= \frac{\eta}{2} u_0 v_0 (q_x^+ + q_x^-) \\ &\quad \sum_{l=1,2} (-1)^{l-1} \frac{1}{D_l} e^{-i(k_{el} - k_{hl})X} \sin[(k_{el} + k_{hl})x/2], \end{aligned} \quad (44)$$

where

$$D_l \equiv u_0^2 (k_{el} + q_x^+) (k_{hl} + q_x^-) + v_0^2 (k_{hl} - q_x^+) (-k_{el} + q_x^-). \quad (45)$$

On the superconducting side of the interface, where $x_1, x_2 > 0$, the nonzero even- and odd-frequency singlet and triplet retarded anomalous Green's functions are given by

$$\begin{aligned} F_0^{r,E}(X, x, p_y; \omega) &= -\frac{\eta}{2i} \frac{u_0 v_0}{(u_0^2 - v_0^2)} \left\{ e^{i(q_x^+ - q_x^-)X} \right. \\ &\quad \cos[(q_x^+ + q_x^-)x/2] \sum_{l=1,2} \frac{1}{D_l} (k_{el} + k_{hl}) \\ &\quad - \left(\frac{1}{q_x^+} e^{iq_x^+ |x|} + \frac{1}{q_x^-} e^{-iq_x^- |x|} \right) \\ &\quad \left. - \frac{1}{2} \sum_{l=1,2} \left(\frac{E_l}{D_l} \frac{1}{q_x^+} e^{2iq_x^+ X} + \frac{F_l}{D_l} \frac{1}{q_x^-} e^{-2iq_x^- X} \right) \right\}, \\ F_0^{r,O}(X, x, p_y; \omega) &= \frac{\eta}{2} u_0 v_0 e^{i(q_x^+ - q_x^-)X} \\ &\quad \sin[(q_x^+ + q_x^-)x/2] \sum_{l=1,2} \frac{1}{D_l} (k_{el} + k_{hl}), \\ F_3^{r,E}(X, x, p_y; \omega) &= -\frac{\eta}{2i} \frac{u_0 v_0}{(u_0^2 - v_0^2)} \left\{ e^{i(q_x^+ - q_x^-)X} \right. \\ &\quad \cos[(q_x^+ + q_x^-)x/2] \sum_{l=1,2} (-1)^{l-1} \frac{1}{D_l} (k_{el} + k_{hl}) \\ &\quad \left. - \frac{1}{2} \sum_{l=1,2} (-1)^{l-1} \left(\frac{E_l}{D_l} \frac{1}{q_x^+} e^{2iq_x^+ X} + \frac{F_l}{D_l} \frac{1}{q_x^-} e^{-2iq_x^- X} \right) \right\}, \\ F_3^{r,O}(X, x, p_y; \omega) &= \frac{\eta}{2} u_0 v_0 e^{i(q_x^+ - q_x^-)X} \\ &\quad \sin[(q_x^+ + q_x^-)x/2] \sum_{l=1,2} (-1)^{l-1} \frac{1}{D_l} (k_{el} + k_{hl}), \end{aligned} \quad (46)$$

where

$$\begin{aligned} E_l &\equiv u_0^2(k_{el} - q_x^+)(-k_{hl} - q_x^-) + v_0^2(k_{hl} + q_x^+)(k_{el} - q_x^-), \\ F_l &\equiv u_0^2(k_{el} + q_x^+)(-k_{hl} + q_x^-) + v_0^2(k_{hl} - q_x^+)(k_{el} + q_x^-). \end{aligned} \quad (47)$$

There are no equal-spin triplets in the system.

The F/S system

The even- and odd-frequency singlet and triplet retarded anomalous Green's functions of the F/S system are given by the same expressions as for the SOC/S system with $\mathbf{n} = \mathbf{x}$ if we let $F_3^{r,E}(X, x, p_y; \omega) \leftrightarrow F_3^{r,O}(X, x, p_y; \omega)$ in Eqs. (44) and (46). There are no equal-spin triplets in the system.

The symmetries of the singlet and triplet retarded anomalous Green's functions

Finally, we investigate the spatial symmetries of the singlet and triplet retarded anomalous Green's functions of the SOC/S systems with $\mathbf{n} = \mathbf{x}$ and $\mathbf{n} = \mathbf{z}$ and the F/S system with $\mathbf{m}|\mathbf{z}$. P_x is inversion of the relative x coordinate, $x \rightarrow -x$. P_y is inversion of the momentum along the y axis, $p_y \rightarrow -p_y$. P is total spatial inversion, and must be 1 for F_0^E and F_3^O , and -1 for F_0^O and F_3^E , according to the Pauli principle. For $P = 1$, we may have $P_x = P_y = 1$, which describes an s - or a $d_{x^2-y^2}$ -wave amplitude, or $P_x = P_y = -1$, which describes a d_{xy} -wave amplitude. For $P = -1$, we may have $P_x = 1$ and $P_y = -1$, which describes a p_y -wave amplitude, or $P_x = -1$ and $P_y = 1$, which describes a p_x -wave amplitude. Considering P , P_x , and P_y is not sufficient for determining whether a Green's function has an s -wave or a $d_{x^2-y^2}$ -wave symmetry. In order to prove the presence of s -wave singlets and triplets, we apply the Fourier transform,

$$\begin{aligned} F_{0(3)}^{r,E(O)}(X, p_x, p_y; \omega) \\ = \int_{-\infty}^{\infty} dx F_{0(3)}^{r,E(O)}(X, x, p_y; \omega) e^{-ip_x x}, \end{aligned} \quad (48)$$

and set p_x and p_y to zero, which is equivalent to integrating over all spatial coordinates.

The SOC/S system, $\mathbf{n} = \mathbf{x}$

The symmetries of the Green's functions in Eqs. (44) and (46) under P_x , P_y and P are given in Table I. We see from the table that $F_0^{r,E}$ can represent s - and $d_{x^2-y^2}$ -wave singlets, $F_0^{r,O}$ represents p_x -wave singlets, $F_3^{r,E}$ represents a p_y -wave opposite-spin triplets, and $F_3^{r,O}$ represents d_{xy} -wave opposite-spin triplets. By integrating over all of space, we find that s -wave singlets are present.

	P_x	P_y	P
$F_0^{r,E}$	1	1	1
$F_0^{r,O}$	-1	1	-1
$F_3^{r,E}$	1	-1	-1
$F_3^{r,O}$	-1	-1	1

Table I. The above table shows the parities of the SOC/S system with $\mathbf{n} = \mathbf{x}$ under $x \rightarrow -x$ (P_x), $p_y \rightarrow -p_y$ (P_y), and total spatial inversion (P) for the nonzero singlet and triplet even- and odd-frequency retarded anomalous Green's functions given in Eqs. (44) and (46).

The SOC/S system, $\mathbf{n} = \mathbf{z}$

The symmetries of the Green's functions of the SOC/S system for $\mathbf{n} = \mathbf{z}$ are shown in Table II. These were found numerically by the same approach as for the two other systems. We see that the same singlet and opposite-spin triplet amplitudes are present as for $\mathbf{n} = \mathbf{x}$. In addition, we have nonzero equal-spin triplet amplitudes, that are a mix of triplet amplitudes with different symmetries under P_x and P_y . $F_1^{r,E}$ and $F_2^{r,E}$ are therefore a mix of p_x - and p_y -wave even-frequency triplets, while $F_1^{r,O}$ and $F_2^{r,O}$ are a mix s - and d -wave triplets.

	P_x	P_y	P
$F_0^{r,E}$	1	1	1
$F_0^{r,O}$	-1	1	-1
$F_3^{r,E}$	1	-1	-1
$F_3^{r,O}$	-1	-1	1
$F_1^{r,E}$	-	-	-1
$F_1^{r,O}$	-	-	1
$F_2^{r,E}$	-	-	-1
$F_2^{r,O}$	-	-	1

Table II. The above table shows the parities of the SOC/S system with $\mathbf{n} = \mathbf{z}$ under $x_1 \leftrightarrow -x_2$ (P_x), $p_y \rightarrow -p_y$ (P_y), and total spatial inversion (P) for the singlet and triplet even- and odd-frequency retarded anomalous Green's functions present in the system. In addition to the singlets and triplets present for $\mathbf{n} = \mathbf{x}$ shown in Table I, we have nonzero equal-spin triplet amplitudes with mixing (-) of the possible symmetries in P_x and P_y .

The F/S system

Table III shows the symmetries of the even- and odd-frequency singlet and triplet retarded anomalous Green's functions of the F/S system under P_x , P_y , and P . Due to the lack of symmetry breaking in the y direction, we must conclude that there are no p_y - or d -wave symmetries present. The nonzero singlet and triplet retarded anomalous Green's functions are therefore the s -wave even-frequency singlet, the p_x -wave odd-frequency singlet, the p_x -wave even-frequency opposite-spin triplet and the s -wave odd-frequency opposite-spin triplet.

	P_x	P_y	P
$F_0^{r,E}$	1	1	1
$F_0^{r,O}$	-1	1	-1
$F_3^{r,E}$	-1	1	-1
$F_3^{r,O}$	1	1	1

Table III. The above table shows the parities of the F/S system under $x \rightarrow -x$ (P_x), $p_y \rightarrow -p_y$ (P_y), and total spatial inversion (P).

- [1] Y. A. Bychkov and E. I. Rashba, J. Phys. C: Solid State Phys. **17**, 6039 (1984).
- [2] D. Terrade, *Proximity Effects and Josephson Currents in Ferromagnet - Spin-Triplet Superconductors Junctions*, Ph.D. thesis, Max-Planck-Institut für Festkörperforschung, Universität Stuttgart (2015).
- [3] J. Linder, M. Amundsen, and V. Risinggård, Phys. Rev. B **96**, 094512 (2017).
- [4] L. G. Johnsen, N. Banerjee, and J. Linder, Phys. Rev. B **99**, 134516 (2019).
- [5] J. A. Ouassou, *Density of States and Critical Temperature in Superconductor/Ferromagnet Structures with Spin-Orbit Coupling*, Master's thesis, Norwegian University of Science and Technology (2015).
- [6] J. Bardeen, L. N. Cooper, and J. R. Schrieffer, Phys. Rev. **108**, 5 (1957).
- [7] W. L. McMillan, Phys. Rev. **175**, 559 (1967).
- [8] R. T. W. Koperdraad, R. E. S. Otadoy, M. Blaauboer, and A. Lodder, J. Phys.: Condens. Matter **13**, 8707 (2001).
- [9] S. Kashiwaya and Y. Tanaka, Rep. Prog. Phys. **63**, 1641 (2000).
- [10] A. Furusaki and M. Tsukada, Solid State Commun. **78**, 299 (1991).
- [11] C. Ishii, Prog. Theor. Phys. **44**, 1525 (1970).
- [12] B. Lu and Y. Tanaka, Phil. Trans. R. Soc. A **376**, 20150246 (2016).
- [13] J. Cayao and A. M. Black-Schaffer, Phys. Rev. B **96**, 155426 (2017).
- [14] J. Cayao and A. M. Black-Schaffer, Phys. Rev. B **98**, 075425 (2018).
- [15] C. R. Reeg and D. L. Maslov, Phys. Rev. B **92**, 134512 (2015).

III



REFERENCE

Haakon T. Simensen, Lina G. Johnsen, Jacob Linder, and Arne Brataas,
Spin pumping between noncollinear ferromagnetic insulators through thin superconductors,
Phys. Rev. B **103**, 024524 (2021).

CONTRIBUTIONS

HTS had the main initiative of the project, performed most of the analytical calculations, produced all figures, and wrote most of the manuscript. LGJ performed some of the analytical calculations, and was involved in the discussions and writing of the manuscript. AB and JL supervised the project, contributed to the calculations, discussions and writing of the manuscript.

Spin pumping between noncollinear ferromagnetic insulators through thin superconductors

Haakon T. Simensen , Lina G. Johnsen , Jacob Linder, and Arne Brataas

Center for Quantum Spintronics, Department of Physics, Norwegian University of Science and Technology, NO-7491 Trondheim, Norway



(Received 25 November 2020; revised 11 January 2021; accepted 12 January 2021; published 22 January 2021)

Dynamical magnets can pump spin currents into superconductors. To understand such a phenomenon, we develop a method utilizing the generalized Usadel equation to describe time-dependent situations in superconductors in contact with dynamical ferromagnets. Our proof-of-concept theory is valid when there is sufficient dephasing at finite temperatures, and when the ferromagnetic insulators are weakly polarized. We derive the effective equation of motion for the Keldysh Green's function focusing on a thin film superconductor sandwiched between two noncollinear ferromagnetic insulators, one of which is dynamical. In turn, we compute the spin currents in the system as a function of the temperature and the magnetizations' relative orientations. When the induced Zeeman splitting is weak, we find that the spin accumulation in the superconducting state is smaller than in the normal states due to the lack of quasiparticle states inside the gap. This feature gives a lower backflow spin current from the superconductor as compared to a normal metal. Furthermore, in superconductors, we find that the ratio between the backflow spin current in the parallel and antiparallel magnetization configuration depends strongly on temperature, in contrast to the constant ratio in normal metals.

DOI: [10.1103/PhysRevB.103.024524](https://doi.org/10.1103/PhysRevB.103.024524)

I. INTRODUCTION

Superconductivity and ferromagnetism are conventionally considered antagonistic phenomena. Superconductors (SCs) in contact with ferromagnets (FMs) lead to mutual suppression of both superconductivity and ferromagnetism [1,2]. Despite this apparent lack of compatibility, several intriguing effects also emerge from the interplay between superconductivity and ferromagnetism [3,4]. A singlet *s*-wave SC either in proximity with an inhomogeneous exchange field [5], or experiencing a homogeneous exchange field and spin-orbit coupling [6,7], induces spin-polarized triplet Cooper pairs. The generation of spin-polarized Cooper pairs is of particular interest, paving the way for realizing dissipationless spin transport [4]. In recent developments, the combination of magnetization dynamics and superconductivity has gained attention. This is motivated by spin-pumping experiments reporting observations of pure spin supercurrents [8,9]. Exhibiting a wide range of interesting effects and phenomena, SC-FM hybrids are promising material combinations in the emerging field of spintronics [10].

It is well known that the precessing magnetization in FMs generates spin currents into neighboring materials via spin pumping [11–13]. The injection of a spin current into a neighboring material generates a spin accumulation, which in turn gives rise to a backflow spin current into the FM. Spin pumping has a reactive and a dissipative component, characterized by how it affects the FM's dynamics. Reactive spin currents are polarized along the precession direction of the magnetization, $\dot{\mathbf{m}}$, and they cause a shift in the ferromagnetic resonance (FMR) frequency. Dissipative spin currents resemble Gilbert damping and are polarized along $\mathbf{m} \times \dot{\mathbf{m}}$, relaxing the magnetization toward its principal axis. The dissipative spin current

enhances the effective Gilbert damping coefficient [14], and broadens the FMR linewidth [12,15].

In SCs, both quasiparticles and spin-polarized triplet Cooper pairs can carry spin currents. In the absence of spin-polarized triplet pairs, spin pumping is typically much weaker through a superconducting contact than a normal metal (NM) [16,17]. The reduced efficiency is because the superconducting gap Δ prevents the excitation of quasiparticles by precession frequencies $\omega < 2\Delta$. When spin-polarized triplet pairs are present, spins can flow even for low FMR frequencies as pure spin supercurrents. Reference [8] reported evidence for such pure spin supercurrents. An enhanced FMR linewidth was measured in a FM–SC–heavy-metal hybrid system as it entered the superconducting state, which is a signature of an enlarged dissipative spin current [18]. The authors attributed this observation to spin transport by spin-polarized triplet pairs. These findings and the rapid development of spintronics have lately sparked a renewed interest in spin transport through FM|SC interfaces [9,19–27]. Several earlier works have also considered spin transport resulting from magnetization dynamics in SC-FM hybrids [28–35].

Progress has been made in developing a theoretical understanding of the spin pumping through SCs [17,19,21–23,25]. For instance, assuming suppression of the gap at the interface, Ref. [17] computed the reduced spin-pumping efficiency in the superconducting state using quasiclassical theory. However, to the best of our knowledge, a full understanding of the boundary conditions' complicated time dependence between dynamical ferromagnets and superconductors is not yet in place. This development is required to give improved spin-pumping predictions in multilayers of FMs, SCs, and NMs. Furthermore, spin-pumping in superconducting systems with a noncollinear magnetization configuration remains

theoretically underexplored, but it can provide additional insight into spin-transport properties.

We present a self-consistent method designed to solve the explicit time dependence arising from magnetization dynamics by using the generalized Usadel equation. The explicit time dependence complicates the treatment and understanding of spin-transport properties. We aim to describe a consistent proof-of-concept approach that is as simple as possible to understand. We will therefore use simplifying assumptions that are justified in weak insulating ferromagnets. Hopefully, the main message is then less hindered by subtleties. (i) We explore trilayers with a thin film SC between two noncollinear ferromagnetic insulators (FMIs). (ii) We exclusively consider the imaginary part of the spin-mixing conductance in the contacts between the FMIs and the SC film. (iii) We consider insulating ferromagnets. The first assumption requires that the interface resistance is larger than the superconductor's bulk resistance in the normal state, and that the superconductor is thinner than the coherence length. The second assumption is valid in weak ferromagnets.

Our first main result is the equation of motion for the Green's function in the SC film when the magnetization precesses. Based on these results, we present quantitative predictions for the spin current as a function of temperature and the relative magnetization orientation between the FMIs.

II. THE GENERALIZED USADEL EQUATION AND ITS SOLUTION

In this section, we will first present the generalized Usadel equation, taking into account the magnetization precession. We will demonstrate that it is possible to find an approximate solution to the time dependence when the precession frequency is sufficiently slow. In superconductors, we will discuss how this approach requires sufficient dephasing, since otherwise the peaks in the density of states invalidate the adiabatic assumption. Finally, we will solve the generalized Usadel equation and compute the resulting spin-current driven by the magnetization precession. Our analytical approach is supplemented by a numerical solution demonstrating the consistency of our assumptions.

A. The Generalized Usadel equation in a FMI|SC|FMI trilayer

The generalized Usadel equation determines the time evolution of the electron Green's function \hat{G} in the dirty limit. In a SC the generalized Usadel equation reads [36]

$$-iD\nabla\hat{G}\circ\nabla\hat{G}+i\partial_t\hat{\tau}_3\hat{G}(t_1,t_2)+i\hat{G}(t_1,t_2)\partial_{t_2}\hat{\tau}_3 + [\hat{\Delta}(t_1)\delta(t_1-t'_1)\hat{G}(t',t_2)]=0, \quad (1)$$

where D is the diffusion coefficient and $\delta(t)$ is the Dirac delta function. The symbol \circ denotes time convolution,

$$(a\circ b)(t_1,t_2)=\int_{-\infty}^{\infty}dt'a(t_1,t')b(t',t_2), \quad (2)$$

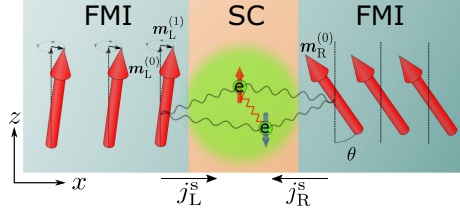


FIG. 1. FMI|SC|FMI trilayer. The superconductor is a thin film. The large red arrows depict the magnetic moments of localized d electrons in the FMIs. The green cloud illustrates a gas of s electrons with spin up (red) and down (blue). An attractive interaction between the s electrons (red sawtooth-like line) gives rise to superconductivity. The s - d exchange interaction at the interfaces gives rise to the indirect exchange interaction between the left and right FMI (wiggly gray lines). The precessing magnetization in the left FMI gives rise to spin currents J_L^s and J_R^s from the FMIs into the SC.

and $[a\circ b]=a\circ b-b\circ a$. \hat{G} and $\hat{\Delta}$ are matrices,

$$\hat{G}=\begin{pmatrix} \hat{G}^R & \hat{G}^K \\ 0 & \hat{G}^A \end{pmatrix}, \quad \hat{\Delta}=\begin{pmatrix} 0 & 0 & 0 & \Delta \\ 0 & 0 & -\Delta & 0 \\ 0 & \Delta^* & 0 & 0 \\ -\Delta^* & 0 & 0 & 0 \end{pmatrix}, \quad (3)$$

where R , A , and K denote the retarded, advanced, and Keldysh components, respectively. Δ is the superconducting gap. We choose to work in the gauge where $\Delta=\Delta^*$ is real. In our notation, the hat (e.g., \hat{G}) denotes 4×4 matrices in the subspace of particle-hole \otimes spin space. The inverted hat (e.g., \check{G}) denotes matrices spanning Keldysh space as well. σ_i are Pauli matrices spanning spin space, where $i\in\{0,x,y,z\}$, and σ_0 is the identity matrix. τ_i are Pauli matrices spanning particle-hole space, where $i\in\{0,1,2,3\}$, and τ_0 is the identity matrix. To simplify the notation, we will omit outer product notation between matrices in spin and particle-hole space. Consequently, $\tau_i\sigma_j$ should be interpreted as the outer product of the matrices τ_i and σ_j . Moreover, we use the following notation for matrices that are identity matrices in spin space: $\hat{\tau}_i\equiv\tau_i\sigma_0$.

We consider thin film SCs sandwiched between two identical, homogeneous, weakly magnetized FMIs, illustrated in Fig. 1. Because of the insulating nature of the FMIs, we disregard any tunneling through the FMIs. The interaction between electrons in the SC region and the FMIs is therefore localized at the interfaces. This s - d exchange interaction couples the localized d electrons in the FMIs to the s electrons in the SC at the interface. In thin film SCs, where the thickness of the superconductor is much shorter than the coherence length, $L_S\ll\xi_S$, we can approximate the effect of the s - d exchange interaction as an induced, homogeneous magnetic field in the SC [37–40]. Furthermore, in computing the transport properties, this assumption requires that the interface resistances (inverse “mixing” conductances) are larger than the SC’s bulk resistance in the normal state. When $L_S\ll\xi_S$, the Green’s function changes little throughout the SC, and we therefore neglect the gradient term in the generalized Usadel equation

within the SC. The resulting effective generalized Usadel equation for the FMI|SC|FMI trilayer then reads

$$i\partial_{t_1}\hat{\tau}_3\check{G}(t_1, t_2) + i\check{G}(t_1, t_2)\partial_{t_2}\hat{\tau}_3 + [\hat{\Delta}(t_1)\delta(t_1 - t')\check{G}(t', t_2)] \\ + m_{\text{eff}}[\mathbf{m}(t_1) \cdot \hat{\boldsymbol{\sigma}}\delta(t_1 - t')\check{G}(t', t_2)] = 0, \quad (4)$$

where $\mathbf{m}(t) = \mathbf{m}_L(t) + \mathbf{m}_R(t)$, and where $\mathbf{m}_{L/R}$ is the magnetization unit vector for the left/right FMI. m_{eff} is the effective magnetic field that each of the two identical FMIs would separately induce in the SC (in units of energy), and $\hat{\boldsymbol{\sigma}} = \text{diag}(\boldsymbol{\sigma}, \boldsymbol{\sigma}^*)$, where $\boldsymbol{\sigma}$ is the vector of Pauli matrices in spin space. Note that when $\mathbf{m}_L = -\mathbf{m}_R$, the effective magnetic field in the superconductor vanishes, in agreement with the conclusions of Ref. [41].

The effective generalized Usadel Eq. (4) was phenomenologically derived. We find the same equation by including boundary conditions to the FMIs [42,43], and then averaging the Green's function over the thickness of the superconductor. In principle, one could also have included other terms that are higher order in both the Green's functions and magnetizations. However, we consider weak ferromagnets, where the phase difference $\Delta\varphi = \varphi_{\uparrow} - \varphi_{\downarrow}$ in the spin-dependent reflection coefficients $r_{\uparrow/\downarrow}$ is small. Then it is sufficient to include the imaginary part of the spin mixing conductance, which results in Eq. (4). In other words, we disregard the real part of the mixing conductance, which is central in strong ferromagnets [17].

B. Gradient expansion in time and energy

The Green's function $\check{G}(t_1, t_2)$ correlates wave functions at times t_1 and t_2 . By shifting variables to relative time $\tau \equiv t_1 - t_2$ and absolute time $t \equiv (t_1 + t_2)/2$, and performing a Fourier transformation in the relative time coordinate, the following identity holds [44,45]:

$$\mathcal{F}\{(a \circ b)(t_1, t_2)\} = \exp\left\{\frac{i}{2}(\partial_{\tau}^a \partial_t^b - \partial_t^a \partial_{\tau}^b)\right\} a(E, t)b(E, t), \quad (5)$$

where \mathcal{F} denotes Fourier transform in τ , $a(E, t)$ and $b(E, t)$ are the Fourier transforms of $a(\tau, t)$ and $b(\tau, t)$ in the relative time coordinate, and $\partial_{E(t)}^{a(b)}$ denotes partial differentiation of the function a (b) with respect to the variable E (t). We will now Fourier transform and rewrite the generalized Usadel Eq. (4) into (E, t) coordinates.

The first two terms of Eq. (4) contain time differential operators. After rewriting these terms as the relative and absolute time coordinates, and Fourier-transforming the relative time coordinate, we find [46]

$$\mathcal{F}\{i\partial_{t_1}\hat{\tau}_3\check{G}(t_1, t_2) + i\check{G}(t_1, t_2)\partial_{t_2}\hat{\tau}_3\} \\ = E[\hat{\tau}_3, \check{G}(E, t)] + \frac{i}{2}\{\hat{\tau}_3, \partial_t\check{G}(E, t)\}. \quad (6)$$

The remaining two terms in Eq. (4) contain commutators of time convolutions of one-point functions $\Delta(t_1)$ and $\mathbf{m}(t_1)$ and the Green's function $\check{G}(t_1, t_2)$. These two terms transform equally. We will therefore consider only the term containing the magnetization in detail. By straightforward substitution into the term containing the magnetization of Eq. (4) into

Eq. (5), we find that

$$\mathcal{F}\{[\mathbf{m}(t_1) \cdot \hat{\boldsymbol{\sigma}}\delta(t_1 - t')\check{G}(t', t_2)]\} \\ = \exp\left\{-\frac{i}{2}\partial_t^m \partial_E \check{G}\right\} \mathbf{m}(t) \cdot \boldsymbol{\sigma} \check{G}(E, t) \\ - \exp\left\{\frac{i}{2}\partial_t^m \partial_E \check{G}\right\} \check{G}(E, t) \mathbf{m}(t) \cdot \boldsymbol{\sigma}. \quad (7)$$

In the following, we drop the arguments E and t to ease the notation.

We proceed by expanding the exponential function with differential operators,

$$\exp\left\{-\frac{i}{2}\partial_t^m \partial_E \check{G}\right\} (\mathbf{m} \cdot \boldsymbol{\sigma}) \check{G} - \exp\left\{\frac{i}{2}\partial_t^m \partial_E \check{G}\right\} \check{G} (\mathbf{m} \cdot \boldsymbol{\sigma}) \\ = [(\mathbf{m} \cdot \hat{\boldsymbol{\sigma}}), \check{G}] - \left(\frac{i}{2}\right) \{\partial_t(\mathbf{m} \cdot \hat{\boldsymbol{\sigma}}), \partial_E \check{G}\} \\ + \frac{1}{2!} \left(\frac{i}{2}\right)^2 [\partial_t^2(\mathbf{m} \cdot \hat{\boldsymbol{\sigma}}), \partial_E^2 \check{G}] \\ - \frac{1}{3!} \left(\frac{i}{2}\right)^3 [\partial_t^3(\mathbf{m} \cdot \hat{\boldsymbol{\sigma}}), \partial_E^3 \check{G}] + (\dots), \quad (8)$$

where $\{\dots, \dots\}$ denotes an anticommutator. Here and later on, for ease of notation, we drop the superscript of the differential operators. Instead, we let the differential operators only act on the factor directly to the right of it. We keep terms only up to linear order in the gradients. This is justified when

$$\left|\frac{1}{2^3}[\partial_t^n(\mathbf{m} \cdot \hat{\boldsymbol{\sigma}}), \partial_E^n \check{G}]_{ij}\right| \ll \left|[\partial_t^{n-2}(\mathbf{m} \cdot \hat{\boldsymbol{\sigma}}), \partial_E^{n-2} \check{G}]_{ij}\right|, \quad (9)$$

$$\left|\frac{1}{2^3}\{\partial_t^n(\mathbf{m} \cdot \hat{\boldsymbol{\sigma}}), \partial_E^n \check{G}\}_{ij}\right| \ll \left|\{\partial_t^{n-2}(\mathbf{m} \cdot \hat{\boldsymbol{\sigma}}), \partial_E^{n-2} \check{G}\}_{ij}\right|, \quad (10)$$

where ∂_t^n denotes the n th partial derivative with respect to t . The magnetization precesses at a frequency ω . Therefore, ω must be much smaller than the energy gradient of the Green's function. First, to avoid a diverging energy gradient of the Green's function, we assume finite temperatures. Second, we add a phenomenological dephasing parameter $\delta = 1/\tau_{\text{dep}}$ to the Green's function, $E \rightarrow E + i\delta$, where τ_{dep} is a characteristic dephasing time. We then find that the requirements (9) and (10) are satisfied when $(\omega\tau_{\text{dep}})^2/8 \ll 1$ and $(\omega\beta)^2/8 \ll 1$, where $\beta = 1/k_B T$ is the inverse temperature.

To linear order, the effective generalized Usadel equation in the FMI|SC|FMI trilayer reads

$$E[\hat{\tau}_3, \check{G}] + \frac{i}{2}\{\hat{\tau}_3, \partial_t \check{G}\} + [\hat{\Delta}, \check{G}] - \frac{i}{2}\{\partial_t \hat{\Delta}, \partial_E \check{G}\} \\ + m_{\text{eff}}[\mathbf{m} \cdot \hat{\boldsymbol{\sigma}}, \check{G}] - \frac{im_{\text{eff}}}{2}\{\partial_t \mathbf{m} \cdot \hat{\boldsymbol{\sigma}}, \partial_E \check{G}\} = 0. \quad (11)$$

In the next section, we will supplement this equation with terms arising from spin-memory loss.

C. Spin relaxation

To obtain a realistic model, we additionally need to include some sort of spin relaxation mechanism in the generalized Usadel Eq. (11). As a simple model, we model the relaxation as a coupling to a NM reservoir, parametrized by the coupling

coefficient V . This coupling relaxes the Green's function in the SC toward the equilibrium solution around the Fermi level in the NM reservoir. The effective generalized Usadel equation including this relaxation reads

$$\begin{aligned} E[\hat{\tau}_3, \check{G}] + \frac{i}{2}[\hat{\tau}_3, \partial_t \check{G}] + [\hat{\Delta}, \check{G}] - \frac{i}{2}[\partial_t \hat{\Delta}, \partial_E \check{G}] \\ + m_{\text{eff}}[\mathbf{m} \cdot \hat{\sigma}, \check{G}] - \frac{im_{\text{eff}}}{2}[\partial_t \mathbf{m} \cdot \hat{\sigma}, \partial_E \check{G}] \\ + iV[\check{N}, \check{G}] - \frac{V}{2}[\partial_E \check{N}, \partial_t \check{G}] = 0, \end{aligned} \quad (12)$$

where \check{N} is the equilibrium Green's function in the NM reservoir. Additionally, this coupling gives a dephasing $E \rightarrow E - iV$ in the Green's function in the SC. This relaxation is therefore a possible source of the dephasing which we have already introduced in Sec. II B.

D. Parametrization

We now aim to express the generalized Usadel Eq. (12) in a form that is easier to treat both analytically and numerically. We use a parametrization [47] that maps the eight nonzero components of \check{G}^R , \check{G}^A , and \check{G}^K onto two scalars (charge

$$\frac{\partial G_0^{R/A}}{\partial t} = m_{\text{eff}} \left(\frac{\partial \mathbf{G}^{R/A}}{\partial E} \right) \cdot \left(\frac{\partial \mathbf{m}}{\partial t} \right) - i \left(\frac{\partial F_0^{R/A}}{\partial E} \right) \left(\frac{\partial \Delta}{\partial t} \right), \quad (15)$$

$$\frac{\partial \mathbf{G}^{R/A}}{\partial t} = 2m_{\text{eff}}(\mathbf{G}^{R/A} \times \mathbf{m}) + m_{\text{eff}} \left(\frac{\partial \mathbf{G}_0^{R/A}}{\partial E} \right) \left(\frac{\partial \mathbf{m}}{\partial t} \right) - i \left(\frac{\partial \Delta}{\partial t} \right) \left(\frac{\partial \mathbf{F}^{R/A}}{\partial E} \right), \quad (16)$$

$$\frac{\partial G_0^K}{\partial t} = m_{\text{eff}} \left(\frac{\partial \mathbf{G}^K}{\partial E} \right) \cdot \left(\frac{\partial \mathbf{m}}{\partial t} \right) - i \left(\frac{\partial F_0^K}{\partial E} \right) \left(\frac{\partial \Delta}{\partial t} \right) - 2V \left[G_0^K - (G_0^R - G_0^A) \tanh \left(\frac{\beta E}{2} \right) \right] - iV \frac{\beta}{2} \left(\frac{\partial G_0^R}{\partial t} + \frac{\partial G_0^A}{\partial t} \right) \text{sech}^2 \left(\frac{\beta E}{2} \right), \quad (17)$$

$$\begin{aligned} \frac{\partial \mathbf{G}^K}{\partial t} = 2m_{\text{eff}}(\mathbf{G}^K \times \mathbf{m}) + m_{\text{eff}} \left(\frac{\partial \mathbf{G}_0^K}{\partial E} \right) \left(\frac{\partial \mathbf{m}}{\partial t} \right) - i \left(\frac{\partial \Delta}{\partial t} \right) \left(\frac{\partial \mathbf{F}^K}{\partial E} \right) \\ - 2V \left[\mathbf{G}^K - (\mathbf{G}^R - \mathbf{G}^A) \tanh \left(\frac{\beta E}{2} \right) \right] - iV \frac{\beta}{2} \left(\frac{\partial \mathbf{G}^R}{\partial t} + \frac{\partial \mathbf{G}^A}{\partial t} \right) \text{sech}^2 \left(\frac{\beta E}{2} \right). \end{aligned} \quad (18)$$

We also obtain additional equations given in Appendix A for the anomalous components F_0 and \mathbf{F} for the R , A , and K components. These equations (A1)–(A4) are large and less transparent algebraic expressions. Lastly, we need the gap equation,

$$\Delta = -i \frac{N_0 \lambda}{4} \int_{-\omega_D}^{\omega_D} dE F_0^K, \quad (19)$$

where ω_D is the Debye cutoff energy, N_0 is the Fermi-level electron density of states, and λ is the BCS electron-phonon coupling constant. We will hereafter refer to Δ_0 as the gap at zero temperature, and Δ as the gap at the temperature and effective magnetic field that is being considered.

For a self-consistent solution, all of the equations (15)–(18), (A1)–(A4), and (19) are needed. If we assume a static gap, however, only Eqs. (15)–(18) are needed to determine the time evolution of the Green's functions once we know their solution at a given time t .

sector) and two vectors (spin sector), one of each reflecting the normal and anomalous parts of the Green's function. We expand the Green's function as (this applies to the R , A , and K components)

$$\hat{G} = \sum_{i \in \{0, 1, 2, 3\}} \sum_{j \in \{0, x, y, z\}} G_{ij} \tau_i \sigma_j, \quad (13)$$

where $G_{ij} = \frac{1}{4} \text{Tr} \hat{G} \tau_i \sigma_j$. We gather the nonzero components into the following functions:

$$\begin{aligned} G_0 &\equiv G_{30}, \\ \mathbf{G} &\equiv [G_{0x}, G_{3y}, G_{0z}], \\ F_0 &\equiv G_{1y}, \\ \mathbf{F} &\equiv [-G_{2z}, G_{10}, G_{2x}]. \end{aligned} \quad (14)$$

The scalar G_0 and the vector \mathbf{G} describe the diagonal elements in particle-hole space of \hat{G} . The scalar F_0 and the vector \mathbf{F} characterize the corresponding anomalous off-diagonal elements of \hat{G} . By inserting the definitions (13) and (14) into the effective generalized Usadel Eq. (12), we arrive at the following parametrized differential equations for the normal components:

E. Spin currents and effects on FMR

The magnetization dynamics in FMs generates spin currents into neighboring materials. In the trilayer FMI|SC|FMI under consideration, these spin currents read

$$j_{X,x}^s = -\frac{iN_0 m_{\text{eff}}}{8} \int_{-\infty}^{\infty} dE \text{Tr} \{ \sigma_x \tau_3 [\mathbf{m}_X \cdot \hat{\sigma} \check{G}]^K \}, \quad (20)$$

$$j_{X,y}^s = -\frac{iN_0 m_{\text{eff}}}{8} \int_{-\infty}^{\infty} dE \text{Tr} \{ \sigma_y \tau_0 [\mathbf{m}_X \cdot \hat{\sigma} \check{G}]^K \}, \quad (21)$$

$$j_{X,z}^s = -\frac{iN_0 m_{\text{eff}}}{8} \int_{-\infty}^{\infty} dE \text{Tr} \{ \sigma_z \tau_3 [\mathbf{m}_X \cdot \hat{\sigma} \check{G}]^K \}, \quad (22)$$

where \mathbf{m}_X is the magnetization at interface $X \in \{L, R\}$, and where positive signs indicate spin-currents going from the FMIs into the SC. After expanding the convolution products in Eqs. (20)–(22) to first order in time and energy gradients, we find

$$\mathbf{j}_X^s = \frac{N_0 m_{\text{eff}}}{4} \int_{-\infty}^{\infty} dE \left[\frac{1}{2} \left(\frac{\partial \mathbf{G}_0^K}{\partial E} \right) \left(\frac{\partial \mathbf{m}_X}{\partial t} \right) + (\mathbf{G}^K \times \mathbf{m}_X) \right]. \quad (23)$$

The first term in this expression is the so-called spin-pumping current arising from the imaginary part of the mixing conductance. The spin-pumping current equals $j^p = (N_0 m_{\text{eff}}/2) \partial \mathbf{m}_X / \partial t$ both in SCs and NMs. The second term in Eq. (23) is the backflow spin current j^b due to spin-accumulation in the SC [48]. The spin-pumping current is independent of temperature, relative magnetization angles, and of whether the system is superconducting or not. The backflow spin current depends on these system parameters, and it will therefore be our main focus henceforth.

If we assume that the magnetizations of the FMIs are uniform, the Landau-Lifshitz-Gilbert equation for the left FMI can be written

$$\frac{\partial \mathbf{m}_L}{\partial t} = -\gamma_0 \mathbf{m}_L \times \mathbf{B}_{\text{eff}} + \alpha_0 \left(\mathbf{m}_L \times \frac{\partial \mathbf{m}_L}{\partial t} \right) - \frac{\gamma_0}{M_s d} \mathbf{j}_L^s, \quad (24)$$

where γ_0 is the gyromagnetic ratio of the ferromagnetic spins, \mathbf{B}_{eff} is the effective field in the FMI, α_0 is the Gilbert damping parameter, M_s is the saturation magnetization in the FMI, and d is the thickness of the FMI. If we express \mathbf{j}_L^s in reactive and dissipative components, $\mathbf{j}_L^s = C_r \frac{\partial \mathbf{m}_L}{\partial t} + C_d (\mathbf{m}_L \times \frac{\partial \mathbf{m}_L}{\partial t})$, we find the following renormalized properties in the FM:

$$\gamma_0 \rightarrow \gamma = \frac{\gamma_0}{1 + \frac{C_r \gamma_0}{M_s d}}, \quad (25)$$

$$\alpha_0 \rightarrow \alpha = \frac{\gamma}{\gamma_0} \left(\alpha_0 + \frac{C_d \gamma_0}{M_s d} \right). \quad (26)$$

For later convenience, we define the reactive and dissipative spin currents, $\mathbf{j}_r^s \equiv C_r \frac{\partial \mathbf{m}_L}{\partial t}$ and $\mathbf{j}_d^s \equiv C_d (\mathbf{m}_L \times \frac{\partial \mathbf{m}_L}{\partial t})$.

III. RESULTS AND DISCUSSIONS

We will now use the equations of motion of (15)–(18), (A1)–(A4), and the gap Eq. (19), to find the spin current generated by FMR in a FMI|SC|FMI trilayer. We consider homogeneous magnetizations \mathbf{m}_L and \mathbf{m}_R in the left and right FMIs, respectively. The angle between the principal axes of the magnetizations is θ . The left magnetization is precessing circularly around its principal axis at a precession angle φ with angular frequency ω . The right magnetization is static. The system is illustrated in Fig. 1.

We will initially search for an analytical solution by treating the dynamic magnetization component as a perturbation from an equilibrium solution. Due to the complexity of the equations, we first assume that the gap is static. This approximation enables us to solve the problem for arbitrary relaxation V . Section III A presents this analytical approach. In principle, it is also possible to find a self-consistent analytical solution. However, the solution becomes extremely complex in the presence of relaxation due to the coupling between the retarded/advanced and Keldysh Green's functions. Hence, the full self-consistent problem is better suited for numerical treatments. In Sec. III B, we compare the results of a self-consistent numerical solution to the analytical solution in Sec. III A. We additionally outline a self-consistent analytical solution in Appendix B in the absence of relaxation. This latter solution has restricted physical relevance, but is supplied for the convenience of further work in this framework.

A. Analytical solution with static gap approximation

We first separate the magnetization vector \mathbf{m} into a static and a dynamic component, $\mathbf{m} = \mathbf{m}^{(0)} + \mathbf{m}^{(1)}$. The static component $\mathbf{m}^{(0)} = \mathbf{m}_L^{(0)} + \mathbf{m}_R^{(0)}$ is the sum of the static magnetizations of the left and right FMIs. The dynamic component $\mathbf{m}^{(1)}$ is the dynamic part of \mathbf{m}_L . It has magnitude δm and precesses around the z axis with angular frequency ω , $\mathbf{m}^{(1)} = \delta m [\cos(\omega t), \sin(\omega t), 0]$. This decomposition of the magnetization vectors is illustrated in Fig. 1. We now assume the following: (i) The dynamic magnetization component is much smaller than the gap, $m_{\text{eff}} \delta m \ll \Delta$. (ii) The fluctuations in the gap are much smaller than the dynamic magnetization amplitude, $\delta \Delta \ll m_{\text{eff}} \delta m$.

Assumption (i) enables us to expand the Keldysh Green's function components in the perturbation δm ,

$$\begin{aligned} G_0^K &= G_0^{K(0)} + G_0^{K(1)} + (\dots), \\ \mathbf{G}^K &= \mathbf{G}^{K(0)} + \mathbf{G}^{K(1)} + (\dots), \end{aligned} \quad (27)$$

where the n th-order terms are assumed to be $\propto \delta m^n$. We consider the first-order expansion in δm only, and we choose therefore to disregard second- and higher-order terms. Assumption (ii) implies that the generalized Usadel equations for the advanced and retarded Green's functions [Eqs. (15) and (16)] decouple from the Keldysh component. In what follows, we will derive the solution for the Keldysh component. The retarded/advanced Green's functions can then be found simply by substituting $K \rightarrow R/A$ and by setting $V = 0$ in the Keldysh component solution.

To first order in δm , the effective generalized Usadel equations for the Keldysh component read

$$\begin{aligned} \frac{\partial G_0^{K(1)}}{\partial t} &= m_{\text{eff}} \left(\frac{\partial \mathbf{G}^{K(0)}}{\partial E} \right) \cdot \left(\frac{\partial \mathbf{m}^{(1)}}{\partial t} \right) \\ &\quad - 2V \left[G_0^{K(1)} - (G_0^{R(1)} - G_0^{A(1)}) \tanh \left(\frac{\beta E}{2} \right) \right], \end{aligned} \quad (28)$$

$$\begin{aligned} \frac{\partial \mathbf{G}^{K(1)}}{\partial t} &= 2m_{\text{eff}} (\mathbf{G}^{K(0)} \times \mathbf{m}^{(1)} + \mathbf{G}^{K(1)} \times \mathbf{m}^{(0)}) \\ &\quad + m_{\text{eff}} \left(\frac{\partial G_0^{K(0)}}{\partial E} \right) \left(\frac{\partial \mathbf{m}^{(1)}}{\partial t} \right) \\ &\quad - 2V \left[\mathbf{G}^{K(1)} - (\mathbf{G}^{R(1)} - \mathbf{G}^{A(1)}) \tanh \left(\frac{\beta E}{2} \right) \right]. \end{aligned} \quad (29)$$

We propose the *Ansätze*

$$\begin{aligned} G_0^{K(1)} &= G_{0+}^{K(1)} e^{i\omega t} + G_{0-}^{K(1)} e^{-i\omega t}, \\ \mathbf{G}^{K(1)} &= \mathbf{G}_+^{K(1)} e^{i\omega t} + \mathbf{G}_-^{K(1)} e^{-i\omega t}. \end{aligned} \quad (30)$$

After inserting the *Ansätze* in Eq. (30) into Eqs. (28) and (29), we note that the differential equations separate into decoupled equations for the $+/-$ components. By solving for $G_{0\pm}^{K(1)}$ and

$\mathbf{G}_{\pm}^{K(1)}$, we obtain

$$\mathbf{G}_{0\pm}^{K(1)} = m_{\text{eff}} \frac{\pm\omega}{\pm\omega + 2V} \left(\frac{\partial \mathbf{G}^{(0)}}{\partial E} \right) \cdot \mathbf{m}_{\pm}^{(1)} + \frac{2V}{\pm\omega + 2V} (\mathbf{G}_0^{R(1)} - \mathbf{G}_0^{A(1)}) \tanh\left(\frac{\beta E}{2}\right), \quad (31)$$

$$\mathbf{G}_{\pm}^{K(1)} = m_{\text{eff}} \mathbf{A}_{\pm\omega}^{-1} \mathbf{B}_{\pm\omega} \mathbf{m}_{\pm}^{(1)} + 2V \mathbf{A}_{\pm\omega}^{-1} (\mathbf{G}^{R(1)} - \mathbf{G}^{A(1)}) \tanh\left(\frac{\beta E}{2}\right), \quad (32)$$

where the matrices $\mathbf{A}_{\pm\omega}$ and $\mathbf{B}_{\pm\omega}$ are defined as

$$\mathbf{A}_{\pm\omega} = \begin{pmatrix} \pm i\omega + 2V & -2m_{\text{eff}}m_z^{(0)} & 2m_{\text{eff}}m_y^{(0)} \\ 2m_{\text{eff}}m_z^{(0)} & \pm i\omega + 2V & -2m_{\text{eff}}m_x^{(0)} \\ -2m_{\text{eff}}m_y^{(0)} & 2m_{\text{eff}}m_x^{(0)} & \pm i\omega + 2V \end{pmatrix}, \quad (33)$$

$$\mathbf{B}_{\pm\omega} = \begin{pmatrix} \pm i\omega C(E) & -2G_z^{K(0)} & 2G_y^{K(0)} \\ 2G_z^{K(0)} & \pm i\omega C(E) & -2G_x^{K(0)} \\ -2G_y^{K(0)} & 2G_x^{K(0)} & \pm i\omega C(E) \end{pmatrix}, \quad (34)$$

and where

$$C(E) = \tanh\left(\frac{\beta E}{2}\right) \left(\frac{\partial \mathbf{G}_0^{R(0)}}{\partial E} - \frac{\partial \mathbf{G}_0^{A(0)}}{\partial E} \right) + \left[(\mathbf{G}_0^{R(0)} - \mathbf{G}_0^{A(0)}) - iV \left[\frac{\partial \mathbf{G}_0^{R(0)}}{\partial E} + \frac{\partial \mathbf{G}_0^{A(0)}}{\partial E} \right] \right] \times \frac{\beta}{2} \text{sech}^2\left(\frac{\beta E}{2}\right). \quad (35)$$

The solution to $\mathbf{G}^{K(1)}$ is particularly simple when $\theta = 0$ or $\theta = \pi$. For $\theta = 0$, we obtain

$$\mathbf{G}_{\theta=0}^{K(1)} = m_{\text{eff}} (2G_z^{K(0)} + \omega C(E)) \frac{(4m_{\text{eff}} + \omega)\mathbf{m}^{(1)} + \frac{2V}{\omega} \frac{\partial \mathbf{m}^{(1)}}{\partial t}}{(2V)^2 + (4m_{\text{eff}} + \omega)^2} + \frac{2V^2 \mathbf{m}^{(1)} - \frac{V}{\omega} (4m_{\text{eff}} + \omega) \frac{\partial \mathbf{m}^{(1)}}{\partial t}}{(2V)^2 + (4m_{\text{eff}} + \omega)^2} G_z^{K(0)}, \quad (36)$$

where we have inserted $m_z^{(0)} = 2$. We observe that a finite V introduces a component of \mathbf{G}^K parallel to $\partial \mathbf{m}_L / \partial t$. When we insert this component into the spin current in Eq. (23), we see that it generates both a reactive and a dissipative backflow current, \mathbf{j}_r^b and \mathbf{j}_d^b . Hence, even though the spin pumping current is purely reactive, the backflow spin current can indeed carry a dissipative part due to relaxation in the SC. Moreover, we note that the effective magnetic field $2m_{\text{eff}}$ suppresses the amplitude of $\mathbf{G}^{K(1)}$. This feature is due to Hanle precession of $\mathbf{G}^{K(1)}$ around the effective magnetic field, which reduces the effect of the excitation.

When $\theta = \pi$, the Hanle precession is more or less absent due to a very small effective magnetic field $\propto m_{\text{eff}} \sin \varphi$. Under the assumption that the precession angle is sufficiently small, $\sin \varphi \ll \omega / m_{\text{eff}}$, we obtain

$$\mathbf{G}_{\theta=\pi}^{K(1)} = m_{\text{eff}} \omega C(E) \frac{\omega \mathbf{m}^{(1)} + \frac{2V}{\omega} \frac{\partial \mathbf{m}^{(1)}}{\partial t}}{(2V)^2 + \omega^2}. \quad (37)$$

As a control check, we can verify that we obtain the instantaneous equilibrium solution $(\mathbf{G}^{R(1)} - \mathbf{G}^{A(1)}) \tanh(\beta E / 2)$ when $V \gg \omega$.

In the second line of $C(E)$ in Eq. (35), we have isolated the source of nonequilibrium behavior of \mathbf{G}^K . This nonequilibrium part arises from the energy gradient of the distribution function, and is therefore proportional to $\text{sech}^2(\frac{\beta E}{2})$. In the normal metal limit, we have $\partial G_0^R / \partial E = 0$, and $\int_{-\infty}^{\infty} dE C(E) = 4$ is therefore constant and independent of temperature. The spin current is therefore independent of temperature in the NM limit.

The coefficient $C(E)$ in Eq. (35) predicts that the nonequilibrium effects mostly arise within a thermal energy interval $\pm \beta^{-1}$ from the Fermi level. There are two tunable parameters that affect the number of quasiparticle states within this energy interval in a SC: First, at higher temperatures, the energy interval in which quasiparticles can be excited broadens. The more overlap there is between this energy window and the gap edge, the larger we expect the spin accumulation to be. Another thermal effect is that the gap Δ decreases with increasing temperature, which enhances the above-mentioned effect. Second, the effective magnetic field introduces a spin-split density of states, which pushes half of the quasiparticle states closer to the Fermi level. An additional effect is that the gap decreases with an increasing effective magnetic field, an effect that moreover is temperature-dependent. Therefore, the effective magnetic field also affects the number of quasiparticle states within a thermal energy interval from the Fermi level. Both the temperature and effective magnetic field can hence be tuned to increase the spin accumulation. The spin accumulation in turn generates a backflow spin current into the FMIs. We therefore expect a larger backflow spin current from a SC at higher temperatures and for stronger effective magnetic fields.

We will now evaluate the angular and temperature dependence of the backflow spin current for a particular FMI|SC|FMI trilayer. We choose the parameters in the SC so that they match those of Nb. That is, we choose $1/V = \tau_{\text{sf}} / 2\pi \sim 10^{-10}$ s [49] and a critical temperature $T_c = 9.26$ K [50]. Moreover, we use an effective magnetic field strength $m_{\text{eff}} = 0.1\Delta_0$, and a magnetization precession angle $\varphi = \arcsin(0.01)$. Last, we use a precession frequency $\omega = 0.005\Delta_0 \approx 10$ GHz, which is an appropriate frequency for, e.g., yttrium iron garnet (YIG). The relaxation introduces a dephasing $V = 0.05\Delta_0$, which is sufficient to justify the gradient expansion. The gap $\Delta = \Delta(T, \theta, m_{\text{eff}})$ is found by solving the gap equation self-consistently [51] to zeroth order in the dynamic magnetization, as well as checking that the free energy of the superconducting state is lower than in the normal metal state. The assumptions (i) and (ii) underlying the static gap approximation can be satisfied for any effective field m_{eff} providing we choose an appropriate precession amplitude, δm , which can be tuned with the ac magnetic field used to excite FMR in the FMI.

In the FMI|SC|FMI trilayer, the expression for the backflow spin current in Eq. (23) implies that there is a static RKKY contribution to the spin current. This RKKY contribution is due to the finite \mathbf{G}^K close to the Fermi level. However, other terms also contribute to the RKKY interaction beyond the quasiclassical theory. Therefore, we subtract the instantaneous RKKY-like static contribution to the spin current.

Figure 2 plots the backflow spin current as a function of θ for two different temperatures, $T = 0.1T_c$ and $T = 0.9T_c$. The

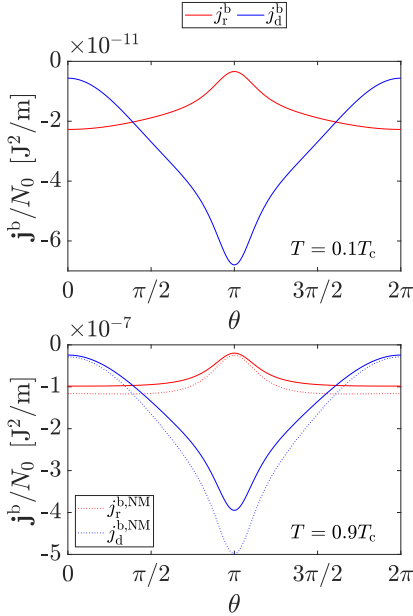


FIG. 2. The reactive (red) and dissipative (blue) backflow spin current, normalized to the density of states N_0 , as a function of θ through the left interface of a FMI|SC|FMI trilayer for two different temperatures, $T = 0.1T_c$ (upper plot) and $T = 0.9T_c$ (lower plot). We have used the parameters given in the main text, with $m_{\text{eff}} = 0.1\Delta_0$. In the lower plot, we have also plotted the spin current through an analogous FMI|NM|FMI trilayer (dotted lines).

spin-pumping currents in both cases are purely reactive and equal to $j^p/N_0 = 10^{-5} J^2/m$. The first striking observation is that the spin current is much lower in the SC system at $T = 0.1T_c$ than at $T = 0.9T_c$. Singlet pair formation hinders injection of spin currents into the superconductor. Next, we observe that the total spin current grows as θ approaches π , which is the case for both the SC and NM systems, and at both temperatures. This is due to the decreased impact of Hanle precession on the spin accumulation as the effective magnetic field decreases. Moreover, we note that the reactive spin current is favored close to $\theta = 0$, whereas the dissipative spin current is favored close to $\theta = \pi$. This is because the Hanle precession affects the reactive and dissipative spin current differently. Inspecting Eq. (36), we see that the reactive and dissipative spin current are suppressed by a factor $\propto (m_{\text{eff}})^{-1}$ and $\propto (m_{\text{eff}})^{-2}$ close to $\theta = 0$, respectively. For large effective magnetic fields, that is, close to $\theta = 0$, the dissipative spin current is therefore strongly suppressed compared to the reactive spin current. Close to $\theta = \pi$, where Hanle precession is negligible, the reactive and dissipative spin currents are suppressed $\propto V^{-2}$ and $\propto V^{-1}$, respectively, as can be seen in

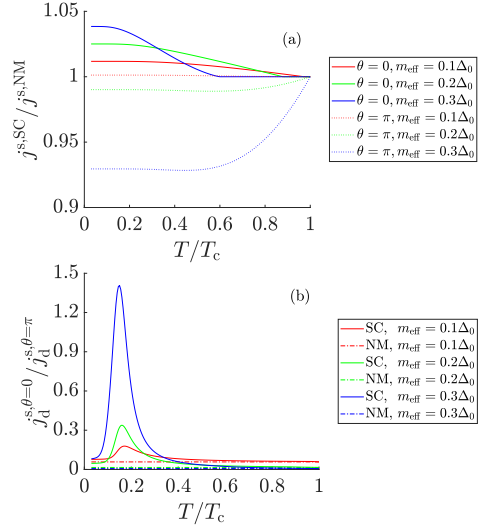


FIG. 3. (a) The temperature dependence of the total spin current in the superconducting system for two relative magnetization angles, $\theta = 0$ and $\theta = \pi$. The spin current is normalized to the normal metal limit, where the spin current is independent of temperature. (b) The ratio $J_d^{s,\theta=0}/J_d^{s,\theta=\pi}$ plotted as a function of temperature for both the SC and NM systems. We have used the parameters given in the main text. The lowest temperature included is $T = 0.03T_c$ in order to ensure that the gradient expansion is justified.

Eq. (37). Hence, the dissipative spin current dominates close to $\theta = \pi$.

Let us now explore the temperature dependence in detail. In Fig. 3(a) we plot the total spin current as a function of temperature for two angles, $\theta = 0$ and $\theta = \pi$, and for different effective field strengths m_{eff} . We have normalized the spin currents with the respect to the analogous NM limit spin currents. The latter are independent of temperature. Due to the gradient expansion, the parameters must satisfy the condition $\beta^{-1} \gg \omega/\sqrt{8} \approx 0.003k_B T_c$. We therefore restrict the temperature analysis to $T \geq 0.03T_c$. First, we observe that the spin currents approach the NM limit at the critical fields for the respective effective magnetic fields. We have already discussed this behavior, which is due to the amount of quasiparticle states within a thermal energy interval from the Fermi energy. This entails an overall decrease in the total spin current for the $\theta = 0$ configuration, and an increase for the $\theta = \pi$ configuration. This is due to the nature of the backflow spin current. In the $\theta = 0$ configuration, the backflow spin current is dominated by a reactive component that counteracts the spin-pumping current. In the $\theta = \pi$ configuration, the backflow spin current is dominated by a dissipative component. This spin current is oriented almost 90° relative to the spin-pumping current, and therefore increases the total spin current.

Next, Fig. 3(a) demonstrates that the temperature dependence of the normalized spin current for the $\theta = 0$ and $\theta = \pi$ states differ. To investigate this further, we plot the ratio between the dissipative spin currents in the parallel and antiparallel configurations, $j_d^{s,\theta=0}/j_d^{s,\theta=\pi}$, both in the NM and SC state, in Fig. 3(b). Here, we observe that this ratio is a constant function of temperature in the NM limit, whereas it depends strongly on temperature in the superconducting state. The ratio peaks at slightly different temperatures for different effective fields m_{eff} in the superconducting state. The height of the peak increases with an increasing effective field m_{eff} . As the temperature approaches T_c , the ratio in the SC state converges toward the NM limit result.

This behavior is due to the aforementioned effect of temperature and effective magnetic field. In the parallel configuration, the effective magnetic fields of the two FMIs add constructively and cause a strong spin-splitting in the density of states. In the antiparallel configuration, the effective fields add destructively and cause only a weakly spin-split density of states. At very low temperatures, the difference between the parallel and antiparallel configurations is small for the chosen values of m_{eff} . This is because neither state has a large density of states close to the almost δ -function-like thermal energy interval around the Fermi level. At slightly higher temperatures, the states that are pushed closer to the Fermi level start overlapping with the thermal energy interval $E_F \pm \beta^{-1}$. The difference between the two states is maximized for some intermediate temperature, $k_B T \lesssim \Delta(T)$, where we observe the peaks in Fig. 3(b). At even higher temperatures, the thermal energy interval broadens further. The difference between the parallel and antiparallel states then starts decreasing for higher temperatures, and eventually approaches the NM limit.

B. Numerical analysis

We aim here to briefly present a numerical solution to the problem that was solved analytically in Sec. III A. Our main goal is to evaluate whether the assumption of a static gap can be justified to a good approximation. A subsidiary goal is to show the time evolution of the gap, and the usefulness of a numerical method in this framework also when the static gap approximation is not valid.

We see from Eqs. (16) and (18) that the vectors \mathbf{G}^A , \mathbf{G}^R , and \mathbf{G}^K precess around the effective magnetic field. For such a class of equations, employing a fourth-order Runge-Kutta method is suitable for obtaining a numerical solution. To test the validity of the static gap approximation, we want to perform a simulation of the system where the oscillations in the gap are maximized. This is expected to occur where the magnitude of the effective field oscillates with the largest amplitude. From Eq. (B9) one can show that this occurs at $\theta = \pi/2$ in the absence of relaxation, and we hence expect it to occur at $\theta = \pi/2$ also with the inclusion of relaxation.

Figure 4(a) for $\theta = \pi/2$ shows the fluctuation of the gap $\delta\Delta(t)$ normalized to Δ_0 over one period $2\pi/\omega$ and for several temperatures T , with $m_{\text{eff}} = 0.1\Delta_0$. The gap oscillates harmonically with frequency ω for all temperatures up to $T = 0.85T_c$. At temperatures close to the critical temperature for the given effective magnetic field, the gap shows a nonlinear response to the dynamical magnetization. This effect

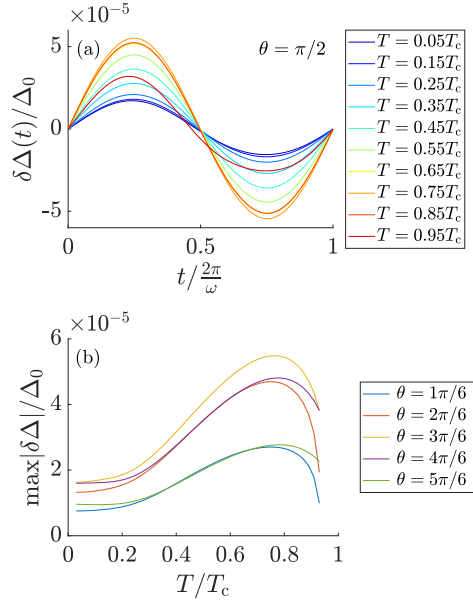


FIG. 4. (a) The fluctuations of the gap $\delta\Delta(t)$ plotted over one period $2\pi/\omega$ at different temperatures for $\theta = \pi/2$. (b) The detailed temperature dependence of the gap fluctuation amplitude $\max|\delta\Delta|$ for different magnetization angles θ . The gap fluctuations are normalized to the gap at zero temperature, Δ_0 , and we have used $m_{\text{eff}} = 0.1\Delta_0$.

is visible for $T = 0.95T_c$, and is due to the increased sensitivity to fluctuations in the magnetic field as the temperature approaches the critical temperature. In Fig. 4(b), we further explore θ and the temperature dependence of the gap fluctuation amplitude, $\max|\delta\Delta|$, in the linear response regime. We observe that the fluctuations are largest at $\theta = \pi/2$, and that they are maximized at about $T \approx 0.8T_c$. Moreover, we observe that the fluctuations are not larger than about $5.5 \times 10^{-5}\Delta_0$. Let us now briefly remind the reader that the formal requirement for the static gap approximation was $\delta\Delta \ll m_{\text{eff}}\delta m$, where δm is the dynamic magnetization amplitude. We have $m_{\text{eff}}\delta m \approx 0.001\Delta_0 \gg \delta\Delta \leq 5.5 \times 10^{-5}\Delta_0$, which implies that the static gap assumption is an excellent approximation in this instance.

IV. CONCLUSION

We have derived an effective, time-dependent generalized Usadel equation in noncollinear FMI|SC|FMI trilayers with a thin superconducting layer and weakly magnetized FMIs. We have provided analytical solutions to these equations in terms of perturbations in the dynamic magnetization, first under the assumption of a static gap, and then a self-consistent solution in the absence of relaxation. Lastly, we have provided

numerical procedures to obtain self-consistent solutions of the full equations without any further simplifications.

From the solutions to the generalized Usadel equation, we computed the spin currents generated by ferromagnetic resonance in one of the FMIs. We have explored this spin current as a function of both temperature and relative magnetization angle between the FMIs. The spin current has been decomposed into a reactive and a dissipative part, which change the effective gyromagnetic ratio and Gilbert damping coefficient of the FMI. We found that the backflow spin current is generally largest when the magnetization orientations of the FMIs are antiparallel. The ratio between the spin current in the parallel and antiparallel configuration strongly depends

on temperature in the SC. The origin is the Zeeman splitting of the quasiparticles at the gap edge. Lastly, we performed a numerical simulation to verify that the static gap assumption is a good approximation in our regime, also showing the usefulness of a numerical solution in this framework.

ACKNOWLEDGMENTS

This work was supported by the Research Council of Norway through its Centres of Excellence funding scheme, Project No. 262633 ‘‘QuSpin,’’ as well as by the European Research Council via Advanced Grant No. 669442 ‘‘Insulatronics.’’

APPENDIX A: ADDITIONAL PARAMETRIZED USADEL EQUATIONS

In the normal text, we provided four of the generalized Usadel equations, Eqs. (15)–(18), that were equations of motion for the normal components of the Green’s functions. The remaining four equations that are needed to solve a system with nonzero anomalous Green’s functions self-consistently are given as follows:

$$F_0^{R/A} = \frac{i(\Delta(m_{\text{eff}}\mathbf{m} \cdot \mathbf{G}^{R/A} - (E - iV)G_0^{R/A}) - \frac{im_{\text{eff}}^3}{2}\mathbf{m} \cdot (\frac{\partial \mathbf{m}}{\partial t} \times \frac{\partial \mathbf{F}^{R/A}}{\partial E}))}{m_{\text{eff}}^2 m^2 - (E - iV)^2}, \quad (\text{A1})$$

$$\begin{aligned} \mathbf{F}^{R/A} = & \frac{i\Delta \mathbf{G}^{R/A}}{(E - iV)} \\ & - \frac{i(m_{\text{eff}}\Delta(m_{\text{eff}}\mathbf{m} \cdot \mathbf{G}^{R/A} - (E - iV)G_0^{R/A})\mathbf{m} - \frac{im_{\text{eff}}^3}{2}[\mathbf{m} \cdot (\frac{\partial \mathbf{m}}{\partial t} \times \frac{\partial \mathbf{F}^{R/A}}{\partial E})]\mathbf{m} + \frac{im_{\text{eff}}}{2}[m_{\text{eff}}^2 m^2 - (E - iV)^2](\frac{\partial \mathbf{m}}{\partial t} \times \frac{\partial \mathbf{F}^{R/A}}{\partial E}))}{(E - iV)[m_{\text{eff}}^2 m^2 - (E - iV)^2]}, \end{aligned} \quad (\text{A2})$$

$$\begin{aligned} F_0^K = & \frac{i(\Delta(m_{\text{eff}}\mathbf{m} \cdot \mathbf{G}^K - EG_0^K) - \frac{im_{\text{eff}}^3}{2}\mathbf{m} \cdot (\frac{\partial \mathbf{m}}{\partial t} \times \frac{\partial \mathbf{F}^K}{\partial E}))}{m_{\text{eff}}^2 m^2 - E^2} - \frac{iV \tanh(\frac{\beta E}{2})[\mathbf{m} \cdot (\mathbf{F}^R + \mathbf{F}^A) - E(F_0^R + F_0^A)]}{(m_{\text{eff}}^2 m^2 - E^2)} \\ & - \frac{\beta V \text{sech}^2(\frac{\beta E}{2})[\mathbf{m} \cdot (\frac{\partial \mathbf{F}^R}{\partial t} - \frac{\partial \mathbf{F}^A}{\partial t}) - E(\frac{\partial F_0^R}{\partial t} - \frac{\partial F_0^A}{\partial t})]}{4(m_{\text{eff}}^2 m^2 - E^2)}, \end{aligned} \quad (\text{A3})$$

$$\begin{aligned} \mathbf{F}^K = & \frac{i\Delta \mathbf{G}^K}{E} - \frac{i(m_{\text{eff}}\Delta(m_{\text{eff}}\mathbf{m} \cdot \mathbf{G}^K - EG_0^K)\mathbf{m} - \frac{im_{\text{eff}}^3}{2}[\mathbf{m} \cdot (\frac{\partial \mathbf{m}}{\partial t} \times \frac{\partial \mathbf{F}^K}{\partial E})]\mathbf{m} + \frac{im_{\text{eff}}}{2}(m_{\text{eff}}^2 m^2 - E^2)(\frac{\partial \mathbf{m}}{\partial t} \times \frac{\partial \mathbf{F}^K}{\partial E}))}{E(m_{\text{eff}}^2 m^2 - E^2)} \\ & + \frac{iV \tanh(\frac{\beta E}{2})[\{\mathbf{m} \cdot (\mathbf{F}^R + \mathbf{F}^A) - E(F_0^R + F_0^A)\}\mathbf{m} - (m^2 - E^2)(\mathbf{F}^R + \mathbf{F}^A)]}{E(m_{\text{eff}}^2 m^2 - E^2)} \\ & + \frac{\beta V \text{sech}^2(\frac{\beta E}{2})[\{\mathbf{m} \cdot (\frac{\partial \mathbf{F}^R}{\partial t} - \frac{\partial \mathbf{F}^A}{\partial t}) - E(\frac{\partial F_0^R}{\partial t} - \frac{\partial F_0^A}{\partial t})\}\mathbf{m} - (m^2 - E^2)(\frac{\partial \mathbf{F}^R}{\partial t} - \frac{\partial \mathbf{F}^A}{\partial t})]}{4E(m_{\text{eff}}^2 m^2 - E^2)}, \end{aligned} \quad (\text{A4})$$

where the notation is defined in the main text.

APPENDIX B: SELF-CONSISTENT SOLUTION IN THE ABSENCE OF SPIN RELAXATION

We will derive here a self-consistent solution to the generalized Usadel equations, Eqs. (15)–(18), Eqs. (A1)–(A4), and the gap Eq. (19), in the absence of spin relaxation ($V = 0$). This solution has restricted physical relevance, and it only applies in the limit where the precession frequency is much larger than the relaxation rate. However, it is included as a proof of concept that a self-consistent solution is in principle possible.

The derivation follows the lines of what was presented in Sec. III A, with a few exceptions. In addition to the perturbation expansion in Eqs. (27), we also expand

$$\begin{aligned} F_0 &= F_0^{(0)} + F_0^{(1)} + F_0^{(2)} + (\dots), \\ \mathbf{F} &= \mathbf{F}^{(0)} + \mathbf{F}^{(1)} + \mathbf{F}^{(2)} + (\dots), \\ \Delta &= \Delta^{(0)} + \Delta^{(1)} + \Delta^{(2)} + (\dots). \end{aligned} \quad (\text{B1})$$

We have dropped the retarded/advanced and Keldysh superscript in order to keep the derivation as general as possible. This derivation hence applies to all Green's-function components. We also propose one additional *Ansatz*,

$$\Delta^{(1)} = \Delta_+^{(1)} e^{i\omega t} + \Delta_-^{(1)} e^{-i\omega t}. \quad (\text{B2})$$

If we insert this into the generalized Usadel equations to first order in δm , and with $V = 0$, we obtain the solutions

$$G_{0\pm}^{(1)} = m_{\text{eff}} \left(\frac{\partial \mathbf{G}^{(0)}}{\partial E} \right) \cdot \mathbf{m}_{\pm}^{(1)} - i \left(\frac{\partial F_0^{(0)}}{\partial E} \right) \Delta_{\pm}^{(1)}, \quad (\text{B3})$$

$$\mathbf{G}_{\pm}^{(1)} = m_{\text{eff}} \tilde{\mathbf{A}}_{\pm\omega}^{-1} \tilde{\mathbf{B}}_{\pm\omega} \mathbf{m}_{\pm}^{(1)} \pm \omega \Delta_{\pm}^{(1)} \tilde{\mathbf{A}}_{\pm\omega}^{-1} \frac{\partial \mathbf{F}^{(0)}}{\partial E}, \quad (\text{B4})$$

where

$$\tilde{\mathbf{A}}_{\pm\omega} = \begin{pmatrix} \pm i\omega & 2m_{\text{eff}} - m_z^{(0)} & 2m_{\text{eff}} m_y^{(0)} \\ 2m_{\text{eff}} m_z^{(0)} & \pm i\omega & -2m_{\text{eff}} m_x^{(0)} \\ -2m_{\text{eff}} m_y^{(0)} & 2m_{\text{eff}} m_x^{(0)} & \pm i\omega \end{pmatrix} \quad (\text{B5})$$

and

$$\tilde{\mathbf{B}}_{\pm\omega} = \begin{pmatrix} \pm i\omega \frac{\partial G_0^{(0)}}{\partial E} & -2G_z^{(0)} & 2G_y^{(0)} \\ 2G_z^{(0)} & \pm i\omega \frac{\partial G_0^{(0)}}{\partial E} & -2G_x^{(0)} \\ -2G_y^{(0)} & 2G_x^{(0)} & \pm i\omega \frac{\partial G_0^{(0)}}{\partial E} \end{pmatrix}. \quad (\text{B6})$$

To solve for $\Delta^{(1)}(t)$, we look closer at the gap equation given in Eq. (19). If we insert the generalized Usadel equation for F_0^K [Eq. (A3)] into the gap equation while using $V = 0$, divide both sides by Δ , and assume that $|m_{\text{eff}} \mathbf{m}^{(1)}| \ll \delta$, the first- and second-order gap equations read

$$1 = \frac{N_0 \lambda}{4} \int_{-\omega_D}^{\omega_D} dE \frac{(m_{\text{eff}} \mathbf{m}^{(0)} \cdot \mathbf{G}^{K(0)} - E G_0^{K(0)})}{m_{\text{eff}}^2 (\mathbf{m}^{(0)})^2 - E^2}, \quad (\text{B7})$$

$$0 = \int_{-\omega_D}^{\omega_D} dE \frac{1}{m_{\text{eff}}^2 (\mathbf{m}^{(0)})^2 - E^2} \left\{ m_{\text{eff}} (\mathbf{m}^{(1)} \cdot \mathbf{G}^{K(0)} + \mathbf{m}^{(0)} \cdot \mathbf{G}^{K(1)}) - E G_0^{K(1)} - 2m_{\text{eff}}^2 (\mathbf{m}^{(0)} \cdot \mathbf{m}^{(1)}) \frac{(m_{\text{eff}} \mathbf{m}^{(0)} \cdot \mathbf{G}^{K(0)} - E G_0^{K(0)})}{m_{\text{eff}}^2 (\mathbf{m}^{(0)})^2 - E^2} \right\}. \quad (\text{B8})$$

Here, we used $\mathbf{m}^{(0)} \cdot (\frac{\partial \mathbf{m}^{(1)}}{\partial t} \times \frac{\partial \mathbf{F}^{K(0)}}{\partial E}) = 0$, since $\mathbf{F}^{K(0)} \parallel \mathbf{m}^{(0)}$. We have moreover used $E \rightarrow E + i\delta$ and $m_{\text{eff}} |\mathbf{m}^{(0)} \cdot \mathbf{m}^{(1)}| \ll |\mathbf{m}^{(0)}| \delta$, ensuring that the expansion is also valid when $\text{Re}[E] \rightarrow m_{\text{eff}} |\mathbf{m}^{(0)}|$. Eq. (B7) is simply the zeroth-order gap equation, while Eq. (B8) must be used to find self-consistent solution to the first-order Green's-function components. All that remains now is to insert the *Ansätze* Eqs. (30) and (B2) into Eq. (B8). The resulting solution for the first-order components $\Delta_{\pm}^{(1)}$ reads

$$\Delta_{\pm}^{(1)} = \frac{1}{T_{\pm}} \int_{-\omega_D}^{\omega_D} dE \frac{m_{\text{eff}}}{m_{\text{eff}}^2 (\mathbf{m}^{(0)})^2 - E^2} \left\{ (\mathbf{m}_{\pm}^{(1)} \cdot \mathbf{G}^{K(0)}) + m_{\text{eff}} ([\tilde{\mathbf{A}}_{\pm\omega}^{-1} \tilde{\mathbf{B}}_{\pm\omega} \mathbf{m}_{\pm}^{(1)}] \cdot \mathbf{m}^{(0)}) - E \left(\mathbf{m}_{\pm}^{(1)} \cdot \frac{\partial \mathbf{G}^{K(0)}}{\partial E} \right) \right. \\ \left. - 2m_{\text{eff}} (\mathbf{m}_{\pm}^{(1)} \cdot \mathbf{m}^{(0)}) \frac{(m_{\text{eff}} \mathbf{m}^{(0)} \cdot \mathbf{G}^{K(0)} - E G_0^{K(0)})}{m_{\text{eff}}^2 (\mathbf{m}^{(0)})^2 - E^2} \right\}, \quad (\text{B9})$$

where T_{\pm} is defined by

$$T_{\pm} = - \int_{-\omega_D}^{\omega_D} dE \frac{\pm \omega m_{\text{eff}} [\tilde{\mathbf{A}}_{\pm\omega}^{-1} \frac{\partial \mathbf{F}^{K(0)}}{\partial E}] \cdot \mathbf{m}^{(0)} + iE \frac{\partial F_0^{K(0)}}{\partial E}}{m_{\text{eff}}^2 (\mathbf{m}^{(0)})^2 - E^2}. \quad (\text{B10})$$

-
- [1] V. L. Ginzburg, Ferromagnetic superconductors, Zh. Eksp. Teor. Fiz. **31**, 202 (1956) [Sov. Phys. JETP **4**, 153 (1957)].
- [2] F. S. Bergeret, K. B. Efetov, and A. I. Larkin, Nonhomogeneous magnetic order in superconductor-ferromagnet multilayers, Phys. Rev. B **62**, 11872 (2000).
- [3] F. S. Bergeret, A. F. Volkov, and K. B. Efetov, Odd triplet superconductivity and related phenomena in superconductor-ferromagnet structures, Rev. Mod. Phys. **77**, 1321 (2005).
- [4] J. Linder and J. W. A. Robinson, Superconducting spintronics, Nat. Phys. **11**, 307 (2015).
- [5] F. S. Bergeret, A. F. Volkov, and K. B. Efetov, Long-Range Proximity Effects in Superconductor-Ferromagnet Structures, Phys. Rev. Lett. **86**, 4096 (2001).
- [6] L. P. Gor'kov and E. I. Rashba, Superconducting 2D System with Lifted Spin Degeneracy: Mixed Singlet-Triplet State, Phys. Rev. Lett. **87**, 037004 (2001).

- [7] F. S. Bergeret and I. V. Tokatly, Spin-orbit coupling as a source of long-range triplet proximity effect in superconductor-ferromagnet hybrid structures, *Phys. Rev. B* **89**, 134517 (2014).
- [8] K.-R. Jeon, C. Ciccarelli, A. J. Ferguson, H. Kurebayashi, L. F. Cohen, X. Montiel, M. Eschrig, J. W. A. Robinson, and M. G. Blamire, Enhanced spin pumping into superconductors provides evidence for superconducting pure spin currents, *Nat. Mater.* **17**, 499 (2018).
- [9] K.-R. Jeon, C. Ciccarelli, H. Kurebayashi, L. F. Cohen, X. Montiel, M. Eschrig, S. Komori, J. W. A. Robinson, and M. G. Blamire, Exchange-field enhancement of superconducting spin pumping, *Phys. Rev. B* **99**, 024507 (2019).
- [10] M. Eschrig, Spin-polarized supercurrents for spintronics, *Phys. Today* **64**(1), 43 (2011).
- [11] A. Brataas, Y. Tserkovnyak, G. E. W. Bauer, and B. I. Halperin, Spin battery operated by ferromagnetic resonance, *Phys. Rev. B* **66**, 060404(R) (2002).
- [12] Y. Tserkovnyak, A. Brataas, and G. E. W. Bauer, Enhanced Gilbert Damping in Thin Ferromagnetic Films, *Phys. Rev. Lett.* **88**, 117601 (2002).
- [13] Y. Tserkovnyak, A. Brataas, and G. E. W. Bauer, Spin pumping and magnetization dynamics in metallic multilayers, *Phys. Rev. B* **66**, 224403 (2002).
- [14] T. L. Gilbert, Classics in magnetism a phenomenological theory of damping in ferromagnetic materials, *IEEE Trans. Magn.* **40**, 3443 (2004).
- [15] Y. Tserkovnyak, A. Brataas, G. E. W. Bauer, and B. I. Halperin, Nonlocal magnetization dynamics in ferromagnetic heterostructures, *Rev. Mod. Phys.* **77**, 1375 (2005).
- [16] C. Bell, S. Milikisyants, M. Huber, and J. Aarts, Spin Dynamics in a Superconductor-Ferromagnet Proximity System, *Phys. Rev. Lett.* **100**, 047002 (2008).
- [17] J. P. Morten, A. Brataas, G. E. W. Bauer, W. Belzig, and Y. Tserkovnyak, Proximity-effect-assisted decay of spin currents in superconductors, *Europhys. Lett.* **84**, 57008 (2008).
- [18] *Dissipative* here refers to its effect on the ferromagnet. In this sense, a dissipative spin current can still be carried through a SC without dissipation by spin-polarized triplet pairs.
- [19] M. Inoue, M. Ichioka, and H. Adachi, Spin pumping into superconductors: A new probe of spin dynamics in a superconducting thin film, *Phys. Rev. B* **96**, 024414 (2017).
- [20] K.-R. Jeon, C. Ciccarelli, H. Kurebayashi, J. Wunderlich, L. F. Cohen, S. Komori, J. W. A. Robinson, and M. G. Blamire, Spin-Pumping-Induced Inverse Spin Hall Effect in Nb/Ni₈₀Fe₂₀ Bilayers and Its Strong Decay Across the Superconducting transition temperature, *Phys. Rev. Appl.* **10**, 014029 (2018).
- [21] Y. Yao, Q. Song, Y. Takamura, J. P. Cascales, W. Yuan, Y. Ma, Y. Yun, X. C. Xie, J. S. Moodera, and W. Han, Probe of spin dynamics in superconducting NbN thin films via spin pumping, *Phys. Rev. B* **97**, 224414 (2018).
- [22] T. Taira, M. Ichioka, S. Takei, and H. Adachi, Spin diffusion equation in superconductors in the vicinity of T_c , *Phys. Rev. B* **98**, 214437 (2018).
- [23] X. Montiel and M. Eschrig, Generation of pure superconducting spin current in magnetic heterostructures via nonlocally induced magnetism due to Landau Fermi liquid effects, *Phys. Rev. B* **98**, 104513 (2018).
- [24] I. V. Bobkova, A. M. Bobkov, and M. A. Silaev, Spin torques and magnetic texture dynamics driven by the supercurrent in superconductor/ferromagnet structures, *Phys. Rev. B* **98**, 014521 (2018).
- [25] T. Kato, Y. Ohnuma, M. Matsuo, J. Rech, T. Jonckheere, and T. Martin, Microscopic theory of spin transport at the interface between a superconductor and a ferromagnetic insulator, *Phys. Rev. B* **99**, 144411 (2019).
- [26] I. A. Golovchanskiy, N. N. Abramov, M. Pfirrmann, T. Piskor, J. N. Voss, D. S. Baranov, R. A. Hovhannisyann, V. S. Stolyarov, C. Dubs, A. A. Golubov, V. V. Ryazanov, A. V. Ustinov, and M. Weides, Interplay of Magnetization Dynamics with a Microwave Waveguide at Cryogenic Temperatures, *Phys. Rev. Appl.* **11**, 044076 (2019).
- [27] I. A. Golovchanskiy, N. N. Abramov, V. S. Stolyarov, V. I. Chichkov, M. Silaev, I. V. Shchetinin, A. A. Golubov, V. V. Ryazanov, A. V. Ustinov, and M. Y. Kupriyanov, Magnetization Dynamics in Proximity-Coupled Superconductor-Ferromagnet-Superconductor Multilayers, *Phys. Rev. Appl.* **14**, 024086 (2020).
- [28] X. Waintal and P. W. Brouwer, Magnetic exchange interaction induced by a Josephson current, *Phys. Rev. B* **65**, 054407 (2002).
- [29] M. Houzet, Ferromagnetic Josephson Junction with Precessing Magnetization, *Phys. Rev. Lett.* **101**, 057009 (2008).
- [30] E. Zhao and J. A. Sauls, Theory of nonequilibrium spin transport and spin-transfer torque in superconducting-ferromagnetic nanostructures, *Phys. Rev. B* **78**, 174511 (2008).
- [31] F. Konschelle and A. Buzdin, Magnetic Moment Manipulation by a Josephson Current, *Phys. Rev. Lett.* **102**, 017001 (2009).
- [32] T. Yokoyama and Y. Tserkovnyak, Tuning odd triplet superconductivity by spin pumping, *Phys. Rev. B* **80**, 104416 (2009).
- [33] S. Teber, C. Holmqvist, and M. Fogelström, Transport and magnetization dynamics in a superconductor/single-molecule magnet/superconductor junction, *Phys. Rev. B* **81**, 174503 (2010).
- [34] J. Linder and T. Yokoyama, Supercurrent-induced magnetization dynamics in a Josephson junction with two misaligned ferromagnetic layers, *Phys. Rev. B* **83**, 012501 (2011).
- [35] I. Kulagina and J. Linder, Spin supercurrent, magnetization dynamics, and ϕ -state in spin-textured Josephson junctions, *Phys. Rev. B* **90**, 054504 (2014).
- [36] K. D. Usadel, Generalized Diffusion Equation for Superconducting Alloys, *Phys. Rev. Lett.* **25**, 507 (1970).
- [37] J. J. Hauser, Coupling between Ferrimagnetic Insulators through a Superconducting Layer, *Phys. Rev. Lett.* **23**, 374 (1969).
- [38] G. Deutscher and F. Meunier, Coupling between ferromagnets through a superconducting layer: Experiments, *IEEE Trans. Magn.* **5**, 434 (1969).
- [39] G. Deutscher and F. Meunier, Coupling between Ferromagnetic Layers through a Superconductor, *Phys. Rev. Lett.* **22**, 395 (1969).
- [40] J. J. Hauser, Coupling between ferrimagnetic insulators through a superconducting layer, *Physica* **55**, 733 (1971).
- [41] P. G. De Gennes, Coupling between ferromagnets through a superconducting layer, *Phys. Lett.* **23**, 10 (1966).
- [42] A. Cottet, D. Huertas-Hernando, W. Belzig, and Y. V. Nazarov, Spin-dependent boundary conditions for isotropic superconducting Green's functions, *Phys. Rev. B* **80**, 184511 (2009).
- [43] M. Eschrig, A. Cottet, W. Belzig, and J. Linder, General boundary conditions for quasiclassical theory of superconductivity

- in the diffusive limit: Application to strongly spin-polarized systems, *New J. Phys.* **17**, 083037 (2015).
- [44] K. S. Tikhonov and M. V. Feigel'man, AC Josephson effect in the long voltage-biased SINIS junction, *JETP Lett.* **89**, 205 (2009).
- [45] J. Rammer and H. Smith, Quantum field-theoretical methods in transport theory of metals, *Rev. Mod. Phys.* **58**, 323 (1986).
- [46] A. Brinkman, A. A. Golubov, H. Rogalla, F. K. Wilhelm, and M. Y. Kupriyanov, Microscopic nonequilibrium theory of double-barrier Josephson junctions, *Phys. Rev. B* **68**, 224513 (2003).
- [47] D. A. Ivanov and Y. V. Fominov, Minigap in superconductor-ferromagnet junctions with inhomogeneous magnetization, *Phys. Rev. B* **73**, 214524 (2006).
- [48] H. J. Jiao and G. E. W. Bauer, Spin Backflow and ac Voltage Generation by Spin Pumping and the Inverse Spin Hall Effect, *Phys. Rev. Lett.* **110**, 217602 (2013).
- [49] M. Johnson, Spin coupled resistance observed in ferromagnet-superconductor-ferromagnet trilayers, *Appl. Phys. Lett.* **65**, 1460 (1994).
- [50] G. Seidel and P. H. Keesom, Specific heat of gallium and zinc in the normal and superconducting states, *Phys. Rev.* **112**, 1083 (1958).
- [51] Z. Zheng, D. Y. Xing, G. Sun, and J. Dong, Andreev reflection effect on spin-polarized transport in ferromagnet/superconductor/ferromagnet double tunnel junctions, *Phys. Rev. B* **62**, 14326 (2000).

IV


REFERENCE

Lina G. Johnsen¹, Sol H. Jacobsen¹, and Jacob Linder,
Magnetic control of superconducting heterostructures using compensated antiferromagnets,
Phys. Rev. B **103**, L060505 (2021).

CONTRIBUTIONS

SHJ performed the analytical calculations and contributed to the numerical calculations. LGJ contributed to the analytical calculations, performed the numerical calculations and wrote the paper. All authors contributed to discussions and revision of the manuscript. JL initiated and supervised the project.

¹ Authors contributed equally.

Magnetic control of superconducting heterostructures using compensated antiferromagnetsLina G. Johnsen^{*,†}, Sol H. Jacobsen[†], and Jacob Linder*Center for Quantum Spintronics, Department of Physics, Norwegian University of Science and Technology (NTNU), NO-7491 Trondheim, Norway* (Received 2 October 2020; revised 17 December 2020; accepted 11 February 2021; published 23 February 2021)

Due to the lack of a net magnetization both at the interface and in the bulk, antiferromagnets with compensated interfaces may appear incapable of influencing the phase transition in an adjacent superconductor via the spin degree of freedom. We here demonstrate that such an assertion is incorrect by showing that proximity coupling a compensated antiferromagnetic layer to a superconductor-ferromagnet heterostructure introduces the possibility of controlling the superconducting phase transition. The superconducting critical temperature can in fact be modulated by rotating the magnetization of the single ferromagnetic layer within the plane of the interface, although the system is invariant under rotations of the magnetization in the absence of the antiferromagnetic layer. Moreover, we predict that the superconducting phase transition can trigger a reorientation of the ground state magnetization. Our results show that a compensated antiferromagnetic interface is in fact able to distinguish between different spin-polarizations of triplet Cooper pairs.

DOI: 10.1103/PhysRevB.103.L060505

Introduction. Proximity effects in heterostructures consisting of ferromagnets (F) and conventional superconductors (S) have been widely studied, in part due to the possibility of creating spin-polarized Cooper pairs [1–4]. When the spin-singlet Cooper pairs of a conventional superconductor enters a ferromagnetic material, the spin-splitting of the energy bands of the ferromagnet gives rise to opposite-spin triplets as spin-up and spin-down electrons acquire different phases upon propagation. Further, the opposite-spin triplets can be rotated into equal-spin triplets with respect to a ferromagnet with a differently oriented magnetization [5,6]. Such triplets can also exist in structures with a single inhomogeneous ferromagnet [7–10]. Equal-spin triplets relative the magnetization direction are more robust to pair-breaking effects from the ferromagnetic exchange field. The generation of equal-spin triplets therefore causes an increased leakage of Cooper pairs from the superconducting region and a weakening of the superconducting condensate. By controlling the singlet to triplet conversion, we can thus manipulate the superconducting condensation energy and the critical temperature [11–15].

The singlet to triplet generation can be controlled by adjusting the misalignment between two ferromagnets proximity-coupled to a superconductor [5,6]. However, when combining these into F/S/F structures, the dominant effect on the superconducting condensation energy and the critical temperature T_c is not the opening of the equal-spin triplet channels. Instead, the mutual compensation of the ferromagnetic exchange fields favor antiparallel alignment of the ferromagnets in order to minimize the field inside the superconductor [16–19]. By arranging the materials in a S/F/F

structure this effect becomes less prominent [20–25]; however, this necessitates the ability to tune the orientations of the ferromagnets independently. It is therefore desirable to reduce the number of magnetic elements required to tune T_c in order to minimize the stray field of the heterostructure. Stray fields would be a disturbance to neighboring elements if the heterostructure was part of a larger device architecture.

Previous studies have suggested introducing heavy-metal layers boosting the interfacial Rashba spin-orbit coupling in a S/F bilayer [26–32]. The Rashba spin-orbit field introduces additional symmetry breaking [33] that allows for control over the spin-triplet channels when rotating the magnetization of the single ferromagnetic layer. However, for a structure with purely Rashba spin-orbit coupling, a variation in the triplet generation for in-plane rotations of the magnetization is only possible in ballistic-limit systems [30], while additional Dresselhaus spin-orbit coupling is needed for such an in-plane effect in the diffusive limit [26]. In this work, we consider another possibility for controlling the spin-triplet channels, namely replacing one of the ferromagnetic layers in the F/S/F structure with an antiferromagnet with a compensated interface.

Antiferromagnets (AF) provide a magnetic structure with zero net magnetization [34]. When proximity-coupling antiferromagnets to other materials, antiferromagnets therefore have the advantage of not emitting an external field to its surroundings. We therefore avoid vortex formation and demagnetizing currents in adjacent superconductors, and the magnetization of an adjacent ferromagnet can be easily controlled. Also, the magnetic moments of the antiferromagnet are insensitive to disturbing magnetic fields [35]. Studies of quasiparticle reflection [36,37], Josephson effects [38–44], the superconducting critical temperature [45–48], and the critical field [48] in uncompensated superconductor-antiferromagnet structures have proved antiferromagnets to be applicable for

*Corresponding author: lina.g.johnsen@ntnu.no

†These authors contributed equally to this work.

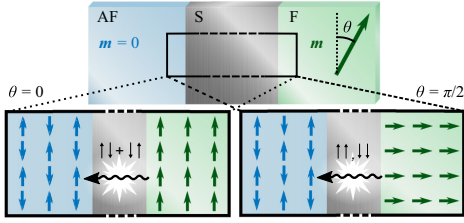


FIG. 1. Although the total magnetization \mathbf{m} of the antiferromagnet is zero (top), the interaction between the local magnetic moments of the antiferromagnet and ferromagnet affects the generation of spin-triplet Cooper pairs. When the magnetic moments are aligned (left), only opposite-spin triplets are present. When they are misaligned, the opposite-spin triplets created at the ferromagnetic interface are partially, or entirely in the perpendicular case (right), rotated into equal-spin triplets relative to the magnetic moments in the antiferromagnet. These triplets scatter differently at the antiferromagnetic interface compared to the triplets that exist in the parallel case, resulting in a weakened singlet condensate. Since the triplet generation only depends on the misalignment between the magnetic moments, we can choose to control the triplet channels by rotating the magnetization within the plane of the interface.

manipulating the superconducting state, despite their zero net magnetization. It has also been shown that uncompensated antiferromagnetic insulators can induce spin-splitting in an adjacent superconductor [49]. Antiferromagnet-ferromagnet structures have shown interesting properties for spintronics applications, e.g., magnetization switching mediated by spin-orbit torques [50,51].

The above-mentioned works have mostly focused on uncompensated antiferromagnetic interfaces where there is an effective magnetization at the interface. Compensated antiferromagnetic interfaces have been claimed to be spin inactive in several recent works, and only a few have reported a nonzero effect on an adjacent superconducting condensate [36,37]. We here consider a heterostructure consisting of a homogeneous ferromagnet, a conventional superconductor, and a compensated antiferromagnetic insulator. We demonstrate that, despite the zero net magnetization in the antiferromagnet, the misalignment between the magnetic moments of the antiferromagnet and ferromagnet allows for control over the spin-triplet amplitude, as illustrated in Fig. 1. This makes it possible to manipulate the superconducting phase transition by rotation of the ferromagnetic magnetization. Moreover, we predict that the suppression of the superconducting gap for misaligned magnetic moments leads to a modulation of the effective ferromagnetic anisotropy, potentially causing a magnetization reorientation driven by the superconducting phase transition. To the best of our knowledge, this Letter presents the first prediction of a compensated antiferromagnetic interface being able to distinguish between different spin-polarizations of triplet Cooper pairs. The T_c variation and magnetization reorientation predicted in our work is a direct manifestation of this new physical effect.

Theoretical framework. We describe the AF/S/F heterostructure by the tight-binding Bogoliubov–de Gennes

Hamiltonian

$$H = -t \sum_{\langle i,j \rangle, \sigma} c_{i,\sigma}^\dagger c_{j,\sigma} - \sum_{i,\sigma} \mu_i c_{i,\sigma}^\dagger c_{i,\sigma} + \sum_{i \in \text{AF}} V_i n_{i,\uparrow} n_{i,\downarrow} - \sum_{i \in \text{S}} U_i n_{i,\uparrow} n_{i,\downarrow} + \sum_{i \in \text{F}, \sigma, \sigma'} c_{i,\sigma}^\dagger (\mathbf{h}_i \cdot \boldsymbol{\sigma})_{\sigma, \sigma'} c_{i,\sigma'}. \quad (1)$$

The first two terms are present throughout the whole structure as they include nearest-neighbor hopping and the chemical potential. Above, t is the hopping integral, μ_i is the chemical potential at lattice site i , and $c_{i,\sigma}^\dagger$ and $c_{i,\sigma}$ are the electron creation and annihilation operators at lattice site i for electrons with spin σ . The remaining three terms are only nonzero in their respective regions. In these terms, $V_i > 0$ is the on-site Coulomb repulsion giving rise to antiferromagnetism, $U_i > 0$ is the attractive on-site interaction giving rise to superconductivity, \mathbf{h}_i is the local magnetic exchange field giving rise to ferromagnetism, $n_{i,\sigma} \equiv c_{i,\sigma}^\dagger c_{i,\sigma}$ is the number operator, and $\boldsymbol{\sigma}$ is the vector of Pauli matrices. We choose the chemical potential in the antiferromagnetic region to be approximately zero so that the antiferromagnet behaves as an insulator. Throughout this work, all energies are scaled by the hopping integral t , and all length scales are scaled by the lattice constant. For simplicity, we set the Boltzmann and reduced Planck constants to 1.

Our theoretical framework is well suited for describing heterostructures consisting of atomically thin layers in the ballistic limit, and it fully accounts for the crystal structure of the system. In our theoretical framework, the particular lattice geometry chosen (square) is not important to understand the triplet generation in the AF/S/F hybrid. Adding disorder and interfacial barriers would influence the magnitude of the predicted T_c change, but not its existence. For simplicity, we therefore consider a two-dimensional (2D) square lattice of size $N_x \times N_y$ with interface normal along the x axis. We assume that the ferromagnetic exchange field is oriented within the plane of the interface and that it is constant throughout the ferromagnetic layer. We describe the ferromagnetic exchange field as $\mathbf{h} = h[0, \sin(\theta), \cos(\theta)]$ in terms of the polar angle θ with respect to the z axis.

The antiferromagnetic contribution is treated by a mean-field approach that preserves the spin-rotational invariance of the antiferromagnetic order parameter $\mathbf{M}_i \equiv 4V_i \langle \mathbf{S}_i \rangle / 3$ [52]. We write the antiferromagnetic term in the Hamiltonian in terms of the spin operator $\mathbf{S}_i \equiv \frac{1}{2} \sum_{\sigma, \sigma'} c_{i,\sigma}^\dagger \boldsymbol{\sigma}_{\sigma, \sigma'} c_{i,\sigma'}$ and assume that the spin operator only weakly fluctuates around its expectation value so that $\mathbf{S}_i = \langle \mathbf{S}_i \rangle + \delta_{\text{AF}}$. We neglect second-order terms in the spin fluctuations δ_{AF} . The superconducting contribution is also treated by a mean-field approach where we similarly write $c_{i,\uparrow} c_{i,\downarrow} = \langle c_{i,\uparrow} c_{i,\downarrow} \rangle + \delta_{\text{S}}$ and neglect second-order terms in the fluctuations δ_{S} . The superconducting gap $\Delta_i \equiv U_i \langle c_{i,\uparrow} c_{i,\downarrow} \rangle$ is treated self-consistently. We assume that the order parameter of the antiferromagnet is large compared to the superconducting gap, so that it is robust under reorientations of the magnetization of the ferromagnet. Under these assumptions it is not necessary to treat the antiferromagnetic order parameter self-consistently, and we assume it to have a constant absolute value M and opposite signs on neighboring lattice sites. By solving both \mathbf{M}_i and Δ_i self-consistently,

we have verified that \mathbf{M}_i remains unchanged as \mathbf{h} is rotated, although Δ_i changes significantly.

We diagonalize the Hamiltonian numerically by assuming periodic boundary conditions in the y direction as outlined in the Supplemental Material [53], and calculate the spin-triplet amplitudes, the superconducting critical temperature T_c , and the free energy of the system. The s -wave odd-frequency opposite- and equal-spin triplet amplitudes are defined as $S_{0,i}(\tau) \equiv \sum_{\sigma} \langle c_{i,\sigma}(\tau) c_{i,-\sigma}(0) \rangle$, and $S_{\sigma,i}(\tau) \equiv \langle c_{i,\sigma}(\tau) c_{i,\sigma}(0) \rangle$, where τ is the relative time coordinate, and $c_{i,\sigma}(\tau) \equiv e^{iH\tau} c_{i,\sigma} e^{-iH\tau}$. The p -wave opposite- and equal-spin triplet amplitudes are defined as $P_{0,i}^n \equiv \sum_{\sigma} (\langle c_{i,\sigma} c_{i+n,-\sigma} \rangle - \langle c_{i,\sigma} c_{i-n,-\sigma} \rangle)$, and $P_{\sigma,i}^n \equiv \langle c_{i,\sigma} c_{i+n,\sigma} \rangle - \langle c_{i,\sigma} c_{i-n,\sigma} \rangle$, where $n \in \{x, y\}$. These are projected along the z axis, but can be rotated to any projection axis. The superconducting critical temperature T_c is calculated by a binomial search where for each temperature we decide whether the gap has increased toward a superconducting state or decreased toward a normal state after a set number of iterative recalculations starting at an initial guess much smaller than the zero-temperature superconducting gap. The free energy is given by $F = -T \ln[\text{Tr}(e^{-H/T})]$ and is calculated using the eigenenergies of the system for a given temperature.

The superconducting critical temperature. We first consider how the superconducting critical temperature of an AF/S/F hybrid structure with a compensated antiferromagnetic interface varies for in-plane rotations of the ferromagnetic magnetization. As shown in Fig. 2, we find that T_c decreases as the magnetization of the ferromagnet and the magnetic moments of the antiferromagnet are increasingly misaligned. Compared to a system where the antiferromagnetic layer is replaced by a ferromagnetic layer of the same thickness and with a magnetic exchange field of magnitude $h = M$, we find that the change in T_c in the AF/S/F structure is only about seven times smaller. For F/S/F hybrids, experiments have demonstrated a difference in T_c between parallel and antiparallel states of several hundreds of millikelvin [19]. This means that the difference in T_c between aligned and perpendicular magnetic moments for an AF/S/F structure with a compensated interface should be measurable.

To understand why an antiferromagnet with a compensated interface, where the net magnetization is zero both in the bulk and at the interface, can be used to control the superconducting condensate, we first consider the more thoroughly studied F/S/F structure. In the F/S/F structure, we have two competing effects that determine T_c . The dominant effect is the partial mutual compensation of the ferromagnetic exchange fields when the ferromagnets have antiparallel components [23]. For parallel alignment, the total magnetic field of the ferromagnets is stronger and superconductivity is more suppressed. This causes the variation in T_c for the F/S/F structure seen in Fig. 2. The second weaker contribution to the T_c variation is caused by spin-triplet generation that depends on the misalignment between the magnetic exchange fields of the two ferromagnets [23]. When the magnetizations of the two ferromagnets are misaligned, opposite-spin s - and p_x -wave triplets generated at one ferromagnetic interface are partly seen as equal-spin triplets with respect to the magnetization of the other ferromagnet. These have a much longer decay length inside the ferromagnet (up to hundreds of nm) compared to

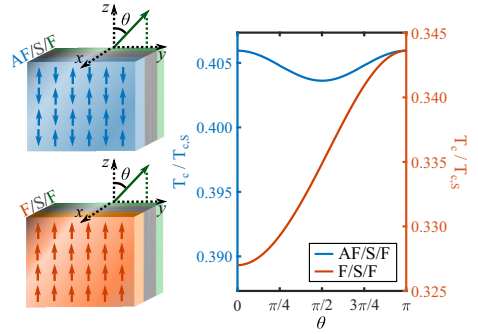


FIG. 2. In the AF/S/F structure, we find a suppression of T_c at $\theta = \pi/2$, when the magnetization of the ferromagnet is perpendicular to the magnetic moments of the antiferromagnet (blue curve). This variation in T_c is only about seven times smaller than the difference in T_c between antiparallel and parallel alignment of the magnetizations of the ferromagnets in a F/S/F structure (orange curve). In the plot, we have compared T_c to the superconducting critical temperature without proximity to the magnetic layers, $T_{c,S}$. The parameters chosen for the AF/S/F system are $N_x^{\text{AF}} = 4$, $N_x^{\text{S}} = 9$, $N_x^{\text{F}} = 3$, $N_y = 90$, $t = 1$, $\mu^{\text{AF}} = 0.0001$, $\mu^{\text{S}} = \mu^{\text{F}} = 0.9$, $M = 0.4$, $U = 2$, and $h = 1$. The coherence length is comparable to the thickness of the superconducting layer. Qualitatively similar behavior in T_c is found also for other choices of parameters. For the F/S/F structure, we replace the antiferromagnet with a ferromagnet with the same chemical potential as the rest of the structure and with magnetic exchange field of magnitude $h = M = 0.4$ along the z axis.

opposite-spin triplets which decay over a short length scale (of order nm). This opening of the equal-spin triplet channels causes a stronger suppression of T_c when the ferromagnets are perpendicular.

In our compensated AF/S/F system, the magnetic field from the antiferromagnet is zero, and the total magnetic field suppressing superconductivity is thus invariant under inversion of the magnetization of the ferromagnet. The dominant effect on T_c in F/S/F structures is therefore absent in the compensated AF/S/F structure. The triplet generation in F/S/F structures only depends on how much the magnetic moments of the two ferromagnets are misaligned, and not on whether they are parallel or antiparallel. However, when inverting the magnetization of one of the ferromagnets, the equal-spin triplet amplitudes with respect to the other ferromagnet changes sign. This means that the amplitude of long-range triplets in the ferromagnet is zero when we average over all up and down spins in the antiferromagnet. On the other hand, when the ferromagnetic magnetization is misaligned with the magnetic moments of the antiferromagnet, there is a finite equal-spin triplet amplitude with respect to the axis along which the magnetic moments of the antiferromagnet are aligned. We find these to be more robust to pair-breaking effects caused by the local magnetic exchange fields associated with the magnetic moments in the antiferromagnet. In contrast, spin-singlet and opposite-spin triplet Cooper pairs are more easily destroyed at the interface of the antiferromagnetic

insulator. This is most likely caused by spin-up and spin-down electrons acquiring a π phase difference upon reflection [36]. At perpendicular alignment between the magnetic moments of the antiferromagnet and ferromagnet, the amplitude of the equal-spin triplets is at its maximum. In this case, more triplets are generated, causing a weakening of the superconducting condensate as more singlets are converted. This causes the T_c variation in the compensated AF/S/F structure seen in Fig. 2. Plots showing the triplet amplitudes and superconducting gap are presented in the Supplemental Material [53].

Since the changes in T_c only depend on the misalignment between the magnetic moments of the ferromagnet and antiferromagnet, not on their orientation with respect to the interface, we can choose to rotate the magnetization within the plane of the interface. This way, no components of the magnetization are perpendicular to the superconducting layer, and we thus avoid the appearance of demagnetizing currents close to the interface, as well as vortex formation. An in-plane magnetization is favored as long as the shape anisotropy of the ferromagnet is sufficiently strong. The T_c variation in the present AF/S/F structure is partially caused by a variation in the s -wave triplet amplitude. We therefore expect the predicted T_c modulation to be robust to impurity scattering and observable in diffusive systems as well as the ballistic limit systems covered by our theoretical framework.

Magnetization reorientation. Until now, we have explained how we can control the triplet channels in a compensated AF/S/F structure in order to manipulate the superconducting critical temperature. We now investigate another consequence of the weakening of the superconducting condensate, namely an increase in the free energy. Since the superconducting condensate is at its weakest for perpendicular alignment of the magnetic moments of the ferromagnet and antiferromagnet, we expect the superconducting contribution to the free energy to be at its maximum. If a perpendicular orientation is preferred for temperatures above T_c , we can achieve a rotation of the ground state magnetization direction by decreasing the temperature below T_c , as shown in Fig. 3. Assuming that the shape anisotropy of the ferromagnet enforces in-plane magnetization, it is thus possible to have $\pi/2$ magnetization reorientation within the plane of the interface driven by the superconducting phase transition. Similar predictions for S/F structures with interfacial spin-orbit coupling [30] have been supported by experiments [32].

The normal-state free energy shown in Fig. 3 only gives an example of a possible normal-state free energy curve for the compensated AF/S/F system. For experimentally realizing the magnetization reorientation, one must ensure that the magnetization in the normal-state is not aligned with the magnetic moments of the antiferromagnet. Using our Bogoliubov–de Gennes theoretical framework, the normal-state free energy depends strongly on the choice of parameters. The exaggerated variation in the normal-state free energy under rotations of the magnetization is a thermal effect caused by an overestimated critical temperature, for the following reason. When considering a Bogoliubov–de Gennes Hamiltonian for a lattice structure, the lattice needs to be scaled down for the system to be computationally manageable. Since the superconducting coherence length is inversely proportional to the zero-temperature superconducting gap, we need the super-

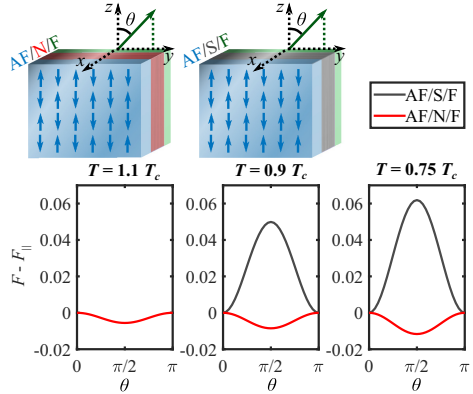


FIG. 3. When decreasing the temperature below T_c , a peak develops in the free energy F for a magnetization perpendicular to the magnetic moments of the antiferromagnet (grey curve). This causes a shift in the free energy minimum compared to the normal state (red curve) allowing for a $\pi/2$ in-plane rotation of the magnetization. The free energy is plotted relative to the free energy F_{\parallel} for parallel alignment for easier comparison between the normal-state and superconducting free energy. The parameters used are $N_x^{\text{AF}} = 4$, $N_x^{\text{S}} = 12$, $N_x^{\text{F}} = 3$, $N_y = 60$, $t = 1$, $\mu^{\text{AF}} = 0.0001$, $\mu^{\text{S}} = \mu^{\text{F}} = 0.9$, $M = 0.5$, $U = 1.7$, and $h = 0.7$. This corresponds to a coherence length comparable to the thickness of the superconducting region.

conducting gap and thus T_c to be large in order to have a coherence length comparable to the thickness of the superconductor. However, it is only the normal-state free energy that is substantially affected by the high temperatures. This is because the temperature dependence of the free energy strongly depends on the eigenenergies close to zero energy [30]. In the presence of a superconducting gap, few eigenenergies exist in this range. We have chosen our parameters so that the coherence length is comparable to the thickness of the superconductor, and the magnetic exchange field is about one order of magnitude larger than the superconducting gap. Predictions based on similar scaling have previously corresponded well to experiments (see e.g., Refs. [54,55] and Refs. [29,30,32]).

Concluding remarks. In this Letter, we have shown that the misalignment between the magnetic moments of an antiferromagnet and a ferromagnet is sufficient for controlling the triplet channels in an AF/S/F heterostructure, even when the antiferromagnetic interface is compensated and thus has zero effective interfacial magnetization. This provides the possibility of tuning the superconducting critical temperature by rotating the magnetization of a single ferromagnetic layer within the plane of the interface. In this way, the superconducting condensate can easily be controlled without having to deal with multiple ferromagnetic regions or out-of-plane magnetic fields causing demagnetizing currents and vortex formation in the superconducting region. Furthermore, we find that the superconducting transition can trigger a $\pi/2$ rotation of the ferromagnetic magnetization within the plane

of the interface, allowing for temperature-controlled magnetic switching.

Acknowledgments. We thank V. Risinggaard, A. Kamra, and I. Bobkova for useful discussions. We acknowledge fund-

ing via the “Outstanding Academic Fellows” program at NTNU and the Research Council of Norway via Grant No. 302315 as well as through its Centres of Excellence funding scheme, Project No. 262633, QuSpin.

- [1] A. A. Golubov, M. Yu. Kupriyanov, and E. Il'ichev, The current-phase relation in Josephson junctions, *Rev. Mod. Phys.* **76**, 411 (2004).
- [2] A. I. Buzdin, Proximity effects in superconductor-ferromagnet heterostructures, *Rev. Mod. Phys.* **77**, 935 (2005).
- [3] F. S. Bergeret, A. F. Volkov, and K. B. Efetov, Odd triplet superconductivity and related phenomena in superconductor-ferromagnet structures, *Rev. Mod. Phys.* **77**, 1321 (2005).
- [4] Yu. A. Izyumov, Yu. N. Proshin, and M. G. Khusainov, Competition between superconductivity and magnetism in ferromagnet/superconductor heterostructures, *Phys. Usp.* **45**, 109 (2002).
- [5] M. Eschrig, Spin-polarized supercurrents for spintronics, *Phys. Today* **64**(1), 43 (2011).
- [6] M. Eschrig, Spin-polarized supercurrents for spintronics: a review of current progress, *Rep. Prog. Phys.* **78**, 104501 (2015).
- [7] F. S. Bergeret, A. F. Volkov, and K. B. Efetov, Long-Range Proximity Effects in Superconductor-Ferromagnet Structures, *Phys. Rev. Lett.* **86**, 4096 (2001).
- [8] A. Kadıgrov, R. I. Shekhter, and M. Jonson, Quantum spin fluctuations as a source of long-range proximity effects in diffusive ferromagnet-superconductor structures, *Europhys. Lett.* **54**, 394 (2001).
- [9] C.-T. Wu, O. T. Valls, and K. Halterman, Reentrant Superconducting Phase in Conical-Ferromagnet-Superconductor Nanostructures, *Phys. Rev. Lett.* **108**, 117005 (2012).
- [10] F. Chiodi, J. D. S. Witt, R. G. J. Smits, L. Qu, G. B. Halász, C.-T. Wu, O. T. Valls, K. Halterman, J. W. A. Robinson, and M. G. Blamire, Supra-oscillatory critical temperature dependence of Nb-Ho bilayers, *Europhys. Lett.* **101**, 37002 (2013).
- [11] A. I. Buzdin and M. Y. Kupriyanov, Transition-temperature of a superconductor-ferromagnet superlattice, *Pis'ma Zh. Eksp. Teor. Fiz.* **52**, 1089 (1990) [*JETP Lett.* **52**, 487 (1990)].
- [12] Z. Radović, M. Ledvij, L. Dobrosavljević-Grujić, A. I. Buzdin, and J. R. Clem, Transition temperatures of superconductor-ferromagnet superlattices, *Phys. Rev. B* **44**, 759 (1991).
- [13] A. I. Buzdin and M. Y. Kupriyanov, Josephson junction with a ferromagnetic layer, *Pis'ma Zh. Eksp. Teor. Fiz.* **53**, 308 (1991) [*JETP Lett.* **53**, 321 (1991)].
- [14] J. S. Jiang, D. Davidović, D. H. Reich, and C. L. Chien, Oscillatory Superconducting Transition Temperature in Nb/Gd Multilayers, *Phys. Rev. Lett.* **74**, 314 (1995).
- [15] L. V. Mercaldo, C. Attanasio, C. Coccorese, L. Maritato, S. L. Prischepa, and M. Salvato, Superconducting-critical-temperature oscillations in Nb/CuMn multilayers, *Phys. Rev. B* **53**, 14040 (1996).
- [16] J. Y. Gu, C.-Y. You, J. S. Jiang, J. Pearson, Ya. B. Bazaliy, and S. D. Bader, Magnetization-Orientation Dependence of the Superconducting Transition Temperature in the Ferromagnet-Superconductor-Ferromagnet System: CuNi/Nb/CuNi, *Phys. Rev. Lett.* **89**, 267001 (2002).
- [17] I. C. Moraru, W. P. Pratt, and N. O. Birge, Magnetization-Dependent T_c Shift in Ferromagnet/Superconductor/Ferromagnet Trilayers with a Strong Ferromagnet, *Phys. Rev. Lett.* **96**, 037004 (2006).
- [18] N. Banerjee, C. B. Smiet, R. G. J. Smits, A. Ozaeta, F. S. Bergeret, M. G. Blamire, and J. W. A. Robinson, Evidence for spin selectivity of triplet pairs in superconducting spin valves, *Nat. Commun.* **5**, 3048 (2014).
- [19] Y. Gu, G. B. Halász, J. W. A. Robinson, and M. G. Blamire, Large Superconducting Spin Valve Effect and Ultrasmall Exchange Splitting in Epitaxial Rare-Earth-Niobium Trilayers, *Phys. Rev. Lett.* **115**, 067201 (2015).
- [20] F. S. Bergeret, A. F. Volkov, and K. B. Efetov, Enhancement of the Josephson Current by an Exchange Field in Superconductor-Ferromagnet Structures, *Phys. Rev. Lett.* **86**, 3140 (2001).
- [21] Y. A. Fominov, A. A. Golubov, T. Yu. Karminskaya, M. Yu. Kupriyanov, R. G. Deminov, and L. R. Tagirov, Superconducting triplet spin valve, *JETP Lett.* **91**, 308 (2010).
- [22] C.-T. Wu, O. T. Valls, and K. Halterman, Proximity effects and triplet correlations in ferromagnet/ferromagnet/superconductor nanostructures, *Phys. Rev. B* **86**, 014523 (2012).
- [23] P. V. Leksin, N. N. Garif'yanov, I. A. Garifullin, Ya. V. Fominov, J. Schumann, Y. Krupskaya, V. Kataev, O. G. Schmidt, and B. Büchner, Evidence for Triplet Superconductivity in a Superconductor-Ferromagnet Spin Valve, *Phys. Rev. Lett.* **109**, 057005 (2012).
- [24] A. A. Jara, C. Safranski, I. N. Krivorotov, C.-T. Wu, A. N. Malmi-Kakkada, O. T. Valls, and K. Halterman, Angular dependence of superconductivity in superconductor/spin-valve heterostructures, *Phys. Rev. B* **89**, 184502 (2014).
- [25] X. L. Wang, A. Di Bernardo, N. Banerjee, A. Wells, F. S. Bergeret, M. G. Blamire, and J. W. A. Robinson, Giant triplet proximity effect in superconducting pseudo spin valves with engineered anisotropy, *Phys. Rev. B* **89**, 140508(R) (2014).
- [26] S. H. Jacobsen, J. A. Ouassou, and J. Linder, Critical temperature and tunneling spectroscopy of superconductor-ferromagnet hybrids with intrinsic Rashba-Dresselhaus spin-orbit coupling, *Phys. Rev. B* **92**, 024510 (2015).
- [27] J. A. Ouassou, A. D. Bernardo, J. W. A. Robinson, and J. Linder, Electric control of superconducting transition through a spin-orbit coupled interface, *Sci. Rep.* **6**, 29312 (2016).
- [28] H. T. Simensen and J. Linder, Tunable superconducting critical temperature in ballistic hybrid structures with strong spin-orbit coupling, *Phys. Rev. B* **97**, 054518 (2018).
- [29] N. Banerjee, J. A. Ouassou, Y. Zhu, N. A. Stelmashenko, J. Linder, and M. G. Blamire, Controlling the superconducting transition by spin-orbit coupling, *Phys. Rev. B* **97**, 184521 (2018).
- [30] L. G. Johnsen, N. Banerjee, and J. Linder, Magnetization reorientation due to the superconducting transition in heavy-metal heterostructures, *Phys. Rev. B* **99**, 134516 (2019).

- [31] J. R. Eskilt, M. Amundsen, N. Banerjee, and J. Linder, Long-ranged triplet supercurrent in a single in-plane ferromagnet with spin-orbit coupled contacts to superconductors, *Phys. Rev. B* **100**, 224519 (2019).
- [32] C. González-Ruano, L. G. Johnsen, D. Caso, C. Tiusan, M. Hehn, N. Banerjee, J. Linder, and F. G. Aliev, Superconductivity-induced change in magnetic anisotropy in epitaxial ferromagnet-superconductor hybrids with spin-orbit interaction, *Phys. Rev. B* **102**, 020405(R) (2020).
- [33] L. G. Johnsen, K. Svalland, and J. Linder, Controlling the Superconducting Transition by Rotation of an Inversion Symmetry-Breaking Axis, *Phys. Rev. Lett.* **125**, 107002 (2020).
- [34] V. Baltz, A. Manchon, M. Tsoi, T. Moriyama, T. Ono, and Y. Tserkovnyak, Antiferromagnetic spintronics, *Rev. Mod. Phys.* **90**, 015005 (2018).
- [35] T. Jungwirth, X. Marti, P. Wadley, and J. Wunderlich, Antiferromagnetic spintronics, *Nat. Nanotechnol.* **11**, 231 (2016).
- [36] I. V. Bobkova, P. J. Hirschfeld, and Y. S. Barash, Spin-Dependent Quasiparticle Reflection and Bound States at Interfaces with Itinerant Antiferromagnets, *Phys. Rev. Lett.* **94**, 037005 (2005).
- [37] B. M. Andersen, I. V. Bobkova, P. J. Hirschfeld, and Y. S. Barash, Bound states at the interface between antiferromagnets and superconductors, *Phys. Rev. B* **72**, 184510 (2005).
- [38] C. Bell, E. J. Tarte, G. Burnell, C. W. Leung, D.-J. Kang, and M. G. Blamire, Proximity and josephson effects in superconductor/antiferromagnetic Nb/ γ -Fe₅₀Mn₅₀ heterostructures, *Phys. Rev. B* **68**, 144517 (2003).
- [39] B. M. Andersen, I. V. Bobkova, P. J. Hirschfeld, and Y. S. Barash, $0 - \pi$ Transitions in Josephson Junctions with Antiferromagnetic Interlayers, *Phys. Rev. Lett.* **96**, 117005 (2006).
- [40] P. Komissinskiy, G. A. Ovsyannikov, I. V. Borisenko, Yu. V. Kislinskii, K. Y. Constantinian, A. V. Zaitsev, and D. Winkler, Josephson Effect in Hybrid Oxide Heterostructures with an Antiferromagnetic Layer, *Phys. Rev. Lett.* **99**, 017004 (2007).
- [41] H. Enoksen, J. Linder, and A. Sudbø, Pressure-induced $0-\pi$ transitions and supercurrent crossover in antiferromagnetic weak links, *Phys. Rev. B* **88**, 214512 (2013).
- [42] L. Bulaevskii, R. Eneias, and A. Ferraz, Superconductor-antiferromagnet-superconductor π Josephson junction based on an antiferromagnetic barrier, *Phys. Rev. B* **95**, 104513 (2017).
- [43] X. Zhou, M. Lan, Y. Ye, Y. Feng, X. Zhai, L. Gong, H. Wang, J. Zhao, and Y. Xu, Andreev reflection and $0-\pi$ transition in graphene-based antiferromagnetic superconducting junctions, *Europhys. Lett.* **125**, 37001 (2019).
- [44] D. S. Rabinovich, I. V. Bobkova, and A. M. Bobkov, Anomalous phase shift in a Josephson junction via an antiferromagnetic interlayer, *Phys. Rev. Res.* **1**, 033095 (2019).
- [45] M. Hübener, D. Tikhonov, I. A. Garifullin, K. Westerholt, and H. Zabel, Proximity effects near the interface between d -wave superconductors and ferro/antiferromagnets, *J. Phys.: Condens. Matter* **14**, 8687 (2002).
- [46] K. Westerholt, D. Sprungmann, H. Zabel, R. Brucas, B. Hjörvarsson, D. A. Tikhonov, and I. A. Garifullin, Superconducting Spin Valve Effect of a V Layer Coupled to an Antiferromagnetic [Fe/V] Superlattice, *Phys. Rev. Lett.* **95**, 097003 (2005).
- [47] J. W. A. Robinson, G. Halász, and M. G. Blamire, Parity-dependent proximity effect in superconductor/antiferromagnet heterostructures, [arXiv:0808.0166](https://arxiv.org/abs/0808.0166).
- [48] B. L. Wu, Y. M. Yang, Z. B. Guo, Y. H. Wu, and J. J. Qiu, Suppression of superconductivity in Nb by IrMn in IrMn/Nb bilayers, *Appl. Phys. Lett.* **103**, 152602 (2013).
- [49] A. Kamra, A. Rezaei, and W. Belzig, Spin Splitting Induced in a Superconductor by an Antiferromagnetic Insulator, *Phys. Rev. Lett.* **121**, 247702 (2018).
- [50] S. Fukami, C. Zhang, S. Dutta Gupta, A. Kurenkov, and H. Ohno, Magnetization switching by spin-orbit torque in an antiferromagnet-ferromagnet bilayer system, *Nat. Mater.* **15**, 535 (2016).
- [51] Y. Wang, D. Zhu, Y. Yang, K. Lee, R. Mishra, G. Go, S.-H. Oh, D.-H. Kim, K. Cai, E. Liu, S. D. Pollard, S. Shi, J. Lee, K. L. Teo, Wu Y., K.-J. Lee, and Yang H., Magnetization switching by magnon-mediated spin torque through an antiferromagnetic insulator, *Science* **366**, 1125 (2019).
- [52] B. M. Andersen, Coexistence of magnetic and superconducting order in the high-Tc materials, Ph.D. thesis, Niels Bohr Institute, University of Copenhagen, 2004, <https://www.nbi.ku.dk/english/theses/phd-theses/brian-moeller-andersen/>.
- [53] See Supplemental Material at <http://link.aps.org/supplemental/10.1103/PhysRevB.103.L060505> for a further description of the theoretical framework used in this Letter, and for a discussion of the triplet amplitudes present in the AF/S/F structure.
- [54] A. M. Black-Schaffer and J. Linder, Strongly anharmonic current-phase relation in ballistic graphene josephson junctions, *Phys. Rev. B* **82**, 184522 (2010).
- [55] C. D. English, D. R. Hamilton, C. Chialvo, I. C. Moraru, N. Mason, and D. J. Van Harlingen, Observation of nonsinusoidal current-phase relation in graphene Josephson junctions, *Phys. Rev. B* **94**, 115435 (2016).

Supplemental Material to: Magnetic Control of Superconducting Heterostructures Using Compensated Antiferromagnets

Lina G. Johnsen,^{1,2,*} Sol H. Jacobsen,^{1,2} and Jacob Linder¹

¹Center for Quantum Spintronics, Department of Physics, Norwegian University of Science and Technology (NTNU), NO-7491 Trondheim, Norway

²These authors contributed equally to this work

We here provide a more detailed description of our theoretical framework (Section I), where we describe the mean-field treatment and diagonalization of the Hamiltonian, as well as how we calculate the superconducting gap, coherence length, critical temperature, and the free energy. We use a similar approach as in Refs. [1–4]. We also provide further discussion of the triplet amplitudes present in the AF/S/F structure (Section II).

I. THEORETICAL FRAMEWORK

We first use the mean-field approximation described in the main text on the antiferromagnetic and superconducting terms in the Hamiltonian given in Eq. (1) in the Letter. The antiferromagnetic contribution to the Hamiltonian takes the form

$$H_{AF} = \frac{3}{8} \sum_i \frac{M_i^2}{V_i} - \sum_i M_i (n_{i,\uparrow} - n_{i,\downarrow}) \quad (1)$$

while the superconducting contribution takes the form

$$H_S = \sum_i \frac{|\Delta_i|}{U_i} + \sum_i (\Delta_i c_{i\uparrow}^\dagger c_{i\downarrow}^\dagger + \text{h.c.}). \quad (2)$$

The superconducting gap Δ_i is calculated self-consistently. The absolute value of antiferromagnetic order parameter M_i is assumed to be constant inside the antiferromagnetic region, while the sign alternates between neighboring lattice sites.

Bogoliubov–de Gennes lattice models are typically simplified by Fourier transforming in directions other than along the junction normal. For our 2D lattice we therefore apply periodic boundary conditions in the y direction. The two-sublattice periodic ordering of antiferromagnets has oscillating magnetic order parameter. This means we can still perform the Fourier transform if we take account of the doubling of the magnetic period [1, 5]. In effect, this means that the magnetic order parameter must have a $\{\mathbf{k}, \mathbf{k} + \mathbf{Q}\}$ symmetry for a reciprocal lattice vector $2\mathbf{Q}$, doubling the size of the matrix space. The general expression for the Fourier transform in the y direction is given by

$$c_{i,\sigma} = \frac{1}{\sqrt{N_y}} \sum_{k_y} c_{i_x, k_y, \sigma} e^{ik_y i_y}. \quad (3)$$

When Fourier transforming the antiferromagnetic term, we take account of the oscillation at every lattice point explicitly by including $(-1)^{i_y} \equiv e^{2\pi i(i_y)}$, which gives the $\{\mathbf{k}, \mathbf{k} + \mathbf{Q}\}$ symmetry when using

$$\frac{1}{\sqrt{N_y}} \sum_{i_y} e^{i(k_y - k'_y) i_y} = \delta_{k_y, k'_y}. \quad (4)$$

After Fourier transforming, we write the Hamiltonian as

$$H = H_0 + \frac{1}{2} \sum_{i_x, j_x, k_y} B_{i_x, k_y}^\dagger H_{i_x, j_x, k_y} B_{j_x, k_y}, \quad (5)$$

where we have introduced the basis

$$B_{i_x, k_y}^\dagger = \left[c_{i_x, k_y, \uparrow}^\dagger, c_{i_x, k_y, \downarrow}^\dagger, c_{i_x, k_y + \mathbf{Q}, \uparrow}^\dagger, c_{i_x, k_y + \mathbf{Q}, \downarrow}^\dagger, c_{i_x, -k_y, \uparrow}, c_{i_x, -k_y, \downarrow}, c_{i_x, -k_y - \mathbf{Q}, \uparrow}, c_{i_x, -k_y - \mathbf{Q}, \downarrow} \right]. \quad (6)$$

The matrix H_{i_x, j_x, k_y} is given by

$$\begin{aligned} H_{i_x, j_x, k_y} = & - \left[\frac{t}{2} (\delta_{i_x, j_x - 1} + \delta_{i_x, j_x + 1}) + \frac{\mu}{2} \delta_{i_x, j_x} \right] \hat{\tau}_3 \hat{\rho}_0 \hat{\sigma}_0 \\ & - t \cos(k_y) \delta_{i_x, j_x} \hat{\tau}_3 \hat{\rho}_3 \hat{\sigma}_0 - \frac{1}{2} M_{i_x} \delta_{i_x, j_x} \hat{\tau}_3 \hat{\rho}_1 \hat{\sigma}_3 \\ & + \frac{\delta_{i_x, j_x}}{2} \left(h_x^x \hat{\tau}_3 \hat{\rho}_0 \hat{\sigma}_1 + h_x^y \hat{\tau}_0 \hat{\rho}_0 \hat{\sigma}_2 + h_x^z \hat{\tau}_3 \hat{\rho}_0 \hat{\sigma}_3 \right) \\ & + \frac{i}{2} \delta_{i_x, j_x} \Delta_{i_x} \hat{\tau}^+ \hat{\rho}_0 \hat{\sigma}_2 - \frac{i}{2} \delta_{i_x, j_x} \Delta_{i_x}^* \hat{\tau}^- \hat{\rho}_0 \hat{\sigma}_2. \end{aligned} \quad (7)$$

Here the matrices $\hat{\tau}_i$, $\hat{\rho}_i$ and $\hat{\sigma}_i$ for $i = \{0, 1, 2, 3\}$ are the usual $SU(2)$ (Pauli) matrices, with $i = 0$ being the identity, and with $\hat{\tau}^\pm = (\hat{\tau}_1 \pm i\hat{\tau}_2)/2$. $\hat{\tau}$ represents particle-hole space, $\hat{\rho}$ the $\{\mathbf{k}, \mathbf{k} + \mathbf{Q}\}$ -space and $\hat{\sigma}$ denotes spin space, as can be identified from the basis choice. The constant term H_0 is given by

$$\begin{aligned} H_0 = & - \frac{1}{2N_y} \sum_{i_x} \mu_{i_x} - \sum_{i_x, k_y} t \cos(k_y) \\ & + \sum_{i_x} \frac{N_y |\Delta_{i_x}|^2}{U_{i_x}} + \frac{3}{8} \sum_{i_x} \frac{N_y M_{i_x}^2}{V_{i_x}}. \end{aligned} \quad (8)$$

By defining another basis,

$$W_{k_y, k_z}^\dagger = [B_{1, k_y}^\dagger, \dots, B_{i_x, k_y}^\dagger, \dots, B_{N_x, k_y}^\dagger], \quad (9)$$

Eq. 5 can be rewritten as

$$H = H_0 + \frac{1}{2} \sum_{k_y} W_{k_y}^\dagger H_{k_y} W_{k_y}, \quad (10)$$

* Corresponding author: lina.g.johnsen@ntnu.no

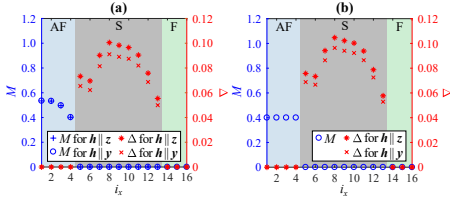


FIG. 1. Panel (a) and (b) show the magnitude of the antiferromagnetic order parameter M and the superconducting gap Δ as a function of the position i_x at temperature $T_C/2$ for the same parameters as used in Fig. 2 in the manuscript. In panel (a) both M and Δ are calculated self-consistently with $V = 2.35$. We see that when rotating the magnetization of the ferromagnet from a parallel ($\mathbf{h}||z$) to a perpendicular ($\mathbf{h}||y$) alignment with respect to the magnetic moments of the antiferromagnet, the superconducting gap changes significantly, while the antiferromagnetic order parameter is unchanged. In panel (b), only Δ is solved self-consistently, as in our manuscript. The order parameter of the antiferromagnet is set equal to its smallest value in the self-consistent solution. We find a similar variation in Δ as in panel (a).

where

$$H_{k_y} = \begin{bmatrix} H_{1,1,k_y} & \cdots & H_{1,N_x,k_y} \\ \vdots & \ddots & \vdots \\ H_{N_x,1,k_y} & \cdots & H_{N_x,N_x,k_y} \end{bmatrix}. \quad (11)$$

We diagonalize H_{k_y} numerically and obtain eigenvalues E_{n,k_y} and eigenvectors Φ_{n,k_y} , given by

$$\begin{aligned} \Phi_{n,k_y} &\equiv [\phi_{1,n,k_y} \cdots \phi_{N_x,n,k_y}]^T, \\ \phi_{i_x,n,k_y} &\equiv [s_{i_x,n,k_y} \quad t_{i_x,n,k_y} \quad u_{i_x,n,k_y} \quad v_{i_x,n,k_y} \\ &\quad w_{i_x,n,k_y} \quad x_{i_x,n,k_y} \quad y_{i_x,n,k_y} \quad z_{i_x,n,k_y}]^T. \end{aligned} \quad (12)$$

In its diagonalized form the Hamiltonian can be written as

$$H = H_0 + \frac{1}{2} \sum_{n,k_y} E_{n,k_y} \gamma_{n,k_y}^\dagger \gamma_{n,k_y}, \quad (13)$$

where the new quasiparticle fermion operators γ_{n,k_y} satisfy

$$\begin{aligned} c_{i_x,k_y,\uparrow} &= \sum_n s_{i_x,n,k_y} \gamma_{n,k_y}, & c_{i_x,-k_y,\uparrow}^\dagger &= \sum_n w_{i_x,n,k_y} \gamma_{n,k_y}, \\ c_{i_x,k_y,\downarrow} &= \sum_n t_{i_x,n,k_y} \gamma_{n,k_y}, & c_{i_x,-k_y,\downarrow}^\dagger &= \sum_n x_{i_x,n,k_y} \gamma_{n,k_y}, \\ c_{i_x,k_y+Q,\uparrow} &= \sum_n u_{i_x,n,k_y} \gamma_{n,k_y}, & c_{i_x,-k_y-Q,\uparrow}^\dagger &= \sum_n y_{i_x,n,k_y} \gamma_{n,k_y}, \\ c_{i_x,k_y+Q,\downarrow} &= \sum_n v_{i_x,n,k_y} \gamma_{n,k_y}, & c_{i_x,-k_y-Q,\downarrow}^\dagger &= \sum_n z_{i_x,n,k_y} \gamma_{n,k_y}. \end{aligned} \quad (14)$$

The Fermi-Dirac distribution function f allows us to calculate expectation values of the form $\langle \gamma_{n,k_y}^\dagger \gamma_{m,k_y} \rangle = f(E_{n,k_y}/2) \delta_{n,m}$.

The superconducting gap is defined $\Delta_i \equiv U_i \langle c_{i,\uparrow} c_{i,\downarrow} \rangle$, and can be expressed in terms of the eigenenergies and elements of the eigenvectors as

$$\begin{aligned} \Delta_{i_x} &= -\frac{U_{i_x}}{2N_y} \sum_{n,k_y} (t_{i_x,n,k_y} w_{i_x,n,k_y}^* \\ &\quad + v_{i_x,n,k_y} y_{i_x,n,k_y}^*) [1 - f(E_{n,k_y}/2)]. \end{aligned} \quad (15)$$

Similarly, the s -wave odd-frequency opposite- and equal-spin triplet amplitudes can be written

$$\begin{aligned} S_{0,i_x}(\tau) &= \frac{1}{2N_y} \sum_{n,k_y} [s_{i_x,n,k_y} x_{i_x,n,k_y}^* + t_{i_x,n,k_y} w_{i_x,n,k_y}^* \\ &\quad + u_{i_x,n,k_y} z_{i_x,n,k_y}^* + v_{i_x,n,k_y} y_{i_x,n,k_y}^*] e^{-iE_{n,k_y} \tau/2} \\ &\quad \cdot [1 - f(E_{n,k_y}/2)], \\ S_{\uparrow,i_x}(\tau) &= \frac{1}{2N_y} \sum_{n,k_y} [s_{i_x,n,k_y} w_{i_x,n,k_y}^* + u_{i_x,n,k_y} y_{i_x,n,k_y}^*] \\ &\quad \cdot e^{-iE_{n,k_y} \tau/2} [1 - f(E_{n,k_y}/2)], \\ S_{\downarrow,i_x}(\tau) &= \frac{1}{2N_y} \sum_{n,k_y} [t_{i_x,n,k_y} x_{i_x,n,k_y}^* + v_{i_x,n,k_y} z_{i_x,n,k_y}^*] \\ &\quad \cdot e^{-iE_{n,k_y} \tau/2} [1 - f(E_{n,k_y}/2)], \end{aligned} \quad (16)$$

and the p_x -wave even-frequency opposite- and equal-spin triplet amplitudes are given by

$$\begin{aligned} P_{0,i_x}^x &= \frac{1}{2N_y} \sum_{n,k_y} [s_{i_x,n,k_y} x_{i_x+1,n,k_y}^* - s_{i_x,n,k_y} x_{i_x-1,n,k_y}^* \\ &\quad + u_{i_x,n,k_y} z_{i_x+1,n,k_y}^* - u_{i_x,n,k_y} z_{i_x-1,n,k_y}^* \\ &\quad + t_{i_x,n,k_y} w_{i_x+1,n,k_y}^* - t_{i_x,n,k_y} w_{i_x-1,n,k_y}^* \\ &\quad + v_{i_x,n,k_y} y_{i_x+1,n,k_y}^* - v_{i_x,n,k_y} y_{i_x-1,n,k_y}^*] \\ &\quad \cdot [1 - f(E_{n,k_y}/2)], \\ P_{\uparrow,i_x}^x &= \frac{1}{2N_y} \sum_{n,k_y} [s_{i_x,n,k_y} w_{i_x+1,n,k_y}^* - s_{i_x,n,k_y} w_{i_x-1,n,k_y}^* \\ &\quad + u_{i_x,n,k_y} y_{i_x+1,n,k_y}^* - u_{i_x,n,k_y} y_{i_x-1,n,k_y}^*] \\ &\quad \cdot [1 - f(E_{n,k_y}/2)], \\ P_{\downarrow,i_x}^x &= \frac{1}{2N_y} \sum_{n,k_y} [t_{i_x,n,k_y} x_{i_x+1,n,k_y}^* - t_{i_x,n,k_y} x_{i_x-1,n,k_y}^* \\ &\quad + v_{i_x,n,k_y} z_{i_x+1,n,k_y}^* - v_{i_x,n,k_y} z_{i_x-1,n,k_y}^*] \\ &\quad \cdot [1 - f(E_{n,k_y}/2)]. \end{aligned} \quad (17)$$

Only s - and p_x -wave triplets are present in the AF/S/F structure. The above spin-triplet amplitudes describe spins projected along the z axis. We rotate the triplets to a new projection axis characterized by the polar coordinate θ and the azimuthal angle

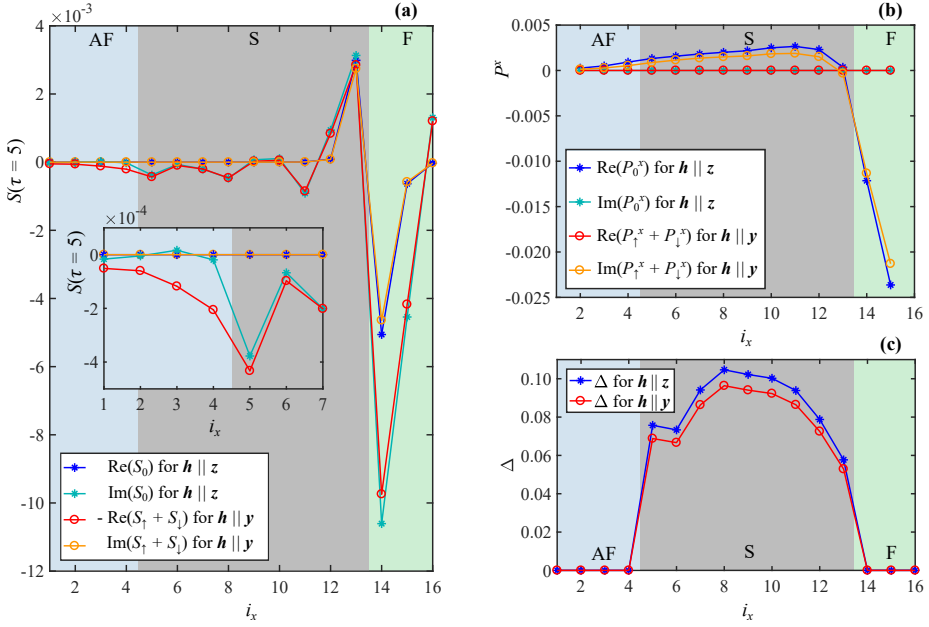


FIG. 2. Panels (a)-(c) show the s -wave triplet amplitude, the p_x -wave triplet amplitude and the superconducting gap, respectively, at temperature $T_c/2$ inside the antiferromagnetic (blue), superconducting (grey) and ferromagnetic (green) region. In all panels we compare the results for parallel ($\mathbf{h} \parallel \mathbf{z}$) and perpendicular ($\mathbf{h} \parallel \mathbf{y}$) alignment of the magnetic moments of the antiferromagnet and ferromagnet. The inset in panel (a) shows the s -wave triplet amplitudes inside and close to the antiferromagnetic region. The parameters used are the same as for Fig. 2 in the main text.

ϕ with respect to the z axis using

$$\begin{aligned}
 (\uparrow\downarrow + \downarrow\uparrow)_{\theta,\phi} &= -\sin(\theta)[e^{-i\phi}(\uparrow\uparrow)_z - e^{i\phi}(\downarrow\downarrow)_z] \\
 &\quad + \cos(\theta)(\uparrow\downarrow + \downarrow\uparrow)_z, \\
 (\uparrow\uparrow)_{\theta,\phi} &= \cos^2(\theta/2)e^{-i\phi}(\uparrow\uparrow)_z + \sin^2(\theta/2)e^{i\phi}(\downarrow\downarrow)_z \\
 &\quad + \sin(\theta/2)\cos(\theta/2)(\uparrow\downarrow + \downarrow\uparrow)_z, \\
 (\downarrow\downarrow)_{\theta,\phi} &= \sin^2(\theta/2)e^{-i\phi}(\uparrow\uparrow)_z + \cos^2(\theta/2)e^{i\phi}(\downarrow\downarrow)_z \\
 &\quad - \sin(\theta/2)\cos(\theta/2)(\uparrow\downarrow + \downarrow\uparrow)_z,
 \end{aligned} \quad (18)$$

where $(\uparrow\downarrow + \downarrow\uparrow)$ represents the opposite-spin triplet amplitude, while $(\uparrow\uparrow)$ and $(\downarrow\downarrow)$ represents the equal-spin triplet amplitudes.

The antiferromagnetic order parameter can be calculated self-consistently from

$$\begin{aligned}
 M_{i_x} &= \frac{V}{4N_y} \sum_{n,k_y} [v_{i_x,n,k_y} l_{i_x,n,k_y}^* + t_{i_x,n,k_y} v_{i_x,n,k_y}^* \\
 &\quad - u_{i_x,n,k_y} s_{i_x,n,k_y}^* - s_{i_x,n,k_y} u_{i_x,n,k_y}^*] [1 - f(E_{n,k_y}/2)]. \quad (19)
 \end{aligned}$$

In Fig. 1, we justify our assumption that a self-consistent calculation of the antiferromagnetic order parameter is unnecessary.

From panel (a), where both the antiferromagnetic and superconducting order parameters are computed self-consistently, we see that the antiferromagnetic order parameter is suppressed close to the interface. However, as seen in panel (b) where only the superconducting order parameter is computed self-consistently, setting the magnetic order parameter equal to the interfacial value of the the magnetic order parameter in panel (a) gives practically identical results for the self-consistently obtained superconducting gap.

The superconducting coherence length is given by $\xi = \hbar v_F / \pi \Delta_0$, where $v_F \equiv \frac{1}{\hbar} \frac{dE_{k_y}}{dk} \Big|_{k=k_F}$ is the normal-state Fermi velocity, E_{k_y} is the normal-state eigenenergies if we instead of accounting for an interface use periodic boundary conditions along all three axes, and k_F is the corresponding Fermi momentum averaged over the Fermi surface.

Our binomial search algorithm for the superconducting critical temperature, is the same as the one we have previously presented in Ref. [4], and we only summarize the main steps here. We divide the temperature interval N_T times. For each of the N_T temperatures considered, we recalculate the

gap N_Δ times from an initial guess with a magnitude much smaller than the zero-temperature superconducting gap. If the gap has increased towards a superconducting solution after N_Δ iterations, we conclude that the current temperature is below T_c . If the gap has decreased towards a normal-state solution, we conclude that the current temperature is above T_c . The advantage of this algorithm is that we are not dependent upon recalculating the gap until it converges. The number of iterations N_Δ must only be large enough that we have an overall increase or decrease in the superconducting gap at all lattice sites inside the superconducting region under recalculation.

The minimum of the free energy defines the ground state of the system. The free energy is given by

$$F = H_0 - T \sum_{n,k_y} \ln(1 + e^{-E_{n,k_y}/2T}). \quad (20)$$

Note also that when $T \rightarrow 0$,

$$F = H_0 + \frac{1}{2} \sum_{n,k_y} E_{n,k_y}, \quad (21)$$

where the sum is restricted to negative eigenenergies.

II. TRIPLET AMPLITUDES

In Fig. 2, we show the s -wave and p_x -wave triplet amplitudes and the superconducting gap inside the AF/S/F structure for parallel ($\mathbf{h}||z$) and perpendicular ($\mathbf{h}||y$) alignment of the magnetic moments inside the antiferromagnet and ferromagnet. To understand how these triplets are generated, we need to comment on two limiting cases: First, in the absence of the

ferromagnetic layer all triplet amplitudes are zero. This means that all triplets in the AF/S/F structure are generated due to the proximity to the ferromagnet. Second, in the absence of the antiferromagnetic layer, all triplet amplitudes are invariant under rotation of the magnetization of the ferromagnet. This means that if we choose a projection axis along the z axis, S_0 and P_0^x for $\mathbf{h}||z$ is equal to $S_\uparrow + S_\downarrow$ and $P_\uparrow^x + P_\downarrow^x$ for $\mathbf{h}||y$, respectively. We now consider an AF/S/F structure where the magnetic moments of the antiferromagnet are directed along $\pm z$. If we first consider the s -wave triplet amplitude (Fig. 2(a)), we find that the amplitude of the equal-spin triplets $S_\uparrow + S_\downarrow$ for $\mathbf{h}||y$ is larger than the amplitude of the opposite-spin triplets S_0 for $\mathbf{h}||z$ close to and inside the antiferromagnetic region (inset of Fig. 2(a)). While opposite-spin triplets hardly penetrate the antiferromagnet at all, the equal-spin triplets seem to have a longer penetration depth. Moreover, they seem to be more robust upon reflection. The robustness of the equal-spin triplets generated when the magnetic moments of the ferromagnet and antiferromagnet are misaligned explains the suppression of the superconducting gap (Fig. 2(c)) and superconducting critical temperature. Close to and inside the ferromagnetic region, the s -wave triplet amplitude is instead weaker for $\mathbf{h}||y$ than for $\mathbf{h}||z$. This is because the triplet generation at the ferromagnetic interface is dependent of the scattering of triplets at the antiferromagnetic interface, via the singlet amplitude. The robustness of the equal-spin triplets close to and inside the antiferromagnet causes the superconducting gap (Fig. 2(c)) and thus the singlet amplitude to be smaller when $\mathbf{h}||z$. The decreased singlet amplitude causes fewer triplets to be created by proximity to the ferromagnet. For the s -wave triplet amplitude this effect only dominates for positions sufficiently far away from the antiferromagnetic region, while for the p_x -wave triplet amplitude (Fig. 2(b)) it dominates in all regions.

-
- [1] B. M. Andersen, I. V. Bobkova, P. J. Hirschfeld, and Y. S. Barash, "Bound states at the interface between antiferromagnets and superconductors," *Phys. Rev. B* **72**, 184510 (2005).
- [2] P. V. Leksin, N. N. Garif'yanov, I. A. Garifullin, Ya. V. Fominov, J. Schumann, Y. Krupskaya, V. Kataev, O. G. Schmidt, and B. Büchner, "Evidence for triplet superconductivity in a superconductor-ferromagnet spin valve," *Phys. Rev. Lett.* **109**, 057005 (2012).
- [3] L. G. Johnsen, N. Banerjee, and J. Linder, "Magnetization reorientation due to the superconducting transition in heavy-metal heterostructures," *Phys. Rev. B* **99**, 134516 (2019).
- [4] L. G. Johnsen, K. Svalland, and J. Linder, "Controlling the superconducting transition by rotation of an inversion symmetry-breaking axis," *Phys. Rev. Lett.* **125**, 107002 (2020).
- [5] B. M. Andersen, *Coexistence of Magnetic and Superconducting Order in the High-Tc Materials*, Ph.D. thesis, Niels Bohr Institute, University of Copenhagen (2004).

V

REFERENCE

César González-Ruano, Diego Caso, Lina G. Johnsen, Coriolan Tiusan, Michel Hehn, Niladri Banerjee, Jacob Linder, and Farkhad G. Aliev,
Superconductivity assisted change of the perpendicular magnetic anisotropy in V/MgO/Fe junctions,
Sci. Rep. **11**, 19041 (2021).

CONTRIBUTIONS

FGA and CT designed the junctions, and CT and MH fabricated the junctions. The measurements were performed by CG-R with the participation of DC. The modelling was developed by LGJ and JL. Micro-magnetic and TDGL calculations have been carried out by DC and CG-R. FGA, CG-R, DC, LGJ, NB and JL analyzed the data and wrote the manuscript. All authors contributed to the study, discussed the results, commented and revised the manuscript. FGA supervised the work.



OPEN Superconductivity assisted change of the perpendicular magnetic anisotropy in V/MgO/Fe junctions

César González-Ruano¹, Diego Caso¹, Lina G. Johnsen², Coriolan Tiusan^{3,4}, Michel Hehn⁴, Niladri Banerjee⁵, Jacob Linder² & Farkhad G. Aliev^{1,5}✉

Controlling the perpendicular magnetic anisotropy (PMA) in thin films has received considerable attention in recent years due to its technological importance. PMA based devices usually involve heavy-metal (oxide)/ferromagnetic-metal bilayers, where, thanks to interfacial spin-orbit coupling (SOC), the in-plane (IP) stability of the magnetisation is broken. Here we show that in V/MgO/Fe(001) epitaxial junctions with competing in-plane and out-of-plane (OOP) magnetic anisotropies, the SOC mediated interaction between a ferromagnet (FM) and a superconductor (SC) enhances the effective PMA below the superconducting transition. This produces a partial magnetisation reorientation without any applied field for all but the largest junctions, where the IP anisotropy is more robust; for the smallest junctions there is a reduction of the field required to induce a complete OOP transition (H_{OOP}) due to the stronger competition between the IP and OOP anisotropies. Our results suggest that the degree of effective PMA could be controlled by the junction lateral size in the presence of superconductivity and an applied electric field. We also discuss how the H_{OOP} field could be affected by the interaction between magnetic stray fields and superconducting vortices. Our experimental findings, supported by numerical modelling of the ferromagnet-superconductor interaction, open pathways to active control of magnetic anisotropy in the emerging dissipation-free superconducting spin electronics.

Control of out-of-plane (OOP) anisotropies in ultra thin ferromagnetic multilayer films have revolutionized magnetic storage and spintronics technologies by mitigating the impact of the demagnetizing energy as the bit and magnetic tunnel junction sizes diminished^{1,2}. Tuning of perpendicular magnetic anisotropy (PMA) by careful selection of structure design^{3,4} and size⁵ has been among the main challenges of spintronics. Besides the variation of the ferromagnet thickness and interface with oxides, OOP magnetisation reorientation can be achieved by a temporary reduction of the IP-OOP barrier using, for example, heat and microwave pulses^{6,7} or a combination of magnetic field and low temperature⁸.

Recently, we demonstrated a fundamentally different route to magnetisation reorientation through the influence of superconductivity on the IP magnetisation anisotropy⁹. The key idea behind this effect is that the magnetisation aligns to minimize the weakening of the superconducting condensate associated with the creation of spin triplet (ST) Cooper pairs¹⁰. The spin triplet generation depends on the magnetisation direction relative to the interfacial Rashba spin-orbit field. Understanding the factors influencing this superconductivity-induced change of magnetic anisotropy is crucial for designing the next generation of cryogenic memories in the emerging field of superconducting spintronics, where control over non-volatile magnetisation states still remains a major challenge^{11–14}.

The main underlying physical mechanisms for the transformation of ST Cooper pairs from singlet to mixed-spin and equal-spin triplet pairs are magnetic inhomogeneities^{15,16}, two misaligned FM layers^{17,18} or SOC¹⁹. Previous experiments focusing on SOC-driven generation of triplets have focused on heavy metal (Pt) layers in

¹Departamento Física de la Materia Condensada C-III, Instituto Nicolás Cabrera (INC) and Condensed Matter Physics Institute (IFIMAC), Universidad Autónoma de Madrid, Madrid 28049, Spain. ²Department of Physics, Center for Quantum Spintronics, Norwegian University of Science and Technology, 7491 Trondheim, Norway. ³Department of Physics and Chemistry, Center of Superconductivity Spintronics and Surface Science C4S, Technical University of Cluj-Napoca, Cluj-Napoca 400114, Romania. ⁴Institut Jean Lamour, Nancy Université, 54506 Vandoeuvre-les-Nancy Cedex, France. ⁵Department of Physics, Loughborough University, Epinal Way, Loughborough LE11 3TU, UK. ✉email: farkhad.aliev@uam.es

non-epitaxial SC/FM structures^{20,21} and Rashba SOC in epitaxial V/MgO/Fe junctions^{9,22} where ST Cooper pairs are generated depending on the magnetisation orientation relative to the Rashba field.

Theoretically, it has been shown¹⁰ that a superconductor coupled to a ferromagnet by SOC could stimulate the modification not only of the IP⁹, but also of the OOP magnetic anisotropy below the superconducting critical temperature (T_C). Due to the stray fields, however, ferromagnetic films are expected to have a stronger interaction with the superconductor when an OOP magnetisation is present, compared to a simple IP variation^{23,24}. Therefore, a careful consideration of the interaction of these stray field generated by the OOP magnetisation and superconducting vortices is essential to fully capture the factors influencing the effective OOP anisotropy.

Here, we investigate the superconductivity-induced OOP magnetisation reorientation in epitaxial Fe(001) films with competing IP and OOP anisotropies, both at zero field and in the presence of out-of-plane applied magnetic fields. The V/MgO/Fe(001) junctions are ideal candidates to verify the predicted modification of the effective perpendicular anisotropy in the superconducting state for several reasons¹⁰. Firstly, the Fe(001) has the required¹⁰ cubic symmetry; secondly, previous studies show that the normal state IP-OOP reorientation transition takes place at a well-defined critical field⁸; thirdly, the system has Rashba type SOC, which is responsible for the PMA in MgO/Fe²⁵; fourthly, the relative contribution of the IP and OOP magnetisation anisotropies can be tuned by changing the junction lateral size, and SOC can be varied by applying an external electric field; finally, the change in magnetisation can be determined with high precision by studying the transport characteristics using a second magnetically hard Fe/Co layer which is magnetostatically decoupled from the soft Fe layer⁸.

For the smallest junctions, where the IP and OOP anisotropies strongly compete, we remarkably observe the full superconductivity-induced IP-OOP magnetisation reorientation predicted in Ref.¹⁰. This results in (i) a decreasing of the required field to induce the full IP-OOP transition below T_C , which is not observed in bigger junctions; and (ii) a spontaneous increasing of the misalignment angle between the two FM layers below T_C in the absence of applied field, which is consistently observed in all but the largest junctions. These differences in the observed behaviour depending on the junctions dimensions are most likely due to the IP anisotropy becoming more dominant with increasing lateral size. We discard the magnetostatic interaction between superconducting vortices and the FM layers as the main cause of the observed effects.

Results

Figure 1 shows the experimental configuration and the different types of OOP transition observed above the vanadium T_C . Figure 1a shows the V(40 nm)/MgO(2 nm)/Fe(10 nm)/MgO(2 nm)/Fe(10 nm)/Co(20 nm) (N(SC)/FM1/FM2) junctions with a hard Fe/Co layer (FM2) sensing the magnetisation alignment of the 10 nm thick Fe(001) soft layer (FM1). Details about the sample growth, characterization and the experimental set-up are explained in the “Methods” section. All junctions were saturated with a 3 kOe IP magnetic field (see the alignment calibration procedure in Supplementary Material, Sect. 1) before each of the OOP magnetoresistance (TMR) measurements, in order to eliminate magnetic inhomogeneities from previous OOP measurements. All except one of the studied junctions showed OOP anisotropy below 3 kOe. On the right side of the vertical axes of Fig. 1b–d, we indicate the TMR values corresponding to the well established parallel (P), perpendicular out-of-plane (OOP) and antiparallel (AP) states for each sample, which are used to calibrate the angle between the two FM layers ($\Delta\phi = \phi_{FM1} - \phi_{FM2}$, where ϕ_{FM1} and ϕ_{FM2} are the angles of each FM layer with respect to the plane of the layers, as shown in Fig. 1a) with the same procedure as described in Refs.^{8,9}. This indicates that the IP-OOP transition also triggers a total or partial reorientation of the sensing (hard) FM2 layer, providing a resistance close to that of an AP state. Previous OOP measurements⁸ above T_C made on only two $20 \times 20 \mu\text{m}^2$ junctions revealed asymmetric transitions into the perpendicular alignment of the soft FM1 layer, without any subsequent transition of the sensing layer with perpendicular fields up to 3 kOe. The present study is made with a total of 16 junctions of four different lateral sizes, where about half of them also demonstrate a transition to an AP configuration when the magnetic field is further increased after the transition to the OOP state has been completed. This AP configuration could potentially be either with the two layers oriented OOP or IP, although it seems rather unlikely that both layers reorient to an IP configuration while the applied OOP field increases. We believe that the high-field-induced transition from OOP to AP alignment or, in some cases, a nearly direct P to AP transition in N/FM1/FM2 junctions could be a consequence of the enhanced antiferromagnetic coupling reported for MgO magnetic tunnel junctions with perpendicular magnetic anisotropy (see²⁶). We cannot exclude the possibility that the AP alignment could be triggered by a partial reorientation of the hard Fe/Co layer (with only the Fe part or the atomic layers closer to the Fe/MgO interface in the hard layer orienting OOP, as shown in the sketches in Fig. 1b,c). However, since we measure the total resistance of the junctions, it is impossible to distinguish between these two cases from transport measurements alone. Therefore, we mainly focus on the influence of superconductivity on the transition between IP and OOP states and the partial OOP reorientation at zero magnetic field. Consequently, for the OOP field range reported here, we will assume that the ϕ_{FM2} angle of the FM2 layer with respect to the in-plane configuration is fixed and close to 0.

Figure 1c shows typical OOP TMR cycles measured in two $20 \times 20 \mu\text{m}^2$ junctions, one of them switching to an AP alignment following an OOP orientation (blue) and the other one only switches to the OOP state (red). Figure 1d shows an OOP TMR for a $30 \times 30 \mu\text{m}^2$ junction where the OOP alignment of the FM1 and FM2 electrodes remains stable up to 3 kOe. Note that all junctions showed remanent OOP alignment of the soft Fe(001) electrode once the perpendicular magnetic field is removed (Fig. 1). This indicates the relatively small number of interfacial defects present in our junctions, as supported by numerical simulations analyzing the OOP configuration robustness as a function of the density of interfacial defects by studying the *inverse* OOP to IP transition, which are discussed in the Supplementary Material, S2.2.

The symmetry broken spin reorientation observed in the OOP TMR experiments shown in Fig. 1 b–d, has been previously explained in Ref.⁸ by the difference in the dislocation density present at the top and bottom

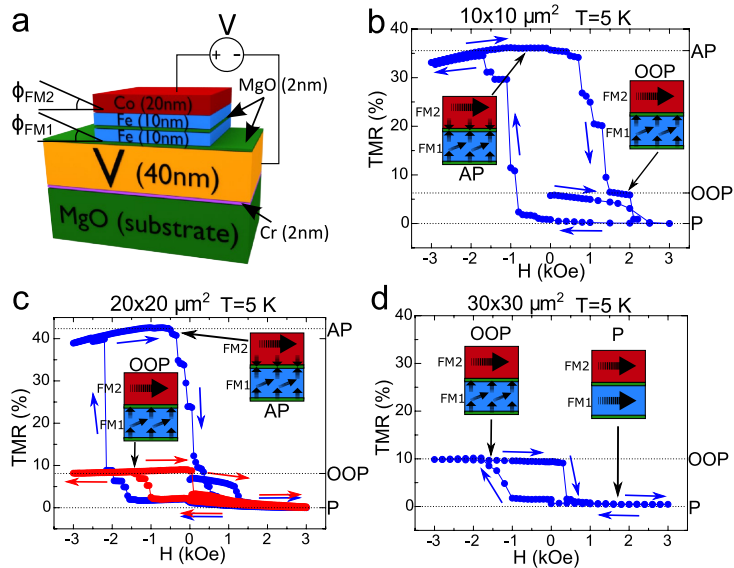


Figure 1. (a) Sketch of the junctions under study where Fe(10 nm) (FM1) is the soft ferromagnet undergoing spin reorientation transitions, while Fe(10 nm)Co(20 nm) (FM2) is the hard (sensing) layer. ϕ_{FM1} and ϕ_{FM2} are the OOP angles of each FM layer (i.e. the angle with respect to the plane of the layers). Since the FM2 layer is normally fixed to act as a sensor, ϕ_{FM2} is assumed to be very close to 0 unless otherwise stated. (b–d) show TMR experiments where the field is applied in the OOP direction in 10×10 , 20×20 and $30 \times 30 \mu\text{m}^2$ junctions respectively, showing the field-induced transition into the nonvolatile OOP state. The right vertical axes indicate the parallel (P), antiparallel (AP) and OOP states for each junction, marked with dotted lines. The inset sketches depict the proposed configuration of the two FM layers in the P (only shown in panel (d)), OOP and AP configurations of the spin valve stack.

surfaces of the soft Fe(001) layer due to the growth process. This differently affects the top and bottom surface anisotropies, which leads to different intensities at each interface resulting in the magnetisation being more easily reoriented into the OOP configuration for one field direction than the other. This asymmetric field behaviour might seem at odds with the Stoner–Rashba model developed in Ref.²⁷. This model suggests that a net Rashba field related to the asymmetric top and bottom interfaces of a ferromagnetic film leads to a pseudo-dipolar contribution to the anisotropy, which would mainly favor an in-plane magnetisation and an uniaxial-like anisotropy favouring the/a perpendicular magnetisation configuration. Correspondingly, the hysteresis curve of a single magnetic (here Fe) layer is expected to be an even function with respect to the external magnetic field. However, we note that the model does not fully account for the complexities discussed below that could lead to the asymmetric hysteresis we observe in our multilayer structures.

The fact that the hysteresis curve is not an even function of the external magnetic field is simply related to the fact that the model is developed for a single ferromagnetic layer while in our complex heterostructure, we do not reverse the Fe/Co interface magnetisation. This is not unreasonable considering a large interface anisotropy. A full magnetisation reversal including interfacial magnetisation would only result in an asymmetric hysteric response. Secondly, in our structures stray fields play a relevant/crucial/central role and importantly the stray fields seen by both interfaces are not similar. The bottom interface experiences the stray field of the Fe/Co top bilayer, while the top interface sees the contribution from the bottom Fe layer. In a macrospin model, increasing the stray fields would decrease the perpendicular anisotropy. To fully understand the complexities of the asymmetric magnetisation response, future studies such as direct OOP magnetisation measurements on the MgO/Fe/MgO structures in the absence of the sensing Fe/Co and V/MgO layers, could be performed.

It is worth mentioning a distinct feature of our junctions, having a strongly preferred IP magnetisation at room temperature⁸, with the OOP configuration of the soft 10 nm Fe layer only becoming non-volatile below 80 K. In the temperature range in which this study takes place (0.3 to 7 K), the magnetic field required to induce an OOP transition in the soft layer does not typically exceed 2 kOe. These relatively low values (with respect to continuous 10 nm thick Fe films) could be explained by the combined influence of a few factors. Firstly, the variation of the relation between the IP and OOP anisotropy energies could vary with temperature, possibly favouring

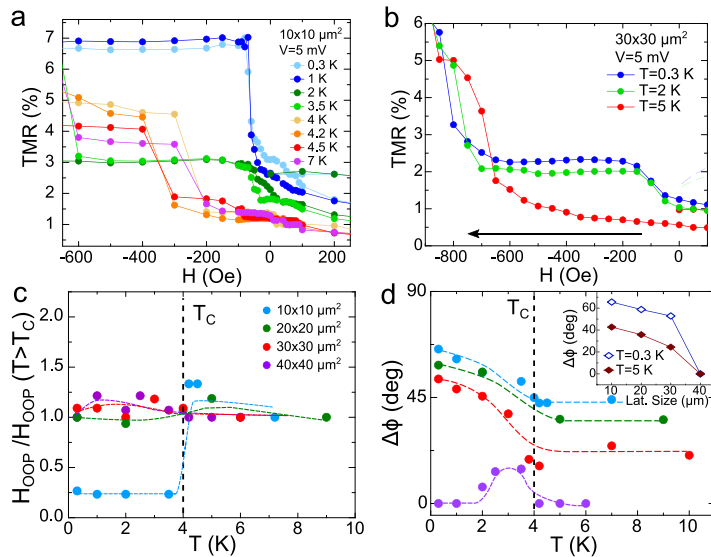


Figure 2. (a) Field induced OOP magnetisation transition in a $10 \times 10 \mu\text{m}^2$ SC/FM1/FM2 junction at different temperatures from above to below T_C . A strong reduction of H_{OOP} takes place below T_C . (b) Shows a similar experiment in a $30 \times 30 \mu\text{m}^2$ junction. In this case, some increasing in the low field TMR is observed, but not enough to be attributed to a complete OOP reorientation. (c) Temperature dependence of the normalized H_{OOP} anisotropy field for junctions with four different lateral sizes. (d) Represents the temperature dependence of the misalignment angle between the two FM layers ($\Delta\phi = \phi_{\text{FM1}} - \phi_{\text{FM2}}$, calibrated following the procedure outlined in Ref.⁷) at zero field for the four different sized samples, using the same color legend as in (c). The inset shows a comparison of the zero field $\Delta\phi$ angle at $T = 5 \text{ K}$ (above T_C) and at $T = 0.3 \text{ K}$ (well below T_C) as a function of the samples' lateral size. The gradual decrease of the zero-field angle above T_C with increasing lateral size points towards a small equilibrium initial angle already existing in the normal state, which we attribute to competing OOP and IP anisotropies. When superconductivity develops below T_C , an additional magnetisation reorientation is observed in all except the bigger samples. The colored dashed lines are guides for the eyes, while the vertical, black, dashed lines indicate the critical temperature.

the OOP configuration at low temperatures²⁸. Secondly, interfacial strain has also demonstrated the potential to induce changes in the perpendicular anisotropy in thin ferromagnetic films²⁹. Thirdly, the IP saturation in this study was carried out with a field of 3 kOe. This value was considered sufficiently high since the resistance values were stable above 1 kOe, but it could be insufficient to induce a perfect IP alignment at low temperatures. This factor could be more relevant for the smallest junctions where edge magnetic charges would have a relatively higher influence on the measured OOP switching field, qualitatively explaining the dependence of this field with the junctions lateral size, as supported by numerical simulations (see Supplementary Material Fig. S5). Finally, as mentioned before, as long as we measure the total resistance of the junction, we can't exclude that the OOP reorientation might take place preferentially in the atomic layers closer to the Fe/MgO interface (where it would be easier to reorient the magnetic moments due to the surface anisotropy). Thus, the surface OOP state (with a thickness of a few nm, close to that of the Fe magnetic exchange length³⁰) might be realized with the aid of interface anisotropy at the Fe/MgO interface and an external OOP magnetic field. This is shown in the sketches of the spin valve configuration in Fig. 1b–d.

Superconductivity induced change of the out-of-plane anisotropy field. Figure 2a shows the temperature dependence of OOP TMRs in a $10 \times 10 \mu\text{m}^2$ junction, in a field range where the field-induced magnetisation reorientation of the FM1 layer (measured at 5 mV) takes place. A decrease of the characteristic H_{OOP} field (defined as the applied magnetic field providing a complete OOP reorientation of the FM1 layer) just below T_C can be observed upon lowering the temperature, as represented in Fig. 2c. We note that the SC-induced full IP-OOP transitions have been clearly observed in the smallest $10 \times 10 \mu\text{m}^2$ lateral size junctions. The larger junctions showed a small low field TMR increase below T_C , which could be interpreted either as a partial FM1 layer reorientation or an inhomogeneous OOP alignment (Fig. 2b). For the $20 \times 20 \mu\text{m}^2$ and larger junctions,

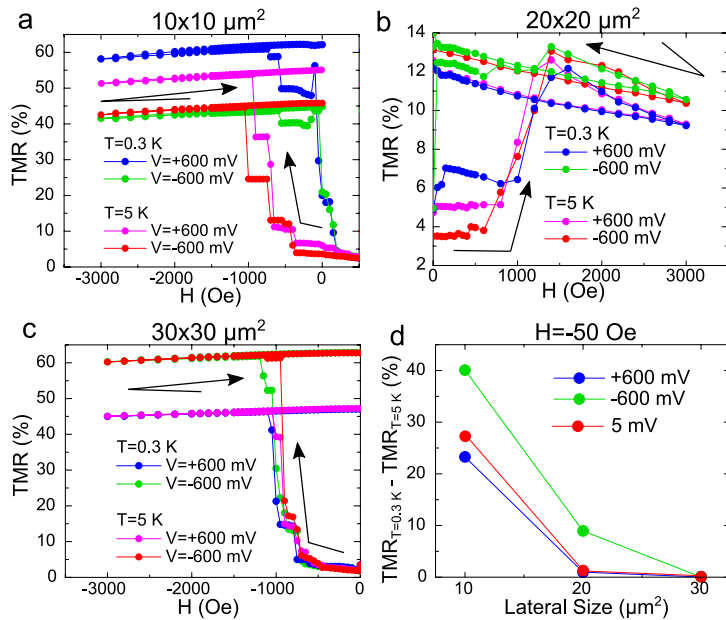


Figure 3. Influence of the electric field on the magnetisation reorientation transition H_{OOP} , above ($T = 5$ K) and below T_C ($T = 0.3$ K). The transition is shown for an applied bias of 600 mV (electric field of about 2.5×10^8 V/m), with both positive and negative polarities, for samples with varying lateral sizes: (a) $10 \times 10 \mu\text{m}^2$, (b) $20 \times 20 \mu\text{m}^2$ and (c) $30 \times 30 \mu\text{m}^2$. (d) shows the difference of TMR with temperature (calculated as $\text{TMR}_{0.3\text{K}} - \text{TMR}_{5\text{K}}$) for both polarities and in the absence of applied electric field ($V = 5$ mV) as a function of the lateral size, for an applied field of $H = -50$ Oe. The superconducting transition seems to have bigger effects on the magnetic OOP reorientation for smaller samples.

the H_{OOP} anisotropy field turned out to be nearly independent of temperature (Fig. 2c). Interestingly, our junctions also revealed spontaneous zero field TMR emerging below T_C (corresponding to a *partial* magnetic reorientation of the soft FM1 layer), which is more pronounced for the smaller samples and diminishes with lateral size, abruptly disappearing for the largest junctions. This is shown in Fig. 2d, where instead of the TMR, the calculated angle between the two FM layer is plotted. It is worth noting that this relative angle calculation is similar to our previous work^{8,9}, and assumes a uniform magnetisation in the whole FM layer. However, the real scenario could be more complex (see Supplementary Material, S2.1).

Influence of electric field on the out-of-plane reorientation. The presence of the MgO barriers allows us to explore the possible influence of high electric fields on the magnetic-field-induced IP-OOP transitions above and below T_C . High electric field influences the PMA anisotropy by modifying the SOC Rashba field in magnetic tunnel junctions²⁷. Our previous study⁸ revealed that roughly two thirds of the voltage drop in our junctions occurs at the V/MgO/Fe barrier, resulting in a high electric field across this interface. The remaining voltage drops at the Fe/MgO/Fe interface, which is responsible for the change in the resistance providing the measured TMR depending on the relative magnetic configuration of the two FM layers.

We have therefore investigated the influence of high bias and its polarity on the IP-OOP transition in junctions with different lateral sizes. Figure 3a–d show that an applied bias of 600 mV (generating an electric field at the V/MgO/Fe interface exceeding 2×10^8 V/m) hardly affects H_{OOP} above T_C , independently of the junctions size. Moreover, the application of a large electric field has also a negligible effect on the superconductivity-induced IP-OOP transition in the larger than $30 \times 30 \mu\text{m}^2$ junctions, with a dominant IP magnetisation alignment (Fig. 3c). However this changes for the smaller junctions, where IP and OOP anisotropy values are comparable leading to an entirely different behaviour. Strikingly, we observe that for $10 \times 10 \mu\text{m}^2$ and $20 \times 20 \mu\text{m}^2$ junctions, the electric field stimulates an IP-OOP transition below T_C at very small values of the applied magnetic field (below 100 Oe).

Figure 3d compares the influence of an electric bias close to 600 mV with different polarities on the magnetisation alignment below T_C (0.3 K) with an applied magnetic field of -50 Oe, within the field range in which

we observed a larger influence of the electric field on the IP-OOP transition for the smaller junctions. This field is about an order of magnitude below the first critical field of our Vanadium films, which was estimated to be close to 400 Oe²², therefore minimizing the presence of vortices in the superconducting layer. We believe that the electric field effect asymmetry could be due to the combined influence of the relatively more dominant proximity effects between the SC and FM states at the V/MgO/Fe interface in smaller junctions, and the electric-field-induced variation of the Rashba field influencing the OOP anisotropy for the non-equivalent interfaces MgO/Fe and Fe/MgO in the junctions²⁷.

Discussion

Evaluation of magnetostatic coupling between superconducting vortices and ferromagnet.

Let us start our discussion by considering different scenarios involving the possible magnetostatic coupling between the superconducting vortices and the ferromagnet³¹. It is tempting to consider the device edges as mainly responsible for the superconductivity-induced spin reorientation, as the edge has a more important contribution for the smallest samples, in which the minimum applied field is enough to fully reorient the magnetisation. However, a few experimental facts contradict this scenario. Firstly, the superconductivity-induced additional zero field OOP angle variation is similar for 10×10 to $30 \times 30 \mu\text{m}^2$ junctions (see inset in Fig. 2d), which would not be the case if the change comes from the device's edges. The superconductivity induced spin reorientation effect abruptly diminishes for the $40 \times 40 \mu\text{m}^2$ junction only (Fig. 2d). Secondly, numerical simulations show that the OOP reorientation due to magnetostatic coupling, if relevant, could potentially be triggered by the nucleation of OOP domains in the interior of the samples rather than at the edges; even if we assume the edges as the initial OOP nucleation places, the resulting vortex distribution would affect the whole FM layer (see Supplementary Material S2.1). Finally, electric field stimulates the OOP transition for relatively small junctions with competing anisotropies (see Fig. 3) which points towards the possible role of the Rashba field.

We have seen from micromagnetic simulations and as an experimental trend that, on average, the normal state H_{OOP} increases with the junctions area (Supplementary Material S2.3). This is in agreement with the gradual decrease of the partial OOP magnetisation reorientation with increasing lateral size seen in the normal state, just above the critical temperature (see Fig. 2d). Within the above picture, a lower H_{OOP} field is required to reorient the magnetisation perpendicularly in the smallest junctions, and therefore one would expect a weaker magnetostatic coupling to SC vortices.

Numerical simulations of the magnetostatic interaction of the V/MgO/Fe system during an OOP TMR experiment such as the ones shown in Fig. 1, where a varying OOP magnetic field is applied, is a complex problem which requires self-consistent treatment of the interaction between magnetic charges and stray fields of superconducting vortices³². The Supplementary Material (Sect. 2.1) introduces a simplified simulation scheme which evaluates this interaction in the presence of the Meissner effect. These results show that the vortex-mediated magnetostatic interaction might only explain a weak enhancement of H_{OOP} in the superconducting state in the largest junctions (Fig. 2c). However, we note that varying the superconducting hysteresis strength or width in the magnetostatic simulations could not explain the strong decrease of H_{OOP} below T_C which was experimentally observed in the smaller junctions. Moreover, a dominant magnetostatic coupling would contradict the observed influence of electric field on TMR below T_C for the smallest junctions (Figs. 2, 3).

Microscopic model. To explain the strong decrease in the OOP anisotropy field below T_C for the smallest junctions and the superconductivity-induced zero field magnetic reorientation in all except the largest ones, as well as the influence of the SOC strength through the application of an electric field, we present a microscopic model describing the observed superconductivity-assisted OOP magnetic reorientation. In heterostructures consisting of superconducting and magnetic layers, the superconducting condensate is weakened as Cooper pairs leak into the magnetic regions³³. This leakage is more efficient when the spin-singlets are transformed into equal-spin triplet pairs polarized along the same axis as the magnetisation. In our system, the MgO layer boosts the Rashba SOC at the SC/FM interface allowing for a generation of equal-spin triplets that depends on the orientation of the magnetisation with respect to the interface^{10,20}.

To show how the efficiency of the triplet leakage affects the critical field for reorienting the magnetisation OOP, we calculate the free energy of the system from a tight-binding Bogoliubov–de Gennes (BdG) Hamiltonian (see Sect. 3 in the Supplementary Material for a complete description of our method). The V/MgO/Fe structure is modelled as a cubic lattice with electron hopping between neighboring sites. We include conventional *s*-wave on-site superconducting pairing potential in the V layer, Rashba SOC in the MgO layer, and an exchange splitting between spins in the Fe layer. Although this model is valid in the ballistic limit, we expect similar results for diffusive materials since spin singlets are partially converted into odd-frequency *s*-wave triplets that are robust to impurity scattering. Moreover, the variation in the singlet population under IP to OOP reorientation of the magnetisation have previously been demonstrated both experimentally and by dirty limit calculations³⁰.

The free energy determined from this model captures the contribution from the superconducting proximity effect, and also includes a normal-state contribution favoring an IP magnetisation. In addition, we include a normal-state anisotropy $K_{\text{IP}}[1 - \cos^4(\Phi_{\text{FM}})] + K_{\text{OOP}}[1 - \sin^2(\Phi_{\text{FM}})]$, where Φ_{FM} ranges from 0° (corresponding to an IP magnetisation of the soft ferromagnet) to 90° (OOP magnetisation). In total this gives a normal-state anisotropy favoring an IP magnetisation, with an additional local minimum for the OOP magnetisation direction. Here we only focus on the superconductivity-assisted deepening of these OOP quasi-minima associated with the spin singlet to spin triplet conversion. The increase in H_{OOP} below T_C discussed in the previous section is not covered by this theoretical framework, as it does not take into account formation of vortices or the size of the junction. The discussion here is therefore relevant to the smaller junctions where the superconductivity-assisted decrease in H_{OOP} dominates.

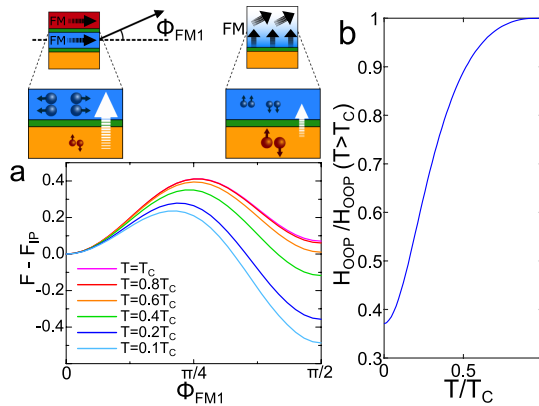


Figure 4. When the magnetisation of the soft ferromagnet is rotated from a parallel to an OOP alignment with respect to the hard ferromagnet, as sketched above (a) (In the upper right part, only the part of the soft FM layer closer to the V is depicted, not to scale, in order to show the possible magnetisation configuration. In the theoretical modelling the magnetisation is considered to be uniform for simplicity, although, as mentioned before, experimentally the magnetisation reorientation is more likely to happen only close to the interface. The FM2 layer is considered to be fixed with an IP orientation), the SOC assisted conversion (white arrows) of singlet Cooper pairs (orange) into equal-spin triplets (blue) is at its minimum for the OOP orientation. The superconducting condensate is therefore stronger when the magnetisation is OOP, causing a decrease in the OOP free energy as the temperature is decreased below T_C (panel a)). The deepening of the OOP minimum causes a decrease in H_{OOP} (b)). In (a), $K_{IP} = 1.5$ and $K_{OOP} = 1.6$, while in (b) $K_{anis} = 0.8$ favoring the IP orientation. The free energy is scaled by the hopping parameter t . For further details about the parameters used in the BdG calculations, see Sect. 3 in the Supplementary Material.

In Fig. 4a), we demonstrate how the local free energy minimum for an OOP magnetisation deepens as the temperature is decreased below T_C . As a simple qualitative model, we calculate the external magnetic field that can be used to force the magnetisation into the OOP orientation as $H_{OOP} = (K_{anis} + F_{OOP} - F_{IP})/\mu_0\mu_{tot}$, where μ_{tot} is the total magnetic moment, K_{anis} is a constant anisotropy favoring the IP orientation that includes the above mentioned parameters for the normal-state IP and OOP anisotropies, K_{IP} and K_{OOP} , as well as an energy barrier associated with the reorientation; and F_{OOP} and F_{IP} are the calculated free energies in the OOP and IP states of the soft layer respectively. In Fig. 4b, we show how H_{OOP} decreases below T_C as observed for the $10 \times 10 \mu\text{m}^2$ junction in Fig. 2c. We have thus demonstrated that the proximity effect enables a strong decrease in H_{OOP} that cannot be explained by the coupling of the ferromagnet to superconducting vortices discussed in the previous section. Moreover, since this variation in H_{OOP} requires that SOC is present, it also explains the dependence on the electric field observed for the smaller junctions (Fig. 3). The fact that H_{OOP} decreases over a longer temperature interval than in the experiments, rather than flattening out for low T , is caused by the downscaling of the lattice that is necessary in our theoretical model. In order to scale down the superconducting coherence length so that it remains comparable to the thickness of the superconducting layer, the on-site interaction must be increased, leading to a higher T_C . Since the temperature interval is larger, a smaller fraction of the temperatures exist in the low-temperature limit where the free energy is temperature independent. Keeping in mind that our measurements of H_{OOP} show a dependence on the magnitude of the Rashba SOC, we can conclude that the SOC induced change in magnetic anisotropy below T_C shown here must strongly contribute to the suppression in H_{OOP} for the $10 \times 10 \mu\text{m}^2$ junctions.

Conclusions

Our experiments point towards the superconductivity induced modification of the perpendicular magnetic anisotropy in the epitaxial Fe(001) films in the V(40 nm)/MgO(2 nm)/Fe(10 nm) system. The behaviour depends on the lateral dimensions of the junctions in the following way: First, for the smallest junctions, the magnetic field necessary for a full OOP magnetisation reorientation drops by an order of magnitude in the superconducting state, while for the rest of the junctions it varies only slightly. Second, in all but the largest junctions, an increase in the OOP misalignment angle between the soft Fe(10 nm) layer and the hard one is observed when the temperature is decreased below T_C without any applied field. This spontaneous reorientation is similar for 10×10 to $30 \times 30 \mu\text{m}^2$ junctions and disappears in the largest ones, suggesting that superconductivity could be affecting the competition between the IP and OOP anisotropies (which is more pronounced for the smaller junctions) rather than being the result of the reorientation taking place at the edges of the samples. The decreasing

of H_{OOP} transition field in the superconducting state, which could also be stimulated by the application of electric field changing the Rashba SOC, is consistent with the theoretical prediction¹⁰ of the absolute minimum of free energy corresponding to the OOP spin direction in SC/SOC/FM hybrids with competing (IP vs OOP) anisotropies just below T_C . The magnetostatic interaction between vortices and magnetic inhomogeneities could explain a weak hardening of the OOP transition in the largest junctions. A detailed theoretical analysis of the mutual interplay between the inhomogeneous magnetisation of the soft ferromagnet and the superconductor is, however, beyond the scope of this work. Our results open a route to active manipulation of perpendicular magnetic anisotropy in the expanding field of dissipation-free superconducting electronics involving spin^{34–36} or spin polarized supercurrents³⁷.

Methods

Samples growth and characterization. The V(40 nm)/MgO(2 nm)/Fe(10 nm)/MgO(2 nm)/Fe(10 nm)/Co(20 nm) MTJ multilayer stacks have been grown by molecular beam epitaxy (MBE) in a chamber with a base pressure of 5×10^{-11} mbar following the procedure described in Ref.³⁸. The samples were grown on (001) MgO substrates. A 10 nm thick seed of anti-diffusion MgO underlayer is grown on the substrate to trap the C from it before the deposition of the Fe (or V). The MgO insulating layer is then epitaxially grown by e-beam evaporation up to a thickness of approximately ~ 2 nm and the same process is then executed for the rest of the layers. Each layer is annealed at 450 °C for 20 min for flattening. After the MBE growth, all the MTJ multilayer stacks are patterned in micrometre-sized square junctions by UV lithography and Ar ion etching, controlled step-by-step in situ by Auger spectroscopy.

Experimental measurement methods. The measurements are performed inside a JANIS³ He³ cryostat (the minimum attainable temperature is 0.3 K). The magnetic field is varied using a 3D vector magnet consisting of one solenoid (Z axis) with $H_{\text{max}} = 3.5$ T and two Helmholtz coils (X and Y axis) with $H_{\text{max}} = 1$ T. In our system the different magnetic states can be distinguished by looking at the resistance, so the relative orientation between two electrodes can be measured. The magnetoresistance measurements are performed by first setting the magnetic field to the desired value, then applying positive and negative current up to the desired voltage (5 mV unless otherwise stated), and averaging the absolute values of the measured voltage for the positive and negative current, obtaining a mean voltage which is used to calculate the resistance at that point. The temperature is measured and controlled with a LakeShore 340 thermometer.

Received: 17 June 2021; Accepted: 30 August 2021

Published online: 24 September 2021

References

- Piramanayagam, S. N. Perpendicular recording media for hard disk drives. *J. Appl. Phys.* **102**, 011301 (2007).
- Dieny, B. & Chshiev, M. Perpendicular magnetic anisotropy at transition metal/oxide interfaces and applications. *Rev. Mod. Phys.* **89**, 025008 (2017).
- Chuang, T. C., Pai, C. F. & Huang, S. Y. Cr-induced perpendicular magnetic anisotropy and field-free spin-orbit-torque switching. *Phys. Rev. Appl.* **11**, 061005 (2019).
- Yi, D. *et al.* Enhanced interface-driven perpendicular magnetic anisotropy by symmetry control in oxide superlattices. *Phys. Rev. Appl.* **15**, 024001 (2021).
- Sun, J. Z. Resistance-area product and size dependence of spin-torque switching efficiency in CoFeB–MgO based magnetic tunnel junctions. *Phys. Rev. B* **96**, 064437 (2017).
- Challener, W. A. *et al.* Heat-assisted magnetic recording by a near-field transducer with efficient optical energy transfer. *Nat. Photonics* **3**, 220–224 (2009).
- Zhu, J.-G., Zhu, X. & Tang, Y. Microwave assisted magnetic recording. *IEEE Trans. Magn.* **44**(1), 125–131 (2008).
- Martinez, I., Tiusan, C., Hehn, M., Chshiev, M. & Aliev, F. G. Symmetry broken spin reorientation transition in epitaxial MgO/Fe/MgO layers with competing anisotropies. *Sci. Rep.* **8**, 9463 (2018).
- González-Ruano, C. *et al.* Superconductivity-induced change in magnetic anisotropy in epitaxial ferromagnet-superconductor hybrids with spin-orbit interaction. *Phys. Rev. B* **102**, 020405(R) (2020).
- Johnsen, L. G., Banerjee, N. & Linder, J. Magnetization reorientation due to superconducting transition in heavy metal heterostructures. *Phys. Rev. B* **99**, 134516 (2019).
- Banerjee, N., Robinson, J. W. A. & Blamire, M. G. Reversible control of spin-polarized supercurrents in ferromagnetic Josephson junctions. *Nat. Commun.* **5**, 4771 (2014).
- Baek, B., Rippard, W. H., Benz, S. P., Russek, S. E. & Dresselhaus, P. D. Hybrid superconducting-magnetic memory device using competing order parameters. *Nat. Commun.* **5**, 3888 (2014).
- Gingrich, E. C. *et al.* Controllable $0-\pi$ Josephson junctions containing a ferromagnetic spin valve. *Nat. Phys.* **12**, 564 (2016).
- Satchell, N. *et al.* Pt and CoB trilayer Josephson π junctions with perpendicular magnetic anisotropy. *Sci. Rep.* **11**, 11173 (2021).
- Bergeret, F. S., Volkov, A. F. & Efetov, K. B. Long-range proximity effects in superconductor-ferromagnet structures. *Phys. Rev. Lett.* **86**, 4096 (2001).
- Keizer, R. S. *et al.* Spin triplet supercurrent through the half-metallic ferromagnet CrO₂. *Nature* **439**, 825 (2006).
- Fominov, Ya. V. *et al.* Superconducting triplet spin valve. *JETP Lett.* **91**, 308 (2010).
- Leksins, P. V. *et al.* Evidence for triplet superconductivity in a superconductor-ferromagnet spin valve. *Phys. Rev. Lett.* **109**, 057005 (2012).
- Bergeret, F. S. & Tokatly, I. V. Singlet-triplet conversion and the long-range proximity effect in superconductor-ferromagnet structures with generic spin dependent fields. *Phys. Rev. Lett.* **110**, 117003 (2013).
- Banerjee, N. *et al.* Controlling the superconducting transition by spin-orbit coupling. *Phys. Rev. B* **97**, 184521 (2018).
- Satchell, N. & Birge, N. O. Supercurrent in ferromagnetic Josephson junctions with heavy metal interlayers. *Phys. Rev. B* **97**, 214509 (2018).
- Martinez, I. *et al.* Interfacial spin-orbit coupling: A platform for superconducting spintronics. *Phys. Rev. Appl.* **13**, 014030 (2020).

23. Dubonos, S. V., Geim, A. K., Novoselov, K. S. & Grigorieva, I. V. Spontaneous magnetization changes and nonlocal effects in mesoscopic ferromagnet-superconductor structures. *Phys. Rev. B* **65**, 220513(R) (2002).
24. Milošević, M. V. & Peeters, F. M. Interaction between a superconducting vortex and an out-of-plane magnetized ferromagnetic disk: Influence of the magnet geometry. *Phys. Rev. B* **68**, 094510 (2003).
25. Yang, H. X., Chshiev, M. & Dieny, B. First-principles investigation of the very large perpendicular magnetic anisotropy at Fe–MgO and Co–MgO interfaces. *Phys. Rev. B* **84**, 054401 (2011).
26. Nistor, L. E. *et al.* Oscillatory interlayer exchange coupling in MgO tunnel junctions with perpendicular magnetic anisotropy. *Phys. Rev. B* **81**, 220407(R) (2010).
27. Barnes, S. E., Ieda, J. & Maekawa, S. Rashba spin-orbit anisotropy and the electric field control of magnetism. *Sci. Rep.* **4**, 4105 (2014).
28. Wang, W. *et al.* Out-of-plane magnetic anisotropy enhancement in $\text{La}_{1-x}\text{Sr}_x\text{CoO}_{3-\delta}/\text{La}_{2/3}\text{Sr}_{1/3}\text{MnO}_3/\text{La}_{1-x}\text{Sr}_x\text{CoO}_{3-\delta}$ thin films. *Phys. Rev. B* **101**, 024406 (2020).
29. Wolloch, M. & Suess, D. Strain-induced control of magnetocrystalline anisotropy energy in FeCo thin films. *J. Magn. Magn. Mater.* **522**, 167542 (2021).
30. Abo, G. S. *et al.* Definition of magnetic exchange length. *IEEE Trans. Magn.* **49**, 8 (2013).
31. Fritzsche, J., Kramer, R. B. G. & Moshchalkov, V. V. Visualization of the vortex-mediated pinning of ferromagnetic domains in superconductor-ferromagnet hybrids. *Phys. Rev. B* **79**, 132501 (2009).
32. Niedzielski, B. & Berakdar, J. Controlled vortex formation at nanostructured superconductor/ferromagnetic junctions. *Phys. Status Solidi B* **257**, 7 (2019).
33. Eschrig, M. Spin-polarized supercurrents for spintronics: A review of current progress. *Rep. Prog. Phys.* **78**, 104501 (2015).
34. Palermo, X. *et al.* Tailored flux pinning in superconductor-ferromagnet multilayers with engineered magnetic domain morphology from stripes to skyrmions. *Phys. Rev. Appl.* **13**, 014043 (2020).
35. Shafraniuk, S. E., Nevirkovets, I. P. & Mukhanov, O. A. Modeling computer memory based on ferromagnetic/superconductor multilayers. *Phys. Rev. Appl.* **11**, 064018 (2019).
36. Golod, T., Kapran, O. M. & Krasnov, V. M. Planar superconductor-ferromagnet-superconductor Josephson junctions as scanning-probe sensors. *Phys. Rev. Appl.* **11**, 014062 (2019).
37. Jeon, K.-R. *et al.* Effect of Meissner screening and trapped magnetic flux on magnetization dynamics in thick Nb/Ni₈₀Fe₂₀/Nb trilayers. *Phys. Rev. Appl.* **11**, 014061 (2019).
38. Tiusan, C. *et al.* Spin tunneling phenomena in single crystal magnetic tunnel junction systems. *J. Phys. Condens. Matter* **19**, 165201 (2007).

Acknowledgements

We acknowledge Antonio Lara and Miguel Granda for help with simulations and Yuan Lu for help in sample preparations. The work in Madrid was supported by Spanish Ministerio de Ciencia (RTI2018-095303-B-C55) and Consejería de Educación e Investigación de la Comunidad de Madrid (NANOMAGCOST-CM Ref. P2018/NMT-4321) Grants. F.G.A. acknowledges financial support from the Spanish Ministry of Science and Innovation, through the “María de Maeztu” Program for Units of Excellence in R&D (CEX2018-000805-M) and “Acción financiada por la Comunidad de Madrid en el marco del convenio plurianual con la Universidad Autónoma de Madrid en Línea 3: Excelencia para el Profesorado Universitario”. D.C. has been supported by Comunidad de Madrid by contract through Consejería de Ciencia, Universidades e Investigación y Fondo Social Europeo (PEJ-2018-AI/IND-10364). NB was supported by EPSRC through the New Investigator Grant EP/S016430/1. The work in Norway was supported by the Research Council of Norway through its Centres of Excellence funding scheme Grant 262633 QuSpin. C.T. acknowledges “EMERSPIN” grant ID PN-III-P4-ID-PCE-2016-0143, No. UEFISCDI: 22/12.07.2017 and “MODESKY” Grant ID PN-III-P4-ID-PCE-2020-0230 No. UEFISCDI: 4/04.01.2021. The work in Nancy was supported by CPER MatDS and the French PIA project “Lorraine Université d’Excellence”, reference ANR-15-IDEX-04-LUE.

Author contributions

F.G.A. and C.T. designed the junctions, and C.T. and M.H. fabricated the junctions. The measurements were performed by C.G.-R. with the participation of D.C. The modelling was developed by L.G.J. and J.L. Micro-magnetic and TDGL calculations have been carried out by D.C. and C.G.-R. F.G.A., C.G.-R., D.C., L.G.J., N.B. and J.L. analyzed the data and wrote the manuscript. All authors contributed to the study, discussed the results, commented and revised the manuscript. F.G.A. supervised the work.

Competing interests

The authors declare no competing interests.

Additional information

Supplementary Information The online version contains supplementary material available at <https://doi.org/10.1038/s41598-021-98079-5>.

Correspondence and requests for materials should be addressed to F.G.A.

Reprints and permissions information is available at www.nature.com/reprints.

Publisher’s note Springer Nature remains neutral with regard to jurisdictional claims in published maps and institutional affiliations.



Open Access This article is licensed under a Creative Commons Attribution 4.0 International License, which permits use, sharing, adaptation, distribution and reproduction in any medium or format, as long as you give appropriate credit to the original author(s) and the source, provide a link to the Creative Commons licence, and indicate if changes were made. The images or other third party material in this article are included in the article's Creative Commons licence, unless indicated otherwise in a credit line to the material. If material is not included in the article's Creative Commons licence and your intended use is not permitted by statutory regulation or exceeds the permitted use, you will need to obtain permission directly from the copyright holder. To view a copy of this licence, visit <http://creativecommons.org/licenses/by/4.0/>.

© The Author(s) 2021

Supplementary Material: Superconductivity assisted change of the perpendicular magnetic anisotropy in V/MgO/Fe junctions

César González-Ruano¹, Diego Caso¹, Lina G. Johnsen², Coriolan Tiusan^{3,4}, Michel Hehn⁴, Niladri Banerjee⁵, Jacob Linder², and Farkhad G. Aliev^{1,*}

¹Departamento Física de la Materia Condensada C-III, Instituto Nicolás Cabrera (INC) and Condensed Matter Physics Institute (IFIMAC), Universidad Autónoma de Madrid, Madrid 28049, Spain

²Center for Quantum Spintronics, Department of Physics, Norwegian University of Science and Technology, NO-7491 Trondheim, Norway

³Department of Physics and Chemistry, Center of Superconductivity Spintronics and Surface Science C4S, Technical University of Cluj-Napoca, Cluj-Napoca, 400114, Romania

⁴Institut Jean Lamour, Nancy Université, 54506 Vandoeuvre-les-Nancy Cedex, France

⁵Department of Physics, Loughborough University, Epinal Way, Loughborough, LE11 3TU, United Kingdom
*farkhad.aliev@uam.es

ABSTRACT

The Supplementary material contains information about the calibration and correction of the superconducting coils alignment with the IP and OOP axis of the samples; the numerical simulations performed to evaluate the influence of Meissner effect, vortex-stray field magnetostatic interaction, microscopic defects and lateral size on the OOP reorientation behaviour; and details about the theoretical model supporting the experimental findings.

1 Correction of the OOP field misalignment

In order to ensure that the magnetic field is perfectly aligned with respect to the FM layers, we calibrate the angle between the V/MgO/Fe plane and the magnetic field created by the vector magnet superconducting coils by performing sub-gap conductance measurements at $T = 0.3$ K for different field directions around each axis. Figure S1 describes the calibration process in detail. The results are robust throughout the studied samples, with a misalignment of 8 ± 1 degrees with respect to the X-axis superconducting coil, which is accounted for in the OOP experiments. There is no observed in-plane misalignment (Y and Z axis coils).

For the highest OOP-AP transition fields measured (about 2000 Oe as shown in Figure 1c in the main text), the uncertainty of 1 degree in the misalignment calibration for the X coil could result in an IP component of the applied field of 35 Oe, which is about 20 times smaller than the IP coercive field of the hard FM layer¹. Therefore, undesired IP field due to misalignment can be ruled out as an explanation for the observed AP transitions.

2 Numerical simulations

Micromagnetic simulations were carried out using the MuMax3² software in order to estimate (i) the possible influence of Meissner effect on the OOP transition dynamics, (ii) the role of magnetic inhomogeneities caused by defects on the volatility of the OOP magnetic state (characterized by the OOP to IP transition field, $H_{\text{OOP-IP}}$) and (iii) the OOP reorientation dynamics. Additional simulations of the OOP transition were performed varying the lateral size of the simulated samples, in order to contrast the results with the observed enhancement of the OOP transition field H_{OOP} with the junctions' lateral size. The following typical Fe magnetic parameters were implemented on the system: saturation magnetization $M_S = 2.13$ T (1.7×10^6 A/m), exchange stiffness $A_{\text{exch}} = 2.1 \times 10^{-11}$ J/m, damping $\alpha = 0.02$ and first order cubic anisotropy $K_{C1} = 4.8 \times 10^4$ J/m³. All simulations were made with $T = 0$ K. The simulation cells of the system were set at 128 for the IP components and at 16 for the OOP component. The lateral size of the simulated samples was $0.4 \times 0.4 \mu\text{m}^2$, with a thickness of 10 nm. The system was additionally surrounded by a vacuum box of an added 100 nm (50 nm on each side) and 3 nm on the top and bottom of the

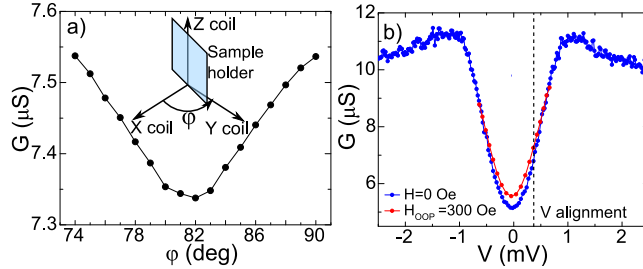


Figure 1. Calibration measurements for the X axis SC coil in a $20 \times 20 \mu\text{m}^2$ junction at $T = 0.3 \text{ K}$. (a) shows the conductance measured at $V = 0.3 \text{ mV}$, inside the SC gap, for different values of the ϕ angle (defined in the inset, which is a sketch of the sample holder situation with respect to the three SC coils). (b) shows two conductance curves at $H = 0$ and $H_{\text{OOP}} = 300 \text{ Oe}$. The dashed line indicates the applied voltage during the calibration process. When an OOP magnetic field is present, the SC gap diminishes and the conductance increases. The misalignment angle is therefore obtained as the one which minimizes the conductance ($\phi = 82 \text{ deg}$ in (a)).

sample, leaving the discretization size of the simulation at $3.9 \times 3.9 \times 1 \text{ nm}$. Higher discretization in the OOP direction has been chosen on purpose to observe the OOP effects with high accuracy in the simulations. Perpendicular magnetic anisotropy (PMA) was introduced on the top and bottom layers of the Fe as surface anisotropy, with a value of $K_{S1} = 8.32 \times 10^{-3} \text{ J/m}^2$. Due to computational limitations on the size and detail of the simulations, the results discussed in this section should be taken as qualitative support for the experimental results, rather than quantitative estimations.

2.1 Influence of Meissner effect on the OOP magnetization reorientation

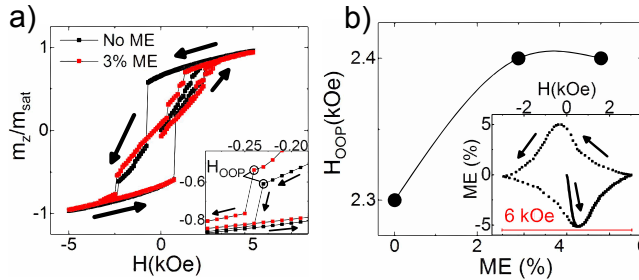


Figure 2. (a) Numerical simulations of the hysteresis loops reproducing the IP to OOP transition for different strengths of ME. (b) shows the simulated OOP transition field H_{OOP} as a function of the strength of the ME.

The influence of superconductivity on the OOP transition has been studied by performing micromagnetic simulations with MuMax3 for 10 nm thick, $0.4 \times 0.4 \mu\text{m}^2$ Fe(001) films under the influence of a superconducting vanadium layer. We simulated OOP hysteresis cycles where a correction to the applied field was added based on a typical Meissner effect (ME) hysteresis cycle (obtained from³, shown in Figure S2b inset), scaled for different values of field contribution from Meissner effect and adapted to the first and second critical fields of vanadium (correspondingly H_{c1} and H_{c2}). The contribution from superconducting vortices was taken into account by using an in-group developed program that numerically solves the time dependent Ginzburg-Landau equations in order to simulate the behaviour of type II superconductors under magnetic fields⁴. The initial stray fields from an in-plane saturated FM simulation were used to generate a distribution of vortices, and then the fields generated by those vortices were calculated⁵ and added into the corrected hysteresis cycle. Our simplified numerical

model, although limited, provides qualitative support for the mutual magnetostatic interaction between the FM and SC as the possible origin of the behaviour of the H_{OOP} field in the superconducting state. We also note that simulations with a contribution exceeding 7% of Meissner effect resulted in the OOP state being volatile in the hysteresis cycle (i.e. the magnetization returns to an IP configuration before returning to zero field), in contradiction with the experimental observations. Consequently, we have not considered larger contributions of Meissner effect as a possible explanation for the observed behaviour of H_{OOP} . We also underline that a complete numerical solution is a great challenge which is outside our current capabilities, as the problem should be solved self-consistently, so the results should be understood in a qualitative way.

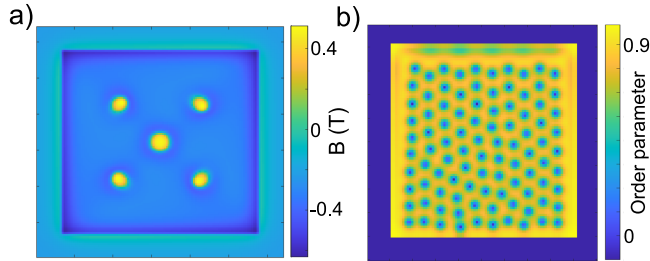


Figure 3. (a) Snapshot of the stray fields calculated in a micromagnetic simulation of a 0.4×0.4 micron Fe sample behaviour under OOP applied fields just before the OOP reorientation. Five domains can be observed with an OOP magnetization resulting in high stray fields, which trigger the reorientation in the rest of the film. (b) shows the stationary state reached in a superconducting simulation on a 0.4×0.4 micron vanadium layer at $T = 2$ K when stray fields are present at the edges of the sample. The vortices fill the interior of the film, which would result in higher OOP fields affecting the neighbouring FM layer and therefore triggering the OOP reorientation.

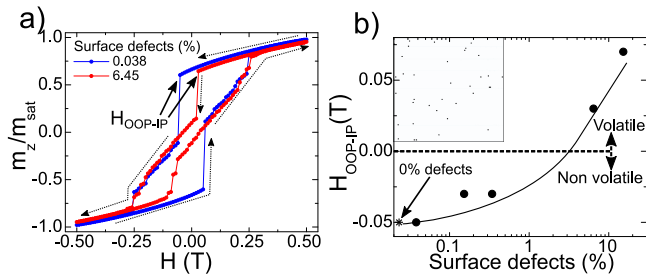


Figure 4. Influence of defects on the spin reorientation transition. (a) shows two OOP hysteresis cycles with different amounts of surface defects. The OOP-IP transition field is indicated by solid line black arrows, while the arrows with dotted lines mark the direction of the cycle. (b) plots the transition field $H_{\text{OOP-IP}}$ against the % of simulated defects (in log scale). An asterisk has been manually added with the transition field for the simulation with no defects. For simulations with more than 1% of defects, the OOP-IP transition becomes volatile (i.e. it happens before the field changes from positive to negative), in contradiction with the experimental results. The solid line is a guide for the eye, while the inset shows an example image of the surface defects introduced.

Another concern about the OOP reorientation is the possibility of it being a trivial effect produced at the edges of the FM layers. As mentioned in the main text, there is experimental evidence pointing against this possibility. However, a more thorough study has been performed in order to fully discard this scenario. First, we simulated the field-induced OOP reorientation in 0.4×0.4 micron Fe films. As shown in figure S3a, the reorientation seems to be triggered by OOP oriented domains in the

interior of the film.

On the other hand, we wanted to see the influence of any possible dominating edge effects on the underlying SC layer. Simulations of 0.4×0.4 micron V films were made using the code for type II superconductors described above at $T = 2$ K, with OOP magnetic fields applied at the edges of the simulated samples. As shown in figure S3b, the stationary state is reached when vortices fill the interior of the film. This would produce high OOP stray fields affecting the interior of the Fe layer, triggering a reorientation in the whole film rather than limiting it to the edges.

2.2 Influence of defects on the OOP-IP magnetization reorientation

In order to better understand the experimentally observed non-volatility of the OOP state in the junctions, we have simulated numerically the influence of randomly distributed surface magnetization defects within the bottom and top layers of the 10 nm thick Fe layer. The defects are introduced in the simulations as spots of enhanced surface saturation magnetization ($M_S(\text{defects}) = 1.25 \times M_S(\text{Fe})$). We have found that the introduction of a small number (about $10^{-3}\%$) of magnetic defects per layer does not affect the non-volatility, but only varies the characteristic field $H_{\text{OOP-IP}}$ of the transition from the OOP state to the IP alignment that takes place after the initial magnetization saturation (Figure S4). Above some critical defect number of about $2 \times 10^{-3}\%$ defects per layer the OOP-IP transition becomes volatile. As long as we always observe experimentally non-volatility of this transition in our junctions, we can conclude that there is a relatively small number of magnetic defects present in the epitaxial MTJs under study.

2.3 Dependence of H_{OOP} with the junctions lateral size

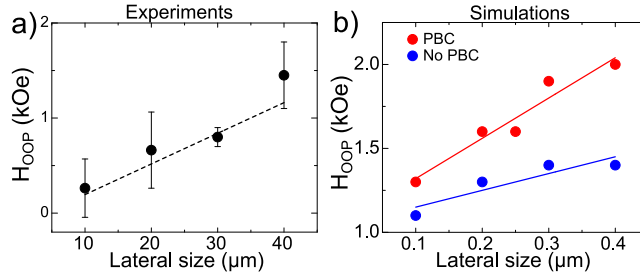


Figure 5. Dependence of the OOP transition field with the lateral size of the junctions. (a) shows experimental results, with the error bars corresponding to the standard deviation of the measured samples for each size. (b) shows the transition field for micromagnetic simulations of different lateral sizes. Note that, due to computational limitations, the simulated sizes are smaller than the actual samples. However, the trend is in qualitative agreement with the experimental results. The lines are linear fittings of the experimental/simulation points, which should serve as guides for the eyes. This trend is accomplished both with or without considering periodic boundary conditions (PBC).

The behaviour of the OOP transition field H_{OOP} has been studied as a function of the samples lateral size, in a total of 14 different samples varying from 10×10 to $40 \times 40 \mu\text{m}^2$. We found an increasing trend of H_{OOP} with the lateral size, as shown in Figure S5a. Micromagnetic simulations of the same transition have been performed in Fe films with lateral sizes of 0.1×0.1 to $0.4 \times 0.4 \mu\text{m}^2$ (as the real dimensions were computationally prohibitive to simulate) with a qualitative agreement to the experimental results, as shown in Figure S5b. These simulations have been made in the absence of previously discussed phenomena such as defects or Meissner effect.

3 Bogoliubov–de Gennes theoretical model

In order to demonstrate how the superconducting proximity effect can cause a change in the magnetic anisotropy, we consider a tight-binding Bogoliubov–de Gennes model for the V/MgO/Fe heterostructure. This model enables us to calculate the free energy of the system, so that we can study how the energy cost for reorienting the magnetization changes with temperature. We here only focus on the superconductivity-induced decrease in H_{OOP} observed for $10 \times 10 \mu\text{m}$ junctions. Vortex formation and the size of the lattice is not taken into account here, and instead discussed in section S2.1 and in the microscopic model section

in the main text. For the microscopic model of the V/MgO/Fe heterostructure, we consider the Hamiltonian

$$H = -t \sum_{\langle i,j \rangle, \sigma} c_{i,\sigma}^\dagger c_{j,\sigma} - \sum_{i,\sigma} (\mu_i - V_i) c_{i,\sigma}^\dagger c_{i,\sigma} - \sum_i U_i n_{i,\uparrow} n_{i,\downarrow} + \sum_{i,\alpha,\beta} c_{i,\alpha}^\dagger (h_i \cdot \sigma)_{\alpha,\beta} c_{i,\beta} - \frac{i}{2} \sum_{\langle i,j \rangle, \alpha,\beta} \lambda_i c_{i,\alpha}^\dagger (\sigma \times d_{i,j})_{\alpha,\beta} c_{j,\beta}. \quad (1)$$

The first term describes the nearest-neighbor hopping, where t is the hopping integral. The second term describes the chemical potential μ_i at each lattice site i , and the potential barrier $V_i > 0$ present in the insulating MgO layers. The third term gives rise to an attractive on-site interaction in the superconducting V layer described by the onsite potential $U_i > 0$. The fourth term introduces a local magnetic exchange field h_i giving rise to ferromagnetism in the Fe layer. The Pauli matrices are contained in the vector σ . The last term describes the Rashba spin-orbit coupling boosted by the MgO layers, where the spin-orbit field has a magnitude λ_i and is directed along the interface normal n . The vector $d_{i,j}$ connects site i and j . In the above Hamiltonian, $c_{i,\sigma}^\dagger$ and $c_{i,\sigma}$ are the second-quantization electron creation and annihilation operators at site i with spin σ , and $n_{i,\sigma} \equiv c_{i,\sigma}^\dagger c_{i,\sigma}$ is the number operator. The superconducting term is treated by a mean-field approach assuming that $c_{i,\uparrow} c_{i,\downarrow} \approx \langle c_{i,\uparrow} c_{i,\downarrow} \rangle + \delta$, where terms to the second order in the fluctuations δ are negligible. The superconducting gap is defined as $\Delta_i \equiv U_i \langle c_{i,\uparrow} c_{i,\downarrow} \rangle$ and must be treated self-consistently. The above model is valid in the ballistic limit, but since the effects considered here depend on the formation of s -wave odd-frequency triplets that are robust to impurity scattering we would obtain qualitatively the same results in the diffusive limit.

We consider a cubic lattice of size $N_x \times N_y \times N_z$ with an interface normal along the x axis. We assume periodic boundary conditions in the y and z directions, and apply the Fourier transform

$$c_{i,\sigma} = \frac{1}{\sqrt{N_y N_z}} \sum_k c_{i,k,\sigma} e^{i(k \cdot i_{\parallel})} \quad (2)$$

along these axes. To simplify notation we have defined $i \equiv i_x, j \equiv j_x, i_{\parallel} = (i_y, i_z)$, and $k \equiv (k_y, k_z)$. We also use that

$$\frac{1}{N_y N_z} \sum_{i_{\parallel}} e^{i(k-k') \cdot i_{\parallel}} = \delta_{k,k'}. \quad (3)$$

The Hamiltonian can be written on the form

$$H = H_0 + \frac{1}{2} \sum_k W_k^\dagger H_k W_k, \quad (4)$$

where the basis is given by

$$W_k^\dagger = [B_{1,k}^\dagger, \dots, B_{N_x,k}^\dagger], \quad B_{i,k}^\dagger = [c_{i,k,\uparrow}^\dagger, c_{i,k,\downarrow}^\dagger, c_{i,-k,\uparrow}, c_{i,-k,\downarrow}], \quad (5)$$

and where the Hamiltonian matrix H_k consists of $N_x \times N_x$ blocks

$$H_{i,j,k} = \varepsilon_{i,j,k} \hat{\tau}_3 \hat{\sigma}_0 + \delta_{i,j} \left[i \Delta_i \hat{\tau}^+ \hat{\sigma}_y - i \Delta_i \hat{\tau}^- \hat{\sigma}_y + h_i^x \hat{\tau}_3 \hat{\sigma}_x + h_i^y \hat{\tau}_0 \hat{\sigma}_y + h_i^z \hat{\tau}_3 \hat{\sigma}_z - \lambda_i \sin(k_y) \hat{\tau}_0 \hat{\sigma}_z + \lambda_i \sin(k_z) \hat{\tau}_3 \hat{\sigma}_y \right], \quad (6)$$

with row and column indices (i, j) . Above, $\hat{\tau}_i \hat{\sigma}_j \equiv \hat{\tau}_i \otimes \hat{\sigma}_j$ is the Kronecker product of the Pauli matrices spanning Nambu and spin space, $\hat{\tau}^\pm \equiv (\hat{\tau}_1 \pm i \hat{\tau}_2)/2$, and

$$\varepsilon_{i,j,k} \equiv -2t [\cos(k_y) + \cos(k_z)] \delta_{i,j} - t (\delta_{i,j+1} + \delta_{i,j-1}) - (\mu_i - V_i) \delta_{i,j}. \quad (7)$$

The constant term is given by

$$H_0 = - \sum_{i,k} \{ 2t [\cos(k_y) + \cos(k_z)] + \mu_i - V_i \} + N_y N_z \sum_i \frac{|\Delta_i|^2}{U_i}. \quad (8)$$

By diagonalizing H_k , we obtain eigenvalues $E_{n,k}$ and eigenvectors

$$\Phi_{n,k}^\dagger = [\phi_{1,n,k}^\dagger, \dots, \phi_{N_x,n,k}^\dagger], \quad \phi_{i,n,k}^\dagger = [u_{i,n,k}^* v_{i,n,k}^* w_{i,n,k}^* x_{i,n,k}^*]. \quad (9)$$

The diagonalized Hamiltonian can be written as

$$H = H_0 - \frac{1}{2} \sum_{n,k} E_{n,k} + \sum_{n,k} E_{n,k} \gamma_{n,k}^\dagger \gamma_{n,k}, \quad (10)$$

where the marked sum goes over $\{n, k_y, k_z > 0\}$, $\{n, k_y > 0, k_z = 0, -\pi\}$, and $\{n$ corresponding to $E_{n, k_y, k_z} > 0, k_y = 0, -\pi, k_z = 0, -\pi\}$. Expectation values of the new operators can now be evaluated according to

$$\langle \gamma_{n,k}^\dagger \gamma_{m,k} \rangle = f(E_{n,k}) \delta_{n,m}, \quad \langle \gamma_{n,k}^\dagger \gamma_{m,k}^\dagger \rangle = \langle \gamma_{n,k} \gamma_{m,k} \rangle = 0, \quad (11)$$

where $f(E_{n,k})$ is the Fermi-Dirac distribution. The new quasi-particle operators are related to the old operators by

$$c_{i,k,\uparrow} = \sum_n u_{i,n,k} \gamma_{n,k}, \quad c_{i,k,\downarrow} = \sum_n v_{i,n,k} \gamma_{n,k}, \quad c_{i,-k,\uparrow}^\dagger = \sum_n w_{i,n,k} \gamma_{n,k}, \quad c_{i,-k,\downarrow}^\dagger = \sum_n x_{i,n,k} \gamma_{n,k}. \quad (12)$$

The eigenenergies $E_{n,k}$ and eigenvectors $\Phi_{n,k}$ obtained in this diagonalization, can be used to calculate physical observables for the system. The superconducting gap is given by

$$\Delta_i = \frac{U_i}{N} \sum_{n,k} \{u_{i,n,k} x_{i,n,k}^* [1 - f(E_{n,k})] + v_{i,n,k} w_{i,n,k}^* f(E_{n,k})\}, \quad (13)$$

and is treated self-consistently.

We can calculate the critical field H_{OOP} for reorienting the magnetization from an IP to an OOP orientation. The Zeeman energy of an external magnetic field H is given by

$$F_{\text{Zeeman}} = -\mu_0 \mu_{\text{tot}} \cdot H, \quad (14)$$

where μ_0 is the vacuum permeability, μ_{tot} is the total magnetic moment, and H is the applied field. If we consider a system where the free energy is minimal for an IP magnetization and maximal for an OOP magnetization, and we want to find the external magnetic field needed to reorient the magnetization to the OOP direction, we must require that $|F_{\text{Zeeman}}| \geq F_{\text{OOP}} - F_{\text{IP}}$. We can then calculate the critical field from

$$H_{\text{OOP}} = \frac{F_{\text{OOP}} - F_{\text{IP}}}{\mu_0 \mu_{\text{tot}}}. \quad (15)$$

To take into account other anisotropy contributions not covered by this model, we let $F_{\text{OOP}} \rightarrow F_{\text{OOP}} + K_{\text{anis}}$. Above, the free energy is given by

$$F = H_0 - \frac{1}{2} \sum_{n,k} E_{n,k} - \frac{1}{\beta} \sum_{n,k} \ln(1 + e^{-\beta E_{n,k}}), \quad (16)$$

where $\beta = (k_B T)^{-1}$. The total magnetic moment of the system for an OOP magnetization is given by

$$\mu_{\text{tot}} = -2\mu_B \sum_{i,n,k} \{ \text{Re}(u_{i,n,k}^* v_{i,n,k}) f(E_{n,k}) + \text{Re}(x_{i,n,k}^* w_{i,n,k}) [1 - f(E_{n,k})] \}, \quad (17)$$

when the interface normal is directed along the x axis.

Since the lattice must be scaled down in order to make the system computationally manageable, we choose the magnitude of the on-site coupling potential U_i so that the superconducting coherence length is comparable to the thickness of the V layer. The superconducting coherence length is given by $\xi = \hbar v_F / \pi \Delta_0$, where $v_F = (1/\hbar) dE_k / dk|_{k=k_F}$ is the Fermi velocity calculated for the normal-state eigenenergy $E_k = -2t[\cos(k_x) + \cos(k_y) + \cos(k_z)] - \mu$, and Δ_0 is the zero-temperature superconducting gap.

We determine the superconducting critical temperature by a binomial search, where we decide if a given temperature is above or below T_C . This is decided by finding whether the superconducting gap measured in the middle of the superconducting region increases towards a superconducting solution or decreases towards a normal state solution from the initial guess $\Delta \ll \Delta(T=0)$ under iterative recalculations.

In Fig. 4 in the main text, we have used the parameters $t = 1$, $\mu_{i \in S} = 0.9$, $\mu_{i \in F} = 0.8$, $V_{i \in \text{SOC}} = 0.79$, $U = 1.4$, $\lambda = 0.4$, $h = 0.8$, $N_x^S = 28$, $N_x^{\text{SOC}} = 3$, $N_x^F = 8$, and $N_y = N_z = 50$. This gives a coherence length of 21 lattice sites. All length scales are scaled by the lattice constant a , all energy scales are scaled by the hopping parameter t , and the magnitude of the spin-orbit coupling is scaled by ta .

References

1. C. González-Ruano, L. G. Johnsen, D. Caso, C. Tiusan, M. Hehn, N. Banerjee, J. Linder, and F. G. Aliev, Superconductivity-induced change in magnetic anisotropy in epitaxial ferromagnet-superconductor hybrids with spin-orbit interaction, *Phys. Rev. B* **102**, 020405(R) (2020).
2. A. Vansteenkiste, J. Leliaert, M. Dvornik, M. Helsen, F. Garcia-Sanchez and B. Van Waeyenberge, The design and verification of MuMax3, *AIP Advances* **4**, 107133 (2014).
3. R. Flükiger, Overview of Superconductivity and Challenges in Applications, *Reviews of Accelerator Science and Technology* **5**, 1-23, (2012).
4. A. Lara, C. González-Ruano and Farkhad G. Aliev, Time-Dependent Ginzburg-Landau Simulations of Superconducting Vortices in Three Dimensions, *Low Temperature Physics/Fizika Nizkikh Temperatur*, **46**, 4, 386-394 (2020).
5. A. M. Chang, H. D. Hallen, L. Harriott, H. F. Hess, H. L. Kao, J. Kwo, R. E. Miller, R. Wolfe and J. van der Ziel, Scanning Hall probe microscopy, *Appl. Phys. Lett.* **61**, 1974 (1992).

VI

REFERENCE

Lina G. Johnsen, and Jacob Linder,

Spin injection and spin relaxation in odd-frequency superconductors,
Phys. Rev. B **104**, 144513 (2021).

CONTRIBUTIONS

LGJ performed the analytical and numerical calculations and wrote the paper. JL initiated and supervised the project, and contributed to discussions and revision of the manuscript.

Spin injection and spin relaxation in odd-frequency superconductorsLina G. Johnsen  and Jacob Linder*Center for Quantum Spintronics, Department of Physics, Norwegian University of Science and Technology, NO-7491 Trondheim, Norway*

(Received 23 August 2021; revised 11 October 2021; accepted 20 October 2021; published 28 October 2021)

The spin transport inside an odd-frequency spin-triplet superconductor differs from that of a conventional superconductor due to its distinct symmetry properties. We study spin transport inside an emergent odd-frequency superconductor by replacing the spin-singlet gap matrix in the Usadel equation with a matrix representing spin-triplet pairing that is odd under inversion of energy. We show that the peculiar nature of the density of states allows for an even larger spin injection than in the normal state. Moreover, when the odd-frequency pairing inherits its temperature dependence from a conventional superconductor through the proximity effect, the density of states can transition from gapless to gapped as the temperature decreases. At the transition point, the spin accumulation inside the odd-frequency superconductor is peaked and larger than in the normal state. While the spin-flip scattering time is known to decrease below the superconducting transition temperature in conventional superconductors, we find that the same is true for the spin-orbit scattering time in odd-frequency superconductors. This renormalization is particularly large for energies close to the gap edge, if such a gap is present.

DOI: [10.1103/PhysRevB.104.144513](https://doi.org/10.1103/PhysRevB.104.144513)

Odd-frequency superconductivity possesses the same robustness against disorder as conventional superconductivity, while allowing for the existence of Cooper pairs that can carry a net spin. These properties are inherited from the *s*-wave spin-triplet symmetry of the Cooper pairs [1], and makes odd-frequency superconductors interesting candidates for dissipationless spin transport [2–5]. Subsequent to the first proposal of odd-frequency pairing as an allowed symmetry of the superconducting state [6], a number of structures have been suggested for realizing odd-frequency superconductivity [7]. Among these are superconductor/ferromagnet hybrids where conventional Cooper pairs are transformed into odd-frequency spin triplets in the presence of the ferromagnetic exchange field [8]. These can penetrate deep into the ferromagnet when, e.g., noncollinear magnetization alignment [9–14], inhomogeneous magnetization [15–18], or spin-orbit coupling [19–21] is used to form equal-spin-triplet pairs unaffected by the Zeeman spin splitting. By now, signatures of odd-frequency triplets have been observed in many different structures, e.g., through modulation of the superconducting critical temperature [22–24], density of states (DOS) [25,26], and magnetic anisotropy [27,28], and through observation of long-range supercurrents in Josephson junctions [11–14, 16–18], and the paramagnetic Meissner effect [29,30].

From a symmetry point of view, the odd-frequency superconducting pairing differs from the conventional one by its spin-triplet symmetry leaving it invariant under exchange of spin coordinates, and an odd parity with respect to exchange of time coordinates for the electrons in the Cooper pair. While the *s*-wave symmetry ensures robustness under regular impurity scattering for both conventional and odd-frequency superconductors, the former is expected to be less robust to magnetic impurities and the latter to spin-orbit scattering

[2,32,33]. As was first discussed in the context of the proximity effect in superconductor/ferromagnet structures [34], another characteristic of odd-frequency pairing is that it alters the local DOS. In an odd-frequency superconductor, the DOS can follow an energy dependence similar to that of the conventional superconductor with a gap around the Fermi energy. However, another possibility is that the DOS is gapless and peaked at zero energy [35,36]. These properties are essential for describing the spin transport inside the odd-frequency superconductor.

In conventional superconductors, Cooper pairs are spinless and quasiparticles are responsible for the spin transport [37,38]. Therefore, spin injection is blocked at energies below the gap edge. The onset of superconductivity also causes the spin-flip scattering length to become energy dependent. For energies close to the gap edge, there is a giant renormalization of the spin-flip scattering length causing a rapid decrease in the spin accumulation inside the superconductor [39]. Additionally, the magnetic impurities causes a weakening of the superconducting gap [40]. The spin-orbit scattering time is not renormalized by conventional superconductivity and remains equal to its normal state value [39].

In this work we instead consider the nonequilibrium spin accumulation in an emergent odd-frequency superconductor in the presence of spin-flip and spin-orbit scattering. We compare our results to the conventional case. Our approach is to consider the Usadel equation for a conventional superconductor, and then to replace the conventional gap matrix with a contribution with a spin-triplet symmetry and odd parity under inversion of energy. We study the system shown in Fig. 1(a), where spin is injected into the odd-frequency or conventional superconductor from a normal-metal contact under an applied spin voltage. The polarization axis of the injected spin is chosen so that the spin transport is carried by quasiparticles only. Although odd-frequency superconductivity has not been found to exist intrinsically in materials, it can be induced

*lina.g.johnsen@ntnu.no

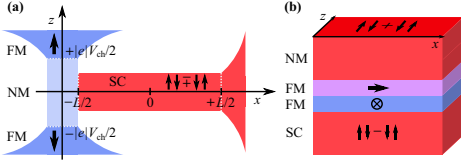


FIG. 1. (a) We study the nonequilibrium spin accumulation in a conventional spin-singlet ($\uparrow\downarrow - \downarrow\uparrow$)₂ and odd-frequency spin-triplet ($\uparrow\downarrow + \downarrow\uparrow$)₂ superconductor (SC) upon applying a spin-dependent voltage $|e|V$ to an adjacent normal metal (NM). The spin-dependent voltage has opposite sign for spin-up and spin-down electrons, and can be induced from an electric voltage $|e|V_{ch}$ applied between two oppositely oriented ferromagnets (FM). The applied electric voltage $|e|V_{ch}$ is in general not equal to the induced spin-dependent voltage $|e|V$ in the NM contact. The FMs are polarized along the z axis so that the spins injected into the SC cannot be carried by the Cooper pairs. The injected spins are relaxed by spin-flip and spin-orbit scattering until equilibrium is reached a distance L from the NM contact. (b) We suggest inducing odd-frequency superconductivity through proximity to a conventional superconductor. Spin-singlet Cooper pairs are partially converted into triplets as they leak from a conventional superconductor into a ferromagnet. Upon leaking through a second sufficiently thick ferromagnet magnetized perpendicularly to the first one, only spin triplets survive [22,23,31]. In the highly disordered materials considered here, only s -wave pairing can be present [1,8]. The remaining triplet pairing then transforms the adjacent normal metal into an emergent odd-frequency superconductor.

by the proximity effect. One way of doing this is presented in Fig. 1(b), where leakage of Cooper pairs through two misaligned ferromagnets effectively converts a normal metal into an emergent odd-frequency spin-triplet superconductor. Therefore, our predictions can be tested experimentally in a hybrid structure.

The odd-frequency superconductivity does not renormalize the spin-flip scattering time caused by magnetic impurities compared to the normal state [2,32,33]. Instead, the spin-orbit scattering length decreases below the superconducting critical temperature. We find that when a gap is present in the DOS, there is a giant renormalization of the spin-orbit scattering length at the gap edge, similar to the renormalization of the spin-flip scattering length in conventional superconductors. Moreover, we find that the distinct features of the DOS [36] causes the temperature dependence of the nonequilibrium spin accumulation to behave qualitatively different from what is expected for a conventional superconductor. It presents a peak when the DOS transitions from peaked to gapped as the temperature decreases. The possibility of a high DOS at low energies also opens the possibility of a higher spin injection than in the normal state.

I. THEORETICAL FRAMEWORK

A. Quasiclassical theory for conventional diffusive superconductors

Our approach will be to generalize the quasiclassical theory for a diffusive conventional superconductor [41,42] in order to describe odd-frequency spin-triplet pairing [35,36].

The motivation behind using this approach is that writing down a microscopic Hamiltonian for the odd-frequency pairing would require adding a time dependence to the electron creation and annihilation operators, which greatly adds to the complexity of the problem. However, we know that the odd-frequency pairing has an even parity under spin inversion and an odd parity under inversion of energy. We can then generalize the result for the conventional pairing so that the pairing satisfies the desired symmetry relations. This comes at the cost of not knowing the gap equation for the odd-frequency pairing.

The impurity-averaged quasiclassical Green's function $\check{g}_{av}^s(\mathbf{R}, \epsilon)$ of a diffusive conventional superconductor can be described by the Usadel equation

$$\nabla_{\mathbf{R}} \cdot \check{\mathbf{I}}(\mathbf{R}, \epsilon) = i[\check{\sigma}(\mathbf{R}, \epsilon), \check{g}_{av}^s(\mathbf{R}, \epsilon)]. \quad (1)$$

Its underlying assumptions and derivation starting from a continuum model is described in Appendix. The Green's function is defined in Keldysh space and has the matrix structure

$$\check{g}_{av}^s(\mathbf{R}, \epsilon) = \begin{pmatrix} [\hat{g}_{av}^s(\mathbf{R}, \epsilon)]^R & [\hat{g}_{av}^s(\mathbf{R}, \epsilon)]^K \\ 0 & [\hat{g}_{av}^s(\mathbf{R}, \epsilon)]^A \end{pmatrix}, \quad (2)$$

where $[\hat{g}_{av}^s(\mathbf{R}, \epsilon)]^R$, $[\hat{g}_{av}^s(\mathbf{R}, \epsilon)]^A$, and $[\hat{g}_{av}^s(\mathbf{R}, \epsilon)]^K$ are the impurity-averaged quasiclassical retarded, advanced, and Keldysh Green's functions, respectively. The check denotes 8×8 matrices in Keldysh space, where $\check{\delta}_0$ is the unit matrix, while the hat denotes 4×4 matrices in Nambu \otimes spin space. We have defined a matrix current

$$\check{\mathbf{I}}(\mathbf{R}, \epsilon) = -D\check{g}_{av}^s(\mathbf{R}, \epsilon)\nabla_{\mathbf{R}}\check{g}_{av}^s(\mathbf{R}, \epsilon), \quad (3)$$

where $D = \tau v_F^2/3$ is the diffusion coefficient. The diffusion coefficient is determined by the Fermi velocity $v_F = p_F/m$, and the scattering time associated with scattering on nonmagnetic impurities $\tau = [2\pi n N_0 \langle |u(\mathbf{e}_{p_F} - \mathbf{e}_{q_F})|^2 \rangle_{p_F, q_F}]^{-1}$. Here n is the density of nonmagnetic impurities, N_0 is the DOS at the Fermi level, and $u(\mathbf{e}_{p_F} - \mathbf{e}_{q_F})$ is the scattering potential of a single nonmagnetic impurity. The scattering potential is averaged over the all possible directions of the momenta $\mathbf{p}_F = p_F \mathbf{e}_{p_F}$ and $\mathbf{q}_F = q_F \mathbf{e}_{q_F}$, where \mathbf{e}_{q_F} and \mathbf{e}_{p_F} are unit vectors. The self-energy matrix $\check{\sigma}(\mathbf{R}, \epsilon) = \hat{\sigma}_0(\epsilon) + \check{\sigma}_{sf}(\mathbf{R}, \epsilon) + \check{\sigma}_{so}(\mathbf{R}, \epsilon) + \hat{\sigma}_{sc}^S(\mathbf{R})$ contains the contributions

$$\hat{\sigma}_0(\epsilon) = \epsilon \hat{\rho}_3, \quad (4)$$

$$\check{\sigma}_{sf}(\mathbf{R}, \epsilon) = (i/8\tau_{sf})\hat{\sigma} \cdot \check{g}_{av}^s(\mathbf{R}, \epsilon)\hat{\sigma}, \quad (5)$$

$$\check{\sigma}_{so}(\mathbf{R}, \epsilon) = (i/8\tau_{so})\hat{\rho}_3\hat{\sigma} \cdot \check{g}_{av}^s(\mathbf{R}, \epsilon)\hat{\rho}_3\hat{\sigma}, \quad (6)$$

$$\hat{\sigma}_{sc}^S(\mathbf{R}) = \hat{\Delta}^S(\mathbf{R}). \quad (7)$$

Above, ϵ is the quasiparticle energy, \mathbf{R} is the center-of-mass coordinate associated with the Green's function, $\hat{\rho}_3 = \text{diag}(1, 1, -1, -1)$, and $\hat{\sigma} = \text{diag}(\sigma, \sigma^*)$, where σ is the vector of Pauli matrices. The self-energies $\check{\sigma}_{sf}(\mathbf{R}, \epsilon)$ and $\check{\sigma}_{so}(\mathbf{R}, \epsilon)$ describe the spin-flip scattering on magnetic impurities and the spin-orbit scattering on nonmagnetic impurities, respectively. The respective scattering times are given by $\tau_{sf} = [8\pi n_m N_0 \langle |u_m(\mathbf{e}_{p_F} - \mathbf{e}_{q_F})|^2 \rangle_{p_F, q_F} S(S+1)/3]^{-1}$ and

$\tau_{\text{so}} = 9\tau / (8\alpha^2 p_F^4)$. Here n_m is the density of the magnetic impurities, $u_m(\mathbf{e}_{p_f} - \mathbf{e}_{q_i})$ and S are the scattering potential and the spin of a single magnetic impurity, and α is the Rashba parameter. We have assumed that $\tau_{\text{so}}, \tau_{\text{sf}} \gg \tau$ so that scattering on nonmagnetic impurities dominates over the spin-orbit and spin-flip scattering. The spin-singlet superconducting pairing is described by the gap matrix

$$\hat{\Delta}^S = \text{antidiag}\{\Delta^S, -\Delta^S, [\Delta^S]^*, -[\Delta^S]^*\}. \quad (8)$$

In this work we will assume the spin-singlet superconducting gap Δ^S to be spatially independent and follow a standard Bardeen-Cooper-Schrieffer temperature dependence given by $\Delta^S(T) = \Delta_0 f(T)$, where

$$\Delta_0 = 1.76T_c, \quad (9)$$

$$f(T) = \tanh\left(1.74\sqrt{\frac{T_c}{T}}\right) \quad (10)$$

are the zero-temperature gap and the temperature dependence of the gap, respectively. Above, T_c is the superconducting critical temperature. The assumption that the superconducting gap, and in particular its phase, is spatially independent holds as long as we only consider spin transport. This is because spin can only be carried by the quasiparticles. Charge can on the other hand be carried by both quasiparticles and Cooper pairs. This causes a conversion between quasiparticle and Cooper pair transport that leads to a renormalization of the gap and makes a spatially dependent phase of the order parameter necessary.

B. Model for odd-frequency superconductivity

In order to describe an odd-frequency spin-triplet superconductor, we replace the spin-singlet contribution to the Usadel equation $\hat{\sigma}^S$ by an energy-dependent contribution $\hat{\sigma}^T(\epsilon) = \hat{\Delta}^T(\epsilon)$ which has an odd parity with respect to inversion of energy. Providing the order parameter with a dependence on ϵ in this way produces the correct relation between the retarded and advanced Green function required for odd-frequency pairing, $f_{\alpha\beta}^R(\epsilon) = -f_{\alpha\beta}^A(-\epsilon)$, corresponding to an odd parity with respect to exchange of time coordinates [5]. We also alter the structure of the gap matrix

$$\hat{\Delta}^T(\epsilon) = \text{antidiag}\{\Delta^T(\epsilon), \Delta^T(\epsilon), -[\Delta^T(\epsilon)]^*, -[\Delta^T(\epsilon)]^*\} \quad (11)$$

in order to describe spin-triplet pairing. We model the spin-triplet pairing by two different plausible models [36]:

$$\Delta^T(\epsilon, T) = \frac{Cf(T)\epsilon}{1 + \left(\frac{C\epsilon}{2\Delta_{\text{max}}}\right)^2}, \quad (12)$$

$$\Delta^T(\epsilon, T) = \frac{Cf(T)\epsilon}{\sqrt{1 + \left(\frac{C\epsilon}{\Delta_{\infty}}\right)^2}}, \quad (13)$$

giving rise to similar results. Equation (12) describes a pairing that has a linear form $Cf(T)\epsilon$ for small energies, reaches its maximum Δ_{max} , and then decays as $\sim 1/\epsilon$ for large energies. Equation (13) describes a pairing that has the same linear form for small energies, and that approaches a constant value Δ_{∞} for large energies. We set the maximum

pairing Δ_{max} and Δ_{∞} of the above models equal to the zero-temperature singlet gap Δ_0 . As can be seen from the above equations, we have assumed the temperature dependence to be the same as for the singlet pairing. This is because when the odd-frequency triplet pairing is produced by the proximity effect as described in Fig. 1(b), the temperature dependence is inherited from the original singlet pairing. Both of the above models produce a gapped DOS similar to that of a spin-singlet superconductor for $Cf(T) > 1$. The gap is of magnitude $(2\Delta_{\text{max}}/C)\sqrt{Cf(T)-1}$ for the pairing in Eq. (12) and $(\Delta_{\infty}/C)\sqrt{[Cf(T)]^2-1}$ for the pairing in Eq. (13). For $0 < Cf(T) \leq 1$, the DOS is instead gapless and peaked around $\epsilon = 0$ [35,36]. Note that the assumption that the pairing is spatially independent also holds for the odd-frequency pairing considered here. The triplet pairs considered ($S_z = 0$) cannot carry any spin supercurrent polarized in the z direction, and thus we may consider a spatially homogeneous order parameter.

C. The kinetic equations and the nonequilibrium spin accumulation

The Usadel equation is subject to a normalization condition

$$\hat{g}_{\text{av}}^{\text{S}}(\mathbf{R}, \epsilon) \hat{g}_{\text{av}}^{\text{S}}(\mathbf{R}, \epsilon) = \hat{\rho}_0 \quad (14)$$

for the quasiclassical Green's function. It follows from the normalization condition that the quasiclassical Keldysh Green's function can be written in terms of the retarded and advanced Green's functions as

$$[\hat{g}_{\text{av}}^{\text{S}}(\mathbf{R}, \epsilon)]^K = [\hat{g}_{\text{av}}^{\text{S}}(\mathbf{R}, \epsilon)]^R \hat{h}(\mathbf{R}, \epsilon) - \hat{h}(\mathbf{R}, \epsilon) [\hat{g}_{\text{av}}^{\text{S}}(\mathbf{R}, \epsilon)]^A, \quad (15)$$

where $\hat{h}(\mathbf{R}, \epsilon)$ is the distribution matrix. Moreover, it follows from the definitions of the retarded and advanced Green's functions that these are related by $[\hat{g}_{\text{av}}^{\text{S}}(\mathbf{R}, \epsilon)]^A = -\{\hat{\rho}_3 [\hat{g}_{\text{av}}^{\text{S}}(\mathbf{R}, \epsilon)]^R \hat{\rho}_3\}^\dagger$. In order to solve the Usadel equation for our system, we therefore only need expressions for the distribution matrix and the retarded Green's function. We assume that the distribution matrix is diagonal, and write it as

$$\hat{h}(\mathbf{R}, \epsilon) = \hat{\rho}_0 h_L(\mathbf{R}, \epsilon) + \hat{\rho}_3 h_T(\mathbf{R}, \epsilon) + \sum_i (\hat{\sigma}_i) h_{iLS}^i(\mathbf{R}, \epsilon) + \sum_i \hat{\rho}_3 (\hat{\sigma}_i) h_{iTS}^i(\mathbf{R}, \epsilon), \quad (16)$$

where $i \in \{x, y, z\}$ refers to the spin projection axis. Above, $h_L(\mathbf{R}, \epsilon)$, $h_T(\mathbf{R}, \epsilon)$, $h_{iLS}^i(\mathbf{R}, \epsilon)$, and $h_{iTS}^i(\mathbf{R}, \epsilon)$ are the energy, charge, spin-energy, and spin distribution functions, respectively. We define corresponding current densities

$$\mathbf{j}_L(\mathbf{R}, \epsilon) = \text{Tr}\{\hat{\mathbf{I}}^K(\mathbf{R}, \epsilon)\}/4, \quad (17)$$

$$\mathbf{j}_T(\mathbf{R}, \epsilon) = \text{Tr}\{\hat{\rho}_3 \hat{\mathbf{I}}^K(\mathbf{R}, \epsilon)\}/4, \quad (18)$$

$$\hat{\mathbf{j}}_{iLS}^i(\mathbf{R}, \epsilon) = \text{Tr}\{(\hat{\sigma}_i) \hat{\mathbf{I}}^K(\mathbf{R}, \epsilon)\}/4, \quad (19)$$

$$\hat{\mathbf{j}}_{iTS}^i(\mathbf{R}, \epsilon) = \text{Tr}\{\hat{\rho}_3 (\hat{\sigma}_i) \hat{\mathbf{I}}^K(\mathbf{R}, \epsilon)\}/4 \quad (20)$$

in terms of the Keldysh part of the current matrix. We set the retarded Green's function for the spin-singlet (spin-triplet) superconductor equal to its equilibrium solution,

$$\{[\hat{g}_{\text{av}}^s(\epsilon)]^R\}^{\text{S(T)}} = [\hat{\rho}_3\epsilon + \hat{\Delta}^{\text{S(T)}}(\epsilon)]I^{\text{S(T)}}(\epsilon), \quad (21)$$

$$I^{\text{S(T)}}(\epsilon) = \frac{\text{sgn}(\epsilon)\Theta(\epsilon^2 - |\Delta^{\text{S(T)}}(\epsilon)|^2)}{\sqrt{\epsilon^2 - |\Delta^{\text{S(T)}}(\epsilon)|^2}} - \frac{i\Theta(|\Delta^{\text{S(T)}}(\epsilon)|^2 - \epsilon^2)}{\sqrt{|\Delta^{\text{S(T)}}(\epsilon)|^2 - \epsilon^2}}, \quad (22)$$

throughout the superconducting region. Above, $\Theta(\epsilon)$ is the Heaviside step function. We have neglected the influence of magnetic and spin-orbit impurity scattering on the retarded Green's function and instead study how the impurity scattering affects the spin distribution function. A study of how the above-mentioned scattering changes the Green's function would require a self-consistent solution for the superconducting pairing and would reveal a renormalization of the superconducting gap. A self-consistent solution is not possible for the spin-triplet superconductor for which the gap equation is unknown. Although a self-consistent solution would not reveal a mixing between conventional and odd-frequency pairing in the present framework, it has been shown to occur close to single magnetic impurities in clean superconductors [43,44]. If such a mixing were present, there would be a contribution from both types of pairing to the nonequilibrium spin accumulation.

Focusing now on the spin transport, we insert the equilibrium retarded Green's function and the definition of the distribution functions into the Keldysh component of the Usadel equation. For the spin-singlet (spin-triplet) superconducting pairing we find a relation

$$\nabla_{\mathbf{R}} \cdot [j_{\text{TTS}}^z(\mathbf{R}, \epsilon)]^{\text{S(T)}} = -2\alpha_{\text{TSTS}}^{\text{S(T)}}(\epsilon)[h_{\text{TTS}}^z(\mathbf{R}, \epsilon)]^{\text{S(T)}}, \quad (23)$$

$$\alpha_{\text{TSTS}}^{\text{S}}(\epsilon) = \left(\frac{1}{\tau_{\text{so}}} + \frac{1}{\tau_{\text{sf}}} \frac{\epsilon^2 + |\Delta|^2}{\epsilon^2 - |\Delta|^2} \right) \Theta(\epsilon^2 - |\Delta|^2), \quad (24)$$

$$\alpha_{\text{TSTS}}^{\text{T}}(\epsilon) = \left(\frac{1}{\tau_{\text{sf}}} + \frac{1}{\tau_{\text{so}}} \frac{\epsilon^2 + |\Delta(\epsilon)|^2}{\epsilon^2 - |\Delta(\epsilon)|^2} \right) \Theta(\epsilon^2 - |\Delta(\epsilon)|^2) \quad (25)$$

between the spin current density $j_{\text{TTS}}^z(\mathbf{R}, \epsilon)$ and the spin distribution function $h_{\text{TTS}}^z(\mathbf{R}, \epsilon)$. Notice that while spin-singlet superconductivity renormalizes the spin-flip scattering time, the odd-frequency spin-triplet superconductivity instead renormalizes the spin-orbit scattering time. For a gapped triplet superconductor [$Cf(T) > 1$], we see from the above expression that there occurs a giant renormalization at the gap edge $\epsilon \rightarrow \Delta(\epsilon)$ causing rapid spin-orbit relaxation. From the definition of the spin current density, we find that

$$[j_{\text{TTS}}^z(\mathbf{R}, \epsilon)]^{\text{S(T)}} = -2D_{\text{L}}^{\text{S(T)}}(\epsilon)\nabla_{\mathbf{R}}[h_{\text{TTS}}^z(\mathbf{R}, \epsilon)]^{\text{S(T)}}, \quad (26)$$

$$D_{\text{L}}^{\text{S}}(\epsilon) = D\Theta(\epsilon^2 - |\Delta|^2), \quad (27)$$

$$D_{\text{L}}^{\text{T}}(\epsilon) = D\Theta(\epsilon^2 - |\Delta(\epsilon)|^2). \quad (28)$$

In order to study the spin distribution $[h_{\text{TTS}}^z(\mathbf{R}, \epsilon)]^{\text{S(T)}}$ inside a singlet (triplet) superconductor under spin injection, we introduce for simplicity transparent boundaries to a normal metal with a spin voltage $V_{\uparrow} = -V_{\downarrow} = V/2$ at position $x = -L/2$. Using more realistic tunneling boundary conditions simply diminishes the magnitude of the spin injection, regardless of whether we consider a conventional superconductor or an odd-frequency superconductor, and does not change any of our conclusions. We assume the spin injected into the singlet or triplet superconductor from the normal metal to have relaxed completely at $x = L/2$. This corresponds to the system introduced in Fig. 1(a). This situation can be described by the boundary conditions

$$h_{\text{TTS}}^z(-L/2, \epsilon) = \frac{1}{2} \left[\tanh\left(\frac{\epsilon + eV_{\uparrow}}{2T}\right) - \tanh\left(\frac{\epsilon + eV_{\downarrow}}{2T}\right) \right], \quad (29)$$

$$h_{\text{TTS}}^z(L/2, \epsilon) = 0, \quad (30)$$

where the temperature T is constant throughout the material. Solving Eqs. (23) and (26) with these boundary conditions, we find that the spin distribution function for the singlet (triplet) superconductor is given by

$$[h_{\text{TTS}}^z(x, \epsilon)]^{\text{S(T)}} = \frac{1}{2} h_{\text{TTS}}^z(-L/2, \epsilon) [H_{\text{TTS}}^z(x, \epsilon)]^{\text{S(T)}} \Theta(\epsilon^2 - |\Delta^{\text{S(T)}}(\epsilon)|^2), \quad (31)$$

$$[H_{\text{TTS}}^z(x, \epsilon)]^{\text{S}} = \left\{ \frac{\cosh\left(\sqrt{\frac{1}{l_{\text{so}}}^2} + \frac{1}{l_{\text{sf}}}^2} \frac{\epsilon^2 + |\Delta^{\text{S}}|^2}{\epsilon^2 - |\Delta^{\text{S}}|^2} x\right)}{\cosh\left(\sqrt{\frac{1}{l_{\text{so}}}^2} + \frac{1}{l_{\text{sf}}}^2} \frac{\epsilon^2 + |\Delta^{\text{S}}|^2}{\epsilon^2 - |\Delta^{\text{S}}|^2} \frac{L}{2}\right)} - \frac{\sinh\left(\sqrt{\frac{1}{l_{\text{so}}}^2} + \frac{1}{l_{\text{sf}}}^2} \frac{\epsilon^2 + |\Delta^{\text{S}}|^2}{\epsilon^2 - |\Delta^{\text{S}}|^2} x\right)}{\sinh\left(\sqrt{\frac{1}{l_{\text{so}}}^2} + \frac{1}{l_{\text{sf}}}^2} \frac{\epsilon^2 + |\Delta^{\text{S}}|^2}{\epsilon^2 - |\Delta^{\text{S}}|^2} \frac{L}{2}\right)} \right\}, \quad (32)$$

$$[H_{\text{TTS}}^z(x, \epsilon)]^{\text{T}} = \left\{ \frac{\cosh\left(\sqrt{\frac{1}{l_{\text{so}}}^2} + \frac{1}{l_{\text{sf}}}^2} \frac{\epsilon^2 + |\Delta^{\text{T}}(\epsilon)|^2}{\epsilon^2 - |\Delta^{\text{T}}(\epsilon)|^2} x\right)}{\cosh\left(\sqrt{\frac{1}{l_{\text{so}}}^2} + \frac{1}{l_{\text{sf}}}^2} \frac{\epsilon^2 + |\Delta^{\text{T}}(\epsilon)|^2}{\epsilon^2 - |\Delta^{\text{T}}(\epsilon)|^2} \frac{L}{2}\right)} - \frac{\sinh\left(\sqrt{\frac{1}{l_{\text{so}}}^2} + \frac{1}{l_{\text{sf}}}^2} \frac{\epsilon^2 + |\Delta^{\text{T}}(\epsilon)|^2}{\epsilon^2 - |\Delta^{\text{T}}(\epsilon)|^2} x\right)}{\sinh\left(\sqrt{\frac{1}{l_{\text{so}}}^2} + \frac{1}{l_{\text{sf}}}^2} \frac{\epsilon^2 + |\Delta^{\text{T}}(\epsilon)|^2}{\epsilon^2 - |\Delta^{\text{T}}(\epsilon)|^2} \frac{L}{2}\right)} \right\}. \quad (33)$$

We have defined the normal-state spin-flip and spin-orbit relaxation lengths $l_{\text{sf}} = \sqrt{D\tau_{\text{sf}}}$ and $l_{\text{so}} = \sqrt{D\tau_{\text{so}}}$. The nonequilibrium spin accumulation

$$[\mu^z(x)]^{\text{S(T)}} = -\frac{1}{N_0} \int_{-\infty}^{\infty} d\epsilon N^{\text{S(T)}}(\epsilon) [h_{\text{TTS}}^z(x, \epsilon)]^{\text{S(T)}} \quad (34)$$

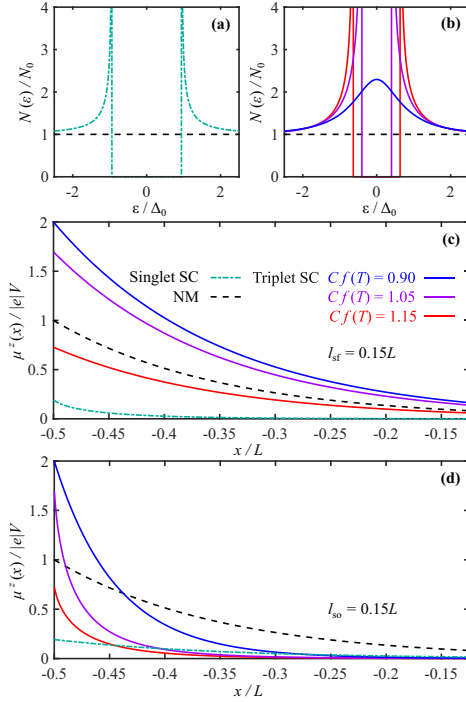


FIG. 2. While the DOS for a singlet superconductor (a) is gapped, the DOS of an odd-frequency superconductor (b) can either be peaked at zero temperature (blue) or gapped (purple and red). The nonequilibrium spin accumulation corresponding to the DOS in (b) is shown for spin-flip scattering with $l_{sf} = 0.15L$ (c) and for spin-orbit scattering with $l_{so} = 0.15L$ (d). All plots correspond to a spin voltage of $|e|V = 0.5\Delta_0$ and temperature $T = 0.5T_c$. The above corresponds to the pairing type described in Eq. (12). The second pairing type described in Eq. (13) gives similar results.

is determined by the spin distribution function given above and the DOS $N^{S(T)}(\epsilon) = N_0 \text{Re}(\{[g_{av}^s(\mathbf{R}, \epsilon)]^R\}^{S(T)})$, where $\{[g_{av}^s(\mathbf{R}, \epsilon)]^R\}^{S(T)} = \epsilon f^{S(T)}(\epsilon)$.

II. THE NONEQUILIBRIUM SPIN ACCUMULATION

A. The density of states

We first discuss how the density of states affects the nonequilibrium spin accumulation inside the superconductor. As shown in Figs. 2(a) and 2(b), the DOS of an odd-frequency superconductor can either be gapped as in the conventional superconductor, or it can be gapless and peaked at zero energy. When the DOS is gapped, the situation is similar to that of a conventional superconductor. There are no available states below the gap edge, and spin is blocked from entering the superconductor. At the gap edge, the DOS is large thus allowing

for a large spin injection. The conventional superconductor always allows for a spin injection that is less than or equal to the spin injection into a normal metal. This is because the total number of states is conserved. For energies up to a given spin voltage just above the gap edge, there will be fewer available quasiparticle states as the available states have been pushed out of the gap region towards higher energies. For the gapped odd-frequency superconductor, the gap is smaller and the peaks at the gap edge broader than in the conventional superconductor. Although this causes the conservation of the total number of states to be broken in our simple model, it has been shown numerically that this problem can be resolved by flanking the peak at the gap edge by a local minimum [36]. Spin voltages that do not allow for spin injection at such high energies can then give rise to a spin injection that is higher than the spin injection in the normal state. For a gapless odd-frequency superconductor, the spin injection can be even larger, since the DOS is always larger than in the normal state, except for at the minima appearing at higher energies [36].

Since the spin injection into an odd-frequency superconductor can be larger than that in the normal state, the nonequilibrium spin accumulation close to the normal-metal contact can also be larger. This is demonstrated in Figs. 2(c) and 2(d) for positions close to $x = -0.5L$. Note that although the additional minima in the DOS are not included in our analytical model, the error is negligible as long as the temperature and spin voltage is sufficiently low. This is because the distribution function of the normal-metal contact [Eq. (29)] becomes negligibly small at the high energies where the minimum appears. For the temperature and spin voltage used in Fig. 2 the spin distribution function of the normal metal is ten (hundred) times smaller than its maximum value at $\epsilon = 1.8\Delta_0$ ($\epsilon = 1.1\Delta_0$).

Another important observation is that since the temperature dependence of the triplet pairing is inherited from the original singlet condensate via the proximity effect [Fig. 1(b)], the coefficient $Cf(T)$ determining whether the DOS is gapped or gapless is also temperature dependent. The coefficient $f(T)$ is equal to one at zero temperature and zero at the superconducting critical temperature. This means that if the DOS start out as gapped at $T = 0$ [$Cf(0) > 1$] it must transition to a peaked DOS as $Cf(T)$ drops below one for higher temperatures. Moreover, the DOS diverges as $Cf(T)$ approaches one. This results in a spin injection that is larger than in the normal state due to the high number of available states at zero energy, as we will demonstrate below.

B. Spin-flip and spin-orbit impurity scattering

While a conventional superconductor has a giant spin-flip relaxation for energies close to the gap edge [39], odd-frequency superconductivity does not renormalize the average spin-flip scattering length. In fact, we find that the roles of the spin-flip and spin-orbit scattering are opposite compared to the spin-singlet case as can be seen from Eqs. (32) and (33). Qualitatively this is reasonable since spin-flip caused by magnetic impurities does not leave the spin part ($\uparrow\downarrow - \downarrow\uparrow$) of a conventional singlet superconductor invariant. Such spin flip does, however, leave the spin part ($\uparrow\downarrow + \downarrow\uparrow$) of an $S_z = 0$ triplet superconductor invariant. The spin-orbit

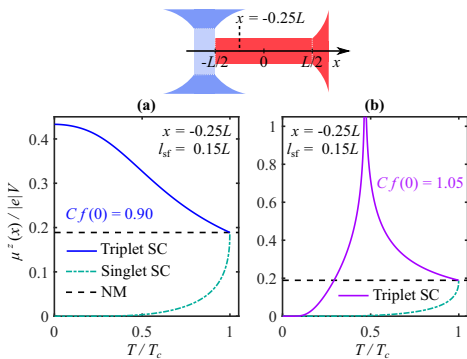


FIG. 3. The nonequilibrium spin accumulation is plotted as a function of temperature in the presence of spin-flip scattering for $l_{sf} = 0.15L$. (a) A gapless DOS where $0 \leq Cf(T) \leq 0.90$ for all temperatures. (b) A DOS that is gapped at low temperatures [$1.05 > Cf(T) > 1$], and gapless at higher temperatures [$0 \leq Cf(T) \leq 1$]. Both are measured at a distance $0.25L$ away from the normal-metal contact and correspond to an applied spin voltage of $|e|V = 0.1\Delta_0$. The triplet pairing follows the model described by Eq. (12), however the model described by Eq. (13) gives similar results.

relaxation length increases at the onset of the odd-frequency superconductivity, and if a gap is present there is a giant renormalization of the spin-orbit relaxation length for energies close to the gap edge. This is demonstrated in Figs. 2(c) and 2(d). In Fig. 2(c) only spin-flip relaxation is present, and the nonequilibrium spin accumulation in the odd-frequency superconductor relaxes at the same rate as in the normal metal. In the conventional superconductor, the spins relax more rapidly. In Fig. 2(d) only spin-orbit relaxation is present, and the nonequilibrium spin accumulation relaxes rapidly inside the odd-frequency superconductor. It relaxes at the same rate for the normal metal and inside the conventional superconductor. In this case, the nonequilibrium spin accumulation crosses from above to below that of the normal state, meaning that the spin accumulation will behave qualitatively different depending on at which position it is measured.

C. Temperature dependence

Finally, we study the temperature dependence of the nonequilibrium spin accumulation. In Fig. 3 we consider the nonequilibrium spin accumulation for $Cf(0) = 0.90$ [Fig. 3(a)] and $Cf(0) = 1.05$ [Fig. 3(b)] in the presence of spin-flip scattering. When $Cf(T) < 1$ at zero temperature, the DOS is gapless for all temperatures up to T_c . The high number of available states causes the spin injection at the normal-metal contact to be higher than in the normal state, and the spin-flip scattering rate is the same. Therefore, the nonequilibrium spin accumulation will stay larger than in the normal state for all temperatures regardless of at which position we choose to measure it. This is demonstrated in Fig. 3(a). In comparison, the spin accumulation in a conventional superconductor relaxes quickly as the temperature is

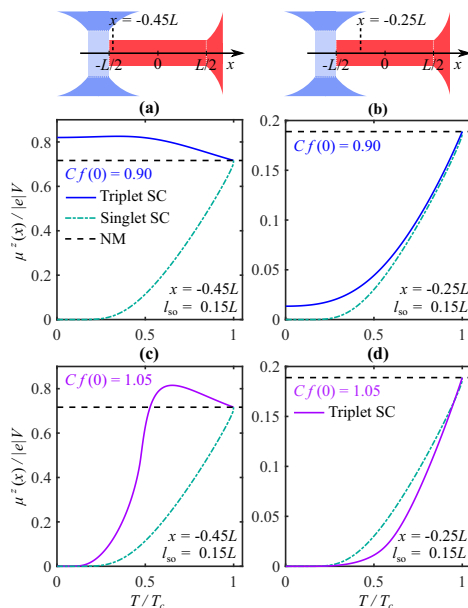


FIG. 4. The nonequilibrium spin accumulation is plotted as a function of temperature in the presence of spin-orbit scattering for $l_{so} = 0.15L$. (a) and (b) A gapless DOS where $0 \leq Cf(T) \leq 0.90$ for all temperatures. (c) and (d) A DOS that is gapped at low temperatures [$1 < Cf(T) < 1.05$], and gapless at higher temperatures [$0 \leq Cf(T) \leq 1$]. (a) and (c) Measured at a distance $0.05L$ away from the normal-metal contact, while (b) and (d) are measured at a distance $0.25L$ away from the normal-metal contact. The applied spin voltage is $|e|V = 0.1\Delta_0$ for all panels. The triplet pairing follows the model described by Eq. (12), however the model described by Eq. (13) gives similar results.

decreased [39]. When $Cf(T) > 1$ at $T = 0$, the DOS goes through a transition from gapped to gapless as the temperature increases. In the absence of spin-orbit relaxation, this causes a sharp peak in the spin accumulation at the temperature where this transition happens, as shown in Fig. 3(b). For lower temperatures, the spin accumulation decreases as the gap widens, leaving fewer available states.

In Fig. 4 we consider the nonequilibrium spin accumulation for the same values of $Cf(T)$ in the presence of spin-orbit scattering. In this case, the spins relax quickly inside the odd-frequency superconductor. Thus, when the superconductor is gapless for all temperatures [$Cf(T) = 0.90$], the spin accumulation can either be larger than in the normal state as shown in Fig. 4(a) or smaller as shown in Fig. 4(b) depending on how close to the normal-metal contact it is measured. In the case where the superconductor transitions from gapped to gapless as the temperature increases, remnants of the peak seen in the absence of spin-orbit scattering [Fig. 3(b)] only appear close to the normal-metal contact as can be seen in Fig. 4(c). Further

away, spin-orbit relaxation causes the spin accumulation to be even smaller than for conventional superconductors.

Note that in Figs. 3 and 4 we have chosen a small spin voltage in order to minimize the error from leaving out the local minimum in the DOS (see Sec. II A). However, close to T_c this will inevitably cause an overestimation in the spin injection from the normal-metal contact. This should however not cause any qualitative changes, since the spin accumulation μ^z has to reach its normal-state value at T_c . It would rather cause a small reduction in the spin accumulation for temperatures close to T_c , and some smoothing of the peak in Fig. 3(b).

III. OUTLOOK AND CONCLUDING REMARKS

In this work we have shown how the nonequilibrium spin accumulation in an odd-frequency superconductor differs qualitatively in several ways from that of a conventional superconductor. First, the density of states of the odd-frequency superconductor allows for a spin injection that is larger than in the normal state. Moreover, it can transition from gapless to gapped as the temperature is decreased, causing a peak in the spin injection at a certain transition temperature below the critical temperature T_c of the superconductor. Second, the roles of the spin-flip and spin-orbit impurity scattering are interchanged compared to what is the case for conventional superconductors. This causes a rapid spin-orbit relaxation, and robustness in the presence of magnetic impurities.

There are several additional interesting effects which can be implemented by adjusting the setup presented in Fig. 1. First, when injecting a spin-polarized charge current directly into a superconductor, it has been shown that the spin injection increases compared to the normal state since the opening of the gap causes a large spin splitting as spins accumulate at the interface [45–47]. At low temperatures, where the density of states is gapped, this should also occur for the odd-frequency superconductors considered here. Second, we have considered the injected spin to be carried entirely by quasiparticles. By allowing the Cooper pairs to be spin polarized with respect to the polarization axis of the injected spins, we open for the possibility that Cooper pairs contribute to the spin transport. Spins can then be injected at energies below the gap edge. However, this can only be described by allowing the retarded Green's function to deviate from its equilibrium value and calls for a self-consistent solution for the superconducting pairing. Third, we have considered an effective odd-frequency superconductor in the absence of spin-splitting fields. Externally applied magnetic fields are known to enhance the spin accumulation inside conventional superconductors [48–51]. In the absence of spin splitting, spin accumulation is a direct consequence of imbalance in the spin distribution function, while in the presence of spin splitting the imbalance in the energy distribution function gives an additional contribution due to coupling between the different modes [52]. A similar coupling is expected to take place for odd-frequency superconductors. Finally, we have considered transparent boundaries between the metallic contact and the superconductor. In reality, there would be some contact resistance restricting the spin injection through the interface. However, a comparison of the spin accumulation above and below the superconducting critical temperature should yield

qualitatively the same result although the overall signal is weaker. In experiments, the advantage of using a tunnel barrier rather than a metallic contact is that it minimizes the proximity effect between the contact and the superconductor, which leads to a suppression in the superconducting gap close to the interface.

ACKNOWLEDGMENTS

This work was supported by the Research Council of Norway through its Centres of Excellence funding scheme Grant No. 262633 QuSpin.

APPENDIX: DERIVATION OF THE USADEL EQUATION

We here give some more details about the underlying assumptions of the Usadel equation given in Eq. (1). Our starting point for deriving the Usadel equation is the continuum Hamiltonian

$$H(\mathbf{r}, t) = \int d\mathbf{r} \sum_{\sigma} \psi_{\sigma}^{\dagger}(\mathbf{r}, t) \left(-\frac{1}{2m} \nabla_{\mathbf{r}}^2 - \mu \right) \psi_{\sigma}(\mathbf{r}, t) + \frac{1}{2} \int d\mathbf{r} [\Delta(\mathbf{r}) \psi_{\uparrow}^{\dagger}(\mathbf{r}, t) \psi_{\downarrow}^{\dagger}(\mathbf{r}, t) + \text{H.c.}] + \int d\mathbf{r} \sum_{\sigma, \sigma'} \psi_{\sigma}^{\dagger}(\mathbf{r}, t) U_{\sigma, \sigma'}^{\text{tot}}(\mathbf{r}) \psi_{\sigma'}(\mathbf{r}, t), \quad (\text{A1})$$

where $\psi_{\sigma}^{(\dagger)}(\mathbf{r}, t)$ is a field operator annihilating (creating) a spin- σ electron at position \mathbf{r} and time t . The first term introduces the kinetic energy for electrons of mass m , and the chemical potential μ . The second term describes superconducting attractive interaction in the mean field approximation. The superconducting gap is defined as $\Delta(\mathbf{r}) = V(\psi_{\uparrow}(\mathbf{r})\psi_{\downarrow}(\mathbf{r}))$. The last term introduces the total scattering potential from the impurities.

We define a four-vector field operator in Nambu \otimes spin space as

$$\hat{\psi}(\mathbf{r}, t) = [\psi_{\uparrow}(\mathbf{r}, t) \quad \psi_{\downarrow}(\mathbf{r}, t) \quad \psi_{\uparrow}^{\dagger}(\mathbf{r}, t) \quad \psi_{\downarrow}^{\dagger}(\mathbf{r}, t)]^T. \quad (\text{A2})$$

We also define the retarded, advanced, and Keldysh Green's functions in Nambu \otimes spin space as

$$[\hat{G}^R(1, 2)]_{i,j} = -i\Theta(t_1 - t_2) \times \sum_k (\hat{\rho}_3)_{ik} \langle \{ [\hat{\psi}(1)]_k, [\hat{\psi}^{\dagger}(2)]_j \} \rangle, \quad (\text{A3})$$

$$[\hat{G}^A(1, 2)]_{i,j} = i\Theta(t_2 - t_1) \times \sum_k (\hat{\rho}_3)_{ik} \langle \{ [\hat{\psi}(1)]_k, [\hat{\psi}^{\dagger}(2)]_j \} \rangle, \quad (\text{A4})$$

$$[\hat{G}^K(1, 2)]_{i,j} = -i \sum_k (\hat{\rho}_3)_{ik} \langle [[\hat{\psi}(1)]_k, [\hat{\psi}^{\dagger}(2)]_j] \rangle, \quad (\text{A5})$$

respectively, where $(1, 2)$ is shorthand notation for $(\mathbf{r}_1, t_1, \mathbf{r}_2, t_2)$. These are elements of the Green's function $\hat{G}(1, 2)$ in Keldysh space as defined for the quasiclassical Green's function in Eq. (2). From the Heisenberg equations of motion for the field operators, we find that the equations

of motion for the Keldysh space Green's function can be written as

$$[i\partial_{t_1}\hat{\rho}_3 - \hat{H}(\mathbf{r}_1)]\check{G}(1, 2) = \delta(1-2)\check{\rho}_0, \quad (\text{A6})$$

$$\check{G}(1, 2)[i\partial_{t_2}\hat{\rho}_3 - \hat{\rho}_3\hat{H}(\mathbf{r}_2)\hat{\rho}_3]^\dagger = \delta(1-2)\check{\rho}_0. \quad (\text{A7})$$

where

$$\hat{H}(\mathbf{r}) = \left(-\frac{1}{2m}\nabla_r^2 - \mu\right)\hat{\rho}_0 - \hat{\Delta}^S(\mathbf{r}) + \hat{U}_{\text{tot}}(\mathbf{r}). \quad (\text{A8})$$

The scattering potential matrix $\hat{U}_{\text{tot}}(\mathbf{r}) = U(\mathbf{r}) + \hat{U}_{\text{so}}(\mathbf{r}) + \hat{U}_{\text{sf}}(\mathbf{r})$ describe scattering on nonmagnetic impurities, spin-orbit impurity scattering, and scattering on magnetic impurities, respectively. The scattering potentials are given by

$$U(\mathbf{r}) = \sum_i u(\mathbf{r} - \mathbf{r}_i), \quad (\text{A9})$$

$$\hat{U}_{\text{so}}(\mathbf{r}) = \sum_i i\alpha[\hat{\rho}_3\hat{\sigma} \times \nabla_r u(\mathbf{r} - \mathbf{r}_i)] \cdot \nabla_r, \quad (\text{A10})$$

$$\hat{U}_{\text{sf}}(\mathbf{r}) = \sum_i u_m(\mathbf{r} - \mathbf{r}_i)\hat{\sigma} \cdot \mathbf{S}_i, \quad (\text{A11})$$

where $u(\mathbf{r} - \mathbf{r}_i)$ and $u_m(\mathbf{r} - \mathbf{r}_i)$ are the scattering potentials of a single nonmagnetic and magnetic impurity, and \mathbf{S}_i is the spin of the magnetic impurity at position \mathbf{r}_i .

In order to solve Eqs. (A6) and (A7), we must replace the impurity potentials by self-energies. To do this, we split the Hamiltonian up into two parts, $\hat{H}(\mathbf{r}) = \hat{H}_0(\mathbf{r}) + \hat{U}_{\text{tot}}(\mathbf{r})$, where $\hat{H}_0(\mathbf{r})$ describes the system in the absence of impurity scattering. We introduce self-energies through the Dyson equations

$$\check{G}(1, 2) = \check{G}_0(1, 2) + \check{G}_0 \bullet \hat{\Sigma} \bullet \check{G}(1, 2), \quad (\text{A12})$$

$$\check{G}(1, 2) = \check{G}_0(1, 2) + \check{G} \bullet \hat{\Sigma}^\dagger \bullet \check{G}_0(1, 2), \quad (\text{A13})$$

where the self-energies are defined as $\hat{\Sigma}(1, 2) = \delta(1-2)\hat{U}_{\text{tot}}(\mathbf{r}_2)$. Above, $\check{G}_0(1, 2)$ is the Green's function in the absence of impurity scattering, and we have introduced the bullet product

$$A \bullet B(1, 2) = \int d3 A(1, 3)B(3, 2). \quad (\text{A14})$$

We solve the Dyson equations iteratively within the self-consistent Born approximation by neglecting terms above the second order in $\hat{\Sigma} \bullet \check{G}$ and $\check{G} \bullet \hat{\Sigma}^\dagger$. Since we are not interested in one specific impurity configuration, we take the average over all impurities,

$$\langle \cdots \rangle_{\text{av}} = \prod_{n=1}^N \left(\frac{1}{\mathcal{V}} \int d\mathbf{r}_n \right) \cdots, \quad (\text{A15})$$

where \mathcal{V} is the volume of the system. We assume that the Green's function is approximately equal to its impurity-averaged value. By acting with $[i\partial_{t_1}\hat{\rho}_3 - \hat{H}_0(\mathbf{r}_1)]$ and $[i\partial_{t_2}\hat{\rho}_3 - \hat{\rho}_3\hat{H}_0(\mathbf{r}_2)\hat{\rho}_3]$ on the resulting equations, we obtain expressions on a similar form as Eqs. (A6) and (A7) where the impurity potentials are replaced by expressions involving self-energies and impurity averaged Green's functions. Subtracting the two

equations, we find that

$$[i\partial_{t_1}\hat{\rho}_3 - \hat{H}_0(\mathbf{r}_1)]\check{G}_{\text{av}}(1, 2) - \check{G}_{\text{av}}(1, 2)[i\partial_{t_2}\hat{\rho}_3 - \hat{\rho}_3\hat{H}_0(\mathbf{r}_2)\hat{\rho}_3]^\dagger - [(\hat{\Sigma} \bullet \check{G}_{\text{av}} \bullet \hat{\Sigma})_{\text{av}} \bullet \check{G}_{\text{av}}](1, 2) = 0. \quad (\text{A16})$$

In order to arrive at Eq. (1) we now need to introduce several approximations to the above equation. We first introduce center-of-mass and relative coordinates $\mathbf{R} = (\mathbf{r}_1 + \mathbf{r}_2)/2$ and $\mathbf{r} = \mathbf{r}_1 - \mathbf{r}_2$, as well as absolute and relative time coordinates $T = (t_1 + t_2)/2$ and $t = t_1 - t_2$. We assume that the Green's function is independent of the absolute time coordinate, and that all quantities varies slowly in space compared to the Fermi wavelength. This allows us to keep only the first order gradients in the center of mass coordinate. We introduce the Fourier transform and its inverse,

$$\check{G}_{\text{av}}(\mathbf{R}, \mathbf{p}, \epsilon) = \int d\mathbf{r} \int dt e^{-i\mathbf{p}\cdot\mathbf{r} + i\epsilon t} \check{G}_{\text{av}}(\mathbf{R}, \mathbf{r}, t), \quad (\text{A17})$$

$$\check{G}_{\text{av}}(\mathbf{R}, \mathbf{r}, t) = \int \frac{d\mathbf{p}}{(2\pi)^3} \int \frac{d\epsilon}{2\pi} e^{i\mathbf{p}\cdot\mathbf{r} - i\epsilon t} \check{G}_{\text{av}}(\mathbf{R}, \mathbf{p}, \epsilon). \quad (\text{A18})$$

Under these assumptions, the Fourier transform of the bullet product between two functions $A(\mathbf{R}, \mathbf{p}, \epsilon)$ and $B(\mathbf{R}, \mathbf{p}, \epsilon)$ is given by

$$A \bullet B(\mathbf{R}, \mathbf{p}, \epsilon) = A(\mathbf{R}, \mathbf{p}, \epsilon)B(\mathbf{R}, \mathbf{p}, \epsilon) + \frac{i}{2}[\nabla_{\mathbf{R}}A(\mathbf{R}, \mathbf{p}, \epsilon) \cdot \nabla_{\mathbf{p}}B(\mathbf{R}, \mathbf{p}, \epsilon) - \nabla_{\mathbf{p}}A(\mathbf{R}, \mathbf{p}, \epsilon) \cdot \nabla_{\mathbf{R}}B(\mathbf{R}, \mathbf{p}, \epsilon)]. \quad (\text{A19})$$

Next, we assume that the absolute value of the momentum p is approximately equal to the Fermi momentum p_F . This allows us to apply the quasiclassical approximation

$$\int \frac{d\mathbf{p}}{(2\pi)^3} \check{G}_{\text{av}}(\mathbf{R}, \mathbf{p}, \epsilon) \approx N_0 \int d\xi_{p_F} \int \frac{d\mathbf{e}_{p_F}}{4\pi} \check{G}_{\text{av}}(\mathbf{R}, \mathbf{p}_F, \epsilon). \quad (\text{A20})$$

Above, N_0 is the DOS at the Fermi level, $\xi_{p_F} = p_F^2/2m$, and $\mathbf{e}_{p_F} = \mathbf{p}_F/p_F$ describes the direction of the momentum. We will use the shorthand notation $\langle \cdots \rangle_{p_F} = \int (d\mathbf{e}_{p_F}/4\pi)$ for the average over all directions of the momentum. Moreover, we introduce the quasiclassical Green's function

$$\check{g}_{\text{av}}(\mathbf{R}, \mathbf{p}_F, \epsilon) = \frac{i}{\pi} \int d\xi_{p_F} \check{G}_{\text{av}}(\mathbf{R}, \mathbf{p}_F, \epsilon). \quad (\text{A21})$$

In the diffusive limit, the quasiclassical Green's function can be approximated as

$$\check{g}_{\text{av}}(\mathbf{R}, \mathbf{p}_F, \epsilon) \approx \check{g}_{\text{av}}^s(\mathbf{R}, \epsilon) + \mathbf{e}_{p_F} \cdot \check{g}_{\text{av}}^p(\mathbf{R}, \epsilon). \quad (\text{A22})$$

We assume that $|\check{g}_{\text{av}}^p(\mathbf{R}, \epsilon)| \ll \check{g}_{\text{av}}^s(\mathbf{R}, \epsilon)$ and neglect terms of second order in $\check{g}_{\text{av}}^p(\mathbf{R}, \epsilon)$.

After applying all these approximations to Eq. (A16), we separate out the even contributions in \mathbf{e}_{p_F} by averaging over all \mathbf{e}_{p_F} . We next separate out the odd contributions in \mathbf{e}_{p_F} by multiplying the equation by \mathbf{e}_{p_F} before doing the averaging. In the odd equation, we assume that the scattering on nonmagnetic impurities dominates over all other terms, and use the normalization condition

$$\check{g}_{\text{av}}(\mathbf{R}, \mathbf{p}_F, \epsilon)\check{g}_{\text{av}}(\mathbf{R}, \mathbf{p}_F, \epsilon) = \check{\rho}_0 \quad (\text{A23})$$

to express $\check{g}_{\text{av}}^{\text{p}}(\mathbf{R}, \epsilon)$ in terms of $\check{g}_{\text{av}}^{\text{s}}(\mathbf{R}, \epsilon)$ as

$$\check{g}_{\text{av}}^{\text{p}}(\mathbf{R}, \epsilon) = -\tau v_F \check{g}_{\text{av}}^{\text{s}}(\mathbf{R}, \epsilon) \nabla_{\mathbf{R}} \check{g}_{\text{av}}^{\text{s}}(\mathbf{R}, \epsilon). \quad (\text{A24})$$

This leaves us with contributions only from second order terms in each of the three scattering potentials. Cross terms including two different types of scattering potential either

disappear when we neglect terms from the odd equation, or they are neglected due to averaging over all directions of the spins of the magnetic impurities. In treating second order terms in the magnetic impurity potential, the same averaging over spin directions causes cross terms between two different magnetic impurities to give zero contribution. We can then write $S_i S_j = S(S+1)\delta_{i,j}$. Inserting Eq. (A24) into the even equation results in the Usadel equation given in Eq. (1).

-
- [1] P. W. Anderson, Theory of dirty superconductors, *J. Phys. Chem. Solids* **11**, 26 (1959).
- [2] F. S. Bergeret, A. F. Volkov, and K. B. Efetov, Odd triplet superconductivity and related phenomena in superconductor-ferromagnet structures, *Rev. Mod. Phys.* **77**, 1321 (2005).
- [3] A. I. Buzdin, Proximity effects in superconductor-ferromagnet heterostructures, *Rev. Mod. Phys.* **77**, 935 (2005).
- [4] Y. Tanaka, M. Sato, and N. Nagaosa, Symmetry and topology in superconductors—Odd-frequency pairing and edge states, *J. Phys. Soc. Jpn.* **81**, 011013 (2012).
- [5] J. Linder and A. V. Balatsky, Odd-frequency superconductivity, *Rev. Mod. Phys.* **91**, 045005 (2019).
- [6] V. L. Berezinskii, New model of the anisotropic phase of superfluid He^3 , *Zh. Eksp. Teor. Fiz. Pis. Red.* **20**, 628 (1974) [*JETP Lett.* **20**, 287 (1974)].
- [7] M. Eschrig, Spin-polarized supercurrents for spintronics: A review of current progress, *Rep. Prog. Phys.* **78**, 104501 (2015).
- [8] F. S. Bergeret, A. F. Volkov, and K. B. Efetov, Long-Range Proximity Effects in Superconductor-Ferromagnet Structures, *Phys. Rev. Lett.* **86**, 4096 (2001).
- [9] A. F. Volkov, F. S. Bergeret, and K. B. Efetov, Odd Triplet Superconductivity in Superconductor-Ferromagnet Multilayered Structures, *Phys. Rev. Lett.* **90**, 117006 (2003).
- [10] F. S. Bergeret, A. F. Volkov, and K. B. Efetov, Manifestation of triplet superconductivity in superconductor-ferromagnet structures, *Phys. Rev. B* **68**, 064513 (2003).
- [11] T. S. Khaire, M. A. Khasawneh, W. P. Pratt, and N. O. Birge, Observation of Spin-Triplet Superconductivity in Co-Based Josephson Junctions, *Phys. Rev. Lett.* **104**, 137002 (2010).
- [12] J. W. A. Robinson, J. D. S. Witt, and M. G. Blamire, Controlled injection of spin-triplet supercurrents into a strong ferromagnet, *Science* **329**, 59 (2010).
- [13] J. W. A. Robinson, G. B. Halász, A. I. Buzdin, and M. G. Blamire, Enhanced Supercurrents in Josephson Junctions Containing Nonparallel Ferromagnetic Domains, *Phys. Rev. Lett.* **104**, 207001 (2010).
- [14] C. Klose, T. S. Khaire, Y. Wang, W. P. Pratt, N. O. Birge, B. J. McMorran, T. P. Ginley, J. A. Borchers, B. J. Kirby, B. B. Maranville, and J. Unguris, Optimization of Spin-Triplet Supercurrent in Ferromagnetic Josephson Junctions, *Phys. Rev. Lett.* **108**, 127002 (2012).
- [15] M. Eschrig, J. Kopu, J. C. Cuevas, and G. Schön, Theory of Half-Metal/Superconductor Heterostructures, *Phys. Rev. Lett.* **90**, 137003 (2003).
- [16] R. S. Keizer, S. T. B. Goennenwein, T. M. Klapwijk, G. Miao, G. Xiao, and A. Gupta, A spin triplet supercurrent through the half-metallic ferromagnet CrO_2 , *Nature (London)* **439**, 825 (2006).
- [17] M. S. Anwar, M. Weldhorst, A. Brinkman, and J. Aarts, Long range supercurrents in ferromagnetic CrO_2 using a multilayer contact structure, *Appl. Phys. Lett.* **100**, 052602 (2012).
- [18] N. Banerjee, J. W. A. Robinson, and M. G. Blamire, Reversible control of spin-polarized supercurrents in ferromagnetic Josephson junctions, *Nat. Commun.* **5**, 4771 (2014).
- [19] F. S. Bergeret and I. V. Tokatly, Singlet-Triplet Conversion and the Long-Range Proximity Effect in Superconductor-Ferromagnet Structures with Generic Spin Dependent Fields, *Phys. Rev. Lett.* **110**, 117003 (2013).
- [20] F. S. Bergeret and I. V. Tokatly, Spin-orbit coupling as a source of long-range triplet proximity effect in superconductor-ferromagnet hybrid structures, *Phys. Rev. B* **89**, 134517 (2014).
- [21] A. Costa, M. Sutula, V. Lauter, J. Song, J. Fabian, and J. S. Moodera, Superconducting triplet pairing in $\text{Al/Al}_2\text{O}_3/\text{Ni/Ga}$ junctions, *arXiv:2102.03083*.
- [22] P. V. Leksin, N. N. Garif'yanov, I. A. Garifullin, Ya. V. Fominov, J. Schumann, Y. Krupskaya, V. Kataev, O. G. Schmidt, and B. Büchner, Evidence For Triplet Superconductivity in a Superconductor-Ferromagnet Spin Valve, *Phys. Rev. Lett.* **109**, 057005 (2012).
- [23] X. L. Wang, A. Di Bernardo, N. Banerjee, A. Wells, F. S. Bergeret, M. G. Blamire, and J. W. A. Robinson, Giant triplet proximity effect in superconducting pseudo spin valves with engineered anisotropy, *Phys. Rev. B* **89**, 140508(R) (2014).
- [24] N. Banerjee, J. A. Ouassou, Y. Zhu, N. A. Stelmashenko, J. Linder, and M. G. Blamire, Controlling the superconducting transition by spin-orbit coupling, *Phys. Rev. B* **97**, 184521 (2018).
- [25] A. Di Bernardo, S. Diesch, Y. Gu, J. Linder, G. Divitini, C. Ducati, E. Scheer, M. G. Blamire, and J. W. A. Robinson, Signature of magnetic-dependent gapless odd frequency states at superconductor/ferromagnet interfaces, *Nat. Commun.* **6**, 8053 (2015).
- [26] S. Diesch, P. Machon, M. Wolz, C. Sürgers, D. Beckmann, W. Belzig, and E. Scheer, Creation of equal-spin triplet superconductivity at the Al/EuS interface, *Nat. Commun.* **9**, 5248 (2018).
- [27] C. González-Ruano, L. G. Johnsen, D. Caso, C. Tiusan, M. Hehn, N. Banerjee, J. Linder, and F. G. Aliev, Superconductivity-induced change in magnetic anisotropy in epitaxial ferromagnet-superconductor hybrids with spin-orbit interaction, *Phys. Rev. B* **102**, 020405(R) (2020).
- [28] C. González-Ruano, D. Caso, L. G. Johnsen, C. Tiusan, M. Hehn, N. Banerjee, J. Linder, and F. G. Aliev, Superconductivity assisted change of the perpendicular magnetic anisotropy in V/MgO/Fe junctions, *Sci. Rep.* **11**, 19041 (2021).
- [29] T. Yokoyama, Y. Tanaka, and N. Nagaosa, Anomalous Meissner Effect in a Normal-Metal-Superconductor Junction

- with a Spin-Active Interface, *Phys. Rev. Lett.* **106**, 246601 (2011).
- [30] A. Di Bernardo, Z. Salman, X. L. Wang, M. Amado, M. Egilmez, M. G. Flokstra, A. Suter, S. L. Lee, J. H. Zhao, T. Prokscha, E. Morenzoni, M. G. Blamire, J. Linder, and J. W. A. Robinson, Intrinsic Paramagnetic Meissner Effect Due to *s*-Wave Odd-Frequency Superconductivity, *Phys. Rev. X* **5**, 041021 (2015).
- [31] A. A. Jara, C. Safranski, I. N. Krivorotov, C.-T. Wu, A. N. Malmi-Kakkada, O. T. Valls, and K. Halterman, Angular dependence of superconductivity in superconductor/spin-valve heterostructures, *Phys. Rev. B* **89**, 184502 (2014).
- [32] E. A. Demler, G. B. Arnold, and M. R. Beasley, Superconducting proximity effects in magnetic metals, *Phys. Rev. B* **55**, 15174 (1997).
- [33] T. Rachatarungsit and S. Yoksan, Spin orbit scattering effect on long-range odd frequency triplet pairing in ferromagnet/superconductor bilayers, *Physica C* **467**, 156 (2007).
- [34] A. Buzdin, Density of states oscillations in a ferromagnetic metal in contact with a superconductor, *Phys. Rev. B* **62**, 11377 (2000).
- [35] Yu. Tanaka, A. A. Golubov, S. Kashiwaya, and M. Ueda, Anomalous Josephson Effect Between Even- and Odd-Frequency Superconductors, *Phys. Rev. Lett.* **99**, 037005 (2007).
- [36] P. O. Sukhachov and A. V. Balatsky, Spectroscopic and optical response of odd-frequency superconductors, *Phys. Rev. B* **100**, 134516 (2019).
- [37] M. Johnson, Spin coupled resistance observed in ferromagnet-superconductor-ferromagnet trilayers, *Appl. Phys. Lett.* **65**, 1460 (1994).
- [38] H. L. Zhao and S. Hershfield, Tunneling, relaxation of spin-polarized quasiparticles, and spin-charge separation in superconductors, *Phys. Rev. B* **52**, 3632 (1995).
- [39] J. P. Morten, A. Brataas, and W. Belzig, Spin transport in diffusive superconductors, *Phys. Rev. B* **70**, 212508 (2004).
- [40] J. P. Morten, A. Brataas, and W. Belzig, Spin transport and magnetoresistance in ferromagnet/superconductor/ferromagnet spin valves, *Phys. Rev. B* **72**, 014510 (2005).
- [41] U. Eckern and A. Schmid, Quasiclassical Green's function in the BCS pairing theory, *J. Low Temp. Phys.* **45**, 137 (1981).
- [42] W. Belzig, F. K. Wilhelm, C. Bruder, G. Schön, and A. D. Zaikin, Quasiclassical Green's function approach to mesoscopic superconductivity, *Superlattices Microstruct.* **25**, 1251 (1999).
- [43] D. Kuzmanovski, R. S. Souto, and A. V. Balatsky, Odd-frequency superconductivity near a magnetic impurity in a conventional superconductor, *Phys. Rev. B* **101**, 094505 (2020).
- [44] V. Perrin, F. L. N. Santos, G. C. Ménard, C. Brun, T. Cren, M. Civelli, and P. Simon, Unveiling Odd-Frequency Pairing Around a Magnetic Impurity in a Superconductor, *Phys. Rev. Lett.* **125**, 117003 (2020).
- [45] F. J. Jedema, B. J. van Wees, B. H. Hoving, A. T. Filip, and T. M. Klapwijk, Spin-accumulation-induced resistance in mesoscopic ferromagnet-superconductor junctions, *Phys. Rev. B* **60**, 16549 (1999).
- [46] S. Takahashi and S. Maekawa, Spin injection and detection in magnetic nanostructures, *Phys. Rev. B* **67**, 052409 (2003).
- [47] N. Poli, J. P. Morten, M. Urech, A. Brataas, D. B. Haviland, and V. Korenivski, Spin Injection and Relaxation in a Mesoscopic Superconductor, *Phys. Rev. Lett.* **100**, 136601 (2008).
- [48] H. Yang, S.-H. Yang, S. Takahashi, S. Maekawa, and S. S. P. Parkin, Extremely long quasiparticle spin lifetimes in superconducting aluminium using MgO tunnel spin injectors, *Nat. Mater.* **9**, 586 (2010).
- [49] F. Hübner, M. J. Wolf, D. Beckmann, and H. v. Löhneysen, Long-Range Spin-Polarized Quasiparticle Transport in Mesoscopic al Superconductors with a Zeeman Splitting, *Phys. Rev. Lett.* **109**, 207001 (2012).
- [50] C. H. L. Quay, D. Chevallier, C. Bena, and M. Aprili, Spin imbalance and spin-charge separation in a mesoscopic superconductor, *Nat. Phys.* **9**, 84 (2013).
- [51] M. J. Wolf, F. Hübner, S. Kolenda, H. v. Löhneysen, and D. Beckmann, Spin injection from a normal metal into a mesoscopic superconductor, *Phys. Rev. B* **87**, 024517 (2013).
- [52] M. Silaev, P. Virtanen, F. S. Bergeret, and T. T. Heikkilä, Long-Range Spin Accumulation from Heat Injection in Mesoscopic Superconductors with Zeeman Splitting, *Phys. Rev. Lett.* **114**, 167002 (2015).

VII

REFERENCE

Lina G. Johnsen, Haakon T. Simensen, Arne Brataas, and Jacob Linder,
Magnon spin current induced by triplet Cooper pair supercurrents,
Phys. Rev. Lett. **127**, 207001 (2021).

CONTRIBUTIONS

LGJ performed the analytical and numerical calculations and wrote the paper. HTS, AB, and JL contributed to discussions and revision of the manuscript. JL initiated and supervised the project.

Magnon Spin Current Induced by Triplet Cooper Pair Supercurrents

Lina G. Johnsen[✉],* Haakon T. Simensen[✉], Arne Brataas, and Jacob Linder
*Center for Quantum Spintronics, Department of Physics, Norwegian University of Science and Technology,
 NO-7491 Trondheim, Norway*

 (Received 12 May 2021; accepted 15 October 2021; published 10 November 2021)

At the interface between a ferromagnetic insulator and a superconductor there is a coupling between the spins of the two materials. We show that when a supercurrent carried by triplet Cooper pairs flows through the superconductor, the coupling induces a magnon spin current in the adjacent ferromagnetic insulator. The effect is dominated by Cooper pairs polarized in the same direction as the ferromagnetic insulator, so that charge and spin supercurrents produce similar results. Our findings demonstrate a way of converting Cooper pair supercurrents to magnon spin currents.

DOI: 10.1103/PhysRevLett.127.207001

Introduction.—Ferromagnetic insulators (FIs) are of high relevance for spin transport applications due to their ability to carry pure spin currents over long distances [1]. The study of how these spin currents can be converted into conventional electron-based charge and spin currents, and vice versa, has therefore attracted much attention over a number of years [2–4].

Early research on the topic showed that spin-polarized electron currents can excite the magnetization of a metallic ferromagnet via a spin-transfer torque [5–8], thus causing propagating spin waves [9–11]. The spin-polarized electron current can be obtained by sending a charge current through a homogeneous magnetic region [7], or through the spin-dependent scattering of a charge current via the spin-Hall effect [12–15]. In this way, one may convert charge currents into magnon spin currents. Conversely, precession of the magnetization of a FI causes spin pumping where spin is injected into an adjacent normal metal [16–20]. The injected spin current can further be transformed into a charge current through the inverse spin-Hall effect [21–26].

The precession of the magnetization of a FI can similarly cause injection of quasiparticle spin currents into a conventional *s*-wave superconductor (*S*). Early reports showed a decrease in the spin injection causing a reduced Gilbert damping [27]. This follows from the fact that the appearance of an energy gap below the superconducting critical temperature makes spin injection and transport in the form of quasiparticles possible only at energies above the gap edge [28]. Contrary to these observations [27,29], other works found a coherence peak in the Gilbert damping just below the superconducting critical temperature [30,31]. Theoretical works have followed the experimental advances [32–36] considering, e.g., noncolinear magnetizations [37], and the effects of a spin-splitting field [38,39]. The latter has been shown experimentally to cause a giant enhancement of the spin transport across the interface [40]. The converse effect, a conversion from

quasiparticle to magnon spin currents, has been predicted when the population of one of the quasiparticle spin species is higher [41].

Superconductors can however also carry charge and spin supercurrents [42]. In conventional singlet superconductors, the Cooper pairs carry zero net spin and are easily destroyed by magnetic fields. Supercurrents carried by spin-polarized triplet Cooper pairs are, on the other hand, robust to the spin-dependent pair-breaking effect of magnetic fields and allow for dissipationless spin transport [43–45]. Moreover, they have attracted a lot of attention in the light of recent spin-pumping experiments where both spin-polarized supercurrents [46–49] and quasiparticle spin currents [50] have been pointed out as potential explanations for the observed effects. Motivated by these advances, we pose the following fundamental question: Is it possible for a triplet Cooper pair supercurrent to induce a magnon spin current?

To answer this question, we study the coupling between the spins in a ferromagnetic insulator and a *p*-wave superconductor carrying triplet Cooper pair supercurrents. We find that to the first order in perturbation theory, a supercurrent only causes a renormalization of the magnon gap. To the second order, both charge and spin supercurrents induce a magnon spin current in the adjacent FI. This effect is dominated by Cooper pairs polarized parallel to the magnetization. The magnon spin current appears due to a symmetry breaking in the magnon energy spectrum with respect to momentum inversion. The asymmetry originates from the coupling to the superconductor, which due to the presence of the supercurrent has an energy spectrum that is tilted in momentum space. We propose that the supercurrent-induced magnon spin current can be measured in the *S*-FI structure shown in Fig. 1. However, as we will discuss further, an intrinsic triplet superconductor is not necessarily required, since such superconductivity can be established even in nonsuperconducting materials via

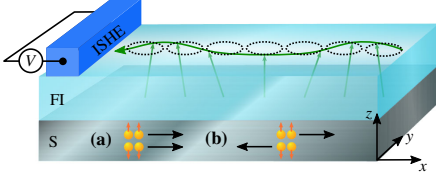


FIG. 1. A superconductor (S) can carry (a) a charge supercurrent consisting of an equal number of spin-up and spin-down triplet Cooper pairs traveling in the same direction or (b) a spin supercurrent where the spin-up and spin-down triplets travel in opposite directions. Because of a coupling between the spins in the superconductor and in an adjacent ferromagnetic insulator (FI), these supercurrents induce a magnon spin current in the FI (green). The induced spin current can be measured through a normal-metal contact via the inverse spin-Hall effect (ISHE). In order to couple the currents, we only require that the Cooper pairs must carry a net spin along the easy axis of the FI which is fixed along the z axis. The orientation of the interface is not restricted by our model, so that the Cooper pair-induced magnon spin current also occurs if the FI is instead polarized in plane, in that case with an interface in the xz plane.

the proximity effect [42–45]. In the following, we present our model for describing this structure.

Microscopic model.—To describe the S-FI structure, we need a Hamiltonian $H = H_S + H_{\text{FI}} + H_c$ describing the superconductor, the ferromagnetic insulator, and the coupling between these, respectively. We describe this system as two separate translationally invariant two-dimensional (2D) layers on top of each other, where coupling between the layers exists for lattice sites corresponding to the same location in the plane. This allows us to describe our Hamiltonian in momentum space. Details on how the Hamiltonian can be derived from a lattice model is described in the Supplemental Material (SM) [51].

We describe the current-carrying state of the superconductor by the mean-field Hamiltonian,

$$H_S = \sum_{k,\sigma} \epsilon_k c_{k,\sigma}^\dagger c_{k,\sigma} - \frac{1}{2} \sum_{k,\sigma} [\Delta_{k,\sigma}^\delta c_{k+Q^\sigma}^\dagger c_{-k+Q^\sigma}^\dagger + \text{H.c.}], \quad (1)$$

$$\epsilon_k = -\mu - 2t \sum_{\delta} \cos(\mathbf{k} \cdot \boldsymbol{\delta}), \quad \Delta_{k,\sigma}^\delta = f_\sigma^\delta \sin(\mathbf{k} \cdot \boldsymbol{\delta}), \quad (2)$$

corresponding to $p_{x(y)}$ -wave superconductivity for $\Delta_{k,\sigma}^{x(y)}$. The first term in H_S sets the chemical potential μ and describes hopping between nearest neighbor sites, where t is the hopping integral. For layers with a square lattice structure, the vectors $\boldsymbol{\delta}$ from a given lattice site to all nearest neighbors is a set of two perpendicular vectors. We can also describe a one-dimensional (1D) chain by eliminating one of the vectors in the set. The second term gives rise to p -

wave superconducting triplet pairing between electrons of equal spin. The Cooper pairs have a center-of-mass momentum of $2Q^\sigma$ so that we have a supercurrent of spin- σ Cooper pairs inside the superconductor. The supercurrent is enforced by an externally applied homogeneous phase gradient [51–53], which can be obtained experimentally via electric contacts at each end of the superconductor. The applied current is assumed to be smaller than the critical supercurrent of the system. The strength of the superconducting order parameter $\Delta_{k,\sigma}^\delta$ is given by the real parameter f_σ^δ . The operators $c_{k,\sigma}^{(\dagger)}$ annihilate (create) an electron with momentum k and spin σ .

The Hamiltonian describing the ferromagnetic insulator is obtained from a Heisenberg model with uniaxial anisotropy favoring parallel spins aligned along the z axis. By performing a Holstein-Primakoff (HP) transformation to the second order in the bosonic operators, we arrive at

$$H_{\text{FI}} = \sum_q \omega_q a_q^\dagger a_q, \quad \omega_q = 4S \left(K + J \sum_{\delta} [1 - \cos(\mathbf{q} \cdot \boldsymbol{\delta})] \right). \quad (3)$$

The strength of the coupling between spins on neighboring lattice sites is $J > 0$, and S is the magnitude of the spins. The anisotropy favoring alignment along the z axis gives rise to a magnon gap whose magnitude is determined by $K > 0$. We include the magnon gap to make contact with an experimentally realistic setting, and also to satisfy the condition that the coupling strength must be small compared to the original magnon energies for all momenta. The operators $a_q^{(\dagger)}$ annihilate (create) a magnon of momentum q . Since the FI is polarized along the z axis, all magnons have spin along $-z$.

We now consider the coupling between the superconductor and the ferromagnetic insulator. By performing a HP transformation to the second order in the bosonic operators on the coupling $H_c = -\sum_i \Lambda s_i \cdot S_i$ between the electron spins s_i in the superconductor and the spins S_i in the ferromagnetic insulator, we find that the coupling $H_c = H_c^{2c} + H_c^{2c1a} + H_c^{2c2a}$ consists of three terms. These are given by

$$H_c^{2c} = -\lambda \sqrt{\frac{NS}{2}} \sum_{k,\sigma} \sigma c_{k,\sigma}^\dagger c_{k,\sigma}, \quad (4)$$

$$H_c^{2c1a} = -\lambda \sum_{k,q} (c_{k+q,\uparrow}^\dagger c_{k,\downarrow} a_{-q}^\dagger + c_{k+q,\downarrow}^\dagger c_{k,\uparrow} a_q), \quad (5)$$

$$H_c^{2c2a} = \frac{\lambda}{\sqrt{2NS}} \sum_{k,q,q',\sigma} \sigma c_{k+q,\sigma}^\dagger c_{k-q',\sigma} a_{-q}^\dagger a_{q'}. \quad (6)$$

Above, N is the total number of lattice sites, and $\lambda = \Lambda \sqrt{S/2N} > 0$ is the coupling strength, where we have

absorbed a factor into the coupling strength for simplicity of notation. The first term, H_c^{2c} , describes a spin splitting of the fermionic energy spectrum. We absorb this term into H_S by letting $\epsilon_k \rightarrow \epsilon_{k,\sigma} = \epsilon_k - \sigma\lambda\sqrt{NS/2}$. In the absence of magnons, $H_S + H_c^{2c}$ reproduces the familiar energy spectrum of a triplet superconductor in a spin-splitting field. The second term, H_c^{2c1a} , transfers spin between fermion and boson operators and will turn out to be significant for inducing a magnon spin current. The third term, H_c^{2c2a} , only gives a constant shift in the magnon energy spectrum to the first order in perturbation theory and is projected out to the second order.

Before we start analyzing how the coupling affects the magnonic part of the Hamiltonian, we first write the superconducting part in the diagonal form:

$$H_S = \sum_{k,\sigma} E_{k-Q^\sigma} \gamma_{k,\sigma}^\dagger \gamma_{k,\sigma}, \quad (7)$$

$$E_{k,\sigma} = \frac{1}{2}(\epsilon_{k+Q^\sigma} - \epsilon_{-k+Q^\sigma}) + \sqrt{\left[\frac{1}{2}(\epsilon_{k+Q^\sigma} + \epsilon_{-k+Q^\sigma})\right]^2 + |\Delta_k|^2}. \quad (8)$$

We have assumed the magnitude of the superconducting order parameter $|\Delta_k|$ to be spin independent. The old operators are related to the new ones by

$$c_{k+Q^\sigma} = u_{k,\sigma} \gamma_{k+Q^\sigma} + \text{sgn}(\Delta_k^\dagger) v_{k,\sigma} \gamma_{-k+Q^\sigma}^\dagger, \quad (9)$$

with coefficients

$$\begin{aligned} u_{k,\sigma} &= \left[\frac{1}{2} \left(1_{(-)}^+ \frac{\frac{1}{2}(\epsilon_{k+Q^\sigma} + \epsilon_{-k+Q^\sigma})}{\sqrt{\left[\frac{1}{2}(\epsilon_{k+Q^\sigma} + \epsilon_{-k+Q^\sigma})\right]^2 + |\Delta_k|^2}} \right) \right]^{1/2}, \\ v_{k,\sigma} &= \left[\frac{1}{2} \left(1_{(-)}^- \frac{\frac{1}{2}(\epsilon_{k+Q^\sigma} + \epsilon_{-k+Q^\sigma})}{\sqrt{\left[\frac{1}{2}(\epsilon_{k+Q^\sigma} + \epsilon_{-k+Q^\sigma})\right]^2 + |\Delta_k|^2}} \right) \right]^{1/2}. \end{aligned} \quad (10)$$

Using the above relation, we also express the coupling terms in Eqs. (5) and (6) in terms of the new fermion operators. Note that while the coefficients $u_{k,\sigma}$ and $v_{k,\sigma}$ remain invariant under inversion of \mathbf{k} , a finite supercurrent ($Q^\sigma \neq 0$) breaks the momentum inversion symmetry of the eigenenergies $E_{k,\sigma}$.

To the first order in perturbation theory.—We first investigate what happens if we only take into account first-order terms in perturbation theory. This is done by evaluating the expectation values with respect to the new fermion operators, using that

$$\langle \gamma_{k,\sigma}^\dagger \gamma_{k',\sigma'} \rangle_\gamma = f_{\text{FD}}(E_{k-Q^\sigma}) \delta_{k,k'} \delta_{\sigma,\sigma'}, \quad (11)$$

$$\langle \gamma_{k,\sigma}^\dagger \gamma_{k',\sigma'}^\dagger \rangle_\gamma = \langle \gamma_{k,\sigma} \gamma_{k',\sigma'} \rangle_\gamma = 0, \quad (12)$$

where $f_{\text{FD}}(E_{k,\sigma})$ is the Fermi-Dirac (FD) distribution. Neglecting terms that are constant in the boson operators, we find that

$$\langle H \rangle_\gamma = \sum_q (\omega_q + \omega_\lambda) a_q^\dagger a_q, \quad (13)$$

$$\omega_\lambda = \frac{\lambda}{\sqrt{2NS}} \sum_{k,\sigma} \sigma \{ (u_{k,\sigma}^2 - v_{k,\sigma}^2) f_{\text{FD}}(E_{k,\sigma}) + v_{k,\sigma}^2 \}. \quad (14)$$

Since the coupling only results in a \mathbf{q} independent renormalization of the magnon gap, there is no magnon spin current generated. The renormalization of the magnon gap is caused by the spin splitting of the quasiparticle energy spectrum and exists even in the absence of supercurrents. Since the spin splitting originates from the adjacent FI, there is an excess population of spin-up electrons, and the magnon gap is always increased. A further renormalization occurs in the presence of supercurrents due to the tilting of the quasiparticle energy spectrum.

To the second order in perturbation theory.—Next, we want to perform a Schrieffer–Wolff (SW) transformation to obtain an effective Hamiltonian to the second order in perturbation theory [54]. We define a transformed Hamiltonian $H_{\text{eff}} = e^{iS} H e^{-iS}$, and use the Baker-Campbell-Hausdorff formula to expand it. By requiring that

$$H_c^{2c1a} + H_c^{2c2a} = i[H_{\text{FI}} + H_S, S], \quad (15)$$

we project out first-order terms that do not commute with $H_{\text{FI}} + H_S$. Keeping terms up to the second order, the effective Hamiltonian can be written as

$$H_{\text{eff}} = H_{\text{FI}} + H_S + \frac{i}{2} [S, H_c^{2c1a} + H_c^{2c2a}], \quad (16)$$

where H_c^{2c} is absorbed into H_S . In order to determine S , we make an ansatz that it consists of two types of terms, S^{2c1a} and S^{2c2a} , that are of the same form as H_c^{2c1a} and H_c^{2c2a} , respectively. The coefficients are determined by solving Eq. (15). By disregarding terms above second order in the fluctuations $a_q^{(\dagger)}$, and also neglecting all terms related to renormalization of the superconductivity caused by magnons (terms with four fermion operators), we are left with only one nonzero commutator $[S^{2c1a}, H_c^{2c1a}]$. After computing the commutator, evaluating the expectation value of the Hamiltonian with respect to the fermion operators, and diagonalizing with respect to the boson operators, we end up with an effective Hamiltonian of the form

$$\langle H_{\text{eff}} \rangle_\gamma = \sum_q \Omega_q \alpha_q^\dagger \alpha_q, \quad (17)$$

$$\Omega_q = \Omega_{q+(Q^1-Q^i)}^+ + \Omega_{q-(Q^1-Q^i)}^-, \quad (18)$$

$$\begin{aligned} \Omega_q^\pm &= \pm \frac{1}{2} (M_q^{(11)} - M_{-q}^{(11)}) \\ &+ \sqrt{\left[\frac{1}{2} (M_q^{(11)} + M_{-q}^{(11)}) \right]^2 - (M_q^{(12)})^2}, \end{aligned} \quad (19)$$

$$M_q^{(11)} = \frac{1}{2} \omega_{q-(Q^1-Q^i)} + \sum_k A_{k,q}^{(11)}, \quad (20)$$

$$M_q^{(12)} = \sum_k A_{k,q}^{(12)}. \quad (21)$$

The coefficients $A_{k,q}^{(11)}$ and $A_{k,q}^{(12)}$ are given in the SM [51]. The old magnon operators are related to the new ones by

$$a_{q-(Q^\dagger-Q^\downarrow)} = x_q \alpha_{q-(Q^\dagger-Q^\downarrow)} - w_q \alpha_{-q-(Q^\dagger-Q^\downarrow)}^\dagger, \quad (22)$$

with coefficients

$$x_q = \left\{ \frac{1}{2} \left[1 + \frac{\frac{1}{2}(M_q^{(11)} + M_{-q}^{(11)})}{\sqrt{[\frac{1}{2}(M_q^{(11)} + M_{-q}^{(11)})]^2 - (M_q^{(12)})^2}} \right] \right\}^{1/2}. \quad (23)$$

We can now evaluate expectation values of the new operators according to

$$\langle \alpha_q^\dagger \alpha_q \rangle_\alpha = f_{\text{BE}}(\Omega_q) \delta_{q,q'}, \quad (24)$$

$$\langle \alpha_q^\dagger \alpha_{q'}^\dagger \rangle_\alpha = \langle \alpha_q \alpha_{q'} \rangle_\alpha = 0, \quad (25)$$

where $f_{\text{BE}}(\Omega_q)$ is the Bose-Einstein (BE) distribution.

Finally, we define the magnon spin current density [55,56] polarized along z traveling in the δ direction:

$$j_\delta^z = \frac{1}{N} \sum_q v_q^\delta \langle S_q^z \rangle_\alpha, \quad v_q^\delta = (\Omega_{q+\delta} - \Omega_{q-\delta})/2|\delta|, \quad (26)$$

$$\langle S_q^z \rangle_\alpha = -[|x_{q+(Q^\dagger-Q^\downarrow)}|^2 + |w_{-q-(Q^\dagger-Q^\downarrow)}|^2] f_{\text{BE}}(\Omega_q). \quad (27)$$

Above, v_q^δ is the velocity associated with a momentum mode q , and $\langle S_q^z \rangle_\alpha$ is the spin associated with the new magnon operators for a momentum mode q .

Induced magnon spin current.—Before presenting the results for the magnon spin current, we argue that Curie's principle allows for charge and spin supercurrents to induce magnon spin currents traveling along the same axis. Curie's principle states that an effect should obey the symmetries of the cause. The symmetry of our system is that of a square lattice with a magnetization along z . The p -wave order parameter does not impose any further restrictions on the symmetry. Since the presence of a charge or spin supercurrent in the plane perpendicular to the z axis breaks both the C^4 rotational symmetry around the z axis and the mirror symmetry in the xy plane, these leave the system without any symmetry restrictions and allow for resulting magnon spin currents in any direction. A spin or charge supercurrent along the z axis however only allows for a magnon spin current along the same axis. Since the expression for the magnon spin current density [Eq. (26)] is the same regardless of whether the supercurrent is traveling parallel or perpendicular to the magnetization, the magnon spin

current has to abide by the strictest restriction. Thus, charge and spin supercurrents can only induce magnon spin currents along the same axis. In the following, we only present the results for two coupled S and FI 1D chains, since these are qualitatively the same as for two coupled square lattice layers.

In Fig. 2, we show that both a charge and a spin supercurrent induce the same finite magnon spin current in the adjacent FI. A finite center-of-mass momentum ($Q^\sigma \neq 0$) of the spin- σ Cooper pairs causes a symmetry breaking in the eigenenergies $E_{k,\sigma}$ of the superconductor [Eq. (8)] with respect to inversion of the momentum. The momentum inversion symmetry is broken irrespective of the relative directions of Q^\dagger and Q^\downarrow . The asymmetry is transferred to the eigenenergy spectrum Ω_q of the new boson operators [Eqs. (18) and (19)] via the coupling

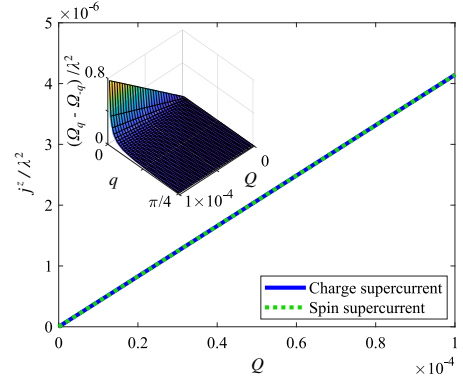


FIG. 2. Both a charge ($Q^\dagger = Q^\downarrow = Q$) and a spin ($Q^\dagger = -Q^\downarrow = Q$) supercurrent induce the same finite magnon spin current density j^z in an adjacent ferromagnetic insulator. This is because spin-up Cooper pairs dominate in inducing the magnon spin current. The supercurrents induce the magnon spin current through an asymmetry in the eigenenergy spectrum Ω_q of the new boson operators with respect to inversion of the momentum q (inset). The results are robust to changes in the parameters, and for this particular figure we have chosen $\mu = -0.5$, $\lambda = 10^{-4}$, $f_\uparrow = f_\downarrow = 10^{-4}$, $S = 1/2$, $J = 10^{-2}$, $K = 10^{-3}$ for a 1D chain of $N = 365$ lattice sites at temperature $T = 0.001$. For a square lattice with a p_x - or p_y -wave symmetry, the results are qualitatively the same as in 1D. A supercurrent of spin-up Cooper pairs induces a current of spin-down magnons in the opposite direction, while transverse currents are not allowed. All energies, as well as the magnon spin current density, are scaled by the hopping parameter t . The temperature is scaled by t/k_B , where k_B is the Boltzmann constant. The momenta q and Q are both scaled by \hbar/a , where \hbar is the reduced Planck constant and a is the lattice constant.

[Eq. (5)]. To second order, the coupling transfers momentum between quasiparticles and magnons. The eigenenergies Ω_q enter into the expression for the magnon spin current through the velocity of each momentum mode v_q and the Bose-Einstein distribution function $f_{\text{BE}}(\Omega_q)$ in Eqs. (26) and (27). Supercurrents of spin- σ Cooper pairs are thus able to introduce a momentum inversion symmetry breaking that causes a finite magnon spin current. We illustrate this lack of symmetry by plotting $\Omega_q - \Omega_{-q}$ for $q > 0$ in the inset of Fig. 2. The asymmetry in the magnon energy spectrum disappears for large momenta q , because the renormalization of the quasiparticle energy spectrum is also small for large momenta [see Eq. (8)].

The contribution from the spin-down Cooper pairs in inducing the magnon spin current is negligible compared to the contribution from the spin-up Cooper pairs. This can be seen from the results for the charge and spin supercurrents in Fig. 2. A charge supercurrent corresponds to spin-up and spin-down Cooper pairs traveling in the same direction, while for a spin supercurrent the spin-down Cooper pairs instead travel in the opposite direction. The fact that inverting the propagation direction of the spin-down Cooper pairs has no visible effect on the magnon spin current density implies that it is mostly spin-up Cooper pairs that contribute in inducing the magnon spin current. The fact that spin-up and spin-down Cooper pairs do not contribute equally follows from the coupling between spins in the superconductor and ferromagnetic insulator, where the FI breaks the up-down symmetry by having a majority spin polarization along z . We observe that this asymmetry must be introduced through Eq. (5), since neglecting the spin-splitting term [Eq. (4)] only slightly alters the results.

Outlook.—Our results provides a proof of principle, showing that it is possible to convert both charge and spin supercurrents into a magnon spin current. Although we presented results for a p_x -wave symmetry in one dimension, we expect similar results with a different symmetry, e.g., a $p_x + ip_y$ -wave symmetry [57]. In fact, from results for a square lattice, we have verified that we obtain qualitatively the same results for a p_x - and a p_y -wave superconducting order parameter when the supercurrent travels along the x axis. Other structures that have been shown to carry spin-polarized supercurrents include heterostructures where conventional superconductors are combined with half-metals [58–61], magnetic multilayers [62–64], or structures with spiral magnetic order [65–68]. These structures may also be relevant, since the crucial ingredient for a broken momentum inversion symmetry is the presence of spin-polarized triplet supercurrents, and not the particular symmetry of the superconducting order parameter. We therefore posit that together with the p -wave superconductor discussed in this work, supercurrents of odd-frequency triplets could also be potential

candidates for inducing magnon spin currents in an adjacent ferromagnetic insulator.

This work was supported by the Research Council of Norway through its Centres of Excellence funding scheme, Project No. 262633 “QuSpin.”

*Corresponding author.
lina.g.johnsen@ntnu.no

- [1] L. J. Cornelissen, J. Liu, R. A. Duine, J. Ben Youssef, and B. J. van Wees, Long-distance transport of magnon spin information in a magnetic insulator at room temperature, *Nat. Phys.* **11**, 1022 (2015).
- [2] A. V. Chumak, V. I. Vasyuchka, A. A. Serga, and B. Hillebrands, Magnon spintronics, *Nat. Phys.* **11**, 453 (2015).
- [3] W. Han, S. Maekawa, and X.-C. Xie, Spin current as a probe of quantum materials, *Nat. Mater.* **19**, 139 (2020).
- [4] A. Brataas, B. van Wees, O. Klein, G. de Loubens, and M. Viret, Spin insulatronics, *Phys. Rep.* **885**, 1 (2020).
- [5] J. C. Slonczewski, Current-driven excitation of magnetic multilayers, *J. Magn. Magn. Mater.* **159**, L1 (1996).
- [6] L. Berger, Emission of spin waves by a magnetic multilayer traversed by a current, *Phys. Rev. B* **54**, 9353 (1996).
- [7] M. Tsoi, A. G. M. Jansen, J. Bass, W.-C. Chiang, M. Seck, V. Tsoi, and P. Wyder, Excitation of a Magnetic Multilayer by an Electric Current, *Phys. Rev. Lett.* **80**, 4281 (1998).
- [8] A. Manchon, J. Železný, I. M. Miron, T. Jungwirth, J. Sinova, A. Thiaville, K. Garello, and P. Gambardella, Current-induced spin-orbit torques in ferromagnetic and antiferromagnetic systems, *Rev. Mod. Phys.* **91**, 035004 (2019).
- [9] V. E. Demidov, S. Urazhdin, and S. O. Demokritov, Direct observation and mapping of spin waves emitted by spin-torque nano-oscillators, *Nat. Mater.* **9**, 984 (2010).
- [10] M. Madami, S. Bonetti, G. Consolo, S. Tacchi, G. Carlotti, G. Gubbiotti, F. B. Mancoff, M. A. Yar, and J. Åkerman, Direct observation of a propagating spin wave induced by spin-transfer torque, *Nat. Nanotechnol.* **6**, 635 (2011).
- [11] Z. Wang, Y. Sun, M. Wu, V. Tiberkevich, and A. Slavin, Control of Spin Waves in a Thin Film Ferromagnetic Insulator through Interfacial Spin Scattering, *Phys. Rev. Lett.* **107**, 146602 (2011).
- [12] M. I. Dyakonov and V. I. Perel, Current-induced spin orientation of electrons in semiconductors, *Phys. Lett.* **35A**, 459 (1971).
- [13] K. Ando, S. Takahashi, K. Harii, K. Sasage, J. Ieda, S. Maekawa, and E. Saitoh, Electric Manipulation of Spin Relaxation using the Spin Hall Effect, *Phys. Rev. Lett.* **101**, 036601 (2008).
- [14] Y. Kajiwara, K. Harii, S. Takahashi, J. Ohe, K. Uchida, M. Mizuguchi, H. Umezawa, H. Kawai, K. Ando, K. Takanashi, S. Maekawa, and E. Saitoh, Transmission of electrical signals by spin-wave interconversion in a magnetic insulator, *Nature (London)* **464**, 262 (2010).
- [15] V. E. Demidov, S. Urazhdin, E. R. J. Edwards, and S. O. Demokritov, Wide-range control of ferromagnetic resonance by spin Hall effect, *Appl. Phys. Lett.* **99**, 172501 (2011).

- [16] Y. Tserkovnyak, A. Brataas, and G. E. W. Bauer, Enhanced Gilbert Damping in Thin Ferromagnetic Films, *Phys. Rev. Lett.* **88**, 117601 (2002).
- [17] E. Šimánek and B. Heinrich, Gilbert damping in magnetic multilayers, *Phys. Rev. B* **67**, 144418 (2003).
- [18] G. Woltersdorf, M. Buess, B. Heinrich, and C. H. Back, Time Resolved Magnetization Dynamics of Ultrathin Fe(001) Films: Spin-Pumping and Two-Magnon Scattering, *Phys. Rev. Lett.* **95**, 037401 (2005).
- [19] M. V. Costache, M. Sladkov, S. M. Watts, C. H. van der Wal, and B. J. van Wees, Electrical Detection of Spin Pumping due to the Precessing Magnetization of a Single Ferromagnet, *Phys. Rev. Lett.* **97**, 216603 (2006).
- [20] Y. Tserkovnyak, A. Brataas, G. E. W. Bauer, and B. I. Halperin, Nonlocal magnetization dynamics in ferromagnetic heterostructures, *Rev. Mod. Phys.* **77**, 1375 (2005).
- [21] E. Saitoh, M. Ueda, and H. Miyajima, Conversion of spin current into charge current at room temperature: Inverse spin-Hall effect, *Appl. Phys. Lett.* **88**, 182509 (2006).
- [22] C. W. Sandweg, Y. Kajiwara, A. V. Chumak, A. A. Serga, V. I. Vasyuchka, M. B. Jungfleisch, E. Saitoh, and B. Hillebrands, Spin Pumping by Parametrically Excited Exchange Magnons, *Phys. Rev. Lett.* **106**, 216601 (2011).
- [23] F. D. Czeschka, L. Dreher, M. S. Brandt, M. Weiler, M. Althammer, I.-M. Imort, G. Reiss, A. Thomas, W. Schoch, W. Limmer, H. Huebl, R. Gross, and S. T. B. Goennenwein, Scaling Behavior of the Spin Pumping Effect in Ferromagnet-Platinum Bilayers, *Phys. Rev. Lett.* **107**, 046601 (2011).
- [24] V. Castel, N. Vlietstra, J. Ben Youssef, and B. J. van Wees, Platinum thickness dependence of the inverse spin-Hall voltage from spin pumping in a hybrid yttrium iron garnet/platinum system, *Appl. Phys. Lett.* **101**, 132414 (2012).
- [25] C. Hahn, G. de Loubens, O. Klein, M. Viret, V. V. Naletov, and J. Ben Youssef, Comparative measurements of inverse spin Hall effects and magnetoresistance in YIG/Pt and YIG/Ta, *Phys. Rev. B* **87**, 174417 (2013).
- [26] M. Weiler, M. Althammer, M. Schreier, J. Lotze, M. Perpeintner, S. Meyer, H. Huebl, R. Gross, A. Kamra, J. Xiao, Y.-T. Chen, H. J. Jiao, G. E. W. Bauer, and S. T. B. Goennenwein, Experimental Test of the Spin Mixing Interface Conductivity Concept, *Phys. Rev. Lett.* **111**, 176601 (2013).
- [27] C. Bell, S. Milikisyants, M. Huber, and J. Aarts, Spin Dynamics in a Superconductor-Ferromagnet Proximity System, *Phys. Rev. Lett.* **100**, 047002 (2008).
- [28] H. Yang, S.-H. Yang, S. Takahashi, S. Maekawa, and S. S. P. Parkin, Extremely long quasiparticle spin lifetimes in superconducting aluminium using MgO tunnel spin injectors, *Nat. Mater.* **9**, 586 (2010).
- [29] K.-R. Jeon, C. Ciccarelli, H. Kurebayashi, J. Wunderlich, L. F. Cohen, S. Komori, J. W. A. Robinson, and M. G. Blamire, Spin-pumping-induced inverse spin Hall effect in Nb/Ni₈₀Fe₂₀ bilayers and its strong decay across the superconducting transition temperature, *Phys. Rev. Applied* **10**, 014029 (2018).
- [30] M. Inoue, M. Ichioka, and H. Adachi, Spin pumping into superconductors: A new probe of spin dynamics in a superconducting thin film, *Phys. Rev. B* **96**, 024414 (2017).
- [31] Y. Yao, Q. Song, Y. Takamura, J. P. Cascales, W. Yuan, Y. Ma, Y. Yun, X. C. Xie, J. S. Moodera, and W. Han, Probe of spin dynamics in superconducting nbn thin films via spin pumping, *Phys. Rev. B* **97**, 224414 (2018).
- [32] T. Kato, Y. Ohnuma, M. Matsuo, J. Rech, T. Jonckheere, and T. Martin, Microscopic theory of spin transport at the interface between a superconductor and a ferromagnetic insulator, *Phys. Rev. B* **99**, 144411 (2019).
- [33] M. A. Silaev, Finite-frequency spin susceptibility and spin pumping in superconductors with spin-orbit relaxation, *Phys. Rev. B* **102**, 144521 (2020).
- [34] M. A. Silaev, Large enhancement of spin pumping due to the surface bound states in normal metal–superconductor structures, *Phys. Rev. B* **102**, 180502(R) (2020).
- [35] M. Tanhayi Ahari and Y. Tserkovnyak, Superconductivity-enhanced spin pumping: Role of andreev resonances, *Phys. Rev. B* **103**, L100406 (2021).
- [36] Y. Ominato, A. Yamakage, and M. Matsuo, Anisotropic superconducting spin transport at magnetic interfaces, arXiv:2103.05871.
- [37] H. T. Simensen, L. G. Johnsen, J. Linder, and A. Brataas, Spin pumping between noncollinear ferromagnetic insulators through thin superconductors, *Phys. Rev. B* **103**, 024524 (2021).
- [38] R. Ojajarvi, J. Manninen, T. T. Heikkilä, and P. Virtanen, Nonlinear spin torque, pumping, and cooling in superconductor/ferromagnet systems, *Phys. Rev. B* **101**, 115406 (2020).
- [39] T. T. Heikkilä, M. Silaev, P. Virtanen, and F. S. Bergeret, Thermal, electric and spin transport in superconductor/ferromagnetic-insulator structures, *Prog. Surf. Sci.* **94**, 100540 (2019).
- [40] K.-R. Jeon, J.-C. Jeon, X. Zhou, A. Migliorini, J. Yoon, and S. S. P. Parkin, Giant transition-state enhancement of quasiparticle spin-Hall effect in an exchange-spin-split superconductor detected by non-local magnon spin-transport, *ACS Nano* **14**, 15874 (2020).
- [41] V. S. U. A. Vargas and A. R. Moura, Injection of spin current at the superconductor/ferromagnetic insulator interface, *J. Magn. Magn. Mater.* **494**, 165813 (2020).
- [42] M. Eschrig, Spin-polarized supercurrents for spintronics: A review of current progress, *Rep. Prog. Phys.* **78**, 104501 (2015).
- [43] F. S. Bergeret, A. F. Volkov, and K. B. Efetov, Odd triplet superconductivity and related phenomena in superconductor-ferromagnet structures, *Rev. Mod. Phys.* **77**, 1321 (2005).
- [44] A. I. Buzdin, Proximity effects in superconductor-ferromagnet heterostructures, *Rev. Mod. Phys.* **77**, 935 (2005).
- [45] J. Linder and J. W. A. Robinson, Superconducting spintronics, *Nat. Phys.* **11**, 307 (2015).
- [46] K.-R. Jeon, C. Ciccarelli, A. J. Ferguson, H. Kurebayashi, L. F. Cohen, X. Montiel, M. Eschrig, J. W. A. Robinson, and M. G. Blamire, Enhanced spin pumping into superconductors provides evidence for superconducting pure spin currents, *Nat. Mater.* **17**, 499 (2018).
- [47] K.-R. Jeon, C. Ciccarelli, H. Kurebayashi, L. F. Cohen, X. Montiel, M. Eschrig, S. Komori, J. W. A. Robinson, and M. G. Blamire, Exchange-field enhancement of superconducting spin pumping, *Phys. Rev. B* **99**, 024507 (2019).

- [48] K.-R. Jeon, C. Ciccarelli, H. Kurebayashi, L. F. Cohen, X. Montiel, M. Eschrig, T. Wagner, S. Komori, A. Srivastava, J. W. A. Robinson, and M. G. Blamire, Effect of Meissner screening and trapped magnetic flux on magnetization dynamics in thick Nb/Ni₈₀Fe₂₀/Nb trilayers, *Phys. Rev. Applied* **11**, 014061 (2019).
- [49] K.-R. Jeon, C. Ciccarelli, H. Kurebayashi, L. F. Cohen, S. Komori, J. W. A. Robinson, and M. G. Blamire, Abrikosov vortex nucleation and its detrimental effect on superconducting spin pumping in Pt/Nb/Ni₈₀Fe₂₀/Nb/Pt proximity structures, *Phys. Rev. B* **99**, 144503 (2019).
- [50] M. Müller, L. Liensberger, L. Flacke, H. Huebl, A. Kamra, W. Belzig, R. Gross, M. Weiler, and M. Althammer, Temperature-Dependent Spin Transport and Current-Induced Torques in Superconductor-Ferromagnet Heterostructures, *Phys. Rev. Lett.* **126**, 087201 (2021).
- [51] See Supplemental Material at <http://link.aps.org/supplemental/10.1103/PhysRevLett.127.207001> for more details on the derivation of the momentum space Hamiltonian and for expressions of the coefficients in Eqs. (20) and (21).
- [52] R. Takashima, S. Fujimoto, and T. Yokoyama, Adiabatic and nonadiabatic spin torques induced by a spin-triplet supercurrent, *Phys. Rev. B* **96**, 121203(R) (2017).
- [53] S.-H. Lin, M. V. Milošević, B. Jankó, and F. M. Peeters, Quantum rotor in nanostructured superconductors, *Sci. Rep.* **4**, 4542 (2014).
- [54] S. Bravyi, D. P. DiVincenzo, and D. Loss, Schrieffer-Wolff transformation for quantum many-body systems, *Ann. Phys. (Amsterdam)* **326**, 2793 (2011).
- [55] S. M. Rezende, A. Azevedo, and R. L. Rodríguez-Suárez, Introduction to antiferromagnetic magnons, *J. Appl. Phys.* **126**, 151101 (2019).
- [56] N. Okuma, Magnon Spin-Momentum Locking: Various Spin Vortices and Dirac Magnons in Noncollinear Antiferromagnets, *Phys. Rev. Lett.* **119**, 107205 (2017).
- [57] A. P. Mackenzie and Y. Maeno, The superconductivity of Sr₂RuO₄ and the physics of spin-triplet pairing, *Rev. Mod. Phys.* **75**, 657 (2003).
- [58] M. Eschrig, J. Kopu, J. C. Cuevas, and Gerd Schön, Theory of Half-Metal/Superconductor Heterostructures, *Phys. Rev. Lett.* **90**, 137003 (2003).
- [59] R. S. Keizer, S. T. B. Goennenwein, T. M. Klapwijk, G. Miao, G. Xiao, and A. Gupta, A spin triplet supercurrent through the half-metallic ferromagnet CrO₂, *Nature (London)* **439**, 825 (2006).
- [60] D. Sprungmann, K. Westerholt, H. Zabel, M. Weides, and H. Kohlstedt, Evidence for triplet superconductivity in Josephson junctions with barriers of the ferromagnetic heusler alloy Cu₂MnAl, *Phys. Rev. B* **82**, 060505(R) (2010).
- [61] M. S. Anwar, M. Veldhorst, A. Brinkman, and J. Aarts, Long range supercurrents in ferromagnetic CrO₂ using a multilayer contact structure, *Appl. Phys. Lett.* **100**, 052602 (2012).
- [62] T. S. Khaire, M. A. Khasawneh, W. P. Pratt, and N. O. Birge, Observation of Spin-Triplet Superconductivity in Co-Based Josephson Junctions, *Phys. Rev. Lett.* **104**, 137002 (2010).
- [63] C. Klose, T. S. Khaire, Y. Wang, W. P. Pratt, N. O. Birge, B. J. McMorran, T. P. Ginley, J. A. Borchers, B. J. Kirby, B. B. Maranville, and J. Unguris, Optimization of Spin-Triplet Supercurrent in Ferromagnetic Josephson Junctions, *Phys. Rev. Lett.* **108**, 127002 (2012).
- [64] E. C. Gingrich, P. Quarterman, Y. Wang, R. Loloee, W. P. Pratt, and Norman O. Birge, Spin-triplet supercurrent in Co/Ni multilayer Josephson junctions with perpendicular anisotropy, *Phys. Rev. B* **86**, 224506 (2012).
- [65] M. Houzet and A. I. Buzdin, Long range triplet Josephson effect through a ferromagnetic trilayer, *Phys. Rev. B* **76**, 060504(R) (2007).
- [66] J. W. A. Robinson, J. D. S. Witt, and M. G. Blamire, Controlled injection of spin-triplet supercurrents into a strong ferromagnet, *Science* **329**, 59 (2010).
- [67] M. Alidoust, J. Linder, G. Rashedi, and T. Yokoyama, A. Sudbø, Spin-polarized Josephson current in superconductor/ferromagnet/superconductor junctions with inhomogeneous magnetization, *Phys. Rev. B* **81**, 014512 (2010).
- [68] G. B. Halász, M. G. Blamire, and J. W. A. Robinson, Magnetic-coupling-dependent spin-triplet supercurrents in helimagnet/ferromagnet Josephson junctions, *Phys. Rev. B* **84**, 024517 (2011).

Supplemental Material to: Magnon spin current induced by triplet Cooper pair supercurrents

Lina G. Johnsen, Haakon T. Simensen, Arne Brataas, and Jacob Linder
 Center for Quantum Spintronics, Department of Physics, Norwegian
 University of Science and Technology, NO-7491 Trondheim, Norway
 (Dated: October 14, 2021)

In Sec. I, we present further details on the derivation of our momentum space Hamiltonian from a lattice model. In Sec. II, we present expressions for $A_{k,q}^{(1)}$ and $A_{k,q}^{(2)}$ from the Eqs. (20) and (21) in the main text.

I. THE HAMILTONIAN

A. The superconductor

The momentum space Hamiltonian for the superconductor (Eqs. (1) and (2) in the main text) is derived starting from

$$H_S = - \sum_{\langle i,j \rangle, \sigma} t_{i,j} c_{i,\sigma}^\dagger c_{j,\sigma} - \sum_{i,\sigma} \mu_i c_{i,\sigma}^\dagger c_{i,\sigma} - \frac{1}{4} \sum_{\langle i,j \rangle, \sigma} U_{i,j} n_{i,\sigma} n_{j,\sigma}. \quad (1)$$

The first term describes nearest-neighbor hopping between sites i and j , where $t_{i,j}$ is the hopping integral. The second term introduces a chemical potential μ_i at lattice site i . In the third term, $U_{i,j} > 0$ gives rise to the attractive nearest-neighbor interaction associated with superconductivity. We assume the structure to be either a one-dimensional (1D) chain, or a square lattice. Above, $c_{i,\sigma}$ and $c_{i,\sigma}^\dagger$ are second quantization annihilation and creation operators for electrons with spin σ at lattice site i , and $n_{i,\sigma} \equiv c_{i,\sigma}^\dagger c_{i,\sigma}$ is the number operator. We treat the superconducting term by a mean-field approach, where we assume that $c_{i,\sigma} c_{j,\sigma} \approx \langle c_{i,\sigma} c_{j,\sigma} \rangle + \delta_S$ and neglect second order terms in the fluctuations δ_S . We define the superconducting order parameter as

$$\Delta_{i,j}^\sigma \equiv U_{i,j} \langle c_{i,\sigma} c_{j,\sigma} \rangle. \quad (2)$$

We want to describe a superconductor that carries a charge or spin supercurrent. Such a supercurrent can be enforced by an externally applied phase gradient. To have a finite supercurrent in the system, we must require that the Cooper pairs have a finite center-of-mass velocity. This is satisfied if we write the superconducting order parameter on the form

$$\Delta_{i,j}^\sigma = \Delta_{i-j}^\sigma e^{i\mathcal{Q}^\sigma \cdot (i+j)}, \quad (3)$$

describing a propagation of the center-of-mass of a spin- σ Cooper pair along the \mathcal{Q}^σ direction [1, 2]. The assumption that the phase gradient $2\mathcal{Q}^\sigma$ is homogeneous follows from current conservation. The superconducting order parameter can be written on this form as long as the center-of-mass velocity is small enough that the amplitude Δ_{i-j}^σ is independent of the center-of-mass coordinate. To arrive at the momentum space

Hamiltonian in Eqs. (1) and (2) in the main text, we assume all parameters to be constant throughout the whole material, perform the Fourier transform (FT)

$$c_{i,\sigma} = \frac{1}{\sqrt{N}} \sum_{\mathbf{k}} c_{k,\sigma} e^{i\mathbf{k} \cdot \mathbf{i}}, \quad (4)$$

and use the relation

$$\frac{1}{N} \sum_{\mathbf{i}} e^{i(\mathbf{k}+\mathbf{k}') \cdot \mathbf{i}} = \delta_{\mathbf{k},\mathbf{k}'}. \quad (5)$$

Here, N is the total number of lattice sites.

Note that although we choose to set the strength of the order parameter f_σ^δ in Eq. (2) in the main text to a constant value, it can in principle be solved for self-consistently. This parameter is real and has the value $f_\sigma^\delta = \Im m[\Delta_\sigma^\delta]$, where

$$\Delta_\sigma^\delta = -\frac{U}{N} \sum_{\mathbf{k}} \langle c_{\mathbf{k}+\mathcal{Q}^\sigma, \sigma} c_{-\mathbf{k}+\mathcal{Q}^\sigma, \sigma} \rangle e^{i\mathbf{k} \cdot \delta}. \quad (6)$$

B. The ferromagnetic insulator

The momentum space Hamiltonian for the ferromagnetic insulator (Eq. (3) in the main text), we start from the Heisenberg Hamiltonian

$$H_{FI} = - \sum_{\langle i,j \rangle} J_{i,j} \mathbf{S}_i \cdot \mathbf{S}_j - \sum_{\langle i,j \rangle} K_{i,j} S_i^z S_j^z. \quad (7)$$

The first term describes the ferromagnetic coupling between neighboring spins for $J_{i,j} > 0$. The second term introduces an anisotropy favoring alignment of the spins along the z direction for $K_{i,j} > 0$. Above, \mathbf{S}_i is the total spin and S_i^z the spin polarized along the z axis at lattice site i . The spin is assumed to mainly be directed along the z axis with weak spin fluctuations only. We can therefore apply a Holstein-Primakoff (HP) transformation to the second order in the magnon annihilation and creation operators a_i and a_i^\dagger ,

$$S_i^+ = \sqrt{2S} a_i, \quad (8)$$

$$S_i^- = \sqrt{2S} a_i^\dagger, \quad (9)$$

$$S_i^z = S - n_i. \quad (10)$$

Above, S is the magnitude of the spins in the ferromagnetic insulator, $S_i^\pm = S_i^x \pm iS_i^y$, and $n_i = a_i^\dagger a_i$ is the number operator. By assuming that $J_{i,j}$ and K_i are constant, and applying a similar FT as for the fermion operators,

$$a_i = \frac{1}{\sqrt{N}} \sum_{\mathbf{q}} a_{\mathbf{q}} e^{i\mathbf{q} \cdot \mathbf{i}}, \quad (11)$$

we arrive at the momentum space Hamiltonian for the ferromagnetic insulator given in Eq. (3) in the main text.

C. The coupling

In order to describe a coupling between spins at the interface between the superconductor and the ferromagnetic insulator, we introduce

$$H_c = - \sum_i \Lambda s_i \cdot S_i, \quad (12)$$

where $\Lambda > 0$ is the coupling strength and

$$s_i = \frac{1}{2} \sum_{\sigma, \sigma'} c_{i, \sigma}^\dagger \sigma_{\sigma, \sigma'} c_{i, \sigma'}, \quad (13)$$

is the electron spin and σ is the vector of Pauli matrices. We apply the HP transformation in Eqs. (8)-(10) to the spin S_i in the ferromagnetic insulator. Performing the dot product between the two spin operators, we obtain

$$H_c = - \Lambda \sum_i \sigma n_{i, \sigma} (S - a_i^\dagger a_i) - \Lambda \sqrt{2S} \sum_i (c_{i, \uparrow}^\dagger c_{i, \downarrow} a_i^\dagger + c_{i, \downarrow}^\dagger c_{i, \uparrow} a_i). \quad (14)$$

The first sum comes from the z component of the spins and gives rise to spin-splitting in the quasi-particle energy spectrum and the renormalization of the magnon gap. The second sum comes from the x and y components and gives rise to magnon spin currents in the ferromagnetic insulator if supercurrents are present in the superconductor. We apply the FT in Eq. (4) to the fermion operators and the FT in Eq. (11) to the magnon operators in order to arrive at the momentum space Hamiltonian for the coupling given in Eqs. (4)-(6) in the main text. In these equations we have renamed the coupling terms to $\lambda = \Lambda \sqrt{S/2N}$ for simplicity of notation.

II. EXPRESSIONS FOR THE COEFFICIENTS

The coefficients $A_{k, q}^{(11)}$ and $A_{k, q}^{(12)}$ in Eqs. (20) and (21) in the main text are given by

$$A_{k, q}^{(11)} = \frac{\lambda^2}{2} \left\{ (u_{k, \uparrow})^2 (u_{k+q, \downarrow})^2 \frac{[f_{\text{FD}}(E_{k, \uparrow}) - f_{\text{FD}}(E_{k+q, \downarrow})]}{(E_{k, \uparrow} - E_{k+q, \downarrow}) + \omega_{q-(Q^\uparrow-Q^\downarrow)}} + (v_{k, \uparrow})^2 (u_{k+q, \downarrow})^2 \frac{[(1 - f_{\text{FD}}(E_{-k, \uparrow})) - f_{\text{FD}}(E_{k+q, \downarrow})]}{-(E_{-k, \uparrow} + E_{k+q, \downarrow}) + \omega_{q-(Q^\uparrow-Q^\downarrow)}} \right. \\ \left. + (u_{k, \uparrow})^2 (v_{k+q, \downarrow})^2 \frac{[f_{\text{FD}}(E_{k, \uparrow}) - (1 - f_{\text{FD}}(E_{-k-q, \downarrow}))]}{(E_{k, \uparrow} + E_{-k-q, \downarrow}) + \omega_{q-(Q^\uparrow-Q^\downarrow)}} + (v_{k, \uparrow})^2 (v_{k+q, \downarrow})^2 \frac{[(1 - f_{\text{FD}}(E_{-k, \uparrow})) - (1 - f_{\text{FD}}(E_{-k-q, \downarrow}))]}{-(E_{-k, \uparrow} - E_{-k-q, \downarrow}) + \omega_{q-(Q^\uparrow-Q^\downarrow)}} \right\}, \quad (15)$$

$$A_{k, q}^{(12)} = \frac{\lambda^2}{2} u_{k+q, \uparrow} u_{k, \downarrow} \text{sgn}(\Delta_{k+q}^\uparrow) v_{k+q, \uparrow} \text{sgn}(\Delta_k^\downarrow) v_{k, \downarrow} \left\{ \frac{[f_{\text{FD}}(E_{k+q, \uparrow}) - f_{\text{FD}}(E_{k, \downarrow})]}{-(E_{k+q, \uparrow} - E_{k, \downarrow}) + \omega_{q-(Q^\uparrow-Q^\downarrow)}} - \frac{[f_{\text{FD}}(E_{k+q, \uparrow}) - (1 - f_{\text{FD}}(E_{-k, \downarrow}))]}{-(E_{k+q, \uparrow} + E_{-k, \downarrow}) + \omega_{q-(Q^\uparrow-Q^\downarrow)}} \right. \\ \left. - \frac{[(1 - f_{\text{FD}}(E_{-k-q, \uparrow})) - f_{\text{FD}}(E_{k, \downarrow})]}{(E_{-k-q, \uparrow} + E_{k, \downarrow}) + \omega_{q-(Q^\uparrow-Q^\downarrow)}} + \frac{[(1 - f_{\text{FD}}(E_{-k-q, \uparrow})) - (1 - f_{\text{FD}}(E_{-k, \downarrow}))]}{(E_{-k-q, \uparrow} - E_{-k, \downarrow}) + \omega_{q-(Q^\uparrow-Q^\downarrow)}} \right\}. \quad (16)$$

[1] R. Takashima, S. Fujimoto, and T. Yokoyama, "Adiabatic and nonadiabatic spin torques induced by a spin-triplet supercurrent," *Phys. Rev. B* **96**, 121203 (2017).

[2] S.-H. Lin, M. V. Milošević, B. Jankó, and F. M. Peeters, "Quantum rotor in nanostructured superconductors," *Sci. Rep.* **4**, 4542 (2014).

VIII

REFERENCE

Linde A. B. Olde Olthof, Lina G. Johnsen, Jason W. A. Robinson, and Jacob Linder,

Controllable enhancement of p-wave superconductivity via magnetic coupling to a conventional superconductor,

Phys. Rev. Lett. **127**, 267001 (2021).

CONTRIBUTIONS

LABOO performed the analytical and numerical calculations and wrote the paper. LGJ contributed with expertise on lattice models and ways to implement matrices in Matlab to make the code more efficient. LGJ, JWAR, and JL were involved in discussions and writing of the manuscript. JL initiated and supervised the project.

Controllable Enhancement of p -Wave Superconductivity via Magnetic Coupling to a Conventional Superconductor

Linde A. B. Olde Olthof^{1,*}, Lina G. Johnsen², Jason W. A. Robinson^{1,‡} and Jacob Linder^{2,†}

¹Department of Materials Science & Metallurgy, University of Cambridge, CB3 0FS Cambridge, United Kingdom

²Center for Quantum Spintronics, Department of Physics, Norwegian University of Science and Technology, NO-7491 Trondheim, Norway

 (Received 21 July 2021; accepted 16 November 2021; published 23 December 2021)

Unconventional superconductors are of high interest due to their rich physics, a topical example being topological edge states associated with p -wave superconductivity. A practical obstacle in studying such systems is the very low critical temperature T_c that is required to realize a p -wave superconducting phase in a material. We predict that the T_c of an intrinsic p -wave superconductor can be significantly enhanced by coupling to a conventional s -wave or d -wave superconductor with a higher critical temperature via an atomically thin ferromagnetic (F) layer. We show that this T_c boost is tunable via the direction of the magnetization in F . Moreover, we show that the enhancement in T_c can also be achieved using the Zeeman effect of an external magnetic field. Our findings provide a way to increase T_c in p -wave superconductors in a controllable way and make the exotic physics associated with such materials more easily accessible experimentally.

DOI: 10.1103/PhysRevLett.127.267001

Introduction.—Superconductivity is one of the most exotic states of matter and is often described as conventional or unconventional, depending on the symmetry of the underlying order parameter. Conventional spin-singlet superconductors have an s -wave order parameter that is isotropic in momentum space. Unconventional superconductors can instead have a highly anisotropic order parameter, both in magnitude and in phase. The spin-triplet p -wave ($p_x + ip_y$) order parameter is a prototypical example [1], which is of high interest due to its edge states. Such edge states may arise at interfaces of unconventional superconductors where reflection causes the order parameter to change sign [2–4] with energies lying midgap at the normal-state Fermi level. Previous work has shown that edge states arising from a p -wave superconductor can be topologically protected from decoherence [5–7], making them interesting as building blocks for qubits in topological quantum computation [8,9].

Candidate materials for topological superconductivity include ³He B-phase [10], the surface of Sr₂RuO₄ [11], Cu-doped Bi₂Se₃ [12–14], p -type TlBiTe₂ [15], and BC₃ [16]. Sr₂RuO₄ is the most studied although the exact underlying superconducting order parameter is hotly debated [17–19]. Sr₂RuO₄ has a critical temperature T_c of 1.5 K [20] and is highly sensitive to disorder [21], making it challenging to utilize.

A way to locally increase the T_c of Sr₂RuO₄ is via the 3 K phase, which involves embedding Ru inclusions [22]. Similar local T_c enhancement has been predicted near dislocations [23]. The 3 K phase was later attributed to local stress induced by the Ru inclusions [24] and are mimicked

in pure Sr₂RuO₄ by applying uniaxial pressure [25,26]. Piezoelectric techniques can increase the T_c globally to 3.4 K [27,28]. By linking the uniaxial strain to spin and charge fluctuations, the latter could serve as a further mechanism for increasing T_c [24].

Finding a general method to enhance T_c of unconventional superconductors in order to easily access their interesting physics is an important, yet challenging, goal. Proximity enhancement of T_c in s -wave systems has been predicted theoretically [29] and recently shown experimentally [30]. However, in a junction between a singlet and triplet superconductor, there is no enhancement of the critical temperature in the low- T_c superconductor, since singlet Cooper pairs do not couple to triplet pairs [31,32].

In the case of transition-metal compounds, strong intratomic spin-orbit coupling can enhance triplet superconductivity in a three-layer oxide heterostructure [33]. Hence, to couple singlet and triplet superconductors, a spin-active interface is required to facilitate conversion between singlet and triplet Cooper pairs. Ferromagnets [34–36] and spin-orbit coupling [37–39] are commonly used for generating spin-triplet Cooper pairs from conventional superconducting pairing. In particular, both ferromagnets [40–42] and spin-orbit coupling [43,44] have been used to study the Josephson effect in s -wave- p -wave (SP) junctions.

In this Letter, we present a method to boost T_c of a triplet superconductor. The key is to couple a low- T_c triplet superconductor to a higher- T_c spin-singlet superconductor (either s -wave or d -wave) via a ferromagnetic interface (F). This is achievable using different types of ferromagnets, but here we consider an atomically thin ferromagnetic

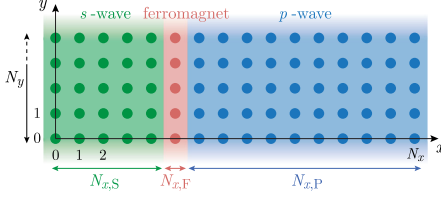


FIG. 1. Schematic illustration of the two-dimensional *SFP* cubic $N_x \times N_y$ lattice structure, with layer thicknesses of $N_{x,S}$, $N_{x,F}$ and $N_{x,P}$ lattice sites, respectively. The y direction is translationally invariant by using periodic boundary conditions and $N_y \gg N_x$.

interlayer. Using numerical diagonalization of a lattice-model, we predict that such a coupling strongly enhances the T_c of the triplet superconductor. Moreover, we show that the T_c boost is controllable by rotating the ferromagnetic exchange field with respect to the p -wave d vector. Finally, we show that the enhancement of T_c is also obtained via a Zeeman effect from an external magnetic field.

Model.—We model a two-dimensional *SFP* junction using the tight-binding Bogoliubov-de Gennes framework [45–49] with a square $N_x \times N_y$ lattice structure [50], as illustrated in Fig. 1. The interface normal is along the x axis and we assume periodic boundary conditions along y . The Hamiltonian in terms of the second quantization electron creation and annihilation operators $c_{i\sigma}^\dagger$ and $c_{i\sigma}$ is

$$H = -t \sum_{\langle ij \rangle, \sigma} c_{i\sigma}^\dagger c_{j\sigma} - \sum_{i, \sigma} \mu_i n_{i\sigma} - \sum_i U_i n_{i\uparrow} n_{i\downarrow} - \frac{1}{2} \sum_{\langle ij \rangle, \sigma} V_{ij} n_{i\sigma} n_{j, -\sigma} + \sum_{i, \sigma, \sigma'} c_{i\sigma}^\dagger (\mathbf{h}_i \cdot \boldsymbol{\sigma})_{\sigma\sigma'} c_{i\sigma'}, \quad (1)$$

where $\mathbf{i} = (i_x, i_y)$ is the lattice site, t is the hopping amplitude, μ_i is the chemical potential, and $n_{i\sigma} \equiv c_{i\sigma}^\dagger c_{i\sigma}$ is the number operator. The attractive on-site interaction ($U_i > 0$) gives rise to isotropic singlet superconductivity in S , while the nearest-neighbor interaction ($V_{ij} > 0$) between opposite spin electrons at sites \mathbf{i} and \mathbf{j} results in spin-triplet superconductivity in P . The last term describes a spin-splitting field \mathbf{h}_i interacting with the Pauli spin matrices $\boldsymbol{\sigma} = (\sigma_x, \sigma_y, \sigma_z)$ to give a net spin polarization of the itinerant electrons in F .

The two superconducting terms are treated by a mean-field approach, assuming $c_{i\uparrow} c_{i\downarrow} = \langle c_{i\uparrow} c_{i\downarrow} \rangle + \delta$ and neglecting second order fluctuations in δ . These fluctuations can be neglected for type I superconductors with a conventional metallic normal state [51]. We obtain one on-site pair correlation $F_{s,i} = \langle c_{i\uparrow} c_{i\downarrow} \rangle$ and four nearest-neighbor pair

correlations $F_{i\pm\hat{x}} = \langle c_{i\uparrow} c_{i\pm\hat{x},\downarrow} \rangle$ and $F_{i\pm\hat{y}} = \langle c_{i\uparrow} c_{i\pm\hat{y},\downarrow} \rangle$. These are anomalous Green's functions quantifying the strength of the superconducting correlations in the material and vanishing at T_c . \hat{x} and \hat{y} are vectors connecting nearest-neighbor sites along the x and y axes, respectively. The Hamiltonian is diagonalized numerically and solved iteratively for these five pair correlations. To describe the triplet symmetry, we introduce the symmetrized nearest-neighbor triplet pair correlation $F_{ij}^{(\text{triplet})} = (F_{ij} - F_{ji})/2$. After convergence, we calculate the superconducting order parameters

$$\Delta_{s,i} = UF_{s,i}, \quad (2)$$

$$\Delta_{p_x,i} = VF_{p_x,i} = \frac{V}{2} (F_{i\pm\hat{x}}^{(\text{triplet})} - F_{i\mp\hat{x}}^{(\text{triplet})}), \quad (3)$$

$$\Delta_{p_y,i} = VF_{p_y,i} = \frac{V}{2} (F_{i\pm\hat{y}}^{(\text{triplet})} - F_{i\mp\hat{y}}^{(\text{triplet})}). \quad (4)$$

The anomalous Green's functions $F_{s,i}$, $F_{p_x,i}$, and $F_{p_y,i}$ have their own critical temperatures T_c^s , $T_c^{p_x}$, and $T_c^{p_y}$, respectively, in the sense that they become smaller than some tolerance level at a specific temperature. The highest T_c of an anomalous Green's function determines the temperature at which the material becomes superconducting. The full derivation of the model is given in [52]. The nearest-neighbor model can describe a variety of superconducting symmetries. To stabilize the p -wave pairing, the V and μ_P parameters are chosen in accordance with the free energy minimization in Ref. [53] and previously used values for Sr_2RuO_4 [47]. The parameters U and μ_S are calibrated to give $T_c^s \sim 10T_c^{p_x}$ (in bulk systems), which is realistic for common s -wave superconductors like Nb. However, the resulting $U/t = 5.3$ is too large to be realistic for an actual Bardeen-Cooper-Schrieffer superconductor and is a result of downscaling the lattice to a computationally manageable system size. Nevertheless, it is the relative ratio of the critical temperatures that is important to enhance T_c of the p -wave superconductor and for this reason we expect that our predictions hold for larger system sizes as well. The parameters h_z and μ_F are optimized to give the largest effect. In the following, we study F_{p_x} and F_{p_y} to determine how the coupling between the superconductors in Fig. 1 through an atomically thin ferromagnet influences the triplet superconductivity.

T_c boost via singlet-triplet coupling.—We first consider the pair correlations close to the surface of a finite two-dimensional $p_x + ip_y$ superconductor shown in Fig. 2(a). In a single P (interfaced with vacuum), electrons are reflected with opposite momentum in the x direction ($k_x \mapsto -k_x$), while the momentum in the y direction is conserved. The p_x orbital symmetry $\sin(k_x)$ is odd under inversion of k_x . This symmetry relation $\Delta(k_x) = -\Delta(-k_x)$ gives the criterion for having a midgap surface state [2,4]. A Cooper pair thus experiences an opposite sign after

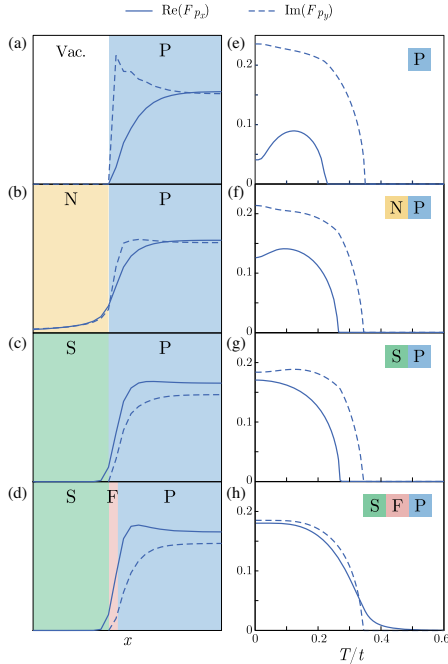


FIG. 2. Spatial pair correlation profiles $\text{Re}(F_{p_x})$ (solid) and $\text{Im}(F_{p_y})$ (dashed) at the interface of (a) vacuum or P , (b) NP , (c) SP , and (d) SFP at zero temperature. The pair correlations vs normalized temperature for (e) thin single P , (f) thin-layer NP , (g) SP , and (h) SFP junctions ($N_{x,N} = N_{x,S} = 5$, $N_{x,F} = 1$, $N_{x,P} = 10$). The thin single P is severely suppressed. The suppression is recovered in NP and SP . Singlet-triplet conversion in SFP results in a tail in T_c . The parameters for all plots are $N_y = 200$, $\mu_N/t = \mu_S/t = 1.2$, $U/t = 5.3$, $\mu_F/t = 1.4$, $h_z/t = 0.9$, $\mu_P/t = 1.8$, and $V/t = 1.5$.

reflection. This causes the pair breaking that gives the cancellation of F_{p_x} near the surface [3,54]. As a result, there are more electrons present to form Cooper pairs in the y direction and F_{p_y} increases close to the surface.

By bringing the P into contact with a normal metal (N) in Fig. 2(b), F_{p_x} is no longer fully canceled at the interface since Cooper pairs can enter the N via the proximity effect, resulting in a suppression of the midgap states. In fact, replacing the vacuum with any conducting material suppresses the midgap states since the reflection probability goes from 1 to < 1 . On the other hand F_{p_y} simply decreases at the interface since Cooper pairs can now tunnel into N . Both F_{p_x} and F_{p_y} decay exponentially in N . In Fig. 2(c),

we replace N with a conventional superconductor S , forming a SP junction. The proximity effect is strongly suppressed [31,32] and spans only a few lattice sites on either side of the interface. Consequently, F_{p_x} and F_{p_y} reach their bulk values close to the interface. Like the NP case, midgap surface state reflections are also suppressed in SP and F_{p_x} overtakes F_{p_y} . Finally, by sandwiching a F in between the S and P , as shown in Fig. 2(d), conversion of an s -wave singlet into p_x -wave triplets takes place and F_{p_x} is boosted at the interface. Increasing the exchange field results in an enhancement of singlet-to-triplet pair conversion efficiency. Additionally, increasing the field weakens the influence of the midgap surface state [40], thus strengthening F_{p_x} .

Having demonstrated the behavior of the triplet correlations F_{p_x} and F_{p_y} in different types of heterostructures in Figs. 2(a)–2(d), we now consider the temperature dependence of these correlations in order to demonstrate that T_c of the triplet superconductor can be enhanced. First, consider a system where P is thin ($N_{x,P}$ small) enough that the midgap surface states of the two surfaces partially overlap. If P is interfaced by vacuum on either side, F_{p_x} vanishes at both interfaces and is severely or even fully suppressed over the whole width of the superconductor. Hence, its T_c (taken in the middle of the P) is suppressed as well, as shown in Fig. 2(e). The behavior of $F_{p_x}(T)$ is nonmonotonic which is a known result in the presence of midgap surface states in a thin P [3,4,55]. Placing the P in contact with an N or S instead of a vacuum, F_{p_x} can be recovered by reducing midgap surface state reflections, which is visible in Figs. 2(f)–2(g) for the SP junction. The T_c in this case matches the T_c of a bulk P .

The SFP junction shows an additional effect. The S has a higher T_c than P ; for our parameters, $T_c^S \approx 10T_c^P$. Once the intrinsic T_c of P is exceeded, there is still a small amount of triplets coming from the SF interface, stabilizing F_{p_x} above its intrinsic T_c . This results in a tail in T_c^P , as seen in Fig. 2(h). For the optimal parameters, it is possible to nearly double T_c^P . Only T_c^P is boosted while T_c^S remains the same as a result of the structural symmetry. In this setup, the interface normal is parallel to the x axis, meaning spatial inversion symmetry is broken along x . The SF bilayer converts even-frequency s -wave singlets into even-frequency p_x -wave triplets and odd-frequency s -wave triplets [56]. The latter do not contribute to the T_c enhancement discussed here. Since there is no symmetry breaking in the y direction, there is no conversion to p_y -wave triplets [56]. Furthermore, the increase in the magnitude of F_{p_x} is accompanied with a decrease in F_{p_y} since less midgap surface states appear at the P interface.

The increase in T_c^P is limited by the T_c of the superconductor with the highest T_c in the heterostructure and by the interface transparency. The effective interface transparency depends on the presence of an explicit barrier

(not included in our model) and the Fermi surface mismatch, i.e., different choices of μ . There is no intrinsic enhancement of the pairing mechanism, since U and V stay constant throughout our calculations. Regarding the layer thicknesses, $T_c^{p_x}$ is doubled in *SFP* compared to a thin single P with suppressed $T_c^{p_x}$. The same effect is expected in thicker layers, although the absolute $T_c^{p_x}$ increase will be smaller.

It is known that triplet superconductivity is also induced in *SF* bilayers [34,41]. However, both singlet and triplet correlations occur simultaneously in these systems, leading to mixed-pairing superconductivity. In contrast, in our case only the triplet correlations have a non-negligible magnitude in the temperature regime exceeding the intrinsic $T_c^{p_x}$, distinguishing it from the *SF* bilayer.

Controlling T_c enhancement via magnetization direction.—Triplet superconductivity is generally described by the \mathbf{d} vector $\mathbf{d} \equiv [(\Delta_{\downarrow\downarrow} - \Delta_{\uparrow\uparrow})/2, -i(\Delta_{\uparrow\uparrow} + \Delta_{\downarrow\downarrow})/2, \Delta_{\uparrow\downarrow}]$ [36]. We consider $p_x + ip_y$ pairing happens between opposite spin electrons so that \mathbf{d} is along \hat{z} . We study the effect of changing the direction of the F spin-splitting field \mathbf{h} with respect to \mathbf{d} . The S is isotropic and the $|\uparrow\downarrow\rangle - |\downarrow\uparrow\rangle$ spin-singlet Cooper pair is rotationally invariant. The three spin-triplet states $|\uparrow\downarrow\rangle + |\downarrow\uparrow\rangle$, $|\uparrow\uparrow\rangle$, and $|\downarrow\downarrow\rangle$ transform into each other when the quantization axis changes [36,57], and we choose this axis to be along \mathbf{h} . Thus, a spin-splitting field h_z converts singlets to $|\uparrow\downarrow\rangle + |\downarrow\uparrow\rangle$ triplets polarized along the z axis. This is the native triplet Cooper pairs of the P and hence boosts $T_c^{p_x}$. By changing the exchange field direction from h_z to h_x or h_y , singlets are converted to $|\uparrow\downarrow\rangle + |\downarrow\uparrow\rangle$ triplets with a quantization axis along the x and y axis, respectively. In the reference frame of the $p_x + ip_y$ -wave superconductor, this corresponds to $|\uparrow\uparrow\rangle$ and $|\downarrow\downarrow\rangle$ triplets. These triplets suppress $T_c^{p_x}$, as seen in Fig. 3. For the optimal parameters, $T_c^{p_x}$ corresponding to h_z is double the $T_c^{p_x}$ for h_x or h_y . The F also converts triplets originating from P into singlets, but

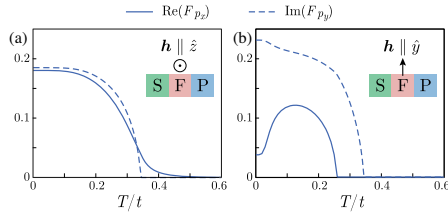


FIG. 3. Pair correlations vs normalized temperature for *SFP* with the exchange field in F (a) along \hat{z} and (b) along \hat{y} . Rotating the exchange field changes T_c dramatically. The parameters are $N_{x,S} = 5$, $N_{x,F} = 1$, $N_{x,P} = 10$, $N_y = 200$, $\mu_S/t = 1.2$, $U/t = 5.3$, $\mu_F/t = 1.4$, $h_z/t = h_y/t = 0.9$, $\mu_P/t = 1.8$, and $V/t = 1.5$.

since the S is isotropic, this contribution is independent of the exchange field direction.

The fact that the T_c enhancement is controlled by the magnetization direction of F is an important observation which could lead to interesting device concepts and a means to further probe p -wave superconductivity. The exchange field direction is tunable via an applied magnetic field, meaning that $T_c^{p_x}$ can be tuned externally, while T_c^s remains largely unchanged. This can serve as a switch in a device. Similarly, to observe a Josephson current in a *SFP* junction, an exchange field component parallel to the \mathbf{d} vector of the triplet order parameter (here pointing along z) is required [42]. By extension, one could control the Josephson current by rotating an applied magnetic field.

T_c boost via external magnetic field.—Finally, we compare the *SFP* junction to a S/P junction with an external field B_z along \hat{z} . When the superconductors are much smaller than the magnetic penetration depth λ , the orbital effect of B_z is quenched and superconductivity coexists with a Zeeman splitting throughout both superconductors up to the Clogston-Chandrasekhar limit [58,59]. This results in a spin polarization across the whole junction. Since F_{p_x} and F_{p_y} have different magnitudes and different T_c , they also have different critical fields $B_c^{p_x}$ and $B_c^{p_y}$, respectively, with $B_c^{p_x} > B_c^{p_y}$.

By applying the magnetic field, F_{p_x} first decreases. Since fewer Cooper pairs are converted from F_{p_x} to F_{p_y} , this results in a net increase in F_{p_x} . The F_{p_x} -to- F_{p_y} conversion stops at $B_c^{p_x}$, and F_{p_x} saturates to a maximum amplitude. This case is shown in Fig. 4. Similar to h_z , B_z facilitates singlet-to-triplet conversion and $T_c^{p_x}$ shows a tail. Interestingly, the magnitude of F_{p_x} in *SP* with B_z is significantly larger than in *SFP*, due to the lack of F_{p_x} -to- F_{p_y} conversion.

However, B_z also introduces a gradient of F_s over the full width of the P (positive at the *SP* interface, zero in the middle, negative at the P or vacuum interface).

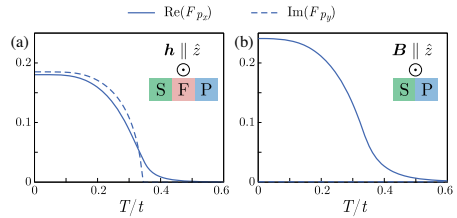


FIG. 4. Comparison between the pair correlations in a *SFP* (a) with exchange field h_z and (b) *SP* in an external field B_z , vs normalized temperature. The external field is chosen as $B_z/t = B_c^{p_x} = 0.3$, for which F_{p_x} is maximized. The parameters are $N_{x,S} = 5$, $N_{x,F} = 1$, $N_{x,P} = 10$, $N_y = 200$, $\mu_S/t = 1.2$, $U/t = 5.3$, $\mu_F/t = 1.4$, $h_z/t = 0.9$, $\mu_P/t = 1.8$, and $V/t = 1.5$.

The magnitude of F_s at the interfaces is approximately half the magnitude of F_{p_x} , which is significant, especially since the interesting physics unique to P superconductivity are generally situated at the edges. In this respect, the SFP structure is favorable since it maintains the pure p -wave correlations in the P throughout the regime of increased critical temperature. Increasing B_z further, our model shows Fulde-Ferrell-Larkin-Ovchinnikov oscillations in the P .

Having demonstrated that T_c is enhanced in a P by proximity to an S , it is interesting to explore enhancing T_c further using a high- T_c cuprate $d_{x^2-y^2}$ -wave superconductor (D). The theoretical framework used in this *Letter* does not allow us to address the D case. The reason is that when solved self-consistently, as is required to compute T_c , our model tends to stabilize $d + p_x$ symmetry in D rather than pure d -wave [53]. However, our findings for the SFP case are indicative that a much larger T_c^c could be possible if one is able to experimentally realize a high- T_c superconductor or FP junction.

Possible materials combinations with Sr_2RuO_4 include the transition metal ferromagnet SrRuO_3 [60], the highly spin-polarized manganites such as $\text{La}_{0.7}\text{Ca}_{0.3}\text{MnO}_3$ [61,62], and the oxide superconductors $\text{YBa}_2\text{Cu}_3\text{O}_{7-x}$ [63] and $\text{Pr}_{1.85}\text{Ce}_{0.15}\text{CuO}_4$ [64]. Other materials to consider are two-dimensional ferromagnets including $\text{Cr}_2\text{Ge}_2\text{Te}_6$ [65], CrI_3 [66], and VSe_2 [67].

Concluding remarks.—We have shown that the T_c of a spin-triplet p -wave superconductor is controllable in an SFP junction, where S has a higher T_c than P . A ferromagnetic interlayer facilitates singlet-to-triplet conversion, providing the P with triplets even above its intrinsic T_c . This shows up as a tail in the order parameter-temperature phase diagram. Rotating the F exchange field direction with respect to the p -wave d vector controls the triplets, and therefore, T_c . An exchange field parallel to d is able to nearly double T_c , whereas an exchange field perpendicular to d converts singlets to the wrong type of triplets and suppresses T_c . Hence, the exchange field direction serves as a T_c switch and can by extension control a Josephson current. In our model, we considered an atomically thin F . Qualitatively similar results are expected for thicker F .

Enhancing the T_c of a p -wave superconductor above liquid helium temperatures would have massive practical advantages from a device operation point of view. In the case of Sr_2RuO_4 with its T_c of 1.5 K, the doubling of T_c is still not enough, although it might be sufficient for different p -wave materials. However, our results indicate that by replacing the s -wave with a high- T_c cuprate d -wave superconductor the p -wave T_c will be boosted even further.

L. A. B. O. O. and J. W. A. R. were supported by the EPSRC through the EPSRC-JSPS Core-to-Core International Network ‘‘Oxide Superspin’’ (EP/P026311/1), the ‘‘Superconducting Spintronics’’ Programme Grant

(EP/N017242/1), the Doctoral Training Partnership Grant (EP/N509620/1), and the Cambridge NanoDTC (EP/S022953/1). L. G. J. and J. L. were supported by the Research Council of Norway through its Centres of Excellence funding scheme grant 262633 QuSpin.

[†]labo2@cam.ac.uk

[‡]jacob.linder@ntnu.no

[§]jjr33@cam.ac.uk

- [1] A. P. Mackenzie and Y. Maeno, *Rev. Mod. Phys.* **75**, 657 (2003).
- [2] C.-R. Hu, *Phys. Rev. Lett.* **72**, 1526 (1994).
- [3] J. Hara and K. Nagai, *Prog. Theor. Phys.* **76**, 1237 (1986).
- [4] Y. Nagato and K. Nagai, *Phys. Rev. B* **51**, 16254 (1995).
- [5] A. Y. Kitaev, *Phys. Usp.* **44**, 131 (2001).
- [6] N. Read and D. Green, *Phys. Rev. B* **61**, 10267 (2000).
- [7] N. V. Gnezdilov, B. van Heck, M. Diez, J. A. Hutasoit, and C. W. J. Beenakker, *Phys. Rev. B* **92**, 121406(R) (2015).
- [8] C. Beenakker, *Annu. Rev. Condens. Matter Phys.* **4**, 113 (2013).
- [9] M. Sato and S. Fujimoto, *J. Phys. Soc. Jpn.* **85**, 072001 (2016).
- [10] S. B. Chung and S.-C. Zhang, *Phys. Rev. Lett.* **103**, 235301 (2009).
- [11] Y. Tada, N. Kawakami, and S. Fujimoto, *New J. Phys.* **11**, 055070 (2009).
- [12] L. Fu and E. Berg, *Phys. Rev. Lett.* **105**, 097001 (2010).
- [13] T. H. Hsieh and L. Fu, *Phys. Rev. Lett.* **108**, 107005 (2012).
- [14] S. Sasaki, M. Kriener, K. Segawa, K. Yada, Y. Tanaka, M. Sato, and Y. Ando, *Phys. Rev. Lett.* **107**, 217001 (2011).
- [15] B. Yan, C.-X. Liu, H.-J. Zhang, C.-Y. Yam, X.-L. Qi, T. Frauenheim, and S.-C. Zhang, *Europhys. Lett.* **90**, 37002 (2010).
- [16] X. Chen, Y. Yao, H. Yao, F. Yang, and J. Ni, *Phys. Rev. B* **92**, 174503 (2015).
- [17] A. P. Mackenzie and Y. Maeno, *Rev. Mod. Phys.* **75**, 657 (2003).
- [18] Y. Maeno, S. Kittaka, T. Nomura, S. Yonezawa, and K. Ishida, *J. Phys. Soc. Jpn.* **81**, 011009 (2012).
- [19] C. Kallin, *Rep. Prog. Phys.* **75**, 042501 (2012).
- [20] Y. Maeno, H. Hashimoto, K. Yoshida, S. Nishizaki, T. Fujita, J. Bednorz, and F. Lichtenberg, *Nature (London)* **372**, 532 (1994).
- [21] A. P. Mackenzie, R. K. W. Haselwimmer, A. W. Tyler, G. G. Lonzarich, Y. Mori, S. Nishizaki, and Y. Maeno, *Phys. Rev. Lett.* **80**, 161 (1998).
- [22] Y. Maeno, T. Ando, Y. Mori, E. Ohmichi, S. Ikeda, S. Nishizaki, and S. Nakatsuiji, *Phys. Rev. Lett.* **81**, 3765 (1998).
- [23] Y. Ying, N. Staley, Y. Xin, K. Sun, X. Cai, D. Fobes, T. Liu, Z. Mao, and Y. Liu, *Nat. Commun.* **4**, 2596 (2013).
- [24] S. Acharya, D. Pashov, C. Weber, H. Park, L. Sponza, and M. Van Schilfgaarde, *Commun. Phys.* **2**, 163 (2019).
- [25] S. Kittaka, H. Yaguchi, and Y. Maeno, *J. Phys. Soc. Jpn.* **78**, 103705 (2009).
- [26] S. Kittaka, H. Taniguchi, S. Yonezawa, H. Yaguchi, and Y. Maeno, *Phys. Rev. B* **81**, 180510(R) (2010).

- [27] C. Hicks, D. Daniel O. Brodsky, E. Yelland, A. Gibbs, J. Bruin, M. Barber, S. Edkins, K. Nishimura, S. Yonezawa, Y. Maeno, and A. Mackenzie, *Science* **344**, 283 (2014).
- [28] A. Steppke, L. Zhao, M. E. Barber, T. Scaffidi, F. Jerzembeck, H. Rosner, A. S. Gibbs, Y. Maeno, S. H. Simon, A. P. Mackenzie, and C. W. Hicks, *Science* **355**, eaaf9398 (2017).
- [29] M. E. Farrell and M. F. Bishop, *Phys. Rev. B* **40**, 10786 (1989).
- [30] H. Han, J. Ling, W. Liu, H. Li, C. Zhang, and J. Wang, *Appl. Phys. Lett.* **118**, 253101 (2021).
- [31] E. Fenton, *Solid State Commun.* **34**, 917 (1980).
- [32] A. Millis, *Physica (Amsterdam)* **135B+C**, 69 (1985).
- [33] M. Horsdal, G. Khaliullin, T. Hyart, and B. Rosenow, *Phys. Rev. B* **93**, 220502(R) (2016).
- [34] F. S. Bergeret, A. F. Volkov, and K. B. Efetov, *Phys. Rev. Lett.* **86**, 4096 (2001).
- [35] A. I. Buzdin, *Rev. Mod. Phys.* **77**, 935 (2005).
- [36] J. Linder and J. W. Robinson, *Nat. Phys.* **11**, 307 (2015).
- [37] L. P. Gor'kov and E. I. Rashba, *Phys. Rev. Lett.* **87**, 037004 (2001).
- [38] G. Annunziata, D. Manske, and J. Linder, *Phys. Rev. B* **86**, 174514 (2012).
- [39] F. S. Bergeret and I. V. Tokatly, *Phys. Rev. Lett.* **110**, 117003 (2013).
- [40] Y. Tanaka and S. Kashiwaya, *J. Phys. Soc. Jpn.* **68**, 3485 (1999).
- [41] T. Yokoyama, Y. Tanaka, and A. A. Golubov, *Phys. Rev. B* **75**, 094514 (2007).
- [42] P. M. R. Brydon, W. Chen, Y. Asano, and D. Manske, *Phys. Rev. B* **88**, 054509 (2013).
- [43] Y. Hasegawa, *J. Phys. Soc. Jpn.* **67**, 3699 (1998).
- [44] Y. Asano, Y. Tanaka, M. Sigrist, and S. Kashiwaya, *Phys. Rev. B* **67**, 184505 (2003).
- [45] J.-X. Zhu and C. S. Ting, *Phys. Rev. B* **61**, 1456 (2000).
- [46] K. Kuboki and H. Takahashi, *Phys. Rev. B* **70**, 214524 (2004).
- [47] D. Terrade, P. Gentile, M. Cuoco, and D. Manske, *Phys. Rev. B* **88**, 054516 (2013).
- [48] D. Terrade, D. Manske, and M. Cuoco, *Phys. Rev. B* **93**, 104523 (2016).
- [49] L. G. Johnsen, N. Banerjee, and J. Linder, *Phys. Rev. B* **99**, 134516 (2019).
- [50] We expect the results to be qualitatively the same for a rectangular lattice or a three-dimensional model.
- [51] V. Emery and S. Kivelson, *Nature (London)* **374**, 434 (1995).
- [52] See Supplemental Material at <http://link.aps.org/supplemental/10.1103/PhysRevLett.127.267001> for details of the model.
- [53] K. Kuboki, *J. Phys. Soc. Jpn.* **70**, 2698 (2001).
- [54] V. Ambegaokar, P. G. deGennes, and D. Rainer, *Phys. Rev. A* **9**, 2676 (1974).
- [55] A. Vorontsov, *Phil. Trans. R. Soc. A* **376**, 20150144 (2018).
- [56] L. G. Johnsen, K. Svalland, and J. Linder, *Phys. Rev. Lett.* **125**, 107002 (2020).
- [57] M. Eschrig, *Phys. Today* **64**, No. 1, 43 (2011).
- [58] A. M. Clogston, *Phys. Rev. Lett.* **9**, 266 (1962).
- [59] B. S. Chandrasekhar, *Appl. Phys. Lett.* **1**, 7 (1962).
- [60] Y. Sugimoto, M. S. Anwar, S. R. Lee, Y. J. Shin, S. Yonezawa, T. W. Noh, and Y. Maeno, *Phys. Procedia* **75**, 413 (2015).
- [61] V. Peña, Z. Sefrioui, D. Arias, C. Leon, J. Santamaria, M. Varela, S. J. Pennycook, and J. L. Martinez, *Phys. Rev. B* **69**, 224502 (2004).
- [62] A. Srivastava, L. A. B. Olde Olthof, A. Di Bernardo, S. Komori, M. Amado, C. Palomares-Garcia, M. Alidoust, K. Halterman, M. G. Blamire, and J. W. A. Robinson, *Phys. Rev. Applied* **8**, 044008 (2017).
- [63] M. K. Wu, J. R. Ashburn, C. J. Torng, P. H. Hor, R. L. Meng, L. Gao, Z. J. Huang, Y. Q. Wang, and C. W. Chu, *Phys. Rev. Lett.* **58**, 908 (1987).
- [64] A. Di Bernardo, O. Millo, M. Barbone, H. Alpern, Y. Kalcheim, U. Sassi, A. Ott, D. De Fazio, D. Yoon, M. Amado, A. Ferrari, L. J., and J. Robinson, *Nat. Commun.* **8**, 14024 (2017).
- [65] C. Gong, L. Li, Z. Li, H. Ji, A. Stern, Y. Xia, T. Cao, W. Bao, C. Wang, Y. Wang, Z. Q. Qiu, R. J. Cava, S. G. Louie, J. Xia, and X. Zhang, *Nature (London)* **546**, 265 (2017).
- [66] B. Huang, G. Clark, E. Navarro-Moratalla, D. R. Klein, R. Cheng, K. L. Seyler, D. Zhong, E. Schmidgall, M. A. McGuire, D. H. Cobden, W. Yao, D. Xiao, P. Jarillo-Herrero, and X. Xu, *Nature (London)* **546**, 270 (2017).
- [67] M. Bonilla, S. Kolekar, Y. Ma, H. C. Diaz, V. Kalappattil, R. Das, T. Eggers, H. R. Gutierrez, M.-H. Phan, and M. Batzill, *Nat. Nanotechnol.* **13**, 289 (2018).

Supplemental materials:
Controllable enhancement of p -wave superconductivity via magnetic coupling to a conventional superconductor

Linde A. B. Olde Olthof,¹ Lina G. Johnsen,² Jason W. A. Robinson,¹ and Jacob Linder²

¹*Department of Materials Science & Metallurgy, University of Cambridge, CB3 0FS Cambridge, United Kingdom*

²*Center for Quantum Spintronics, Department of Physics, Norwegian University of Science and Technology, NO-7491 Trondheim, Norway*

S1. INTRODUCTION

We model a two-dimensional S/F/P junction using the lattice tight-binding Bogoliubov-de Gennes framework with a cubic $N_x \times N_y$ lattice structure. The interface normal is parallel to the x -axis and we assume periodic boundary conditions along y . The physics at each site and interactions between adjacent sites are expressed in the second quantisation electron creation ($c_{i\sigma}^\dagger$) and annihilation ($c_{i\sigma}$) operators at lattice site $\mathbf{i} = (i_x, i_y)$ with spin σ . The number operator $n_{i\sigma} \equiv c_{i\sigma}^\dagger c_{i\sigma}$ counts the number of electrons occupying state \mathbf{i} with spin σ . The Hamiltonian (1) in the main text has five contributions:

1. The hopping term describes hopping between nearest neighbours. The hopping amplitude t_{ij} is the probability of an electron moving from site \mathbf{j} to \mathbf{i} , i.e. an electron being created at site \mathbf{i} and annihilated at site \mathbf{j} . The hopping Hamiltonian is

$$H_t = - \sum_{\langle \mathbf{i}, \mathbf{j} \rangle, \sigma} t_{ij} c_{i\sigma}^\dagger c_{j\sigma}.$$

We assume that the hopping amplitude is the same everywhere ($t_{ij} = t$). In two dimensions, every lattice site has four nearest neighbours and H_t reduces to

$$H_t = -t \sum_{\mathbf{i}, \sigma} c_{i\sigma}^\dagger c_{i+\hat{x}, \sigma} + c_{i\sigma}^\dagger c_{i-\hat{x}, \sigma} + c_{i\sigma}^\dagger c_{i+\hat{y}, \sigma} + c_{i\sigma}^\dagger c_{i-\hat{y}, \sigma}. \quad (\text{S1})$$

2. The chemical potential μ_i is a material parameter that generally differs between the different layers. It acts as a constant offset to the electronic spectrum and is given by

$$H_\mu = - \sum_{\mathbf{i}, \sigma} \mu_i n_{i\sigma}. \quad (\text{S2})$$

3. The s -wave superconductor is modelled using by the attractive on-site interaction U_i between electrons with opposite spin (with $U_i > 0$).

$$H_U = - \sum_{\mathbf{i}} U_i n_{i\uparrow} n_{i\downarrow}. \quad (\text{S3})$$

4. More complicated superconducting symmetries, such as p -wave and d -wave, are modelled using the

nearest neighbour interaction V_{ij} (with $V_{ij} > 0$). Generally, the nearest neighbour interaction can contain all possible spin and momentum dependence interactions. Here, we focus on $p_x + ip_y$ symmetry corresponding to opposite-spin pairing ($\uparrow\downarrow + \downarrow\uparrow$). Therefore, the nearest neighbour Hamiltonian is written as

$$H_V = - \frac{1}{2} \sum_{\langle \mathbf{i}, \mathbf{j} \rangle, \sigma} V_{ij} n_{i\sigma} n_{j, -\sigma}. \quad (\text{S4})$$

5. The ferromagnet is introduced using the itinerant Stoner model. We model a local magnetic exchange field \mathbf{h} which splits the energy spectrum of spin-up and spin-down electrons. The exchange field interacts with the spin as

$$H_h = \sum_{\mathbf{i}} \mathbf{h}_i \cdot \mathbf{s}_i$$

where the spin density \mathbf{s}_i at lattice site \mathbf{i} is determined by the probability of an electron changing its spin from σ' to σ in accordance with the Pauli spin matrices $\boldsymbol{\sigma} = (\sigma_x, \sigma_y, \sigma_z)$, that is

$$\mathbf{s}_i = \sum_{\sigma, \sigma'} c_{i\sigma}^\dagger \boldsymbol{\sigma}_{\sigma\sigma'} c_{i\sigma'}.$$

The ferromagnet Hamiltonian is then given by

$$H_h = \sum_{\mathbf{i}, \sigma, \sigma'} c_{i\sigma}^\dagger (\mathbf{h}_i \cdot \boldsymbol{\sigma})_{\sigma\sigma'} c_{i\sigma}. \quad (\text{S5})$$

We note that H_U , H_V and H_h are only present in their respective regions.

S2. MEAN-FIELD APPROXIMATION

The superconducting terms H_U and H_V contain quadratic terms which are decoupled using the Hartree-Fock mean-field approximation. This method assumes that the exact value of a product of operators can be approximated by a small fluctuation around its expectation value, i.e. $c_{i\uparrow} c_{i\downarrow} = \langle c_{i\uparrow} c_{i\downarrow} \rangle + \delta$ and $c_{i\uparrow}^\dagger c_{i\downarrow}^\dagger = \langle c_{i\uparrow}^\dagger c_{i\downarrow}^\dagger \rangle - \delta^\dagger$. Applying this directly to the on-site superconductor Hamiltonian (S3) gives

$$H_U = \sum_{\mathbf{i}} U_i \left(\langle c_{i\uparrow}^\dagger c_{i\downarrow}^\dagger \rangle \langle c_{i\uparrow} c_{i\downarrow} \rangle + \delta^\dagger \langle c_{i\uparrow} c_{i\downarrow} \rangle + \delta \langle c_{i\uparrow}^\dagger c_{i\downarrow}^\dagger \rangle \right),$$

where we neglected second order fluctuations in δ . We introduce the s -wave superconducting gap $\Delta_{\mathbf{i}} \equiv U_{\mathbf{i}} \langle c_{\mathbf{i}\uparrow} c_{\mathbf{i}\downarrow} \rangle$ such that H_U becomes

$$H_U = \sum_{\mathbf{i}} \frac{|\Delta_{\mathbf{i}}|^2}{U_{\mathbf{i}}} + \Delta_{\mathbf{i}} c_{\mathbf{i}\uparrow}^\dagger c_{\mathbf{i}\downarrow}^\dagger + \Delta_{\mathbf{i}}^* c_{\mathbf{i}\uparrow} c_{\mathbf{i}\downarrow}.$$

The first term gives a constant contribution E_U to the total energy of the electron system, and can therefore be neglected when calculating eigenvalues and eigenvectors.

The nearest-neighbour superconductor Hamiltonian (S4) is treated in a similar fashion. We introduce the pair correlation function between electrons located at sites \mathbf{i} and \mathbf{j} with opposite spin as $F_{ij}^{\sigma,-\sigma} \equiv \langle c_{i\sigma} c_{j,-\sigma} \rangle$. The nearest-neighbour Hamiltonian H_V is expressed in the pair correlation function as

$$H_V = -\frac{1}{2} \sum_{(\mathbf{i},\mathbf{j}),\sigma} V_{ij} \left(|F_{ij}^{\sigma,-\sigma}|^2 + F_{ij}^{\sigma,-\sigma} c_{i\sigma}^\dagger c_{j,-\sigma}^\dagger + \left(F_{ij}^{\sigma,-\sigma} \right)^* c_{i\sigma} c_{j,-\sigma} \right).$$

The first term is again a constant energy contribution, E_V . We expand the summation over σ , use that nearest-neighbour interaction is symmetric ($V_{ij} = V_{ji}$) and $F_{ji}^{\uparrow\downarrow} = -F_{ij}^{\downarrow\uparrow}$, such that H_V becomes

$$H_V = E_V - \sum_{(\mathbf{i},\mathbf{j})} V_{ij} \left[F_{ij}^{\uparrow\downarrow} c_{i\downarrow}^\dagger c_{j\uparrow}^\dagger + \left(F_{ij}^{\uparrow\downarrow} \right)^* c_{i\uparrow} c_{j\downarrow} \right].$$

Since V_{ij} only acts on the nearest neighbours, the summation over \mathbf{j} yields four terms, similar to the hopping Hamiltonian (S1). For brevity, we refer to the terms originating from $\left(F_{ij}^{\uparrow\downarrow} \right)^*$ as ‘‘h.c.’’ (hermitian conjugate). H_V becomes

$$\begin{aligned} H_V = E_V - \sum_{\mathbf{i}} & V_{\mathbf{i},\mathbf{i}+\hat{x}} F_{\mathbf{i},\mathbf{i}+\hat{x}} c_{\mathbf{i}\uparrow}^\dagger c_{\mathbf{i}+\hat{x},\downarrow}^\dagger \\ & + V_{\mathbf{i},\mathbf{i}-\hat{x}} F_{\mathbf{i},\mathbf{i}-\hat{x}} c_{\mathbf{i}\uparrow}^\dagger c_{\mathbf{i}-\hat{x},\downarrow}^\dagger \\ & + V_{\mathbf{i},\mathbf{i}+\hat{y}} F_{\mathbf{i},\mathbf{i}+\hat{y}} c_{\mathbf{i}\uparrow}^\dagger c_{\mathbf{i}+\hat{y},\downarrow}^\dagger \\ & + V_{\mathbf{i},\mathbf{i}-\hat{y}} F_{\mathbf{i},\mathbf{i}-\hat{y}} c_{\mathbf{i}\uparrow}^\dagger c_{\mathbf{i}-\hat{y},\downarrow}^\dagger + \text{h.c.} \end{aligned}$$

S3. THE HAMILTONIAN IN k -SPACE

In our system, the interfaces are located along x and we assume periodic boundary conditions in the infinite y -direction. We write $k_y = 2\pi n/N_y$, where $n \in \mathbb{Z}$. To implement the periodic boundary condition, we use the

Fourier transform

$$c_{\mathbf{i}\sigma} = \frac{1}{\sqrt{N_y}} \sum_{k_y} c_{i_x, k_y, \sigma} e^{ik_y i_y}. \quad (\text{S6})$$

The sum over k_y spans the first Brillouin zone, such that $k_y \in (-\pi, \pi]$. We also note that, if the function inside the summation does not depend on i_y , the sum over i_y gives

$$\frac{1}{N_y} \sum_{i_y, k_y, k'_y} f(k_y, k'_y) e^{-i(k_y - k'_y) i_y} = \sum_{k_y} f(k_y, k'_y) \delta_{k_y, k'_y}. \quad (\text{S7})$$

Applying the Fourier transform (S6) and using the relation (S7), the individual Hamiltonian contributions become

$$\begin{aligned} H_t &= -t \sum_{i,j,k,\sigma} c_{ik\sigma}^\dagger c_{jk\sigma} (\delta_{i,j+1} + \delta_{i,j-1} + 2 \cos(k_y) \delta_{ij}), \\ H_\mu &= - \sum_{i,k,\sigma} \mu_i c_{ik\sigma}^\dagger c_{ik\sigma}, \\ H_U &= E_U + \sum_{i,k} \Delta_i c_{ik\uparrow}^\dagger c_{i,-k\downarrow}^\dagger + \Delta_i^* c_{i,-k\downarrow} c_{ik\uparrow}, \\ H_V &= E_V + \sum_{i,j,k} F_{ijk} c_{ik\uparrow}^\dagger c_{j,-k\downarrow}^\dagger + F_{ijk}^* c_{j,-k\downarrow} c_{ik\uparrow} \\ &\quad \text{with } F_{ijk} = -V_{ij} \left[F_i^{x+} \delta_{i,j+1} + F_i^{x-} \delta_{i,j-1} \right. \\ &\quad \quad \left. + (F_i^{y+} e^{ik} + F_i^{y-} e^{-ik}) \delta_{ij} \right], \\ H_h &= \sum_{i,k,\sigma,\sigma'} (\mathbf{h}_i \cdot \boldsymbol{\sigma})_{\sigma\sigma'} c_{ik\sigma}^\dagger c_{ik\sigma'}, \end{aligned}$$

where we have dropped the subscripts $i = i_x, j = j_x$ and $k = k_y$ and introduced the notation $F_i^{x\pm} \equiv F_{i,i\pm\hat{x}}$ and $F_i^{y\pm} \equiv F_{i,i\pm\hat{y}}$. The broken translation symmetry in the x -direction leads to non-diagonal terms in H_t and H_V in the x -indices. In H_t , the $\delta_{i,j+1}$ and $\delta_{i,j-1}$ represent hopping to nearest neighbours in x , whereas the $2 \cos(k_y)$ is the standard electronic spectrum (the dispersion relation).

S4. DIAGONALISATION

To diagonalise the full Hamiltonian H , we first have to express it in its current basis of single-electron creation and annihilation operators. We define the basis $B_{ik}^\dagger = [c_{ik\uparrow}^\dagger, c_{ik\downarrow}^\dagger, c_{i,-k\uparrow}, c_{i,-k\downarrow}]$, such that the Hamiltonian H_V can be written as

$$H = E_U + E_V + \frac{1}{2} \sum_{i,j,k} B_{ik}^\dagger H_{ijk} B_{jk} \quad (\text{S8})$$

with

$$H_{ijk} = \begin{bmatrix} \epsilon_{ijk} + h_i^z \delta_{ij} & (h_i^x - ih_i^y) \delta_{ij} & 0 & \Delta_i \delta_{ij} + F_{ijk} \\ (h_i^x + ih_i^y) \delta_{ij} & \epsilon_{ijk} - h_i^z \delta_{ij} & -\Delta_i \delta_{ij} - F_{j,i,-k} & 0 \\ 0 & -\Delta_i^* \delta_{ij} - F_{i,j,-k}^* & -\epsilon_{ijk} - h_i^z \delta_{ij} & -(h_i^x + ih_i^y) \delta_{ij} \\ \Delta_i^* \delta_{ij} + F_{ijk}^* & 0 & (-h_i^x + ih_i^y) \delta_{ij} & -\epsilon_{ijk} + h_i^z \delta_{ij} \end{bmatrix}. \quad (\text{S9})$$

where $\epsilon_{ijk} = -t\delta_{i,j+1} - t\delta_{i,j-1} - (2t \cos(k) + \mu_i) \delta_{ij}$. We define a new basis W_k , which stacks the N_x separate B_{ik} vectors into one long vector, i.e. $W_k^\dagger = [B_{1k}^\dagger \ B_{2k}^\dagger \ \dots \ B_{N_x,k}^\dagger]$, such that

$$H = E_U + E_V + \frac{1}{2} \sum_k W_k^\dagger H_k W_k.$$

The matrix H_k is Hermitian and is diagonalised numerically with eigenvalues E_{nk} and eigenvectors γ_{nk} as

$$H = E_U + E_V + \frac{1}{2} \sum_{n,k} E_{nk} \gamma_{nk}^\dagger \gamma_{nk}. \quad (\text{S10})$$

Diagonalising the Hamiltonian effectively transforms the system from the single-electron operator basis (denoted by c, c^\dagger) to the Bogoliubov quasiparticle basis (denoted by γ, γ^\dagger). Since Bogoliubov quasiparticles are part electron and part hole, the Bogoliubov operators are linear combinations of electron creation and annihilation operators. The coherence factors u, v, w and x are associated with the probability of electron-like and hole-like states with spin-up and spin-down being occupied. The Bogoliubov creation operator is

$$\gamma_{nk}^\dagger = \sum_i \left(u_{ink} c_{ik\uparrow}^\dagger + v_{ink} c_{ik\downarrow}^\dagger + w_{ink} c_{i,-k\uparrow} + x_{ink} c_{i,-k\downarrow} \right). \quad (\text{S11})$$

However, in the summation in (S10), not all γ_{nk} are independent for all k -values. Since Cooper pairs impose momentum restrictions on the pairing, there is a symmetry relation between quasiparticles with $+k$ and $-k$. We find that $\gamma_{n,-k}^\dagger = \gamma_{nk}$ and $E_{n,-k} = -E_{nk}$. To account for this, we split the sum over k in (S10) in $k > 0$ and $k < 0$ and $k = 0$ and use these symmetry relations to rewrite them. We obtain

$$H = E_U + E_V + \sum_{n,k>0} E_{nk} \left(\gamma_{nk}^\dagger \gamma_{nk} - \frac{1}{2} \right) + \sum_{E_{n0} \geq 0} E_{n0} \left(\gamma_{n0}^\dagger \gamma_{n0} - \frac{1}{2} \right),$$

where the notation $\sum_{E_{n0} \geq 0}$ is the summation over all positive eigenvalues, including one zero-energy eigenvalue.

Taking the inverse of (S11), the single-electron op-

erators are related to quasiparticles as

$$c_{ik\uparrow} = \sum_n u_{ink} \gamma_{nk}, \quad c_{i,-k\uparrow}^\dagger = \sum_n w_{ink} \gamma_{nk}, \\ c_{ik\downarrow} = \sum_n v_{ink} \gamma_{nk}, \quad c_{i,-k\downarrow}^\dagger = \sum_n x_{ink} \gamma_{nk}. \quad (\text{S12})$$

These expressions are the main ingredient to evaluate the pair correlations in terms of the eigenvalues and eigenvectors of the system.

5. SELF-CONSISTENT SOLUTION

The Hamiltonian H_k depends on the s -wave superconducting gap Δ_i and the pair correlations $F_i^{x\pm}$ and $F_i^{y\pm}$ which are initially unknown. By substituting (S12) we express $\Delta_i, F_i^{x\pm}$ and $F_i^{y\pm}$ in the eigenvalues and eigenvectors of H_k . The self-consistent calculation consists of choosing initial values for $\Delta_i, F_i^{x\pm}$ and $F_i^{y\pm}$, diagonalising H_k to obtain the eigenvectors and eigenvalues, using these to calculate new values for $\Delta_i, F_i^{x\pm}$ and $F_i^{y\pm}$, substituting these back into H_k and repeating this procedure until $\Delta_i, F_i^{x\pm}$ and $F_i^{y\pm}$ have converged.

The s -wave gap Δ_i in terms of the eigenvectors and eigenvalues is

$$\Delta_i = U_i \langle c_{i\uparrow} c_{i\downarrow} \rangle = \frac{U_i}{N_y} \left(\sum_n u_{in0} x_{in0}^* \langle \gamma_{n0}^\dagger \gamma_{n0} \rangle + \sum_{k>0,n} u_{ink} x_{ink}^* \langle \gamma_{nk}^\dagger \gamma_{nk} \rangle + v_{ink} w_{ink}^* \langle \gamma_{nk}^\dagger \gamma_{nk} \rangle \right).$$

We arrange the eigenvectors in the diagonalising matrix such that the first $2N_x$ are positive and the last $2N_x$ are negative. Then, $u_{i,2N_x+n,0} = w_{in0}^*$, $x_{i\pm 1,2N_x+n,0} = v_{i\pm 1,n0}^*$ and $\gamma_{2N_x+n,0} = \gamma_{n0}^\dagger$. The Fermi-Dirac function is defined as the expectation value of independent γ -operators as $f(E_{nk}) = \langle \gamma_{nk}^\dagger \gamma_{nk} \rangle$. The s -wave gap becomes

$$\Delta_i = \frac{U_i}{N_y} \left(\sum_{k>0,n} u_{ink} x_{ink}^* [1 - f(E_{nk})] + v_{ink} w_{ink}^* f(E_{nk}) + \sum_{E_{n0} \geq 0} u_{in0} x_{in0}^* [1 - f(E_{n0})] + v_{in0} w_{in0}^* f(E_{n0}) \right). \quad (\text{S13})$$

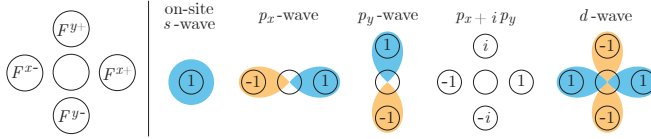


FIG. S1. Symmetries of the nearest-neighbour pair correlations F^{x+} , F^{x-} , F^{y+} and F^{y-} based on the spherical harmonics for different superconducting pairing symmetries.

The nearest neighbour pair correlation $F_i^{x\pm}$ is

$$F_i^{x\pm} = \langle c_{i\uparrow} c_{i\pm\hat{x},\downarrow} \rangle = \frac{1}{N_y} \left(K_{x0} + \sum_{k>0,n} u_{ink} x_{i\pm 1,nk}^* [1 - f(E_{nk})] + v_{i\pm 1,nk} w_{ink}^* f(E_{nk}) \right), \quad (\text{S14})$$

where K_{x0} corresponds to $k = 0$ and is given by

$$K_{x0} = \sum_{E_n \geq 0} u_{in0} x_{i\pm 1,n0}^* [1 - f(E_{n0})] + v_{i\pm 1,n0} w_{in0}^* f(E_{n0}).$$

Similarly, $F_i^{y\pm} = F_{i,i\pm\hat{y}}$ becomes

$$F_i^{y\pm} = \langle c_{i\uparrow} c_{i\pm\hat{y},\downarrow} \rangle = \frac{1}{N_y} \left(K_{y0} + \sum_{k>0,n} u_{ink} x_{ink}^* [1 - f(E_{nk})] e^{\pm ik} + v_{ink} w_{ink}^* f(E_{nk}) e^{\mp ik} \right), \quad (\text{S15})$$

with

$$K_{y0} = \sum_{E_n \geq 0} u_{in0} x_{in0}^* [1 - f(E_{n0})] + v_{in0} w_{in0}^* f(E_{n0}).$$

S6. SUPERCONDUCTING ORDER PARAMETERS

After convergence, the self-consistency solutions (S13), (S14) and (S15) are used to calculate the superconducting order parameters. The self-consistent s -wave gap (S13) is directly the on-site s -wave order parameter, as described in (2) in the main text. Linear combinations of the pair amplitudes $F_i^{x\pm}$ and $F_i^{y\pm}$ provide order parameters with distinct symmetry properties. These linear combinations originate from the spherical harmonic symmetry projected onto the lattice, as illustrated in Figure S1.

As given by (3) and (4) in the main text, the order parameters for p_x -wave, p_y -wave and d -wave ($d_{x^2-y^2}$) at lattice site i are, respectively,

$$\begin{aligned} \Delta_{p_x,i} &= V F_{p_x,i} = \frac{V}{2} \left(F_i^{x+(T)} - F_i^{x-(T)} \right), \\ \Delta_{p_y,i} &= V F_{p_y,i} = \frac{V}{2} \left(F_i^{y+(T)} - F_i^{y-(T)} \right), \\ \Delta_{d,i} &= V F_{d,i} = \frac{V}{4} \left(F_i^{x+(S)} + F_i^{x-(S)} - F_i^{y+(S)} - F_i^{y-(S)} \right). \end{aligned}$$

The superscripts correspond to spin-singlet (S) and spin-triplet (T) symmetries. Hence $F^{(S)}$ has to be anti-symmetric under spin exchange, while $F^{(T)}$ is symmetric. Therefore, they are defined as

$$F_{ij}^{(S)} = \frac{F_{ij} + F_{ji}}{2}, \quad F_{ij}^{(T)} = \frac{F_{ij} - F_{ji}}{2}.$$

IX

REFERENCE

Lina G. Johnsen,

The magnetic field driven superconductor–metal transition in disordered hole-overdoped cuprates,

J. Phys.: Condens. Matter **35**, 115601 (2023).

CONTRIBUTIONS

LGJ initiated the project, performed all analytical and numerical calculations, and wrote the paper.

The magnetic field driven superconductor–metal transition in disordered hole-overdoped cuprates

Lina G Johnsen 

Center for Quantum Spintronics, Department of Physics, Norwegian University of Science and Technology, NO-7491 Trondheim, Norway

E-mail: lina.g.johnsen@ntnu.no

Received 28 August 2022, revised 15 December 2022

Accepted for publication 29 December 2022

Published 9 January 2023



Abstract

By solving the Bogoliubov–de Gennes equations for a d -wave superconductor, we explore how the interplay between disorder and the orbital depairing of an external magnetic field influences the superconductor–metal transition of the hole-overdoped cuprates. For highly disordered systems, we find granular Cooper pairing to persist above the critical field where the superfluid stiffness goes to zero. We also show that because the vortices are attracted to regions where the superconducting pairing is already weak, the Caroli–de Gennes–Matricon zero-bias peak in the local density of states at the vortex cores disappears already at moderate disorder.

Keywords: superconducting phase transition, disorder, critical field, hole-overdoped cuprates, Bogoliubov–de Gennes equations

(Some figures may appear in colour only in the online journal)

1. Introduction

The rich phase diagram of the cuprates allow for the study of a variety of different phases by adjusting the concentration of dopants [1, 2]. While undoped cuprates are antiferromagnetic Mott insulators, a sufficient level of doping can cause the onset of high-temperature superconductivity [3]. In the hole-underdoped and optimally doped regimes, superconductivity can no longer be described by Bardeen–Cooper–Schrieffer (BCS) theory [4]. In these regimes, the normal state is not a Fermi-liquid, but rather a pseudogap phase or a strange metal [2, 5–7]. As the temperature is decreased, the onset of superconductivity is determined by the superfluid stiffness rather than the Cooper pairing [8]. Moreover, the competition between superconducting and antiferromagnetic order causes magnetic structures to arise around impurities [9–11] and vortex cores [12–17].

In the less studied hole-overdoped regime, a large Fermi surface with well-defined quasi-particles makes Fermi-liquid

theory a more suitable description of the normal-state [18, 19]. In the superconducting state, experimental observations fit better with BCS theory [2, 20]. However, some puzzling observations include Cooper pairs forming above the superconducting critical temperature (T_c) in $\text{Bi}_2\text{Sr}_2\text{CaCu}_2\text{O}_{8+x}$ (Bi2212) [21–23], and a large fraction of uncondensed electrons below T_c in several of the hole-overdoped cuprates [24–28]. Recent experimental studies of $\text{La}_{2-x}\text{Sr}_x\text{CuO}_4$ (LSCO) [27, 29–31] found that the superfluid stiffness decreases linearly with increasing temperature, and that the critical temperature depends on the zero-temperature superfluid stiffness. The claim that these findings go beyond BCS theory has been challenged by theoretical works [32–34]. No consensus has yet been reached, but it is clear that the relation between the superconducting pairing and superfluid stiffness shows interesting properties even when described within the dirty BCS framework.

As a prime example, Li *et al* [35] predicted that upon increasing the concentration of non-magnetic impurities in

hole-overdoped Bi2212, the superfluid stiffness is lost, and the superconductor transitions into a state with granular Cooper pairing and spontaneous supercurrent loops. Since the hole-overdoped cuprates are d -wave superconductors, they are not protected by Anderson's theorem [36–38] and superconductivity is strongly suppressed in the vicinity of non-magnetic impurities [39, 40]. In [23, 35] modeling Bi2212, the authors in particular highlight the importance of flat bands in the anti-nodal regions causing increased pair-breaking and the transition into the granular state.

In this work, we study how the interplay between disorder and the orbital depairing of an external magnetic field influences the superconductor–metal transition of the hole-overdoped cuprates. By solving the Bogoliubov–de Gennes (BdG) equations for a disordered d -wave superconductor, we study the superfluid stiffness and superconducting pairing close to the transition. Like Li *et al* [35], we consider a band-structure fitting experimental measurements of Bi2212 [23] with a band-filling that gives rise to flat bands close to the Fermi level in the antinodal regions. We find that when the system becomes sufficiently disordered, granular Cooper pairing persists beyond the magnetic field driven superconductor to metal transition. This allows us to conveniently reach the intermediate regime predicted for the disorder driven superconductor–metal transition in [35] by tuning an external magnetic field. Moreover, we show that the Caroli–de Gennes–Matricon (CdGM) zero-bias peak in the local density of states (LDOS) at the vortex cores vanishes at moderate disorder, as the vortices start penetrating regions where the superconductivity is already weak. This sensitivity to disorder could contribute to the elusiveness of the CdGM zero-bias peak in experimental studies [41–45].

2. Model

We consider a disordered type-II d -wave superconductor under an applied magnetic field. The lattice structure considered is a two-dimensional (2D) square lattice, which to good approximation models the quasi-2D structure of the cuprates [1]. Moreover, we assume the superconducting film to be thin enough that the orbital effect of the perpendicular magnetic field dominates over the Zeeman splitting. This system can be described by the Hamiltonian

$$H = - \sum_{i,j,\sigma} t_{i,j} e^{i\phi_{i,j}} c_{i,\sigma}^\dagger c_{j,\sigma} - \sum_{i,\sigma} (\mu - V_i) n_{i,\sigma} + \sum_{\langle i,j \rangle} \left(\Delta_{i,j} c_{i,\uparrow}^\dagger c_{j,\downarrow}^\dagger + \text{h.c.} \right). \quad (1)$$

Here, $c_{i,\sigma}^\dagger$, $c_{i,\sigma}$, and $n_{i,\sigma} = c_{i,\sigma}^\dagger c_{i,\sigma}$ are the creation, annihilation, and number operators associated with a spin- σ electron at lattice site i . Each of the above terms are explained in the following.

The first term describes hopping between neighboring lattice sites. We include hopping between nearest, next nearest

and third nearest neighbors. These three types of hopping are associated with hopping parameters $t_{ij} = t, t', t''$, respectively. The applied magnetic field introduces an accumulated Peierls phase

$$\phi_{i,j} = - \frac{\pi}{\Phi_0^{\text{SC}}} \int_{r_j}^{r_i} d\mathbf{r} \cdot \mathbf{A}(\mathbf{r}) \quad (2)$$

when an electron moves from position r_j to position r_i . Here, $\Phi_0^{\text{SC}} = hc/2e$ is the superconducting flux quantum, and $\mathbf{A}(\mathbf{r}) = B(0, x, 0)$ is the vector potential in the Landau gauge resulting from a homogeneous external magnetic field B .

The second term in equation (1) introduces the chemical potential μ and the disorder potential V_i . We consider a random disorder potential in the range $V_i \in [-V, V]$. The chemical potential is adjusted in order to fix the hole density x while considering different disorder strengths. The hole density is given by

$$x = \frac{1}{N_x N_y} \sum_{i,\sigma} \langle 1 - n_{i,\sigma} \rangle. \quad (3)$$

We consider hole-doped superconductors ($0 < x \leq 1$) far away from half-filling ($x = 0$). In this regime, the cuprates are purely superconducting without competing antiferromagnetic order. Experimental observations suggest a more conventional behavior, where BCS theory captures many aspects of the superconductivity well [1, 2].

The last term in equation (1) introduces the superconducting pairing arising from a nearest-neighbor interaction described within the mean field approximation [46]. The pairing correlation $\Delta_{ij} = J \langle c_{i,\uparrow} c_{j,\downarrow} \rangle$ is used to calculate the spin-singlet pairing $\Delta_{i,j}^s = (\Delta_{i,j} + \Delta_{j,i})/2$. The d -wave spin-singlet pairing is defined as

$$\Delta_i^d = \frac{1}{4} (\Delta_i^{+x} + \Delta_i^{-x} - \Delta_i^{+y} - \Delta_i^{-y}), \quad (4)$$

where $\Delta_i^{\pm x(y)} = \Delta_{i,i \pm x(y)} \exp(i\phi_{i,i \pm x(y)})$. In order to make the numerical calculations feasible, we need to scale down the lattice size compared to a realistic system. The parameter J should ideally be chosen large enough that the vortex diameter is much smaller than the width of the system, but still small enough that the vortex spans at least a few lattice sites. The parameters chosen for each plot is given in the corresponding figure text. We consider the zero-temperature limit as our theoretical framework do not capture the effect of thermal fluctuations.

We calculate the spin-singlet d -wave pairing self-consistently from the Bogoliubov–de Gennes equations of the Hamiltonian in equation (1). We follow the method in [46]. For details, see the [appendix](#). In order to reduce the system size without disturbance from edge effects, we define a magnetic unit cell containing an even number of superconducting flux quanta and apply periodic boundary conditions at its edges. Thus, we can solve the BdG equations for a periodic array of $M_x \times M_y$ magnetic unit cells of size $N_x \times N_y$.

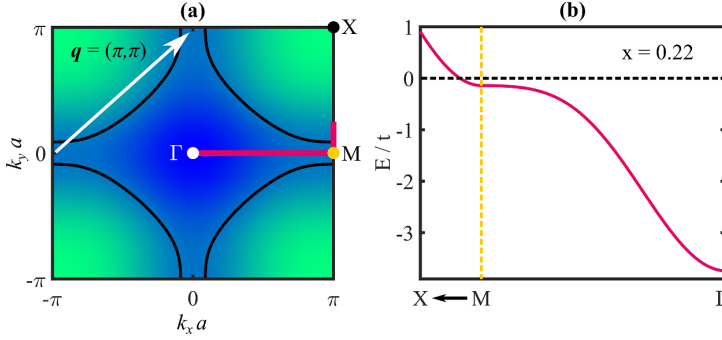


Figure 1. We consider a normal state band structure fitting experimental measurements of Bi2212 at 22% hole doping [23] using next nearest and third nearest neighbor hopping parameters $t'/t = -0.05$ and $t''/t = 0.2$, respectively [35]. Panel (a) shows the Fermi surface (black lines), and panel (b) the bandstructure along the red line in panel (a). The band structure is plotted from the Γ point to the M point and towards the X point. The position of the Γ , M, and X points in the first Brillouin zone are indicated by a white, yellow, and black dot, respectively. In panel (b), the Fermi level is marked by the black dotted line, and the M point is marked by the yellow dotted line. Scattering between the antinodal regions by a wave vector $\mathbf{q} = (\pm\pi, \pm\pi)$, as illustrated by the white arrow in panel (a), is pair breaking due to the d -wave pairing having opposite signs in the antinodal regions around $(\pm\pi, 0)$ and $(0, \pm\pi)$ [50]. The flat band shown in panel (b) increases the scattering between the antinodal regions, thus making the d -wave pairing more sensitive to impurities [51].

In highly disordered materials, the existence of superconducting pairing is no longer a good measure for whether the material is superconducting. This is because pairing can exist locally without any global phase coherence. For defining the superconducting phase transition, we therefore introduce the superfluid stiffness D_s . We calculate the superfluid stiffness from the Kubo formula [46–48]

$$\frac{D_s}{\pi e^2} = \langle -K_x \rangle - \Lambda_{xx}(q_x = 0, q_y \rightarrow 0, \omega = 0), \quad (5)$$

that describes the linear response to a vector potential $A_x e^{i(\mathbf{q} \cdot \mathbf{r}_i - \omega t)}$ applied in the x direction. Above, $\langle K_x \rangle$ is the expectation value of the kinetic energy and $\Lambda_{xx}(\mathbf{q}, \omega)$ is the current-current correlation function. The kinetic energy associated with the x oriented bonds is given by

$$K_x = -\frac{1}{N_x N_y} \sum_{i, \delta} \delta_x^2 (t_{i+\delta, i} c_{i+\delta, \sigma}^\dagger c_{i, \sigma} + \text{h.c.}). \quad (6)$$

The current-current correlation function is given by

$$\Lambda_{xx}(\mathbf{q}, \omega) = \frac{i}{N_x N_y} \int_0^\infty dt e^{i\omega t} \langle [J_x(\mathbf{q}, t), J_x(-\mathbf{q}, 0)] \rangle, \quad (7)$$

where $J_x(\mathbf{q}, t) = \sum_i \exp(-i\mathbf{q} \cdot \mathbf{r}_i) J_x(\mathbf{r}_i, t)$ is the Fourier transform of the x oriented particle current

$$J(\mathbf{r}_i, t) = i \sum_{\delta, \sigma} \delta_x (t_{i+\delta, i} e^{i\phi_{i+\delta, i}} c_{i+\delta, \sigma}^\dagger c_{i, \sigma} - \text{h.c.}). \quad (8)$$

With these physical quantities, we are able to study whether superconducting pairing is present, whether the material is superconducting, and how currents flow inside the material.

Finally, we define the LDOSs in terms of the retarded Green's function [46]

$$N_i = -\frac{1}{\pi} \sum_{\sigma} \Im \text{m} [G_{i, \sigma, i, \sigma}^R(\omega)], \quad (9)$$

$$G_{i, \alpha, j, \beta}^R(\omega) = -i \int_0^\infty dt e^{i\omega t} \langle \{c_{i, \alpha}(t), c_{j, \beta}^\dagger(0)\} \rangle. \quad (10)$$

This furthermore allows us to study the LDOSs inside the vortex cores.

3. Results

In order to study how the strong pair breaking associated with the d -wave pairing symmetry affects the magnetic field driven superconducting transition, we choose parameters modeling Bi2212 at 22% hole doping. As shown in figure 1, this band filling gives rise to flat bands close to the Fermi surface in the antinodal regions, causing increased scattering between regions where the superconducting pairing has opposite signs [23]. For the case of zero external magnetic field, such flat bands have been shown to cause a strong suppression of the superconducting pairing and superfluid stiffness under increasing disorder [35]. By choosing parameters giving a high sensitivity to disorder, our parameters allow us to study the opposite limit compared to the robust conventional superconductor studied in [49].

We first consider the how the superconducting pairing evolves under increasing disorder in the presence of a constant magnetic field. Figures 2(a)–(e) show the superconducting pairing inside a magnetic unit cell penetrated by four superconducting flux quanta for various disorder strengths.

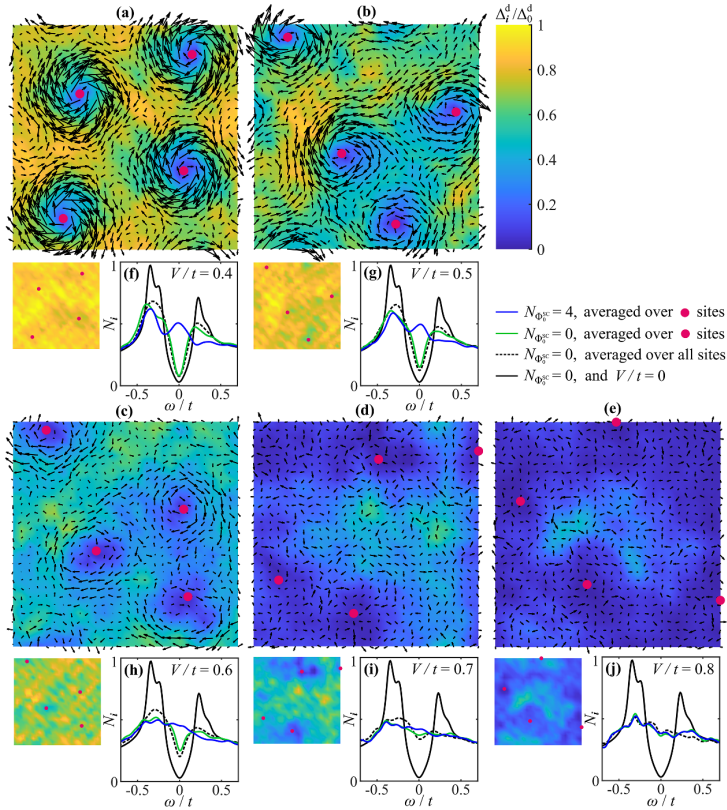


Figure 2. Panels (a)–(e): the d -wave pairing Δ_v^d in a magnetic unit cell containing 4 vortices for impurity potentials $V/t = 0.4, 0.5, 0.6, 0.7,$ and $0.8,$ respectively. The corresponding plots for zero magnetic field are shown below each panel. The pairing is scaled by its value Δ_0^d in a clean system without vortices. The arrows represent the net current through each lattice site, and the red dots mark the positions of the vortex cores determined from the phase of Δ_v^d . Panels (f)–(j): the local density of states at the vortex cores in panels (a)–(e) (blue), and at the corresponding lattice sites for zero magnetic field (green). The LDOS is averaged over all vortex sites and their nearest and next nearest neighbors. The black curves show the LDOS averaged over all lattice sites in the absence of the magnetic field for the given impurity potential (dotted) and in a clean system (solid). (Parameters: $J/t = 0.9, N_{x(y)} = 28, M_{x(y)} = 10.$)

While the vortices in a clean system form a regular lattice due to the mutual repulsion between vortices, increasing disorder causes the vortices to shift towards highly disordered regions where the superconducting pairing is already weak. In figures 2(a)–(e), we typically find one vortex where the superconducting pairing is at its weakest, and the other three vortices in or close to local minima sufficiently far away from other vortices. In the highly disordered systems, a vortex can be located close to a grain boundary if the vortex repulsion makes this energetically favorable. It is however very unlikely to find vortices in the middle of a superconducting grain. The magnetic field therefore suppresses the Cooper pairing in the regions where the pairing is already weak, and causes

superconducting pairing to survive in grains surrounded by regions where the pairing is absent. We will later show that this granularity is associated with a vanishing superfluid stiffness.

In figures 2(f)–(j), we study how the LDOSs at the vortex cores changes as the disorder increases. When the disorder is low, the LDOS at the vortex core show a clear CdGM zero-bias peak [52]. However, the CdGM zero-bias peak vanishes already at moderate disorder where the pairing is not yet granular in the absence of magnetic fields. This is clearly seen from figures 2(c) and (h). The zero-bias peak is nearly absent, although before applying the magnetic field there is a clear superconducting gap in the average density of states and the superconducting pairing always remains above 40% of its value

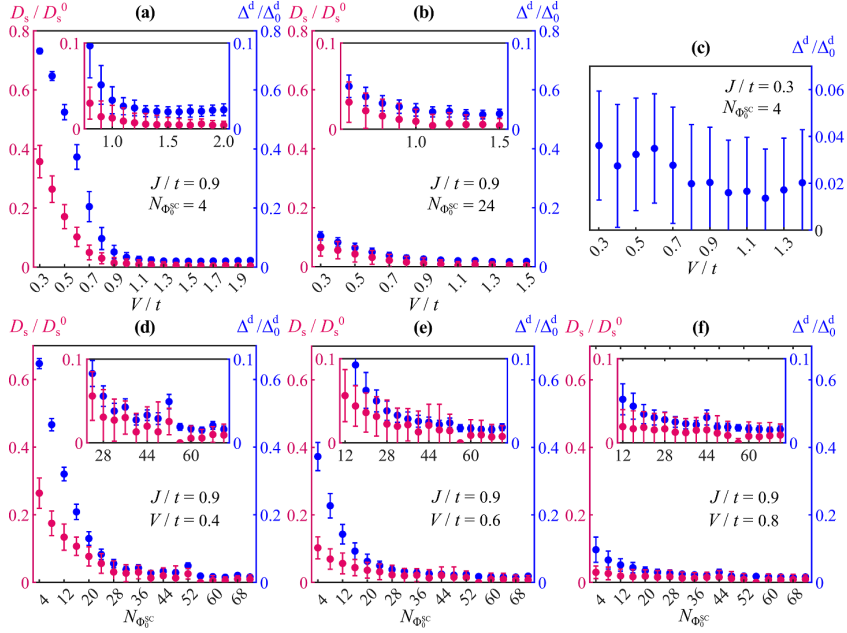


Figure 3. Panels (a) and (b): the superconducting pairing Δ^d and superfluid stiffness D_s under increasing disorder for a system penetrated by 4 and 24 vortices, respectively, for pairing potential $J/t = 0.9$. Panel (c): the superconducting pairing and superfluid stiffness as a function of the number of vortices penetrating the system for disorder strengths $V/t = 0.4$, $V/t = 0.6$, and $V/t = 0.8$ for pairing potential $J/t = 0.9$. In all panels, the superconducting pairing and superfluid stiffness are averaged over all lattice sites and impurity configurations, and plotted with respect to their values Δ_0^d and D_s^0 in a clean system with zero external magnetic field. The insets show a zoom in on the data in on the data in the main plots. The error bars represent the standard deviation. (In this figure, $N_x = N_y = 28$, and $M_x = M_y = 1$.)

in the clean system. Since the vortices are being attracted to regions of high disorder where the superconducting pairing is minimal, the suppression of the zero-bias peak is determined by the disorder potential in the most strongly disordered regions. In these regions, we see that the superconducting gap in the LDOS in the absence of an external magnetic field is more filled up than when we average over the whole system, see especially panel (h). The sensitivity to disorder could be a contributing factor to the absence of the CdGM zero-bias peak in hole-overdoped cuprates. The zero-bias peak has been observed in conventional superconductors [53] and more recently also in the cuprate $\text{YBa}_2\text{Cu}_3\text{O}_{7-\delta}$ (Y123) [54]. Observing the CdGM zero-bias peak in cuprates have otherwise proved difficult, and experimental studies of Bi2212 have not shown signatures of a robust zero-bias peak [41–45].

In figure 3, we plot the superconducting pairing and superfluid stiffness as a function of the disorder strength and the applied magnetic field. Each data point is calculated by averaging over all lattice sites and 70–100 impurity configurations. The error bars represent the standard deviation. The standard error of the mean is 12%–10% of the standard deviation.

Since we are considering relatively small lattice sizes, the superconducting transition is sensitive not only to the magnetic field and the impurity strength, but also the impurity configuration. Although the superconducting transition is sharper for a specific impurity configuration, the superconducting transition is seen in our plots as a gradual transition where an increasing fraction of the impurity configurations result in zero superfluid stiffness. This is represented by the error bars dropping down to zero and the data points gradually approaching zero. Note that when plotting the superconducting pairing and superfluid stiffness as a function of the magnetic field, we will not get a purely monotonous decrease, particularly for weaker disorder strengths. This is because not all of the field strengths can produce a square lattice of vortices in a clean system. This error decreases with increasing system size and disorder.

In figures 3(a)–(c), we plot the average superconducting pairing and superfluid stiffness as a function of disorder for a system under a constant applied magnetic field. In panel (a) where the applied magnetic field is weak, the superconducting pairing remains finite for all impurity strengths and configurations, while the superfluid stiffness

goes to zero for an increasing fraction of the impurity configurations as the disorder is increased. For strong disorder, we thus find a regime of finite superconducting pairing beyond the superconducting transition as was predicted in [35] for zero applied magnetic field. The superconducting pairing survives in islands that grow smaller and fewer in number as the disorder increases. Such islands survive for much higher disorder strengths than what is presented in the figure. In panel (b), we consider an applied field that is closer to the critical field of the superconductor. While the superfluid stiffness is still more suppressed than the superconducting pairing, the difference is smaller than for weaker field strengths. In panel (c), we show the average superconducting pairing as a function of the disorder strength for a weaker pairing potential. This demonstrates that there is a second transition where the superconducting pairing also goes to zero. However, this transition happens for a higher disorder strength and magnetic field than what is reasonable to consider for the band width and system size in panels (a) and (b).

In figures 3(d)–(f) we study the average superconducting pairing and superfluid stiffness as a function of the applied magnetic field for different disorder strengths. Despite the non-monotonous behavior caused by the small system size, we see that the average pairing always remain finite, while some fraction of the impurity configurations result in zero superfluid stiffness for the higher field strengths, similar to the results in panels (a) and (b). These results differs qualitatively for what is expected for a clean system, where we know that the superconducting pairing and superfluid stiffness must go to zero simultaneously at the critical field. Instead, we find that in disordered systems, the intermediate granular regime appears also beyond the magnetic field driven superconducting transition. In panel (f), where the disorder strength is high, the superfluid stiffness starts its transition at lower field strengths than in panels (d) and (e). This, together with the results from panels (a) and (b), indicates that the intermediate granular regime appears at lower field strengths with increasing disorder. As shown in figure 2, the vortices contribute to suppressing superconductivity in the already disordered regions and thus makes the superconductivity granular. Once the system is granular, the magnetic field does not punch additional holes in the superconducting condensate and the pairing decreases very slowly as the field is increased. It is interesting to note that the separation between the two transitions where the superfluid stiffness and superconducting pairing vanishes, also found for a conventional *s*-wave superconductor in [49], persists despite our conservative choice of parameters where the flat bands makes the *d*-wave pairing very sensitive to impurity scattering. As a result, the intermediate regime of remnant superconducting pairing in the superconductor–metal transition can be conveniently studied by tuning the external magnetic field, provided that the system is sufficiently disordered.

4. Concluding remarks

We have here provided a description of the magnetic field driven superconductor–metal transition in the disordered

hole-overdoped cuprates when described solely within the dirty-BCS theory. We find that the CdGM zero-bias peak in the LDOSs at the vortex cores vanishes already at moderate disorder, due to the vortices being attracted to the most disordered regions. We also show that there is an intermediate regime with remnant superconducting pairing at the superconductor–metal transition, which can be reached by tuning an external magnetic field. It still debated to what extent the more unconventional nature of the cuprates needs to be taken into account in the description of the hole-overdoped regime. While we have here studied the low-temperature limit, it is likely that at temperatures closer to the critical temperature, thermal fluctuations could be the dominant cause for the loss of phase coherence of the Cooper pairs. Moreover, experiments predict a pseudogap to exist in the antinodal regions of the Fermi surface above the superconducting critical temperature, particularly in underdoped to weakly overdoped samples [55]. It is unclear whether a second pseudogap could enter the density of states also beyond the disorder and field driven superconducting transition in the highly disordered overdoped samples considered here. Another open question is what the exact nature of the material is at disorder and field strengths where both the superfluid stiffness and superconducting pairing is absent. Experimental studies suggest that the hole-overdoped cuprates are metallic rather than insulating in the normal-state suggesting that the material could be conducting beyond the two transitions [30]. Although it far outside the scope of this work to resolve this debate, we find that the superconductor–metal transition in the disordered hole-overdoped cuprates show some interesting features even when described within the BdG framework.

Data availability statement

All data that support the findings of this study are included within the article (and any supplementary files).

Acknowledgment

This work was supported by the Research Council of Norway through its Centres of Excellence funding scheme, Project No. 262633 ‘QuSpin’.

Appendix. Theoretical framework

The full Bogoliubov–de Gennes equations

In order to diagonalize the Hamiltonian in equation (1), we solve the Bogoliubov–de Gennes equations of the system following the approach in [46, 56]. We first define a basis

$$\psi_i = (c_{i,\uparrow} \ c_{i,\downarrow} \ c_{i,\uparrow}^\dagger \ c_{i,\downarrow}^\dagger)^T, \quad (\text{A.1})$$

and write the Hamiltonian in the form

$$H = H_0 + \frac{1}{2} \sum_{i,j} \psi_i^\dagger H_{i,j} \psi_j. \quad (\text{A.2})$$

Above, H_0 is a constant and H_{ij} is a 4×4 matrix. The Hamiltonian can be written in a diagonal form

$$H = H_0 + \frac{1}{2} \sum_n E_n \gamma_n^\dagger \gamma_n \quad (\text{A.3})$$

by solving the full BdG equations

$$\sum_j H_{i,j} \phi_{j,n} = E_n \phi_{i,n}. \quad (\text{A.4})$$

Here, E_n are the eigenenergies and $\phi_{i,n}$ the eigenvectors labeled by $n \in [1, 4N_x N_y]$. There are seemingly twice as many fermionic operators γ_n compared to our original operators $c_{i,\sigma}$, which means pairs of the new operators must relate to each other. It can be shown that there are two equivalent solutions

$$E_n, \phi_{i,n} = (u_{i,n\uparrow} \ u_{i,n\downarrow} \ v_{i,n\uparrow} \ v_{i,n\downarrow})^T, \quad (\text{A.5})$$

$$-E_n, \phi_{i,n} = (v_{i,n\uparrow}^* \ v_{i,n\downarrow}^* \ u_{i,n\uparrow}^* \ u_{i,n\downarrow}^*)^T. \quad (\text{A.6})$$

Since the eigenenergies of these equivalent solutions differ only by a sign, we can write the the Hamiltonian in a diagonal form

$$H = H_0 - \frac{1}{2} \sum_{n \text{ for } E_n > 0} E_n + \sum_{n \text{ for } E_n > 0} E_n \gamma_n^\dagger \gamma_n \quad (\text{A.7})$$

including only positive eigenenergies. The old operators are related to the new ones by

$$c_{i,\sigma} = \sum_{n \text{ for } E_n > 0} (u_{i,n,\sigma} \gamma_n + v_{i,n,\sigma}^* \gamma_n^\dagger). \quad (\text{A.8})$$

Since the operators in the diagonalized Hamiltonian are now independent, the expectation values of the new operators can be evaluated as

$$\langle \gamma_n^\dagger \gamma_m \rangle = f_{\text{FD}}(E_n) \delta_{n,m}, \quad (\text{A.9})$$

$$\langle \gamma_n^\dagger \gamma_m^\dagger \rangle = \langle \gamma_n \gamma_m \rangle = 0 \quad (\text{A.10})$$

for $E_n > 0$, where $f_{\text{FD}}(E_n)$ is the Fermi–Dirac distribution.

The reduced Bogoliubov–de Gennes equations

We can simplify our calculation by realizing that in the absence of spin–orbit coupling and spin–flip scattering, the Hamiltonian matrix contains two independent blocks [46]. It turns out that the two independent sets of BdG equations can be written in exactly the same form and that while one results in positive eigenenergies, the other results in negative eigenenergies. It is therefore far more efficient to solve the reduced BdG equations

$$\sum_j \begin{pmatrix} \epsilon_{ij} & \Delta_{ij} \\ \Delta_{ji}^* & -\epsilon_{ji} \end{pmatrix} \begin{pmatrix} u_{j,n} \\ v_{j,n} \end{pmatrix} = E_n \begin{pmatrix} u_{i,n} \\ v_{i,n} \end{pmatrix} \quad (\text{A.11})$$

for all positive and negative eigenenergies labeled by $n \in [1, 2N_x N_y]$. For simplicity of notation, we have defined

$$\epsilon_{i,j} = -t_{i,j} e^{i\phi_{i,j}} - (\mu - V_i) \delta_{i,j}. \quad (\text{A.12})$$

The diagonalized Hamiltonian can then be written in the form

$$H = H_0 - \frac{1}{2} \sum_n |E_n| + \sum_n |E_n| \gamma_n^\dagger \gamma_n, \quad (\text{A.13})$$

where the old operators can be written in terms of new operators using the relations

$$c_{i,\uparrow} = \sum_{n \text{ for } E_n > 0} u_{i,n} \gamma_n + \sum_{n \text{ for } E_n < 0} u_{i,n} \gamma_n^\dagger, \quad (\text{A.14})$$

$$c_{i,\downarrow} = \sum_{n \text{ for } E_n > 0} v_{i,n}^* \gamma_n^\dagger + \sum_{n \text{ for } E_n < 0} v_{i,n}^* \gamma_n. \quad (\text{A.15})$$

The expectation values of the new operators are given by

$$\langle \gamma_n^\dagger \gamma_m \rangle = f_{\text{FD}}(|E_n|) \delta_{n,m}, \quad (\text{A.16})$$

$$\langle \gamma_n^\dagger \gamma_m^\dagger \rangle = \langle \gamma_n \gamma_m \rangle = 0. \quad (\text{A.17})$$

The reduced BdG equations in their current form is suitable for studying systems of a finite size. However, when studying vortex formation, it is beneficial to consider a larger systems. Therefore, we next introduce periodic boundary conditions to eliminate edge effects.

Boundary conditions and self-consistent solution

When applying an external magnetic field perpendicular to the sample, the translational invariance of the lattice is broken by the Peierls phase. However, by introducing magnetic unit cells containing an even number of superconducting flux quanta, we can regain the translational invariance of the lattice under translation between equivalent sites in different magnetic unit cells [46, 57, 58]. This allows us to use periodic boundary conditions, and we can consider smaller lattice sizes without the disturbance of edge effects.

We consider $M_x \times M_y$ magnetic unit cells of size $N_x \times N_y$. A translation between magnetic unit cells is described by a vector $\mathbf{R}_{l_x, l_y} = (l_x N_x a, l_y N_y a, 0)$, where $l_{x(y)} \in [0, M_{x(y)} - 1]$ and a is the lattice constant. By applying periodic boundary conditions through the magnetic Bloch theorem [59], our eigenvectors and eigenenergies acquire an index

$$\mathbf{k} = \frac{2\pi l_x}{M_x N_x a} \mathbf{x} + \frac{2\pi l_y}{M_y N_y a} \mathbf{y}. \quad (\text{A.18})$$

This allows us to solve the BdG equations for a system size of $N_x \times N_y$ for $M_x M_y$ values of \mathbf{k} , rather than for a system of size $N_x M_x \times N_y M_y$. We choose to absorb a \mathbf{k} dependent phase factor into the eigenvector so that

$$\begin{pmatrix} u_{i,n,\mathbf{k}} \\ v_{i,n,\mathbf{k}} \end{pmatrix} = e^{i\mathbf{k} \cdot \mathbf{r}_i} \begin{pmatrix} \tilde{u}_{i,n,\mathbf{k}} \\ \tilde{v}_{i,n,\mathbf{k}} \end{pmatrix}. \quad (\text{A.19})$$

The BdG equations now take the form

$$\sum_j e^{ik \cdot (r_j - r_i)} \begin{pmatrix} \epsilon_{ij} & \Delta_{ij} \\ \Delta_{ji}^* & -\epsilon_{ji} \end{pmatrix} \begin{pmatrix} \tilde{u}_{j,n,k} \\ \tilde{v}_{j,n,k} \end{pmatrix} = E_{n,k} \begin{pmatrix} \tilde{u}_{i,n,k} \\ \tilde{v}_{i,n,k} \end{pmatrix}. \quad (\text{A.20})$$

These are solved together with the self-consistency equation for the superconducting pairing correlations

$$\Delta_{ij} = \frac{U}{M_x M_y} \sum_{n,k} e^{ik \cdot (r_i - r_j)} \tilde{u}_{i,n,k} (\tilde{v}_{j,n,k})^* [1 - f_{\text{FD}}(E_{n,k})]. \quad (\text{A.21})$$

Inside a magnetic unit cell, the only phase factors we need to consider are the Peierls phases associated with electron hopping. The nonzero Peierls phases are $\phi_{i \pm y, i} = \mp \pi \phi_x$ for nearest neighbor hopping, $\phi_{i \pm x \pm y, i} = \mp' \pi \phi (\tilde{i}_x \pm 1/2)$ for next nearest neighbor hopping, and $\phi_{i \pm y, i} = \mp 2\pi \phi_{i_x}$ for third nearest neighbor hopping. These depend on the magnetic field through $\phi = N_{\text{B}_0^{\text{SC}}} / N_x N_y = B a^2 / \Phi_0^{\text{SC}}$. When site i and j in equations (A.20) and (A.21) lies in different magnetic unit cells, we need to apply the translation \mathbf{R}_{l_x, l_y} to one of the eigenvectors so that all eigenvalues lie in the same magnetic unit cell. Upon such a translation, the eigenvalues pick up an additional phase through the boundary condition

$$\begin{pmatrix} \tilde{u}_{i,n,k}(\mathbf{r}_i + \mathbf{R}_{l_x, l_y}) \\ \tilde{v}_{i,n,k}(\mathbf{r}_i + \mathbf{R}_{l_x, l_y}) \end{pmatrix} = \begin{pmatrix} e^{-i\chi(\mathbf{r}_i, \mathbf{R}_{l_x, l_y})/2} \tilde{u}_{i,n,k}(\mathbf{r}_i) \\ e^{+i\chi(\mathbf{r}_i, \mathbf{R}_{l_x, l_y})/2} \tilde{v}_{i,n,k}(\mathbf{r}_i) \end{pmatrix}. \quad (\text{A.22})$$

The phase

$$\chi(\mathbf{r}_i, \mathbf{R}_{l_x, l_y}) = \frac{2\pi}{\Phi_0^{\text{SC}}} \mathbf{A}(\mathbf{R}_{l_x, l_y}) \cdot \mathbf{r}_i = 2\pi \phi l_x N_x l_y. \quad (\text{A.23})$$

is the total phase picked up by the superconducting pairing through the translation

$$\Delta_i^d(\mathbf{r}_i - \mathbf{R}_{l_x, l_y}) = \Delta_i^d(\mathbf{r}_i) e^{i\chi(\mathbf{r}_i, \mathbf{R}_{l_x, l_y})}. \quad (\text{A.24})$$

By solving the reduced BdG equation in equation (A.20) together with the self-consistency equation in equation (A.21) and the boundary condition in equation (A.22), we obtain eigenenergies and eigenvalues that we can use to calculate physical observables.

Physical observables

We here give the expressions for the physical observables in terms of the eigenenergies and eigenvalues. The hole concentration is given by

$$x = \frac{1}{N_x N_y M_x M_y} \sum_{i,n,k} \{1 - |\tilde{u}_{i,n,k}|^2 f_{\text{FD}}(E_{n,k}) - |\tilde{v}_{i,n,k}|^2 \times [1 - f_{\text{FD}}(E_{n,k})]\} \quad (\text{A.25})$$

and determines the doping level. The d -wave superconducting pairing is calculated using equations (4) and (A.21). The superfluid stiffness is calculated from the Kubo formula in

equation (5), where we insert the expectation value of the kinetic energy associated with the x oriented bonds

$$\langle -K_x \rangle = \frac{1}{N_x N_y M_x M_y} \sum_{i,\delta,n,k} \delta_x^2 (t_{i+\delta, i} e^{i\phi_{i+\delta, i}} \{ \tilde{u}_{i+\delta, n,k}^* \tilde{u}_{i,n,k} e^{-ik \cdot \delta} \times f_{\text{FD}}(E_n) + \tilde{v}_{i,n,k}^* \tilde{v}_{i+\delta, n,k} e^{ik \cdot \delta} [1 - f_{\text{FD}}(E_n)] \}) + \text{c.c.} \quad (\text{A.26})$$

and the current-current correlation function

$$\Lambda_{xx}(\mathbf{q}, \omega) = \frac{1}{N_x N_y (M_x M_y)^2} \sum_{n,k,m,k'} \frac{f_{\text{FD}}(E_{n,k}) - f_{\text{FD}}(E_{m,k'})}{\omega + i\delta + E_{n,k} - E_{m,k'}} \times A_{n,k,m,k'}(-\mathbf{q}) A_{m,k',n,k}(\mathbf{q}). \quad (\text{A.27})$$

Above, $\delta = \{x, y, x \pm y, 2x, 2y\}$ and

$$A_{m,k',n,k}(\mathbf{q}) = \sum_{i,\delta} \delta_x t_{i+\delta, i} e^{i(\mathbf{q} - \mathbf{k}' + \mathbf{k}) \cdot \mathbf{r}_i} [(\tilde{u}_{i+\delta, m,k'}^* \tilde{u}_{i,n,k} e^{-ik' \cdot \delta} - \tilde{v}_{i,m,k'}^* \tilde{v}_{i+\delta, n,k} e^{ik \cdot \delta}) e^{i\phi_{i+\delta, i}} + (\tilde{v}_{i+\delta, m,k'}^* \tilde{v}_{i,n,k} \times e^{-ik' \cdot \delta} - \tilde{u}_{i,m,k'}^* \tilde{u}_{i+\delta, n,k} e^{ik \cdot \delta}) e^{-i\phi_{i+\delta, i}}]. \quad (\text{A.28})$$

The bond currents can be obtained by multiplying equation (A.26) with i and reversing the sign of the complex conjugate. In figure 2, we have included bond currents along all bonds by removing the factor δ_x^2 . Finally, the LDOS is given by

$$N_i = \frac{1}{M_x M_y} \sum_{n,k} [|\tilde{u}_{i,n,k}|^2 \delta(\omega - E_{n,k}) + |\tilde{v}_{i,n,k}|^2 \delta(\omega + E_{n,k})]. \quad (\text{A.29})$$

In our numerical calculation, the δ -function is approximated by $\delta(x) = (1/\pi) [\Gamma / (x^2 + \Gamma^2)]$, where $\Gamma = 0.05$.

ORCID iD

Lina G Johnsen  <https://orcid.org/0000-0003-2845-1738>

References

- [1] Damascelli A, Hussain Z and Shen Z-X 2003 Angle-resolved photoemission studies of the cuprate superconductors *Rev. Mod. Phys.* **75** 473–541
- [2] Alloul H, Bobroff J, Gabay M and Hirschfeld P J 2009 Defects in correlated metals and superconductors *Rev. Mod. Phys.* **81** 45–108
- [3] Bednorz J G and Müller K A 1986 Possible high T_c superconductivity in the Ba–La–Cu–O system *Z. Phys. B* **64** 189–93
- [4] Bardeen J, Cooper L N and Schrieffer J R 1957 Theory of superconductivity *Phys. Rev.* **108** 1175–204
- [5] Varma C M, Littlewood P B, Schmitt-Rink S, Abrahams E and Ruckenstein A E 1989 Phenomenology of the normal state of Cu-O high-temperature superconductors *Phys. Rev. Lett.* **63** 1996–9
- [6] Alloul H, Ohno T and Mendels P 1989 ^{89}Y NMR evidence for a Fermi-liquid behavior in $\text{YBa}_2\text{Cu}_3\text{O}_{6+x}$ *Phys. Rev. Lett.* **63** 1700–3

- [7] Rossat-Mignod J, Regnault L P, Vettier C, Bourges P, Burlat P, Bossy J, Henry J Y and Lapertot G 1991 Neutron scattering study of the $\text{YBa}_2\text{Cu}_3\text{O}_{6+x}$ system *Physica C* **185** 86–92
- [8] Emery V J and Kivelson S A 1995 Importance of phase fluctuations in superconductors with small superfluid density *Nature* **374** 434–7
- [9] Julien M-H, Fehér T, Horvatic M, Berthier C, Bakharev O N, Ségransan P, Collin G and Maruccio J-F 2000 ^{63}Cu NMR evidence for enhanced antiferromagnetic correlations around Zn impurities in $\text{YBa}_2\text{Cu}_3\text{O}_{6.7}$ *Phys. Rev. Lett.* **84** 3422–5
- [10] Wang Z and Lee P A 2002 Local moment formation in the superconducting state of a doped Mott insulator *Phys. Rev. Lett.* **89** 217002
- [11] Andersen B M, Hirschfeld P J, Kampf A P and Schmid M 2007 Disorder-induced static antiferromagnetism in cuprate superconductors *Phys. Rev. Lett.* **99** 147002
- [12] Lake B *et al* 2001 Spins in the vortices of a high-temperature superconductor *Science* **291** 1759–62
- [13] Demler E, Sachdev S and Zhang Y 2001 Spin-ordering quantum transitions of superconductors in a magnetic field *Phys. Rev. Lett.* **87** 067202
- [14] Zhu J-X and Ting C S 2001 Quasiparticle states at a d -wave vortex core in high- T_c superconductors: induction of local spin density wave order *Phys. Rev. Lett.* **87** 147002
- [15] Lake B *et al* 2002 Antiferromagnetic order induced by an applied magnetic field in a high-temperature superconductor *Nature* **415** 299–302
- [16] Hoffman J E, Hudson E W, Lang K M, Madhavan V, Eisaki H, Uchida S and Davis J C 2002 A four unit cell periodic pattern of quasi-particle states surrounding vortex cores in $\text{Bi}_2\text{Sr}_2\text{CaCu}_2\text{O}_{8+\delta}$ *Science* **295** 466–9
- [17] Zhu J-X, Martin I and Bishop A R 2002 Spin and charge order around vortices and impurities in high- T_c superconductors *Phys. Rev. Lett.* **89** 067003
- [18] Platé M *et al* 2005 Fermi surface and quasiparticle excitations of overdoped $\text{Tl}_2\text{Ba}_2\text{CuO}_{6+\delta}$ *Phys. Rev. Lett.* **95** 077001
- [19] Vignolle B, Carrington A, Cooper R A, French M M J, Mackenzie A P, Jaudet C, Vignolles D, Proust C and Hussey N E 2008 Quantum oscillations in an overdoped high- T_c superconductor *Nature* **455** 952–5
- [20] Simard O, Hébert C-D, Foley A, Sénéchal D and Tremblay A-M S 2019 Superfluid stiffness in cuprates: effect of Mott transition and phase competition *Phys. Rev. B* **100** 094506
- [21] Gomes K K, Pasupathy A N, Pushp A, Ono S, Ando Y and Yazdani A 2007 Visualizing pair formation on the atomic scale in the high- T_c superconductor $\text{Bi}_2\text{Sr}_2\text{CaCu}_2\text{O}_{8+\delta}$ *Nature* **447** 569–72
- [22] Pasupathy A N, Pushp A, Gomes K K, Parker C V, Wen J, Xu Z, Gu G, Ono S, Ando Y and Yazdani A 2008 Electronic origin of the inhomogeneous pairing interaction in the high- T_c superconductor $\text{Bi}_2\text{Sr}_2\text{CaCu}_2\text{O}_{8+\delta}$ *Science* **320** 196–201
- [23] He Y *et al* 2021 Superconducting fluctuations in overdoped $\text{Bi}_2\text{Sr}_2\text{CaCu}_2\text{O}_{8+\delta}$ *Phys. Rev. X* **11** 031068
- [24] Uemura Y J *et al* 1993 Magnetic-field penetration depth in $\text{Tl}_2\text{Ba}_2\text{CuO}_{6+\delta}$ in the overdoped regime *Nature* **364** 605–7
- [25] Niedermayer C, Bernhard C, Binninger U, Glücker H, Tallon J L, Ansaldo E J and Budnick J I 1993 Muon spin rotation study of the correlation between T_c and n_s/m^* in overdoped $\text{Tl}_2\text{Ba}_2\text{CuO}_{6+\delta}$ *Phys. Rev. Lett.* **71** 1764–7
- [26] Rourke P M C *et al* 2011 Phase-fluctuating superconductivity in overdoped $\text{La}_{2-x}\text{Sr}_x\text{CuO}_4$ *Nature* **7** 455–8
- [27] Božović I, He X, Wu J and Bollinger A T 2016 Dependence of the critical temperature in overdoped copper oxides on superfluid density *Nature* **536** 309–11
- [28] Mahmood F, He X, Božović I and Armitage N P 2019 Locating the missing superconducting electrons in the overdoped cuprates $\text{La}_{2-x}\text{Sr}_x\text{CuO}_4$ *Phys. Rev. Lett.* **122** 027003
- [29] Wu J, Bollinger A T, He X and Božović I 2017 Spontaneous breaking of rotational symmetry in copper oxide superconductors *Nature* **547** 432–5
- [30] Božović I, He X, Wu J and Bollinger A T 2018 The vanishing superfluid density in cuprates - and why it matters *J. Supercond. Nov. Magn.* **31** 2683–90
- [31] Herrera C, Franklin J, Božović I, He X and Sochnikov I 2021 Scanning SQUID characterization of extremely overdoped $\text{La}_{2-x}\text{Sr}_x\text{CuO}_4$ *Phys. Rev. B* **103** 024528
- [32] Lee-Hone N R, Dodge J S and Broun D M 2017 Disorder and superfluid density in overdoped cuprate superconductors *Phys. Rev. B* **96** 024501
- [33] Lee-Hone N R, Özdemiř H U, Mishra V, Broun D M and Hirschfeld P J 2020 Low energy phenomenology of the overdoped cuprates: viability of the Landau-BCS paradigm *Phys. Rev. Res.* **2** 013228
- [34] Wang D, Xu J-Q, Zhang H-J and Wang Q-H 2022 Anisotropic scattering caused by apical oxygen vacancies in thin films of overdoped high-temperature cuprate superconductors *Phys. Rev. Lett.* **128** 137001
- [35] Li Z-X, Kivelson S A and Lee D H 2021 Superconductor-to-metal transition in overdoped cuprates *npj Quantum Mater.* **6** 36
- [36] Anderson P W 1959 Theory of dirty superconductors *J. Phys. Chem. Solids* **11** 26–30
- [37] Abrikosov A A and Gor'kov L P 1960 Contribution to the theory of superconducting alloys with paramagnetic impurities *Zh. Eksp. Teor. Fiz.* **39** 1781
- [38] Balatsky A V, Vekhter I and Zhu J-X 2006 Impurity-induced states in conventional and unconventional superconductors *Rev. Mod. Phys.* **78** 373–433
- [39] Franz M, Kallin C, Berlinsky A J and Salkola M I 1997 Critical temperature and superfluid density suppression in disordered high- T_c cuprate superconductors *Phys. Rev. B* **56** 7882–5
- [40] Ghosal A, Randeria M and Trivedi N 2000 Spatial inhomogeneities in disordered d -wave superconductors *Phys. Rev. B* **63** 020505
- [41] Renner C, Revaz B, Kadowaki K, Maggio-Aprile I and Fischer Ø 1998 Observation of the low temperature pseudogap in the vortex cores of $\text{Bi}_2\text{Sr}_2\text{CaCu}_2\text{O}_{8+\delta}$ *Phys. Rev. Lett.* **80** 3606–9
- [42] Hoogenboom B W, Renner C, Revaz B, Maggio-Aprile I and Fischer Ø 2000 Low-energy structures in vortex core tunneling spectra in $\text{Bi}_2\text{Sr}_2\text{CaCu}_2\text{O}_{8+\delta}$ *Physica C* **332** 440–4
- [43] Pan S H, Hudson E W, Gupta A K, Ng K-W, Eisaki H, Uchida S and Davis J C 2000 STM studies of the electronic structure of vortex cores in $\text{Bi}_2\text{Sr}_2\text{CaCu}_2\text{O}_{8+\delta}$ *Phys. Rev. Lett.* **85** 1536–9
- [44] Levy G, Kugler M, Manuel A A, Fischer Ø and Li M 2005 Fourfold structure of vortex-core states in $\text{Bi}_2\text{Sr}_2\text{CaCu}_2\text{O}_{8+\delta}$ *Phys. Rev. Lett.* **95** 257005
- [45] Yoshizawa S, Koseki T, Matsuba K, Mochiku T, Hirata K and Nishida N 2013 High-resolution scanning tunneling spectroscopy of vortex cores in inhomogeneous electronic states of $\text{Bi}_2\text{Sr}_2\text{CaCu}_2\text{O}_x$ *J. Phys. Soc. Japan* **82** 083706
- [46] Zhu J-X 2016 *Bogoliubov-de Gennes Method and its Applications* (Cham: Springer)
- [47] Scalapino D J, White S R and Zhang S C 1992 Superfluid density and the Drude weight of the Hubbard model *Phys. Rev. Lett.* **68** 2830–3

- [48] Scalapino D J, White S R and Zhang S 1993 Insulator, metal, or superconductor: the criteria *Phys. Rev. B* **47** 7995–8007
- [49] Datta A, Banerjee A, Trivedi N and Ghosal A 2021 New paradigm for a disordered superconductor in a magnetic field (arXiv:2101.00220)
- [50] He Y *et al* 2014 Fermi surface and pseudogap evolution in a cuprate superconductor *Science* **344** 608–11
- [51] Zou C, Hao Z, Luo X, Ye S, Gao Q, Li X, Xu M, Cai P, Lin C, Zhou X, Lee D-H and Wang Y 2021 Particle-hole asymmetric superconducting coherence peaks in overdoped cuprates (arXiv:2103.06094)
- [52] Caroli C, De Gennes P G and Matricon J 1964 Bound fermion states on a vortex line in a type II superconductor *Phys. Lett.* **9** 307–9
- [53] Hess H F, Robinson R B, Dynes R C, Valles J M and Waszczak J V 1989 Scanning-tunneling-microscope observation of the Abrikosov flux lattice and the density of states near and inside a fluxoid *Phys. Rev. Lett.* **62** 214–6
- [54] Berthod C, Maggio-Aprile I, Bruér J, Erb A and Renner C 2017 Observation of Caroli–de Gennes–Matricon vortex states in $\text{YBa}_2\text{Cu}_3\text{O}_{7-\delta}$ *Phys. Rev. Lett.* **119** 237001
- [55] Fradkin E, Kivelson S A and Tranquada J M 2015 Colloquium: theory of intertwined orders in high temperature superconductors *Rev. Mod. Phys.* **87** 457–82
- [56] Hermansen C 2018 Vortices in s-wave superconductors *Master thesis* University of Copenhagen (available at: https://nbi.ku.dk/english/theses/bachelor-theses/cecilie-hermansen/bsc_final.pdf)
- [57] Han Q, Zhang L-Y and Wang Z D 2000 Effect of a point impurity on the vortex bound states in an s-wave superconductor: a self-consistent analysis *Phys. Rev. B* **62** 5936–41
- [58] Schmid M, Andersen B M, Kampf A P and Hirschfeld P J 2010 d-wave superconductivity as a catalyst for antiferromagnetism in underdoped cuprates *New J. Phys.* **12** 053043
- [59] Brown E 1964 Bloch electrons in a uniform magnetic field *Phys. Rev.* **133** A1038–44

X

REFERENCE

Simran Chourasia, Lina Johnsen Kamra, Irina V. Bobkova, and Akashdeep Kamra,

Generation of spin-triplet Cooper pairs via a canted antiferromagnet,
arXiv:2303.18145 (2023).

CONTRIBUTIONS

SC performed the analytical and numerical calculations. LJK supervised the analytical calculations and contributed with expertise on the theoretical framework and the numerical algorithm. IVB derived the spin-triplet correlation expressions. SC and AK wrote the manuscript. All coauthors were involved in discussions and revision of the manuscript. AK initiated and supervised the project.

Generation of spin-triplet Cooper pairs via a canted antiferromagnet

Simran Chourasia,^{1,*} Lina Johnsen Kamra,² Irina V. Bobkova,^{3,4} and Akashdeep Kamra¹

¹*Condensed Matter Physics Center (IFIMAC) and
Departamento de Física Teórica de la Materia Condensada,
Universidad Autónoma de Madrid, E-28049 Madrid, Spain*

²*Center for Quantum Spintronics, Department of Physics,
Norwegian University of Science and Technology, NO-7491 Trondheim, Norway*

³*Moscow Institute of Physics and Technology,
Dolgoprudny, 141700 Moscow, Russia*

⁴*National Research University Higher School of Economics, Moscow, 101000 Russia*

Abstract

Spinful triplet Cooper pairs can be generated from their singlet counterparts available in a conventional superconductor (S) using two or more noncollinear magnetic moments, typically contributed by different magnets in a multilayered heterostructure. Here, we theoretically demonstrate that an S interfaced with a canted antiferromagnet (AF) harbors spinful triplet Cooper pairs capitalizing on the intrinsic noncollinearity between the two AF sublattice magnetizations. As the AF canting can be controlled by an applied field, our work proposes a simple bilayer structure that admits controllable generation of spin-triplet Cooper pairs. Employing the Bogoliubov-de Gennes framework, we delineate the spatial dependence of the spin-triplet correlations. We further evaluate the superconducting critical temperature as a function of the AF canting, which provides one experimental observable associated with the emergence of these triplet correlations.

I. INTRODUCTION

The dissipationless flow of charge in superconductors is partly responsible for their central role in the various emerging quantum technologies [1, 2]. The widely available conventional superconductors, such as Al and Nb, are made of spin-singlet Cooper pairs, which harbor no net spin [3]. A superconductor hosting spin-triplet Cooper pairs can support dissipationless spin currents [4–8], deemed valuable for switching magnetic memories [9–13], as well as exotic excitations, such as Majorana bound states [14]. Such an unconventional superconductor can be engineered from its conventional counterpart employing heterostructures incorporating magnetic multilayers [5–8, 15]. The basic requirement for achieving spinful triplets from spin-singlets is exposing the latter to two or more noncollinear spin-splitting fields. A wide variety of multilayered hybrids comprising conventional superconductors (S) and ferromagnets (F) has been employed to achieve the desired spinful triplets [16–29], coming a long way from the initial critical temperature studies [30, 31].

Since a Néel ordered antiferromagnet (AF) bears no net spin or magnetic moment, for some time it was considered inert at causing spin-splitting in an adjacent superconductor. Indeed, early experiments found a metallic AF to behave just like a normal metal when considering its effect on an adjacent superconductor [32]. More recent experiments, on the

* simran.chourasia@uam.es

other hand, found the AF to substantially affect the adjacent S with intriguing dependencies [33–38]. From the theory perspective, Josephson junctions [39, 40] and interfaces [41] involving itinerant AFs were shown to exhibit non-trivial properties due to quasiparticle reflections. Moreover, a recent work demonstrates that an uncompensated interface of an insulating AF with an adjacent S induces a strong spin-splitting as well as spin-flip scattering thereby strongly influencing the S [42]. Subsequent work found even the fully compensated interface between the AF and S to be spin-active [43]. This has been understood as due to the AF inducing Néel triplets whose pairing amplitude has an alternating sign in space similar to the AF spin [44]. Altogether, the potential usefulness of AFs [45] in engineering novel superconducting effects and devices, such as a filter [46], is starting to be understood.

Pekar and Rashba [47] already recognized long ago that even though the net spin vanishes in an AF, at the lattice constant length scale, the AF harbors a spin or magnetization profile that rapidly varies in space changing its sign from one lattice site to the next, which should manifest itself in physical observables. As a result, the AF with its two sublattice magnetizations antiparallel to each other generates zero-spin Néel triplets [44]. Proceeding further along this line of thought, a homogeneous canted AF with its sublattice magnetizations deviating from an antiparallel alignment effectively harbors a noncollinear spin texture capable of generating spinful triplet Cooper pairs in an adjacent S. This exciting possibility is theoretically examined in the present work.

Here, employing the Bogoliubov-de Gennes (BdG) framework [48], we theoretically investigate a bilayer structure consisting of an insulating AF exchange coupled via a compensated interface to an adjacent S. We examine the critical temperature and spin-triplet correlations in the S as a function of the canting in the AF, which allows us to continuously tune the AF from its collinear antiparallel state to it effectively becoming an F. We find that Néel triplets are generated in the S both from the interband pairing channel considered recently [44], and from the conventional intraband pairing. We find that the latter channel results in Néel triplets formation due to an imprinting of the Néel character by the AF on the normal state electronic wavefunctions in the S. Although this channel of Néel triplet generation is found to be much weaker than the interband pairing channel, it admits qualitatively new effects. We show that it is only in the intraband pairing channel that spinful Néel triplets are generated due to the intrinsic noncollinearity of a canted AF. The S critical temperature variation as a function of the AF canting angle is found to be consistent with the intraband Néel triplets

being weaker than their interband counterparts, and may offer a convenient experimental signature of this interplay.

The paper is organized as follows. Section II introduces the model and BdG framework employed in our analysis. The dependence of spin-triplet correlations on space and AF canting is discussed in Sec. III, while the variation of superconducting critical temperature is discussed in Sec. IV. Until this point, we consider a one-dimensional model that allows a simple and semianalytic understanding of the essential physics. In Sec. V, we employ a two-dimensional model for the S to validate our prior results and further examine the spatial dependence of the triplet correlations. We conclude with discussion and summary of the key points in Sec. VI. The appendices provide details of the BdG framework, analytic evaluation of the normal state electronic properties in the bilayer, triplet correlations for a different configuration of the AF sublattice magnetizations, and the parameters employed in our numerical routines.

II. AF/S BILAYER MODEL

We consider a bilayer structure comprising an insulating AF exchange coupled via a compensated interface to the S layer, as depicted schematically in Fig. 1(a). We anticipate that all three kinds of spin-triplet correlations will be generated in the S when the AF sublattice magnetizations are canted [Fig. 1(a)]. We employ the Bogoliubov-de Gennes method and numerically evaluate the superconducting properties self-consistently [48]. The canted-AF is taken to be an ideal insulator with a large band-gap. Consequently, the Hamiltonian is formulated only for the itinerant electrons in S. The AF's influence on the S is accounted for by incorporating a spatially dependent spin-splitting caused by the AF spins [42, 49, 50]. Furthermore, with the aim of allowing a semianalytic understanding to the essential physics, we consider a one-dimensional model as depicted schematically in Fig. 1(b). The resulting Hamiltonian is given by

$$\begin{aligned}
 H = & -\mu \sum_{j,\sigma} c_{j,\sigma}^\dagger c_{j,\sigma} - t \sum_{\langle i,j \rangle} \sum_{\sigma} c_{i,\sigma}^\dagger c_{j,\sigma} - \frac{J}{2} \sum_j \vec{M}_j \cdot \vec{S}_j \\
 & + \sum_j \left(\frac{|\Delta_j|^2}{U} + \Delta_j^* c_{j,\downarrow} c_{j,\uparrow} + \Delta_j c_{j,\uparrow}^\dagger c_{j,\downarrow}^\dagger \right), \tag{1}
 \end{aligned}$$

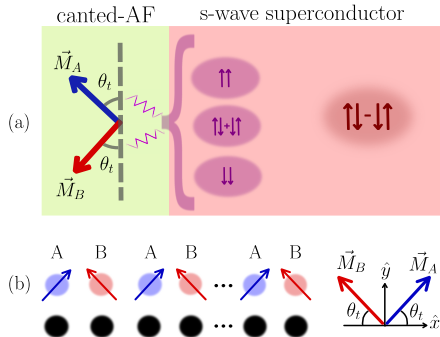


FIG. 1. (a) Schematic depiction of the system and key physics under investigation. Equal-spin and zero-spin triplet correlations are generated in a conventional s-wave spin-singlet superconductor when it is interfaced with a canted antiferromagnet (canted-AF). This results from the intrinsic noncollinearity between the two AF sublattice magnetizations. (b) Schematic depiction of our model investigated using the Bogoliubov-de Gennes method. The black circles represent lattice sites of the superconductor and blue (red) circles represent A (B) sublattice sites of the canted-AF. The blue and red arrows denote the local AF magnetic moments. The canting angle θ_t allows us to vary the magnet from being a collinear AF ($\theta_t = 0$) to a ferromagnet ($\theta_t = \pi/2$).

where $c_{j,\sigma}^\dagger$ ($c_{j,\sigma}$) is the creation (annihilation) operator of an electron with spin σ at site j of the S layer, with $j = 1, 2, \dots, N$ as the site index. Here, the spin quantization axis is taken along the z -axis. We further consider periodic boundary conditions by allowing electrons to hop between sites $j = 1$ and $j = N$.

In Eq. (1), μ is the chemical potential. Within our theoretical method, it is determined via the filling factor f , which is the fraction of filled electronic states in the system. For $f = 0.5$ (half-filled band), we obtain $\mu = 0$. This corresponds to the Fermi wave-vector $k_F = \pi/2a$ located at the AF Brillouin zone boundary, where a is the lattice constant. The normal state electronic dispersion and properties for the case of an AF in its collinear anti-parallel state have been discussed in Appendix A. For $f \neq 0.5$, μ is non-zero and the Fermi level is away from the AF Brillouin zone boundary. In the following analysis, we will consider the two qualitatively distinct cases of $f = 0.5$ and $f \neq 0.5$, corresponding to $\mu = 0$

and $\mu \neq 0$.

The second term in Eq. (1) is the kinetic energy term, describing hopping between nearest neighboring sites $\langle i, j \rangle$ with $t > 0$ as the hopping parameter.

The third term in the Hamiltonian [Eq. (1)] accounts for the spin-splitting due to the localized magnetic moments in the canted-AF [6, 51, 52]. $J\vec{M}_j/2$ is the local spin-splitting field which causes an energy shift of spin-up and spin-down electrons by $\mp J/2$, with respect to the local spin-quantization axis along \vec{M}_j . Here, $\vec{M}_j = [(-1)^{j+1} \cos \theta_t \hat{x} + \sin \theta_t \hat{y}]$ is the unit vector along the direction of local magnetic moment at the j^{th} canted-AF site. The AF sublattice magnetizations are taken to be in the x-y plane to examine the spin-triplet correlation with the quantization axis (z) perpendicular to this plane. A different magnetic configuration has also been investigated and discussed in the appendix. $\vec{S}_j = [(c_{j,\uparrow}^\dagger c_{j,\uparrow} - c_{j,\downarrow}^\dagger c_{j,\downarrow})\hat{z} + (c_{j,\uparrow}^\dagger c_{j,\downarrow} + c_{j,\downarrow}^\dagger c_{j,\uparrow})\hat{x} + (-ic_{j,\uparrow}^\dagger c_{j,\downarrow} + ic_{j,\downarrow}^\dagger c_{j,\uparrow})\hat{y}]$ is the spin operator of an electron at site j of the superconductor.

The last term in Eq. (1) accounts for the conventional s-wave spin-singlet superconducting correlations. It is obtained by mean field approximation of the pairing interaction $-U \sum_j n_{j,\uparrow} n_{j,\downarrow}$, where $U > 0$ is the attractive pairing potential and $n_{j,\sigma} = c_{j,\sigma}^\dagger c_{j,\sigma}$ is the number operator [48]. $\Delta_j = -U \langle c_{j,\downarrow} c_{j,\uparrow} \rangle$ is the resulting superconducting order parameter.

The total Hamiltonian Eq. (1) is numerically diagonalized and the superconducting state is determined self-consistently as detailed in Appendix B. The exact parameters employed in our numerical routines have been specified in Appendix C.

III. TRIPLET CORRELATIONS

In this section, we quantify and investigate the different spin-triplet correlations in the S. Consider the anomalous Matsubara Green's function $F_{jj,\sigma\sigma'}(\tau) = -\langle T_\tau c_{j,\sigma}(\tau) c_{j,\sigma'}(0) \rangle$, where $\tau = i\tilde{t}$ is the imaginary time with \tilde{t} as the time [53, 54]. Further, T_τ is the ordering operator for imaginary time τ . In the Fourier space, we obtain

$$F_{jj,\sigma\sigma'}(i\omega_l) = \int_0^\beta e^{i\omega_l \tau} F_{jj,\sigma\sigma'}(\tau) d\tau, \quad (2)$$

where $\beta = \hbar/k_B T$, k_B is the Boltzmann constant, T is the temperature, and $\omega_l = (2l + 1)\pi/\beta$ are the fermionic Matsubara frequencies with integer l . See Appendix B for further calculation details. Since the spin-triplet correlations are odd in frequency [5], we take a

sum over all positive Matsubara frequencies to define an appropriate dimensionless quantity that would allow us to quantify the correlations

$$F_{j,\sigma\sigma'} = \frac{1}{\beta} \sum_{\omega_l > 0} F_{jj,\sigma\sigma'}(i\omega_l). \quad (3)$$

Employing this notation, we express the relevant superconducting correlations

$$F_j^s = \frac{1}{2} (F_{j,\downarrow\uparrow} - F_{j,\uparrow\downarrow}), \quad (4)$$

$$F_j^{t,z} = -\frac{1}{2} (F_{j,\downarrow\uparrow} + F_{j,\uparrow\downarrow}), \quad (5)$$

$$F_j^{t,x} = \frac{1}{2} (F_{j,\uparrow\uparrow} - F_{j,\downarrow\downarrow}), \quad (6)$$

$$F_j^{t,y} = \frac{i}{2} (F_{j,\uparrow\uparrow} + F_{j,\downarrow\downarrow}). \quad (7)$$

F^s is the spin-singlet correlation. $F^{t,z}$, $F^{t,x}$, and $F^{t,y}$ are the zero-spin triplet correlations when spin is measured along z -, x -, and y -axis respectively. Together, the latter three [Eqs. (5)-(7)] allow us to express all three kinds of the spin-triplet correlations with z quantization axis. We evaluate the quantities defined in Eqs. (4)-(7) to investigate the different superconducting correlations in our system.

A. Numerical results

In an isolated conventional superconductor, only F^s is non-zero while $F^{t,x}$, $F^{t,y}$, and $F^{t,z}$ are zero. Now, if we consider an F/S bilayer, then the electrons with opposite spins acquire a relative phase. This causes the zero-spin triplet correlation with spin-quantization axis along the F magnetization to become non-zero [5, 55]. For example, if the magnetization of the ferromagnet is along the z -axis, then $F^{t,z}$ becomes non-zero while $F^{t,x}$ and $F^{t,y}$ remain zero. Similarly, $F^{t,x}$ and $F^{t,y}$ become non-zero when magnetization of the ferromagnet is along x - and y -axis, respectively.

Quasiclassical theory [53, 54] shows that the triplet vector $\vec{F}_j^t = F_j^{t,x}\hat{x} + F_j^{t,y}\hat{y} + F_j^{t,z}\hat{z}$ always has a component aligning with the local exchange field $J\vec{M}_j/2$ whether the magnetization of the ferromagnet in a F/S bilayer is homogeneous or inhomogeneous [4, 56]. We, therefore, study these correlations in order to decompose the contribution of antiferromagnetic and ferromagnetic components of the canted-AF.

For $\theta_t = 0$ (Fig. 1), our considered AF becomes a collinear antiferromagnet with the axis of magnetic moments along the x -direction. As we increase the value of θ_t by a small amount,

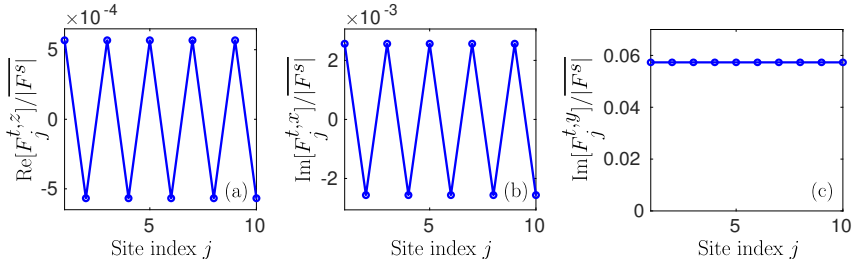


FIG. 2. Spatial variation of the normalized triplet correlations for 10 lattice sites considering maximal noncollinearity corresponding to the canting angle $\theta_t = \pi/4$ and filling factor $f = 0.6$ ($\mu/\Delta_0 \approx 37$, where $2\Delta_0$ is the zero-temperature superconducting gap without the adjacent AF). We plot the real part of the zero-spin triplet correlation $F_j^{t,z}$ [panel (a)], and the imaginary parts of the spin-triplet correlations $F_j^{t,x}$ [panel (b)] and $F_j^{t,y}$ [panel (c)]. The imaginary part of the former and the real parts of the latter two are zero. All the correlations are normalized by the spatially averaged magnitude of the singlet correlation $|\overline{F^s}|$. The detailed parameters employed for the numerical evaluation are specified in Appendix C.

the canted-AF acquires a net magnetization along the y -direction. So the canted-AF can be decomposed into an antiferromagnetic component (along the x -axis) and a ferromagnetic component (along the y -axis). For a collinear AF, we obtain Néel triplets. This means the component of \vec{F}_j^t parallel to the axis of the Néel vector modulates with the Néel order of the AF [44]. For $\theta_t = \pi/2$, we effectively obtain a F/S structure with the F magnetization along the y -axis.

We now investigate the case of $\theta_t = \pi/4$ that produces maximum noncollinearity between the two AF sublattice magnetization. In Fig. 2, triplet correlations for a canted-AF/S bilayer have been plotted as a function of space for filling factor $f = 0.6$. We see that $F^{t,z}$, the component of \vec{F}^t perpendicular to the canted-AF sublattice magnetizations plane, is also being generated along with the in-plane components $F^{t,x}$ and $F^{t,y}$. It oscillates from a constant positive to negative value with Néel order. However, it only appears for non-zero μ , and is zero at half-filling ($f = 0.5$) where $\mu = 0$. $F^{t,x}$ too oscillates between a constant positive and negative value with Néel order, while $F^{t,y}$ is constant in space. Both $F^{t,x}$ and

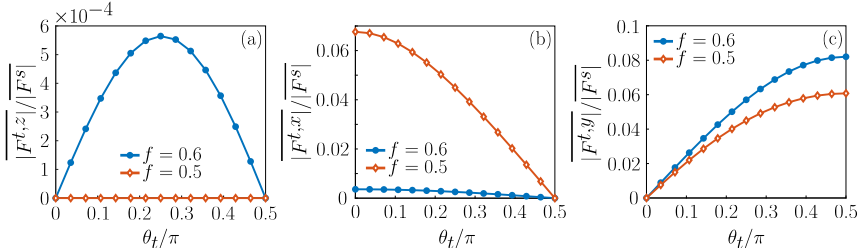


FIG. 3. Variation of triplet correlations with canting angle θ_t for filling factors $f = 0.5$ ($\mu = 0$) and $f = 0.6$ ($\mu/\Delta_0 \approx 37$), where Δ_0 represents the zero-temperature value of the superconducting order parameter in absence of the canted-AF layer. (a) The average magnitude of the normalized spin-triplet correlation $F^{t,z}$ is maximum when the noncollinearity between the two sublattices is maximum, i.e. at $\theta_t = \pi/4$. However, it is zero at half-filling ($f = 0.5$). (b) Average magnitude of the normalized spin-triplet correlation $F^{t,x} = [F_{\uparrow\uparrow} - F_{\downarrow\downarrow}]/2$ decreases as the effective antiferromagnetism becomes weaker with increasing θ_t . (c) The average magnitude of the normalized spin-triplet correlation $F^{t,y} = [i(F_{\uparrow\uparrow} + F_{\downarrow\downarrow})]/2$ increases as the effective ferromagnetism becomes stronger with increasing θ_t . The averages are taken over all the sites and are denoted via an overhead bar. The detailed parameters employed for the numerical evaluation are specified in Appendix C.

$F^{t,y}$ are imaginary, consistent with previous theoretical results for F/S bilayers [55, 56]. The AF sublattice magnetization configuration has been so chosen here to obtain and focus on the non-zero and spatially constant sum of the equal-spin triplets $F_{\uparrow\uparrow}$ and $F_{\downarrow\downarrow}$. In Appendix D, we present the correlations for a configuration when the AF Néel order is aligned with the z -axis [44]. To conclude this discussion, the intrinsic noncollinearity of the canted AF successfully generates all three components of the spin-triplet correlations.

We now examine the dependence of these spin-triplets on the canting angle. To this end, we plot the average magnitudes of the three spin-triplet correlations vs. the canting angle θ_t in Fig. 3. As we change θ_t from 0 to $\pi/2$ the system changes from a collinear AF (along x -axis) to a collinear F (along y -axis). As discussed above, $F^{t,z}$ is found to vanish identically at $\mu = 0$ ($f = 0.5$) for all canting angles. This will be explained further below. However, for non-zero μ (away from the half-filling case), it increases from 0 to a finite value

as we go from a collinear antiferromagnetic alignment to maximal noncollinearity between the sublattice magnetic moments, and decreases back to zero in the ferromagnetic alignment [Fig. 3(a)]. This component thus results directly due to the AF sublattice magnetization noncollinearity.

The spatially averaged value of $|F^{t,x}|$ decreases as θ_t goes from 0 to $\pi/2$ [Fig. 3(b)]. This component, therefore, essentially follows the Néel vector magnitude and appears to stem directly from the antiferromagnetism [44]. It has been understood as being due to the interband pairing, which is feasible when μ is smaller or comparable to the superconducting gap. However, we also find such Néel triplets to be present for $\mu \approx 37\Delta_0$ ($f = 0.6$), although they are significantly weaker than for the case of $\mu = 0$ [Fig. 3(b)]. We attribute this observation to a modification of the normal state electronic wavefunctions by the AF, so that even the conventional intraband pairing causes a finite generation of the Néel triplets. Finally, the average value of $|F^{t,y}|$ increases with the canting angle and it appears to be caused primarily by the net magnetization.

B. Insights from simplified analytics

In order to understand the difference between $\mu = 0$ and $\mu \neq 0$ cases, we examine the electronic properties of a bilayer comprising a normal metal and an AF, as detailed in Appendix A. For $\mu = 0$, the Fermi wave-vector is $k_F = \pi/2a$. This means that the electrons participating in the formation of Cooper pairs have $|k| \sim \pi/2a$. The eigenfunctions with $|k| \sim \pi/2a$ are such that the probability of finding an electron is non-zero on one sublattice while it is zero on the other sublattice. Now, the electrons near the Fermi level of the superconductor which interact with sublattice A do not see sublattice B and vice-versa. Therefore the triplet correlations are generated independently by sublattices A and B. The resultant correlations we obtain are a sum of correlations generated by the two sublattices. So, the only non-zero components are $F^{t,x}$ and $F^{t,y}$. This separation of the two sublattices at a special value of the electronic chemical potential is reminiscent of a similar result obtained for spin pumping via AFs [57–60].

In contrast, for $\mu \neq 0$, the Fermi level is within one of the bands and the wavefunctions of the states near the Fermi energy are such that the electrons on a site of the A sublattice also have a non-zero probability at the sites of the B sublattice. There is no way for the electrons

to arrange themselves to decouple the two sublattices [59, 60]. The electrons experience a spin-splitting field in one direction at site 1 (of sublattice A) and in another direction at site 2 (of sublattice B), then again the first orientation at site 3 (of sublattice A). So, the electrons see the noncollinearity between the magnetic moments on the adjacent lattice sites. Therefore, the correlation $F^{t,z}$ along the direction perpendicular to the plane of magnetic moments of the canted-AF becomes non-zero along with the in-plane components $F^{t,x}$ and $F^{t,y}$ when $\mu \neq 0$. At the same time, the electronic amplitudes at the two sublattices are different due to the adjacent AF, as detailed in Appendix A. This lends the normal electronic states a weak Néel character which manifests itself in the emergence of Néel triplets even for the conventional intraband pairing.

IV. CRITICAL TEMPERATURE

The formation of spin-triplet Cooper pairs comes at the cost of destroying their spin-singlet counterparts that are originally produced in and stabilize the superconducting state [52, 61, 62]. Hence, the critical temperature is reduced with the formation of spin-triplets, which may offer a convenient experimental signature. Thus, we investigate the critical temperature of our AF/S bilayer now via numerical self-consistent solution of the BdG equation (1).

Critical temperature T_c vs. canting angle θ_t is plotted in Fig. 4 for (a) $f = 0.5$ ($\mu = 0$) and (b) $f = 0.6$ ($\mu \approx 37\Delta_0$). We find that for $\mu = 0$, T_c increases with θ_t while it manifests the opposite dependence for $\mu \neq 0$. These intriguing and distinct dependencies can be understood based on our analysis of spin-triplets generation above.

Let us first consider the $f = 0.5$, corresponding to $\mu = 0$, case presented in Fig. 4(a). In this case, a strong generation of spin-zero Néel triplets [Fig. 3(b)] due to interband pairing leads to maximal T_c suppression at $\theta_t = 0$. Hence, the T_c increases with θ_t since the T_c suppression is stronger for the collinear AF case ($\theta_t = 0$) than for the F case ($\theta_t = \pi/2$). Further, when the exchange field is large enough, we find a complete suppression of superconductivity at $\theta_t = 0$ corresponding to a vanishing T_c . The abrupt change in T_c with θ_t here is attributed to the additional contribution to superconductivity suppression by the opening of a normal dispersion bandgap by the AF, as described in Appendix A. This normal state bandgap predominantly affects the superconducting pairing at half-filling

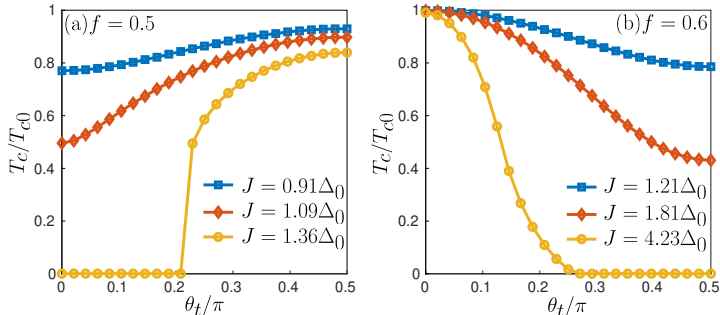


FIG. 4. (a) Normalized critical temperature T_c vs. canting angle θ_t for filling factor (a) $f = 0.5$ and (b) $f = 0.6$ considering different values of the spin-splitting J . Here, T_{c0} and $2\Delta_0$ are respectively the critical temperature and the zero-temperature superconducting gap of the same superconductor without the AF layer. The detailed parameters employed for the numerical evaluation are specified in Appendix C.

when $\mu = 0$.

For the case of $f = 0.6$, the Néel spin-triplets generation by the antiferromagnetic order is much weaker (Fig. 3). On the other hand, the ordinary spin-triplets generation by a ferromagnet remain of the same order of magnitude as for $f = 0.5$. Thus, T_c is largest for $\theta_t = 0$ and it decreases with θ_t . The amplitude of spin-triplets generated due to the noncollinearity [Fig. 3(a)] remains small and does not seem to affect the T_c dependence substantially. Contrary to the $\mu = 0$ case, the variation of T_c with θ_t is smooth even for large values of the exchange field J .

V. CORRELATIONS IN 2-D

In our discussion above, we have considered a one-dimensional (1-D) superconductor with the aim of examining essential physics employing analytic results discussed in Appendix A. We now validate these results using a two-dimensional (2-D) model for the S. This further allows us to examine how the spin-triplet correlations vary with space as we move away from the S/AF interface.

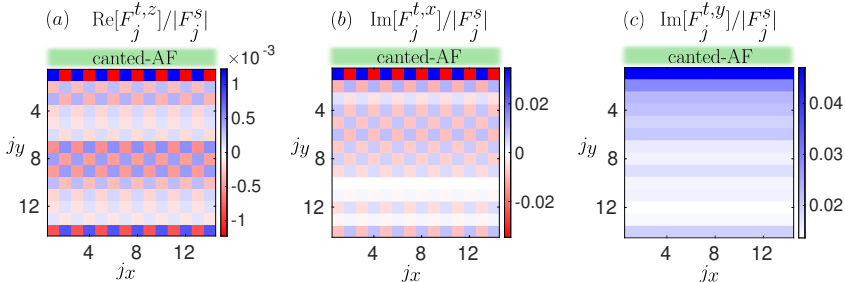


FIG. 5. Spatial variation of the spin-triplet correlations for a 2-D superconductor. The sites are indexed as (j_x, j_y) . The sites with index $(j_x, 1)$ form the layer adjacent to the AF. A small section of size 14×14 of a superconducting sheet of size 102×14 has been plotted here for clarity. The real part of the normalized zero-spin triplet correlation $F_j^{t,z}$ [panel (a)], and the imaginary parts of the normalized spin-triplet correlations $F_j^{t,x}$ [panel (b)] and $F_j^{t,y}$ [panel (c)] have been plotted as colormaps. The imaginary part of the former and the real parts of the latter two are zero. We consider maximal noncollinearity ($\theta_t = \pi/4$) and filling fraction $f = 0.6$ ($|\mu| \gg |\Delta_0|$). All the correlations are normalized with respect to the magnitude of the singlet correlation $|F_j^s|$. The detailed parameters employed for the numerical evaluation are specified in Appendix C.

In Fig. 1(b), the superconducting lattice is along the x -axis. We add more such 1-D layers in the y -direction to create our 2-D model for the S. Each site of this 2-D sheet is indexed as (j_x, j_y) so that j_x takes a value between 1 to N_x , and j_y takes a value between 1 to N_y , where N_x and N_y are the number of sites along x - and y -direction, respectively. The spin-splitting effect is experienced only by the electrons at the sites next to the AF/S interface. Thus, it suffices to treat the AF via the same 1-D model as before. Overall, the Hamiltonian of Eq. (1) is modified by letting all site indices j take the form (j_x, j_y) . Summation in the spin-splitting term is now over the sites with indices of the form $(j_x, 1)$. We continue to consider periodic boundary condition along the x -axis, like in the 1-D case.

Carrying out the BdG diagonalization self-consistently and numerically, we evaluate the spatially-resolved spin-triplet correlations [Eqs. (4)-(7)] for this system and plot them in Fig. 5. We have the same observations in the first layer (along the AF/S interface) of the 2-D sheet as the 1-D case discussed in section III. Additional calculations not presented

here confirm that $F^{t,z}$ appears only when μ is non-zero. We observe that $F^{t,x}$ and $F^{t,z}$ show modulation between positive and negative values along the y -axis apart from along the x -axis. This is interesting because the system has nothing imposing Néel order along the y -axis on the correlations. In addition, we find some layers in which the alternating pattern of positive and negative values is skipped. This is attributed to Friedel-like oscillations [44, 48]. We found that these skipping of pattern only appears for non-zero μ while we get a perfect alternating pattern along the y -axis for $\mu = 0$ case. The correlation component $F^{t,y}$ [Fig. 5(c)] is constant in each layer along the interface (along the x -axis) but decays as we move away from the interface along the y -direction. So, the 2-D case is consistent with and corroborates our 1-D results. We find that the spatial pattern (oscillating with Néel order or being constant in space) imposed on superconducting correlations along the interfacial direction also manifests itself perpendicular to the AF/S interface.

VI. CONCLUDING REMARKS

We have theoretically demonstrated the generation of all, including the spinful, spin-triplet Cooper pairs in a conventional superconductor by an adjacent canted antiferromagnet. Our proposal leverages the intrinsic noncollinearity between the two sublattice magnetizations in a canted antiferromagnet for applications in superconducting hybrids. This canting can be induced intrinsically by Dzyaloshinskii-Moriya interaction, such as in hematite [63]. Additionally, it can be induced and controlled using an applied magnetic field [64]. The resulting spin-triplets have a predominantly Néel character, i.e., their amplitude oscillates in space on the lattice length scale similar to the Néel spin order. The superconducting critical temperature is more strongly suppressed by the interband Néel spin-triplets than by a ferromagnetic spin-splitting field of similar magnitude, thereby offering an experimental signature of their generation. Altogether, our analysis highlights the noncollinear nature of homogeneous canted antiferromagnets by employing them for generating spin-triplet Cooper pairs in a simple superconducting bilayer. This manner of generating noncollinearity using a homogeneous antiferromagnet is expected to find use in other phenomena that have traditionally relied on magnetic multilayers or spin textures.

Appendix A: Normal metal interfaced with an antiferromagnet

In order to understand when interband and intraband pairing is favored, we consider the normal-state wave functions of an AF/normal metal bilayer. The Hamiltonian for the conducting electrons of a normal metal interfaced with an insulating AF is modeled as [65]

$$H = -\mu \sum_{j,\sigma} c_{j,\sigma}^\dagger c_{j,\sigma} - t \sum_{\langle i,j \rangle} \sum_{\sigma} c_{i,\sigma}^\dagger c_{j,\sigma} - \frac{J}{2} \sum_j \vec{M}_j \cdot \vec{S}_j, \quad (\text{A1})$$

where $\vec{M}_j = (-1)^{j+1} \hat{z}$ gives the magnetic texture of a collinear AF. Other symbols have the same meaning as in section II of the main text.

In order to calculate the eigenenergies and eigenvectors, the Hamiltonian is written in terms of creation and annihilation operators for electrons at sublattices A and B. Creation operators for electrons at sublattices A and B are defined as $a_{j,\sigma}^\dagger = c_{2j-1,\sigma}^\dagger$, and $b_{j,\sigma}^\dagger = c_{2j,\sigma}^\dagger$, where $j = 1, 2, \dots, N/2$. Then, the basis is changed from Wannier wavefunctions to Bloch wavefunctions using the relation

$$a_{j,\sigma}^\dagger = \sum_{k \in \text{FBZ}} \frac{1}{\sqrt{N/2}} e^{-ik(2j-2)a} a_{k,\sigma}^\dagger, \quad \text{and} \quad b_{j,\sigma}^\dagger = \sum_{k \in \text{FBZ}} \frac{1}{\sqrt{N/2}} e^{-ik(2j-1)a} b_{k,\sigma}^\dagger, \quad (\text{A2})$$

where a is the lattice constant, and k is a reciprocal lattice vector in the first Brillouin zone (FBZ). Now, the Hamiltonian can be written in the form

$$H = \sum_k \begin{pmatrix} a_{k,\uparrow}^\dagger & a_{k,\downarrow}^\dagger & b_{k,\uparrow}^\dagger & b_{k,\downarrow}^\dagger \end{pmatrix} H(k) \begin{pmatrix} a_{k,\uparrow} & a_{k,\downarrow} & b_{k,\uparrow} & b_{k,\downarrow} \end{pmatrix}^T, \quad (\text{A3})$$

giving the dispersion relation

$$E_{\pm}(k) = -\mu \pm \sqrt{4t^2 \cos^2(ka) + (J/2)^2}, \quad (\text{A4})$$

where the two energy bands $E_{\pm}(k)$ are two-fold degenerate. The eigenvectors for energy band $E_-(k)$ are

$$\psi_1(k) = \mathcal{N}_2 \begin{pmatrix} 2t \cos(ka) \\ 0 \\ -J/2 + \sqrt{4t^2 \cos^2(ka) + (J/2)^2} \\ 0 \end{pmatrix} = \begin{pmatrix} u_{Ak\uparrow}^{(1)} \\ u_{Ak\downarrow}^{(1)} \\ u_{Bk\uparrow}^{(1)} \\ u_{Bk\downarrow}^{(1)} \end{pmatrix}, \quad \text{and} \quad (\text{A5})$$

$$\psi_2(k) = \mathcal{N}_1 \begin{pmatrix} 0 \\ 2t \cos(ka) \\ 0 \\ J/2 + \sqrt{4t^2 \cos^2(ka) + (J/2)^2} \end{pmatrix} = \begin{pmatrix} u_{Ak\uparrow}^{(2)} \\ u_{Ak\downarrow}^{(2)} \\ u_{Bk\uparrow}^{(2)} \\ u_{Bk\downarrow}^{(2)} \end{pmatrix}. \quad (\text{A6})$$

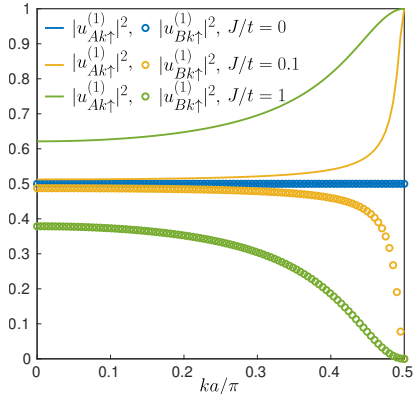


FIG. 6. Non-zero components of eigenfunction ψ_1 (Eq. (A5)) of a normal metal/AF bilayer for different strengths of magnetic exchange interaction as a function of positive k values in the first Brillouin zone.

Whereas the eigenvectors for the energy band $E_+(k)$ are

$$\psi_3(k) = \mathcal{N}_1 \begin{pmatrix} 2t \cos(ka) \\ 0 \\ -J/2 - \sqrt{4t^2 \cos^2(ka) + (J/2)^2} \\ 0 \end{pmatrix} = \begin{pmatrix} u_{Ak\uparrow}^{(3)} \\ u_{Ak\downarrow}^{(3)} \\ u_{Bk\uparrow}^{(3)} \\ u_{Bk\downarrow}^{(3)} \end{pmatrix}, \text{ and} \quad (\text{A7})$$

$$\psi_4(k) = \mathcal{N}_2 \begin{pmatrix} 0 \\ 2t \cos(ka) \\ 0 \\ J/2 - \sqrt{4t^2 \cos^2(ka) + (J/2)^2} \end{pmatrix} = \begin{pmatrix} u_{Ak\uparrow}^{(4)} \\ u_{Ak\downarrow}^{(4)} \\ u_{Bk\uparrow}^{(4)} \\ u_{Bk\downarrow}^{(4)} \end{pmatrix}. \quad (\text{A8})$$

Here, \mathcal{N}_1 and \mathcal{N}_2 are the normalization factors of the eigenvectors. ψ_1 and ψ_3 correspond to the wavefunctions of spin \uparrow electrons, whereas ψ_2 and ψ_4 correspond to spin \downarrow electrons. Fig. 6 shows a plot of the non-zero components of ψ_1 for positive k values. Let us compare the case of $J = 0$ and $J \neq 0$ to study how the states of a metal are modified when it is brought in contact with an AF.

From Fig. 6, we see that the probabilities of finding a spin \uparrow electron at sites of sublattice A and B are equal for $J = 0$. However, for $J \neq 0$, the probability on A sublattice is more

than that on B sublattice. It is important to note that the probability of finding spin \uparrow electrons at sublattice A sites becomes 1 and that for sublattice B becomes 0 at $k = \pi/2a$. Similar asymmetries in the sublattices arise for states ψ_2 , ψ_3 , and ψ_4 as soon as we make J non-zero. For ψ_2 , the probability of finding a spin \downarrow electron at sublattice site B becomes more than that for sublattice A. For the states of $E_+(k)$ band (ψ_3 and ψ_4), the roles of sublattices A and B are interchanged with respect to spin.

Near the Brillouin zone boundary (BZB) of band $E_-(k)$ (i.e. ψ_1 and ψ_2), all the spin \uparrow electrons get localized to the sites of sublattice A and all the spin \downarrow electrons get localized to the sites of sublattice B. For the band $E_+(k)$, sublattices A and B interchange their roles and we find that spin \uparrow electrons get localized at sublattice B and spin \downarrow electrons get localized at sublattice A near the BZB. This property of the electronic states near the BZB is the reason why interband pairing is the dominant mechanism for the formation of on-site opposite-spin Cooper pairs in an AF/S bilayer when the Fermi level lies within the antiferromagnetic band gap $E_+ - E_-$. On the other hand, intraband pairing is the dominant mechanism when the Fermi level lies within one of the two bands.

Appendix B: Bogoliubov-de Gennes calculation

The Hamiltonian in Eq. (1) can be written as

$$H = -\mu N + \sum_j \frac{|\Delta_j|^2}{U} + \frac{1}{2} \sum_{i,j} \Psi_i^\dagger \tilde{H}_{i,j} \Psi_j, \quad (\text{B1})$$

where $\Psi_j^\dagger = (c_{j,\uparrow}^\dagger, c_{j,\downarrow}^\dagger, c_{j,\uparrow}, c_{j,\downarrow})$ and N is the total number of sites. The matrix \tilde{H} is diagonalized by solving the BdG equations

$$\sum_j \tilde{H}_{i,j} \phi_{j,n} = E_n \phi_{i,n}, \quad \text{where} \quad (\text{B2})$$

$$\phi_{i,n} = \begin{pmatrix} u_{i,n,\uparrow} & u_{i,n,\downarrow} & v_{i,n,\uparrow} & v_{i,n,\downarrow} \end{pmatrix}^T, \quad (\text{B3})$$

is the eigenvector and E_n the eigenenergies of \tilde{H} . Now the Hamiltonian can be written as

$$H = -\mu N + \sum_j \frac{|\Delta_j|^2}{U} + \sum_n \tilde{\Gamma}_n^\dagger E_n \Gamma_n, \quad (\text{B4})$$

where $\tilde{\sum}_n$ represents sum over positive eigenenergies, and Γ_n 's are Bogoliubov fermionic operators related to the old fermionic operators by $c_{j,\sigma} = \sum_n (u_{j,n,\sigma} \Gamma_n + v_{j,n,\sigma}^* \Gamma_n^\dagger)$. The

superconducting order parameter is calculated self-consistently using the relation

$$\Delta_j = -U \sum_n^{\tilde{\infty}} [u_{j,n,\downarrow} v_{j,n,\uparrow}^* [1 - f_{FD}(E_n)] + v_{j,n,\downarrow}^* u_{j,n,\uparrow} f_{FD}(E_n)], \quad (\text{B5})$$

where $f_{FD}(E_n) = \langle \Gamma_n^\dagger \Gamma_n \rangle = 1/(e^{E_n/k_B T} + 1)$ is the Fermi-Dirac distribution.

In order to calculate the spin-triplet correlations, we consider the anomalous Matsubara Green's function $F_{jj,\sigma\sigma'}(\tau) = -\langle T_\tau c_{j,\sigma}(\tau) c_{j,\sigma'}(0) \rangle$, where $\tau = i\tilde{t}$ is the imaginary time, \tilde{t} is the time, and T_τ is the ordering operator for τ . Taking its Fourier transform, we get

$$F_{jj,\sigma\sigma'}(i\omega_l) = \int_0^\beta e^{i\omega_l \tau} F_{jj,\sigma\sigma'}(\tau) d\tau = \sum_n^{\tilde{\infty}} \left[\frac{u_{j,n,\sigma} v_{j,n,\sigma'}^*}{i\omega_l - E_n/\hbar} + \frac{v_{j,n,\sigma}^* u_{j,n,\sigma'}}{i\omega_l + E_n/\hbar} \right], \quad (\text{B6})$$

where $\beta = \hbar/k_B T$, k_B is the Boltzmann constant, T is the temperature, and $\omega_l = (2l+1)\pi/\beta$ is a Matsubara frequency for fermions with integer l . This expression is used in calculating the correlations in Eq. (3) and their relevant components Eqs. (4)- (7).

Appendix C: Numerical parameters

The parameters used for each of the figures are

- **Fig. 2:** Number of sites $N = 302$, hopping parameter $t = 10$, pair potential $U/t = 1$, temperature $T/T_c = 0.1$, canting angle $\theta_t = \pi/4$, filling factor $f = 0.6$ ($\mu/\Delta = 37$), magnetic exchange interaction strength $J = 0.018t$ ($= 1.09\Delta$).
- **Fig. 3:** $N = 302$, $t = 10$, $U/t = 1$, $k_B T/t = 0.001$. For filling factor $f = 0.5$ ($\mu/\Delta_0 = 0$), $J = 0.012t = 1.09\Delta_0$ was taken. For $f = 0.6$ ($\mu/\Delta_0 = 37$), $J = 0.018t = 1.09\Delta_0$ was taken. Here, $2\Delta_0$ represents the superconducting gap in the absence of the canted-AF at zero-temperature.
- **Fig. 4:** $N = 302$, $t = 10$, $U/t = 1$ was used for the calculation of T_c for filling factors $f = 0.5$ ($\mu/\Delta_0 = 0$) and $f = 0.6$ ($\mu/\Delta_0 = 37$). The critical temperature of the isolated superconductor T_{c0} for $f = 0.5$ is $0.0101t/k_B$ and $f = 0.6$ is $0.0076t/k_B$.
- **Fig. 5:** A 2-D sheet with $N_x = 102$, $N_y = 14$, $t = 10$, $J = 0.1t = 4.4\overline{|\Delta|}$, $\theta_t = \pi/4$, $U/t = 1$, $f = 0.6$ ($\mu/\overline{|\Delta|} = 19$), and at $k_B T/t = 0.001$ was used to calculate the correlations. Here, $\overline{|\Delta|}$ represents the average magnitude of the superconducting order parameter.

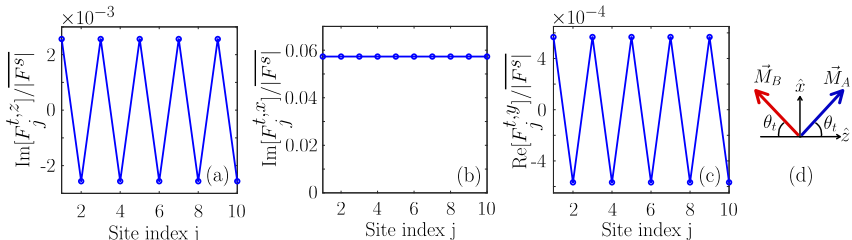


FIG. 7. Spatial variation of normalized triplet correlations for 10 lattice sites considering $\theta_t = \pi/4$ and $\mu/\Delta = 37$, corresponding to filling factor $f = 0.6$. We show the imaginary part of the triplet correlations $F_j^{t,z}$ [panel (a)] and $F_j^{t,x}$ [panel (b)], and the real part of the triplet correlation $F_j^{t,y}$ [panel (c)]. The real part of the two former and the imaginary part of the latter are zero. All the correlations are normalized by the spatially averaged magnitude of the singlet correlation $\overline{|F^s|}$. (d) Orientation of the magnetic moments of sublattices A and B of the AF in the rotated configuration.

Appendix D: Canted-AF/S with rotated magnetic moments

To compare the results of this article with Ref. [44], one needs to rotate the magnetic moments of the Hamiltonian [Eq. (1)] to $\vec{M}_j = [(-1)^{j+1} \cos \theta_t \hat{z} + \sin \theta_t \hat{x}]$ (see Fig. 7(d)). The correlations for this rotated system is plotted in Fig. 7. Here, $F^{t,z}$ is the Néel triplet correlation coming from the antiferromagnetic component of the canted-AF, $F^{t,x}$ comes from the ferromagnetic component, and $F^{t,y}$ comes from the noncollinearity in the canted-AF.

ACKNOWLEDGMENTS

SC and AK acknowledge financial support from the Spanish Ministry for Science and Innovation – AEI Grant CEX2018-000805-M (through the “Maria de Maeztu” Programme for Units of Excellence in R&D). LJK acknowledges support from the Research Council of Norway through its Centres of Excellence funding scheme, Project No. 262633 ‘QuSpin’.

IVB acknowledges support from MIPT, Project FSMG-2023-0014.

- [1] Z.-L. Xiang, S. Ashhab, J. Q. You, and F. Nori, Hybrid quantum circuits: Superconducting circuits interacting with other quantum systems, *Rev. Mod. Phys.* **85**, 623 (2013).
- [2] P. Krantz, M. Kjaergaard, F. Yan, T. P. Orlando, S. Gustavsson, and W. D. Oliver, A quantum engineer's guide to superconducting qubits, *Applied Physics Reviews* **6**, 021318 (2019).
- [3] M. Sigrist and K. Ueda, Phenomenological theory of unconventional superconductivity, *Rev. Mod. Phys.* **63**, 239 (1991).
- [4] M. Eschrig, Spin-polarized supercurrents for spintronics: a review of current progress, *Reports On Progress In Physics* **78**, 104501 (2015).
- [5] F. S. Bergeret, A. F. Volkov, and K. B. Efetov, Odd triplet superconductivity and related phenomena in superconductor-ferromagnet structures, *Rev. Mod. Phys.* **77**, 1321 (2005).
- [6] F. S. Bergeret, M. Silaev, P. Virtanen, and T. T. Heikkilä, Colloquium: Nonequilibrium effects in superconductors with a spin-splitting field, *Rev. Mod. Phys.* **90**, 041001 (2018).
- [7] A. I. Buzdin, Proximity effects in superconductor-ferromagnet heterostructures, *Rev. Mod. Phys.* **77**, 935 (2005).
- [8] J. Linder and J. W. A. Robinson, Superconducting spintronics, *Nature Physics* **11**, 307 (2015).
- [9] G. Yang, C. Ciccarelli, and J. W. A. Robinson, Boosting spintronics with superconductivity, *APL Materials* **9**, 050703 (2021).
- [10] I. V. Bobkova, A. M. Bobkov, and M. A. Silaev, Spin torques and magnetic texture dynamics driven by the supercurrent in superconductor/ferromagnet structures, *Phys. Rev. B* **98**, 014521 (2018).
- [11] X. Waintal and P. W. Brouwer, Magnetic exchange interaction induced by a josephson current, *Phys. Rev. B* **65**, 054407 (2002).
- [12] K. Halterman and M. Alidoust, Josephson currents and spin-transfer torques in ballistic SFSFS nanojunctions, *Superconductor Science and Technology* **29**, 055007 (2016).
- [13] J. Linder and T. Yokoyama, Supercurrent-induced magnetization dynamics in a josephson junction with two misaligned ferromagnetic layers, *Phys. Rev. B* **83**, 012501 (2011).
- [14] L. Fu and C. L. Kane, Superconducting proximity effect and majorana fermions at the surface of a topological insulator, *Phys. Rev. Lett.* **100**, 096407 (2008).

- [15] M. Eschrig and T. Löfwander, Triplet supercurrents in clean and disordered half-metallic ferromagnets, *Nature Physics* **4**, 138 (2008).
- [16] R. S. Keizer, S. T. B. Goennenwein, T. M. Klapwijk, G. Miao, G. Xiao, and A. Gupta, A spin triplet supercurrent through the half-metallic ferromagnet CrO₂, *Nature* **439**, 825 (2006).
- [17] T. S. Khaire, M. A. Khasawneh, W. P. Pratt, and N. O. Birge, Observation of spin-triplet superconductivity in co-based josephson junctions, *Phys. Rev. Lett.* **104**, 137002 (2010).
- [18] K.-R. Jeon, C. Ciccarelli, A. J. Ferguson, H. Kurebayashi, L. F. Cohen, X. Montiel, M. Eschrig, J. W. A. Robinson, and M. G. Blamire, Enhanced spin pumping into superconductors provides evidence for superconducting pure spin currents, *Nature Materials* **17**, 499 (2018).
- [19] K.-R. Jeon, X. Montiel, S. Komori, C. Ciccarelli, J. Haigh, H. Kurebayashi, L. F. Cohen, A. K. Chan, K. D. Stenning, C.-M. Lee, M. Eschrig, M. G. Blamire, and J. W. A. Robinson, Tunable pure spin supercurrents and the demonstration of their gateability in a spin-wave device, *Phys. Rev. X* **10**, 031020 (2020).
- [20] S. Diesch, P. Machon, M. Wolz, C. Sürgers, D. Beckmann, W. Belzig, and E. Scheer, Creation of equal-spin triplet superconductivity at the Al/EuS interface, *Nature Communications* **9**, 5248 (2018).
- [21] A. Costa, M. Sutula, V. Lauter, J. Song, J. Fabian, and J. S. Moodera, Signatures of superconducting triplet pairing in Ni-Ga-bilayer junctions, *New Journal of Physics* **24**, 033046 (2022).
- [22] A. Hijano, V. N. Golovach, and F. S. Bergeret, Quasiparticle density of states and triplet correlations in superconductor/ferromagnetic-insulator structures across a sharp domain wall, *Phys. Rev. B* **105**, 174507 (2022).
- [23] J. W. A. Robinson, J. D. S. Witt, and M. G. Blamire, Controlled injection of spin-triplet supercurrents into a strong ferromagnet, *Science* **329**, 59 (2010).
- [24] F. Chiodi, J. D. S. Witt, R. G. J. Smits, L. Qu, G. B. Halász, C.-T. Wu, O. T. Valls, K. Halterman, J. W. A. Robinson, and M. G. Blamire, Supra-oscillatory critical temperature dependence of Nb-Ho bilayers, *EPL (Europhysics Letters)* **101**, 37002 (2013).
- [25] C. González-Ruano, L. G. Johnsen, D. Caso, C. Tiusan, M. Hehn, N. Banerjee, J. Linder, and F. G. Aliev, Superconductivity-induced change in magnetic anisotropy in epitaxial ferromagnet-superconductor hybrids with spin-orbit interaction, *Phys. Rev. B* **102**, 020405 (2020).

- [26] C.-T. Wu, O. T. Valls, and K. Halterman, Reentrant superconducting phase in conical-ferromagnet–superconductor nanostructures, *Phys. Rev. Lett.* **108**, 117005 (2012).
- [27] N. Banerjee, J. A. Ouassou, Y. Zhu, N. A. Stelmashenko, J. Linder, and M. G. Blamire, Controlling the superconducting transition by spin-orbit coupling, *Phys. Rev. B* **97**, 184521 (2018).
- [28] L. G. Johnsen, N. Banerjee, and J. Linder, Magnetization reorientation due to the superconducting transition in heavy-metal heterostructures, *Phys. Rev. B* **99**, 134516 (2019).
- [29] S. H. Jacobsen, J. A. Ouassou, and J. Linder, Critical temperature and tunneling spectroscopy of superconductor-ferromagnet hybrids with intrinsic rashba-dresselhaus spin-orbit coupling, *Phys. Rev. B* **92**, 024510 (2015).
- [30] A. Buzdin and M. Kupriyanov, Transition-temperature of a superconductor-ferromagnet superlattice, *JETP Letters* **52**, 487 (1990).
- [31] Z. Radović, M. Ledvij, L. Dobrosavljević-Grujić, A. I. Buzdin, and J. R. Clem, Transition temperatures of superconductor-ferromagnet superlattices, *Phys. Rev. B* **44**, 759 (1991).
- [32] J. J. Hauser, H. C. Theuerer, and N. R. Werthamer, Proximity effects between superconducting and magnetic films, *Phys. Rev.* **142**, 118 (1966).
- [33] M. Hübener, D. Tikhonov, I. A. Garifullin, K. Westerholt, and H. Zabel, The antiferromagnet/superconductor proximity effect in Cr/V/Cr trilayers, *Journal Of Physics-Condensed Matter* **14**, 8687 (2002).
- [34] C. Bell, E. J. Tarte, G. Burnell, C. W. Leung, D.-J. Kang, and M. G. Blamire, Proximity and josephson effects in superconductor/antiferromagnetic Nb/ γ -Fe₅₀Mn₅₀ heterostructures, *Phys. Rev. B* **68**, 144517 (2003).
- [35] B. L. Wu, Y. M. Yang, Z. B. Guo, Y. H. Wu, and J. J. Qiu, Suppression of superconductivity in Nb by IrMn in IrMn/Nb bilayers, *Applied Physics Letters* **103**, 152602 (2013).
- [36] R. L. Seeger, G. Forestier, O. Gladii, M. Leiviskä, S. Auffret, I. Joumard, C. Gomez, M. Rubio-Roy, A. I. Buzdin, M. Houzet, and V. Baltz, Penetration depth of cooper pairs in the IrMn antiferromagnet, *Phys. Rev. B* **104**, 054413 (2021).
- [37] A. Mani, T. G. Kumary, D. Hsu, J. G. Lin, and C.-H. Chern, Modulation of superconductivity by spin canting in a hybrid antiferromagnet/superconductor oxide, *Applied Physics Letters* **94**, 072509 (2009).

- [38] A. Mani, T. G. Kumary, and J. G. Lin, Thickness controlled proximity effects in c-type antiferromagnet/superconductor heterostructure, *Scientific Reports* **5**, 12780 (2015).
- [39] I. V. Bobkova, P. J. Hirschfeld, and Y. S. Barash, Spin-dependent quasiparticle reflection and bound states at interfaces with itinerant antiferromagnets, *Phys. Rev. Lett.* **94**, 037005 (2005).
- [40] B. M. Andersen, I. V. Bobkova, P. J. Hirschfeld, and Y. S. Barash, $0 - \pi$ transitions in josephson junctions with antiferromagnetic interlayers, *Phys. Rev. Lett.* **96**, 117005 (2006).
- [41] B. M. Andersen, I. V. Bobkova, P. J. Hirschfeld, and Y. S. Barash, Bound states at the interface between antiferromagnets and superconductors, *Phys. Rev. B* **72**, 184510 (2005).
- [42] A. Kamra, A. Rezaei, and W. Belzig, Spin splitting induced in a superconductor by an antiferromagnetic insulator, *Phys. Rev. Lett.* **121**, 247702 (2018).
- [43] L. G. Johnsen, S. H. Jacobsen, and J. Linder, Magnetic control of superconducting heterostructures using compensated antiferromagnets, *Phys. Rev. B* **103**, L060505 (2021).
- [44] G. A. Bobkov, I. V. Bobkova, A. M. Bobkov, and A. Kamra, Néel proximity effect at antiferromagnet/superconductor interfaces, *Phys. Rev. B* **106**, 144512 (2022).
- [45] V. Baltz, A. Manchon, M. Tsoi, T. Moriyama, T. Ono, and Y. Tserkovnyak, Antiferromagnetic spintronics, *Rev. Mod. Phys.* **90**, 015005 (2018).
- [46] E. H. Fyhn, A. Brataas, A. Qaiumzadeh, and J. Linder, Superconducting proximity effect and long-ranged triplets in dirty metallic antiferromagnets (2022), arXiv:2210.09325 [cond-mat.supr-con].
- [47] S. I. Pekar and E. I. Rashba, Combined Resonance in Crystals in Inhomogeneous Magnetic Fields, *Zh. Eksperim. Teor. Fiz.* **47**, 1927 (1964).
- [48] J. Zhu, *Bogoliubov-de Gennes Method and Its Applications*, Lecture Notes in Physics (Springer International Publishing, 2016).
- [49] A. Cottet, D. Huertas-Hernando, W. Belzig, and Y. V. Nazarov, Spin-dependent boundary conditions for isotropic superconducting green's functions, *Phys. Rev. B* **80**, 184511 (2009).
- [50] M. Eschrig, A. Cottet, W. Belzig, and J. Linder, General boundary conditions for quasiclassical theory of superconductivity in the diffusive limit: application to strongly spin-polarized systems, *New Journal of Physics* **17**, 083037 (2015).
- [51] M. Kiwi, Exchange bias theory, *Journal of Magnetism and Magnetic materials* **234**, 584 (2001).
- [52] K. Maki and T. Tsuneto, Pauli paramagnetism and superconducting state, *Progress of Theoretical Physics* **31**, 945 (1964).

- [53] N. Kopnin, *Theory of Nonequilibrium Superconductivity*, International Series of Monographs (Clarendon Press, 2001).
- [54] W. Belzig, F. K. Wilhelm, C. Bruder, G. Schön, and A. D. Zaikin, Quasiclassical green's function approach to mesoscopic superconductivity, *Superlattices and Microstructures* **25**, 1251 (1999).
- [55] M. Eschrig, T. Löfwander, T. Champel, J. C. Cuevas, J. Kopu, and G. Schön, Symmetries of pairing correlations in superconductor–ferromagnet nanostructures, *Journal of Low Temperature Physics* **147**, 457 (2007).
- [56] T. Champel and M. Eschrig, Effect of an inhomogeneous exchange field on the proximity effect in disordered superconductor-ferromagnet hybrid structures, *Phys. Rev. B* **72**, 054523 (2005).
- [57] S. Takei, B. I. Halperin, A. Yacoby, and Y. Tserkovnyak, Superfluid spin transport through antiferromagnetic insulators, *Phys. Rev. B* **90**, 094408 (2014).
- [58] R. Cheng, J. Xiao, Q. Niu, and A. Brataas, Spin pumping and spin-transfer torques in anti-ferromagnets, *Phys. Rev. Lett.* **113**, 057601 (2014).
- [59] A. Kamra and W. Belzig, Spin pumping and shot noise in ferrimagnets: Bridging ferro- and antiferromagnets, *Phys. Rev. Lett.* **119**, 197201 (2017).
- [60] Q. Liu, H. Y. Yuan, K. Xia, and Z. Yuan, Mode-dependent damping in metallic antiferromagnets due to intersublattice spin pumping, *Phys. Rev. Mater.* **1**, 061401 (2017).
- [61] B. S. Chandrasekhar, A note on the maximum critical field of high-field superconductors, *Applied Physics Letters* **1**, 7 (1962).
- [62] A. M. Clogston, Upper limit for the critical field in hard superconductors, *Phys. Rev. Lett.* **9**, 266 (1962).
- [63] A. H. Morrish, *Canted Antiferromagnetism: Hematite* (WORLD SCIENTIFIC, 1995).
- [64] T. Wimmer, A. Kamra, J. Gückelhorn, M. Opel, S. Geprägs, R. Gross, H. Huebl, and M. Althammer, Observation of antiferromagnetic magnon pseudospin dynamics and the hanle effect, *Phys. Rev. Lett.* **125**, 247204 (2020).
- [65] H. T. Simensen, A. Kamra, R. E. Troncoso, and A. Brataas, Magnon decay theory of gilbert damping in metallic antiferromagnets, *Phys. Rev. B* **101**, 020403 (2020).

XI

REFERENCE

Lina Johnsen Kamra, and Jacob Linder,

Inverse spin-Hall effect and spin-swapping in spin-split superconductors,
Manuscript under preparation.

CONTRIBUTIONS

LJK performed the analytical and numerical calculations. LJK and JL both contributed to the writing of the manuscript. JL initiated and supervised the project, and contributed to discussions.

COMMENTS

This draft includes analytic results describing the spin-Hall and spin-swap angles associated with the transversal charge and spin currents in a spin-split superconductor. We have also plotted the relevant spin-Hall and spin-swap angles by solving the gap equation self-consistently. Before submission, additional numerical results for the non-equilibrium charge and spin accumulations will be included.

This paper is under preparation and not yet published and is therefore not included.

ISBN 978-82-326-7134-2 (printed ver.)
ISBN 978-82-326-7133-5 (electronic ver.)
ISSN 1503-8181 (printed ver.)
ISSN 2703-8084 (online ver.)



NTNU

Norwegian University of
Science and Technology